BioMed Research International

Animal Models of Human Pathology 2016

Guest Editors: Monica Fedele, Oreste Gualillo, and Andrea Vecchione

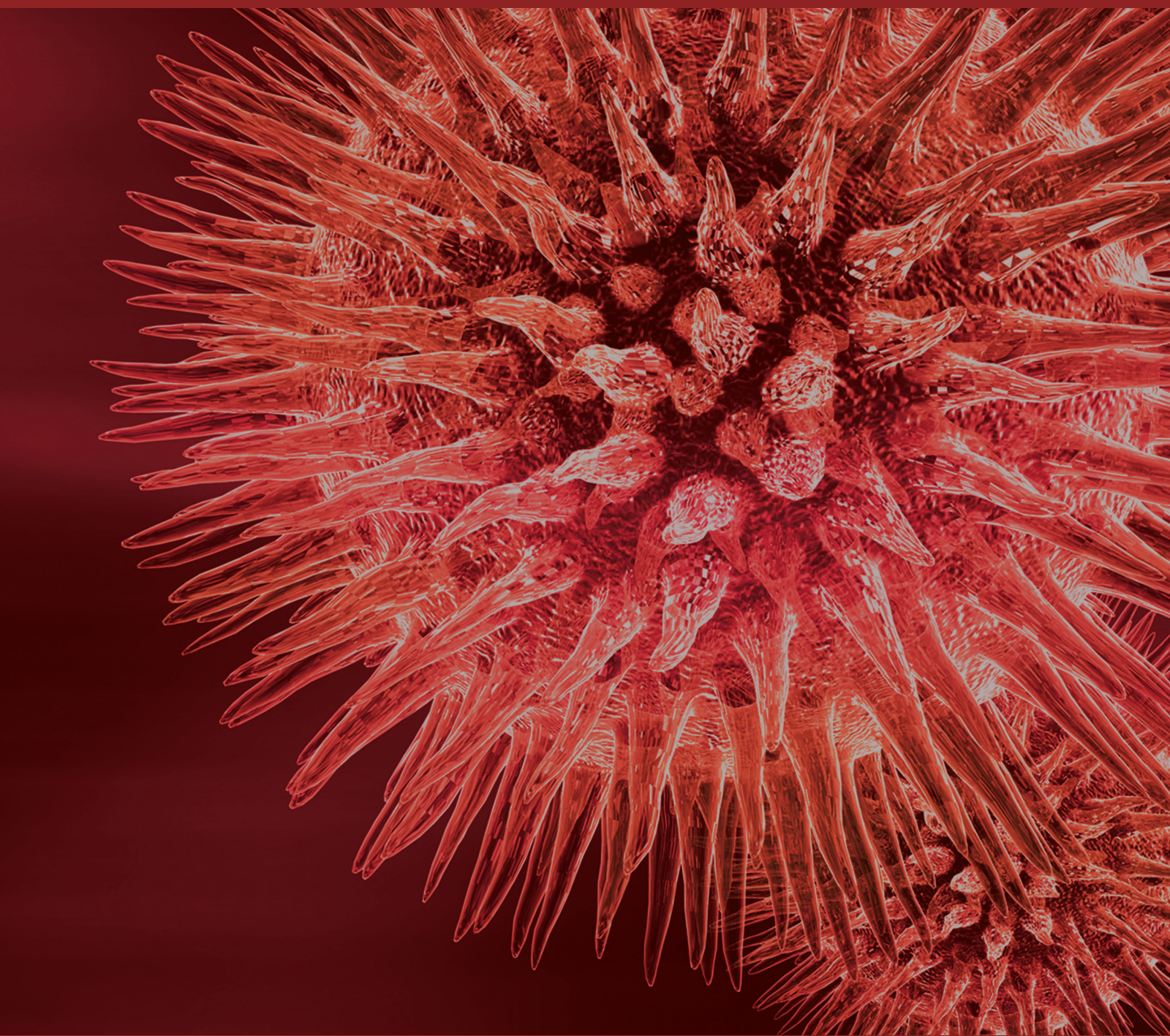

Animal Models of Human Pathology 2016

BioMed Research International

Animal Models of Human Pathology 2016

Guest Editors: Monica Fedele, Oreste Gualillo,
and Andrea Vecchione

Contents

Hindawi Publishing Corporation
BioMed Research International
Volume 2016, Article ID 4023982, 2 pages
http://dx.doi.org/10.1155/2016/4023982

Editorial

Animal Models of Human Pathology 2016

Monica Fedele,[1] Oreste Gualillo,[2] and Andrea Vecchione[3,4]

[1]*Istituto per l'Endocrinologia e l'Oncologia Sperimentale (IEOS), CNR, 80131 Naples, Italy*
[2]*Santiago University Clinical Hospital, Instituto de Investigación Sanitaria de Santiago (IDIS), 15706 Santiago de Compostela, Spain*
[3]*Human Cancer Genetics Program/CCC, The Ohio State University, Columbus, OH 43210, USA*
[4]*Department of Clinical and Molecular Medicine, Sapienza University of Rome, 00100 Rome, Italy*

Correspondence should be addressed to Monica Fedele; mfedele@unina.it

Received 29 November 2016; Accepted 29 November 2016

Biomedical research is a complicated process that needs tools capable of mimicking the human body level of complexity. Despite increasingly sophisticated *in vitro* model systems, animal models remain irreplaceable allies for the study of human disease. The paraphrase "*in vivo veritas*" is today more relevant than ever, so that the scientific community is doing its best to develop animal models ever closer to man. In the last few years, with the development of humanized mice, increasingly optimized to mimic human immune system and allow the efficient engraftment of human cells, we entered in a new era of translational research, where animal models are very close to humans and play a crucial role in the development of new therapeutic strategies for human pathologies.

In this new collection of articles (15 research articles and 5 reviews) focused on animal models of human pathology, we have gathered interesting evidences of how, through the use of animal models, we can understand, ever more closely, the pathogenic mechanisms of a human disease. Moreover, we have learned about new animal models and new therapeutic strategies for different human diseases. Most of the animal models used are small rodents, such as mice and rats, but you will also read about rabbits, dogs, goats, pigs, zebrafish, chick embryos, ferrets, and primates.

C. Daly, M. Fusellier, and respective coauthors faced the problem of the intervertebral disc degeneration, from pathophysiology to the clinic. Other pathologies approached by animal models in this special issue include cerebral and kidney ischemic events, dialed by I. Novitzky, S.-J. Chang, A. Lazaro, and respective coauthors; diabetes mellitus, with the contribution of M. Du et al.; inflammation, addressed by W.-R. Lin, S. Biesmans, and respective coauthors; cystic fibrosis, contributed by G. M. Lavelle et al.; and obesity, with the article by K. Nakadate et al. that continue their recent studies carried out on this pathology and its relationship with metabolic syndrome.

Among the contributions to cancer, three articles dial with colorectal cancer, optimizing patient-derived xenograft models (M. Gock et al.), studying the protective effect of Vitamin A (I. Okayasu et al.), and reviewing the role of deficiencies of DNA repair mechanisms (M. A. Mcilhatton et al.) through mouse models. In this field you will also read the timely and updated reviews of D. Rea et al. about prostate cancer and M. M. Stei et al. about uveal melanoma.

New animal models of human disease are addressed by S. H. Abdul Aziz et al. that describe the development of a rat model of gestational diabetes mellitus based on the combination of high fat sucrose diet with streptozotocin and nicotinamide STZ; J. Bogomolovas et al. that develop a novel murine model of parvovirus associated dilated cardiomyopathy; and V. Sala et al., with their new transgenic mouse model of heart failure and cardiac cachexia.

Lastly, the antifatigue effects of an asiatic mushroom and the protective effect of erythropoietin treatment in animals exposed to ventricular fibrillation were studied by Q. Li et al. and A. Faa et al., respectively.

Acknowledgments

We thank all authors for their contribution and the expert reviewers for their critical analysis of the manuscripts, hoping

that, once again, we provided the readership with an interesting overview of what it is going on in the biomedical field thanks to the lessons learned from animal models.

Monica Fedele
Oreste Gualillo
Andrea Vecchione

Hindawi Publishing Corporation
BioMed Research International
Volume 2016, Article ID 1715053, 7 pages
http://dx.doi.org/10.1155/2016/1715053

Research Article

Tumor Take Rate Optimization for Colorectal Carcinoma Patient-Derived Xenograft Models

Michael Gock,[1] Florian Kühn,[1] Christina Susanne Mullins,[1] Mathias Krohn,[1] Friedrich Prall,[2] Ernst Klar,[1] and Michael Linnebacher[1]

[1]*Department of General, Vascular, Thoracic and Transplantation Surgery, University of Rostock, Schillingallee 35, 18055 Rostock, Germany*
[2]*Institute of Pathology, University of Rostock, Strempelstraße 14, 18055 Rostock, Germany*

Correspondence should be addressed to Michael Linnebacher; michael.linnebacher@med.uni-rostock.de

Received 18 February 2016; Revised 23 September 2016; Accepted 7 November 2016

Academic Editor: Andrea Vecchione

Background. For development of individualized treatment on a routine basis, transfer of patients' tumor tissue in a xenograft model (i.e., generation of patient-derived xenografts (PDX)) is desirable for molecular, biochemical, or functional analyses. Drawbacks are dissatisfactory tumor take rates, the necessity of fast tumor tissue processing, and extensive logistics demanding teamwork of surgeons, pathologists, and laboratory researchers. *Methods*. The take rates of ten colorectal cancer (CRC) tissue samples in immunodeficient mice were compared after direct cryopreservation and after a 24 h cooling period at 4°C prior to cryopreservation. Additionally, the effect of simultaneous Matrigel application on the take rates was investigated. Beside take rates, tumor growth characteristics and cell culture success were analyzed. *Results*. Tumor takes of CRC tissue samples were significantly improved after Matrigel application (8 versus 15 takes, $p = 0.04$). As expected, they diminished furthermore after 24 h cooling. Application of Matrigel could counteract this decrease significantly (2 versus 7 takes, $p = 0.03$). Cumulative take rate after cryopreservation was satisfactory (70%). *Conclusion*. Matrigel application after 24 h delay in tissue processing facilitates CRC PDX model development. These data help developing strategies for individualized tumor therapies in the context of multicenter clinical studies and for basic research on primary patient tumors.

1. Introduction

The milestone paper of Vogelstein et al. established a new era for understanding genetic alterations during colorectal cancer (CRC) development leading to a complete new comprehension of colorectal tumorigenesis [1]. Subsequently, major developments were accomplished in defining the main molecular classes of CRC as chromosomal and microsatellite instability and the CpG island methylator phenotype, which are recognized as key pathogenetic mechanisms [2, 3]. The analysis of these fundamental sequences led to five molecular subtypes of CRC [3, 4]. As a result of these discoveries, additional mutational analyses have revealed that in an individual cancer only a limited number of pathways are dysregulated by some "driver" mutations from a circumscribed number of about 80 candidate cancer genes [5, 6]. Transferring these findings into day-to-day clinical practice triggered the conception of targeted treatments including EGF-receptor blockade (with the prerequisite of K-Ras mutational analysis) [7, 8]. It is extremely plausible that in the near future additional "individual" molecular testing of patients' tumor tissue might become a regular step towards individual guiding and improving anticancer therapy regimens.

Tumor pieces xenografted into and expanded in immunodeficient mice, so-called patient-derived xenografts (PDX), as models of the original tumor enable, in contrast to conventional paraffin-embedded specimens, beside extensive molecular analysis also functional testing. They might thus be a central step towards truly patient orientated and individualized therapy [9–11]. Even models of metastatic diseases may be achieved as valuable research instruments for additional multidisciplinary research [12].

Yet, there are still several drawbacks hampering the use of PDX models, although standardization of processes facilitates their generation. Profound expertise and a very close teamwork encompassing several fields (surgery, pathology, and molecular and cell biology as well as animal care) are obligatory to manage logistical and technical difficulties [13]. Thus, cryopreservation of tumor samples is an effective way to resolve this situation since date and location of tumor harvesting and pathological analysis can be easily parted from tumor engrafting and subsequent molecular and functional investigations [13]. Nevertheless, facilities and corresponding expertise of cryopreservation are very limited, for the most part in nonresearch institutions. Procedures making the workflow easier, simplifying the creation, and increasing the success rate in generation of PDX models are extremely sought for.

Matrigel, a commercially available mixture of components usually found in the extracellular matrix, is well known to enhance the engrafting outcome of tumor specimen [14, 15].

We here report on a relatively easy procedure to optimize tumor take rate after xenografting of CRC specimen using Matrigel. Specifically, xenografting success rates of cryopreserved tumors with or without application of Matrigel were analyzed side by side in a consecutive series of CRCs collected *ad hoc*. In addition, we examined the feasibility of a storing routine comprising preservation of tumor specimen for one day on ice prior to cryopreservation, in order to simulate a transport of tumor samples to a facility capable of cryopreservation and/or xenografting.

2. Methods

2.1. Harvesting of Tumor Specimens and Cryopreservation. Tumor specimens ($n = 10$, primary CRC without prior chemotherapy) were received fresh from surgery. Tumor tissue cubes ($3 \times 3 \times 3$ mm) were cut from deep invasive parts with a sterile scalpel blade. For direct cryopreservation, four tumor pieces were transferred into sterile cryotubes (Greiner-Bio-One, Frickenhausen, Germany) containing 1.5 ml freezing medium (fetal calf serum containing 10% DMSO), sealed in a freezing container (Nalgene, Rochester, NY, USA), and placed immediately at −80°C. Until transplantation, tubes were kept at −80°C (for a maximum of 6 weeks), or after overnight cooling, and transferred into liquid nitrogen for longer storage periods.

For delayed cryopreservation as simulation of transport, tumor specimens were preserved on ice in a 15 ml tube in 5 ml NaCl (0.9%) for a period of 24 hours (24 h cooling) and were thereafter processed according to the above-described protocol.

For xenografting, cryopreserved tumor pieces were thawed at 37°C immediately before the xenografting procedure.

Prior written informed consent was obtained from all patients, and all procedures were approved by the Ethics Committee of the University of Rostock (reference number II HV 43/2004) in accordance with generally accepted guidelines for the use of human material.

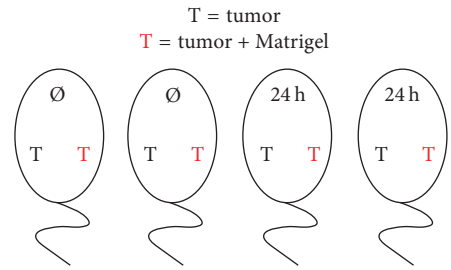

Figure 1: Mode of implantation of the tumor specimens in one and the same animal. Ø: no cooling; 24 h: 24 h cooling; T: tumor piece implanted (black: without and red: with Matrigel).

2.2. Tumor Xenografting. Experiments were performed as described in detail elsewhere [13] on female 6–8-weak-old NMRI (nu/nu) nude mice ($n = 40$) weighting 18–20 g. Tumor pieces were implanted subcutaneously bilaterally into the animals' flanks under anesthesia (ketamine-xylazine (1 : 1) mixture (1.3 μl per g body weight)). Mode of implantation is depicted in Figure 1 and allows direct comparison of Matrigel application in one and the same animal at a given time point. Tumor specimens for the Matrigel group were soaked in 100 μl of Matrigel (BD Biosciences, Heidelberg, Germany) for 20 seconds at 20°C immediately prior to xenografting.

Mice were kept in the animal facilities of the medical faculty of the University of Rostock and maintained in specified pathogen-free conditions. Animals were exposed to 12 h light/12 h darkness cycles and standard food and water including antibiotics (Cotrimoxazole) *ad libitum*. Their care and housing were in accordance with guidelines as put forth by the German Ethical Committee and the Guide for the Care and Use of Laboratory Animals (Institute of Laboratory Animal Resources, National Research Council; NIH Guide, volume 25, number 28, 1996). The protocol was approved by the Committee on the Ethics of Animal Experiments of the University of Rostock (Landesamt für Landwirtschaft, Lebensmittelsicherheit und Fischerei Mecklenburg- Vorpommern; Thierfelder Str. 18, 18059 Rostock, Germany; permit number: LALLF M-V/TSD/7221.3-1.1-071-10). Growth of tumors to volumes of 1–1.5 cm^3 was taken as evidence of successful xenografting, and the animals were then sacrificed for collection of tumor tissues for further studies.

2.3. Verification of the Human Origin of the Harvested Tumors and Genetic Fingerprint. For verification of the human origin of our harvested tumors, a human specific PCR was performed by amplification of a portion of the human mitochondrial cytochrome b gene as previously described [16]. Briefly, the reaction mixture (25 μl) contained 25 ng of gDNA, 0.1 mM of each primer (L15674: TAGCAATAATCCCCATCCTCCATATAT, H15782: ACTTGTCCAATGATGGTAAAAGG), 200 μM dNTPs, 1x standard reaction buffer, and 0.1 U Taq DNA polymerase (Bioron, Ludwigshafen, Germany). PCR was performed in a standard thermal cycler for 40 cycles of 30 s at 96°C, 40 s at 59°C, and 1 min at 72°C. Products were separated on a 1% agarose gel and results were scored positive with the appearance of a band of 157 bp.

Table 1

Tumor ID	Age	Sex	TNM	Localization
HROC107	74 y	Male	pT3pN2cM1 G2 R0 L1 V0	Sigmoid
HROC118	70 y	Male	pT4pN1cM0 G2 R0 L0 V1	Ascending colon
HROC119	72 y	Male	pT3pN0cM0G3 R0 L1 V0	Coecum
HROC122	80 y	Male	pT4pN0cM0 G3 R2 L0 V1	Sigmoid
HROC123	74 y	Male	T4 N2 M0G3 R0 L0 V0	Descending colon
HROC125	84 y	Female	pT3pN1cM0 G2 R0 L0 V0	Sigmoid
HROC129	76 y	Female	pT3pN1cM0 G2R0L1V0	Transversal colon
HROC130	60 y	Male	pT3pN1cM1 G3R2L0V0	Sigmoid
HROC131	73 y	Female	pT3pN1cM0 G3R0L0V0	Ascending colon
HROC135	75 y	Male	pT3pN1cM0 G3R0L0V0	Ascending colon

The identity of each cell line was checked by a short tandem repeat analysis at 9 different loci (D5S818, D13S317, D7S820, D16S539, vWA, TH01, TPOX, CSF1PO, and amelogenin for sex determination). Multiplex PCR amplicons were separated by capillary electrophoresis and analyzed using GeneMapperID software from Life Technologies (Darmstadt, Germany).

2.4. Cell Line Generation from PDX Material. Cell line generation has previously been described in detail [17]. Briefly, PDX tumors were minced; cells were released from surrounding tissue by scraping and passage through a nylon mesh (100 μm) to obtain single cell suspensions. This was seeded on collagen-coated 6-well plates in medium supplemented with 10% FCS, 200 mM L-glutamine, antibiotics (penicillin G 10.000 IU/L; streptomycin 130 mg/L), and antimycotics (Amphotericin B 6 mg/L). Plates were incubated at 37°C in a humidified atmosphere of 5% CO_2. All cell culture reagents were obtained from Pan Biotech (Aidenbach, Germany); antibiotics and antifungal agents were from the pharmacy of the university hospital Rostock. Medium was regularly changed and cells were passaged into 25 cm^2 culture flasks when tumor cell growth was observed.

2.5. Histopathological Analysis. Histopathological examinations of the primary tumors were done according to standard protocols for surgical pathology reports of CRCs [18]. Primary and PDX tumor tissue were embedded in paraffin and 4 μm H&E sections were made. Morphology of tumor architecture, growth pattern, and cytological features of primary and xenograft tumors were examined and compared.

2.6. Statistical Analysis. A Chi-square test (one or two sided) was used to test whether differences between two groups were significant. Analyses were performed using GraphPad Prism 5 software and p values <0.05 were considered significant.

3. Results

In this study, 10 colorectal adenocarcinomas were consecutively collected. Localization and TNM staging as well as patients data are presented in Table 1. In addition, length of cryopreservation (40 to 293 days) prior to implantation is depicted in Table 2.

Vital tumor pieces from the invasive front were first cryoconserved and subsequently engrafted into nude mice. A side-by-side comparison was performed with tumor pieces immediately frozen after the tissue preparation and a second set of tumor pieces left at approximately 4°C for a 24 h cooling period before cryopreservation. A second systematic comparison was performed by either briefly soaking the tumor pieces in Matrigel or not before subcutaneously implanting soaked and unsoaked pieces of the same tumor into different sides of the same animals. The overall outcome is given in Table 2.

3.1. Overall Xenografting Success Rate. The general analysis of the 10 CRC included into this study revealed that outgrowing PDX were obtained in seven out of the ten cases, thus summing up to a 70% take rate (actual results are summarized in Table 2).

3.2. Effect of Delayed Cryopreservation. For simulation of a time delay in the tissue handling process such as transport and the like, tumor tissue was preserved for a 24 h period on ice (24 h cooling). Thereafter, cryopreservation was done according to the protocol. Take rate analysis of this group (24 h cooling) compared to the group of direct cryopreservation (no cooling) revealed a profoundly diminished take rate which barely failed to reach statistical significance (without Matrigel: $n = 6$ takes with no cooling versus $n = 2$ takes with 24 h cooling; $p = 0.06$).

3.3. Effect of Matrigel Application. In order to allow best analysis of the effects of Matrigel application, animals received tumor implantation in a bilateral manner: one side without and the other side with presoaking in Matrigel. In both groups (no cooling and 24 h cooling) combined, application of Matrigel resulted in a significantly improved tumor take rate ($n = 15$ takes with Matrigel versus $n = 8$ takes without Matrigel; $p = 0.04$ Chi-square test). Analysis of the group of directly cryopreserved tumors (no cooling) showed that application of Matrigel had only a minor, statistically not

Table 2

Tumor ID	Outcome		Days frozen
	No cooling	24 h cooling	
HROC107	M1(+/+); M2(+/−)	M3(−/+); M4(−/+)	293
HROC118	M1(−/+); M2(−/−)	M3(−/+); M4(−/+)	174
HROC119	M1(−/−); M2(−/−)	M3(−/−); M4(−/−)	154
HROC122	M1(−/−); M2(−/−)	M3(−/−); M4(−/−)	130
HROC123	M1(+/−); M2(−/−)	M3(−/−); M4(−/−)	130
HROC125	M1(−/−); M2(−/−)	M3(−/−); M4(−/−)	74
HROC129	M1(+/+); M2(−/+)	M3(−/−); M4(−/−)	61
HROC130	M1(−/+); M2(−/−)	M3(−/−); M4(−/−)	57
HROC131	M1(+/+); M2(+/+)	M3(+/+); M4(+/+)	54
HROC135	M1(−/+); M2(−/−)	M3(−/−); M4(−/+)	40
Ø Matrigel	6/20	2/20	
With Matrigel	8/20	7/20	

A total of 4 mice were implanted on both flanks with human CRC tissue samples. M denotes individual animals xenografted; the outcome is given in parentheses as index + (outgrowing tumor) or index − (no outgrowth). Tumor tissues presoaked with Matrigel are indicated in underlined signs. The overall number of successful sites with and without the addition of Matrigel is given for the total of 20 sides implanted.

significant effect on take rate (no cooling with Matrigel $n = 8$ takes versus no cooling without Matrigel $n = 6$ takes; $p = 0.25$ Chi-square test).

More importantly, in the group of delayed cryopreserving (24 h cooling), application of Matrigel ameliorated tumor take rate significantly (24 h cooling with Matrigel $n = 7$ takes, versus 24 h cooling without Matrigel $n = 2$ takes; $p = 0.03$ Chi-square test).

3.4. Morphological Analysis of Histopathology, Molecular Analysis, and Demonstration of Tumor Cell Viability. Analysis performed by an expert pathologist (FP) showed that, histologically, the PDX closely resembled their primaries (Figure 2). Additionally, the group of delayed cryopreserving showed similar tumor architecture, growth pattern, and cytological features compared to the group of directly cryopreserved tumors (Figure 2(b) versus Figure 2(c)).

In addition, PCR studies amplifying part of the human mitochondrial cytochrome b gene confirmed the human origin of the PDX tumors (data not shown).

Subsequent to the PDX generation, we also routinely generated primary cell cultures out of the established PDX. This procedure was successful in all cases with no observed differences between the no cooling and 24 h cooling PDX. Thus, the viability of the PDX-derived tumor cells was obviously not affected from the 24 h cooling procedure nor from the presence or absence of Matrigel at the time of tumor tissue implantation. Of note, in two cases, permanent cell lines were generated from the PDX primary cultures of the 24 h delay group (i.e., HROC107 and HROC131) (Figure 3). Fingerprint analyses of these two cell lines again confirmed human origin as well as genetic identity with the patients' tumors and PDX models they were generated from (Table 3(a)). A basic analysis of relevant mutations for CRC and further genetic features performed side by side with the PDX models and the primary tumors also revealed no differences (Table 3(b)). Accordingly, HROC107 could be classified as a sporadic standard type CRC whereas HROC131 is sporadic microsatellite instable (Table 3(b); classification according to [3]) CRC.

4. Discussion

Generating models of individual human tumors is an important step towards truly individualized therapy since it facilitates functional testing in addition to pure molecular analysis [9–11]. However, creation of these models is still challenging. On the one hand, the success rate for generation of individual permanent cell lines for CRC is reported to rarely exceed 10% [19], and on the other hand, exquisite expertise and a close teamwork of surgery and pathology as well as molecular and cell biology and animal care are involved in PDX establishment [13, 20, 21]. Recently, we could show that xenografting of prior cryopreserved tumor specimen may be equally successful as xenografting of fresh tumor material [13]. This is an approach to minimize logistical and timing problems when fresh tumor tissue is being engrafted. The pure tumor harvesting can thus be spatiotemporally separated from the xenografting [13] disentangling the logistical problems. Nevertheless, a close teamwork of surgery, pathology, and laboratory is mandatory for fast processing of tumor samples. Capability of cryopreservation of tumor samples is limited to a low number of institutions and therefore new and optimized methods are required to overcome these restrictions.

In order to improve the "take rate" of xenografted tumor specimen, we here systematically analyzed effects of soaking the tumor specimens in Matrigel prior to implantation. This approach was previously reported in PDX generation from pancreatic and other carcinomas [21, 22], but a systematical and comparative approach has so far not been reported. Our mode of implantation allows such a systematical and direct comparison of engraftment with and without Matrigel in one

Table 3

(a)

ID	vWA	TH01	TPOX	CSF1 PO	D5S818	D13S317	D7S820	D16S539	Sex
HROC107	16, 17	8, 9	10, 11	10, 12	11, 13	8	10, 11	10, 13	m
HROC131	16	10	8	11	12, 13	12	11, 13	8, 12	f

(b)

ID	Molecular type	Ploidy status	Mutations		K-Ras	N-Ras	H-Ras	PIK3CA	B-Raf	CIMP-number	MSI - status
			p53	APC							
HROC107	spStd	Aneuploid	Ex8	mut	G12D	wt	wt	E542K	wt	2	MSS
HROC131	spMSI-H	Aneuploid	n.a.	n.a.	wt	wt	wt	wt	mut	5	MSI-H

(a) Fingerprint analysis of cases HROC107 and HROC131. The alleles of nine classical markers are displayed. No differences were observed between the original tumor and both the PDX models and the tumor cell lines generated from the 24 h PDX models.
(b) The results of the molecular analysis of cases HROC107 and HROC131 (according to [3]) are displayed. Mutations in the CRC-relevant target genes p53, APC, K-, N-, and H-Ras, PIK3CA, and B-Raf were analyzed. Together with the CIMP and MSI analysis results, the underlying molecular type could be identified as spSTD for HROC107 and spMSI-H for HROC131.
ID: pseudonym of case, sex: result of the amelogenin marker analysis, m: male, f: female, sp: sporadic, Std: standard type, Ex8: exon number 8, mut: mutated, wt: wild type, n.a.: not analyzed, CIMP: CpG island methylator phenotype, MSI: microsatellite instability, MSS: microsatellite stable, MSI-H: high grade microsatellite instable.

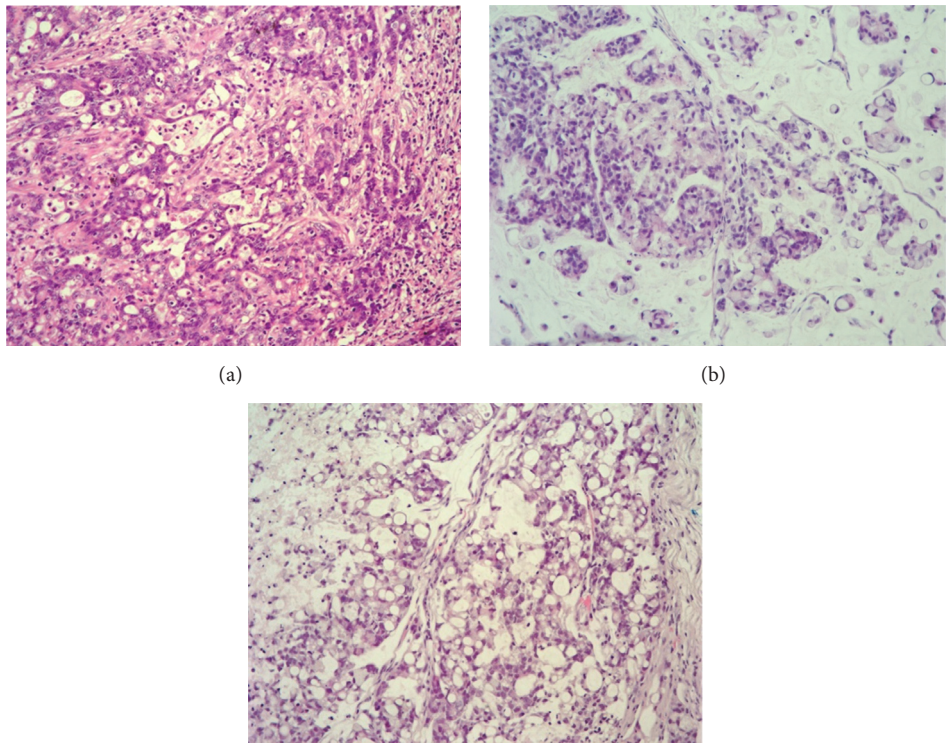

(a) (b) (c)

Figure 2: Tumor morphology (20x). Exemplary HE stains from HROC131. (a) Primary tumor; (b) the PDX generated according to the no cooling and (c) the PDX generated according to the 24 h cooling protocol. (b) and (c) are from the cases with the addition of Matrigel. Tumor architecture, growth pattern, and cytological features of the primary tumor are well preserved in the PDX.

and the same animal at a given time point thus allowing a concrete analysis and minimizing potential bias from the experimental animal side.

With the intention to simulate a logistical delay between tumor surgery and the cryopreservation procedure, as would necessarily be the case when tumor tissue is acquired from distant institutions, especially nonuniversity outpatient clinics, we analyzed the effects of Matrigel in an additional group with a 24-hour 4°C cooling delay before cryopreservation. Analysis of delayed xenografting after this 24 h cooling period of specimen storage on ice showed a considerable reduction of tumor take rate. Though not significant, however showing

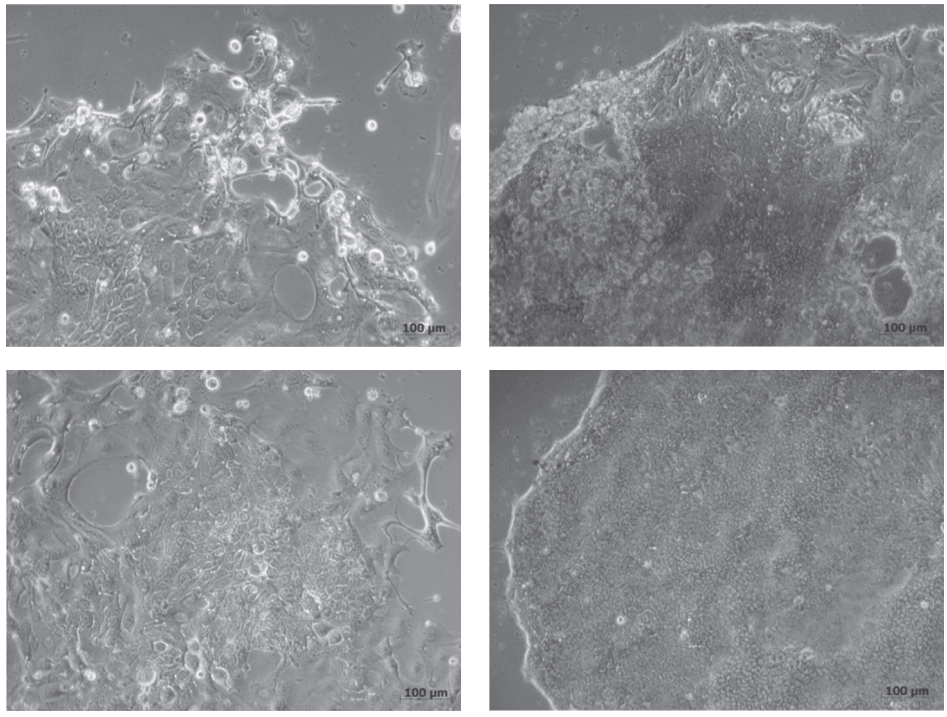

(a) (b)

Figure 3: Depicted are the two successfully established cell lines form this series in passage number 1. Two different areas are displayed to demonstrate the minor morphological differences. (a) HROC107. Note the hem of obviously dying cells in the upper left picture. In the colony center (also of the lower left picture), a population of cells with a copper-stone phenotype can be found which dominated the culture in subsequent passages. (b) HROC131. Similar to HROC107, areas with a larger cell type can be observed in the upper right picture. Smaller cells (displayed in the lower right picture), again with a copper-stone phenotype, took over in the culture in later passages, too.

a strong trend ($p = 0.06$), this result could be explained by biological degradation processes impairing cell viability and fitness.

On the other hand, we could show that application of Matrigel resulted in a significantly improved tumor take rate in this group of delayed xenografting. Contrary to this, Matrigel pretreatment of directly cryopreserved tumors had only a minor effect on take rate.

Therefore, addition of Matrigel seems to counteract the deterioration of delayed cryopreserving after a 24 h cooling period on ice. Interestingly, our cumulative take rate was 70% and was as satisfying as in our previously reported series with a cumulative take rate of 71% [13]. In accordance with these previous findings, the length of the cryopreservation period had no influence on take rate ($p = 0.9489$).

This addendum to our cryopreservation protocol may help to overcome the well-known logistical limits of individual tumor model generation especially if site of tumor harvesting and place of cryopreservation (e.g., hospital and laboratory) are geographically distant and thus may allow preclinical studies or individual testing of targeting therapies in patient tumor tissue of centers without the ability of the complex cryopreservation procedure on site.

Since primary cell cultures could also successfully be established from the PDX tissues obtained, one can safely assume that cell viability is not generally or at least not sustainably impaired from the delay in cryopreservation. Sustained cellular fitness is further corroborated by the fact that two permanent cell lines (HROC107 and HROC131) were successfully established from these primary cultures.

At last, the option of a delayed cryopreservation will greatly facilitate selection and establishment of different tumor models, especially if low passage PDX (or cell line) models are mandatory. This might be an important step towards more individual guided and improved anticancer therapy regimens

Competing Interests

The authors declare that they have no competing interests.

References

[1] B. Vogelstein, E. R. Fearon, S. R. Hamilton et al., "Genetic alterations during colorectal-tumor development," *The New England Journal of Medicine*, vol. 319, no. 9, pp. 525–532, 1988.

[2] J. R. Jass, "Molecular heterogeneity of colorectal cancer: implications for cancer control," *Surgical Oncology*, vol. 16, no. 1, pp. 7–9, 2007.

[3] C. Ostwald, M. Linnebacher, V. Weirich, and F. Prall, "Chromosomally and microsatellite stable colorectal carcinomas without the CpG island methylator phenotype in a molecular classification," *International Journal of Oncology*, vol. 35, no. 2, pp. 321–327, 2009.

[4] J. R. Jass, "Classification of colorectal cancer based on correlation of clinical, morphological and molecular features," *Histopathology*, vol. 50, no. 1, pp. 113–130, 2007.

[5] L. D. Wood, D. W. Parsons, S. Jones et al., "The genomic landscapes of human breast and colorectal cancers," *Science*, vol. 318, no. 5853, pp. 1108–1113, 2007.

[6] V. E. Velculescu, "Defining the blueprint of the cancer genome," *Carcinogenesis*, vol. 29, no. 6, pp. 1087–1091, 2008.

[7] D. J. Freeman, T. Juan, M. Reiner et al., "Association of K-ras mutational status and clinical outcomes in patients with metastatic colorectal cancer receiving panitumumab alone," *Clinical Colorectal Cancer*, vol. 7, no. 3, pp. 184–190, 2008.

[8] R. G. Amado, M. Wolf, M. Peeters et al., "Wild-type KRAS is required for panitumumab efficacy in patients with metastatic colorectal cancer," *Journal of Clinical Oncology*, vol. 26, no. 10, pp. 1626–1634, 2008.

[9] R. S. Kerbel, "Human tumor xenografts as predictive preclinical models for anticancer drug activity in humans: better than commonly perceived-but they can be improved," *Cancer Biology & Therapy*, vol. 2, no. 4, pp. 134–139, 2003.

[10] E. A. Sausville and A. M. Burger, "Contributions of human tumor xenografts to anticancer drug development," *Cancer Research*, vol. 66, no. 7, pp. 3351–3354, 2006.

[11] T. Voskoglou-Nomikos, J. L. Pater, and L. Seymour, "Clinical predictive value of the in vitro cell line, human xenograft, and mouse allograft preclinical cancer models," *Clinical Cancer Research*, vol. 9, no. 11, pp. 4227–4239, 2003.

[12] R. R. Mehta, J. M. Graves, A. Shilkaitis, and T. K. Das Gupta, "Development of a new metastatic human breast carcinoma xenograft line," *British Journal of Cancer*, vol. 77, no. 4, pp. 595–604, 1998.

[13] M. Linnebacher, C. Maletzki, C. Ostwald et al., "Cryopreservation of human colorectal carcinomas prior to xenografting," *BMC Cancer*, vol. 10, article 362, 2010.

[14] T. G. Pretlow, C. M. Delmoro, G. G. Dilley, C. G. Spadafora, and T. P. Pretlow, "Transplantation of human prostatic carcinoma into nude mice in matrigel," *Cancer Research*, vol. 51, no. 14, pp. 3814–3817, 1991.

[15] A. Noël, M.-C. De Pauw-Gillet, G. Purnell, B. Nusgens, C.-M. Lapiere, and J.-M. Foidart, "Enhancement of tumorigenicity of human breast adenocarcinoma cells in nude mice by matrigel and fibroblasts," *British Journal of Cancer*, vol. 68, no. 5, pp. 909–915, 1993.

[16] H. Matsuda, Y. Seo, E. Kakizaki, S. Kozawa, E. Muraoka, and N. Yukawa, "Identification of DNA of human origin based on amplification of human-specific mitochondrial cytochrome b region," *Forensic Science International*, vol. 152, no. 2-3, pp. 109–114, 2005.

[17] C. Maletzki, S. Stier, U. Gruenert et al., "Establishment, characterization and chemosensitivity of three mismatch repair deficient cell lines from sporadic and inherited colorectal carcinomas," *PLoS ONE*, vol. 7, no. 12, Article ID e52485, 2012.

[18] L. P. Fielding, P. A. Arsenault, P. H. Chapuis et al., "Clinicopathological staging for colorectal cancer: an international documentation system (IDS) and an international comprehensive anatomical terminology (ICAT)," *Journal of Gastroenterology and Hepatology*, vol. 6, no. 4, pp. 325–344, 1991.

[19] V. Dangles-Marie, M. Pocard, S. Richon et al., "Establishment of human colon cancer cell lines from fresh tumors versus xenografts: comparison of success rate and cell line features," *Cancer Research*, vol. 67, no. 1, pp. 398–407, 2007.

[20] S. Julien, A. Merino-Trigo, L. Lacroix et al., "Characterization of a large panel of patient-derived tumor xenografts representing the clinical heterogeneity of human colorectal cancer," *Clinical Cancer Research*, vol. 18, no. 19, pp. 5314–5328, 2012.

[21] C. Sorio, A. Bonora, S. Orlandini et al., "Successful xenografting of cryopreserved primary pancreatic cancers," *Virchows Archiv*, vol. 438, no. 2, pp. 154–158, 2001.

[22] E. Fujii, M. Suzuki, K. Matsubara et al., "Establishment and characterization of in vivo human tumor models in the NOD/SCID/γcnull mouse," *Pathology International*, vol. 58, no. 9, pp. 559–567, 2008.

Hindawi Publishing Corporation
BioMed Research International
Volume 2016, Article ID 1627184, 9 pages
http://dx.doi.org/10.1155/2016/1627184

Research Article

A Novel Murine Model of Parvovirus Associated Dilated Cardiomyopathy Induced by Immunization with VP1-Unique Region of Parvovirus B19

Julijus Bogomolovas,[1,2] Egidijus Šimoliūnas,[3] Ieva Rinkūnaitė,[3] Luka Smalinskaitė,[1] Andrej Podkopajev,[2] Daiva Bironaitė,[4] Cleo-Aron Weis,[5] Alexander Marx,[5] Virginija Bukelskienė,[3] Norbert Gretz,[6] Virginija Grabauskienė,[2] Dittmar Labeit,[1] and Siegfried Labeit[1]

[1]*Department of Integrative Pathophysiology, Medical Faculty Mannheim, Mannheim, Germany*
[2]*Department of Pathology, Forensic Medicine and Pharmacology, Faculty of Medicine, Vilnius University, Vilnius, Lithuania*
[3]*Department of Biological Models, Institute of Biochemistry, Vilnius University, Vilnius, Lithuania*
[4]*State Research Institute, Centre for Innovative Medicine, Department of Stem Cell Biology, Vilnius, Lithuania*
[5]*Medical Faculty Mannheim, Institute of Pathology, Mannheim, Germany*
[6]*Medical Faculty Mannheim, Medical Research Centre, Mannheim, Germany*

Correspondence should be addressed to Julijus Bogomolovas; julius.bogomolovas@medma.uni-heidelberg.de

Received 17 May 2016; Revised 9 August 2016; Accepted 14 September 2016

Academic Editor: Andrea Vecchione

Background. Parvovirus B19 (B19V) is a common finding in endomyocardial biopsy specimens from myocarditis and dilated cardiomyopathy patients. However, current understanding of how B19V is contributing to cardiac damage is rather limited due to the lack of appropriate mice models. In this work we demonstrate that immunization of BALB/c mice with the major immunogenic determinant of B19V located in the unique sequence of capsid protein VP1 (VP1u) is an adequate model to study B19V associated heart damage. *Methods and Results*. We immunized mice in the experimental group with recombinant VP1u; immunization with cardiac myosin derived peptide served as a positive reference and phosphate buffered saline served as negative control. Cardiac function and dimensions were followed echocardiographically 69 days after immunization. Progressive dilatation of left ventricle and decline of ejection fraction were observed in VP1u- and myosin-immunized mice. Histologically, severe cardiac fibrosis and accumulation of heart failure cells in lungs were observed 69 days after immunization. Transcriptomic profiling revealed ongoing cardiac remodeling and immune process in VP1u- and myosin-immunized mice. *Conclusions*. Immunization of BALB/c mice with VP1u induces dilated cardiomyopathy in BALB/c mice and it could be used as a model to study clinically relevant B19V associated cardiac damage.

1. Introduction

Dilated cardiomyopathy (DCM) remains the leading cause of heart failure leading to heart transplantation. When therapeutic and prophylactic measures are applied early, a progression of ischemic cardiomyopathy can be stopped and patient can be saved from the heart transplantation. However, only in selected cases progression of primary nonischemic dilated cardiomyopathy can be circumvented with the currently available therapy. Thus, a high demand for new DCM therapies exists. Improved diagnostics revealed that up to 70% of primary nonischemic DCM cases might be due to an unfortunate combination of immunological factors and viral agents [1].

Numerous reports on the presence of parvovirus B19 (B19V) in the hearts of DCM patients imply that B19V might be causatively linked to the heart damage, but the understanding of its pathogenicity in heart diseases is rather

limited [2]. B19V infection in humans typically manifests as *erythema infectiosum*, hydrops fetalis in pregnant women or aplastic crisis, infecting and replicating in erythroid progenitor cells. Up to 60% of adult population are positive for B19V IgG antibodies indicating a previous infection [3]. Following the B19V infection, a dominant immune response is elicited by the VP1-unique region (VP1u), which harbors potent neutralizing epitopes [4, 5]. VP1u is an N-terminal 227 amino acid long region distinguishing minor capsid component VP1 from the major VP2 protein. VP1u region possesses phospholipase activity critical for infectivity [6] and acts as a major determinant of viral tropism [7]. Upon cardiac B19V infection, viral genomes are detected only in endothelial cells and not in myocytes [2]. Therefore, it is very likely that mechanisms beyond the viral infection are involved in the pathogenesis of B19 related DCM. It has been proposed that viral infection can trigger pathological immune response leading to the development of DCM [1].

So far two studies reported on cardiac response to VP1u immunization. Active immunization of BALB/c mice with VP1u induced cardiac inflammation and increased blood levels of nonspecific cytosolic enzymes [8]. Passive immunization of ZB/W F1 mice with rabbit anti-B19-VP1u IgG elicited foci of cardiac infiltration and upregulation of cardiac matrix metalloproteinase-9 (MMP9) activity. However, no significant differences in the cardiac atrial natriuretic peptide, brain natriuretic peptide, heart-type fatty acid-binding protein, and creatine kinase MB levels were detected among all experimental groups [9]. Nevertheless, cardiac function was not evaluated in these studies and progression/resolution of cardiac damage was not followed in these studies. Thus, in this work we demonstrate that VP1u holds cardiopathic potential in the experimental paradigm of widely accepted myosin-induced myocarditis model. Cardiac damage is induced by immunization of BALB/c mice with a cardiac myosin derived peptide. Immunized animals developed acute myocarditis accompanied inflammatory infiltrates about 21 days after immunization and subsequent progression to DCM marked by cardiac fibrosis and impaired systolic function around 40 to 70 days after immunization [10]. To our knowledge, this is the first murine model to study B19V induced DCM.

2. Materials and Methods

2.1. Animal Experiments. Experiments were performed on 6–8-week-old BALB/c male mice. Animals were housed in standard plastic cages in an animal room with controlled environmental conditions and maintained on standard food and water *ad libitum*. Experimental procedures conformed to Directive 2010/63/EU requirements and were approved by the Lithuanian State Food and Veterinary Service (approval number G2-17, 2014/11/11).

2.2. Immunization Protocol. Mice were immunized as described [10]. A peptide derived from α-myosin (MyHC-α6 14-62 RSLKLMATLFSTYASADR) or recombinant VP1u (residues 3–229, UniProtKB/Swiss-Prot: P07299.1) produced in endotoxin-deficient ClearColi (Lucigen) *E. coli* strain as described earlier [11] was used for immunization. 150 μg/animal of cardiac myosin or 500 μg/animal of VP1u was used per immunization. Animals were immunized twice in a 7-day interval. Peptide and protein dissolved in PBS were mixed with equal amount of Freund's complete adjuvant for the first and incomplete Freud's adjuvant for second immunization, emulsified using sonifier, and injected subcutaneously. During the first immunization, animals were stimulated with 500 ng intraperitoneal injection of *Pertussis* toxin in bovine serum albumin supplemented sterile saline. Control animals were immunized using PBS mixed with Freund's adjuvant following the same protocol described above.

2.3. Echocardiography. Transthoracic M-mode echocardiography was performed under isoflurane (1% in pure oxygen) anesthesia, using linear 13 MHz sensor coupled to HITACHI EUB-7000HV ultrasound system. The heart was viewed in short parasternal axis at the papillary muscle level. Six cardiac cycles per measurement were used for averaging. Animals were examined on the day of the first immunization and then 20, 47, and within 60–69 days later. LV ejection fraction was calculated using Teichholz method from M-mode images [12].

2.4. Histology. 60 to 69 days after immunization, animals were sacrificed and heart and lungs were fixed in 10% neutral buffered formalin, embedded in paraffin, sectioned at 6 μm, and stained with picrosirius or Prussian blue (ScyTek) following manufacturer's recommendations. The degree of fibrosis was graded by an experienced pathologist on picrosirius stained sections under white light; density of alveolar siderophages in lung parenchyma was quantified using semiautomated routine in Fiji [13]. For CD45 immunohistochemistry, reagents from Dako Ltd. were used. Heat-mediated antigen retrieval was performed. Dakoreal™ EN Vision TM Detection System Peroxidase/DAB was used to visualize the signal. Rabbit polyclonal anti-CD45 antibody (Abcam ab10558) was used at 1 : 1000 dilution. CD45 positive foci were quantified by counting in 10 random fields (magnification 400x).

2.5. Expression Profiling. Total RNA was extracted from frozen apical LV region using TRIzol® Plus RNA Purification Kit (ThermoFisher Scientific). Gene expression profiling with Affymetrix system using GeneChip® Mouse Gene 2.0 ST Arrays was performed in Microarray Core Facility at Medical Research Center. Arrays were processed using software package JMP® Genomics. Gene set enrichment analysis was performed using GSEA-P [14] with KEGG pathway database derived gene sets [15]. Gene sets with p value and q-val FDR < 0.05 were considered significantly dysregulated and visualized with Enrichment Map [16].

2.6. Statistics. Changes in echocardiographic parameters were statistically evaluated using mixed ANOVA. Differences between fibrosis scores and alveolar siderophage densities were statistically assessed using The Kruskal-Wallis H test. The analysis was performed using SPSS 23; p values < 0.05 were considered significant.

Table 1: Echocardiographic parameters of immunized animals.

Antigen	Days after immunization	LV end-diastolic diameter (mm)	LV end-systolic diameter (mm)	Fractional shortening (%)	LV ejection fraction (%)
		Mean ± SE	Mean ± SE	Mean ± SE	Mean ± SE
PBS	0	3.93 ± 0.10	2.64 ± 0.10	32.9 ± 1.3	61.9 ± 1.8
	20	4.12 ± 0.14	2.70 ± 0.14	34.7 ± 1.5	64.2 ± 2.1
	47	4.05 ± 0.10	2.66 ± 0.07	34.4 ± 1.3	64.0 ± 1.8
	60–69	4.25 ± 0.10	2.83 ± 0.19	33.6 ± 3.2	62.3 ± 4.2
Simple main effect for measurement time		*$F(3, 9) = 1.025$, $p = 0.426$, partial $\eta^2 = 0.255$*	*$F(3, 9) = 0.574$, $p = 0.646$, partial $\eta^2 = 0.161$*	*$F(3, 9) = 1.010$, $p = 0.432$, partial $\eta^2 = 0.252$*	*$F(3, 9) = 1.060$, $p = 0.413$, partial $\eta^2 = 0.261$*
Cardiac myosin	0	3.83 ± 0.05	2.39 ± 0.09	37.5 ± 1.6	68.1 ± 2.1
	20	4.12 ± 0.10	2.98 ± 0.13	27.7 ± 1.8	54.0 ± 2.7
	47	4.46 ± 0.12	3.46 ± 0.11	22.6 ± 0.5	45.7 ± 0.9
	60–69	4.48 ± 0.04	3.57 ± 0.06	20.4 ± 0.9	41.7 ± 1.5
Simple main effect for measurement time		*$F(3, 12) = 25.761$, $p < 0.0005$, partial $\eta^2 = 0.866$*	*$F(3, 12) = 37.638$, $p < 0.0005$, partial $\eta^2 = 0.904$*	*$F(3, 12) = 35.975$, $p < 0.0005$, partial $\eta^2 = 0.900$*	*$F(3, 12) = 36.057$, $p < 0.0005$, partial $\eta^2 = 0.900$*
VP1u	0	3.71 ± 0.07	2.43 ± 0.07	34.5 ± 1.7	64.1 ± 2.4
	20	4.00 ± 0.06	2.77 ± 0.11	30.8 ± 20	58.7 ± 3.0
	47	4.33 ± 0.09	3.26 ± 0.05	24.7 ± 1.1	49.1 ± 1.8
	60–69	4.39 ± 0.14	3.21 ± 0.15	26.9 ± 1.5	52.6 ± 2.4
Simple main effect for measurement time		*$F(3, 15) = 9.760$, $p < 0.005$, partial $\eta^2 = 0.661$*	*$F(3, 15) = 18.526$, $p < 0.0005$, partial $\eta^2 = 0.787$*	*$F(3, 15) = 13.968$, $p < 0.0005$, partial $\eta^2 = 0.736$*	*$F(3, 15) = 13.707$, $p < 0.0005$, partial $\eta^2 = 0.733$*
Two-way interaction between immunization and the time on echocardiographic parameter		*$F(6, 36) = 3.755$, $p < 0.005$, partial $\eta^2 = 0.385$*	*$F(6, 36) = 8.669$, $p < 0.0005$, partial $\eta^2 = 0.591$*	*$F(6, 36) = 9.225$, $p < 0.0005$, partial $\eta^2 = 0.606$*	*$F(6, 36) = 9.460$, $p < 0.0005$, partial $\eta^2 = 0.612$*

3. Results

3.1. Immunization with VP1u Causes Progressive Worsening of Systolic Function in BALB/c Mice. We have followed heart morphology and cardiac function in mice by echocardiography over the course of 69 days after immunization (pi). Given timeframe encloses acute myocarditis (21 days pi) and DCM (60 days pi) phases reported for the established myosin-induced myocarditis/DCM model [17, 18].

There was a statistically significant effect of the antigen on echocardiographic parameters in time-dependent manner. Immunizations with cardiac myosin and VP1u, but not with PBS, lead to statistically significant changes in LV end-diastolic and end-systolic diameters, fractional shortening, and LV ejection fraction over time (Table 1). Immunization with cardiac myosin and VP1u caused progressive dilatation of LV, resulting in gradual increase of LV diameter at systole and diastole (Figure 1). In good agreement with DCM phenotype, remodeling of LV was accompanied by the worsening of systolic function, measured by fractional shortening and ejection fraction. Immunization with cardiac myosin and VP1u resulted in statistically significant decrease of EF and FS as early as 20 days pi (Figure 1).

3.2. Immunization with VP1u Leads to Cardiac Fibrosis. 69 days after immunization hearts and lungs were examined histologically. Cardiac sections were stained with picrosirius red to visualize fibrosis and imaged under the white and polarized light (Figure 2). In cardiac sections of PBS-immunized mice no to mild fibrosis could be observed, evenly distributed through myocardium, physiologically more intensive around the vessels. Under polarized light, mostly green birefringence was observed, typical for thin collagen fibers. Myosin-immunized mice developed severe fibrosis clustering into multiple foci, mostly located in the pericardium, consisting of thick (red) and thin (green) collagen fibers. In VP1u animals, fibrotic foci developed around the vessels, mimicking pathological picture of "hypertensive" cardiomyopathy. Moreover, under the polarized light, extensive spread of interstitial fibrosis could be seen. The extent of cardiac fibrosis was graded by an experienced pathologist in a blinded manner. A Kruskal-Wallis H test confirmed significantly different median fibrosis scores between studied groups, $H(2) = 9.987$, $p = 0.007$. Pairwise comparisons were performed using Dunn's procedure with a Bonferroni correction for multiple comparisons. Adjusted p values are presented. This *post hoc* analysis revealed statistically significant differences in median fibrosis scores between the PBS (4.62) and cardiac myosin (13) ($p = 0.013$) and VP1u- (6.08) and cardiac myosin-immunized animals ($p = 0.028$), but not between VP1u- (5.50) and PBS-immunized animals.

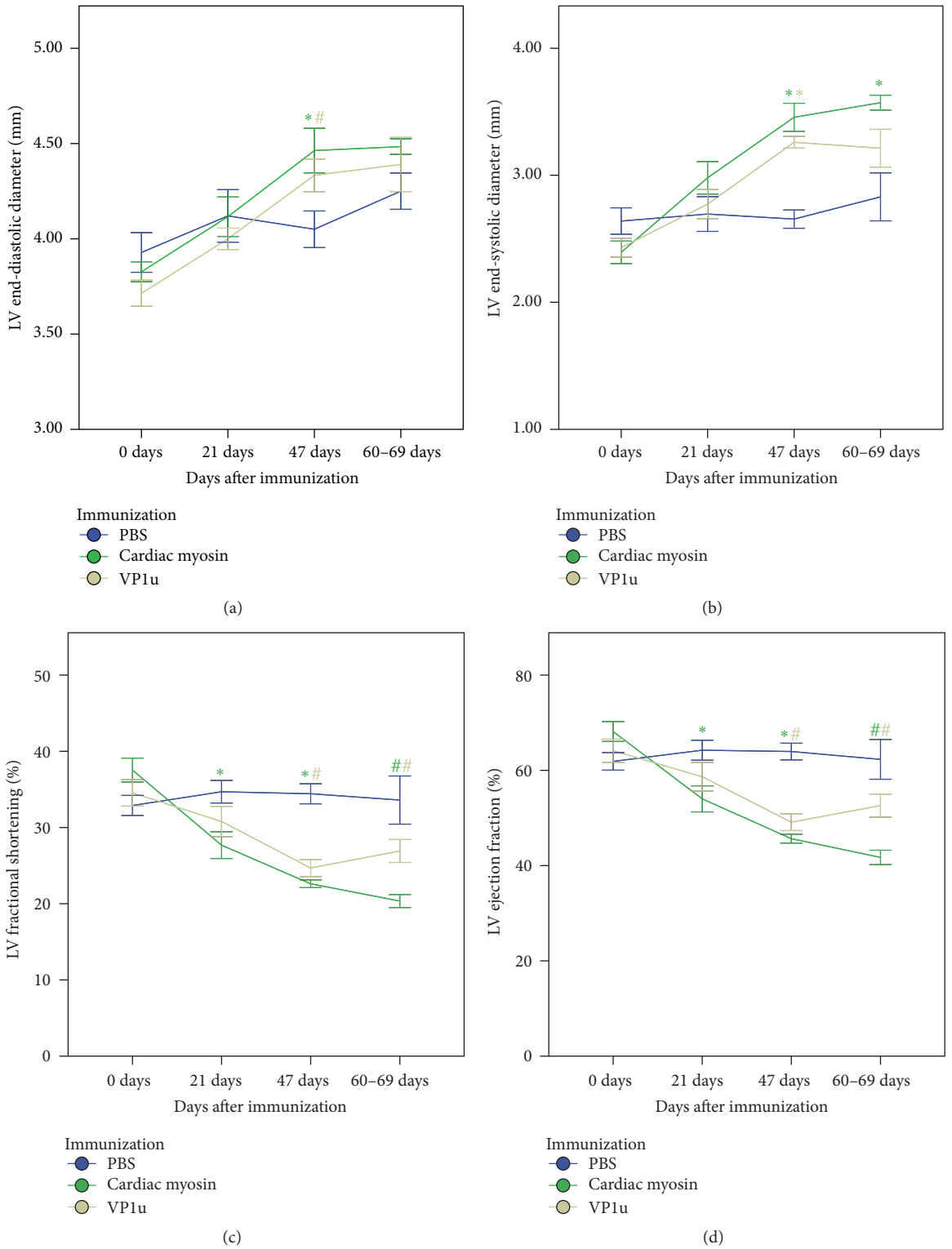

Figure 1: Serial echocardiographic measurements of immunized animals. All parameters were determined from serial echocardiography images obtained at given intervals in isoflurane-anesthetized mice. LV diameters were measured in M-mode at the short parasternal axis. Data are expressed as means ± SEM; $n = 6$–10; ∗ denotes $p < 0.005$; # denotes $p < 0.05$, from 0 days.

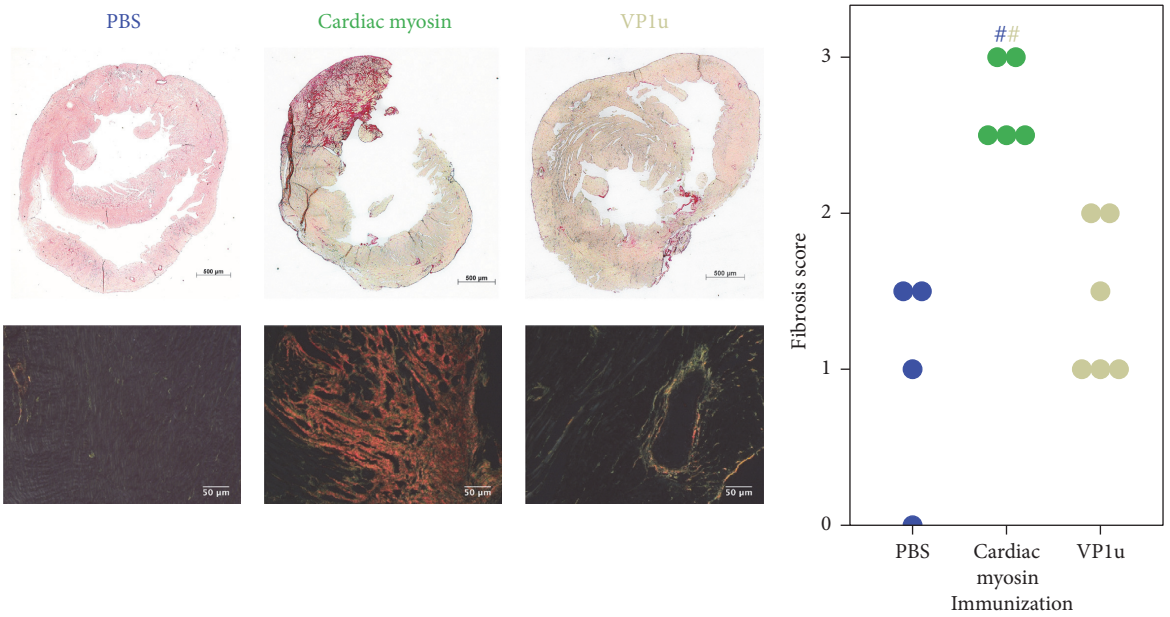

FIGURE 2: Fibrotic changes in the myocardium. Representative fields for each group are shown. Sections are photographed under white light (fibrosis-red, cardiac tissue-yellow to pink, upper panel) and under polarized light (thin collagen fibers are green, thick-red; the background is black, lower column). Distribution of fibrosis scores is given in (b). # denotes $p < 0.05$; color marks the compared group, $n = 4–6$.

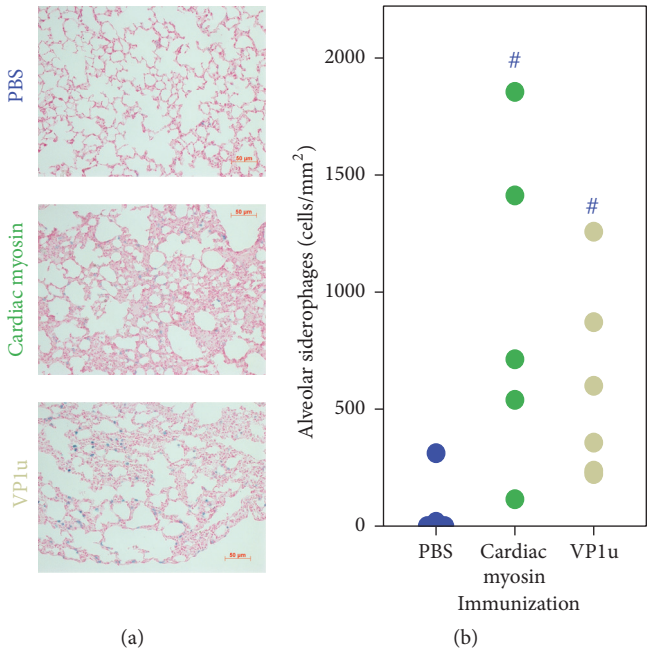

FIGURE 3: Accumulation of alveolar siderophages, indicative of heart failure in lungs of cardiac myosin- or VP1u-immunized animals. Representative fields are shown for each group. Siderophages stain blue in red counterstained lung tissue. Distribution of median alveolar siderophage densities is given in (b); # denotes $p < 0.05$; color marks the compared group, $n = 4–6$.

3.3. Accumulation of Heart Failure Cells in Lungs of VP1u-Immunized Animals. We have stained lungs of animals with Prussian blue for the visualization of siderophages known as the heart failure cells (Figure 3). Upon left heart failure, increased pulmonary blood pressure causes red blood cells to leak out, where they are engulfed by macrophages. The resulting accumulation of hemosiderin in macrophages stains blue. Cardiac myosin-immunized animals displayed the accumulation of alveolar siderophages compared to physiological levels observed in lungs of PBS-immunized

Table 2: Top 10 dysregulated transcripts.

		Fold change	p value			Fold change	p value
PBS *versus* cardiac myosin							
Igkc	Immunoglobulin kappa constant	−2.47	0.04	Timp4	Tissue inhibitor of metalloproteinase 4	2.94	0.01
Tfrc	Transferrin receptor	−1.80	0.01	Pdk4	Pyruvate dehydrogenase kinase, isoenzyme	2.65	0.02
Tcrg-C4	T cell receptor gamma, constant 4	−1.68	0.04	Fkbp5	FK506 binding protein 5	2.49	0.02
Mmp3	Matrix metallopeptidase 3	−1.45	0.05	Zbtb16	Zinc finger and BTB domain containing 16	2.09	0.02
Comp	Cartilage oligomeric matrix protein	−1.36	0.05	Fam107a	Family with sequence similarity 107, mem	2.06	0.02
Rrad	Ras-related associated with diabetes	−1.33	0.02	Map3k6	Mitogen-activated protein kinase kinase	2.04	0.02
Ighm	Immunoglobulin heavy constant mu	−1.31	0.02	Ucp3	Uncoupling protein 3 (mitochondrial, pro	1.97	0.03
Gpr22	G protein-coupled receptor 22	−1.06	0.01	Cdkn1a	Cyclin-dependent kinase inhibitor 1A (p21)	1.73	0.05
Map2k6	Mitogen-activated protein kinase kinase	−1.04	0.03	Ms4a4a	Membrane-spanning 4-domain, subfamily A	1.51	0.02
Igkj5	Immunoglobulin kappa joining 5	−1.04	0.04	Klhl38	Kelch-like 38	1.45	0.04
PBS *versus* VP1u							
Rrad	Ras-related associated with diabetes	−1.69	0.01	Fkbp5	FK506 binding protein 5	2.39	0.02
Kcnj2	Potassium inwardly-rectifying channel	−1.05	0.01	Timp4	Tissue inhibitor of metalloproteinase 4	2.04	0.03
Arhgap18	Rho GTPase activating protein 18	−1.01	0.01	Cdkn1a	Cyclin-dependent kinase inhibitor 1A (p21)	2.02	0.03
Ighm	Immunoglobulin heavy constant mu	−0.88	0.05	Map3k6	Mitogen-activated protein kinase kinase	2.01	0.02
Lphn2	Latrophilin 2	−0.86	0.03	Fam107a	Family with sequence similarity 107, mem	2.00	0.03
Tfrc	Transferrin receptor	−0.82	0.02	Serpine1	Serine (or cysteine) peptidase inhibitor	1.72	0.01
Dusp18	Dual specificity phosphatase 18	−0.71	0.03	Zbtb16	Zinc finger and BTB domain containing 16	1.71	0.03
Slc26a10	Solute carrier family 26, member 10	−0.68	0.01	8430408G22Rik	RIKEN cDNA 8430408G22 gene	1.69	0.02
Slc6a6	Solute carrier family 6 (neurotransmitter transporter, taurine), member 6	−0.68	0.04	Ms4a4a	Membrane-spanning 4-domain, subfamily A	1.60	0.02
Kctd12b	Potassium channel tetramerisation domain	−0.66	0.03	Ctgf	Connective tissue growth factor	1.32	0.01
Cardiac myosin *versus* VP1u							
Pdk4	Pyruvate dehydrogenase kinase, isoenzyme	−1.86	0.04	Igkc	Immunoglobulin kappa constant	2.54	0.03
Ces1d	Carboxylesterase 1D	−1.27	0.03	Trbj1-1	T cell receptor beta joining 1-1	1.73	0.04
Apln	Apelin	−0.96	0.05	Igj	Immunoglobulin joining chain	1.56	0.04
Ttn	Titin	−0.96	0.04	Comp	Cartilage oligomeric matrix protein	1.38	0.04
Klf15	Kruppel-like factor 15	−0.93	0.04	Mmp3	Matrix metallopeptidase 3	1.34	0.05
Ctnnal1	Catenin (cadherin associated protein), a	−0.93	0.01	Nox4	NADPH oxidase 4	1.07	0.04

Table 2: Continued.

		Fold change	p value			Fold change	p value
Tacc2	Transforming Acidic Coiled-Coil Containing Protein 2	−0.84	0.02	Mcpt4	Mast cell protease 4	1.03	0.04
Scn4a	Sodium channel, voltage-gated, type IV	−0.82	0.03	Tfrc	Transferrin receptor	0.98	0.01
Gpam	Glycerol-3-phosphate acyltransferase, mi	−0.74	0.03	Rab2b	RAB2B, member RAS oncogene family	0.94	0.04
Cited2	Cbp/p300-interacting transactivator, wit	−0.73	0.04	Snord71	Small nucleolar RNA, C/D box 71	0.93	0.04
Fbxo32	F-box protein 32	−0.73145	0.04	Mgl2	Macrophage galactose N-acetyl-galactosamine specific lectin 2	0.91	0.01
Glul	Glutamate-ammonia ligase (glutamine synthase)	−0.68506	0.01	Glipr1	GLI pathogenesis-related 1 (glioma)	0.84	0.04

animals. A Kruskal-Wallis H test confirmed significantly different median siderophage densities between studied groups, $H(2) = 6.514$, $p = 0.039$. Pairwise comparisons were performed using Dunn's procedure with a Bonferroni correction for multiple comparisons. Adjusted p values are presented. This *post hoc* analysis revealed statistically significant differences in median fibrosis scores between the PBS (3.25) and cardiac myosin (10.6) ($p = 0.043$) and between VP1u- (9.0) and PBS-immunized animals ($p = 0.049$).

3.4. Transcriptomic Profiling of Immunized Animals. To gain molecular insights into VP1u immunization triggered heart damage we have performed gene expression profiling on left ventricular samples. 362 genes were found statistically significantly dysregulated between studied groups (Supplementary Table 1 in Supplementary Material available online at http://dx.doi.org/10.1155/2016/1627184). The list of top 10 dysregulated genes (Table 2) demonstrated shared and unique molecular features between myosin and VP1u triggered cardiac damage. In both animal models (compared to PBS control) matrix metallopeptidase 3 was upregulated, and tissue inhibitor of metalloprotease 4 was downregulated. This expression pattern resembles changes in the proteome, marking cardiac remodeling typical for the DCM [19, 20]. Moreover, commonly upregulated set of inflammation-related genes (*Igkc*, *Ighm*, and *Tcrg-C4*) imply activation of the immune system in the myocardium. However, studied models share some differences in gene expression patterns. Immunization with the VP1u results in less pronounced immune activation of the myocardium, when compared to myosin-immunized mice, resulting in downregulation of immunity-related genes (*Igkc, Igj, Trbj1-1, Mcpt4, and Mgl2*). The cellular basis of this phenomenon could be related to a significant accumulation of CD45 positive immune cells in hearts of myosin-immunized animals (Figure 4). Set of genes involved in central energy metabolism (*Pdk4, Gpam, and Glul*) was upregulated in VP1u-immunized animals. Speculatively, this could indicate a relatively spared energy metabolism in a less damaged myocardium of VP1u-immunized animals; on another hand this might mean differing molecular mechanisms leading to heart damage. Gene set enrichment analysis using KEGG annotation based gene set exemplifies differences between expression patterns of myosin- and VP1u-immunized animals. Gene sets related to inflammation and immune response are underrepresented in VP1u-immunized animals, whereas gene sets involved in energy metabolism are overrepresented.

4. Discussion

Echocardiographic and histological assessment of cardiac function and structure in VP1u-immunized animals revealed gradual remodeling of LV and worsening of systolic function. Observed changes are typical for DCM phenotype and follow the pattern of heart damage caused by established myosin-induced myocarditis/DCM model, used in this work as a positive reference. Thus immunization with VP1u can be applied as a model to study clinically relevant B19V associated DCM.

Our findings are in good agreement with previous studies, demonstrating that active or passive immunization of susceptible mice strain with VP1u alone can elicit heart damage [8, 9]. However, in this study we demonstrated that immunization with VP1u could progress beyond the phase of acute cardiac inflammation reported by Nie et al. and lead to LV dilatation, impaired systolic function, and cardiac fibrosis consistent with the development of DCM. This pattern closely resembles progression of heart damage elicited by the immunization with cardiac myosin derived peptide used in the established experimental autoimmune myocarditis/DCM model [10, 17].

However, cardiac damage in VP1u-immunized animals has unique features when compared to the cardiac myosin-immunized group. Animals in the VP1u-immunized group developed milder cardiac damage with less LV dilatation, lesser cardiac fibrosis, and fewer heart failure cells in lungs. Moreover, slight LV reverse remodeling was observed in VP1u-immunized animals 47 to 60–69 days after immunization. It is noteworthy that spontaneous recovery of cardiac function is well documented in clinical practice [21] and presented model could at least partly be used to study this relevant phenomenon.

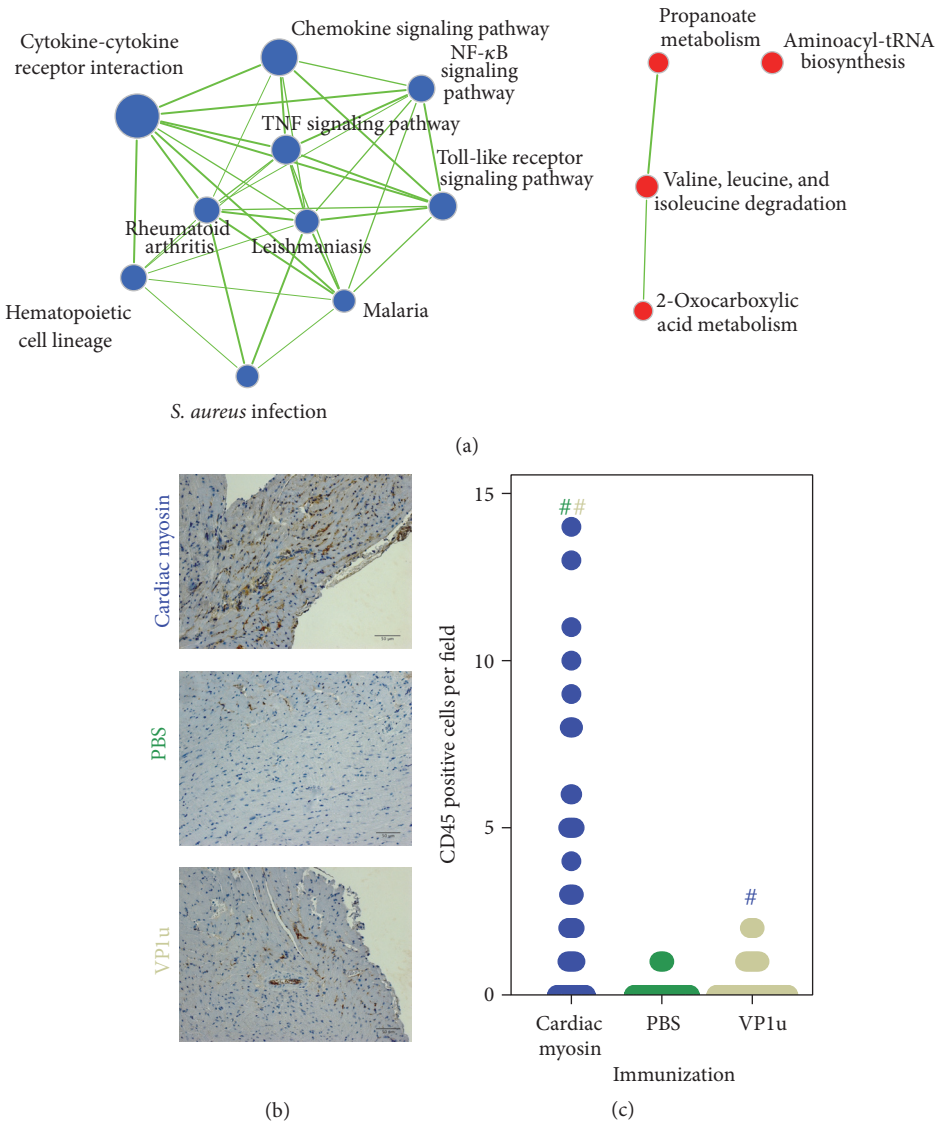

Figure 4: Immune infiltration in immunized animals. Network representation of under- and overrepresented gene sets between cardiac myosin- and VP1u-immunized animals (a). Gene sets related to immunity and infection are underrepresented in VP1u-immunized animals (blue nodes), whereas gene sets involved in catabolic and anabolic processes are overrepresented (red nodes). Accumulation of CD45 positive foci in cardiac myosin-immunized animals (b). Number of CD45 positive cells is given in (c); # denotes $p < 0.05$; color marks the compared group.

At the molecular level, comparative transcriptomic profiling revealed that immunization with VP1u resulted in less pronounced upregulation of inflammation-related genes than immunization with cardiac myosin. Conversely, immunization with VP1u upregulated set of energy metabolism genes. Speculatively, observed differences in gene expression patterns might reflect the varying severity of heart damage caused by the immunization with distinct antigens. Significant accumulation of CD45 positive immune cells in hearts of the cardiac myosin-immunized animals supports this observation. However, these differences might also imply differing molecular mechanisms leading to the heart damage.

Intriguingly, cardiac fibrosis in VP1u animals clustered around the vessels and resembled the histological picture of hypertrophic cardiomyopathy. It was shown that B19V myocarditis is an endothelial cell-mediated disease [22, 23] and anti-B19V antibodies alone can activate endothelial cells *in vitro* [24]. Thus, endothelium of cardiac vessels might be a primary autoimmune target in VP1u-immunized animals.

In conclusion, presented data indicate that immunization of BALB/c mice with the recombinant VP1u protein causes heart damage compatible with the DCM phenotype. Described model can be useful to study clinically relevant B19V associated heart damage.

Competing Interests

The authors declare that they have no competing interests.

Acknowledgments

This work has been funded by a Grant (MIP-011/2014) from the Research Council of Lithuania. The authors acknowledge the financial support of the Leducq Foundation (TNE-13CVD04) and the European Commission Marie Skłodowska-Curie Individual Fellowship (Titin Signals, 656636). The authors thank Roma Grinienė for histochemical stainings performed. The authors are grateful to Microarray Technology core facility at Medical Research Centre and specially Carolina De La Torre and Carsten Sticht for microarray processing.

References

[1] C. Kawai, "From myocarditis to cardiomyopathy: mechanisms of inflammation and cell death: learning from the past for the future," *Circulation*, vol. 99, no. 8, pp. 1091–1100, 1999.

[2] S. Pankuweit and K. Klingel, "Viral myocarditis: from experimental models to molecular diagnosis in patients," *Heart Failure Reviews*, vol. 18, no. 6, pp. 683–702, 2013.

[3] E. D. Heegaard and K. E. Brown, "Human parvovirus B19," *Clinical Microbiology Reviews*, vol. 15, no. 3, pp. 485–505, 2002.

[4] E. Zuffi, E. Manaresi, G. Gallinella et al., "Identification of an immunodominant peptide in the parvovirus B19 VP1 unique region able to elicit a long-lasting immune response in humans," *Viral Immunology*, vol. 14, no. 2, pp. 151–158, 2001.

[5] T. Saikawa, S. Anderson, M. Momoeda, S. Kajigaya, and N. S. Young, "Neutralizing linear epitopes of b19 parvovirus cluster in the vP1 unique and vP1-vP2 junction regions," *Journal of Virology*, vol. 67, no. 6, pp. 3004–3009, 1993.

[6] C. Filippone, N. Zhi, S. Wong et al., "VP1u phospholipase activity is critical for infectivity of full-length parvovirus B19 genomic clones," *Virology*, vol. 374, no. 2, pp. 444–452, 2008.

[7] R. Leisi, N. Ruprecht, C. Kempf, and C. Ros, "Parvovirus B19 uptake is a highly selective process controlled by VP1u, a novel determinant of viral tropism," *Journal of Virology*, vol. 87, no. 24, pp. 13161–13167, 2013.

[8] X. Nie, G. Zhang, D. Xu et al., "The VP1-unique region of parvovirus B19 induces myocardial injury in mice," *Scandinavian Journal of Infectious Diseases*, vol. 42, no. 2, pp. 121–128, 2010.

[9] B.-S. Tzang, T.-M. Lin, C.-C. Tsai, J.-D. Hsu, L.-C. Yang, and T.-C. Hsu, "Increased cardiac injury in NZB/W F1 mice received antibody against human parvovirus B19 VP1 unique region protein," *Molecular Immunology*, vol. 48, no. 12-13, pp. 1518–1524, 2011.

[10] D. Čiháková, R. B. Sharma, D. Fairweather, M. Afanasyeva, and N. R. Rose, "Animal models for autoimmune myocarditis and autoimmune thyroiditis," in *Autoimmunity*, vol. 102 of *Methods in Molecular Medicine*, pp. 175–193, Humana Press, Totowa, NJ, USA, 2004.

[11] J. Bogomolovas, B. Simon, M. Sattler, and G. Stier, "Screening of fusion partners for high yield expression and purification of bioactive viscotoxins," *Protein Expression and Purification*, vol. 64, no. 1, pp. 16–23, 2009.

[12] L. E. Teichholz, T. Kreulen, M. V. Herman, and R. Gorlin, "Problems in echocardiographic volume determinations: echocardiographic-angiographic correlations in the presence or absence of asynergy," *The American Journal of Cardiology*, vol. 37, no. 1, pp. 7–11, 1976.

[13] J. Schindelin, I. Arganda-Carreras, E. Frise et al., "Fiji: an open-source platform for biological-image analysis," *Nature Methods*, vol. 9, no. 7, pp. 676–682, 2012.

[14] A. Subramanian, H. Kuehn, J. Gould, P. Tamayo, and J. P. Mesirov, "GSEA-P: a desktop application for gene set enrichment analysis," *Bioinformatics*, vol. 23, no. 23, pp. 3251–3253, 2007.

[15] M. Kanehisa and S. Goto, "KEGG: kyoto encyclopedia of genes and genomes," *Nucleic Acids Research*, vol. 28, no. 1, pp. 27–30, 2000.

[16] D. Merico, R. Isserlin, O. Stueker, A. Emili, and G. D. Bader, "Enrichment map: a network-based method for gene-set enrichment visualization and interpretation," *PLoS ONE*, vol. 5, no. 11, Article ID e13984, 2010.

[17] M. Afanasyeva, D. Georgakopoulos, D. F. Belardi et al., "Quantitative analysis of myocardial inflammation by flow cytometry in murine autoimmune myocarditis: correlation with cardiac function," *The American Journal of Pathology*, vol. 164, no. 3, pp. 807–815, 2004.

[18] M. Afanasyeva, D. Georgakopoulos, and N. R. Rose, "Autoimmune myocarditis: cellular mediators of cardiac dysfunction," *Autoimmunity Reviews*, vol. 3, no. 7-8, pp. 476–486, 2004.

[19] C. V. Thomas, M. L. Coker, J. L. Zellner, J. R. Handy, A. J. Crumbley III, and F. G. Spinale, "Increased matrix metalloproteinase activity and selective upregulation in LV myocardium from patients with end-stage dilated cardiomyopathy," *Circulation*, vol. 97, no. 17, pp. 1708–1715, 1998.

[20] C. M. Tummalapalli, B. J. Heath, and S. C. Tyagi, "Tissue inhibitor of metalloproteinase-4 instigates apoptosis in transformed cardiac fibroblasts," *Journal of Cellular Biochemistry*, vol. 80, no. 4, pp. 512–521, 2001.

[21] A. D'Ambrosio, G. Patti, A. Manzoli et al., "The fate of acute myocarditis between spontaneous improvement and evolution to dilated cardiomyopathy: a review," *Heart*, vol. 85, no. 5, pp. 499–504, 2001.

[22] H. Mahrholdt, A. Wagner, C. C. Deluigi et al., "Presentation, patterns of myocardial damage, and clinical course of viral myocarditis," *Circulation*, vol. 114, no. 15, pp. 1581–1590, 2006.

[23] B. D. Bültmann, K. Klingel, K. Sotlar et al., "Fatal parvovirus b19–associated myocarditis clinically mimicking ischemic heart disease: an endothelial cell–mediated disease," *Human Pathology*, vol. 34, no. 1, pp. 92–95, 2003.

[24] B.-S. Tzang, C.-C. Tsai, C.-C. Chiu, J.-Y. Shi, and T.-C. Hsu, "Up-regulation of adhesion molecule expression and induction of TNF-α on vascular endothelial cells by antibody against human parvovirus B19 VP1 unique region protein," *Clinica Chimica Acta*, vol. 395, no. 1-2, pp. 77–83, 2008.

Hindawi Publishing Corporation
BioMed Research International
Volume 2016, Article ID 3819052, 9 pages
http://dx.doi.org/10.1155/2016/3819052

Research Article

Transneuronal Degeneration of Thalamic Nuclei following Middle Cerebral Artery Occlusion in Rats

Shu-Jen Chang,[1] Juin-Hong Cherng,[2] Ding-Han Wang,[1] Shu-Ping Yu,[2] Nien-Hsien Liou,[2] and Ming-Lun Hsu[1]

[1]*School of Dentistry, National Yang-Ming University, No. 155, Section 2, Li-Non Street, Taipei 112, Taiwan*
[2]*Department and Graduate Institute of Biology and Anatomy, National Defense Medical Center, No. 161, Section 6, Minquan E. Road, Taipei 114, Taiwan*

Correspondence should be addressed to Ming-Lun Hsu; mlhsu@ym.edu.tw

Received 18 February 2016; Revised 22 June 2016; Accepted 8 July 2016

Academic Editor: Andrea Vecchione

Objective. Postinfarction transneuronal degeneration refers to secondary neuronal death that occurs within a few days to weeks following the disruption of input or output to synapsed neurons sustaining ischemic insults. The thalamus receives its blood supply from the posterior circulation; however, infarctions of the middle cerebral arterial may cause secondary transneuronal degeneration in the thalamus. In this study, we presented the areas of ischemia and associated transneuronal degeneration following MCAo in a rat model. *Materials and Methods.* Eighteen 12-week-old male Sprague-Dawley rats were randomly assigned to receive middle cerebral artery occlusion surgery for 1, 7, and 14 days. Cerebral atrophy was assessed by 2,3,5-triphenyltetrazolium hydrochloride staining. Postural reflex and open field tests were performed prior to animal sacrifice to assess the effects of occlusion on behavior. *Results.* Myelin loss was observed at the lesion site following ischemia. Gliosis was also observed in thalamic regions 14 days following occlusion. Differential degrees of increased vascular endothelial growth factor expression were observed at each stage of infarction. Increases in myelin basic protein levels were also observed in the 14-day group. *Conclusion.* The present rat model of ischemia provides evidence of transneuronal degeneration within the first 14 days of occlusion. The observed changes in protein expression may be associated with self-repair mechanisms in the damaged brain.

1. Introduction

The brain and spinal cord consist of neurons with different functions, such as movement control and sensory information processing. The loss of function of neurons in the brain and spinal cord is known as neurodegeneration [1, 2]. Current research suggests that transneuronal degeneration plays a significant role in a number of neurodegenerative diseases, including Alzheimer's disease, Parkinson's disease, Huntington's disease, and amyotrophic lateral sclerosis [3–7].

Transneuronal degeneration is also referred to as secondary neuronal degeneration and includes the following four stages: axonal transection, anterograde degeneration, retrograde degeneration, and associated neuronal degeneration [7]. In the human brain, the pathological processes induced by physical trauma or vascular blockages may cause neuronal damage, resulting in a disruption of axonal transmission in which both input and output information cannot be received by the associated neurons, following which anterograde and retrograde degeneration occur.

Ischemic stroke, also known as cerebral infarction, may occur at the bifurcation of the middle cerebral artery (MCA). The MCA, supplying 80% of the blood supply to the brain, is the largest branch of the internal carotid artery (ICA) and the most common site for the occurrence of cerebral embolism. Research has revealed that severe ischemic stroke in the MCA results in damage and eventual necrosis of neurons in the striatum and substantia nigra due to the resulting disruption in blood supply. Saji and Reis, for example, reported that MCA occlusion (MCAo) leads to decreased GABAergic input to the substantia nigra (SN) as well as elevated blood flow, metabolism, and neuronal activity in SN neurons [8]. Loss

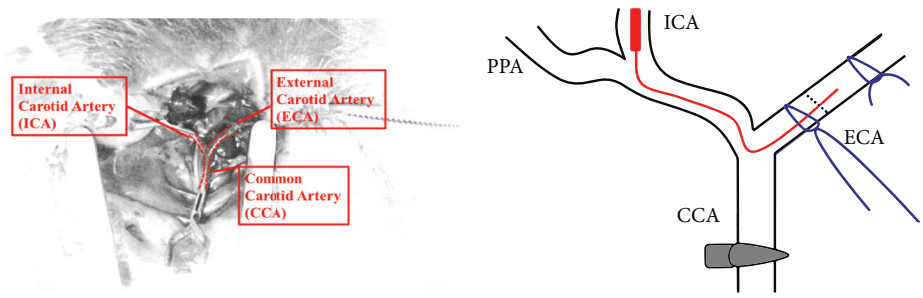

FIGURE 1: Illustration of middle cerebral artery occlusion procedure. (a) The sternocleidomastoid muscle and sternohyoid gap are located in the vicinity of the right common carotid artery, dividing in the neck to form the external and internal carotid arteries. (b) A 4-0 nylon suture (red line) is inserted and moved towards the internal carotid artery bifurcation, and the blood supply from the external carotid artery is cut off. The 4-0 nylon suture is inserted 20–22 mm into the internal carotid artery in order to slowly occlude the middle cerebral artery. CCA: common carotid artery, ECA: external carotid artery, ICA: internal carotid artery, and PPA: pterygopalatine artery.

of inhibitory GABAergic innervation in the SN following striatal lesions shifts the balance between inhibitory and excitatory input, leading to a state of excessive excitation that ultimately results in neuronal cell death.

Though a number of studies have confirmed that MCAo results in damage to neurons directly supplied by the MCA, researchers have also documented the occurrence of secondary neuronal degeneration in areas with synaptic connections to the ischemic regions, including the thalamus and substantia nigra [9, 10]. Hata et al. further reported that, following MCAo, brain damage may also occur in deep regions connected to the neuronal structures supplied by the MCA, such as the hippocampus, hypothalamus, and globus pallidus, as well as in the substantia nigra ipsilateral to striatal infarction [11]. This form of neuronal atrophy, known as anterograde transneuronal degeneration, occurs following the deafferentation of postsynaptic neurons. However, the mechanisms underlying transneuronal degeneration in remote areas remain poorly understood. In the present study, we investigated areas of ischemia and associated transneuronal degeneration following MCAo in a rat model of cerebral ischemia.

2. Materials and Methods

2.1. Surgical Occlusion of the Middle Cerebral Artery. All experimental procedures of the present study were approved by the Institutional Animal Care and Use Committee of the National Defense Medical Center. All efforts were made to minimize the number of animals utilized and their suffering with Guide for Care and Use of Laboratory Animals. Each group consisted of six male Sprague-Dawley rats (250–300 g) exposed to MCAo for 1 d, 7 d, and 14 d and sham control.

In the present study, we simulated human stroke by inducing focal cerebral ischemia in rats. MCAo was performed according to the experimental methods published by Uluç et al. in 2011 [12]. Prior to the operation, a 22 mm, 4-0 size nylon suture (UNIK Surgical Sutures MFG, Co., Taiwan) was prepared, and its tip was wrapped with Parafilm (Parafilm M®, Bemis, Germany) approximately 1 mm long and 0.1 cm thick. Following Zoletil (20 mg/kg) anesthetization, an approximately 4-cm incision was made in the center of the neck, and the right sternoclavicular mastoid muscle was exposed. The right external carotid artery (ECA) and ICA were located by following the right common carotid artery to the brain (Figure 1(a)). The common carotid artery was fixed with an artery clamp, and an incision was made in the ECA. The prepared 4-0 nylon suture was pushed forward from the incision to the bifurcation of the ECA and ICA. The ECA was ligated and incised (Figure 1(b)). The 4-0 nylon suture was pushed forward between 20 mm and 22 mm into the ICA until the tip reached the MCA in order to complete the occlusion procedure. The ECA and skin incisions were then sutured closed, and the animals were allowed to wake from the anesthesia under a heat lamp. All animals were provided free access to food and water.

2.2. Postural Hang Reflex and Open Field Test. Developed by Bederson et al. [13, 14], the postural hang reflex test was performed in order to evaluate sensorimotor function via assessment of upper body posture. The degree of abnormal posture was estimated by suspending the rats by their tails 100 cm above the floor and slowly lowering them. Mild cases of abnormal posture were defined by flexing the contralateral limb towards the body, while more severe cases were defined by circling towards the ipsilateral side. In addition, each animal individually underwent a single, 3-minute open field test for the assessment of local motor activity.

Both tests were scored according to the following system. A score of zero indicated normal motor activity; a score of 1 was given when the body is consistently bent towards the side contralateral to the occlusion; a score of 2 was given when animal was suspended by its tail, leading to circling behavior of the side contralateral to the occlusion; a score of 3 was given when rats exhibited winding behavior towards the side contralateral to the occlusion; a score of 4 was given when rats exhibited difficulty in/loss of the ability to walk (Table 1).

2.3. Brain Sections Preparation. Brains were removed at various times after reperfusion (MCAo: 1 d, 7 d, and 14 d). The brains of MCAo rats were dissected and sliced using a matrix device (Plastics One Inc., USA) into 2 mm coronary sections.

Table 1: The scoring criteria for locomotor activity test in rats. Rats were subjected to tail suspension and open field tests following middle cerebral artery occlusion and scored as indicated here.

Score	Behavior
0	Rats with normal behavior
1	The forelimb and body of the rat bend consistently to the side contralateral to that of the damaged brain hemisphere
2	The rat can move to both sides, but when its tail is held, it can only circle to the side contralateral to that of the damaged brain hemisphere
3	The rat can only go move in circles in the direction of the side contralateral to that of the damaged brain hemisphere
4	The rat has difficulty in walking or loses its ability to walk

After mediosagittal division, the main portion of the infarct was snap frozen and stored for further analyses.

2.4. TTC Staining. After sectioning, slices were immediately stained with 1% TTC (triphenyltetrazolium hydrochloride, USB Corporation, USA) in 0.9% NaCl at 37°C for 15 min. The sections were then transferred to 10% formaldehyde (Hayashi Pure Chemical IND, LTD, Japan) for 16 h in order to complete fixation.

2.5. Measurement of Infarct Volume. Five equidistant coronal sections 2 mm from bregma +4.0 mm to bregma −7.0 mm were stained with TTC and photographed using a Leica vertical microscope (DM2500, Wetzlar, Germany). The area of the infarct was determined in each slice (Image J 1.45, Wayne Rasband, USA). The infarct volume was calculated by multiplying the sum of the area by the distance between each section. To account for differential shrinkage resulting from tissue processing, the infarct sizes were measured as follows: corrected injury volume = (measured bilateral hemisphere volume − injury volume)/bilateral hemisphere volume.

2.6. Luxol Fast Blue-Cresyl Echt Violet Stain. Brain sections were dehydrated with 75% alcohol and subsequently incubated in Luxol fast blue stain solution at 25°C for 24 h. Sections were then washed with distilled water and quickly dipped in 0.05% lithium carbonate and 70% regent alcohol for gray and white matter differentiation. The sections were then incubated in 0.1% cresyl echt violet stain for 3 min, dipped in 70% regent alcohol 5–10 times, dehydrated through three changes of absolute alcohol, and finally mounted with Permount medium (Thermo Fisher Scientific, USA). The white matter bundles were examined using light microscopy (Zeiss Axio Imager A2, Germany).

2.7. Immunohistochemistry. Brain samples were harvested and kept in 4% paraformaldehyde for 24 h and immersed in 30% sucrose for 3-4 days at 4°C. After cryoprotection in 30% sucrose, the brains were rapidly frozen in isopentane and stored at −80°C. Twenty micrometer cryostat sections at the level of the thalamus (bregma −3.3 mm) according to a stereotaxic atlas [15] were processed for immunohistochemistry. Immunohistochemistry analyses were performed with the UltraVision Quanto Detection System HRP DAB kit (Thermo Fisher Scientific, USA). The primary antibodies utilized were rabbit anti-GFAP antibody (glial fibrillary acidic protein, Santa Cruz Biotechnology, USA, 1 : 200 dilution), anti-VEGF (vascular endothelial growth factor, Millipore Corporation, USA, 1 : 400), and anti-MBP (myelin basic protein, Santa Cruz Biotechnology, USA, 1 : 200). The secondary antibodies utilized were biotinylated goat anti-mouse IgG and goat anti-rabbit IgG (Thermo Fisher Scientific, USA, 1 : 400 dilution). The results were observed using the Leica vertical microscope.

3. Results

3.1. Locomotor Behavior following MCA Occlusion. The locomotor behavior of the animals was tested on the 1st, 7th, or 14th day after surgery, depending on the group to which the rats had been assigned. On the first day after surgery, rats consistently bent their bodies to the side contralateral to that of the damaged brain hemisphere during the postural hang reflex test (Figure 2(a)). In the open field test, the 1-day rats were still able to move, though this movement was restricted to a circular pattern towards the side contralateral to that of the damaged brain hemisphere (Figures 2(b) and 2(c)). Behavioral tests were conducted again on the 7th and 14th days following surgery for the remaining two groups. Though rats in the 7-day group no longer exhibited the contralateral circling behavior, their bodies still bent to the side contralateral to that of the damaged brain hemisphere in the tail suspension test at a rate of 70%. Rats in the 14-day group exhibited no significant differences in behavior from normal rats; though the alignment of their body axes had changed. Contralateral bending again occurred at a rate of 70%.

3.2. Analysis of Brain Mitochondrial Dehydrogenase Activity and Cerebral Infarct Area. TTC (2,3,5-triphenyltetrazolium chloride solution) is a colorless solution that undergoes a reduction reaction with dehydrogenase in the mitochondria of normal cells. After MCAo, no reaction was observed between TTC and mitochondrial dehydrogenase in the damaged brain tissue; therefore, the cerebral ischemic area appeared white after TTC staining (Figure 3(a)). In the 7-day group, the left and right hemispheres differed in size, with the damaged areas exhibiting signs of slight atrophy. In the 14-day postsurgery group, no white patches were observed; however, the morphology of the entire brain had been altered. The damaged areas were more severely atrophic, and the structures were more loosely connected than in the 7-day group. In the 1-day group, red-stained thalamic areas indicated that

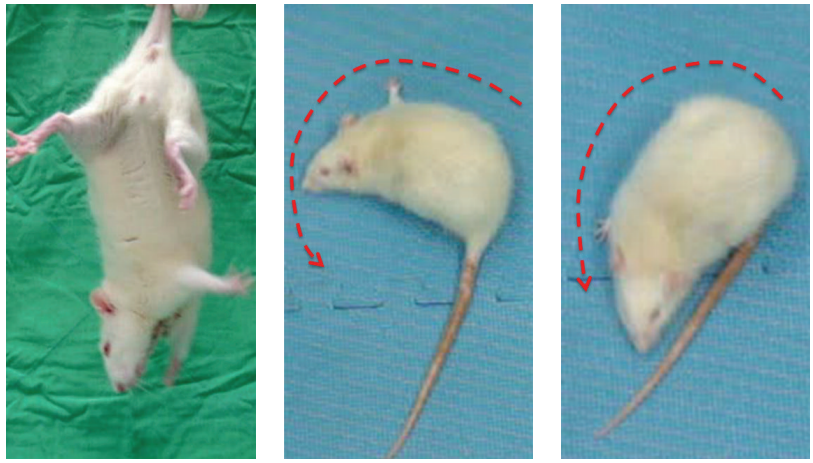

(a) (b) (c)

Figure 2: Confirmation of locomotor activity in rats on postsurgery day 1. (a) The body of the rat bent consistently to the side contralateral to that of the damaged brain hemisphere. (b, c) The rat could only circle to the side contralateral to that of the damaged brain hemisphere.

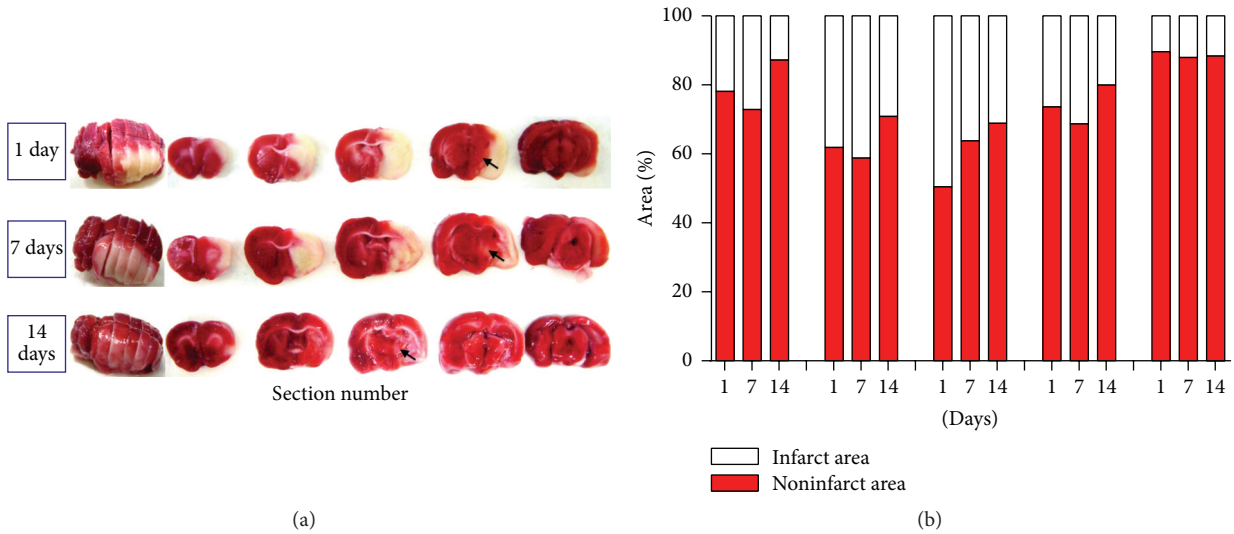

(a) (b)

Figure 3: Results of 2,3,5-triphenyltetrazolium chloride staining and calculation of the infract area. (a) Results of 2,3,5-triphenyltetrazolium chloride staining in the 1-day, 7-day, and 14-day groups. The arrow indicates the thalamus. (b) Quantification of the staining results and percentage of cerebral infarct area. Infarction was most severe at 7 days after surgery.

these regions had not sustained any damage; however, analysis of the remaining groups indicated that white areas had appeared by the 7th day, suggesting changes to the morphology of neurons in the thalamus. Analysis of rat brain sections using Image J software revealed that the area of infarction was most severe at the 7th day after the surgery (Figure 3(b)).

3.3. Functional Manifestation of Brain Nissl Bodies and Myelin. Luxol fast blue staining is commonly used to identify the myelin coating of neural axons. Myelin exhibits a blue color after staining, while other regions remain transparent. Cresyl echt violet stain is used to identify nerve cells and Nissl bodies, which exhibit a magenta color. On days 1 and 14 after MCAo surgery, brain sections were stained with Luxol fast blue and cresyl echt violet (Figure 4). On day 1 after surgery, the myelin of the brain regions supplied by the MCA, including the putamen, had degenerated completely even though the nerve cells themselves remained. At this stage, no change was observed in the thalamus; both myelin and nerve cells were present. Samples taken from rats euthanized on the 14th day after surgery also exhibited an absence of myelin in the brain regions supplied by the MCA.

3.4. Immunohistochemistry. Staining results at days 1 and 14 after surgery revealed that the levels of glial fibrillary acidic protein (GFAP) (Figure 5) and vascular endothelial growth factor (VEGF) (Figure 6) increased remarkably in the damaged areas. Gliosis was observed in both the 1-day and 14-day

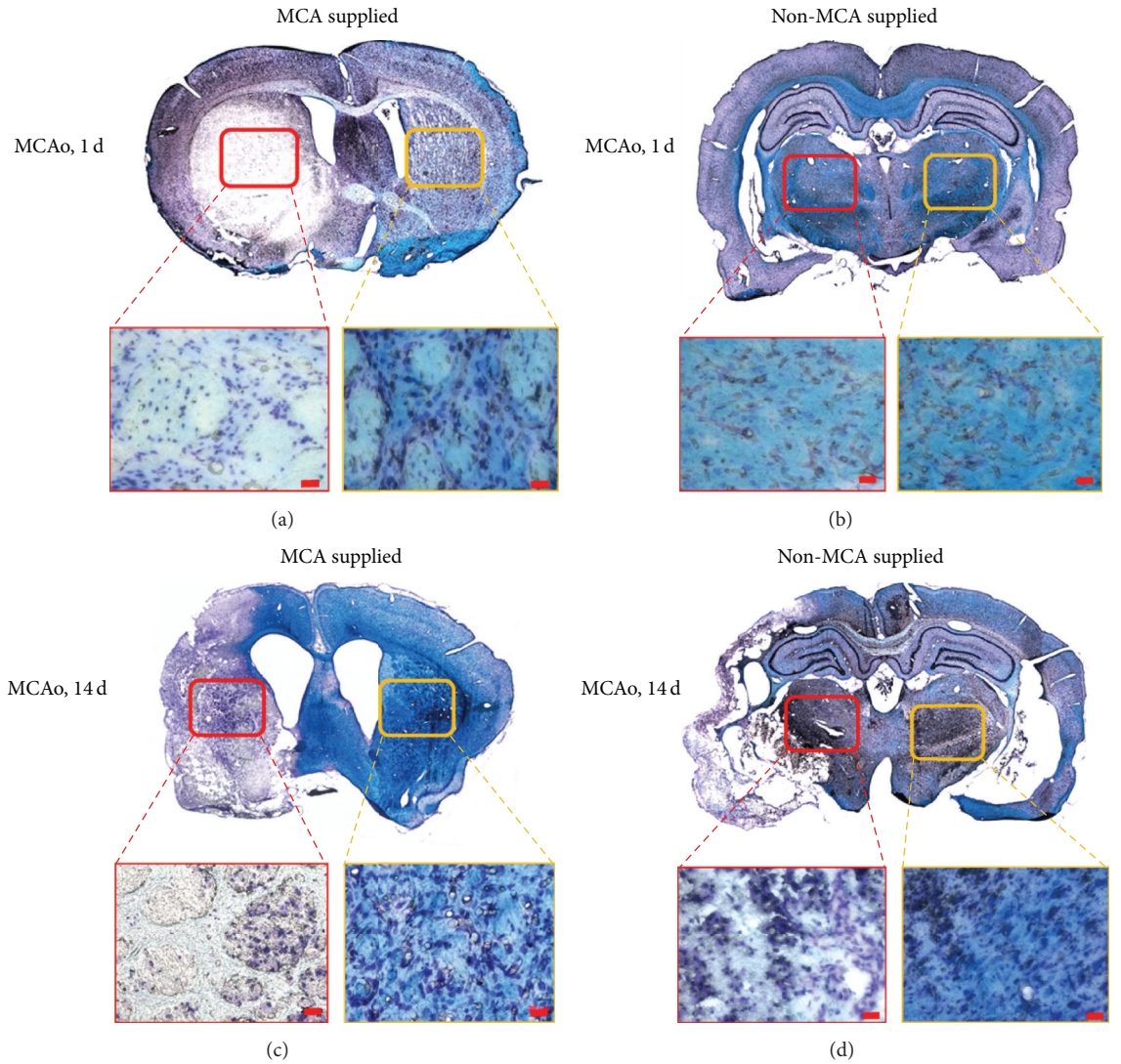

Figure 4: Luxol fast blue and cresyl echt violet staining at 1 and 14 days after MCAo. (a, b) Day 1 after MCAo. (c, d) Day 14 after MCAo. (a, c) Images of the brain indicating areas supplied by the MCA. The red box designates the putamen on the damaged side, and the yellow box designates the putamen on the control side. (b, d) Images of brain areas not supplied by the MCA. The red box designates the thalamic nuclei on the damaged side, and the yellow box designates the thalamic nuclei on the control side. The amount of myelin (blue dots) in the putamen on the damaged side exhibited a decrease in day 1 and day 14 groups. No difference was observed in the amount of thalamic myelin between the affected and control sides in day 1 group. In the 14-day group, the amount of myelin in the thalamus was remarkably reduced on the damaged side compared to the control side, indicating the occurrence of transneuronal degeneration. MCAo: middle cerebral artery occlusion.

groups. Astrocyte proliferation also increased greatly in the damaged areas in these groups (Figure 5). However, certain areas, such as the thalamic nucleus in charge of movement, remained unaffected between day 1 and day 14 after surgery. Marked positive staining for myelin basic protein (MBP) (Figure 7) was observed at day 14 after surgery.

4. Discussion

MCAo in rats is commonly used to model focal brain ischemia in humans. Studies have indicated that stroke survivors usually exhibit chronic disability that tends to worsen with age. In the present study, no changes were observed in the anterolateral region of the thalamus following MCAo. Contralateral circling and bending were also observed in the 1-day group, indicating that MCAo did not affect the animals' ability to move. Previous research has also revealed that damage to the nigrostriatal system following MCAo causes laboratory animals to exhibit circling behavior [16]. However, the authors of this study reported changes in motor function over time. Therefore, the movement behavior test and evaluation proposed by Bederson utilized in the present study may be ill-suited to observing the long-term postoperative behavioral patterns of rats [13].

In addition, TTC staining revealed that the cerebral ischemic area was larger in the 7-day postsurgery group than

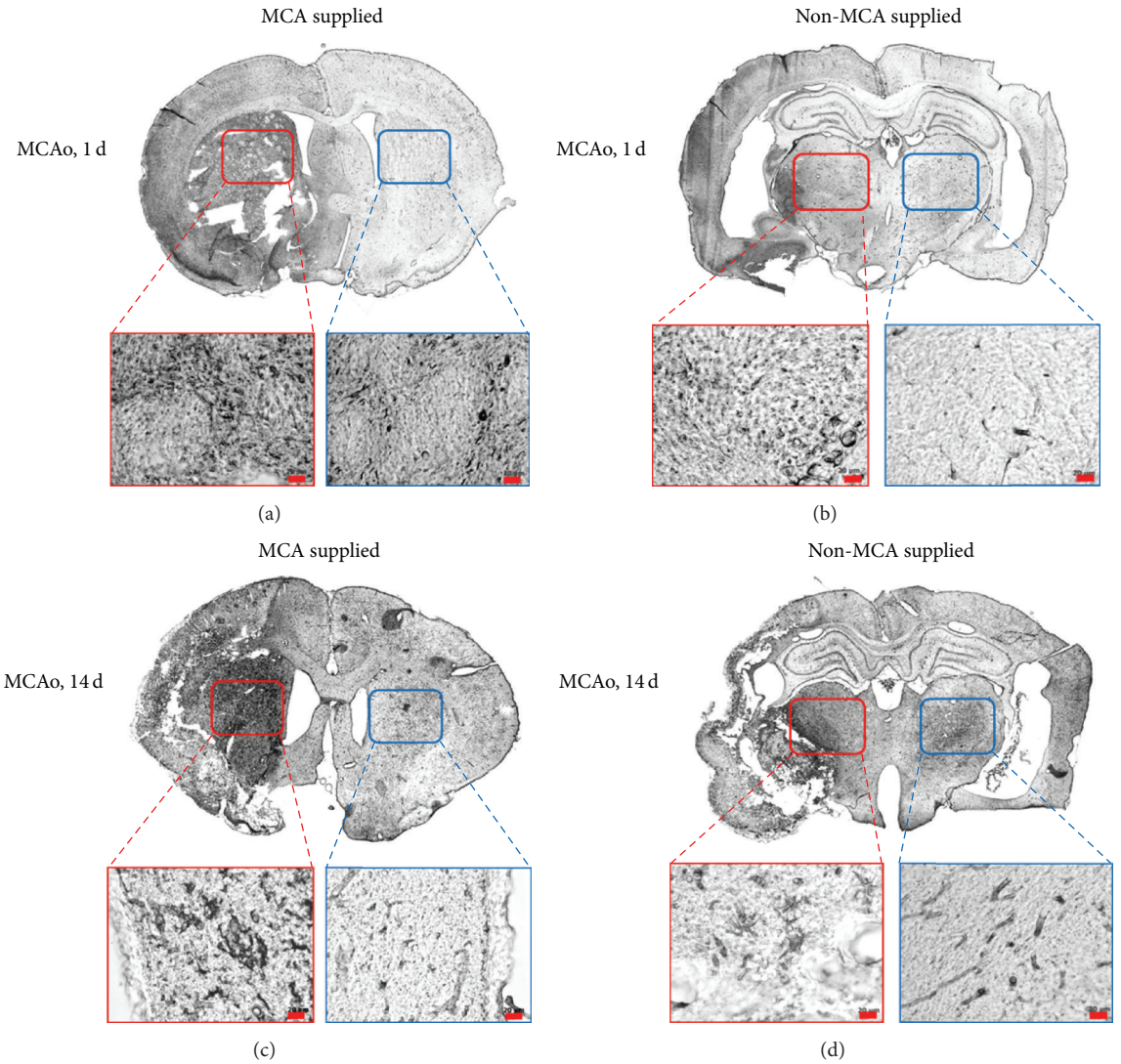

Figure 5: Expression of glial fibrillary acidic protein (GFAP) on day 1 and day 14 after MCAo. (a, b) Day 1. (c, d) Day 14. (a, c) Images of the brain regions supplied by the MCA. The red box designates the putamen on the damaged side. The blue box designates the putamen on the control side. (b, d) Images of brain areas not supplied by the MCA. The red box designates the thalamic nuclei on the damaged side. The blue box designates the thalamic nuclei on the control side. Damaged areas stained positive for GFAP in the 1-day group. GFAP was expressed in the putamen, but not in the thalamus, indicating that neurons in the thalamic regions were not affected at 1 day after surgery. Damaged areas remained positive for GFAP in the 14-day group, though additional staining was also observed in the thalamic region, indicating that transneuronal degeneration and subsequent increases in GFAP expression occurred in the thalamus despite not being directly supplied by the MCA. MCA: middle cerebral artery.

in the remaining groups. Mitochondrial activity also seemed to recover by the 14th day after MCAo surgery, though the brains of rats in the 14-day group were more atrophic than those of the 1-day and 7-day groups. Though TTC staining remains the most common method used for determining the success of cerebral ischemia surgery due to its effectiveness and convenience [17], research has indicated that the results of TTC staining may be affected by the length of occlusion time [18].

Luxol fast blue and cresyl violet staining revealed that the tissue structure of the thalamus was loose in the 14-day group when compared to that of the remaining groups and that the myelin sheath in the same region was remarkably reduced when compared to that of the 1-day group. These results confirm that the thalamic region was affected indirectly by the MCAo, and the self-regeneration might occur by the 14th day after surgery.

In the central nervous system, astrocytes are relatively large glial cells with multiple functions that accumulate in areas where neurons have sustained damage. Glial cell proliferation and neuron loss in certain brain areas have been observed in a number of neurodegenerative disorders. Previous studies have reported widespread areas of necrosis 1 day following MCAo, with loose connective tissue forming

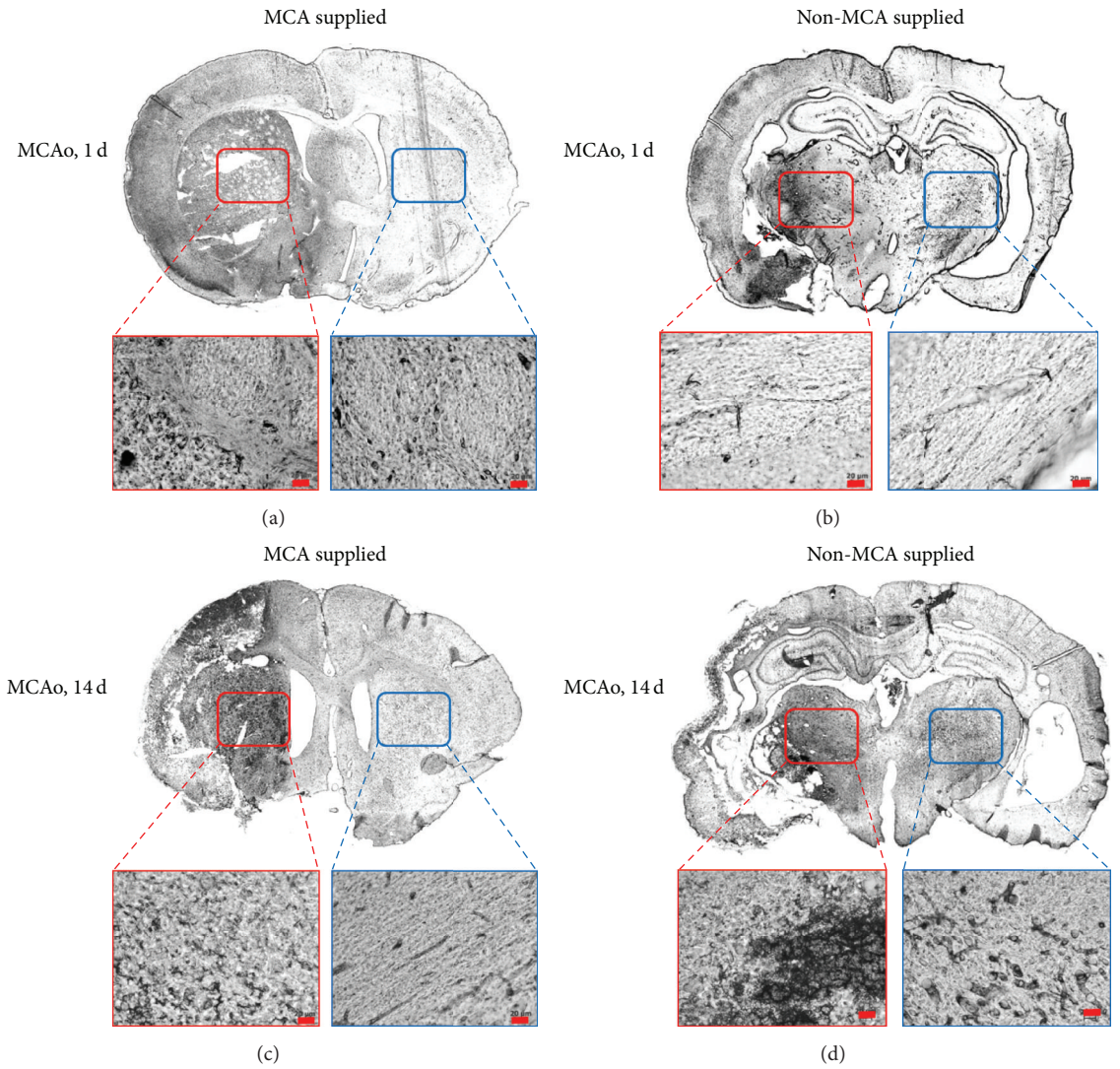

Figure 6: Expression of vascular endothelial growth factor (VEGF) on day 1 and day 14 after MCAo. (a, b) Day 1. (c, d) Day 14. (a, c) Images of the brain regions supplied by the MCA. The red box designates the putamen on the damaged side. The blue box designates the putamen on the control side. (b, d) Images of brain areas not supplied by the MCA. The red box designates the thalamic nuclei on the damaged side. The blue box designates the thalamic nuclei on the control side. Neurons in the damaged area stained positive for VEGF in the 1-day group, though differences in expression were observed in the thalamus and putamen. Staining results indicate that angiogenesis may have occurred in the damaged area 1 day following occlusion. In the 14-day group, neurons at the damaged site also stained positive for VEGF, though staining was also observed in the thalamus—a result remarkably different from that observed in the 1-day group. Staining results indicate that, by 14 days after surgery, levels of VEGF expression and angiogenesis may have increased in the thalamus. MCAo: middle cerebral artery occlusion.

a matrix border along the site of the infraction after the occlusion has been in place for 7–14 days. Moreover, the ischemic area contained a large number of astrocytes expressing GFAP [19]. The immunohistochemical staining results of the present study align with these previously published results.

Brain tissue is very sensitive to ischemia and anoxia. Following cerebral ischemia, the neuronal damage is relatively restricted in mild cases. However, when complete and persistent ischemia occurs, various neurons, glial cells, and endothelial cells inside the ischemic region undergo necrosis. After MCAo, brain tissue in the central necrotic area and surrounding ischemic penumbra become compromised. In the necrotic area, brain cells die due to complete ischemia. However, evidence from the present study seems to suggest that collateral circulation continues to supply some amount of blood to the ischemic penumbra, given the amount of viable neurons. If circulation can be restored rapidly enough to sustain brain metabolism, nerve cells may survive and recover their function. Therefore, protection of these irreversibly damaged neurons is the key to treatment of acute cerebral infarction.

The present study successfully established a rat model of cerebral ischemia and further explored long-term alterations in neural structure after cerebral infarction. VEGF was highly expressed in the damaged areas of the brain in both the 1-day and 14-day groups, indicating the occurrence of angiogenesis.

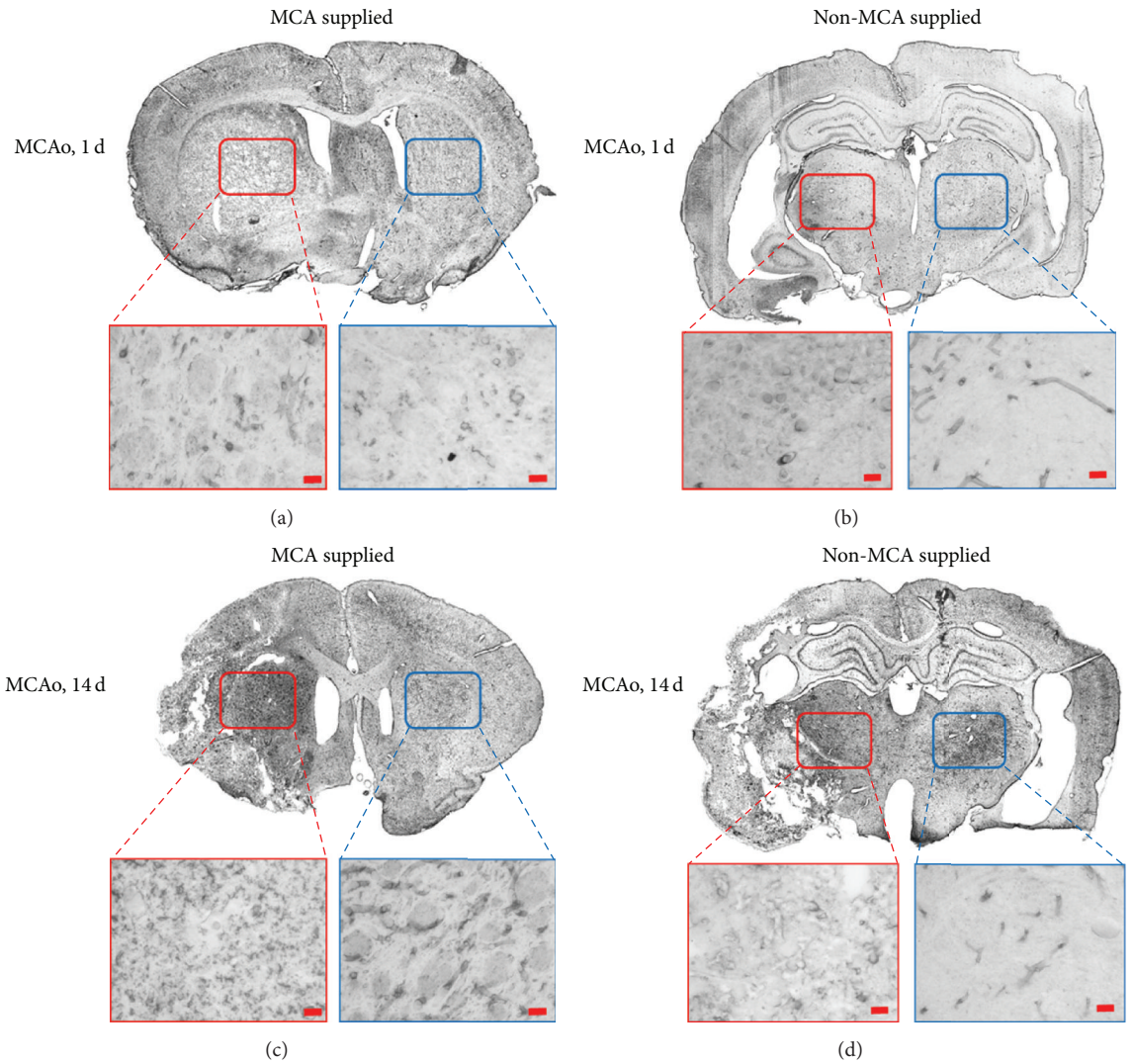

Figure 7: Expression of myelin basic protein (MBP) on the first day after MCAo. Staining results in (a, b) day 1 and (c, d) day 14 groups. (a, c) Images of the brain regions supplied by the MCA. The red box designates the putamen on the damaged side. The blue box designates the putamen on the control side. (b, d) Images of brain areas not supplied by the MCA. The red box designates the thalamic nuclei on the damaged side. The blue box designates the thalamic nuclei on the control side. No expression of MBP was observed at the damaged site in the 1-day group, and there were no differences in MBP expression between the putamen and thalamus. In the 14-day group, MBP expression was detected both at the damage site and in the thalamus. Again, no differences were observed between the putamen and thalamus with regard to MBP expression. The staining results indicate that levels of MBP expression increased by the 14th day following occlusion and that remyelination may have occurred at the damaged site.

Previous studies have documented the neurotrophic and neuroprotective effects of VEGF, in addition to its potential role in stimulating adult neurogenesis [20]. The expression of GFAP is also related to the rehabilitation process following brain injury. Therefore, the interaction between GFAP and VEGF may provide an avenue for future strategies for the treatment of chronic cerebral infarction.

Furthermore, the relative levels of MBP provide more insight into changes that occur following MCAo, as increased expression of MBP indicates remyelination while reduced expression indicates demyelination. In the present study, marked increases in MBP expression were observed in the 14-day group when compared to levels of the 1-day group, indicating the potential involvement of MBP in the proliferation of oligodendrocyte progenitor cells [21]. The increased expression of GFAP, VEGF, and MBP may help the brain to recover temporarily and offset its loss of function and thus may be the key to future treatment for patients who have experienced a stroke.

5. Conclusions

The results of the present study provide evidence of myelin loss in the thalamus, changes in VEGF, and glial responses following middle cerebral artery occlusion in a rate model of ischemia, indicative of neuronal degeneration. In addition,

the increased expression of GFAP and VEGF is observed in the damaged and surrounding areas and may help the brain to recover temporarily and offset losses of function. The rat model for cerebral ischemic stroke established in the present study may be utilized in future research regarding the prevention of transneuronal degeneration before irreversible damage occurs and aid in the development of new treatment strategies for patients with stroke.

Competing Interests

The authors declare that there are no competing interests regarding the publication of this paper.

Authors' Contributions

Juin-Hong Cherng and Ming-Lun Hsu contributed equally to this paper.

Acknowledgments

This study was supported by grants (101F195CY15) from the Cheng-Hsin/Yang-Ming corporate program.

References

[1] S. H. Appel, R. G. Smith, and W. D. Le, "Immune-mediated cell death in neurodegenerative disease," *Advances in Neurology*, vol. 69, pp. 153–159, 1996.

[2] J. Hardy, "Pathways to primary neurodegenerative disease," *Annals of the New York Academy of Sciences*, vol. 924, pp. 29–34, 2000.

[3] C. Soto, "Unfolding the role of protein misfolding in neurodegenerative diseases," *Nature Reviews Neuroscience*, vol. 4, no. 1, pp. 49–60, 2003.

[4] J. H. Su, G. M. Deng, and C. W. Cotman, "Transneuronal degeneration in the spread of Alzheimer's disease pathology: immunohistochemical evidence for the transmission of tau hyperphosphorylation," *Neurobiology of Disease*, vol. 4, no. 5, pp. 365–375, 1997.

[5] L. Stefanis and R. E. Burke, "Transneuronal degeneration in substantia nigra pars reticulata following striatal excitotoxic injury in adult rat: time-course, distribution and morphology of cell death," *Neuroscience*, vol. 74, no. 4, pp. 997–1008, 1996.

[6] A. Eisen and M. Weber, "The motor cortex and amyotrophic lateral sclerosis," *Muscle & Nerve*, vol. 24, no. 4, pp. 564–573, 2001.

[7] E. Knyihár-Csillik, P. Rakic, and B. Csillik, "Transneuronal degeneration in the Rolando substance of the primate spinal cord evoked by axotomy-induced transganglionic degenerative atrophy of central primary sensory terminals," *Cell and Tissue Research*, vol. 258, no. 3, pp. 515–525, 1989.

[8] M. Saji and D. J. Reis, "Delayed transneuronal death of substantia nigra neurons prevented by γ-aminobutyric acid agonist," *Science*, vol. 235, no. 4784, pp. 66–69, 1987.

[9] K. Sakatani, H. Iizuka, and W. Young, "Somatosensory evoked potentials in rat cerebral cortex before and after middle cerebral artery occlusion," *Stroke*, vol. 21, no. 1, pp. 124–132, 1990.

[10] J. Zhang, Y. Zhang, S. Xing, Z. Liang, and J. Zeng, "Secondary neurodegeneration in remote regions after focal cerebral infarction: a new target for stroke management?" *Stroke*, vol. 43, no. 6, pp. 1700–1705, 2012.

[11] R. Hata, G. Mies, C. Wiessner et al., "A reproducible model of middle cerebral artery occlusion in mice: hemodynamic, biochemical, and magnetic resonance imaging," *Journal of Cerebral Blood Flow and Metabolism*, vol. 18, pp. 367–375, 1998.

[12] K. Uluç, A. Miranpuri, G. C. Kujoth, E. Aktüre, and M. K. Başkaya, "Focal cerebral ischemia model by endovascular suture occlusion of the middle cerebral artery in the rat," *Journal of Visualized Experiments*, no. 48, article e1978, 2011.

[13] J. B. Bederson, L. H. Pitts, M. Tsuji, M. C. Nishimura, R. L. Davis, and H. Bartkowski, "Rat middle cerebral artery occlusion: evaluation of the model and development of a neurologic examination," *Stroke*, vol. 17, no. 3, pp. 472–476, 1986.

[14] I. Q. Whishaw, *The Septohippocampal System and Path Integration*, Springer, New York, NY, USA, 2000.

[15] G. Paxinos and C. Watson, *The Rat Brain in Stereotaxic Coordinates*, Academic Press, San Diego, Calif, USA, 2nd edition, 1986.

[16] Y. Wang-Fischer, *Manual of Stroke Models in Rats*, CRC Press, Boca Raton, Fla, USA, 2009.

[17] J. B. Bederson, L. H. Pitts, S. M. Germano, M. C. Nishimura, R. L. Davis, and H. M. Bartkowski, "Evaluation of 2,3,5-triphenyltetrazolium chloride as a stain for detection and quantification of experimental cerebral infarction in rats," *Stroke*, vol. 17, no. 6, pp. 1304–1308, 1986.

[18] A. Popp, N. Jaenisch, O. W. Witte, and C. Frahm, "Identification of ischemic regions in a rat model of stroke," *PLoS ONE*, vol. 4, no. 3, Article ID e4764, pp. 1–8, 2009.

[19] U. Dirnagl, C. Iadecola, and M. A. Moskowitz, "Pathobiology of ischaemic stroke: an integrated view," *Trends in Neurosciences*, vol. 22, no. 9, pp. 391–397, 1999.

[20] M. Mărgăritescu, D. Pirici, and C. Mărgăritescu, "VEGF expression in human brain tissue after acute ischemic stroke," *Romanian Journal of Morphology and Embryology*, vol. 52, no. 4, pp. 1283–1292, 2011.

[21] Y. Chen, Q. Yi, G. Liu, X. Shen, L. Xuan, and Y. Tian, "Cerebral white matter injury and damage to myelin sheath following whole-brain ischemia," *Brain Research*, vol. 1495, pp. 11–17, 2013.

Hindawi Publishing Corporation
BioMed Research International
Volume 2016, Article ID 2518626, 8 pages
http://dx.doi.org/10.1155/2016/2518626

Research Article

Beneficial Effect of Short Pretransplant Period of Hypothermic Pulsatile Perfusion of the Warm-Ischemic Kidney after Cold Storage: Experimental Study

Alberto Lázaro,[1] Blanca Humanes,[1] Juan Carlos Jado,[1] Marina Mojena,[1] María Ángeles González-Nicolás,[1] Juan Francisco del Cañizo,[2,3] Alberto Tejedor,[1,4] and Enrique Lledó-García[5]

[1]*Renal Physiopathology Laboratory, Department of Nephrology, Instituto de Investigación Sanitaria Gregorio Marañón (IiSGM), Hospital General Universitario Gregorio Marañón, 28007 Madrid, Spain*
[2]*Medicine and Surgery Unit, IiSGM, Hospital General Universitario Gregorio Marañón, 28007 Madrid, Spain*
[3]*Department of Surgery, Faculty of Medicine, Complutense University of Madrid, 28040 Madrid, Spain*
[4]*Department of Medicine, Faculty of Medicine, Complutense University of Madrid, 28040 Madrid, Spain*
[5]*Urology Department, IiSGM, Hospital General Universitario Gregorio Marañón, 28007 Madrid, Spain*

Correspondence should be addressed to Alberto Lázaro; alazaro10@gmail.com

Received 17 March 2016; Revised 10 June 2016; Accepted 10 July 2016

Academic Editor: Andrea Vecchione

Warm ischemia (WI) produces a significant deleterious effect in potential kidney grafts. Hypothermic machine perfusion (HMP) seems to improve immediate graft function after transplant. Our aim was to analyze the effect of short pretransplant periods of pulsatile HMP on histology and renal injury in warm-ischemic kidneys. Twelve minipigs were used. WI was achieved in the right kidney by applying a vascular clamp for 45 min. After nephrectomy, autotransplant was performed following one of two strategies: cold storage of the kidneys or cold storage combined with perfusion in pulsatile HMP. The graft was removed early to study renal morphology, inflammation (fibrosis), and apoptosis. Proinflammatory activity and fibrosis were less pronounced after cold storage of the kidneys with HMP than after cold storage only. The use of HMP also decreased apoptosis compared with cold storage only. The detrimental effects on cells of an initial and prolonged period of WI seem to improve with a preservation protocol that includes a short period of pulsatile HMP after cold storage and immediately before the transplant, in comparison with cold storage only.

1. Introduction

Renal graft injury secondary to warm and/or cold ischemia is a critical problem after transplantation. Some authors have associated this event with medium- to long-term graft and patient survival [1–3]. The availability of expanded criteria donor kidneys to date has increased significantly and, consequently, research in this area is of paramount importance if we are to reduce delayed graft function after the transplant. Additionally, it is very important to establish uniform criteria for acceptance or rejection of these kidneys [4].

Preservation techniques play a key role in the success of organ transplantation. Cold storage has traditionally been the most prevalent technique, although, in the setting of warm or prolonged cold ischemia and expanded criteria donor kidneys, hypothermic machine perfusion (HMP) is a useful technique that is also protective for the graft [5, 6], both in preconditioning of the organs and when attempting to obtain hydrodynamic or biochemical information from them. Brief in-house machine perfusion after preceding cold storage (hypothermic reconditioning) has been proposed as a convenient tool for improving organ graft function in livers and kidneys [7]. Thus, in porcine kidney transplants, a two-hour period of pulsatile oxygenated HMP was shown to be as effective as continuous perfusion starting from the time of organ retrieval [8]. Few data have been reported on the

potential positive effect of clinical application of HMP after cold storage or on the duration of perfusion.

This paper reviews the comparative benefits of two protocols for preservation of warm-ischemic kidneys: a single cold storage period and a cold storage period combined with one hour of HMP before the transplant.

2. Materials and Methods

2.1. Pulsatile Machine Perfusion. The perfusion system used was an in-house vacuum pump model controlled by a computerized console [9–11]. Briefly, the pumping device consists of a rigid external chamber (transparent methacrylate) with an elastic internal membrane (polyurethane), which generates a human-like pulsatile waveform with alternative systolic and diastolic pulses by either opening or closing valves. This is achieved by applying a vacuum via a source controlled by a console in the rigid chamber, thus forcing the expansion of the tubular elastic chamber. At a given time, the console stops the vacuum connecting the rigid chamber with the atmosphere, thus inducing elastic recovery, which generates the perfusion impulse. Two valves applied on the input and output tubes (controlled by the console) ensure that the pulses direct the flow appropriately.

Other components of the system include a cool generator (Cooling Frigedor, Lambra S.L., Madrid, Spain), an ultrasonic flowmeter T-108 (Transonic Systems, Inc., Ithaca, NY, USA), and a disposable pressure transducer (Transpac L978-39, Abbot CCS, Dublin, Ireland). The flowmeter measures the flow and the pressure transducer measures the pressure [9–11].

All the information is stored and regulated in real time using a personal computer equipped with a Keithley MetraByte DAS-1600 input-output A/D card. Our in-house electronic interface contains input amplifiers and output circuits to adapt signal levels to the A/D card [9–11].

2.2. Animals. We used 12 minipigs with an average weight of 40 kg. All the procedures were approved by the Ethics Committee on Animal Experimentation from the Instituto de Investigación Sanitaria Gregorio Marañón, Hospital General Universitario Gregorio Marañón, and animals were cared for in accordance with applicable legal regulations in Directive 2010/63/EU and RD 53/2013, on the protection of animals used for experimentation and other scientific purposes.

After laparotomy and isolation of the kidney, warm ischemia was accomplished by applying a vascular arterial clamp to the right kidney for 45 min, with subsequent nephrectomy and cold storage of the organs for 24 h in UW solution. The kidneys were then autotransplanted ($n = 6$). A second group of kidneys ($n = 6$) underwent the same protocol, but the kidneys were perfused immediately before the autotransplant in a pulsatile HMP machine. Perfusion was performed at 4°C with a pressure of 40 mmHg and maintained for 60 minutes with Belzer solution. The kidney was reperfused after the autotransplant, and the graft was removed 60 min later. Tissue samples were obtained from the retrieved organ and stored for subsequent study.

The contralateral kidney (left kidney) of each animal in the two previous groups was removed immediately before the autotransplant and used as a control ($n = 12$, healthy kidney).

2.3. Histopathological Studies. Sections of kidneys were fixed in 4% paraformaldehyde, dehydrated in graded concentrations of alcohol, and embedded in paraffin. Kidney blocks were cut into 4 μm sections and stained with hematoxylin-eosin (Sigma-Aldrich, St. Louis, MO, USA). The kidney injury score was calculated blind by two independent pathologists using a previously described semiquantitative index [12].

2.4. Immunohistochemistry. Immunohistochemistry of cleaved caspase-3 and TGF-β1 was carried out in paraffin-embedded 4 μm thick kidney sections as described previously [12]. After quenching of endogenous peroxidase activity, sections were incubated with a polyclonal rabbit anti-cleaved caspase-3 (Asp175) (1 : 50; Cell Signaling Technology, Inc., Beverly, MA, USA) and a polyclonal anti-transforming growth factor-β1 (TGF-β1) antibody (Santa Cruz Biotechnology, Inc., Beverly, MA, USA, dilution 1 : 100) overnight at 4°C in a humid atmosphere. Thereafter, sections were processed using the Vectastain Elite ABC Kit (Vector Labs, Burlingame, CA, USA), following the manufacturer's protocol. Immunostaining was performed with 3,3′-diaminobenzidine (DAB) (Sigma-Aldrich), and sections were counterstained with Mayer's hematoxylin (Sigma-Aldrich). Negative controls included incubation with a nonspecific Ig of the same isotype as the primary antibody. The surface labelled by the antibodies was evaluated using quantitative image analysis as previously described [13].

2.5. Determination of the Tubular Fibrosis: Sirius Red Staining. Collagen fibers were measured as an index of fibrosis by staining with Sirius Red (Sigma-Aldrich). Four-micrometer sections were dewaxed and rehydrated in decreasing concentrations of alcohol. After rinsing with water, sections were stained with Sirius Red (0.5 g dissolved in 500 mL of saturated aqueous solution of picric acid) for one hour. Thereafter, sections were washed with acidified water and vigorously shaken to remove the acidified water. Sections were then dehydrated using increasing concentrations of alcohol, cleared in xylene, and finally mounted in DPX (EMS, Washington, PA, USA) for microscopy. The staining score was calculated blind by two independent pathologists using the following semiquantitative scale: 0, none; 1, staining between 0 and 25%; 2, staining between 25 and 50%; 3, staining between 50 and 75%; 4, staining >75%.

2.6. In Situ Detection of Apoptosis. Terminal deoxynucleotidyl transferase-mediated dUTP nick end labelling (TUNEL) in paraffin-embedded kidney tissue sections was performed using the in situ Fluorescein FragEL DNA Fragmentation Detection Kit (Calbiochem, San Diego, CA, USA) following the manufacturer's protocol. The TUNEL-positive cells were visualized with a Leica-SP2 confocal microscope

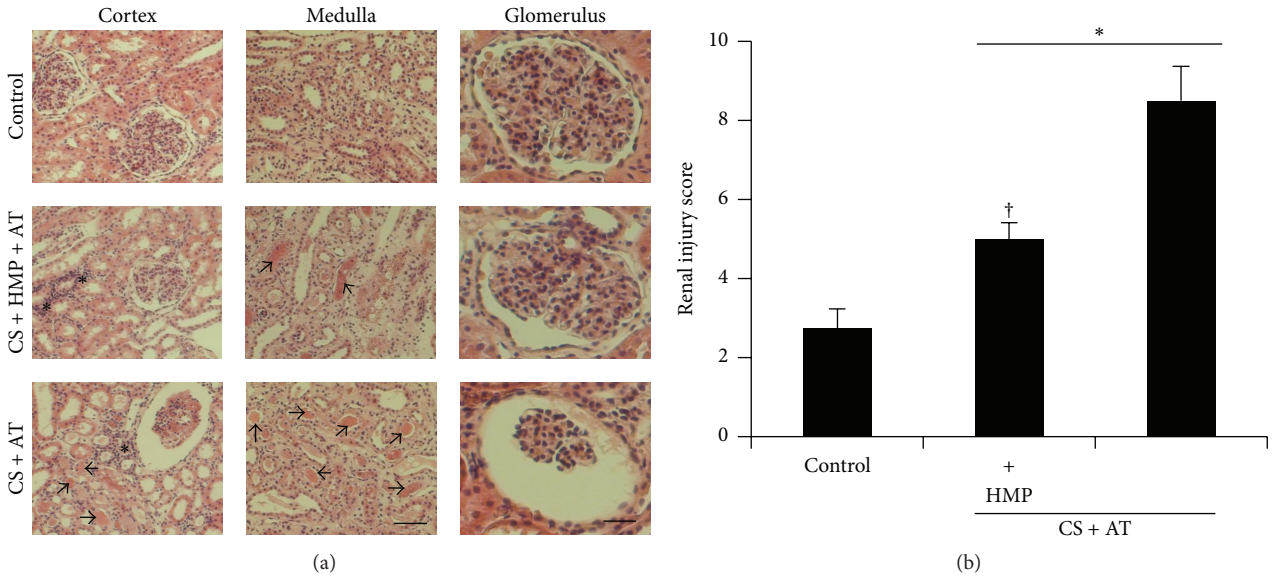

Figure 1: Renal injury is attenuated by the use of pulsatile hypothermic machine perfusion after cold storage. (a) Representative images of renal pathology (hematoxylin-eosin, magnifications ×20 and ×40). Note the signs of inflammation (asterisks) and hyaline casts (arrows) in the kidneys subjected only to cold storage compared with those that also received the perfusion by the use of pulsatile machine. The bar in the cortex or medulla pictures represents 100 μm while in glomerulus images it represents 50 μm. (b) Semiquantitative renal injury score. Results are expressed as mean ± SEM, $n = 6$–12 animals per group. $^{*}P < 0.05$ versus control group; $^{\dagger}P < 0.005$ versus cold storage group. CS: cold storage; HMP: hypothermic machine perfusion; AT: autotransplant.

(Leica Microsystems, Heidelberg, Germany). Various measurements of positive staining fluorescence were taken using Leica confocal software LCS-1537 (Leica Microsystems) in 10 nonoverlapping random fields viewed at ×20 magnification.

2.7. Statistical Analysis. Results are reported as mean ± SEM. Levene's test was used to test equality of variances. Variables with equal variances were studied using analysis of variance. The Kruskal-Wallis test was performed if variances were not equal. Differences between groups were deemed statistically significant at $p < 0.05$. Tests were performed using SPSS 11.5 (SPSS, Chicago, IL, USA).

3. Results

3.1. Kidney Damage. In both protocols, warm ischemia followed by nephrectomy and cold storage of the kidneys before the autotransplant resulted in significant histological renal injury in comparison with the control kidneys (Figure 1). Structural renal damage was characterized by tubular necrosis, mesangial expansion, tubular dilation, interstitial fibrosis, inflammation, and hyaline protein casts in renal tubules (Figure 1). HMP after cold storage decreased the degree of renal injury compared with cold storage only (Figure 1).

3.2. Activation of Apoptotic Mechanisms. Cold storage before the autotransplant was associated with high activation of cleaved caspase-3, the main executioner caspase in apoptotic pathways (Figure 2). However, the use of pulsatile HMP significantly decreased—but did not normalize—caspase-3 activation in comparison with the control kidneys (Figure 2). In addition, we confirmed these results by measuring cell death using the TUNEL assay. The number of apoptotic nuclei increased in kidneys preserved with cold storage only compared with the control kidneys (Figure 3), but the use of HMP significantly decreased the number of TUNEL-positive cells (Figure 3).

3.3. Renal Fibrosis. TGF-β is a proinflammatory and profibrotic cytokine that contributes to a variety of pathophysiological processes. It induces renal cells to produce extracellular matrix proteins leading to tubulointerstitial fibrosis and glomerulosclerosis, thus worsening kidney damage [14]. In the kidneys preserved with cold storage only, increased TGF-β1 levels were noted in renal tubules compared with the control kidneys (Figure 4). The use of pulsatile HMP significantly decreased kidney TGF-β1 levels (Figure 4).

These results correlated well with the extent of fibrosis measured by staining of collagen fibers with Sirius Red. As shown in Figure 5, increased presence of fibrosis was observed in kidneys preserved with cold storage only. The use of pulsatile HMP reduced these levels.

4. Discussion

Adequate preservation of renal allografts for transplantation is important for maintaining and improving transplant outcomes. There are two prevalent methods: HMP and static cold

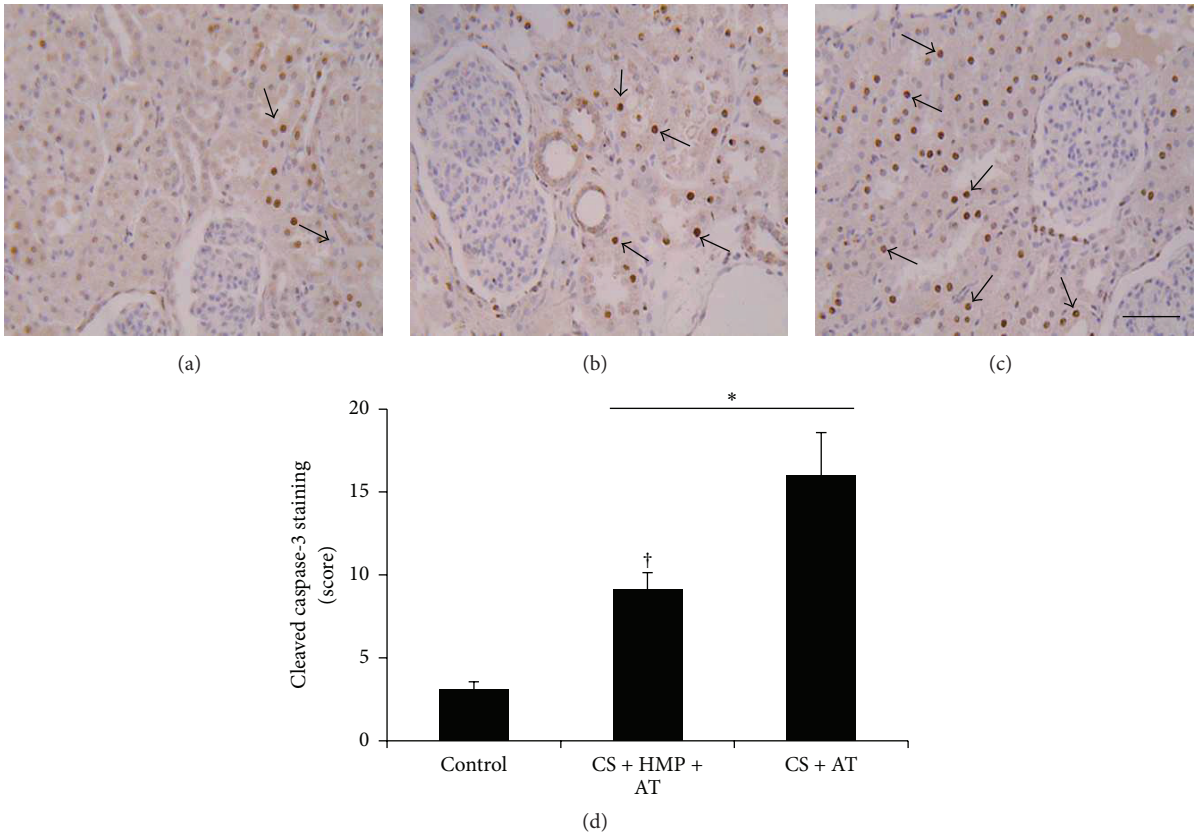

FIGURE 2: The use of pulsatile hypothermic machine perfusion after cold storage diminishes cleaved caspase-3 expression. Localization of active cleaved caspase-3 in kidney sections: (a) control group; (b) cold storage (CS) plus pulsatile machine (HMP) and subsequent transplant (AT) group; (c) cold storage (CS) and subsequent transplant (AT) group. Note that renal tubules are the main site of caspase-3 activation (arrows, magnification ×20). (d) Semiquantification of cleaved caspase-3 immunostaining in renal cells. The use of pulsatile machine decreased but did not normalize caspase-3 activation. Data are represented as means ± SEM (n = 6–12 animals per group). $^{*}p < 0.05$ versus control group; $^{\dagger}p < 0.02$ versus cold storage plus autotransplant group. Bar: 100 μm.

storage. The preferred method of storage, however, remains controversial.

O'Callaghan et al. [15] performed a meta-analysis of the literature on the effect of HMP versus cold storage of kidney allografts on transplant outcomes. Eighteen studies were reviewed. In summary, the overall risk of delayed graft function was lower with HMP than with static cold storage (relative risk: 0.81; 95% confidence interval: 0.71 to 0.92; $p = 0.002$). There was no difference in the rate of primary nonfunction (relative risk: 1.15; 95% confidence interval: 0.46 to 2.90; $p = 0.767$). The authors concluded that HMP reduces delayed graft function compared with cold storage.

The role of HMP should also be evaluated when it is used as the only preservation technique or as a complementary preservation technique in suboptimal/expanded criteria kidneys. Brief in-house machine perfusion after preceding cold storage (hypothermic reconditioning) has been proposed as a convenient tool for improvement of liver and kidney graft function [7, 16]. In porcine kidney transplants, a two-hour period of reconditioning by pulsatile oxygenated HMP was shown to be as effective as continuous perfusion starting from the time of organ retrieval [8]. Subsequent clinical application of HMP after cold storage produced the first clinical evidence of a beneficial effect of the technique [17]. Our group had already reported preliminary results on the theoretical advantages of HMP over cold storage, concluding that short periods of HMP after cold ischemia for warm-ischemic kidneys immediately before the transplant would be beneficial [18].

However, the importance of the duration of HMP prior to transplantation remains open to debate, as does the importance of a pulsatile versus nonpulsatile model of waveform in the perfusion of the organ. We used an in-house HMP pump. The kidneys were perfused at 4°C under a constant flow using the pump to apply vacuum or atmospheric pressure sequentially in order to achieve a truly pulsatile wave (vacuum-powered tubular pump). We have already published our experimental results showing the advantages of this system over the classical roller pump. Nitric oxide values increased inversely with renal vascular resistance in kidneys perfused with a vacuum pump and Belzer solution [11].

The goal of any preservation technique before transplant-reperfusion is to overcome or attenuate the effects of ischemic rewarming injury, which is one of the main risk factors

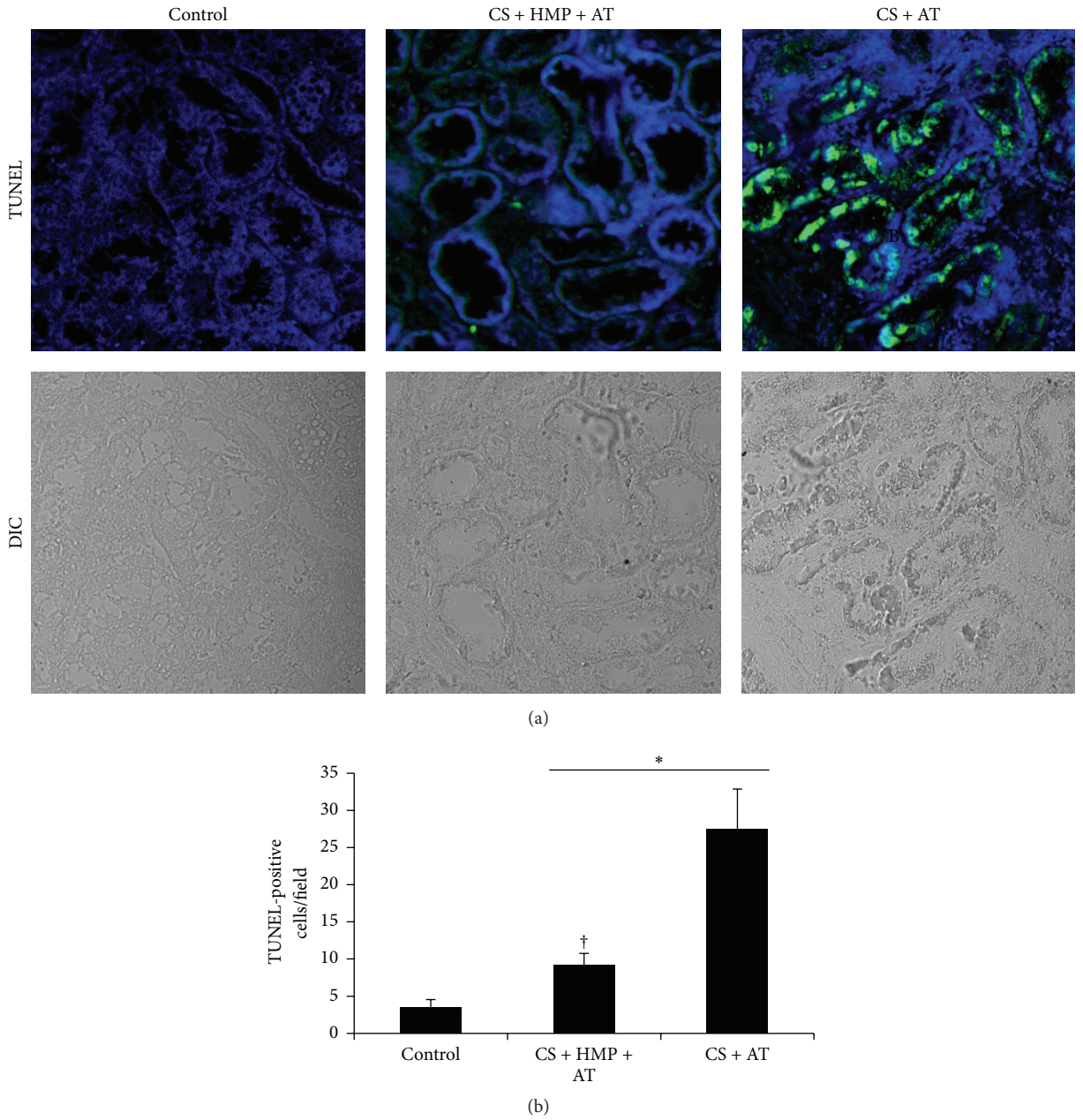

Figure 3: The use of pulsatile hypothermic machine perfusion after cold storage decreases tubular cell apoptosis. (a) Photomicrographs of terminal deoxynucleotidyl transferase- (tdT-) mediated dUTP nick end labelling (TUNEL) staining in the kidneys from control group; cold storage (CS) plus pulsatile machine (HMP) and subsequent transplant (AT) group and cold storage (CS) and subsequent transplant (AT) group. Green fluorescent staining indicates TUNEL-positive nuclei, and blue staining (4,6-diamidino-2-phenylindoles, DAPI) represents all nuclei in the sample (magnification ×40). (b) Quantification of TUNEL staining. Results are expressed as mean ± SEM (n = 6–12 animals per group). $^{*}p < 0.01$ versus control group; $^{\dagger}p < 0.05$ versus cold storage plus autotransplant group.

for acute kidney failure after transplantation and for long-term graft dysfunction. Renal reperfusion induces both microvascular and mitochondrial dysfunction, which are also evident in cultures of kidney cells after cold ischemia and reperfusion [19, 20]. Initial warm ischemia is an insult to the kidney that significantly affects cell and organ viability [21]. In comparison with cold storage only, cold storage combined with HMP can reduce the expression of inflammatory markers. In addition, HMP has been shown to reduce the inflammatory reaction by downregulating the expression of matrix metalloproteinase-9, which may be the mechanism of kidney protection in ischemia/reperfusion injury [22]. In our

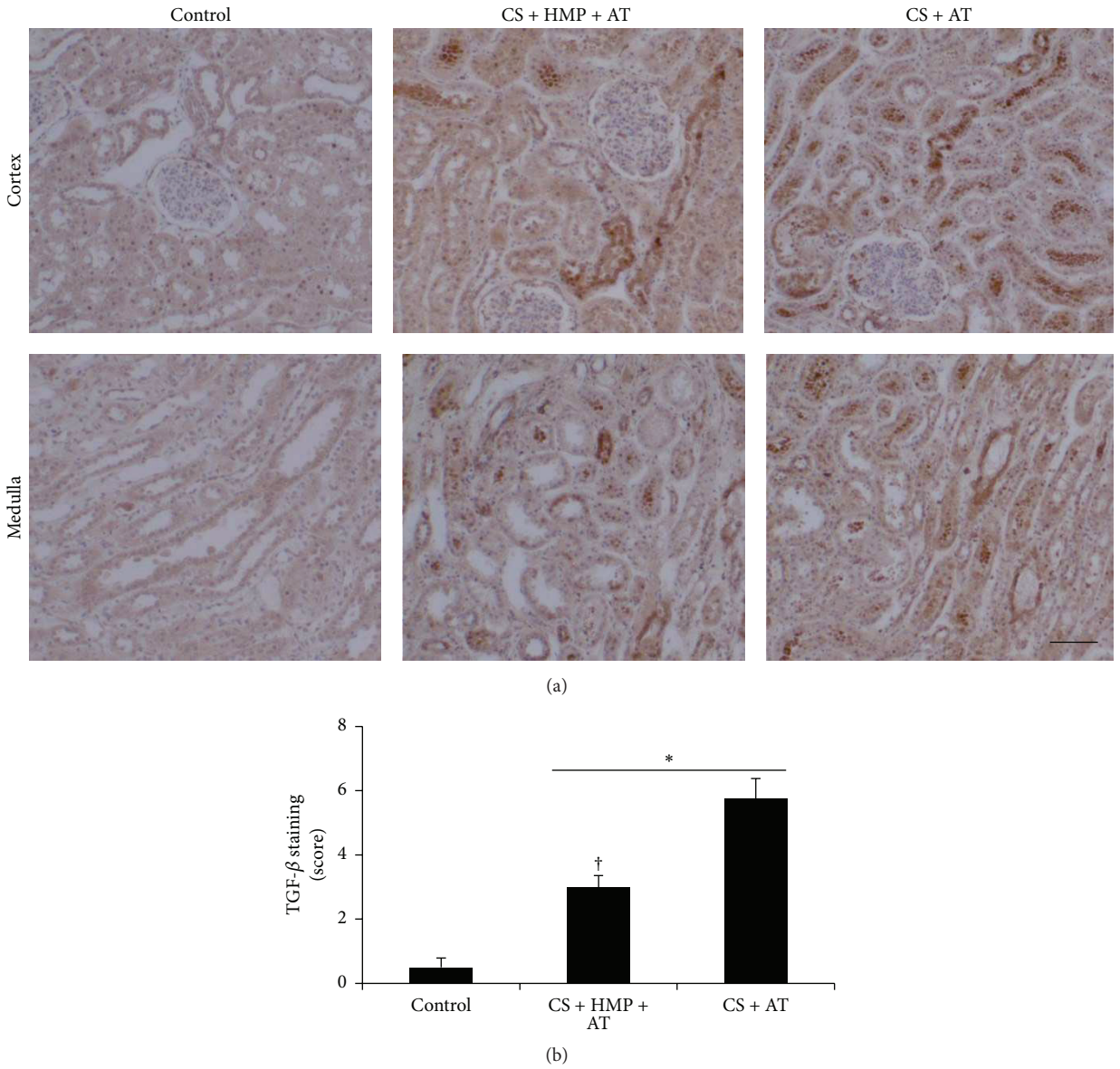

Figure 4: The use of pulsatile hypothermic machine perfusion after cold storage is associated with decreased profibrotic cytokines. (a) Localization of TGF-β in kidney sections. Note the localization in tubules and decreased expression in sections perfused with pulsatile machine after cold storage compared with only cold storage before the autotransplant (magnification 20x). (b) Semiquantification of TGF-β immunostaining in renal cells. Results are expressed as mean ± SEM (n = 6–12 animals per group). $^{*}p < 0.005$ versus control group; $^{\dagger}p < 0.01$ versus cold storage plus autotransplant group. CS: cold storage; HMP: hypothermic pulsatile machine; AT: autotransplant. Bar: 100 μm.

study, we observed less inflammatory and fibrotic activity and lower levels of cleaved caspase-3 with cold storage and HMP. Furthermore, TUNEL showed significantly more apoptosis in kidneys that were not perfused before reperfusion.

Other factors may contribute to the advantages of HMP cold storage or addition of HMP to the previous effect of cold storage, not only with respect to inflammatory factors but also with respect to the potentiation of endothelial vasodilatory factor expression and production. Furthermore, waveform is important for reduction of the shear-stress effect on the endothelium associated with perfusion. Our group previously reported the beneficial consequences of a pulsatile waveform generated by a vacuum pump, which was associated mainly with more marked release of nitric oxide during the perfusion process and probably during the initial rewarming period [18].

In summary, our study shows the positive and beneficial effect of HMP in kidneys transplanted after a warm-ischemic period and preserved either by cold storage alone or by cold storage plus one hour of HMP. However, proinflammatory activity and fibrosis were less marked after cold storage with HMP than after cold storage only.

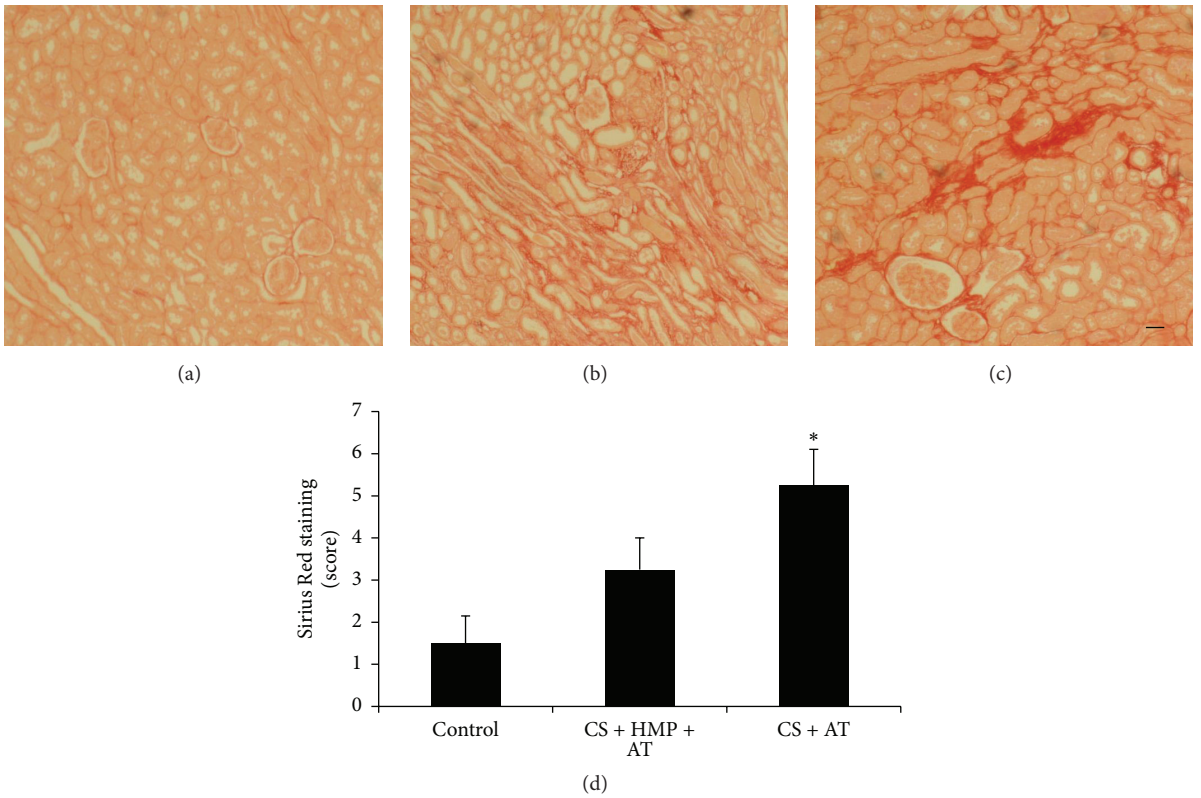

FIGURE 5: The use of pulsatile hypothermic machine perfusion after cold storage is associated with decreased fibrosis. Localization of collagen fibers in kidney sections by staining with Sirius Red: (a) control group; (b) cold storage (CS) plus hypothermic pulsatile machine (HMP) and subsequent transplant (AT) group; (c) cold storage (CS) and subsequent transplant (AT) group. Collagen fibers are stained in red on a yellow background (magnification ×10). (d) Semiquantification of Sirius Red staining in renal sections. Data are represented as mean ± SEM (n = 6–12 animals per group). $^{*}P < 0.01$ versus control group. Bar: 100 μm.

Competing Interests

The authors declare that they have no competing interests.

Acknowledgments

The authors are grateful to Dr. Rafael Samaniego for help with confocal microscopy. This work was supported by Spanish grants from the Ministry of Economy and Competitiveness ISCIII-FIS (PI07/0237 and PI14/01195 cofinanced by FEDER Funds from the European Commission, "A Way of Making Europe") and Comunidad Autónoma de Madrid S2010/BMD2378 (Consorcio para la Investigación del Fracaso Renal Agudo, CIFRA).

References

[1] A. Siedlecki, W. Irish, and D. C. Brennan, "Delayed graft function in the kidney transplant," *American Journal of Transplantation*, vol. 11, no. 11, pp. 2279–2296, 2011.

[2] N. Perico, D. Cattaneo, M. H. Sayegh, and G. Remuzzi, "Delayed graft function in kidney transplantation," *The Lancet*, vol. 364, no. 9447, pp. 1814–1827, 2004.

[3] I. Szwarc, V. Garrigue, S. Delmas, S. Deleuze, G. Chong, and G. Mourad, "Delayed graft function: a frequent but still unsolved problem in renal transplantation," *Nephrologie et Therapeutique*, vol. 1, no. 6, pp. 325–334, 2005.

[4] E. Lledó-García, L. Riera, J. Passas et al., "Spanish consensus document for acceptance and rejection of kidneys from expanded criteria donors," *Clinical transplantation*, vol. 28, no. 10, pp. 1155–1166, 2014.

[5] C. Y. Lee and M. J. Mangino, "Preservation methods for kidney and liver," *Organogenesis*, vol. 5, no. 3, pp. 105–112, 2009.

[6] C. Moers, J. Pirenne, A. Paul, and R. J. Ploeg, "Machine perfusion or cold storage in deceased-donor kidney transplantation," *The New England Journal of Medicine*, vol. 366, no. 8, pp. 770–771, 2012.

[7] T. Minor and A. Paul, "Hypothermic reconditioning in organ transplantation," *Current Opinion in Organ Transplantation*, vol. 18, no. 2, pp. 161–167, 2013.

[8] A. Gallinat, A. Paul, P. Efferz et al., "Hypothermic reconditioning of porcine kidney grafts by short-term preimplantation machine perfusion," *Transplantation*, vol. 93, no. 8, pp. 787–793, 2012.

[9] J. F. Del Cañizo, J. C. Antoranz, J. Duarte, M. M. Desco, and P. García-Barreno, "Tubular vacuum-powered blood-pumping device with active valves," *Artificial Organs*, vol. 20, no. 7, pp. 789–793, 1996.

[10] E. Lledó García, C. Hernández Fernández, J. I. Martínez-Salamanca et al., "Hydrodynamic and biochemical adaptation to perfusion pressure profile in isolated hypothermic renal

perfusion," *Actas Urologicas Espanolas*, vol. 28, no. 7, pp. 513–522, 2004.

[11] E. Lledó-Garcia, C. Hernández-Fernández, J. M. Díez-Cordero, P. García-Barreno, and J. F. del Cañizo-López, "Hydrodynamic and biochemical effects of isolated hypothermic renal perfusion depending on the pump model and perfusion solution," *Transplantation Proceedings*, vol. 35, no. 5, pp. 1661–1663, 2003.

[12] B. Humanes, A. Lazaro, S. Camano et al., "Cilastatin protects against cisplatin-induced nephrotoxicity without compromising its anticancer efficiency in rats," *Kidney International*, vol. 82, no. 6, pp. 652–663, 2012.

[13] A. Lazaro, J. Gallego-Delgado, P. Justo et al., "Long-term blood pressure control prevents oxidative renal injury," *Antioxidants and Redox Signaling*, vol. 7, no. 9-10, pp. 1285–1293, 2005.

[14] I. Loeffler and G. Wolf, "Transforming growth factor-β and the progression of renal disease," *Nephrology, Dialysis, Transplantation*, vol. 29, supplement 1, pp. i37–i45, 2014.

[15] J. M. O'Callaghan, R. D. Morgan, S. R. Knight, and P. J. Morris, "Systematic review and meta-analysis of hypothermic machine perfusion versus static cold storage of kidney allografts on transplant outcomes," *British Journal of Surgery*, vol. 100, no. 8, pp. 991–1001, 2013.

[16] A. Gallinat, P. Efferz, A. Paul, and T. Minor, "One or 4 h of 'in-house' reconditioning by machine perfusion after cold storage improve reperfusion parameters in porcine kidneys," *Transplant International*, vol. 27, no. 11, pp. 1214–1219, 2014.

[17] A. Gallinat, V. Amrillaeva, D. Hoyer et al., "Cold storage followed by short term hypothermic machine perfusion (HMP): a new concept for reconditioning kidneys from expanded criteria donors (ECD)?" *Transplant International*, vol. 26, no. 1, pp. 2–10, 2013.

[18] B. Humanes-Sanchez, A. Lazaro-Fernandez, J. C. Jado et al., "606 Beneficial effect of a short-period of hypothermic pulsatile machine perfusion of warm ischemic kidneys just before the transplant. Experimental study," *European Urology Supplements*, vol. 12, no. 1, pp. e606–e607, 2013.

[19] E. Lledó-García, B. Humanes-Sánchez, M. Mojena-Sánchez et al., "Independent cellular effects of cold ischemia and reperfusion: experimental molecular study," *Transplantation Proceedings*, vol. 45, no. 3, pp. 1260–1263, 2013.

[20] R. Baniene, D. Trumbeckas, M. Kincius et al., "Short ischemia induces rat kidney mitochondria dysfunction," *Journal of Bioenergetics and Biomembranes*, vol. 48, no. 1, pp. 77–85, 2016.

[21] D. Kamińska, K. Kościelska-Kasprzak, P. Chudoba, and M. Klinger, "Kidney injury due to warm ischemia during transplantation can be reduced," *American Journal of Transplantation*, vol. 16, no. 5, p. 1639, 2016.

[22] Z. Fu, Q. Ye, Y. Zhang et al., "Hypothermic machine perfusion reduced inflammatory reaction by downregulating the expression of matrix metalloproteinase 9 in a reperfusion model of donation after cardiac death," *Artificial Organs*, vol. 40, no. 6, pp. E102–E111, 2016.

Hindawi Publishing Corporation
BioMed Research International
Volume 2016, Article ID 9085273, 14 pages
http://dx.doi.org/10.1155/2016/9085273

Research Article

Systematic Analysis of the Cytokine and Anhedonia Response to Peripheral Lipopolysaccharide Administration in Rats

Steven Biesmans,[1,2] Liam J. R. Matthews,[2] Jan A. Bouwknecht,[2] Patrick De Haes,[2] Niels Hellings,[1] Theo F. Meert,[1,2] Rony Nuydens,[2] and Luc Ver Donck[2]

[1]*BIOMED, Hasselt University, Agoralaan C Building, 3590 Diepenbeek, Belgium*
[2]*Neuroscience, Janssen Research & Development, Division of Janssen Pharmaceutica NV, Turnhoutseweg 30, 2340 Beerse, Belgium*

Correspondence should be addressed to Luc Ver Donck; lverdon1@its.jnj.com

Received 17 February 2016; Revised 27 May 2016; Accepted 14 June 2016

Academic Editor: Monica Fedele

Inflammatory processes may cause depression in subsets of vulnerable individuals. Inflammation-associated behavioral changes are commonly modelled in rodents by administration of bacterial lipopolysaccharide (LPS). However, the time frame in which immune activation and depressive-like behavior occur is not very clear. In this study, we showed that systemic administration of LPS robustly increased circulating levels of corticosterone, leptin, pro- and anti-inflammatory cytokines, and chemokines. Serum concentrations of most analytes peaked within the first 6 h after LPS injection and returned to baseline values by 24 h. Chemokine levels, however, remained elevated for up to 96 h. Using an optimized sucrose preference test (SPT) we showed that sickness behavior was present from 2 to 24 h. LPS-induced anhedonia, as measured by decreased sucrose preference, lasted up to 96 h. To mimic the human situation, where depression develops after chronic inflammation, rats were preexposed to repeated LPS administration or subchronic restraint stress and subsequently challenged with LPS. While these procedures did not increase the duration of anhedonia, our results do indicate that inflammation may cause depressive symptoms such as anhedonia. Using our SPT protocol, more elaborate rodent models can be developed to study the mechanisms underlying inflammation-associated depression in humans.

1. Introduction

Major depressive disorder, or depression, is a serious medical illness with a life time prevalence of around 16% [1]. It is predicted that by 2030 depression will be the second leading cause of disability worldwide [2]. Clinical manifestations of depression include a range of symptoms, such as depressed mood, anhedonia (inability to experience pleasure from naturally rewarding activities), feelings of worthlessness or excessive guilt, decreased appetite and weight, fatigue, and recurrent suicidal ideations [3]. For many years, pharmacological research in depression has been focused on the monoamine theory, which proposes that depression is caused by decreased monoamine function in the brain and that drugs which correct this deficit, for example, selective serotonin reuptake inhibitors (SSRIs) and serotonin-norepinephrine reuptake inhibitors (SNRIs), can treat the disorder [4, 5]. Though the monoamine systems are clearly involved in the etiology of depression, it is now generally accepted that a more complex interplay between genetics and environmental factors underlies its pathophysiology. Findings from clinical studies indicate that inflammatory processes might also be involved in the pathogenesis of depression, at least in a subset of susceptible individuals (for reviews see [6–10]).

Based on these observations, several rodent models of inflammation-associated depression have been developed. One of the most used models involves administration of bacterial lipopolysaccharide (LPS), which is a potent activator of the immune system. Behavioral studies in rodents have shown that systemic LPS injection induces a sickness response, characterized by hypolocomotion, social withdrawal, fatigue, anorexia, and alterations in sleep patterns

and cognition [6]. There are some indications that LPS-induced sickness is followed by a depressive-like phenotype in which rodents display behavior similar to clinically relevant symptoms of depression in humans [11–13]. However, the time frame in which potential depressive-like behavior occurs relative to sickness is not clear and findings often vary across labs. Some studies indicate that depressive-like behavior can be observed in the absence of sickness 24 h after systemic LPS administration [11–13], while others report that at this time sickness is still present and hence confounds measurements of depressive-like behavior [14–17]. Indeed, sick animals display reduced locomotor activity, which can confound measurements of immobility used to estimate behavioral despair in paradigms such as the forced swim test [6]. Moreover, sick animals show reduced eating and drinking behavior, thereby potentially confounding measures of sweetened fluid intake in paradigms designed to evaluate anhedonia. Therefore, it is of crucial importance to include measures of sickness when assessing depressive-like behavior.

In a previous study we characterized behavioral changes induced by systemic LPS injection in mice [17]. This work showed that the time course of sickness and anhedonia can be evaluated by measuring total volume intake and sucrose preference in an optimized sucrose preference test (SPT). To extend our previous work, we characterized sickness and the anhedonic response to systemic LPS injection using a SPT in rats. First, the dose dependency of LPS-induced behavioral changes during the first 24 h after LPS administration was evaluated across a panel of behavioral assays. After identifying a dose that induced potential anhedonia, the immunological response to systemic LPS was measured by quantifying serum levels of corticosterone, leptin, and a selection of cytokines and chemokines over time. Then, the time course of sickness and the anhedonic response to systemic LPS was assessed using an optimized SPT. Finally, in an attempt to mimic the chronic nature of depression in humans more carefully, our SPT protocol was used to test whether preexposure to repeated LPS administration or subchronic stress influenced the anhedonic response to a subsequent LPS challenge.

2. Methods

2.1. Animals and LPS. All studies were conducted in male Sprague-Dawley rats (Harlan, Netherlands) weighing 200–220 g on arrival. Animals were housed in groups of 4 in plexiglass individually ventilated cages ($L \times W \times H$: $43 \times 32 \times 18$ cm; Tecniplast, Italy) for one week to acclimate prior to experiments. Procedure rooms were maintained at a temperature of $22 \pm 2^{\circ}$C and a humidity of $54 \pm 2\%$, with a 12 : 12 h light-dark cycle (lights on at 06:00 a.m. with a 30-minute sunrise and dusk phase). Unless mentioned otherwise, food and water were available *ad libitum*. All experimental protocols were approved by the Institutional Ethical Committee on Animal Experimentation, in compliance with Belgian law (Royal Decree on the protection of laboratory animals, April 6, 2010) and conducted in facilities accredited by the Association for the Assessment and Accreditation of Laboratory Animal Care (AAALAC).

Lipopolysaccharide (LPS) from *Escherichia coli* (serotype 055:B5) was purchased from Sigma-Aldrich and freshly dissolved in sterile saline prior to injection.

2.2. Serum Collection. To measure the effect of peripheral LPS administration on serum levels of a selection of analytes, rats were injected i.p. with either vehicle or 0.63 mg/kg LPS ($n = 12$ per group). Just before and at 1 h, 2 h, 6 h, 24 h, 48 h, 72 h, and 96 h after the immune challenge, rats were briefly anesthetized by inhalation of 2% isoflurane, blood was collected from the tail artery, and the rats were returned to their home cage. Serum was obtained by keeping the blood samples in Vacutainer SST II Advance blood tubes (BD Biosciences, product ID 367955) for 30 minutes at room temperature. Then the samples were centrifuged (1300 ×g, 10 min, room temperature), aliquoted, flash frozen in liquid nitrogen, and stored at −80°C until analysis.

2.3. Cytokine Measurements. Serum levels of chemokine (C-X-C motif) ligand 1 (CXCL1), interferon-γ (IFN-γ), interleukin- (IL-) 1β, IL-6, IL-10, leptin, monocyte chemoattractant protein-1 (MCP-1), macrophage inflammatory protein-1α (MIP-1α), and tumor necrosis factor-α (TNF-α) were simultaneously determined using a rat cytokine/chemokine magnetic bead panel kit from Merck Millipore. This assay is based on Luminex™ technology in which magnetic beads with a distinct emitting fluorescence pattern are coated onto antibodies that specifically capture individual cytokines. All steps in the assay were conducted according to the manufacturer's instructions. A Bio-Plex 200 System (Bio-Rad) was used to measure the fluorescent signal and the data was analyzed using Bio-Plex Manager 5.0 software (Bio-Rad) with five-parameter logistic regression curve fitting. Cytokine levels below detection limit were assigned a value equal to the lowest detectable value of that cytokine. Cytokine values outside of the average + 3 times standard deviation range were considered outliers and were excluded from all calculations. This was the case for less than 2% of all measured cytokines.

2.4. Corticosterone Measurements. Serum concentrations of corticosterone were determined using a commercial ELISA kit supplied by Enzo Life Sciences (Product ID 900-097). All procedures were carried out as per manufacturer's instructions.

2.5. Behavioral Tests. The open field test (OFT) and forced swim test (FST) setups were custom-made. In these paradigms, groups of naive rats ($n = 12$ per group) were injected i.p. with 0, 0.31, 0.63, or 1.25 mg/kg LPS and tested at 2 h, 6 h, or 24 h after LPS administration. This dose range of LPS was selected based on results from our previous experiments in mice [17].

2.5.1. Open Field Test. The OFT setup consisted of a circular arena with a diameter of 1.2 m. A video camera with an infrared filter was fixed 1 m above the arena and infrared illumination was provided from the bottom for optimal detection and tracking of the rats. This setup allowed the

testing of one rat at a time. Exactly 2 sec after detection of a rat, tracking was started and performed for 10 min using EthoVision 6.1 software (Noldus, Netherlands), set up to detect immobility time and distance moved. In this test, exploratory behavior by the animal was used to measure locomotor activity.

2.5.2. Forced Swim Test. The FST setup consisted of four independent plexiglass cylinders (diameter 19 cm) which were flushed and filled with water (30 cm deep, 24-25 degrees Celsius). The four cylinders allowed testing of four rats per session. A video camera with an infrared filter was fixed onto a frame in front of each cylinder and infrared illumination was provided to allow optimal detection and tracking of the rats. Exactly 2 sec after detection of each individual rat, tracking was started and performed using EthoVision 6.1 software (Noldus, Netherlands). Each FST test consisted of two sessions: a 15 min training session on the day before LPS administration and a 6 min test session at the relevant time after LPS. Immobility time and distance moved (based on center point of gravity of the detected surface) were measured during each session and the duration of immobility was evaluated as a measure of behavioral despair.

2.5.3. Sucrose Preference Test in Fluid Deprived Rats. Animals were single-housed in individually ventilated cages ($L \times W \times H$: 35 × 31 × 16 cm; Tecniplast, Italy) fitted with two 250 mL drinking bottles and *ad libitum* access to food. Each of the drinking bottles contained either filtered tap water or a 1% sucrose solution. The location of each bottle on the cage was randomized every day, with half the animals receiving sucrose on the left and the other half on the right. Prior to LPS administration, rats were familiarized to the sucrose solution by presenting them with water/water (W/W) or water/sucrose (W/S) for 24 h each on 2 consecutive days. Then, the rats were fluid deprived overnight and injected i.p. with 0, 0.31, 0.63, or 1.25 mg/kg LPS ($n = 12$ per group). At 2 h, 6 h, and 24 h after LPS administration all rats were exposed to preweighed drinking bottles containing W/S. After 1 h the bottles were removed and weighed using Software Wedge for Windows 1.2 (TAL Technologies).

2.5.4. Sucrose Preference Test in Undeprived Rats. All of the remaining SPT experiments started with a 4-day *familiarization phase*, during which the rats were presented for 24 h with two water-filled bottles (W/W) on familiarization day 1 (FAM1) and FAM3 or one water- and one 1% sucrose-filled bottle (W/S) on FAM2 and FAM4 (Figure 1(a)). The bottles were removed between 08:00 and 09:00 a.m. each day and weighed using Software Wedge for Windows 1.2. Then, the animals were weighed and freshly prepared bottles were put onto the cages.

To assess the effect of a single peripheral bolus of LPS on anhedonia over time, the *test phase* started by weighing and injecting rats with either vehicle or 0.63 mg/kg i.p. LPS ($n = 12$ per group). Immediately after LPS administration, the rats were put into their home cage and given access to W/S for 4 consecutive days. This experiment was repeated three times using 12 naive animals per treatment group in each trial and the data was pooled prior to analysis so that the final $n = 36$ per group.

The effect of repeated systemic LPS injection on anhedonia was evaluated by randomizing rats across 4 experimental groups, that is, 5 days of vehicle + vehicle on test day (5 Veh + Veh), 5 days of vehicle + LPS on test day (5 Veh + LPS), 5 days of LPS + vehicle on test day (5 LPS + Veh), and 5 days of LPS + LPS on test day (5 LPS + LPS) ($n = 12$ per group). After the *familiarization phase*, a *preexposure phase* was introduced in which rats from the 5 days of vehicle groups were injected i.p. with vehicle while rats from the 5 days of LPS groups received a daily i.p. injection of 0.63 mg/kg LPS for 5 consecutive days (Figure 1(b)). All rats had *ad libitum* access to food and water during the *preexposure phase*. Three days after the last LPS administration, rats were injected with an acute bolus of either vehicle or 0.63 mg/kg i.p. LPS and presented with W/S for 24 h for 4 consecutive days.

To assess the effect of stress on LPS-induced anhedonia, rats were randomized across 4 experimental groups, that is, no stress + vehicle (NS + Veh), no stress + LPS (NS + LPS), stress + vehicle (S + Veh), and stress + LPS (S + LPS) ($n = 12$ per group), and a *manipulation phase* was introduced in between the *familiarization phase* and *the test phase* (Figure 1(c)). During this *manipulation phase*, animals in the stress groups were weighed and subjected to 1 h of physical restraint per day using a transparent rat restrainer ($D \times H$: 5 × 23 cm; length adjusted to tightly enclose the rat) for 5 consecutive days. To control for possible effects of handling stress, rats from the no stress groups were weighed, handled, and put back in their home cage. All rats had *ad libitum* access to food and water during the *manipulation phase*. The *test phase* started 3 days after the *manipulation phase* by injecting the rats i.p. with either vehicle or 0.63 mg/kg LPS. Immediately after LPS administration, all animals were presented with W/S for 4 consecutive days.

2.5.5. Evaluation of Parameters in Sucrose Preference Test. In all SPT experiments, the amount drunk by a rat was determined by subtracting the weight of a bottle at the start of the observation period and at the end (taking fluid density as 1 g/mL). Total fluid intake was taken as the total change in volume from both bottles combined, while sucrose preference was calculated as a percentage of consumed sucrose solution of the total fluid intake. A total fluid intake greater than the mean + two times standard deviation was considered to be an invalid measure that probably resulted from leaking bottles. Invalid measures were replaced by the mean of all the bottles either on the relevant side (for W/W) or for either water or sucrose (for W/S). This happened for less than 2% of bottle measurements in any given experiment. Total volume intake was evaluated as a primary measure for sickness behavior (reduction versus normal daily intake), while sucrose preference was used as a measure of anhedonia. Change in body weight was calculated by subtracting the weight at a given time point from the weight at the start of the experiment. These time points are specified for each experiment in the Results.

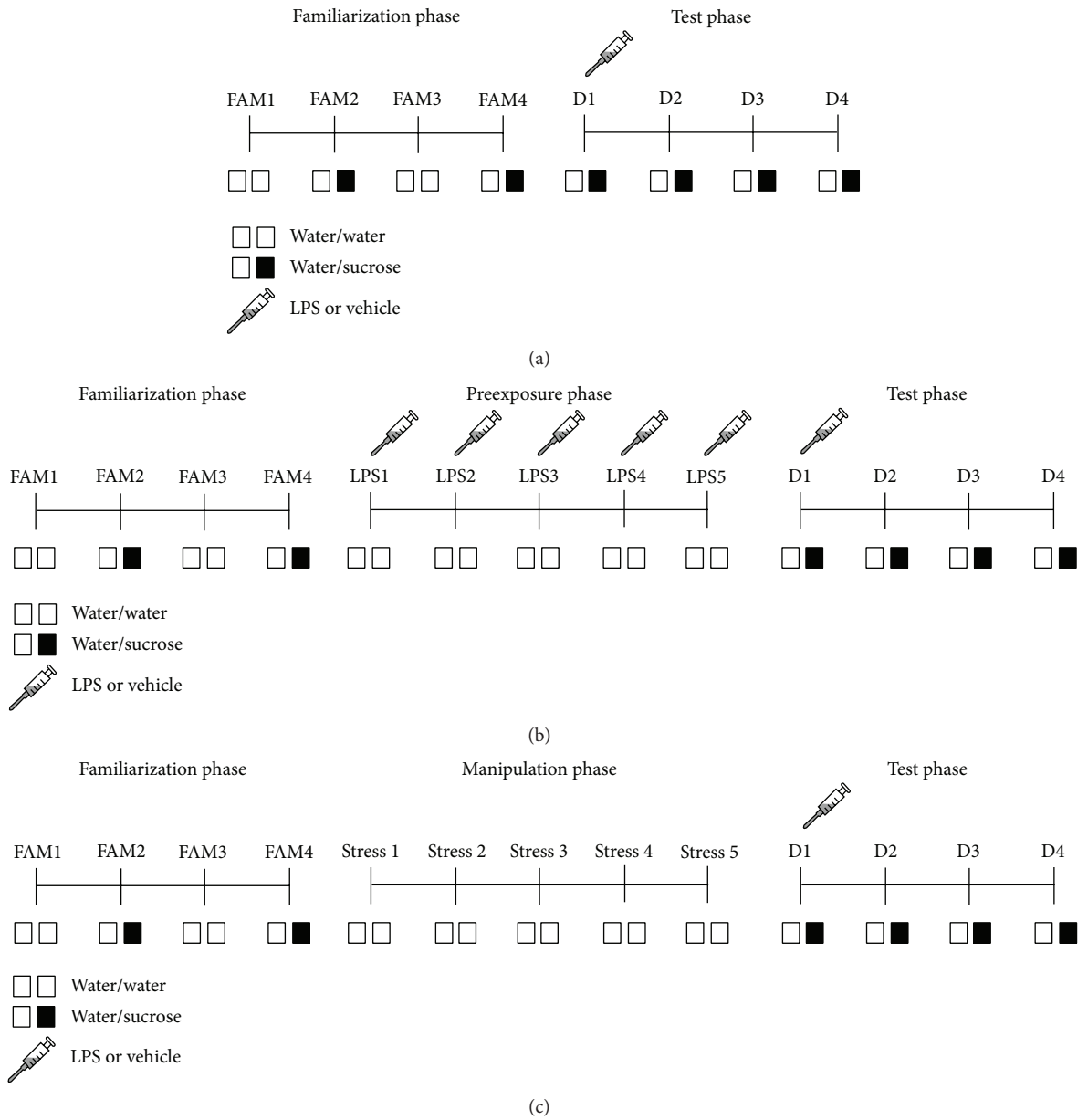

Figure 1: Experimental design of the sucrose preference tests performed using fluid undeprived rats. In the *familiarization phase*, rats were presented for 24 h with two water-filled bottles (W/W) on familiarization day 1 (FAM1) and FAM3, or one water- and one 1% sucrose-filled bottle (W/S) on FAM2 and FAM4. In all studies, the *test phase* started by injecting the rats with LPS (0.63 mg/kg, i.p.) or vehicle. Voluntary consumption of water and sucrose was measured during a period of 24 h for 4 days (D1–D4) in the *test phase* (a–c). The effect of repeated systemic LPS injection on anhedonia was evaluated by preceding the *test phase* by a *preexposure phase* during which rats received a daily i.p. injection of 0.63 mg/kg LPS or vehicle for 5 consecutive days (LPS1–LPS5) (b). To assess the effect of stress on LPS-induced anhedonia, the *test phase* was preceded by a *manipulation phase* during which rats were subjected to 1 h of restraint stress daily for 5 consecutive days (Stress 1–Stress 5) (c).

2.6. Statistical Analysis. Data were analyzed using SPSS Statistics software (Version 20 for Windows, IBM Inc). Analysis of variance (ANOVA) or repeated measure ANOVA (rmANOVA) was performed to assess the statistical significance of differences across treatment groups. A Greenhouse-Geisser correction epsilon (ε) was used in case of repeated measures analysis to correct for potential violation of the sphericity assumption [18]. This correction multiplies both the numerator and the denominator degrees of freedom by epsilon and the significance of the F-ratio is evaluated with the new degrees of freedom, resulting in a more conservative statistical test. To account for the skewness of the data distribution, concentrations of serum analytes were log-transformed prior to analysis. Significance was accepted for the ANOVAs and rmANOVAs when $p < 0.05$. When appropriate, post hoc comparisons were made by using an

independent samples t-test with a Bonferroni-corrected p value. For consistency between the analysis and the visualization of serum analyte concentrations, the group means and its standard error of the mean (SEM) were back-transformed and visually presented on a logarithmic scale. All other data are expressed as mean ± SEM on a linear scale.

3. Results

3.1. Systemic LPS Administration Causes Sickness and Anhedonia in a Dose- and Time-Dependent Manner. The total distance travelled in the OFT is a general measure for exploration and can be used as a marker of sickness behavior. Factorial ANOVA revealed a main effect of LPS dose ($F(3, 110) = 11.1$, $p < 0.001$) and time point ($F(2, 110) = 15.6$, $p < 0.001$) for total distance travelled. Post hoc analysis indicated that systemic LPS administration reduced locomotor activity in a dose-dependent manner at 2 h (Figure 2(a)). This LPS-induced reduction in exploration was more pronounced at 6 h after LPS but disappeared at 24 h.

The effect of systemic LPS administration on behavioral despair was evaluated in the FST by placing the rats in a water-filled cylinder from which they cannot escape and measuring the time they remained immobile. Factorial ANOVA demonstrated that there was no main effect of LPS dose or time point tested. Explorative post hoc analysis indicated that rats injected with 0.63 mg/kg LPS showed a potential increase in immobility time at 6 h after administration (Figure 2(b)). Such an immobility response was not observed at any of the other time points or LPS doses used.

In the sucrose preference paradigm, sickness is evaluated by measuring the total volume of fluid an animal consumes during a predefined observation period, while sucrose preference is used as marker for anhedonia. rmANOVA revealed a significant time × LPS dose interaction for total volume intake ($F(6, 80) = 12.3$, $p < 0.001$, $\varepsilon = 0.98$). Post hoc analysis indicated that LPS reduced total volume intake at 6 h and 24 h to a similar extent at all doses (Figure 2(c)), suggesting suppression of drinking as a consequence of sickness. No main effect of time or LPS dose was found for sucrose preference. However, explorative post hoc analysis demonstrated that, at 24 h, sucrose preference was significantly reduced in rats that were injected with 0.63 or 1.25 mg/kg LPS (Figure 2(d)). Rats injected with 0.31 mg/kg LPS did not show reduced sucrose preference, while at this time they drank much less than vehicle-treated rats. This suggests that LPS-induced anhedonia is potentially detectable at a dose of 0.63 mg/kg and higher.

3.2. Systemic LPS Increases Serum Levels of Corticosterone, Cytokines, and Chemokines in a Time-Dependent Manner. Based on the strong behavioral effects of 0.63 mg/kg LPS, it was decided to analyze the effect of this particular LPS dose on the release of a selection of hormones and cytokines in serum over time. Factorial rmANOVA revealed a significant time × LPS interaction for the analytes corticosterone ($F(7, 140) = 11.2$, $p < 0.001$, $\varepsilon = 0.47$), CXCL1 ($F(7, 133) = 56.7$, $p < 0.001$, $\varepsilon = 0.30$), IFN-γ ($F(7, 140) = 39.8$, $p < 0.001$, $\varepsilon = 0.29$), IL-1β ($F(7, 140) = 14.9$, $p < 0.001$, $\varepsilon = 0.28$), IL-6 ($F(7, 140) = 76.6$, $p < 0.001$, $\varepsilon = 0.19$), IL-10 ($F(7, 140) = 35.1$, $p < 0.001$, $\varepsilon = 0.22$), leptin ($F(7, 140) = 6.5$, $p < 0.001$, $\varepsilon = 0.53$), MCP-1 ($F(7, 140) = 288.4$, $p < 0.001$, $\varepsilon = 0.38$), MIP-1α ($F(7, 140) = 51.1$, $p < 0.001$, $\varepsilon = 0.33$), and TNF-α ($F(7, 140) = 68.2$, $p < 0.001$, $\varepsilon = 0.23$). Post hoc analysis showed that serum levels of corticosterone were elevated at 2 h, 6 h, and 24 h and fell below control values at 48 h after LPS administration (Figure 3). Furthermore, LPS caused a strong but short-lasting increase in the serum concentrations of most cytokines. Interestingly, the peak of this release did not occur at the same time for all cytokines. IL-10 and TNF-α peaked at 1 h, while CXCL1, IL-1β, IL-6, MCP-1, and MIP-1 reached their peak release at 2 h after LPS administration. IFN-γ and leptin were the only analytes that peaked at 6 h after LPS. Apart from the chemokines CXCL1, MCP-1, and MIP-1α all immune molecules had returned to control levels by 24 h.

3.3. LPS-Induced Anhedonia Can Be Measured in the Sucrose Preference Test. Based on the results from the first SPT study (Figure 2) and the time course of LPS-induced cytokine and chemokine release (Figure 3), an extended SPT study was performed to analyze the effects of peripheral LPS administration over a longer period of time. In this optimized experimental design, undeprived rats were subjected to a *familiarization phase* and a *test phase*. During the *familiarization phase* normal daily intake volume was assessed, animals were familiarized with exposure to sucrose, and a stable sucrose preference baseline was obtained. The growth rate of rats during each day of the *familiarization phase* was evaluated by calculating the body weight change against their weight at the first day of the *familiarization phase*. Factorial rmANOVA showed that there was a main effect of time ($F(3, 210) = 563.2$, $p < 0.001$, $\varepsilon = 0.69$) and LPS assignment ($F(1, 70) = 5.1$, $p < 0.05$, $\varepsilon = 0.69$) for change in body weight during the *familiarization phase*. Post hoc analysis indicated that rats in the LPS group had a statistically significant lower change in body weight at familiarization day 1 (FAM1) as compared to animals in the vehicle group (Figure 4(a), left panel). However, this difference was very small and can be considered as not biologically relevant. Rats from both groups continuously grew about 5 g per day throughout the *familiarization phase*, regardless of exposure type (W/W versus W/S). This indicates that the caloric value of sucrose did not influence the change in body weight.

For total volume intake during the *familiarization phase*, there was a flavor × repeat interaction ($F(1, 90) = 8.9$, $p < 0.01$) but no effect of LPS assignment. Post hoc analysis indicated that the total volume intake increased substantially on days that rats were exposed to W/S when compared to W/W days. This increase was slightly reduced upon retesting (i.e., FAM4 versus FAM2) (Figure 4(b), left panel).

There were no time or group effects on sucrose preference during the *familiarization phase* and the rats showed a stable sucrose preference of around 80% on both W/S days (Figure 4(c), left panel).

In the *test phase*, the effect of systemic LPS on change in body weight, total daily intake volume, and sucrose

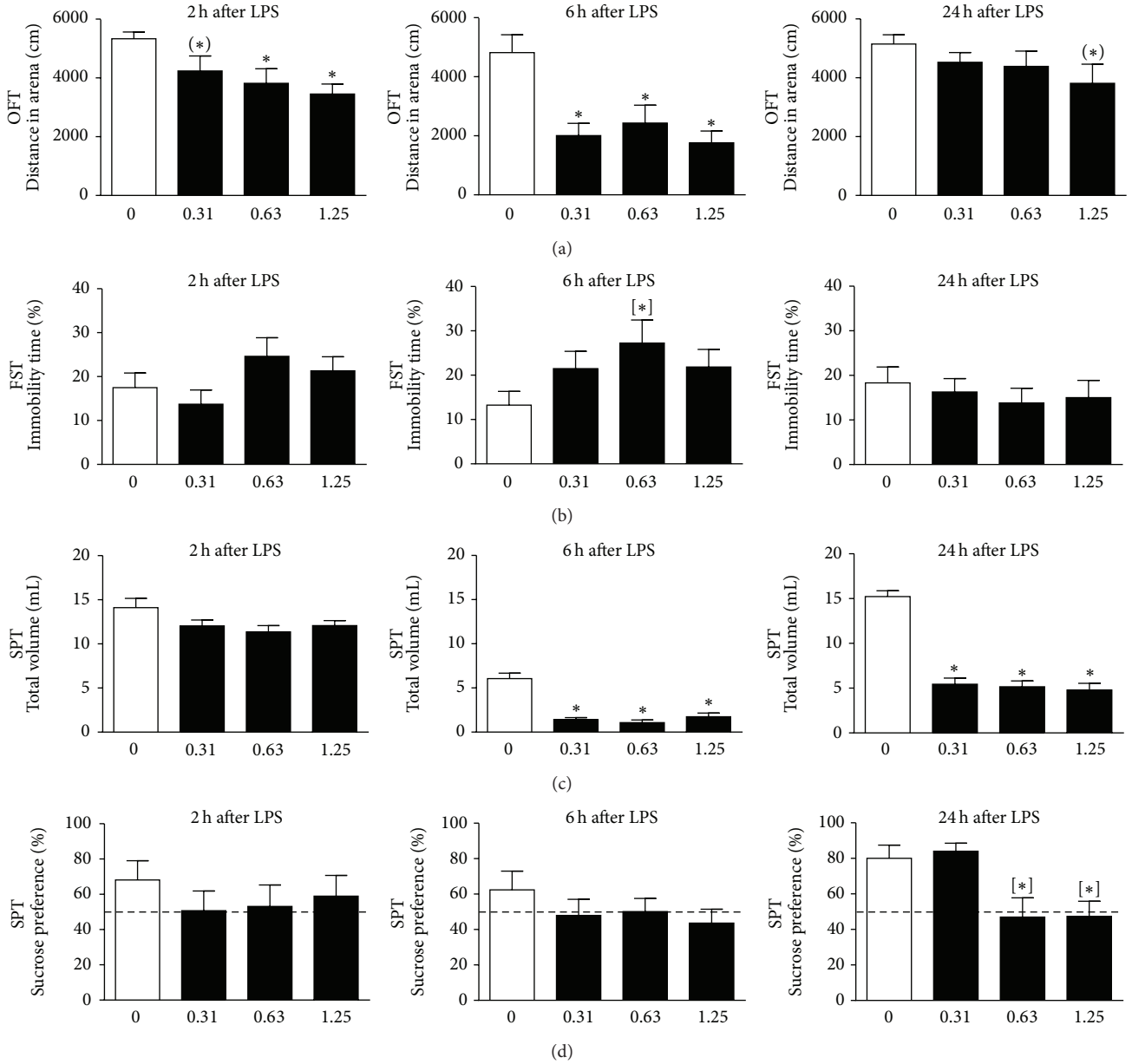

Figure 2: Systemic LPS administration causes sickness and anhedonia in a dose- and time-dependent manner. Intraperitoneal LPS injection induced sickness behavior, as seen by reduced locomotor activity in the open field test (OFT) (a) and decreased total volume intake in the sucrose preference test (SPT) (c). At 24 h after administration, a dose of 0.63 and 1.25 mg/kg LPS reduced sucrose preference (d), thereby potentially indicating development of anhedonia. However, a single i.p. injection of LPS did not induce clear depressive-like behavior in the forced swim test (FST) (b). Please note that in the OFT and FST naive animals were used at all time points, whereas in the SPT rats were tested repeatedly. Dashed lines indicate chance level for sucrose preference. Graphs are plotted as mean + SEM ($n = 12$ per group). OFT and FST data were analyzed by multivariate ANOVA, SPT data by rmANOVA, and followed by independent samples t-test. $^{(*)}0.1 < p < 0.05$; $^{*}p < 0.05$ compared to 0 mg/kg LPS group; $^{[*]}p < 0.05$ compared to 0 mg/kg LPS group in absence of rmANOVA effects.

preference was assessed over time. The growth rate of rats during each day of the *test phase* was evaluated by calculating the body weight change against their weight right before LPS administration. Factorial rmANOVA revealed a strong time × LPS interaction ($F(3, 210) = 86.2$, $p < 0.001$, $\varepsilon = 0.83$) for change in body weight during the *test phase*. Post hoc analysis showed that systemic LPS injection reduced weight during the first 2 days after injection (D1 and D2) and that this weight decrease remained statistically significant throughout the *test phase* (Figure 4(a), right panel).

For total volume intake during the *test phase*, there was a time × LPS interaction ($F(3, 210) = 50.0$, $p < 0.001$, $\varepsilon = 0.87$). In the first 24 h after administration (D1), LPS reduced total volume intake to less than one-third of the normal daily water intake, suggesting suppression of drinking as a consequence of sickness (Figure 4(b), right panel). On D2, LPS-injected

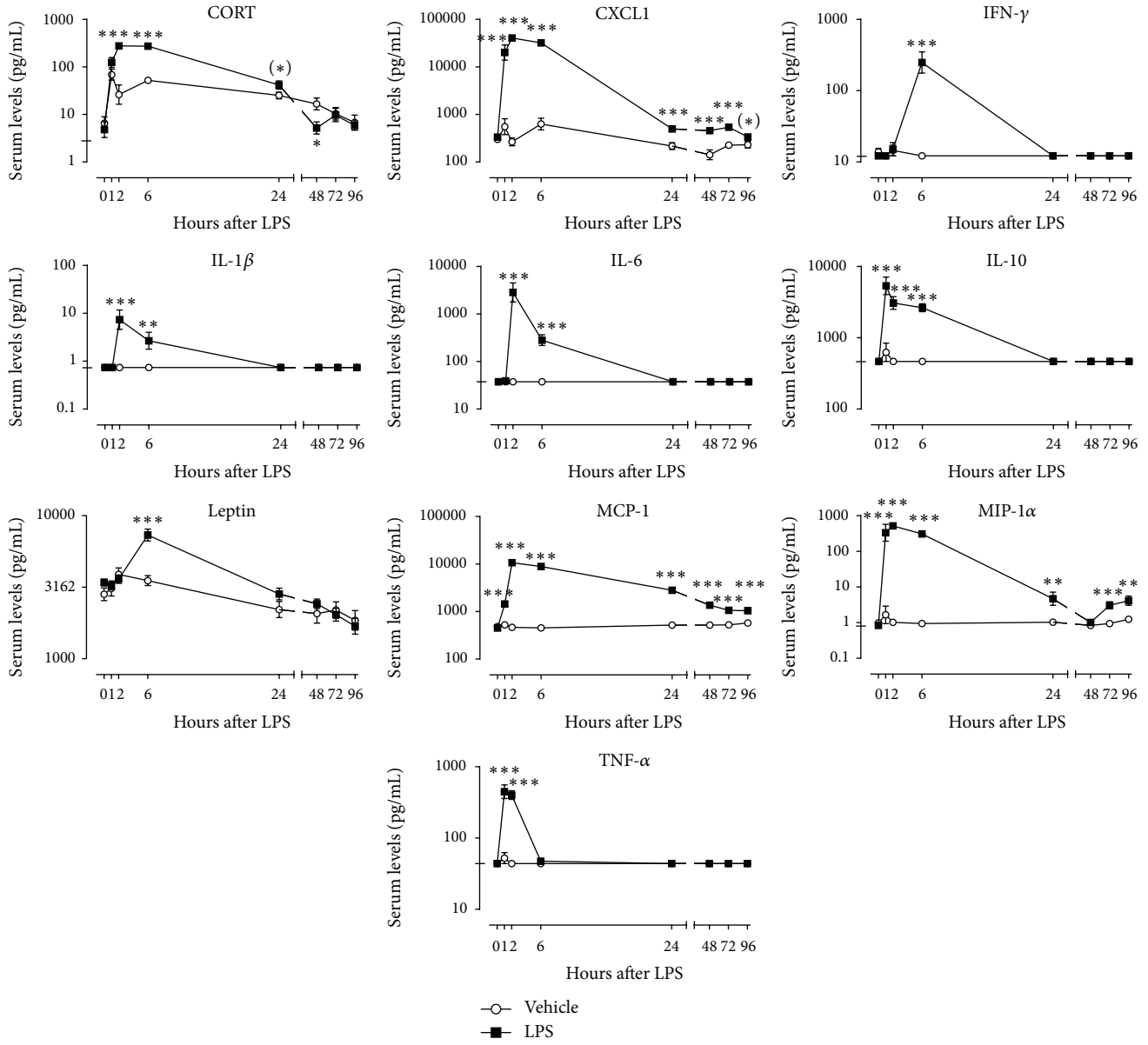

Figure 3: Peripheral LPS administration transiently increases serum levels of corticosterone, leptin, cytokines, and chemokines. Time curves of corticosterone (CORT), chemokine (C-X-C motif) ligand 1 (CXCL1), interferon-γ (IFN-γ), interleukin- (IL-) 1β, IL-6, IL-10, leptin, monocyte chemoattractant protein-1 (MCP-1), macrophage inflammatory protein-1α (MIP-1α), and tumor necrosis factor-α (TNF-α) quantified in serum at 0 h, 1 h, 2 h, 6 h, 24 h, 48 h, 72 h, and 96 h after LPS injection (0.63 mg/kg, i.p.). The detection limit of each analyte is indicated by a tick on the y-axis of its individual graph. Detection limits that fall below the lowest value on the y-axis are not presented. Graphs are plotted as mean ± SEM (n = 12 per group). Data were analyzed by rmANOVA followed by independent samples t-test. $^{(*)}0.1 < p < 0.05$, $^{*}p < 0.05$, $^{**}p < 0.01$, and $^{***}p < 0.001$ compared to vehicle.

rats still drank significantly less than rats that received vehicle, but their total volume intake was no longer lower than the normal daily water intake, thereby indicating that sickness had dissipated. No differences in total volume intake were found on D3 and D4 after LPS treatment.

A time × LPS interaction ($F(3, 210) = 2.8$, $p < 0.05$, $\varepsilon = 0.91$) was also found for sucrose preference during the *test phase*. Post hoc analysis revealed that systemic LPS administration reduced sucrose preference close to chance level (i.e., 50%) on D1 (Figure 4(c), right panel). Interestingly, the LPS-induced decrease of sucrose preference lasted until D3, a time point at which total volume intake had returned to control levels suggesting occurrence of anhedonia in the absence of sickness on D2 and D3.

3.4. Repeated LPS Exposure Protects against Acute LPS-Induced Sickness but Not Anhedonia. The duration of inflammatory processes associated with depression is thought to be

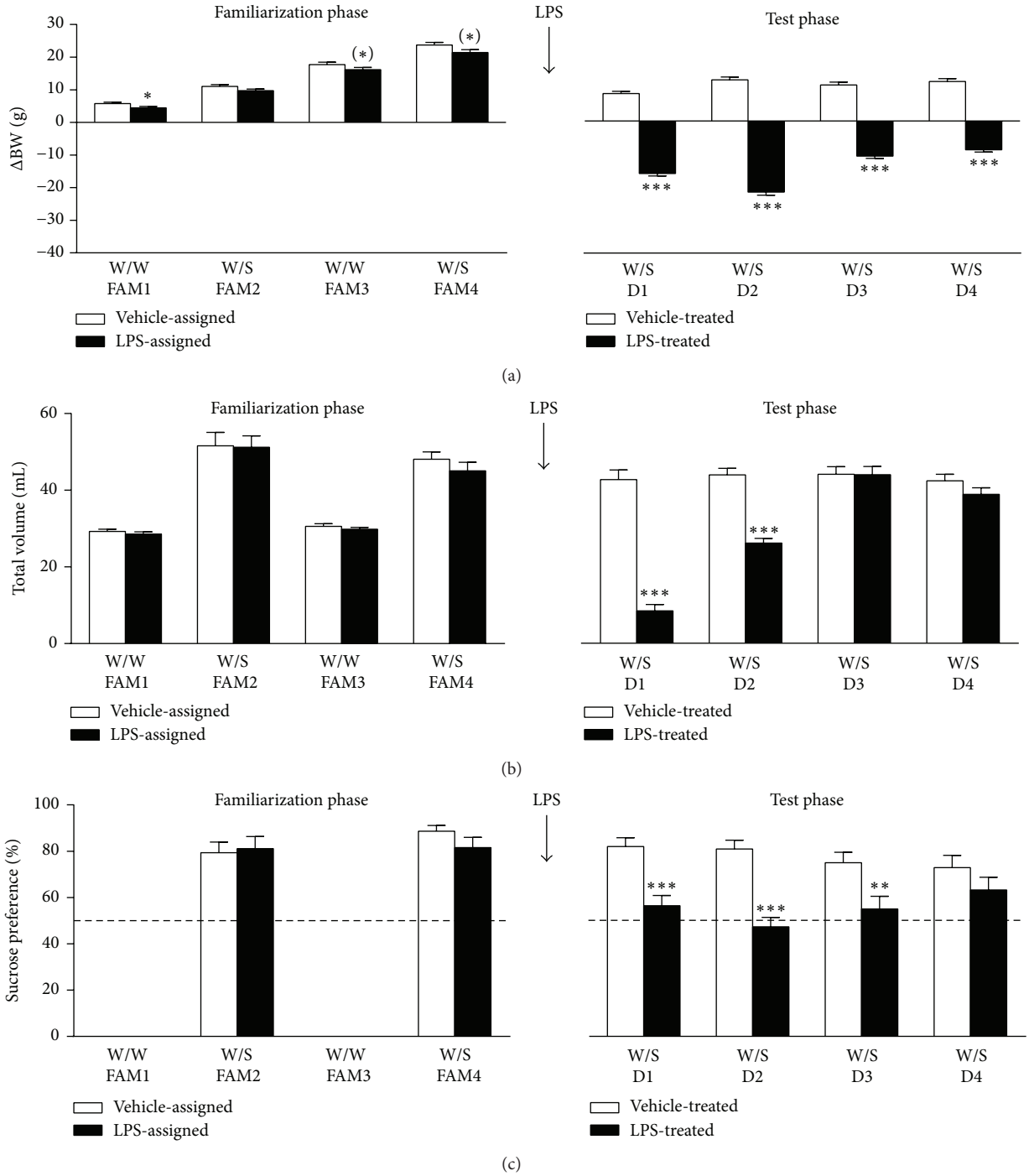

Figure 4: Systemic LPS injection reduces body weight, fluid intake, and sucrose preference in the sucrose preference test. An optimized sucrose preference test was used to evaluate the anhedonic response to LPS. During the *familiarization phase* of the experiment ((a–c) left panels), rats were exposed to 2 bottles of water (W/W) on familiarization day 1 (FAM1) and FAM3, while on FAM2 and FAM4 one bottle was filled with water and the other bottle contained a 1% sucrose solution (W/S). Three days after the *familiarization phase*, rats were injected i.p. with 0.63 mg/kg LPS or vehicle and voluntary consumption of water and sucrose was measured during a period of 24 h for 4 days (D1–D4) in the *test phase* ((a–c) right panels). Note that the growth rate of rats during each day of the *familiarization phase* was evaluated by calculating the body weight change (ΔBW) against their weight at the first day of the *familiarization phase* ((a) left panel). Growth rate in the *test phase* is presented as the body weight change at each day compared to the rats' weight right before LPS administration. Dashed lines in (c) indicate chance level for sucrose preference. Graphs are plotted as mean + SEM and represent pooled data from 3 separate but identical studies using 12 naive animals per treatment group in each experiment (total $n = 36$ per treatment group). Data were analyzed by rmANOVA followed by independent samples t-test. $^{(*)}0.1 < p < 0.05$, $^{*}p < 0.05$, $^{**}p < 0.01$, and $^{***}p < 0.001$ compared to vehicle.

chronic rather than acute. In this experiment, the anhedonic response to a more prolonged immune challenge was investigated by first injecting rats with LPS on 5 consecutive days (*preexposure phase*) and measuring sucrose preference after an acute LPS injection 3 days later (*test phase*).

The effect of repeated LPS administration on the growth rate of rats was determined by calculating the change in body weight versus their weight immediately before the first LPS injection in the *preexposure phase*. Factorial rmANOVA demonstrated a time × preexposure interaction for change in body weight during this *preexposure phase*. Post hoc analysis showed that rats receiving vehicle injections continuously grew, while rats preexposed to LPS showed reduced weight change at all days of the *preexposure phase* (Figure 5(a)).

At the beginning of the *test phase*, rats that were preexposed to LPS weighed significantly less than animals that received vehicle preexposure (i.e., 288.9 ± 2.6 g versus 314.5 ± 3.6 g, $p < 0.001$; data not shown). To evaluate the weight change after a subsequent acute LPS injection, weight measures during the *test phase* were subtracted from the weight at the start of the *test phase*. rmANOVA revealed that there was a time × preexposure × LPS interaction ($F(3, 132) = 13.9$, $p < 0.001$, $\varepsilon = 0.76$) for change in body weight in the *test phase*. Post hoc analysis indicated that all rats lost weight after receiving the acute LPS challenge (Figure 5(b)). Animals that received LPS during the *preexposure phase*, however, lost significantly less weight after the acute LPS injection than rats that were pretreated with vehicle. Moreover, rats preexposed to LPS recovered faster after the acute LPS challenge than rats that received acute LPS after vehicle pretreatment.

There was a time × preexposure × LPS interaction for total volume intake during the *test phase*. All groups that received LPS in the *test phase* drank less than vehicle-injected animals on the first day after acute LPS administration (Figure 5(c)). However, LPS-pretreated rats drank much more upon a subsequent acute LPS challenge than animals that were preexposed to vehicle. On the second day after acute LPS injection, the total volume drank by rats preexposed to LPS had returned to control levels, while this took until day 3 for vehicle-pretreated rats.

Finally, factorial rmANOVA revealed that, for sucrose preference during the *test phase*, there was a main effect of LPS ($F(1, 44) = 24.4$, $p < 0.001$, $\varepsilon = 0.93$) but not of time or preexposure. Rats that were injected with LPS during the *test phase* had a reduced sucrose preference when compared to vehicle-injected animals (Figure 5(d)). However, due to the absence of other main effects no further post hoc analyses could be made.

3.5. Subchronic Restraint Stress Does Not Influence the Anhedonic Response to a Subsequent LPS Challenge. Stress, a known risk factor for depression, influences immunological responses. To test whether stress impacts on the anhedonic response to an immune challenge, rats were first exposed to 1 h of restraint stress per day for 5 consecutive days (*manipulation phase*) and subsequently injected systemically with LPS three days later (*test phase*).

The effect of subchronic restraint stress on the growth rate of rats was determined by calculating the change in body weight during the *manipulation phase* versus the weight just before the first stress session. Factorial rmANOVA revealed a time × stress interaction ($F(3, 138) = 145.6$, $p < 0.001$, $\varepsilon = 0.69$) for change in body weight during the *manipulation phase*. Post hoc analysis indicated that stressed rats continuously lost weight from the first stress session until the last, while nonstressed rats grew steadily during the *manipulation phase* (Figure 6(a)).

Rats that were stressed weighed significantly less than nonstressed animals at the beginning of the *test phase* (i.e., 299.7 ± 3.1 g versus 324.9 ± 2.4 g, $p < 0.001$; data not shown). Weight changes induced by a subsequent acute LPS challenge were determined by subtracting weight measures from the rats' weight at the beginning of the *test phase*. There was a time × LPS ($F(3, 132) = 23.9$, $p < 0.001$, $\varepsilon = 0.63$) and a stress × LPS ($F(1, 44) = 16.0$, $p < 0.001$, $\varepsilon = 0.63$) interaction for change in body weight during the *test phase*. Post hoc analysis showed that LPS decreased weight in stressed and nonstressed rats (Figure 6(b)). This LPS-induced weight loss was most pronounced in the first 2 days after administration and then recovered over time. For total volume intake during the *test phase*, there was a time × stress × LPS interaction ($F(3, 132) = 4.5$, $p < 0.01$, $\varepsilon = 0.75$). On the first 2 days after administration, stressed and nonstressed rats that were injected with LPS drank significantly less than animals that received vehicle (Figure 6(c)). On the third day after LPS administration, stressed rats that received LPS drank less than their vehicle-injected controls, while the total volume intake of LPS-treated nonstressed rats had returned to control values. Finally, factorial rmANOVA indicated that there was a significant LPS effect ($F(1, 44) = 59.0$, $p < 0.001$, $\varepsilon = 0.85$), but no main effect of time or stress for sucrose preference during the *test phase*. LPS-treated rats had a lower sucrose preference than vehicle-injected animals, but the lack of main effects of time and stress did not allow further post hoc analysis (Figure 6(d)).

4. Discussion

Anhedonia, or the inability to experience pleasure from naturally rewarding activities, is a hallmark of clinical depression. While other key symptoms such as depressed mood are challenging to measure in laboratory animals, anhedonia can be estimated fairly easy by measuring the preference an animal develops for a sweetened solution relative to water. It is suggested that a decrease in this preference reflects a state of anhedonia [19].

Systemic administration of LPS has been commonly used to study inflammation-associated depression in rodents. However, discrepancies in the doses administered and time points investigated between labs have made it difficult to establish this approach as a useful animal model to study depressive symptoms. In a previous study, we characterized LPS-induced behavioral changes in mice and demonstrated that the time course of sickness and anhedonia can be evaluated by measuring total volume intake and sucrose preference in the SPT [17]. To extend this work, we assessed the anhedonic response to LPS in rats, while paying close attention to the dose- and time-dependency of LPS-induced

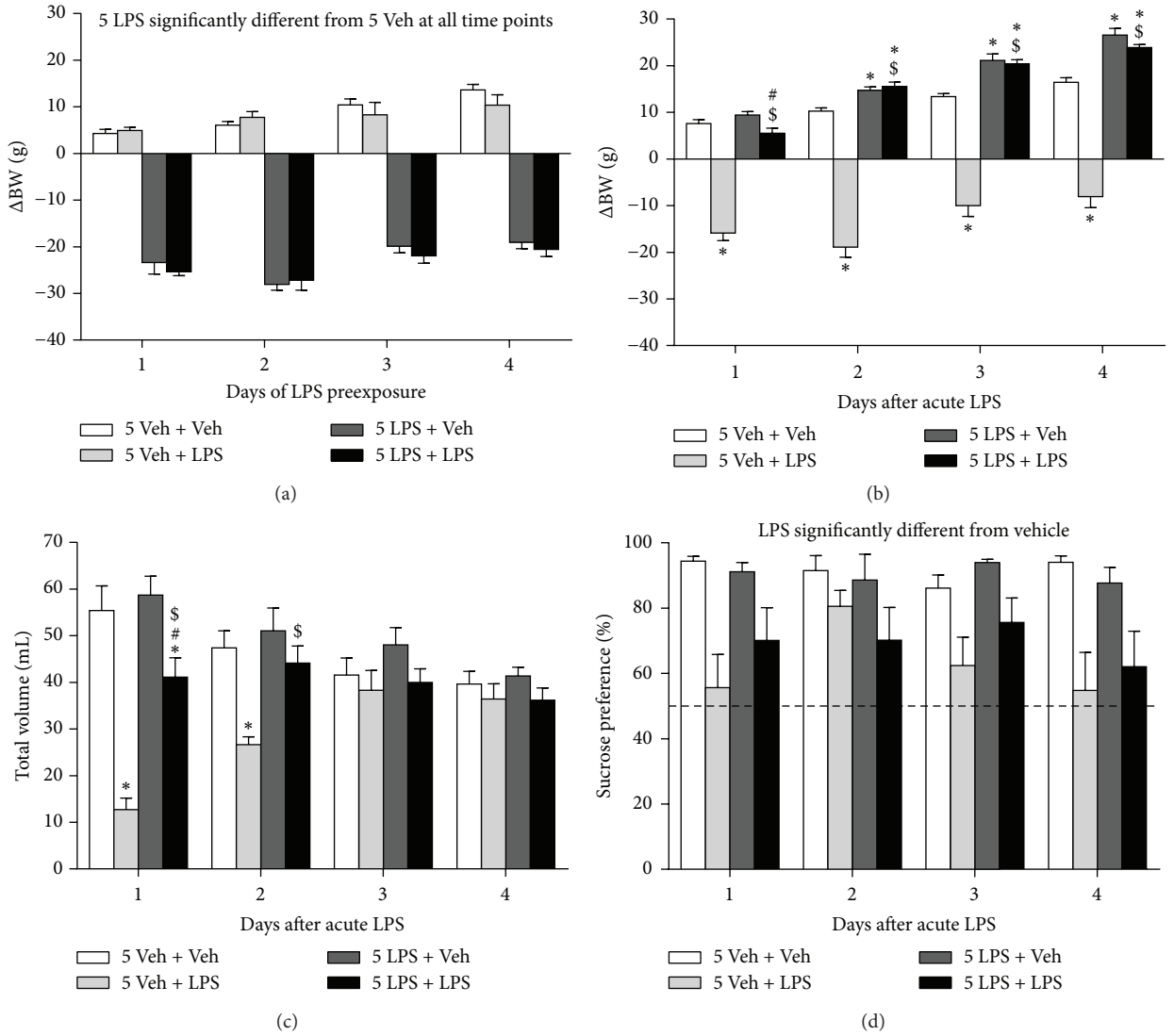

Figure 5: Repeated LPS administration protects against LPS-induced sickness but not anhedonia. After the *familiarization phase* (data not shown), rats received daily i.p. injections of either 0.63 mg/kg LPS (5 LPS) or vehicle (5 Veh) for 5 consecutive days. Three days after this *preexposure phase*, an acute systemic injection was administered to rats of either 0.63 mg/kg LPS or vehicle (Veh) and voluntary consumption of water and sucrose was measured during a period of 24 h for 4 days. Repeated peripheral LPS administration reduced body weight during the *preexposure phase* (a). At the beginning of the *test phase*, rats preexposed to LPS had a significant lower weight than animals that received vehicle preexposure (288.9 ± 2.6 g versus 314.5 ± 3.6 g, $p < 0.001$; data not shown). Weight only decreased mildly upon rechallenge with LPS, while weight reduction in LPS naive rats was more pronounced (b). On the first day of the *test phase*, LPS-challenged rats drank less than their vehicle-injected controls but this effect was less pronounced in rats that were preexposed to LPS (c). Sucrose preference was reduced in LPS-treated rats but no effect of preexposure was found (d). Dashed lines indicate chance level for sucrose preference. Graphs are plotted as mean + SEM ($n = 12$ per group). Data were analyzed by rmANOVA followed by independent samples t-test. $^{*}p < 0.05$ compared to 5 Veh + Veh, $^{\#}p < 0.05$ compared to 5 LPS + Veh, and $^{\$}p < 0.05$ compared to 5 Veh + LPS. 5 Veh + Veh: 5 days of vehicle followed by acute vehicle, 5 Veh + LPS: 5 days of vehicle followed by acute LPS, 5 LPS + Veh: 5 days of LPS followed by acute vehicle, and 5 LPS + LPS: 5 days of LPS followed by acute LPS.

sickness behavior because this may confound behavioral readouts being interpreted as depressive-like symptoms.

First, LPS-induced behavioral changes were evaluated in automated, investigator-independent assays commonly used to measure sickness and depressive-like behavior in rodents. In this study the animals were naive to testing at each time point measured, thus excluding potential confounding effects caused by habituation to repeated testing at different time points. Sickness, as measured by reduced locomotor activity in the OFT, was present as soon as 2 h after LPS administration and started to dissipate at 24 h. However, total volume intake in the SPT was still decreased at this time, thereby indicating that sickness had not disappeared completely. Interestingly, sucrose preference in rats injected

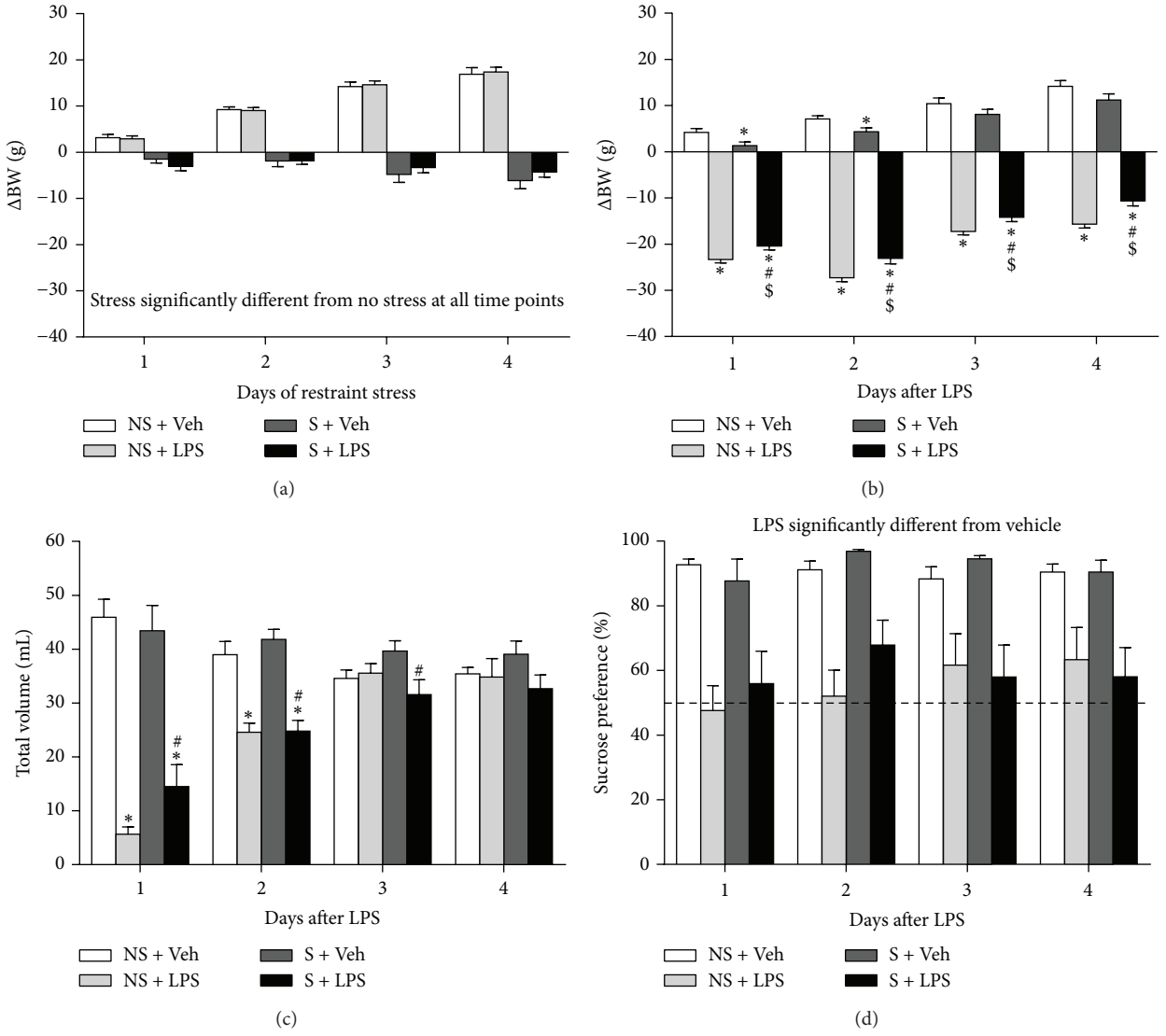

Figure 6: Subchronic restraint stress does not influence the anhedonic response to a subsequent LPS challenge. After the *familiarization phase* (data not shown), rats were exposed to 1 h of restraint stress daily for 5 consecutive days. Three days after the last stress session animals received an i.p. injection of either vehicle or 0.63 mg/kg LPS. Daily restraint stress reduced body weight (a). At the beginning of the *test phase*, rats that were stressed during the *manipulation phase* had a significant lower body weight than animals that were nonstressed (299.7 ± 3.1 g versus 324.9 ± 2.4 g, $p < 0.001$; data not shown). A subsequent acute LPS challenge reduced weight in nonstressed rats and to a slightly lesser extent in stressed animals (b). Systemic LPS administration also reduced total volume intake (c) and sucrose preference (d), but no differences could be found between stressed and nonstressed rats. Dashed lines indicate chance level for sucrose preference. Graphs are plotted as mean + SEM ($n = 12$ per group). Data were analyzed by rmANOVA followed by independent samples t-test. $^{*}p < 0.05$ compared to NS + Veh, $^{\#}p < 0.05$ compared to S + Veh, and $^{\$}p < 0.05$ compared to S + LPS. NS: nonstressed, S: stressed, and Veh: vehicle.

with the low dose of LPS (0.31 mg/kg) had returned to control levels at 24 h, despite the fact that these animals still drank much less than vehicle-treated rats. Rats injected with higher doses of LPS, in contrast, showed reduced total volume intake and decreased sucrose preference at this time. This may indicate that, at a dose of 0.63 mg/kg (and higher), LPS causes more pronounced anhedonia and therefore this particular dose was selected for further experimentation.

While the immunological response to LPS in mice and its relationship to behavioral changes are well documented, this is not the case for rats. Currently available literature on the effect of systemic LPS administration on circulating levels of inflammatory mediators in the rat is limited by the number of analytes measured and/or time points used. We have previously shown that in the mouse LPS administration leads to a rapid release of proinflammatory cytokines such as TNF-α, IL-1β, and IL-6 [17]. The present study for the first time provides the serum profile of a broad panel of immune molecules over a prolonged period of time after LPS administration. We show that systemic LPS injection in rats leads to

a response comparable to that in mice, with serum levels of proinflammatory cytokines peaking between 1 and 2 h after LPS administration and returning to baseline levels at 24 h. These findings are in line with Goble et al., who previously reported rapid, but short-lasting, increases in circulating IL-1β and IL-6 in LPS-challenged rats [20]. In our study, the release of the anti-inflammatory cytokine IL-10 peaked at 1 h and faded in the first 24 h after LPS. This confirms that the strong inflammatory response to a peripheral immune challenge is tightly regulated and rapidly attenuated by anti-inflammatory mediators. The appetite suppressing hormone leptin, whose primary function is to regulate energy balance [21], is also known to be an important mediator of sickness during systemic inflammation [22]. In line with other studies [23, 24], we found that peripheral LPS administration increased circulating levels of leptin. Although this effect was short lasting, it is not unlikely that leptin plays a role in the reduction of fluid intake and body weight that follows after LPS injection. The LPS-induced changes in serum levels of most analytes had dissipated by 24 h. However, circulating levels of the chemokines CXCL1, MCP-1, and MIP-1α remained elevated up to 96 h after treatment. These chemokines play an important role in leukocyte migration and activation, and their serum profile suggests that the immunological response to systemically administered LPS lasted for several days. Future studies should reveal whether levels of circulating chemokines could be used as a biomarker for inflammation-associated depressive symptoms such as anhedonia.

Activation of the immune system is known to deregulate the HPA axis, a physiological finding which is frequently observed in depression [25]. In agreement with previous findings [20, 26], we found that systemic LPS injection increased serum levels of corticosterone. This release of corticosterone into the circulation occurred promptly after LPS administration and had decreased substantially by 24 h. Corticosterone levels also increased in vehicle-injected rats. However, this happened to a lesser extent than following LPS administration and probably occurred as a consequence of stress related to the experimental procedure. While it is clear that inflammation can induce behavioral changes through secretion of systemic mediators, the precise relationship between specific cytokines and behavioral changes is not yet well understood. Sickness behavior is a normal physiological response that evolved to help organisms cope with infections [27]. It is thus unlikely that short-lived increases in cytokines playing a role in sickness behavior (such as IL-1β, IL-6, and TNF-α) will induce depression. Nevertheless, these cytokines may cause depressive symptoms such as anhedonia and thus add to the understanding of the pathological mechanisms of depression.

In our extended SPT study we showed that a single bolus of LPS reduces fluid intake in the first 2 days after administration. More specifically, on the first day after administration, LPS decreased total volume intake to approximately one-third of the normal daily intake (i.e., unchallenged on a W/W day). This suppressed drinking is a clear indication of sickness and precludes interpreting reduced sucrose preference as a sign of anhedonia. On the second day, however, LPS-injected rats also drank less than vehicle-treated controls but their total volume intake did reach normal daily intake levels. Therefore, the reduced sucrose preference seen on this day can be interpreted as an anhedonic response to the LPS challenge. This became even clearer on the third day where there was no difference in total volume intake between treatment groups, but still a significant reduction in sucrose preference in LPS-injected rats. The fact that rats treated with LPS started to gain weight at day three further indicates that sickness had dissipated at this point. In line with previously reported rat data [28, 29], LPS administration did not alter water intake at any of the time points (data not shown). This highlights the importance of including measures of total volume intake to estimate sickness in paradigms such as the SPT.

In our model of acute systemic LPS administration, anhedonia was present in the absence of apparent sickness from 2 to 3 days after injection. Depressive episodes in humans, however, can last up to several months [30]. Moreover, inflammation-associated depression in humans develops on a background of persistent inflammation. In order to mimic the human situation more closely, we decided to evaluate the anhedonic response to a longer lasting immune challenge. It was found that preexposure to LPS reduced the sickness response to a subsequent acute LPS challenge, suggesting the induction of tolerance to LPS. This phenomenon involves downregulation of proinflammatory responses to repeated LPS exposure and is thought to protect an organism from excessive tissue damage and the development of pathological states during prolonged or uncontrolled inflammation [31, 32]. Moreover, in our study, the secondary LPS challenge reduced sucrose preference in all rats, regardless of their preexposure. This indicates that, in our model to study anhedonia, repeated LPS administration does not offer an advantage over a single peripheral injection. Kubera and coworkers recently described a model in which repeated LPS injections given at one-month intervals induced a chronic state of anhedonia in female, but not in male mice [33]. Our study was performed in male rats, which could be an explanation for the lack of effect. Additionally, it is possible that a more specific or elaborate LPS dosing scheme is required to induce more pronounced and/or longer lasting anhedonia.

Stress is a major risk factor for the development of depression [34]. In a second approach to create a model of anhedonia that relates to the human situation, we tested whether exposure to stress alters anhedonic responses to a subsequent immune challenge. It was observed that repeated daily exposure to restraint stress decreased body weight, indicating that the rats underwent stress. Previous work by other labs has shown that repeated restraint stress can induce depressive-like behavior, including anhedonia [35–39]. Moreover, in studies using social disruption as a model of psychological stress the sickness response to a secondary LPS challenge was aggravated [40, 41]. In our study, repeated restraint stress did not alter measures of sickness or anhedonia in response to a subsequent LPS challenge. These findings are in line with results from a study by Wohleb et al., where repeated social defeat stress in mice did not exacerbate

anxiety behavior following a secondary LPS challenge [42]. It is possible that the restraint stress protocol used in our study was too mild and thus not sufficient to alter the sickness and/or anhedonic response to a subsequent immune challenge. Indeed, in most studies where anhedonia was reported following repeated restraint stress, the animals were restrained for several hours per day (versus 1 hour in our study), during several weeks (versus 5 days in our study) [36, 38, 39], and when shorter lasting restraint stress protocols were used, anhedonia was evaluated immediately after the last restraint session [35].

In the experiments where we tested the effect of LPS preexposure or stress on the anhedonia response to a subsequent LPS administration, LPS-injected rats showed reduced sucrose preference across the test phase. These findings are not in line with the acute LPS experiment where sucrose preference was only reduced at days 2 and 3 but had recovered at day 4. This discrepancy can potentially be explained by the fact that in our more elaborate experimental protocols a third phase was introduced between the *familiarization phase* and *test phase*. It may be possible that this extra week of individual housing and handling confounded measures of sucrose preference after a subsequent systemic LPS injection.

5. Conclusion

This study provides a systematic analysis of the time course of cytokine release and behavioral changes following peripheral LPS administration in rats. We report a SPT protocol that includes measurements of total volume intake, sucrose preference, and body weight and demonstrated that, by assessing these measurements and their interaction, this SPT protocol provides a way of separating LPS-induced anhedonia from sickness. This anhedonic response to LPS is robust but only lasts for 2 days. Therefore, caution is needed when studying the mechanisms underlying inflammation-associated depression using a single LPS injection in rats. To model the chronic nature of depression in humans more carefully, our SPT protocol was used to test whether preexposure to repeated LPS administration or subchronic stress influences the anhedonic response to a subsequent LPS challenge. While these procedures did not affect the time course of anhedonia, our results provide useful insights into the behavioral consequences of peripheral immune activation using LPS and may contribute to the development of more elaborate rodent models of inflammation-associated depression.

Disclosure

Jan A. Bouwknecht, Patrick De Haes, Theo F. Meert, Rony Nuydens, and Luc Ver Donck hold a permanent position at Janssen Pharmaceutica NV. Niels Hellings holds a permanent position at Hasselt University.

Competing Interests

The authors have no conflict of interests to declare.

Authors' Contributions

Steven Biesmans and Liam J. R. Matthews contributed equally to this work.

Acknowledgments

This work was fully funded by Janssen Research & Development, Division of Janssen Pharmaceutica NV.

References

[1] R. C. Kessler, P. Berglund, O. Demler, R. Jin, K. R. Merikangas, and E. E. Walters, "Lifetime prevalence and age-of-onset distributions of DSM-IV disorders in the national comorbidity survey replication," *Archives of General Psychiatry*, vol. 62, no. 6, pp. 593–602, 2005.

[2] C. D. Mathers and D. Loncar, "Projections of global mortality and burden of disease from 2002 to 2030," *PLoS Medicine*, vol. 3, no. 11, article e442, 2006.

[3] American Psychiatric Association, "Mood Disorders," in *Diagnostic and Statistical Manual of Mental Disorders, Text Revision (DSM-IV-TR)*, 2000.

[4] O. Berton and E. J. Nestler, "New approaches to antidepressant drug discovery: beyond monoamines," *Nature Reviews Neuroscience*, vol. 7, no. 2, pp. 137–151, 2006.

[5] V. Krishnan and E. J. Nestler, "The molecular neurobiology of depression," *Nature*, vol. 455, no. 7215, pp. 894–902, 2008.

[6] R. Dantzer, J. C. O'Connor, G. G. Freund, R. W. Johnson, and K. W. Kelley, "From inflammation to sickness and depression: when the immune system subjugates the brain," *Nature Reviews Neuroscience*, vol. 9, no. 1, pp. 46–56, 2008.

[7] A. H. Miller, V. Maletic, and C. L. Raison, "Inflammation and its discontents: the role of cytokines in the pathophysiology of major depression," *Biological Psychiatry*, vol. 65, no. 9, pp. 732–741, 2009.

[8] J. Blume, S. D. Douglas, and D. L. Evans, "Immune suppression and immune activation in depression," *Brain, Behavior, and Immunity*, vol. 25, no. 2, pp. 221–229, 2011.

[9] R. Krishnadas and J. Cavanagh, "Depression: an inflammatory illness?" *Journal of Neurology, Neurosurgery and Psychiatry*, vol. 83, no. 5, pp. 495–502, 2012.

[10] S. M. Gibney and H. A. Drexhage, "Evidence for a dysregulated immune system in the etiology of psychiatric disorders," *Journal of Neuroimmune Pharmacology*, vol. 8, no. 4, pp. 900–920, 2013.

[11] C. J. Henry, Y. Huang, A. Wynne et al., "Minocycline attenuates lipopolysaccharide (LPS)-induced neuroinflammation, sickness behavior, and anhedonia," *Journal of Neuroinflammation*, vol. 5, article 15, 2008.

[12] F. Frenois, M. Moreau, J. O'Connor et al., "Lipopolysaccharide induces delayed FosB/DeltaFosB immunostaining within the mouse extended amygdala, hippocampus and hypothalamus, that parallel the expression of depressive-like behavior," *Psychoneuroendocrinology*, vol. 32, no. 5, pp. 516–531, 2007.

[13] J. C. O'Connor, M. A. Lawson, C. André et al., "Lipopolysaccharide-induced depressive-like behavior is mediated by indoleamine 2,3-dioxygenase activation in mice," *Molecular Psychiatry*, vol. 14, no. 5, pp. 511–522, 2009.

[14] B. M. Berg, J. P. Godbout, K. W. Kelley, and R. W. Johnson, "α-Tocopherol attenuates lipopolysaccharide-induced sickness

behavior in mice," *Brain, Behavior, and Immunity*, vol. 18, no. 2, pp. 149–157, 2004.

[15] J. P. Godbout, J. Chen, J. Abraham et al., "Exaggerated neuroinflammation and sickness behavior in aged mice following activation of the peripheral innate immune system," *The FASEB Journal*, vol. 19, no. 10, pp. 1329–1331, 2005.

[16] J. P. Godbout, M. Moreau, J. Lestage et al., "Aging exacerbates depressive-like behavior in mice in response to activation of the peripheral innate immune system," *Neuropsychopharmacology*, vol. 33, no. 10, pp. 2341–2351, 2008.

[17] S. Biesmans, T. F. Meert, J. A. Bouwknecht et al., "Systemic immune activation leads to neuroinflammation and sickness behavior in mice," *Mediators of Inflammation*, vol. 2013, Article ID 271359, 14 pages, 2013.

[18] M. W. Vasey and J. F. Thayer, "The continuing problem of false positives in repeated measures ANOVA in psychophysiology: a multivariate solution," *Psychophysiology*, vol. 24, no. 4, pp. 479–486, 1987.

[19] A. Der-Avakian and A. Markou, "The neurobiology of anhedonia and other reward-related deficits," *Trends in Neurosciences*, vol. 35, no. 1, pp. 68–77, 2012.

[20] K. H. Goble, Z. A. Bain, V. A. Padow, P. Lui, Z. A. Klein, and R. D. Romeo, "Pubertal-related changes in hypothalamic-pituitary-adrenal axis reactivity and cytokine secretion in response to an immunological stressor," *Journal of Neuroendocrinology*, vol. 23, no. 2, pp. 129–135, 2011.

[21] J. M. Friedman, "Leptin, leptin receptors, and the control of body weight," *Nutrition Reviews*, vol. 56, no. 2, pp. s38–s46, 1998.

[22] C. Rummel, W. Inoue, S. Poole, and G. N. Luheshi, "Leptin regulates leukocyte recruitment into the brain following systemic LPS-induced inflammation," *Molecular Psychiatry*, vol. 15, no. 5, pp. 523–534, 2010.

[23] P. Sarraf, R. C. Frederich, E. M. Turner et al., "Multiple cytokines and acute inflammation raise mouse leptin levels: potential role in inflammatory anorexia," *The Journal of Experimental Medicine*, vol. 185, no. 1, pp. 171–175, 1997.

[24] R. Faggioni, G. Fantuzzi, J. Fuller, C. A. Dinarello, K. R. Feingold, and C. Grunfeld, "Il-1β mediates leptin induction during inflammation," *American Journal of Physiology—Regulatory Integrative and Comparative Physiology*, vol. 274, no. 1, pp. R204–R208, 1998.

[25] L. Capuron and A. H. Miller, "Immune system to brain signaling: neuropsychopharmacological implications," *Pharmacology and Therapeutics*, vol. 130, no. 2, pp. 226–238, 2011.

[26] S. M. Silva and M. D. Madeira, "Effects of chronic alcohol consumption and withdrawal on the response of the male and female hypothalamic-pituitary-adrenal axis to acute immune stress," *Brain Research*, vol. 1444, pp. 27–37, 2012.

[27] J. P. Konsman, P. Parnet, and R. Dantzer, "Cytokine-induced sickness behaviour: mechanisms and implications," *Trends in Neurosciences*, vol. 25, no. 3, pp. 154–159, 2002.

[28] R. Yirmiya, "Endotoxin produces a depressive-like episode in rats," *Brain Research*, vol. 711, no. 1-2, pp. 163–174, 1996.

[29] Y. Shen, T. J. Connor, Y. Nolan, J. P. Kelly, and B. E. Leonard, "Differential effect of chronic antidepressant treatments on lipopolysaccharide-induced depressive-like behavioural symptoms in the rat," *Life Sciences*, vol. 65, no. 17, pp. 1773–1786, 1999.

[30] J. Spijker, R. De Graaf, R. V. Bijl, A. T. F. Beekman, J. Ormel, and W. A. Nolen, "Duration of major depressive episodes in the general population: results from The Netherlands Mental Health Survey and Incidence Study (NEMESIS)," *British Journal of Psychiatry*, vol. 181, pp. 208–213, 2002.

[31] A. Broad, D. E. J. Jones, and J. A. Kirby, "Toll-like receptor (TLR) response tolerance: a key physiological 'damage limitation' effect and an important potential opportunity for therapy," *Current Medicinal Chemistry*, vol. 13, no. 21, pp. 2487–2502, 2006.

[32] M. Karin, T. Lawrence, and V. Nizet, "Innate immunity gone awry: linking microbial infections to chronic inflammation and cancer," *Cell*, vol. 124, no. 4, pp. 823–835, 2006.

[33] M. Kubera, K. Curzytek, W. Duda et al., "A new animal model of (chronic) depression induced by repeated and intermittent lipopolysaccharide administration for 4months," *Brain, Behavior, and Immunity*, vol. 31, pp. 96–104, 2013.

[34] K. S. Kendler, L. M. Thornton, and C. O. Gardner, "Genetic risk, number of previous depressive episodes, and stressful life events in predicting onset of major depression," *American Journal of Psychiatry*, vol. 158, no. 4, pp. 582–586, 2001.

[35] T. Hayase, "Depression-related anhedonic behaviors caused by immobilization stress: a comparison with nicotine-induced depression-like behavioral alterations and effects of nicotine and/or 'antidepressant' drugs," *Journal of Toxicological Sciences*, vol. 36, no. 1, pp. 31–41, 2011.

[36] L. Eiland, J. Ramroop, M. N. Hill, J. Manley, and B. S. McEwen, "Chronic juvenile stress produces corticolimbic dendritic architectural remodeling and modulates emotional behavior in male and female rats," *Psychoneuroendocrinology*, vol. 37, no. 1, pp. 39–47, 2012.

[37] G. Naert, G. Ixart, T. Maurice, L. Tapia-Arancibia, and L. Givalois, "Brain-derived neurotrophic factor and hypothalamic-pituitary-adrenal axis adaptation processes in a depressive-like state induced by chronic restraint stress," *Molecular and Cellular Neuroscience*, vol. 46, no. 1, pp. 55–66, 2011.

[38] B. Haenisch, A. Bilkei-Gorzo, M. G. Caron, and H. Bönisch, "Knockout of the norepinephrine transporter and pharmacologically diverse antidepressants prevent behavioral and brain neurotrophin alterations in two chronic stress models of depression," *Journal of Neurochemistry*, vol. 111, no. 2, pp. 403–416, 2009.

[39] S. Chiba, T. Numakawa, M. Ninomiya, M. C. Richards, C. Wakabayashi, and H. Kunugi, "Chronic restraint stress causes anxiety- and depression-like behaviors, downregulates glucocorticoid receptor expression, and attenuates glutamate release induced by brain-derived neurotrophic factor in the prefrontal cortex," *Progress in Neuro-Psychopharmacology and Biological Psychiatry*, vol. 39, no. 1, pp. 112–119, 2012.

[40] J. Gibb, S. Hayley, R. Gandhi, M. O. Poulter, and H. Anisman, "Synergistic and additive actions of a psychosocial stressor and endotoxin challenge: circulating and brain cytokines, plasma corticosterone and behavioral changes in mice," *Brain, Behavior, and Immunity*, vol. 22, no. 4, pp. 573–589, 2008.

[41] J. Gibb, S. Hayley, M. O. Poulter, and H. Anisman, "Effects of stressors and immune activating agents on peripheral and central cytokines in mouse strains that differ in stressor responsivity," *Brain, Behavior, and Immunity*, vol. 25, no. 3, pp. 468–482, 2011.

[42] E. S. Wohleb, A. M. Fenn, A. M. Pacenta, N. D. Powell, J. F. Sheridan, and J. P. Godbout, "Peripheral innate immune challenge exaggerated microglia activation, increased the number of inflammatory CNS macrophages, and prolonged social withdrawal in socially defeated mice," *Psychoneuroendocrinology*, vol. 37, no. 9, pp. 1491–1505, 2012.

Hindawi Publishing Corporation
BioMed Research International
Volume 2016, Article ID 7261960, 6 pages
http://dx.doi.org/10.1155/2016/7261960

Research Article

Effects of Erythropoietin Administration on Adrenal Glands of Landrace/Large White Pigs after Ventricular Fibrillation

Armando Faa,[1] Gavino Faa,[1] Apostolos Papalois,[2] Eleonora Obinu,[1] Giorgia Locci,[1] Maria Elena Pais,[1] Pavlos Lelovas,[3] Dimitrios Barouxis,[3] Charalampos Pantazopoulos,[3] Panagiotis V. Vasileiou,[3] Nicoletta Iacovidou,[4] and Theodoros Xanthos[5]

[1]*Department of Surgery, Section of Pathology, University of Cagliari, Cagliari, 09100 Sardinia, Italy*
[2]*ELPEN Experimental Center, Athens, Greece*
[3]*Medical School, National and Kapodistrian University of Athens, Athens, Greece*
[4]*Neonatal Department, Aretaieio Hospital, Medical School, National and Kapodistrian University of Athens, Athens, Greece*
[5]*European University Cyprus, Nicosia, Cyprus*

Correspondence should be addressed to Armando Faa; armando.faa@hotmail.it

Received 19 February 2016; Revised 13 June 2016; Accepted 21 June 2016

Academic Editor: Oreste Gualillo

Aim. To evaluate the effects of erythropoietin administration on the adrenal glands in a swine model of ventricular fibrillation and resuscitation. *Methods*. Ventricular fibrillation was induced *via* pacing wire forwarded into the right ventricle in 20 female Landrace/Large White pigs, allocated into 2 groups: experimental group treated with bolus dose of erythropoietin (EPO) and control group which received normal saline. Cardiopulmonary resuscitation (CPR) was performed immediately after drug administration *as per* the 2010 European Resuscitation Council (ERC) guidelines for Advanced Life Support (ALS) until return of spontaneous circulation (ROSC) or death. Animals who achieved ROSC were monitored, mechanically ventilated, extubated, observed, and euthanized. At necroscopy, adrenal glands samples were formalin-fixed, paraffin-embedded, and routinely processed. Sections were stained with hematoxylin-eosin. *Results.* Oedema and apoptosis were the most frequent histological changes and were detected in all animals in the adrenal cortex and in the medulla. Mild and focal endothelial lesions were also detected. A marked interindividual variability in the degree of the intensity of apoptosis and oedema at cortical and medullary level was observed within groups. Comparing the two groups, higher levels of pathological changes were detected in the control group. No significant difference between the two groups was observed regarding the endothelial changes. *Conclusions*. In animals exposed to ventricular fibrillation, EPO treatment has protective effects on the adrenal gland.

1. Introduction

Cardiac arrest is one of the leading causes of death. After return of spontaneous circulation (ROSC), post-cardiac arrest syndrome represents the predominant disorder in survivors. Besides the postarrest brain injury, the postresuscitation myocardial stunning, and the systemic ischemia/reperfusion response, this syndrome is characterized by adrenal insufficiency, a disorder that often lacks attention and appears to be associated with a poor prognosis in cases of postresuscitation shock [1].

The hormone erythropoietin (EPO), from Greek: *ερυθρός* (red) and *ποιεῖν* (make), controls red blood cell production in the human body. It is a cytokine crucial for erythrocyte precursors production in the fetal liver and, after birth, in the bone marrow. Human EPO has a molecular weight of 34 kDa. The hematopoietic cytokine EPO is produced by the kidney in response to hypoxia and stimulates erythroid progenitor cells to increase the number of mature red blood cells, thereby increasing the O_2 carrying capacity.

It is well established that EPO-receptors are widespread in cells throughout the body, including endothelial cells, myocardiocytes, macrophages, retinal cells, and cells of the adrenal cortex [2].

Erythropoietin treatment influences directly or indirectly the function of endocrine organs; it induces a significant decrease in somatotropin, prolactin, follitropin, lutropin, ACTH, cortisol, plasma renin activity, aldosterone, noradrenaline, adrenaline, dopamine, glucagon, pancreatic polypeptide, and gastrin plasma levels. It also increases plasma insulin, estradiol, testosterone, atrial natriuretic peptide, thyrotropin, and thyroxine levels [3].

Recent studies suggest that adrenal insufficiency might be due to adrenal microvessel contraction; adrenomedullin, a vasodilator peptide with a half-life of about 20 min, might partly be responsible for this phenomenon as it dampens baroreflex-driven responses and buffers sympathetic actions.

As it has been hypothesized that EPO might have a multiorgan protection role [4], the present study aimed at better understanding of the pathophysiology of adrenal insufficiency and the possible protective effects of EPO at adrenal level, in an experimental animal model of ventricular fibrillation (VF).

2. Materials and Methods

The protocol was approved by the Directorate of Veterinary Services of Prefecture of Athens, Attica, Greece, according to Greek legislation regarding ethical and experimental procedures. Twenty female Landrace/Large White pigs, aged 10–15 weeks with an average weight of 19 ± 2 kg, all from the same breeder (Validakis, Athens, Greece) were the study subjects. All animals were prepared in a standardized fashion at ELPEN Experimental-Research Center, Pikermi, Greece, as previously described [5]. Initial sedation was achieved by intramuscular injection of ketamine hydrochloride (10 mg/kg), midazolam (0.5 mg/kg), and atropine (0.05 mg/kg). Anaesthesia was induced with an intravenous (iv) bolus dose of propofol (2 mg/kg) *via* the marginal auricular vein. The pigs were then intubated and mechanically ventilated with a volume-controlled ventilator. End-tidal CO_2 ($ETCO_2$) was monitored by waveform capnography, and respiratory frequency was adjusted to maintain $ETCO_2$ between 35 and 40 mm Hg. A bolus dose of cis-atracurium (0.15 mg/kg) was administered to ascertain synchrony with the ventilator. Continuous infusion of propofol 150 μg/kg/min was used to maintain adequate anaesthetic depth and fentanyl 4 μg/kg to ensure analgesia. Cardiac rhythm and heart rate were monitored by electrocardiography. Right carotid artery and right internal jugular vein were catheterized, and aortic pressure was measured using a fluid-filled catheter. Mean arterial pressure (MAP) was determined by electronic integration of the aortic blood pressure waveform. A catheter was inserted into the right atrium *via* the right jugular vein for continuous measurement of right atrial pressure.

2.1. Experimental Protocol. After surgery, the animals were allowed a 30-minute stabilization period, before baseline data were collected. Ventricular fibrillation was induced with a 9 V ordinary cadmium battery *via* a pacing wire forwarded into the right ventricle through the cannulated right jugular vein, as previously described [6, 7], and was confirmed by electrocardiography and by a sudden drop in MAP. Mechanical ventilation and administration of anaesthetics were discontinued simultaneously with the onset of VF and the animals were left untreated for 8 min. A bolus dose of adrenaline (0.02 mg/kg) was then administered, and the animals ($n = 10$ per group) were randomly treated either with a bolus dose of EPO or with normal saline as placebo. All drugs were injected *via* the marginal auricular vein, followed by a 10 mL normal saline flush to assist faster circulation of medications. The researchers were blinded to the animal's allocation, until the experiment was completed and all haemodynamic and survival data were collected. Cardiopulmonary resuscitation was commenced immediately after drug administration. Mechanical ventilation was resumed with 21% oxygen and automatic continuous precordial compression was initiated at a rate of 100 per minute following the two-minute cycles *as per* the 2010 ERC ALS guidelines [5]. After 2 min of CPR, defibrillation was attempted with a 4 J/kg monophasic shock. Cardiopulmonary resuscitation was resumed for another 2 minutes after each defibrillation attempt. Further bolus doses of adrenaline (0.02 mg/kg) were administered every 4 minutes during CPR. Each experiment continued until ROSC or if asystole/pulseless electrical activity (PEA) occurred >10 min after CPR initiation. Return of spontaneous circulation was defined as the presence of a perfusing cardiac rhythm with a mean arterial pressure of at least 60 mmHg for a minimum of 5 minutes. After ROSC, the animals were monitored closely and mechanically ventilated for 6 hours, under general anaesthesia, with the prearrest settings. No other interventions were made after ROSC. After 6 hours, all catheters were removed; the animals were allowed to recover from anaesthesia and were extubated and transferred to their observation cages. They remained under observation for 48 hours after ROSC before euthanasia with an iv bolus dose of propofol 40 mg, followed by 2 gr thiopental iv. Experimental endpoints were ROSC and 48 h survival.

Histological analyses were carried out in all treated animals. Adrenal tissue samples were fixed in 10% formalin, routinely processed, and paraffin-embedded; the initial block was cut into 6-7 blocks about 2-3 mm wide. Five-micron-thick sections were deparaffinized and hydrated to water. They were then colored with hematoxylin for 15 minutes, washed in running tap water for 20 minutes, and counterstained with eosin for 15 seconds to 2 minutes. Finally, slides were dehydrated in 95% absolute alcohol and cleared in xylene. All hematoxylin-eosin- (H&E-) stained slices were assessed by a pathologist who was blinded to the animal treatment and outcome. For the quantification of the elementary lesions observed in adrenal glands, five fields were randomly selected and observed for the count in each sample. The variables are expressed as mean ± standard deviation (SD) for each elementary lesion found at histology. Repeated Student's t-tests were used to evaluate any possible significant statistical difference between the control group and the experimental group.

Table 1

Cases	Cortical			Medulla		
	Apoptosis	Oedema	Endothelial damage	Apoptosis	Oedema	Endothelial damage
1	2	3	1	1	2	1
2	2	3	1	1	1	1
4	3	3	1	1	1	1
5	3	3	1	1	2	1
6	4	3	1	1	2	1
7	4	3	1	1	2	1
8	4	3	1	1	2	1
9	3	3	1	1	2	1
10	4	3	1	1	2	1
12	2	2	1	1	1	1
13	3	2	1	1	1	1
14	3	3	1	1	1	1
15	2	3	1	1	2	1
15B	2	2	1	1	2	1
15C	2	2	1	1	1	1
16	2	1	1	1	1	1
17	1	1	1	1	1	1
18	1	2	1	1	1	1
20	1	2	1	1	2	1

3. Results

The histological study of adrenal glands of the pigs submitted to VF revealed pathological changes in all animals (see Table 1). The most important changes were oedema and apoptosis of adrenal cells. Moreover, morphological signs of mild and focal endothelial cell damage were detected. All pathological changes were detected both in the adrenal cortex and in the medulla. A marked interindividual variability regarding the degree of adrenal pathology was observed among the animals within the same group: in particular, significant differences were observed among animals of the same group regarding the intensity of apoptosis and oedema at cortical and medullary level. No significant interindividual variability was detected regarding the degree of endothelial changes (see Table 1).

Differences regarding the intensity and diffusion of the pathological changes between the two groups of animals were detected. The adrenal glands of the animals of the control group (group 1) were characterized by higher levels of pathological changes. In particular, apoptosis of cortical adrenal cells was present in the vast majority of animals in this group (Figure 1), contrarily with the presence of scattered apoptotic cells in animals submitted to EPO treatment (group 2). Differences were also detected regarding oedema, which was diffuse in all animals of group 1 (Figure 2), whereas in the EPO-treated animals cortical oedema was focal or mild in the majority of animals (see Table 1). No significant differences between the two groups were found regarding the endothelial changes (mainly endothelial swelling), which were mild (Figure 3) and focally detected in similar degree in the cortex of animals of groups 1 and 2 (see Table 1).

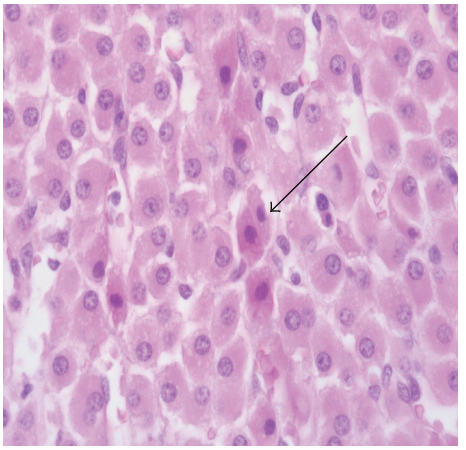

Figure 1: Diffuse apoptosis in the cortex of the adrenal glands. Cells undergoing apoptosis are characterized by cell detachment, chromatin condensation, and eosinophilia of the cytoplasm.

Histological examination of the adrenal medulla showed minor pathological changes, compared with the adrenal cortex. Apoptosis was focal, appearing as scattered apoptotic cells showing a hypereosinophilic cytoplasm and a dark nucleus. Cells undergoing apoptosis appeared intermingled with normal-appearing larger medullary cells (Figure 4). No significant difference regarding the degree of medullary

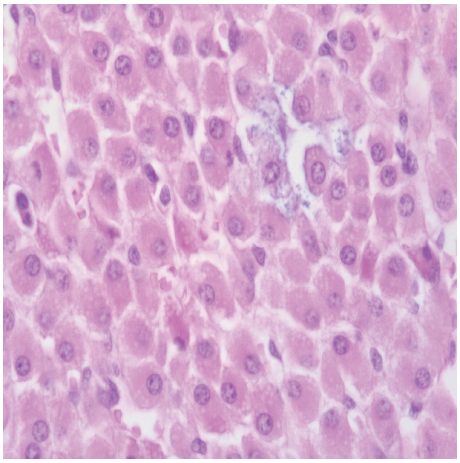

Figure 2: Diffuse oedema in the adrenal cortex. Due to the increase of the interstitial fluid, adrenal cells are detached from each other.

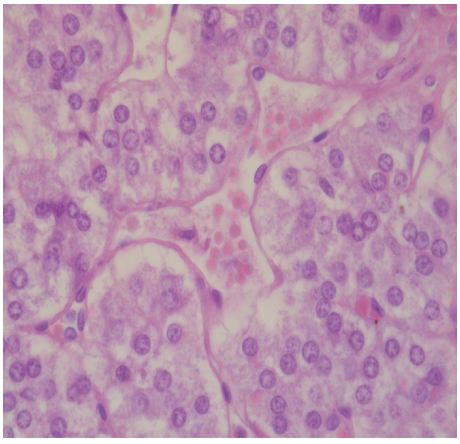

Figure 3: Mild endothelial damage in adrenal vessel, represented by swelling of the nuclei of endothelial cells (center of the picture).

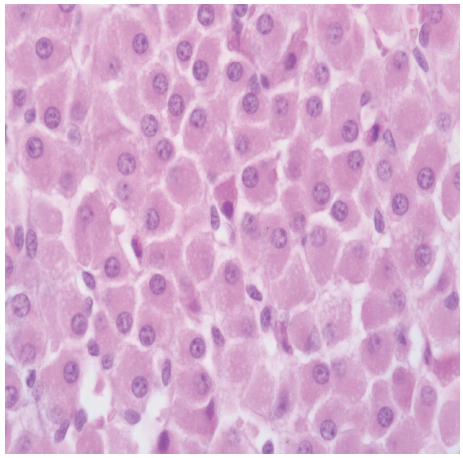

Figure 4: Apoptosis of the adrenal medulla. The scattered cells undergoing apoptosis show a picknotic nucleus and a dense eosinophilic cytoplasm.

apoptosis was detected between the two groups (see Table 1). Oedema was found in the adrenal medulla of all the animals, including those treated with EPO (Table 1).

Regarding the endothelial lesions detected in the medulla, endothelial swelling was the unique lesion focally detected in both groups.

To minimize errors due to sampling variability, the count of histological changes was based on the observation of five high power-fields, randomly selected from adrenal cortex and the medulla of the collected adrenal samples.

4. Discussion

In a previous preliminary study from our team, EPO administration resulted in higher rates of ROSC and higher 48 h survival with improved haemodynamics throughout the resuscitation period [8]. In other studies of experimental model of cardiac ischemia-reperfusion injury, EPO administration had contradictory effects: on one hand, EPO treatment increased functional recovery, suggesting the need of additional studies to evaluate therapeutic applications of EPO administration [4]; on the other hand, EPO did not have any significant protecting effect on cardiomyocytes when exposed to VF [8]. Moreover, EPO was demonstrated to prevent apoptosis of motor neurons in an experimental model of spinal cord ischemic injury [9]. The antiapoptotic role of EPO was also reported in a rat model of cerebral ischemia, where systemic administration of EPO after middle-cerebral artery occlusion dramatically reduced the volume of brain infarction and promoted cell survival by protecting neurons against hypoxia-induced cell death [10]. Conflicting results have recently been reported regarding the mechanisms of neuroprotection of EPO treatment. In particular, the neuroprotective effects of EPO are not restricted to its antiapoptotic role, given the lack of Akt activation after EPO administration. An alternative mechanism, proposed to explain EPO neuroprotection, was blood-brain barrier preservation and prevention of brain oedema [11].

The protective effects of EPO treatment are not restricted to the central nervous system. Pretreatment with EPO has recently been shown to ameliorate the renal injury caused by bilateral renal ischemia-reperfusion, by attenuating oxidative stress in kidney cells [12]. Moreover, the protective effect of EPO on kidney cells was increased by its association with melatonin in a rat model of ischemia-reperfusion injury [13].

With the present study we demonstrate, for the first time to the best of our knowledge, that EPO treatment has protective effects on the adrenal gland injury following VF. This protection was mainly observed in the adrenal cortex. It was evidenced in the medulla but in a minor degree. In the pigs of the control group, oedema was intense and diffuse in the cortex of all animals, indicating the increase in interstitial fluid as a possible mechanism for adrenal gland pathology. In contrast, in animals treated with EPO, oedema of the adrenal cortex was focal and mild in the majority of animals, reaching levels similar to those detected in all animals of the other group only in 2 out of 10 animals.

Striking differences were also found regarding apoptosis of cortical adrenal cells. High levels (degree 3 or 4) of cell shrinkage and cell detachment, typical morphological signs of apoptotic cell death, were observed in 7 out 9 animals of the first group, not receiving EPO treatment. Contrarily, similar high levels of apoptosis were observed in 2 out of 10 animals in the EPO-treated animals (group 2). These data clearly indicate that EPO protects adrenal cortical cells by limiting apoptosis and interstitial oedema. The origin of oedema is not clear, on the basis of our findings. No significant difference between the 2 groups was found, in this study, regarding the occurrence of vascular damage and, in particular, of endothelial damage. Endothelial changes (focal endothelial swelling) were mild in all the animals. As for the levels of endothelial damage, no difference was found between groups, both in the cortical and in the medullary zones.

In our study, the protective effects of EPO treatment were mainly observed in the cortical zones. Apoptotic cells were observed to be scattered even in the medulla, suggesting the existence of mild medullary pathological changes due to VF. The absence of any difference, regarding apoptosis of medullary cells, between the 2 groups might suggest that the antiapoptotic protective effects of EPO in this experimental model are restricted to cortical adrenal cells. These findings might be related to previous studies on an uneven distribution of EPO-receptors in the adrenal glands, indicating a preferential localization of EPO-receptors in the adrenal cortex [3].

Some differences were observed between the 2 groups regarding the degree of oedema in the medulla: the finding of a mild and focal oedema (grade 1) in the medulla of 7 out of 10 animals in the EPO-treated group contrasted with the detection of grade 1 oedema in 2 out of 9 animals of the control group. These findings confirm previous studies, suggesting that the protective role of EPO should not be restricted to its antiapoptotic effect [9], and lay stress on the ability of EPO treatment to end or decrease the levels of interstitial oedema in the adrenal gland, as previously reported in the brain [11].

There are significant limitations in the current study. This is an animal study and extrapolation to humans should be done with caution. Moreover, the number of animals was relatively low and in the current study we did not measure cytokines and stress hormones' levels such as epinephrine and norepinephrine.

In conclusion, our study clearly shows that EPO treatment during resuscitation of Landrace/Large White pigs submitted to VF has a clear protective effect on adrenal glands. The mechanism of this action might be multifactorial, resulting in a marked decrease in the degree of apoptosis of cortical adrenal cells and a decrease in oedema, both in the cortex and in the adrenal medulla.

Competing Interests

The authors declare that they have no competing interests.

Authors' Contributions

Contribution of each author to the project and production of the paper is as follows: Armando Faa analysed and interpreted the data and prepared the paper. Theodoros Xanthos and Nicoletta Iacovidou performed the animal experiment and critically revised the paper. Pavlos Lelovas, Panagiotis V. Vasileiou, Dimitrios Barouxis, Charalampos Pantazopoulos, and Apostolos Papalois performed the animal experiment. Giorgia Locci and Eleonora Obinu performed interpretation of histological and immunohistochemical data. Maria Elena Pais participated to the interpretation of data and to preparation of the paper. Gavino Faa contributed to the conception and design of the present study.

References

[1] F. Pene, H. Hyvernat, V. Mallet et al., "Prognostic value of relative adrenal insufficiency after out-of-hospital cardiac arrest," *Intensive Care Medicine*, vol. 31, no. 5, pp. 627–633, 2005.

[2] S. E. Juul, A. T. Yachnis, and R. D. Christensen, "Tissue distribution of erythropoietin and erythropoietin receptor in the developing human fetus," *Early Human Development*, vol. 52, no. 3, pp. 235–249, 1998.

[3] F. Kokot, A. Wiecek, H. Schmidt-Gayk et al., "Function of endocrine organs in hemodialyzed patients of long-term erythropoietin therapy," *Artificial Organs*, vol. 19, no. 5, pp. 428–435, 1995.

[4] Z. Cai, D. J. Manalo, G. Wei et al., "Hearts from rodents exposed to intermittent hypoxia or erythropoietin are protected against ischemia-reperfusion injury," *Circulation*, vol. 108, no. 1, pp. 79–85, 2003.

[5] T. Xanthos, P. Lelovas, I. Vlachos et al., "Cardiopulmonary arrest and resuscitation in Landrace/Large White swine: a research model," *Laboratory Animals*, vol. 41, no. 3, pp. 353–362, 2007.

[6] S. V. Rao and J. S. Stamler, "Eythropoietin , anemia, and orthostatic hypotension: the evidence mounts," *Clinical Autonomic Research*, vol. 12, no. 3, pp. 141–143, 2002.

[7] C. J. Parsa, J. Kim, R. U. Riel et al., "Cardioprotective effects of erythropoietin in the reperfused ischemic heart: a potential role for cardiac fibroblasts," *The Journal of Biological Chemistry*, vol. 279, no. 20, pp. 20655–20662, 2004.

[8] P. V. S. Vasileiou, T. Xanthos, D. Barouxis et al., "Erythropoietin administration facilitates return of spontaneous circulation and improves survival in a pig model of cardiac arrest," *American Journal of Emergency Medicine*, vol. 32, no. 8, pp. 871–877, 2014.

[9] M. Celik, N. Gökmen, S. Erbayraktar et al., "Erythropoietin prevents motor neuron apoptosis and neurologic disability in experimental spinal cord ischemic injury," *Proceedings of the National Academy of Sciences of the United States of America*, vol. 99, no. 4, pp. 2258–2263, 2002.

[10] A.-L. Sirén, M. Fratelli, M. Brines et al., "Erythropoietin prevents neuronal apoptosis after cerebral ischemia and metabolic stress," *Proceedings of the National Academy of Sciences of the United States of America*, vol. 98, no. 7, pp. 4044–4049, 2001.

[11] B. O. Ratilal, M. M. C. Arroja, J. P. F. Rocha et al., "Neuroprotective effects of erythropoietin pretreatment in a rodent model of transient middle cerebral artery occlusion," *Journal of Neurosurgery*, vol. 121, no. 1, pp. 55–62, 2014.

[12] M. Elshiekh, M. Kadkhodaee, B. Seifi, M. Ranjbaran, and P. Ahghari, "Ameliorative effect of recombinant human erythropoietin and ischemic preconditioning on renal ischemia reperfusion injury in rats," *Nephro-Urology Monthly*, vol. 7, no. 6, Article ID e31152, 2015.

[13] N. Ahmadiasl, S. Banaei, A. Alihemati, B. Baradaran, and E. Azimian, "Effect of a combined treatment with erythropoietin and melatonin on renal ischemia reperfusion injury in male rats," *Clinical and Experimental Nephrology*, vol. 18, no. 6, pp. 855–864, 2014.

Hindawi Publishing Corporation
BioMed Research International
Volume 2016, Article ID 5251738, 9 pages
http://dx.doi.org/10.1155/2016/5251738

Research Article

Progressive Depletion of Rough Endoplasmic Reticulum in Epithelial Cells of the Small Intestine in Monosodium Glutamate Mice Model of Obesity

Kazuhiko Nakadate,[1] Kento Motojima,[2] Tomoya Hirakawa,[2] and Sawako Tanaka-Nakadate[3]

[1]*Department of Basic Science, Educational and Research Center for Pharmacy, Meiji Pharmaceutical University, Tokyo 204-8588, Japan*
[2]*Faculty of Pharmaceutical Sciences, Meiji Pharmaceutical University, Tokyo 204-8588, Japan*
[3]*Department of Pharmacology and Toxicology, Dokkyo Medical University School of Medicine, Tochigi 321-0293, Japan*

Correspondence should be addressed to Kazuhiko Nakadate; nakadate@my-pharm.ac.jp

Received 7 February 2016; Revised 26 May 2016; Accepted 2 June 2016

Academic Editor: Monica Fedele

Chronic obesity is a known risk factor for metabolic syndrome. However, little is known about pathological changes in the small intestine associated with chronic obesity. This study investigated cellular and subcellular level changes in the small intestine of obese mice. In this study, a mouse model of obesity was established by early postnatal administration of monosodium glutamate. Changes in body weight were monitored, and pathological changes in the small intestine were evaluated using hematoxylin-eosin and Nissl staining and light and electron microscopy. Consequently, obese mice were significantly heavier compared with controls from 9 weeks of age. Villi in the small intestine of obese mice were elongated and thinned. There was reduced hematoxylin staining in the epithelium of the small intestine of obese mice. Electron microscopy revealed a significant decrease in and shortening of rough endoplasmic reticulum in epithelial cells of the small intestine of obese mice compared with normal mice. The decrease in rough endoplasmic reticulum in the small intestine epithelial cells of obese mice indicates that obesity starting in childhood influences various functions of the small intestine, such as protein synthesis, and could impair both the defense mechanism against invasion of pathogenic microbes and nutritional absorption.

1. Introduction

Obesity has recently become a major cause of the metabolic syndrome worldwide [1, 2]. Moreover, the incidence of obesity has more than doubled in children and quadrupled in adolescents in the past 30 years [3]. Obese children and adolescents are likely to be obese as adults; therefore, they are at an increased risk of adult health problems, such as heart disease, cardiovascular disease, type 2 diabetes, stroke, and osteoarthritis [4–8]. Chronic obesity is also associated with an increased risk of many types of cancer, including cancer of the breast, colon, endometrium, esophagus, kidney, pancreas, gall bladder, thyroid, ovary, cervix, and prostate as well as multiple myeloma and Hodgkin's lymphoma [9]. Furthermore, metabolic syndrome is a major predictor of nonalcoholic fatty liver disease (NAFLD) [10, 11]. In NAFLD, a steadily progressive disease, the findings of hepatitis and fibrosis and changes in hepatocytes are similar to those seen in alcoholic liver disease [12]. Many patients with NAFLD are obese and have comorbid hyperlipidemia, hypertension, and insulin resistance. Therefore, NAFLD is now recognized as the hepatic manifestation of metabolic syndrome [13–15]. The pathogenesis of NAFLD remains unclear. However, it is thought that inflammation and fibrosis in the liver are caused by a two-phase process [16]. The first step involves an increase in fatty acid biosynthesis or blockade of fatty acid combustion, and the second step involves an increase in factors, such as oxidative stress and lipid peroxidation. In terms of

an immunological pathogenesis, it has been suggested that lifestyle factors, such as overeating or unbalanced diet, alter the quality and/or quantity of bacterial flora in the intestine. This can result in the translocation of Gram-negative bacteria from the gut into the portal vein, which activates resident liver macrophages (Kupffer cells), setting up an immune response.

The intestinal mucous membrane epithelium has a defense mechanism to prevent the invasion of pathogenic microbes such as bacteria. When the permeability of this intestinal epithelium is increased by excessive alcohol intake or overeating, the defense mechanism can fail [17]. Liver damage is caused by an inflow of bacteria and endotoxins through the lining of the intestinal tract into the bloodstream, including the portal vein. Therefore, failure of the defense mechanism of the intestinal mucous membrane is very important in the pathogenesis of various chronic liver diseases [17, 18]. The transport of material through the intestinal epithelium is either transcellular via the intracellular pathway, or paracellular via the intercellular pathway. The paracellular pathway is involved in the absorption of minerals such as calcium and is controlled by an intercellular barrier. The transcellular pathway is involved in the intake of nutrients and is controlled by regulation of the many transporters and channels on the membrane of intestinal epithelium cells. Failure of the defense mechanism provided by the intestinal mucous membrane underlies many pathological conditions.

In a previous study of mice with monosodium glutamate- (MSG-) induced obesity, we found that lipid droplets accumulated in the hepatocytes of obese mice and levels of nonesterified fatty acid (NEFA), low-density lipoprotein cholesterol (LDL-C), high-density lipoprotein cholesterol (HDL-C), and triglyceride (TG) were increased compared to controls [19]. Other studies have also reported that lipid droplets accumulate in hepatocytes in chronic obesity and NAFLD [1, 20]. Moreover, our recent scanning electron microscopic analysis of the livers of mice with MSG-induced obesity showed sinusoidal dilatation and swelling of sinusoidal fenestrations [21]. However, little is known about pathological changes in the small intestine associated with chronic obesity. It is possible that obesity leads to functional changes in the small intestine, such as altered nutritional absorption through the epithelial cells into blood vessels. Therefore, we used light and electron microscopy to investigate structural details of the small intestinal epithelium in mice with obesity induced using MSG during the early perinatal period.

2. Materials and Methods

2.1. Animals. A total of 16 C57BL/6J male mice (Charles River, Japan) were used in this study. The mice were housed under temperature and humidity controlled conditions with a 12 : 12 h light-dark cycle and free access to food and water. All experiments were performed in accordance with the National Institutes of Health Guide for the Care and Use of Laboratory Animals. The animal research committee of Meiji Pharmaceutical University approved the experimental protocol. All efforts were made to minimize the suffering of animals and to reduce the number of animals used in the present study.

2.2. Induction of Obesity. As reported in our previous studies, MSG was used to induce obesity [19, 21]. On postnatal days 1, 2, 4, 6, 8, and 10, eight male C57BL/6J mice were intrasubcutaneously injected with MSG (2 mg/g of body weight; Wako Pure Chemical Industries, Ltd., Japan). The other eight male mice were intrasubcutaneously injected with saline on the same days to serve as controls. After weaning, the body weight of each mouse was measured once a week.

2.3. Tissue Preparation. At 15 weeks of age, all mice were anesthetized with an overdose of Sodium pentobarbital (50 mg/kg, ip, Nembutal; Abbott Lab., North Chicago, IL), and their digestive system was quickly removed. The total length of small intestine from all animals and the diameter of their small intestines (5 places/animal) were measured, and then the wet volumes of their small intestines were weighted. For histological analysis using light microscopy, a section of the small intestine was immersed in fixative containing 4% paraformaldehyde in 0.1 M phosphate buffer (PB; pH 7.4) for 2 days at 4°C. After fixation, the small intestine was trimmed, washed with PB, dehydrated through graded concentrations of ethanol, cleared in xylene, and embedded in paraffin. For transmission electron microscopy, a section of small intestine was immersed in fixative containing 4% paraformaldehyde and 2% glutaraldehyde in 0.1 M PB for 2 days at 4°C. After washing with PB, the small intestine was immersed in 1% osmium tetroxide solution, dehydrated through graded concentrations of ethanol, saturated in propylene oxide, and embedded in Epon-812 resin (TAAB Co., Switzerland).

2.4. Histological Analysis. For hematoxylin-eosin (HE) and toluidine blue (Nissl) staining and to further investigate rough endoplasmic reticulum (rER), Golgi apparatus, and tight junction, the small intestine blocks were cut into 3 μm thick sections on a microtome (REM-710; Yamato, Japan). The sections were mounted on glass slides, deparaffinized with xylene, and immersed in degraded concentrations of ethanol. After washing in distilled water, several sections from each group were stained with HE or Nissl solution. After washing, the sections were dehydrated through graded concentrations of ethanol, cleared with xylene, and cover slipped. The rER and Golgi apparatus in mucosal epithelial cells in the small intestine samples from each group were stained using anti-GRP78 Bip antibody (ab21685, Abcam, Cambridge, MA) or anti-golgin 97 antibody (ab84340, Abcam, Cambridge, MA), respectively. And to identify the tight junction between epithelia, the sections were stained with anti-ZO-1 antibody (gift from Dr. M. Itoh, Department of Biochemistry, School of Medicine, Dokkyo Medical University, Japan). After immunofluorescence procedures, the sections were cover slipped. All images of stained sections were captured using a CCD camera system (BZ-X700; Keyence, Japan).

2.5. Electron Microscopic Analysis. All small intestine blocks embedded in Epon-812 resin were trimmed using light microscopy. Several sections (3 μm) were cut with an MT-XL ultramicrotome (Research and Manufacturing Company, Tucson, AZ) and stained with Nissl solution, and images were

Table 1: Macroscopic anatomical changes of small intestine at 15 weeks of age.

	Length (cm)	Weight (g)	Diameter (mm)
Control ($n = 8$)	41.7 ± 1.40	1.36 ± 0.11	2.17 ± 0.23
MSG ($n = 8$)	40.2 ± 1.24	1.39 ± 0.09	2.15 ± 0.18

The data are expressed as mean ± standard error values. MSG: monosodium glutamate.

Table 2: Lengths and thickness of villi in small intestine at 15 weeks of age.

	Length (μm)	Thickness (μm)
Control ($n = 4$)	375.70 ± 24.23	92.55 ± 8.59
MSG ($n = 4$)	394.11 ± 22.30*	69.14 ± 9.69*

The data are expressed as mean ± standard error values. *$P < 0.05$, compared with the age-matched controls. MSG: monosodium glutamate.

captured using the CCD camera system (BZ-X700; Keyence). The other sections were checked, reembedded in Epon-812 resin, cut with an MT-XL ultramicrotome into ultrathin sections (70 nm), and picked up on grids (Veco Co., Eerbeek, Holland). The ultrathin sections were stained with electron stain and examined with a conventional transmission electron microscope (JEM-1011; JEOL LTD., Tokyo, Japan), and the images captured using the CCD camera system.

2.6. Data Analysis. All images captured using the CCD camera system were measured using the ImageJ software according to the user manual. The lengths of villi (control group: 40 villi from 4 animals; MSG-induced obesity group: 40 villi from 4 animals) and thicknesses of villi (control group: 80 villi from 4 animals; MSG-induced obesity group: 80 villi from 4 animals) were measured. The volume of cytoplasm and nucleus of small intestinal epithelia from each group were also measured (control group: 80 cells from 4 animals; MSG-induced obesity group: 80 cells from 4 animals). According to the morphometric aspect of rER [22], the length of rER in cells from each group was measured (control group: 414 rER from 10 cells; MSG-induced obesity group: 415 rER from 17 cells). According to the morphometric aspect of mitochondria [22], the area of mitochondria in small intestinal epithelia from each group was measured (control group: 30 cells; MSG-induced obesity group: 30 cells). All data were expressed as mean ± standard deviation. Statistical analysis was performed using the StatView statistical software (SAS Institute Inc., Cary, NC). The differences between control mice and MSG-induced obese mice were analyzed using Student's t-test. P values < 0.05 were considered statistically significant.

3. Results

3.1. Body Weight and Macroscopic Changes in the Small Intestine. Similar to our previous studies, obesity was induced in mice using MSG [19, 21]. In the present study, pathological changes in the small intestine of MSG-induced obese mice were examined to gain insight into changes occurring in chronic obesity in humans. MSG-induced obese mice were slightly heavier compared with control mice at 5 weeks of age, and from 9 to 15 weeks of age, the obese mice were significantly heavier (Figure 1(a)). The small intestines from the 15-week-old mice were examined macroscopically. There was no difference in length or thickness of the small intestines between the obese and control mice (Figure 1(b) and Table 1).

3.2. Histopathological Changes in the Small Intestine. Pathological changes in the small intestinal mucosa were examined using HE-stained tissue sections (Figure 2). The tissues from control mice were healthy (Figure 2(a)). In MSG-induced obese mice, the villi were elongated compared with those from control mice (Table 2). Moreover, the villi from the obese mice were thinner compared with those from control mice (Figure 2(b) and Table 2). The single-layered epithelium in samples from MSG-induced obese mice appeared almost normal and there was no difference in the distribution and frequency of goblet cells in the epithelium between control and obese mice. In addition, there was no difference in the appearance of the central lacteals between the two groups. The mucosal epithelial cells from control mice appeared healthy, and the brush borders showed a normal structure (Figure 2(c)). There was no obvious difference between control and MSG-induced obese mice in terms of the shape and dimensions of the mucosal epithelial cells (Figure 2(d) and Table 3). However, many intensely hematoxylin-stained regions were identified in the mucosal epithelial cells from control mice (arrowheads in Figure 2(c)), but there was only slight or negative hematoxylin staining in the mucosal epithelial cells from MSG-induced obese mice (double arrowheads in Figure 2(d)). Because hematoxylin solution stains the acidic regions in cytoplasm, it was possible that the hematoxylin-stained regions were rER, which is acidic.

3.3. Ultrastructural Changes in the Small Intestine. Next, pathological changes in mucosal epithelial cells were investigated using electron microscopy. On Nissl staining of sections embedded in epoxy resin, rERs in the mucosal epithelial cells of control mice were clearly detected, but few or none were detected in sections from MSG-induced obese mice (data not shown). Under electron microscopy, many rERs were detected in mucosal epithelial cells from control mice (Figure 3(a) low magnification view, Figure 3(b) high magnification view, and Figure 3(b′) rERs were highlighted by red color lines). Compared with the cells from control mice, rER was significantly decreased in cells from

Table 3: Volume of cytoplasm and nucleus in small intestinal epithelia at 15 weeks of age.

	Area of cytoplasm (μm^2)	Area of nucleus (μm^2)
Control ($n = 4$)	168.36 ± 39.29	21.83 ± 5.41
MSG ($n = 4$)	162.58 ± 32.25	21.66 ± 7.07

The data are expressed as mean ± standard error values. MSG: monosodium glutamate.

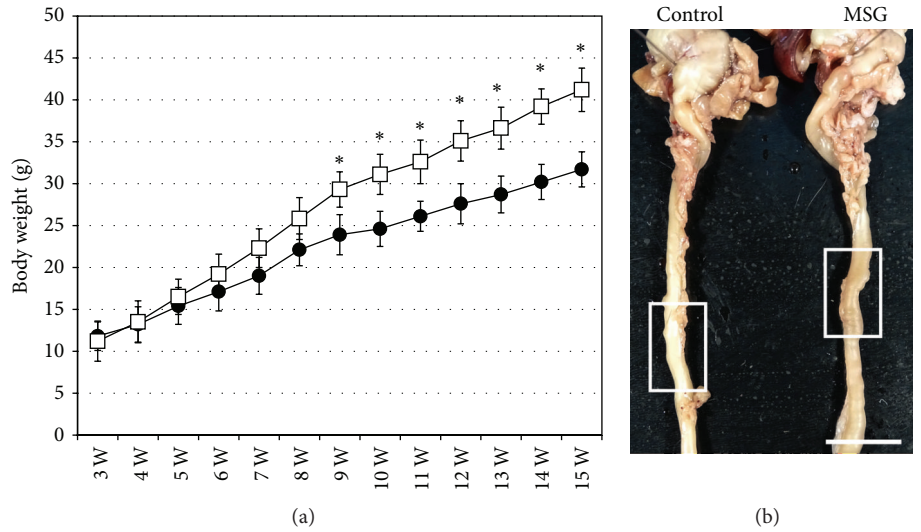

Figure 1: Changes in body weight and macroscopic observation of the small intestine. (a) Plot of body weight from 3 weeks to 15 weeks of age for monosodium glutamate- (MSG-) induced obese mice (white squares) and control mice (black circles). The mean ± standard deviation is shown for each group. $^*P < 0.05$. (b) Representative samples of the stomach and small intestine from control and MSG-induced obese mice. The white boxes indicate the area selected to investigate pathological changes. Scale bar in (b) = 1 cm.

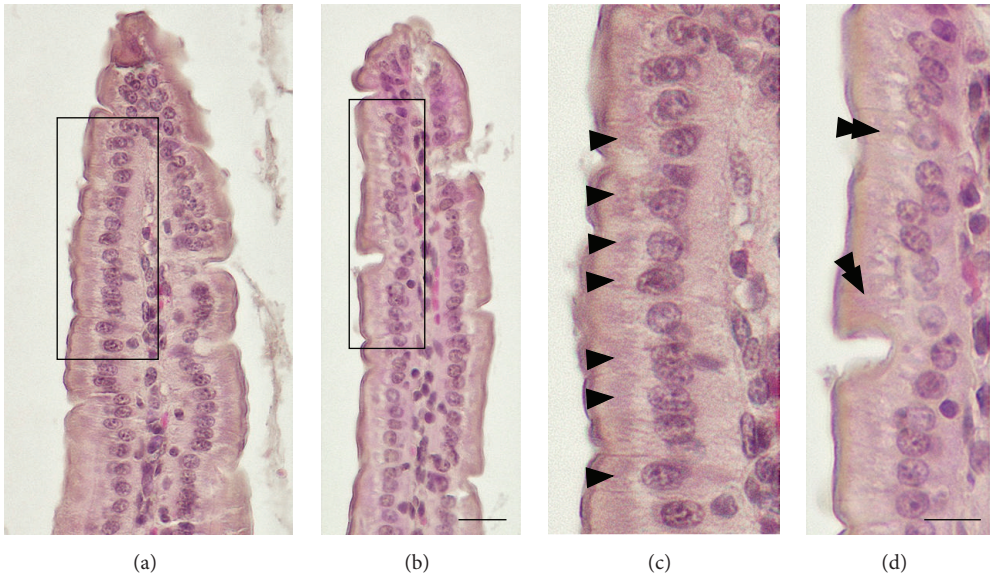

Figure 2: Representative light microscopy images showing histopathology of the small intestine. (a) Low magnification view of a hematoxylin-eosin- (HE-) stained section of small intestine from control mice. (b) Low magnification view of a HE-stained section of small intestine from monosodium glutamate- (MSG-) induced obese mice. Black boxes in (a) and (b) show the areas enlarged in (c) and (d), respectively. Arrowheads in (c) indicate intensely hematoxylin-stained regions in the cytoplasm. Double arrowheads in (d) indicate slight or negative hematoxylin-stained regions in the cytoplasm. Scale bars in (a) and (b) = 20 μm and (c) and (d) = 10 μm, respectively.

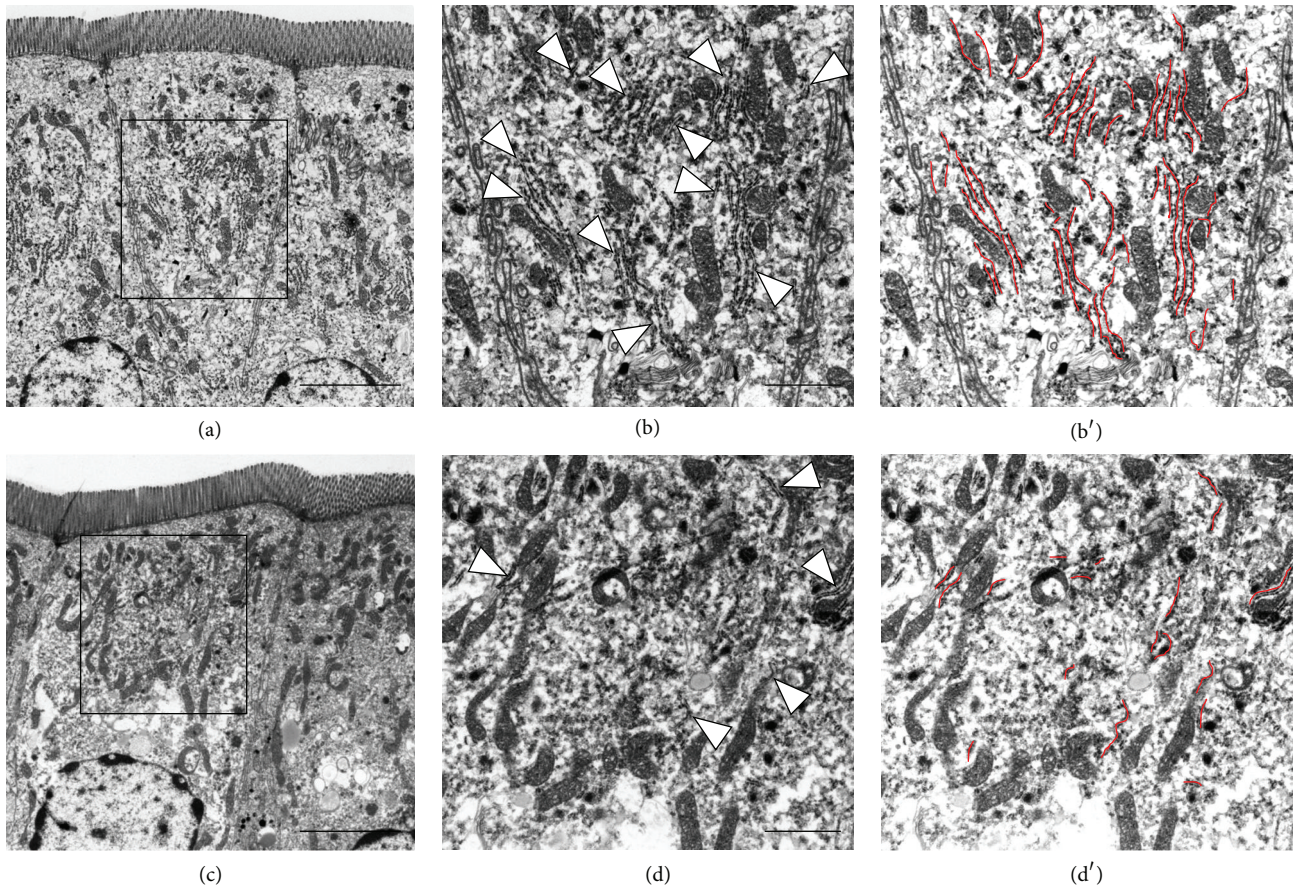

Figure 3: Representative electron microscopy images showing the distribution of rough endoplasmic reticulum (rER) in small intestine mucosal epithelial cells. Mucosal epithelial cells from control mice ((a) low magnification; (b) high magnification). Mucosal epithelial cells from monosodium glutamate- (MSG-) induced obese mice ((c) low magnification; (d) high magnification). Arrowheads in (b) and (d) indicate rER. Scale bars in (a) and (c) = 5 μm and (b) and (d) = 2 μm.

MSG-induced obese mice (Figure 3(c) low magnification view, Figure 3(d) high magnification view, and Figure 3(d′) rERs were highlighted by red color lines). Similar numbers of rER from both groups were measured for length using transmission electron microscopy (control 414 rER; MSG-induced obese mice 415 rER; Figure 4(a)). The length of rER in cells from control mice showed a peak at approximately 3 μm. The distribution of the rER length in cells from MSG-induced obese mice peaked at a shorter length and showed a narrower distribution compared with that for control mice. Therefore, the length of rER in cells from MSG-induced obese mice was significantly shorter compared with that from control mice. The rER density in cells from MSG-induced obese mice was also significantly decreased by approximately 45% compared with that in control mice (Figure 4(b)). The average length of rER in cells from MSG-induced obese mice was significantly decreased by approximately 60% compared with that in cells from control mice (Figure 4(c)). Next we demonstrated that the volumes of mitochondria from both groups were also measured. The volumes of mitochondria from MSG-induced mice were not significantly changed compared to that of control mice (Table 4).

Table 4: The occupancy of mitochondria in small intestinal epithelia at 15 weeks of age.

	Occupancy of mitochondria (%)
Control (n = 4)	9.81 ± 0.92
MSG (n = 4)	10.43 ± 1.13

The data are expressed as mean ± standard error values. MSG: monosodium glutamate.

3.4. Histopathological Changes Using Histological Staining in the Small Intestine. To confirm whether rERs were decreased in the mucosal epithelial cells from MSG-induced obese mice, the mucosal epithelial cells embedded in paraffin were stained using Nissl solution, a basic aniline dye (Figures 5(a) and 5(b)). Nissl solution identifies rER as Nissl bodies or tigroid substance. In mucosal epithelial cells from control mice, there were many Nissl-stained regions (arrowheads in Figure 5(a)). In cells from the MSG-induced obese mice, there was only slight or negative Nissl staining in the same regions stained with hematoxylin (double arrowheads in Figure 5(b)). Moreover, the rER of mucosal epithelial cells were stained using anti-GRP78 Bip antibody (Figures 5(c)

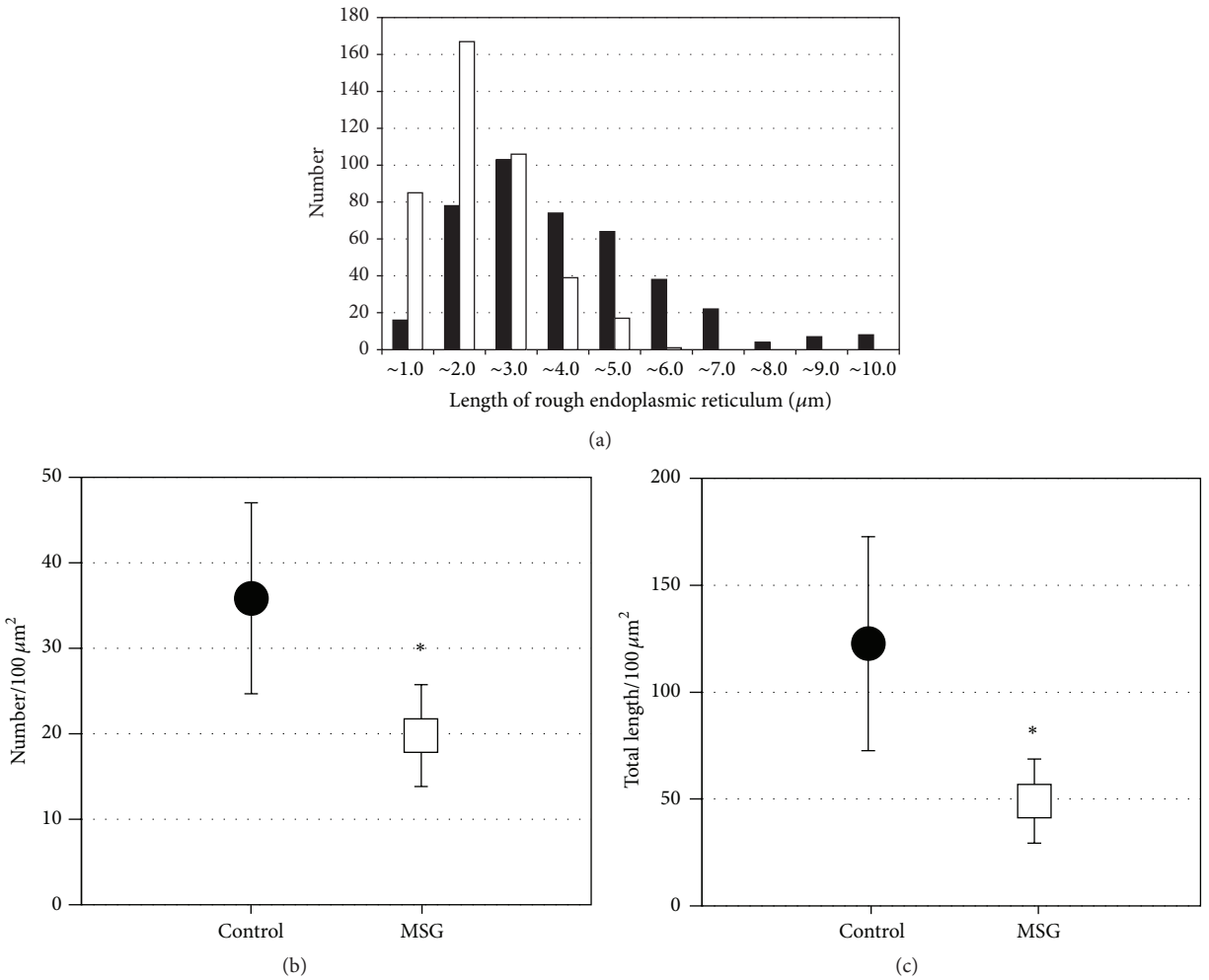

Figure 4: Size distribution and density of rough endoplasmic reticulum (rER) profiles measured using transmission electron microscopy. (a) Histogram of the size of individual rER profiles in small intestine mucosal epithelial cells. (b) Density of rER in small intestine mucosal epithelial cells. (c) Total length of rER in small intestine mucosal epithelial cells. The black bars and circles and the white bars and squares indicate the number of control mice and monosodium glutamate- (MSG-) induced obese mice, respectively. $^{*}P < 0.05$.

and 5(d)). In control mice, many rERs (green color) were identified (white arrows in Figure 5(c)), but there were fewer rERs in the mucosal epithelial cells of the MSG-induced obese mice compared with the controls (Figure 5(d)). And the Golgi apparatuses of mucosal epithelial cells were also stained using anti-golgin 97 antibody (Figures 5(e) and 5(f)). Many Golgi apparatuses (green color) were detected in cells from control mice (white arrows in Figure 5(e)). However, in cells from the MSG-induced obese mice, there was increased staining intensity compared with the controls (white arrows in Figure 5(f)), indicating enlargement and/or expansion of Golgi apparatus, in particular around the nucleus and basal side of the epithelial cells.

Finally, to identify the tight junction between epithelia, the mucosal epithelial cells sections were stained with anti-ZO-1 antibody (Figures 5(g)–5(i)). As previously described [23], many tight junctions were identified in between epithelia from control mice (white arrows in Figure 5(g)). In MSG-induced obesity mice, many tight junctions were also maintained in between epithelia (white arrows in Figure 5(h)); however, there were some poorly stained regions by tight junctional marker (Figure 5(i)).

4. Discussion

The objective of this study was to determine whether small intestinal epithelial cells show pathological changes associated with obesity. We induced obesity in mice soon after birth using MSG, as a model of obesity starting in childhood. Based on past evidence of clinical conditions in chronic obesity, we hypothesized that pathology causing functional changes in nutritional absorption and/or the integrity of the gut barrier would be observed. In human society, childhood obesity has become an increasing problem worldwide [3]. Obese children are likely to become obese adults at increased risk for many health problems [4–8]. Importantly, metabolic syndrome associated with chronic obesity is a major predictor of NAFLD, a progressive and potentially fatal disease [10, 11]. While the pathogenesis of NAFLD is partly understood, to date, little is known about structural changes in the small

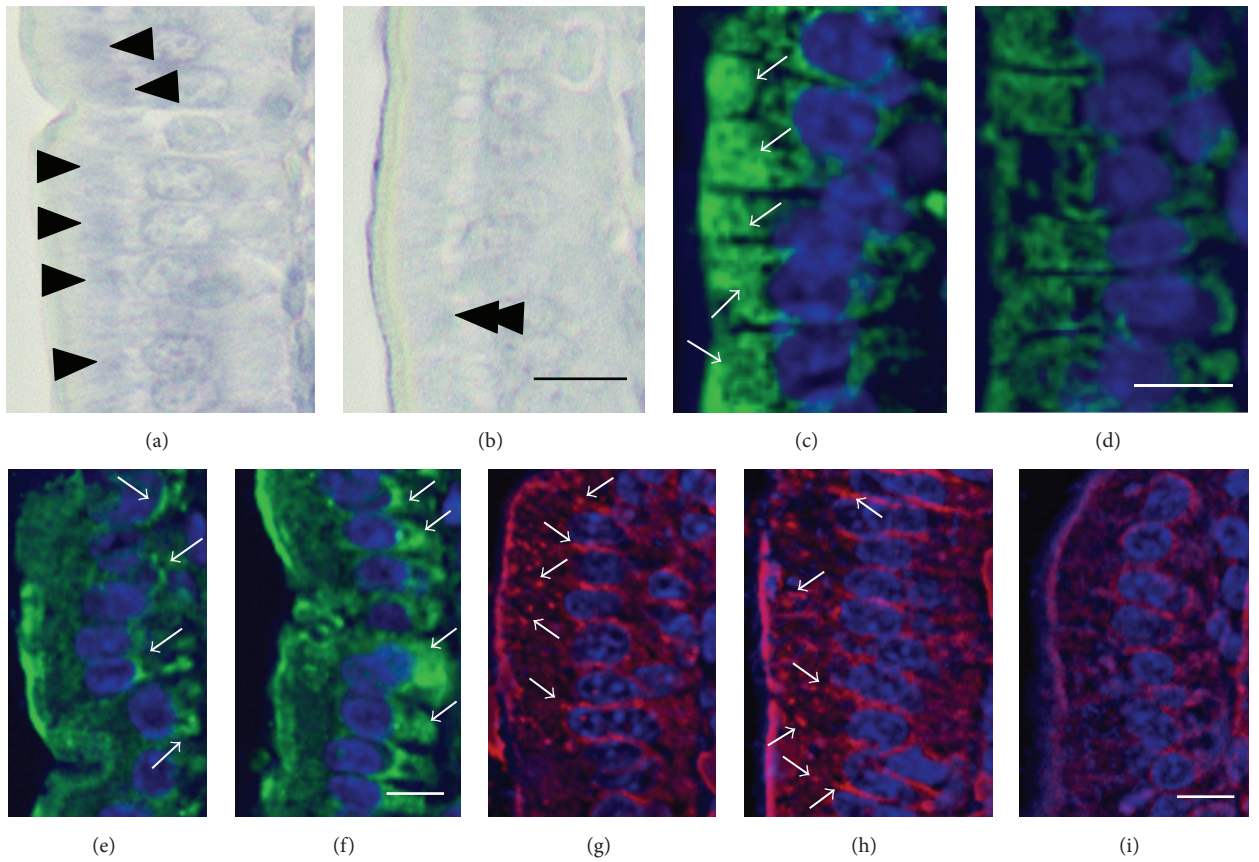

Figure 5: Representative light microscopy images showing the distribution of rough endoplasmic reticulum (rER) in small intestine mucosal epithelial cells. ((a) and (b)) High magnification views of Nissl-stained sections of small intestine from control mice and monosodium glutamate- (MSG-) induced obese mice, respectively. ((c) and (d)) High magnification views of rER-stained sections small intestine from control mice and MSG-induced obese mice, respectively. ((e) and (f)) High magnification views of Golgi apparatus-stained sections of small intestine from control mice and MSG-induced obese mice, respectively. (g) High magnification view of tight junction-stained sections of small intestine from control mice. ((h) and (i)) High magnification views of tight junction-stained sections of small intestine from MSG-induced obese mice. Arrowheads in (a) indicate intensely Nissl-stained regions in the cytoplasm. Double arrowheads in (b) indicate slightly or negative Nissl-stained regions in the cytoplasm. White arrows in (c) and (d) indicate rER. White arrows in (e) and (f) indicate Golgi apparatus. White arrows in (g) and (h) indicate tight junctions. All scale bars = 10 μm.

intestine associated with chronic obesity. Therefore, in the present study, we conducted a structural and ultrastructural investigation of the small intestinal mucosa in a mouse model of obesity immediately after birth.

While the macroscopic anatomy did not differ between control and obese mice, light microcopy identified elongated and thinned villi in the small intestine of the obese mice. It is possible that these changes could affect the function of the small intestine. In addition to the absorption of nutrients, the intestinal mucous membrane epithelium provides a defense mechanism to prevent the invasion of the pathogenic microbes such as bacteria. If this gut barrier is compromised, pathogens can pass through the intestinal mucous membrane epithelium into the blood stream. Translocation of bacteria into the portal vein is one of the causes of liver damage in NAFLD. Therefore, it is possible that functional failure of the intestinal epithelial barrier occurs in chronic obesity. Similar to the findings of the present study, the villi in diabetic model rats (streptozotocin-induced rats) and obese rats (Otsuka Long-Evans Tokushima Fatty rats) were also elongated and thin [24]. In another study using male ICR strain MSG-induced obese mice examined at 4, 8, and 12 weeks of age, the villi gradually elongated with age [25]. Therefore, elongation of the villi of the small intestine might be a change associated with obesity.

The balance between energy supply and energy consumption should be taken into consideration in the investigation of obesity. In terms of energy supply, impulsive overeating by MSG-induced obese mice has been reported in a number of studies [19, 21, 26, 27]. Body weight in these mice starts to increase compared to control mice, soon after weaning [19, 21]. It is possible that hyperplasia of the small intestine is caused by an acceleration of absorptive function. Energy consumption includes basal metabolism, thermogenesis, and physical activity. In a previous study, MSG-induced obese mice showed lower spontaneous activity compared to controls from one month of age [28]. Furthermore, growth hormone and thyroid hormone levels in MSG-induced obese

mice are reduced [28–32]. The reduction of these hormones would affect energy balance by reducing basal metabolism. Therefore, in MSG-induced obese mice, obesity results from a combination of reduced energy consumption and overeating. The elongated villi in the small intestinal mucosa of obese mice observed in the present study may lead to accelerated absorption, resulting in the progression of obesity.

There was a decrease in the amount of and shortening of rER and an increase in the numbers of Golgi apparatus in the small intestinal epithelium of the MSG-induced obese mice in the present study. Moreover, many tight junctions were maintained but partly damaged in MSG-induced obesity mice. The rER has many general functions, including the folding of proteins in cisternae and the transport of synthesized proteins in vesicles to the Golgi apparatus. By limiting the passage of proinflammatory agents from the small intestine into the circulation, the barrier function of small intestine plays an important role in limiting the development of diabetes and metabolic disease. A lipoglycan-like lipopolysaccharide found on the cell surface of Gram-negative bacteria interacts with toll-like receptor 4 (TLR4) and initiates the release of proinflammatory cytokines [33, 34]. Glucagon-like peptide-1 (GLP-1) and glucagon-like peptide-2 (GLP-2) play a pivotal role in intestinal adaptation, epithelial cell proliferation, and maintenance of intestinal functions [35]. GLP-2 elicits improvements in gut permeability and endotoxemia and increases expression of zonula occludens-1 (ZO-1) and occludin [35]. ZO-1 and occludin are related to the barrier function of the intestinal mucosa [36–38]. Therefore, in addition to effects on absorptive function, a decrease in rER in the small intestinal epithelium may influence the biosynthesis of many of the proteins involved in the function of the gut barrier. Newly synthesized proteins are folded in the rER, and only properly folded proteins are transported from the rER to the Golgi apparatus. As part of the ER stress response that occurs with viral infections, folding of newly synthesized proteins is slowed leading to an increase in unfolded proteins. This ER stress is emerging as a potential cause of damage in some disorders, for example, insulin resistance in diabetes mellitus. Therefore, it is possible that a decrease in the amount of and shortening of rER in the small intestinal mucosa associated with chronic obesity could lead to dysfunction of the epithelium of the small intestine, for example, dysfunction of gut barrier by limiting the passage of proinflammatory agents, and/or the changes of nutrition absorption.

5. Conclusions

There was a decrease in hematoxylin-stained regions in the small intestinal epithelium of obese mice compared with controls. Furthermore, electron microscopy revealed a decrease in numbers and shortening of rER in the small intestinal epithelium of the obese mice. These results suggest that dysfunction of the small intestinal epithelium could occur in chronic obesity starting in childhood. Moreover, dysfunction of the small intestinal epithelium could affect functions such as protein synthesis and the defense mechanism that prevents the invasion of pathogenic microbes. These mechanisms could be involved in the pathogenesis of serious disorders associated with chronic obesity starting in childhood.

Competing Interests

The authors have declared that there are no competing interests.

Acknowledgments

This work was supported in part by a Grant-in-Aid for Scientific Research (C) and the Suzuken Memorial Foundation. The authors thank Dr. M. Itoh for providing the anti-Zo-1 antibody.

References

[1] R. Mailloux, J. Lemire, and V. Appanna, "Aluminum-induced mitochondrial dysfunction leads to lipid accumulation in human hepatocytes: a link to obesity," *Cellular Physiology and Biochemistry*, vol. 20, no. 5, pp. 627–638, 2007.

[2] M. Ng, T. Fleming, M. Robinson et al., "Global, regional, and national prevalence of overweight and obesity in children and adults during 1980–2013: a systematic analysis for the Global Burden of Disease study 2013," *The Lancet*, vol. 384, no. 9945, pp. 766–781, 2014.

[3] C. L. Ogden, M. D. Carroll, B. K. Kit, and K. M. Flegal, "Prevalence of childhood and adult obesity in the United States, 2011–2012," *The Journal of the American Medical Association*, vol. 311, no. 8, pp. 806–814, 2014.

[4] D. S. Freedman, L. K. Khan, W. H. Dietz, S. R. Srinivasan, and G. S. Berenson, "Relationship of childhood obesity to coronary heart disease risk factors in adulthood: the Bogalusa heart study," *Pediatrics*, vol. 108, no. 3, pp. 712–718, 2001.

[5] D. S. Freedman, L. K. Khan, M. K. Serdula, W. H. Dietz, S. R. Srinivasan, and G. S. Berenson, "The relation of childhood BMI to adult adiposity: The Bogalusa Heart Study," *Pediatrics*, vol. 115, no. 1, pp. 22–27, 2005.

[6] D. S. Freedman, J. Wang, J. C. Thornton et al., "Classification of body fatness by body mass index-for-age categories among children," *Archives of Pediatrics & Adolescent Medicine*, vol. 163, no. 9, pp. 805–811, 2009.

[7] S. S. Guo and W. C. Chumlea, "Tracking of body mass index in children in relation to overweight in adulthood," *The American Journal of Clinical Nutrition*, vol. 70, no. 1, pp. 145S–148S, 1999.

[8] P. A. Sarafidis and P. M. Nilsson, "The metabolic syndrome: a glance at its history," *Journal of Hypertension*, vol. 24, no. 4, pp. 621–626, 2006.

[9] L. H. Kushi, T. Byers, C. Doyle et al., "American cancer society guidelines on nutrition and physical activity for cancer prevention: reducing the risk of cancer with healthy food choices and physical activity," *CA: A Cancer Journal for Clinicians*, vol. 56, no. 5, pp. 254–314, 2006.

[10] A. Kotronen, L. Juurinen, A. Hakkarainen et al., "Liver fat is increased in type 2 diabetic patients and underestimated by serum alanine aminotransferase compared with equally obese nondiabetic subjects," *Diabetes Care*, vol. 31, no. 1, pp. 165–169, 2008.

[11] A. Kotronen, J. Westerbacka, R. Bergholm, K. H. Pietiläinen, and H. Yki-Järvinen, "Liver fat in the metabolic syndrome," *The*

Journal of Clinical Endocrinology and Metabolism, vol. 92, no. 9, pp. 3490–3497, 2007.

[12] C. P. Day and O. F. W. James, "Steatohepatitis: a tale of two 'Hits'?" *Gastroenterology*, vol. 114, no. 4 I, pp. 842–845, 1998.

[13] G. Bedogni, L. Miglioli, F. Masutti, C. Tiribelli, G. Marchesini, and S. Bellentani, "Prevalence of and risk factors for nonalcoholic fatty liver disease: the dionysos nutrition and liver study," *Hepatology*, vol. 42, no. 1, pp. 44–52, 2005.

[14] J. D. Browning, L. S. Szczepaniak, R. Dobbins et al., "Prevalence of hepatic steatosis in an urban population in the United States: impact of ethnicity," *Hepatology*, vol. 40, no. 6, pp. 1387–1395, 2004.

[15] G. Targher, L. Bertolini, R. Padovani et al., "Prevalence of nonalcoholic fatty liver disease and its association with cardiovascular disease among type 2 diabetic patients," *Diabetes Care*, vol. 30, no. 5, pp. 1212–1218, 2007.

[16] M. Malaguarnera, M. Di Rosa, F. Nicoletti, and L. Malaguarnera, "Molecular mechanisms involved in NAFLD progression," *Journal of Molecular Medicine*, vol. 87, no. 7, pp. 679–695, 2009.

[17] N. Enomoto, K. Ikejima, B. Bradford et al., "Alcohol causes both tolerance and sensitization of rat Kupffer cells via mechanisms dependent on endotoxin," *Gastroenterology*, vol. 115, no. 2, pp. 443–495, 1998.

[18] K. Ikejima, N. Enomoto, Y. Iimuro et al., "Estrogen increases sensitivity of hepatic Kupffer cells to endotoxin," *American Journal of Physiology—Gastrointestinal and Liver Physiology*, vol. 274, no. 4, part 1, pp. G669–G676, 1998.

[19] K. Nakadate, K. Motojima, S. Kamata, T. Yoshida, M. Hikita, and H. Wakamatsu, "Pathological changes in hepatocytes of mice with obesity-induced type 2 diabetes by monosodium glutamate," *Yakugaku Zasshi*, vol. 134, no. 7, pp. 829–838, 2014.

[20] S. H. Caldwell, J. A. Redick, C. Y. Chang, C. A. Davis, C. K. Argo, and K. A. Al Osaimi, "Enlarged hepatocytes in NAFLD examined with osmium fixation: does microsteatosis underlie cellular ballooning in NASH?" *American Journal of Gastroenterology*, vol. 101, no. 7, pp. 1677–1678, 2006.

[21] K. Nakadate, K. Motojima, and S. Tanaka-Nakadate, "Dilatation of sinusoidal capillary and swelling of sinusoidal fenestration in obesity: an ultrastructural study," *Ultrastructural Pathology*, vol. 39, no. 1, pp. 30–37, 2015.

[22] D. W. Fawcett, *The Cell*, WB Saunders, Philadelphia, Pa, USA, 1981.

[23] M. Itoh, S. Yonemura, A. Nagafuchi, S. Tsukita, and S. Tsukita, "A 220-kD undercoat-constitutive protein: its specific localization at cadherin-based cell-cell adhesion sites," *Journal of Cell Biology*, vol. 115, no. 5, pp. 1449–1462, 1991.

[24] T. Adachi, C. Mori, K. Sakurai, N. Shihara, K. Tsuda, and K. Yasuda, "Morphological changes and increased sucrase and isomaltase activity in small intestines of insulin-deficient and type 2 diabetic rats," *Endocrine Journal*, vol. 50, no. 3, pp. 271–279, 2003.

[25] K. Hamaoka and T. Kusunoki, "Morphological and cell proliferative study on the growth of visceral organs in monosodium L-glutamate-treated obese mice," *Journal of Nutritional Science and Vitaminology*, vol. 32, no. 4, pp. 395–411, 1986.

[26] J. Bunyan, E. A. Murrell, and P. P. Shah, "The induction of obesity in rodents by means of monosodium glutamate," *British Journal of Nutrition*, vol. 35, no. 1, pp. 25–39, 1976.

[27] K. Tanaka, M. Shimada, K. Nakao, and T. Kusunoki, "Hypothalamic lesion induced by injection of monosodium glutamate in suckling period and subsequent development of obesity," *Experimental Neurology*, vol. 62, no. 1, pp. 191–199, 1978.

[28] C. B. Nemeroff, L. D. Grant, G. Bissette, G. N. Ervin, L. E. Harrell, and A. J. Prange Jr., "Growth, endocrinological and behavioral deficits after monosodium L glutamate in the neonatal rat: possible involvement of arcuate dopamine neuron damage," *Psychoneuroendocrinology*, vol. 2, no. 2, pp. 179–196, 1977.

[29] J. L. Bakke, N. Lawrence, J. Bennett, S. Robinson, and C. Y. Bowers, "Late endocrine effects of administering monosodium glutamate to neonatal rats," *Neuroendocrinology*, vol. 26, no. 4, pp. 220–228, 1978.

[30] C. B. Nemeroff, R. J. Konkol, G. Bissette et al., "Analysis of the disruption in hypothalamic-pituitary regulation in rats treated neonatally with monosodium L-glutamate (MSG): evidence for the involvement of tuberoinfundibular cholinergic and dopaminergic systems in neuroendocrine regulation," *Endocrinology*, vol. 101, no. 2, pp. 613–622, 1977.

[31] C. B. Nemeroff, M. A. Lipton, and J. S. Kizer, "Models of neuroendocrine regulation: use of monosodium glutamate as an investigational tool," *Developmental Neuroscience*, vol. 1, no. 2, pp. 102–109, 1978.

[32] T. W. Redding, A. V. Schally, A. Arimura, and I. Wakabayashi, "Effect of monosodium glutamate on some endocrine functions," *Neuroendocrinology*, vol. 8, no. 3, pp. 245–255, 1971.

[33] M. S. H. Akash, K. Rehman, and S. Chen, "Role of inflammatory mechanisms in pathogenesis of type 2 diabetes mellitus," *Journal of Cellular Biochemistry*, vol. 114, no. 3, pp. 525–531, 2013.

[34] Y.-C. Lu, W.-C. Yeh, and P. S. Ohashi, "LPS/TLR4 signal transduction pathway," *Cytokine*, vol. 42, no. 2, pp. 145–151, 2008.

[35] P. D. Cani, S. Possemiers, T. Van De Wiele et al., "Changes in gut microbiota control inflammation in obese mice through a mechanism involving GLP-2-driven improvement of gut permeability," *Gut*, vol. 58, no. 8, pp. 1091–1103, 2009.

[36] E. A. Felinski and D. A. Antonetti, "Glucocorticoid regulation of endothelial cell tight junction gene expression: novel treatments for diabetic retinopathy," *Current Eye Research*, vol. 30, no. 11, pp. 949–957, 2005.

[37] C. Förster, "Tight junctions and the modulation of barrier function in disease," *Histochemistry and Cell Biology*, vol. 130, no. 1, pp. 55–70, 2008.

[38] M. Itoh and M. J. Bissell, "The organization of tight junctions in epithelia: implications for mammary gland biology and breast tumorigenesis," *Journal of Mammary Gland Biology and Neoplasia*, vol. 8, no. 4, pp. 449–462, 2003.

Hindawi Publishing Corporation
BioMed Research International
Volume 2016, Article ID 1414383, 18 pages
http://dx.doi.org/10.1155/2016/1414383

Review Article

Manipulation of DNA Repair Proficiency in Mouse Models of Colorectal Cancer

Michael A. Mcilhatton,[1] Gregory P. Boivin,[2] and Joanna Groden[1]

[1]*Department of Cancer Biology and Genetics, The Ohio State University, 460 West 12th Avenue, Columbus, OH 43210, USA*
[2]*Department of Pathology, Boonshoft School of Medicine, Wright State University, Health Sciences Building 053, 3640 Colonel Glenn Highway, Dayton, OH 45435, USA*

Correspondence should be addressed to Joanna Groden; joanna.groden@osumc.edu

Received 18 March 2016; Accepted 9 May 2016

Academic Editor: Monica Fedele

Technical and biological innovations have enabled the development of more sophisticated and focused murine models that increasingly recapitulate the complex pathologies of human diseases, in particular cancer. Mouse models provide excellent *in vivo* systems for deciphering the intricacies of cancer biology within the context of precise experimental settings. They present biologically relevant, adaptable platforms that are amenable to continual improvement and refinement. We discuss how recent advances in our understanding of tumorigenesis and the underlying deficiencies of DNA repair mechanisms that drive it have been informed by using genetically engineered mice to create defined, well-characterized models of human colorectal cancer. In particular, we focus on how mechanisms of DNA repair can be manipulated precisely to create *in vivo* models whereby the underlying processes of tumorigenesis are accelerated or attenuated, dependent on the composite alleles carried by the mouse model. Such models have evolved to the stage where they now reflect the initiation and progression of sporadic cancers. The review is focused on mouse models of colorectal cancer and how insights from these models have been instrumental in shaping our understanding of the processes and potential therapies for this disease.

1. The Mouse as a Model Organism for Colorectal Cancer Studies

The study of cancer biology advances continually and generates complex emergent data. In the area of biological sciences, technology has arguably outpaced our ability to fully interpret the wealth of available data and subsequent implications for understanding cancer pathogenesis [1]. Evolving platforms for sequence analyses, expression arrays, and proteomic and metabolomic characterization of tumor tissues relentlessly refine our resolution of the crucial biological processes inherent to the initiation and progression of human cancers [2].

The development of more effective therapeutic modalities for cancer treatment remains a driving priority of modern biomedical science. This imperative requires appropriate models to provide conceptual frameworks for deciphering the various biological pathways that collaborate in the initiation and progression of human cancers. Ideally these models will mimic the complexity of cancer development and provide a biological system for both identifying and assessing relevant therapeutic targets [3, 4]. The mouse presents a useful animal surrogate for unraveling the complexities of human tumor biology in an *in vivo* setting. Furthermore, the genomic sequences of common laboratory strains have been determined, revealing the high degree of conservation between mouse genes and their cognate human counterparts [5]. Mouse models have made tremendous contributions to our understanding of the pathologies of many diseases, including cancer [3, 4], but a comprehensive evaluation is beyond the scope of this review. Instead, we will confine this discussion to the utility of the mouse as a model for studying colorectal cancer, a focus of our laboratory for many years.

There are significant gaps in our ability to predict the inherited risk of developing colorectal cancer and in our understanding of the biological mechanisms that lead to its initiation and progression. Colorectal cancer is the second

leading cause of cancer-related death in the Western world and is currently the third most common form of cancer. Although constitutional genetics is well established as a contributor to susceptibility and screening recommendations are a well-accepted part of best clinical practices, nearly 140,000 new cases of colorectal cancer are diagnosed each year in the United States, and >50,000 attributable deaths occur annually [6]. Approximately 8 to 35% of sporadic colorectal cancer is estimated to be due to genetic variance [7–9], but genome-wide association studies (GWAS) for colorectal cancer susceptibility have only uncovered approximately 1–9% of the estimated heritable risk [9–12]. Inflammation is a known risk factor for multiple tumor types including colorectal cancer, inflammatory bowel disease (IBD), and several other conditions [13–15]. Inflammatory bowel diseases, such as Crohn's disease (CD) and ulcerative colitis (UC), are also estimated to have a high degree of heritable risk: 25–42% for CD and 4–15% for UC [16, 17]. Although more than 201 risk loci for IBD have been identified, these are estimated to only account for a little over one-third of the estimated genetic risk [18–21]. Additionally, individuals with IBD, especially those diagnosed with ulcerative colitis which specifically affects the large intestine, are at an increased risk for the development of colorectal cancer: 2% at 10 years, 8% at 20 years, and 18% at 30 years [22]. Finally, regardless of our understanding of some major risk factors for and the pathways dysregulated in colorectal cancer fifty percent of those diagnosed with localized invasive disease die within five years [6].

Mouse models are uniquely suited to test hypotheses about tumor formation in intestinal cancer *in vivo* and more than one model should be used to represent the complicated risk factors that affect tumor susceptibility within the human population. Disease pathogenesis recapitulates the adenoma-carcinoma transition of human colorectal cancer, at least at the early stages [23, 24]. Expression analyses have revealed critical similarities, and also important differences, in transcriptional profiles between various mouse models and human colorectal tumors [25]. *In vivo* modeling of colorectal cancer advances a greater understanding of human tumors through insight into the cellular mechanisms that initiate and promote tumor progression. Ultimately, this knowledge can provide better patient treatment, either through more informed therapeutic interventions or through rationales which provide personalized treatments.

2. Genomic Instability: A Critical Element of Colorectal Cancer

The majority of colorectal cancers develop sporadically (85%), with the remaining cases arising in the context of hereditary cancer syndromes, mainly familial adenomatous polyposis coli (FAP) and Lynch syndrome, also known as hereditary nonpolyposis colon cancer (HNPCC), or against the background of inflammatory bowel disease [39]. The contribution of genomic instability to colorectal cancer has been established by numerous studies on FAP and Lynch syndrome. It was demonstrated that inactivation of the mismatch repair system (MMR) was a prerequisite for tumor development in those with Lynch syndrome [40]. The genomic instability intrinsic in tumors from these individuals is characterized by mutations at the nucleotide level, typically demonstrated by the emergence of microsatellite instability (MSI) [41, 42].

Heterogeneous deficiencies in a number of DNA repair and signaling pathways may collectively manifest as a second category of DNA instability, designated chromosomal instability (CIN), which is characterized by allelic losses, amplifications, and translocations at the chromosomal level of genomic organization. A signature phenotype of FAP is CIN, which develops as a consequence of mutations predominantly in the *APC* tumor suppressor gene [39, 43]. FAP requires the inheritance of one mutated allele of the adenomatous polyposis coli (*APC*) gene [44]. Depending on the nature of the inherited germline allele, second-hit inactivation of the wild-type allele is achieved either by loss of heterozygosity (LOH) of the (wild-type) *APC* locus or by intragenic mutation of the *APC* gene [45, 46]. APC is also inactivated by intragenic mutation in 70–80% of individuals with sporadic colorectal cancer [47, 48]. Many germline and sporadic human mutations have been mapped to codons 1250 to 1464 of the *APC* gene [47–49]. This region has been designated the mutation cluster region (MCR) and includes a mutational hotspot at codon 1309, with a second hotspot falling outside the region at codon 1061 [48, 49]. These mutations generate truncated APC proteins that lack part or all of key β-catenin-binding domains.

Mutation of *APC* subsequently disrupts the WNT/β-catenin signaling pathway [39, 43]. In the absence of *APC* mutation, alterations in β-catenin (*CATNB*) or other downstream genes compromise signaling in the WNT pathway [50, 51]. The variable mechanisms by which APC is targeted and the nature and distribution of the inactivating mutations themselves have led to the proposal that, dependent on mutational context, an optimal activation of WNT signaling is required for subsequent tumorigenesis [45, 46]. This is known as the "just-right" hypothesis—"just-the-right (dysregulated) level of WNT." Persistent activation of the canonical WNT pathway in the colonic epithelium appears to be a required event to initiate subsequent adenoma formation. The pathogenic signature of FAP is revealed by the development of hundreds of small adenomatous polyps throughout the colon, a small percentage of which ultimately progress to malignant adenocarcinomas (reviewed in [39]). The inevitable outcome is colorectal cancer, mandating preemptive surgical intervention.

3. Models of Familial Adenomatous Polyposis Coli

The archetypical animal model of FAP is the multiple intestinal neoplasia (Min) mouse which was originally identified following a mutagenesis screen with N-ethyl-N-nitrosourea (ENU) [26]. It was subsequently shown that the "Min" phenotype was conferred by a truncating mutation at codon 850 in the *Apc* gene. The resulting truncated Apc lacked all the motifs for interacting with β-catenin and consequently failed to regulate cellular levels of this protein, promoting

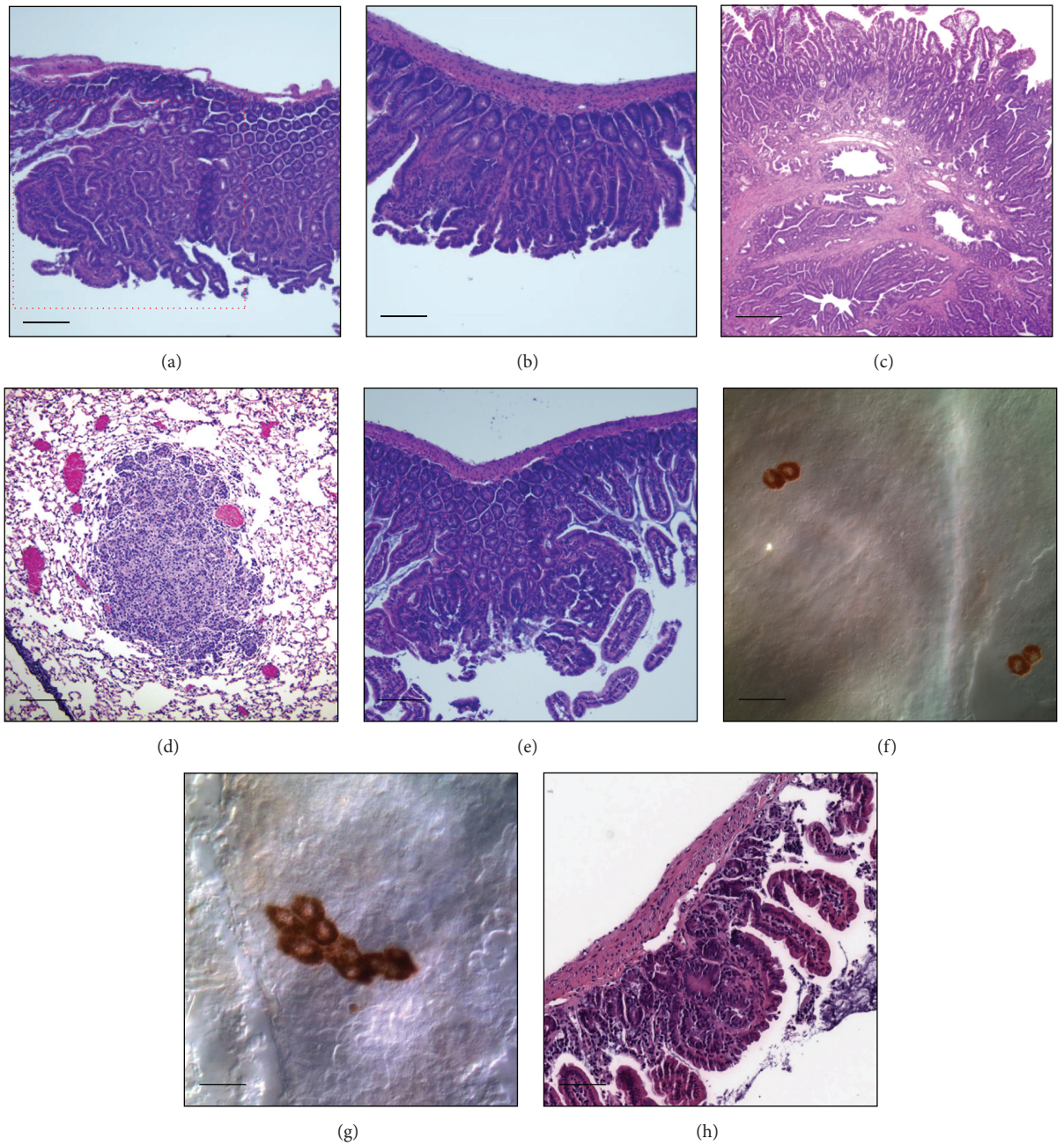

FIGURE 1: Pathology of intestinal lesions in $Apc^{Min/+}$ and *Blm/BLM* mice. (a) Gastrointestinal neoplasia (red box) in $Apc^{Min/+}$ mouse intestine; (b) adenoma in $Apc^{Min/+}$ mouse intestine (ileum); (c) carcinoma in $Apc^{Min/+}$;$Blm^{Cin/+}$ mouse intestine; (d) adenoma in *Ccsp/fgf-10*;$Blm^{Cin/+}$ lung tissue; (e) adenoma in $Apc^{Min/+}$;BLM^{Tg} mouse intestine; (f) isolated retinal pigment epithelial (RPE) cells in a $p^{un/un}$;BLM^{Tg} mouse retina; (g) a cluster of RPE cells in a $p^{un/un}$;BLM^{Tg} mouse retina; and (h) adenoma in $Apc^{Min/+}$;BLM^{Tg};$Msh2^{\Delta 7N/\Delta 7N}$ mouse intestine.

tumorigenesis. Apc^{Min} is embryonic lethal in the homozygous state; animals must be maintained as heterozygotes. In addition to gastrointestinal neoplasia (GIN), which is defined as "histologically apparent areas of dysplasia that are not visible grossly, <0.5–1.0 mm" [23], $Apc^{Min/+}$ mice develop numerous small intestinal polyps, both pedunculated and flat adenomas (Figures 1(a) and 1(b)). Tumors in this model are characterized by activated Wnt signaling [25]. The wild-type *Apc* allele is inactivated by a LOH mechanism at the locus on mouse chromosome 18 and most tumors are homozygously mutated for *Apc*. This initiating event is required for promoting tumor progression in the $Apc^{Min/+}$ model of intestinal neoplasia, although the wild-type allele can be inactivated by point mutations in other genetic contexts [46, 52, 53].

Min mouse tumor burden varies according to background and may even vary on the same background between different laboratories [54]. In our laboratory, we routinely observe a median of 50 polyps in the intestine of mice on

a C57Bl/6J background. A number of factors, both genetic and environmental, affect intestinal polyp multiplicity in the $Apc^{Min/+}$ model. For example, it is well documented that $Apc^{Min/+}$ mice maintained on a high-fat (Western) diet develop more polyps than those on the Mediterranean diet [55, 56]. Increased dietary fat has been shown to directly increase the number and proliferation of mouse intestinal stem cells, leading to a greater incidence of spontaneous adenomas [57]. Increased dietary fat induced upregulation of PPAR-δ which in turn activated signaling through the Wnt/β-catenin pathway. Furthermore, the resident gut microflora of $Apc^{Min/+}$ mice influences tumorigenesis and intestinal polyp numbers; manipulating the gut microflora can effect a reduction in the overall tumor burden [58, 59]. Intestinal polyp numbers in $Apc^{Min/+}$ mice are also modulated by several genetic modifiers, collectively termed modifier(s) of Min (*Mom*). These may be defined genes (*Mom1*) [60] or less well-defined loci of indeterminate function such as *Mom12* and *Mom13* [61]. Compared to C57Bl/6J $Apc^{Min/+}$ mice, mice on a mixed C57Bl/AKR background have a reduced tumor burden of 6.0 ± 4.7 polyps [62]. *Mom1*, the first reported modifier of Min, is predominantly responsible for the observed phenotype [63, 64]. *Mom1* was subsequently identified as phospholipase A2 (*Pla2g2a*) [60, 65]. However, it should be noted that the role of *Mom1* is complicated by the presence of other unlinked modifiers on the AKR/J background which additionally impact polyp multiplicity [60, 63]. Other modifiers of Min are reviewed in [66].

Since the derivation of the $Apc^{Min/+}$ mouse, genetically engineered mice have been generated which collectively model a series of different *Apc* mutations. This series highlights the strength of the mouse as a model system, namely, the capacity to study a range of clinically related mutations under comparable *in vivo* settings. Previous models provide the rational foundations for the development of more refined models that deepen our overall understanding of how mutations in key cellular genes can give rise to tumors in humans. In all of the Apc models, loss or inactivation of the wild-type allele is required for tumor initiation and progression. Although age of onset, location, and tumor number vary according to the specific *Apc* mutation and genetic background, tumor histology is similar across the different models [23]. Relevant mutant alleles of *Apc* have been outlined in Table 1. A more exhaustive, but not necessarily comprehensive, list of *Apc* mutations, derived from the Mouse Genomic Informatics website, currently lists 26 *Apc* alleles on 53 different backgrounds (http://www.informatics.jax.org/marker/phenotypes/MGI:88039). Allelic series of mutations, such as those generated for the *Apc* gene, have facilitated dissection of the key roles played by tumor suppressor and oncogenes in fundamental cellular processes and how dysregulation of such processes leads to aberrant cell growth and subsequent tumorigenesis.

A thorough discussion of the available mouse models of Apc is constrained by the limits of this review. However, it is clear that the location, as well as nature, of the inactivating mutation affects tumor incidence across different Apc models (Table 1). Variation in intestinal polyp numbers has been correlated with the location of the inactivating *Apc* mutation relative to the MCR. This has been alluded to previously in the context of the "just-right" hypothesis [45, 46]. The concomitant levels of altered Wnt signaling, for example, in $Apc^{\Delta e1-15}$ [27], $Apc^{15lox/+}$ [28], and $Apc^{1322T/+}$ [29] mice, determine, at least in part, the severity and number of intestinal polyps. Although differential signaling by submaximal levels of Wnt supports the observed incidence of intestinal polyp multiplicity for several of the Apc models listed in Table 1, unfortunately it cannot account for such differences in all models. Moreover, it is worth noting that similar, or supposedly identical, models may vary in the phenotypes they present. For example, $Apc^{580S/+}$ [30], $Apc^{\Delta 14/+}$ [31], and $Apc^{\Delta 580/+}$ [32] mice were all engineered using similar Cre-*loxP* targeting strategies to produce truncated Apc proteins through frameshifts at codon 580. Over the course of their life spans, these animals develop approximately 7, 65, and 120 adenomas, respectively. The $Apc^{\Delta 14/+}$ and $Apc^{\Delta 580/+}$ models highlight how institutional differences, perhaps such as diet and intestinal microbiome, between independently maintained colonies can skew tumor phenotypes. The inactivating mutation in $Apc^{1638N/+}$ mice results in a frameshift at codon 1638 [33] whereas $Apc^{1638T/+}$ mice have been generated with a stop at codon 1638 [34]. $Apc^{1638N/+}$ mice develop ~10 colonic polyploid hyperplastic lesions whereas Apc^{1638T} develop 0 polyps. Moreover, $Apc^{1638T/1638T}$ mice are viable, albeit with developmental and growth abnormalities, whereas $Apc^{1638N/1638N}$ are embryonic lethal. The same selectable neomycin marker was used to generate both $Apc^{1638N/+}$ and $Apc^{1638T/+}$ mice, but in the latter case the marker was inserted in the sense orientation. A truncated 182 kD Apc protein could only be detected in $Apc^{1638T/+}$ mice; insertion of the marker in the antisense orientation abolished Apc expression in $Apc^{1638N/+}$ mice [34]. This is an exemplary illustration of how targeting strategy can subsequently influence the resulting phenotype of genetically engineered mouse models. Such variation of phenotypes in what should be genetically similar models could be interpreted as an inherent flaw of studying human cancers in mouse systems, but such serendipity extends and enriches the versatility of these models and presents greater opportunities for understanding the tumorigenic processes. Given the complexity and number of available Apc models and the number of potentially confounding factors, including genetic modifiers/background, composition of the intestinal microbiome, animal diet, and the possible effects of environmental parameters, such as temperature [67] on tumorigenesis, it is not surprising that phenotypic analyses and interpretation remain challenging. Regardless, the tumor pathology of the Apc mouse and its years of experimental study continue to keep it as the preferred animal model for FAP.

Mutant models of Apc have also been generated in the rat and, more recently, the pig. Polyposis in the rat colon (Pirc) model has been derived from an ENU-induced stop codon at position 1137 in the rat *Apc* gene [68]. Homozygosity for the Apc^{am1137} mutation is embryonic lethal, similar to mouse Apc^{Min}. Heterozygous animals develop both polyps in

Table 1: Genetically engineered alleles of the mouse *Apc* gene.

Apc allele	Mutation	Polyp number	Pathology/comments	Ref
$Apc^{Min/+}$	Frameshift at codon 850 (ENU induced)	~30–>100	Polypoid, papillary and sessile adenomas; cystic crypts, no colonic ACF	[26]
$Apc^{\Delta e1-15}$	Floxed exons 1–15, no protein	~210 ♀ ~150 ♂	Polypoid, papillary and sessile adenomas; cystic crypts, no colonic ACF	[27]
$Apc^{15lox/+}$	Floxed exon 15, frameshift at codon 650, truncation at 667	~185	Polypoid and sessile adenomas; cystic crypts; few colonic lesions	[28]
$Apc^{1322T/+}$	Neomycin cassette inserted into exon 15; stop at codon 1322	~200	Polyps predominantly in the first and second segments of the small intestine; few gastric and colonic polyps; polyps have reduced Wnt signaling relative to Apc^{Min} polyps	[29]
$Apc^{580S/+}$	Floxed exon 14, frameshift at codon 580, truncation at 605	~7	Exposure to adenoviral-Cre; adenomas localized near anus	[30]
$Apc^{\Delta 14/+}$	Floxed exon 14, frameshift at codon 580, truncation at 605	~65	Polypoid and sessile adenomas; increase in colonic polyps, ACF, and rectal prolapses	[31]
$Apc^{\Delta 580/+}$	Floxed exon 14, frameshift at codon 580, truncation at 605	~120	Crossed to K14-Cre mouse line; polyploid and sessile adenomas; increase in colonic polyps, with additional abnormalities in the skin, thymus, and tooth	[32]
Apc^{1638N}	Neomycin cassette inserted into exon 15 in antisense; frameshift at codon 1638	~10	Colonic polyploid hyperplastic lesions, villous/tubulovillous adenomas; moderately to highly differentiated adenocarcinoma; rare gastric lesions	[33]
Apc^{1638T}	PGK-hygromycin cassette inserted in sense orientation; stop at codon 1638	0	Developmental abnormalities; growth retardation; absence of preputial glands	[34]
$Apc^{\Delta 716/+}$	Neomycin cassette inserted into exon 15; frameshift at codon 716	~254	Polypoid, papillary, and sessile adenomas; no colonic ACF	[35]
$Apc^{1309/+}$	Frameshift at codon 1309	~34	Polyps mainly in small intestine but also in the stomach and colon	[36]
$Apc^{\Delta 474/+}$	Neomycin cassette inserted into exon 9; duplication of exons 7–10; frameshift at codon 474	~122	Sessile-type polyps; rare mammary adenocarcinomas	[37]
Apc^{neoF} Apc^{neoR}	Neomycin cassette inserted into intron 13 in both sense and antisense orientations	neoF ~ 1.00 neoR ~ 0.25	Dysplastic adenomas similar to those from $Apc^{\Delta 716}$ mice	[38]

A more extensive list of *Apc* mouse alleles can be found at http://www.informatics.jax.org/marker/phenotypes/MGI:88039.

the small intestine and colon with 100% incidence. Longer-lived $Apc^{am1137/+}$ rats develop adenocarcinomas. A second rat model, the Kyoto Apc Delta (KAD) rat, originates from a separate ENU mutagenesis screen [69]. This model also contains a stop codon, but at Apc position 2523 that, in contrast to the Pirc rat, retains the β-catenin-binding region of the protein. Unlike the Pirc rat, animals homozygous for $Apc^{\Delta 2523}$ are viable and do not develop spontaneous intestinal tumors. However, they are highly sensitive to AOM/DSS induced colitis-associated colon carcinogenesis. Gene targeting, rather than mutagenesis by ENU, has generated germline stop codons at both positions in APC^{1061} and APC^{1311} cloned pigs [70]. These knock-in alleles are orthologous to the clinically relevant FAP mutations occurring at human APC codons 1061 and 1309 [48, 49]. $APC^{1311/+}$ pigs presented with polyps in the colon and rectum at one year of age; aberrant crypt foci (ACF) were detectable in the colon. A similar pathology occurs during the development of FAP in (young) human patients, signifying that the pig is also a suitable model for the study of this type of colorectal cancer.

4. Compound *Apc* Models Recapitulate the Pathology of FAP More Precisely

Cancer is considered to be a multistage process, requiring the cumulative acquisition and integration of a number of cellular, genomic, and possibly epigenomic alterations operationally grouped into several defining hallmarks [71]. The eventual outcome is cellular transformation, clonal expansion, and tumor formation. Important as it is, mutation of *Apc*

is not the sole criterion required for colorectal tumorigenesis. *Apc* mutant mice can be crossed with mice "knocked out," or deficient, at other loci or with other alleles to generate compound animals. Combination of *Apc* mutant backgrounds with mouse strains knockout or defective in key DNA repair genes can be used to recapitulate the FAP phenotype more thoroughly and extend the versatility of this colorectal cancer model. Any changes of the tumor phenotype on the *Apc* mouse background provide a biological readout for assessing the effects of knockout, or overexpression, of other genes. Such crosses are instructive for assessing the relative contribution of known or newly discovered genes to the development of colorectal cancer.

The list of *Apc* compound knockouts is extensive and continually growing. We will briefly discuss some examples and highlight key insights that helped to further our understanding of the biological mechanisms involved in colorectal cancer. (1) $Apc^{\Delta 716/+}$;$Smad4^{+/-}$ heterozygote mice develop intestinal polyps which progress more quickly to invasive adenocarcinoma [72]. Although *Apc* loss of function is required for adenoma formation, loss of function of other genes, such as *Smad4*, is necessary for malignant progression. (2) Certain genes exert regional-specific effects on polyposis along the intestinal tract. $Apc^{\Delta 716/+}$;$Cdx^{+/-}$ mice develop 6-fold more polyps in their colons but 9-fold less polyps in their small intestines compared to $Apc^{\Delta 716/+}$ mice [73]. The increase in colonic polyps is caused by upregulation of *mTor* signaling which thus presents a possible therapeutic target. (3) $Apc^{Min/+}$;$BubR1^{+/-}$ mice also develop more colonic polyps, by a factor of ten, than $Apc^{Min/+}$ mice. It was concluded that both *Apc* and *BubR1* functionally interact in regulating metaphase-anaphase transition [74]. Haploinsufficiency of these proteins in the compound heterozygotes increased chromosomal instability as a function of spindle checkpoint deregulation which accelerated cancer development and progression. (4) Specific deletion of both *Apc* and *Myc* was achieved in the small intestine using the Apc^{580S} allele crossed to an $Ah\text{-}Cre^{+}$;$Myc^{fl/fl}$ compound mouse [75]. Expression array analyses of tumor tissues from these mice revealed that, upon *Apc* loss, *Myc* becomes a critical mediator of concomitant neoplasia and highlighted the potential of *Myc* as a possible therapeutic target in intestinal tumorigenesis. (5) Haploinsufficiency for *Blm* on an $Apc^{Min/+}$ background increased tumor formation about 2-fold [76]. Genomic analyses indicated that increased tumor formation was due to an increase in somatic recombination, which facilitated inactivation of the wild-type *Apc* allele by interchromosomal recombination leading to LOH (see below). These observations are of relevance to human populations, with similar conclusions being reached about carriers of the BLM^{Ash} mutation and their susceptibility to colorectal cancer [77].

5. Models of Lynch Syndrome/Hereditary Nonpolyposis Colon Cancer

Lynch syndrome is an autosomal dominant predisposition to colorectal cancer that was first described over a century ago [78] and comprehensively studied over many years, by Lynch and colleagues, among others [79, 80]. It is the most common cancer predisposition syndrome in the human population and has been estimated to occur at an incidence of 1 in 660 individuals, although, given that screening methods are not 100% inclusive, the actual incidence is probably lower [81]. Consensus criteria for Lynch syndrome diagnosis were internationally agreed upon [82] and have been refined subsequently to reflect the better understanding of this disease at both the clinical and mechanistic levels [83–85]. Patients develop early-onset colorectal cancers and a subset of these is also associated with extracolonic tumors at sites including the stomach, small intestine, ovaries, and endometrium [40, 83, 84]. Individuals predisposed to Lynch syndrome carry heterozygous mutations in various genes of the MMR pathway, most notably *MSH2*, *MSH6*, *MLH1*, and *PMS2* [40, 84, 86]. MMR constitutes a postreplicative DNA repair system and the mechanistic details of this pathway have been reviewed elsewhere [87]. Around 15% of sporadic colorectal cancers also display MMR defects; hereditary and sporadic tumors can be differentially stratified on the basis of various molecular and morphological criteria [86]. Cells lose their wild-type MMR allele by various somatic means, facilitating tumor development due to the increased mutation rates normally suppressed by the MMR system [40, 85, 86]. The resultant mutator phenotype, a genetic hallmark coupled to MSI, provides the environment for the accumulation of multiple secondary mutations. Changes in the length of normally stable short DNA repeat sequences (microsatellites) are now standard diagnostic indicators of the MSI classically associated with MMR defects [41, 42]. Tumor tissues from most Lynch syndrome cases associated with MMR defects display MSI [85, 86].

Knockout mouse lines have been generated for all of the genes known to comprise the MMR system: *Msh2* [46, 88], *Msh3* and *Msh6* [89, 90], *Mlh1* [91, 92], *Pms1* and *Pms2* [93], *Mlh3* [94], and *Exo1* [95]. Multiple lines have been made for some of these genes; for example, there are at least nine different alleles for the *Msh2* gene [96]. Although knockout lines have been generated for *Msh4* and *Msh5*, which are acknowledged members of the MMR family, these genes do have traditional functions in postreplicative DNA repair but instead are associated with defects in meiosis [97, 98]. The severity of tumor phenotypes exhibited by mice deficient in various genetic components of MMR correlates well overall with the known roles and contributions of these genes to Lynch syndrome. Mice deficient in *Msh2* and *Mlh1* develop more tumors more quickly and have the shortest median survival times than mice deficient in other aspects of MMR [24, 46, 88, 92]. *MSH2* and *MLH1* are central to MMR function and are mutated with the highest frequencies in Lynch syndrome tumors, indicative of their pivotal importance in this DNA repair pathway, and the inherent selection required for their inactivation leading to tumorigenesis.

Although knockout mice for *Msh2*, *Mlh1*, and *Msh6* gene function develop gastrointestinal tumors, most actually die from lymphomas and thymomas [24, 46, 88–90, 92]. This was long argued to be a weakness of these models, but this perception has been revised with the recent identification of patients

who are constitutively defective in MMR; that is, they possess biallelic inactivating mutations in *MLH1*, *MSH2*, *MSH6*, or *PMS2* [99]. These patients present with early-onset hematological and brain malignancies. In retrospect, the phenotypes of conventional homozygous knockout mice have actually proven to be good models for patients who are constitutively defective in MMR, as opposed to heterozygous carriers at risk of Lynch syndrome.

Conditional mouse models have also been created for the MMR genes most prominently involved in Lynch syndrome. A floxed allele of *Msh2* has been developed that, in combination with an intestinal-specific Cre recombinase transgene, facilitates restriction of *Msh2* inactivation to the intestinal epithelium [100]. In this model, designated $VCMsh2^{loxP}$ (*Villin-Cre*;$Msh2^{loxP/loxP}$) animals do not present with lymphomas. Tumorigenesis is restricted to the intestinal compartment and mice develop 1-2 adenomas or adenocarcinomas within the first year. The $VCMsh2^{loxP}$ line was combined with *Msh2*-null or $Msh2^{G674A}$ alleles to generate allelic phase mutants. These animals were used to investigate the therapeutic potential of specific drugs on colorectal tumorigenesis in an *in vivo* setting. A similar model ($Mlh1^{flox/flox}$) has also been generated for conditional inactivation of *Mlh1* [101]. Conditional targeting has been used to ablate Msh2 expression in the crypt base columnar stem cells (CBCs) of the mouse intestinal crypt [102]. The *Lgr5-CreERT2* mouse line, originally developed by Barker and colleagues [103], was sequentially crossed with *Msh*-null and *Msh* floxed lines to generate *Lgr5-CreERT2*;$Msh2^{flox/-}$ mice. By judicious administration of tamoxifen, it was possible to generate mosaic *Msh2*-inactivation within a small field of CBCs, thus more closely mimicking the mutational developments that occur during early stages of Lynch syndrome. On average, tamoxifen treated *Lgr5-CreERT2*;$Msh2^{flox/-}$ mice developed invasive adenocarcinomas after 19 months [102]. All tumors were negative for Msh2. It is clear that when directed with precision and studied in context, mouse models are useful systems for studying tumor suppression by the MMR system and investigating its role in colorectal tumorigenesis.

6. Models of Sporadic Tumorigenesis

Most colorectal cancers developed are sporadic in nature and develop without selective pressure from genetic predisposition, lacking germline heterozygosity in any inherited mutant allele. The fundamental challenge of developing sporadic models of colorectal cancer, or any other cancer for that matter, is in the adaption of available genetic systems to control biological processes in a stochastic nonheritable way. The final goal is to orchestrate the formation of defined tumor phenotypes in specific tissues under essentially random, yet controllable, conditions. Many sporadic tumor models involve the Cre-*loxP* or FLP-FRT systems. They are routinely designed around a floxed tumor suppressor gene or a floxed latent allele of an activated oncogene and require inducible or stochastically regulated expression of Cre recombinase to direct deletion (tumor suppressor) or activation (oncogenes) of the target gene [3, 104]. Although many sporadic models of tumorigenesis are variations on this theme, two separate models of sporadic Lynch syndrome have been recently reported that uniquely feature an out-of-frame Cre containing a mononucleotide microsatellite sequence [105, 106]. Expression of wild-type Cre is dependent on the acquisition of a frameshift reversion within the mononucleotide sequence, thus restoring an open reading frame. This may, or may not, be due to acquisition of an MSI phenotype. The sporadic expression of wild-type Cre subsequently drives deletion or activation of other floxed alleles.

The RAS family of genes is somatically mutated in about 30% of all tumors and around 50% of colorectal cancers develop mutations specifically in *KRAS*, the majority occurring at codon 12 [39]. One of the earlier models of sporadic cancer featured a latent allele of the *K-ras G12D* activating mutation ($K\text{-}ras^{LA}$) [107]. Activation of this allele was solely dependent on intrachromosomal recombination between contiguous regions of the genetically restructured endogenous *K-ras* locus; no other exogenous agent, such as Cre, was required. Although tumors developed in the lungs of these mice and all mutant animals developed ACF in the colon, intestinal tumors were not observed. This correlates with the detection of *KRAS* mutations in ACF in humans [108]. A similar strategy has been used to direct sporadic activation of a latent allele of *β-catenin* which features a clinically relevant Ser→Phe mutation at codon 37. This mutation ablates a Gsk-3-β phosphorylation site, important for β-catenin regulation, and, after intrachromosomal recombination, results in expression of an oncogenic form of β-catenin [109]. In this model, sporadically activated β-catenin was sufficient for tumor initiation but did not lead to malignant progression. Sporadic multifocal lesions developed only in the stomach; adenomas were not detected in any tissue. This is in contrast to other mouse models of activated β-catenin signaling which demonstrate a clear association between expression of oncogenic forms of β-catenin and intestinal tumorigenesis [110, 111].

The $K\text{-}Ras^{LA}$ model described above [107] was subsequently modified by the incorporation of a Lox-Stop-Lox (LSL) cassette. This enabled activation of the latent Ras^{G12D} allele by Cre recombinase, administrable by various platforms, including adenoviral infection, which removed the intervening LSL cassette and restored transcriptional integrity of the mutant allele at the endogenous locus [112]. Although the LSL $K\text{-}Ras^{G12D}$ model was initially used to investigate *Ras* involvement in lung tumorigenesis, it was quickly coopted for studies in other cancers including leukemia [113], squamous cell carcinoma [114], and of course colorectal cancer [115, 116]. The models demonstrated that oncogenic *K-ras* induced ACF in the colon, but progression to microadenoma was determined by regional-specific factors within this tissue; ACF in the proximal colon progressed to adenoma whereas those in the distal colon did not [115]. Activated *K-ras* affected proliferation and differentiation in the colonic epithelium of nonneoplastic tissues by signaling through Mek but in itself was not sufficient to drive neoplasia [116].

The LSL *K-Ras*^{G12D} allele has been incorporated into yet another mouse model of sporadic colon cancer, one that successfully recapitulates the adenoma-carcinoma-metastasis trajectory common to human colon cancers [117]. This is an important achievement, as it is still challenging to faithfully model metastatic spread of intestinal cancer. The genetic units of this model entail the LSL *K-Ras*^{G12D} and *Apc*$^{\Delta 580}$ alleles and a Cre-expressing adenovirus (Adeno-Cre). Surgical procedures were used to restrict Adeno-Cre delivery to the mouse colon, resulting in an average tumor burden of 3.6 lesions per animal, which contrasts with the tumor multiplicities of the original models: 0 for LSL *K-Ras*^{G12D} [112] and ~120 for *Apc*$^{\Delta 580}$ [32]. The limited tumor burden increased animal survival, a factor undoubtedly contributing to the successful metastatic spread of tumors from the colon to the liver, which started around 24 weeks after infection with Adeno-Cre. Insights from this model are that activated *K-ras* can accelerate tumor progression in conjunction with an established *Apc* mutation and that *K-Ras*^{G12D} has also the capacity to promote metastatic spread, when expressed against the appropriate cellular background.

7. RecQ Helicases: Guardians of the Genome

RecQ helicases are evolutionarily conserved from bacteria to humans and have multiple, sometimes overlapping, roles in DNA metabolism including replication, recombination, and repair [118]. The five known homologs of the mammalian RecQ family, RECQL1, BLM, WRN, RECQL4, and RECQL5, play pivotal roles in the maintenance of genomic stability and cellular homeostasis. Mammalian RecQs can not only form heterologous complexes with other family members but also interact with many other proteins involved in various DNA maintenance/repair pathways [119]. *BLM*, *WRN*, and *RECQL4* are linked to monogenic genetic diseases characterized by genome instability, premature aging, and cancer predisposition [118, 120].

Bloom's syndrome (BS) is a hereditary disease characterized by a predisposition to various types of cancers that first present at a mean age of 24 years [121]. Characteristic phenotypes manifested by BS patients are severe growth retardation and a high susceptibility for cancers of all types [121, 122]. The *BLM* gene is mutated in individuals with BS [123]. The Groden laboratory has studied BLM (and WRN) for many years and we use BS as a paradigm for understanding how DNA repair deficiency impacts both growth and cancer. BLM responds to DNA damage-induced stress sustained during DNA metabolism including the restart/repair of stalled and collapsed replication forks during DNA replication, the repair of interstrand cross-links, the resolution of Holliday junctions, and the suppression of aberrant homologous recombination [119, 120]. BLM also functions in telomere maintenance and is specifically involved in telomerase-independent telomere elongation in the alternative lengthening of telomeres (ALT) pathway [124–126]. Furthermore, our recently published studies have established a role for BLM in regulating rDNA metabolism [127, 128].

BLM deficiency results in major genomic instability—a hallmark of most cancers and a factor that escalates the cancer frequency in those with BS. BLM interacts with many other DNA damage response proteins, including BRCA1, MLH1, MSH2, MSH6, p53, RAD51, topoisomerase IIα, and WRN [129–134]. Some of these partners function as sensors and transducers in DNA damage response pathways, colocalize with BLM in the nucleolus, and physically associate with BLM to facilitate repair functions [126–128, 134–137]. Consistent with its role in DNA repair, BLM deficiency results in the formation of aberrant chromosomal structures and increased sister chromatid exchanges (SCE) [120, 138].

8. RecQ Mutant Mouse Models and Colorectal Cancer

The role of disrupted homologous recombination (HR) in human cancer susceptibility is well established by studies of tumor incidence in BS, where loss of the BLM helicase increases inter- and intrachromosomal recombination [120] and the high incidence of breast and ovarian cancer in carriers of *BRCA1* mutation, where loss of BRCA1 suppresses HR and impedes DNA double-strand break repair [139]. Similarly, decreased DNA repair capacity and/or dysregulated HR in mouse models of cancer lead to increased tumor susceptibility, although some experiments suggest that such alterations can inhibit tumor formation [140]. Published studies show that intestinal tumor number and histological characteristics in mouse models vary when DNA repair proficiency or chromosome stability varies [74, 76, 140, 141].

To date, six different mouse models of Blm have been reported in the literature. In four of these models, *Blm*^{tm1Grd} (*Blm*^{Cin}), *Blm*^{tm1Ches}, *Blm*^{tm2Brd} (*Blm*^{m2}), and *Blm*^{tm3Ches}, homozygosity for the mutated *Blm* allele results in embryonic lethality [76, 142–144]. The *Blm*^{tm3Brd} (*Blm*^{m3}) allele, also generated by Luo and colleagues, was originally reported as a null mutation which ablated Blm expression [143]. However, it has since been recharacterized as a hypomorphic allele which expresses Blm at approximately 25% of wild-type levels [144]. The *Blm*^{tm4Ches} model consists of a conditionally floxed allele which facilitates tissue-specific ablation of *Blm* function when crossed onto the appropriate Cre recombinase background, thus circumventing the developmental issues of embryonic lethality [145, 146]. Cell lines and tissues from the above Blm models exhibit increased levels of DNA damage and SCE [76, 142–146] underscoring the roles of *BLM*/*Blm* in the maintenance of genomic stability. Previous studies using the *Apc*^{Min} mouse model of intestinal tumorigenesis demonstrate that increased tumor dysplasia and tumor number occur in (heterozygous) *Blm*$^{Cin/+}$;*Apc*$^{Min/+}$ (Figure 1(c)) or (hypomorphic) *Blm*$^{m3/m3}$;*Apc*$^{Min/+}$ mice [76, 143]. These changes in tumor biology are driven by increased rates of homologous recombination which facilitates LOH of the remaining wild-type *Apc* allele. In contrast, *Blm* haploinsufficiency had no impact on tumor development, progression, or regression in a *Ccsp/Fgf-10* transgenic model which overexpresses the growth factor Fgf-10 under control of the lung-specific Clara cell secretory protein (*Ccsp*) promoter (Figure 1(d)) (Boivin & Groden,

personal communication). There were no significant differences in the numbers, size, and histologic grade of lung adenomas between transgenic *Fgf-10* and $Blm^{Cin/+}$;*Fgf-10* mice. Indeed, the $Apc^{Min/+}$ intestinal and *Fgf-10* lung models of adenoma formation may differ in their underlying mechanistic basis, but there are undoubtedly tissue-specific contributions affecting the emergent tumor phenotype(s) when Blm levels are genetically modulated in specific cellular compartments.

Werner syndrome (WS) is a segmental progeroid disease that causes premature aging in affected individuals [147, 148]. Patients have an elevated risk for age-related diseases including atherosclerotic cardiovascular disease and a wide range of cancers [149]. Defects in the Werner gene (*WRN*) are the underlying cause of WS. Similar to BLM, WRN is involved in mitotic recombination and is also important in the ALT pathway of telomere maintenance [135, 150]. A small proportion of WS patients develop gastrointestinal tumors, and *WRN* is epigenetically silenced by promoter methylation in colorectal cancer [151, 152]. Specific *WRN* polymorphisms have been investigated in GWAS studies for susceptibility to colorectal cancer, but of these only the WRN Cys1367Arg variant was associated with increased risk [153, 154]. Mouse models have been generated for WRN, but *Wrn*-deficient mice do not recapitulate the phenotype of WS patients [155, 156]. $Wrn^{-/-}$ mice demonstrate neither premature aging nor develop tumors. Overall they appear phenotypically normal, but this may, in part, be due to the fact that mouse telomeres are considerably longer than human. Indeed, when the $Wrn^{-/-}$ knockout background is crossed with the *Terc*- (telomerase RNA template) deficient mouse model and/or the hypomorphic Blm^{m3} model, it accelerates the onset of several phenotypic aspects characteristic of later generation $Terc^{-/-}$ animals by 2-3 generations [157], suggesting a role for *Wrn* and *Blm* in aging. To our knowledge, the $Wrn^{-/-}$ knockout has yet to be crossed with the Apc^{Min} model, so it remains unknown what influence *Wrn*-deficiency will have on intestinal tumorigenesis in this setting. Recql5 is the only other RecQ family member that has been crossed with the Apc^{Min} model. $Recql5^{-/-}$;$Apc^{Min/+}$ mice develop twofold more intestinal adenomas than control $Apc^{Min/+}$ cohorts [158]. Given the known, overlapping roles of the mammalian RecQ family in maintaining genomic stability, it will be no surprise if other members of this group modify the intestinal tumor phenotype of the Apc^{Min} model.

9. *In Vivo* Manipulation of BLM Levels Modulates Intestinal Tumorigenesis

Several lines of evidence indicate that *Blm* dosage is critical for controlling the onset of tumorigenesis in mice. Mouse models demonstrate that chromosomal instability directly correlates with the levels of Blm; as Blm decreases, genomic instability and tumor burden increase [76, 143, 144]. $Blm^{Cin/+}$ mice develop lymphoma earlier than wild-type litter-mates when challenged with murine leukemia virus [76]. Furthermore, haploinsufficiency for *Blm* on the C57Bl/6J $Apc^{Min/+}$ background increases spontaneous adenoma formation and dysplasia facilitated by an increase in HR which leads to LOH and hence loss of the wild-type *Apc* allele. These observations correlate with studies on human carriers of specific *BLM* mutations and their subsequent susceptibilities to colorectal cancer [77]. Homozygous $Blm^{m3/m3}$ mice develop a wide spectrum of different tumors by age of 20 months, analogous to those presented by BS patients [143]. Additionally, the hypomorphic $Blm^{m3/m3}$ mutant accelerates onset of several phenotypic aspects characteristic of later generation *Terc*-deficient mice by 2-3 generations, including reduced life span, increased apoptosis of epithelial crypt cells, and increased chromosome end-to-end fusions [157].

Transgenic mouse models have been developed that overexpress DNA repair genes. Some models develop tumor-resistant phenotypes with increases in animal survival and/or cancer-free survival and significant increases in animal longevity [23, 159–162]. These reports confirm that overexpression of genes involved in DNA repair not only has anti-tumorigenic effects but also positively impacts the myriad of pathways that contribute to organismal aging. We hypothesized that if halving *Blm* gene dosage increased predisposition to tumorigenesis, overexpression would conversely decrease tumor susceptibility and consequently develop a transgenic mouse model that expresses human *BLM* under control of the *PGK* promoter (BLM^{Tg}). This transgene rescues the embryonic lethality of $Blm^{Cin/Cin}$ knockout mice, indicating that BLM expression is appropriately regulated, within the physiological context of our model, to direct normal development in *Blm*-null mice [141]. Given the demonstrated relationship between low or absent expression levels of BLM/Blm and cancer, we investigated whether constitutive overexpression of BLM attenuated adenoma formation in our Apc^{Min} mouse model of intestinal tumorigenesis. Although there is a 50% reduction in the number of intestinal adenomas that spontaneously arise in $Apc^{Min/+}$;BLM^{Tg} mice, there is no difference in tumor pathology (Figure 1(e)). Suppression of adenoma formation by BLM^{Tg} was most evident in the jejunal and ileac segments of the gastrointestinal tract (Figure 2) which is not surprising, as these regions comprise the predominant site of adenoma formation in $Apc^{Min/+}$ [163]. Adenomas were not observed in BLM^{Tg} or wild-type mice.

Given the role of *BLM* in maintaining genomic integrity [118–120], we hypothesized that BLM^{Tg} modulated tumorigenesis in $Apc^{Min/+}$ mice by suppressing HR, thus reducing the rate of LOH and hence loss of the wild-type *Apc* allele and possibly the rate of secondary genomic events that additionally affect genome stability. To investigate further the mechanism of intestinal tumor reduction by BLM overexpression in $Apc^{Min/+}$;BLM^{Tg} mice, we used the pink-eyed unstable (p^{un}) model as an *in vivo* reporter for measuring levels of HR. In this serendipitous model, which originates from a naturally occurring mutation, a somatic intrachromosomal deletion within the mouse *p* gene restores melanin production in the otherwise transparent cells of the retinal pigment epithelium (RPE), generating a clone of brown cells or eyespot [164]. Deletion events occur spontaneously and are absolutely

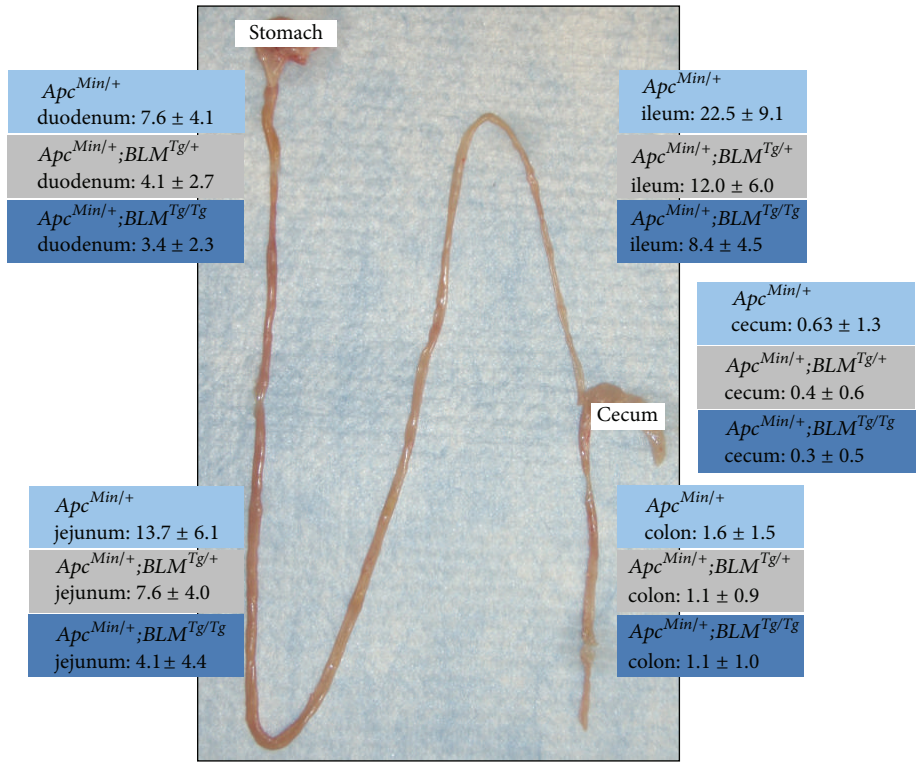

FIGURE 2: BLM^{Tg} reduces intestinal polyp numbers by ~2-fold in $Apc^{Min/+}$ mice. Polyps counts (mean ± σ) for different regions of the gastrointestinal tract are shown for $Apc^{Min/+}$, $Apc^{Min/+};BLM^{Tg/+}$, and $Apc^{Min/+};BLM^{Tg/Tg}$ mice. BLM^{Tg} dose-dependent suppression of adenoma numbers is most evident in the jejunum and ileum. BLM^{Tg} does not change tumor spectrum or location.

dependent on HR. Thus, the number of RPE eyespots is an *in vivo* surrogate for levels of HR within the tissue (Figures 1(f) and 1(g)). The p^{un} model has previously been used to demonstrate the opposing roles that *Blm* and *Brca1* play in HR [165]. A twofold reduction of eyespots in RPE cells of $p^{un/un};BLM^{Tg}$ mice suggests that BLM^{Tg} directly modulates HR in this tissue [141]. Our interpretation of the observed reduction in adenoma numbers in the $Apc^{Min/+};BLM^{Tg}$ model is that elevated levels of BLM/Blm reduce HR in the intestinal epithelia, thus suppressing LOH and hence loss of the wild-type *Apc* allele.

It has been observed that when the Apc^{Min} allele is combined with mismatch repair- (MMR-) null mouse models, either $Mlh1^{-/-}$ or $Msh2^{-/-}$, the mechanism of *Apc* inactivation changes from that of LOH to intragenic mutation. Analyses of adenomas from $Mlh1^{-/-};Apc^{Min/+}$ and $Msh2^{-/-};Apc^{Min/+}$ mice demonstrated intragenic (point) mutation of the wild-type *Apc* allele in 81% and 85% of cases, respectively [46, 52, 53]. This shift in the mechanism of *Apc* inactivation is due to the characteristic mutator phenotypes inherent to these models of MMR deficiency. Given the known roles of *BLM/Blm* in HR, we investigated if our BLM^{Tg} could likewise reduce intestinal adenoma burdens in an $Apc^{Min/+}$ model that was not dependent on LOH as a second-hit mechanism of inactivation. When the $Apc^{Min/+};BLM^{Tg}$ model was crossed onto a $Msh2^{\Delta 7N}$ (MMR-null) background there were no significant differences in intestinal adenoma numbers (Figure 1(h)) between $Apc^{Min/+};BLM^{Tg};Msh2^{\Delta 7N/\Delta 7N}$ and $Apc^{Min/+};Msh2^{\Delta 7N/\Delta 7N}$ mice [141]. Thus, inactivation of the wild-type *Apc* allele by point mutation, due to innate MMR deficiency, rather than by LOH, ablates the protective, suppressive effect of the BLM^{Tg} on intestinal adenoma formation. Although indirect, this observation supports our hypothesis that genetic upregulation of BLM/Blm expression reduces HR in the intestinal epithelia, thus suppressing LOH and hence loss of the wild-type *Apc* allele. Collectively, the data suggest that HR-dependent DNA double-strand break repair capacity can be modulated *in vivo* to alter tumor susceptibility and that perhaps levels of specific DNA repair proteins may be titrated to achieve positive therapeutic outcomes in the context of specific hereditary cancer syndromes, exemplified by FAP.

Cancer (and aging) represents complex phenotypes that develop through the integrated output of numerous biological pathways. It is possible that variation in BLM levels within normal human populations could also confer differential protection from/susceptibility to tumor formation in different individuals. Specific alleles of *BLM* have been associated with human cancers: BLM P868L (rs11852361) with colorectal cancer (odds ratio = 1.29, 95% CI, 1.02–1.64: $p = 0.04$) and BLM rs2532105 with breast cancer (odds ratio = 2.0, 95% CI: 1.2–3.3, $p \leq 0.05$), respectively [153, 166]. Although the observation of decreased adenoma numbers in our $Apc^{Min/+};BLM^{Tg}$ model is associated with overall increased

BLM expression, the example of BLM P868L in colorectal cancer [153] suggests that functional variation within *BLM* alleles might be equally important in contributing to a tumor-resistant/susceptible phenotype. Indeed, *in vitro* analyses of hypomorphic BLM variants, including BLM P868L, have demonstrated that polymorphisms/mutations within the human population have biological consequences for BLM function [167]. It is possible that certain long-lived humans may inherit superior functional variants of *BLM* alleles with elevated expression that contribute to increased genomic stability, protecting against tumorigenesis and thus extending life span. Although loss-of-function *BLM* alleles have been associated with human cancers [153, 166] genome-wide association studies have yet to identify alleles associated with longevity [168]. The early onset of tumorigenesis in BS individuals makes it difficult to resolve the functional protective role(s) that BLM may have in organismal aging [120, 121]. This may in part be due to the highly selective nature of markers chosen for genome-wide association studies and suggests that understanding the effects of specific *BLM* alleles and/or associated haplotypes on tumor repression in humans will remain a future challenge. Understanding the mechanism by which BLM attenuates tumor susceptibility will aid in our fundamental understanding of its roles in maintaining genomic stability and suggest new strategies for cancer prevention involving direct regulation of DNA repair pathways.

10. Therapeutic Insights from Mouse Models

Mouse models have proven good preclinical platforms for assessing the potential efficacy of chemopreventive and chemotherapeutic drugs against colorectal cancer. An unmistakable advantage is the capability to knock in the equivalent of clinically relevant human mutations and study their subsequent effects on tumorigenesis. A trio of common missense mutations identified in the *MSH2*, *MLH1*, and *MSH6* genes of Lynch syndrome patients have been knocked into mouse backgrounds, generating models corresponding to the $Msh2^{G674A}$ [169], $Mlh1^{G67R}$ [170], and $Msh6^{T1217D}$ [171] mutations. These missense models establish additional physiological contexts for recapitulating and unraveling the tumorigenic processes leading to Lynch syndrome and represent genetic systems that facilitate the *in vivo* analyses of clinically important mutations. The $Msh2^{G674A}$, $Mlh1^{G67R}$, and $Msh6^{T1217D}$ mutations have been characterized as separation-of-function alleles and in these animals the normally intertwined processes of mismatch DNA repair and the apoptotic response to DNA damage have been genetically severed, resulting in distinctive phenotypes. Although mutant mice still demonstrated strong tumor dispositions, their normal apoptotic responses to DNA damaging agents such as *N*-methyl-*N*′-nitro-*N*-nitrosoguanidine (MNNG) and cisplatin were intact [169–171]. MMR-deficient cells are traditionally resistant to these types of compounds. However, a recent report conflicts with the finding that $Msh2^{G674A}$ is a separation-of-function allele. Oligonucleotide-directed mutagenesis was used to screen *MSH2* variants of uncertain significance (VUS) in mouse embryonic stem cells hemizygous for *Msh2* ($Msh2^{+PUR/\Delta}$) [172]. In this system, $Msh2^{G674A}$ conferred partial resistance to alkylating agents. It is possible that the $Msh2^{G674A}$ variant functions differently in human and mouse and that differences between the *in vitro* and *in vivo* experimental settings could lead to conflicting biological outcomes.

When the $VCMsh2^{loxP}$ line was combined with *Msh2*-null and $Msh2^{G674A}$ models to generate allelic phase mutants, only tumors from $VCMsh2^{loxP/G674A}$ animals were responsive to treatment with FOLFOX (folinic acid; fluorouracil; oxaliplatin), a chemotherapeutic regime used to treat late-stage colorectal cancer [100]. An obvious implication from these models is that Lynch syndrome patients with certain missense mutations will prove susceptible to treatment with conventional chemotherapeutic agents and this suggests additional criteria that may prove useful for stratifying Lynch syndrome patients with respect to optimal treatment. Treatment of $Lgr5\text{-}CreERT2;Msh2^{flox/-}$ mice with temozolomide (TMZ), a methylating chemotherapeutic agent, provides corroborating data for stratifying therapeutic regimes. TMZ promoted expansion of *Msh2*-deficient crypts over 5-fold in $Lgr5\text{-}CreERT2;Msh2^{flox/-}$ mice, consistent with the interpretation that *Msh2*-deficient CBCs develop a competitive growth advantage in the crypt stem cell niche [102]. This is congruent with the proposed biased drift model of stem cell dynamics that governs the mutational trajectories of CBCs after acquisition, or induction, of oncogenic mutations [173]. Moreover, drug treatment accelerated intestinal tumor development in $Lgr5\text{-}CreERT2;Msh2^{flox/-}$ mice, most likely caused by the increased mutational load from TMZ and compounded by the MSI phenotype of *Msh2*-deficient CBCs [102]. In conclusion, Lynch syndrome patients should not be exposed to TMZ, which is paradoxically a strong risk factor for tumor development, as it selects for and causes expansion of highly tumorigenic *Msh2*-deficient cells in this therapeutic setting.

Various FAP and Lynch syndrome mutant mouse lines have been employed over many years to study the potential of nonsteroidal anti-inflammatory drugs (NSAIDs), a structurally diverse family of compounds, as chemopreventive options in cancer treatment [174, 175]. Epidemiological studies have clearly reported an inverse relationship between the use of certain NSAIDs and the incidence of colorectal cancers [176, 177] and mouse models remain appropriate experimental systems for investigating the anti-tumorigenic mechanisms of these compounds. Although it is accepted that NSAIDs interrupt arachidonic acid metabolism *via* inhibition of COX enzymes, thus modulating the synthesis of prostaglandins [178], they also exhibit pleiotropic effects on other cellular pathways.

Aspirin suppresses the MSI in MMR-deficient human colon tumor cell lines via a genetic selection that appears to enhance apoptosis in critically unstable cells [179]. The long-term outcome is a cell population that has a persistent deficiency in MMR but has paradoxically acquired a largely microsatellite stable (MSS) phenotype. Remarkably, the selection for MSS in cells that were MMR-deficient was independent of the *COX1* or *COX2* genes [179]. Nitric oxide-donating aspirin (NO-aspirin) also suppressed MSI in MMR-deficient cell lines but at concentrations 300- to 3000-fold

less than aspirin [180]. We hypothesized that treatment with aspirin and NO-aspirin would delay and/or prevent tumorigenesis in Lynch syndrome. When aspirin and NO-aspirin were used to treat a mouse model of Lynch syndrome (*Msh2*$^{flox/flox}$*;Villin-Cre*) it was observed that both reagents delayed onset of tumorigenesis and increased animal survival [181]. Furthermore, aspirin appeared to partially stabilize tumor MSI in this model, possibly through an apoptotic process that eliminated critically unstable cells, thus attenuating, but not completely reversing, the intrinsic mutator phenotype. If we can identify and understand important signaling pathways that are important in determining the chemopreventive properties of various NSAIDs, they may reveal new opportunities for alternative, more focused therapies for the treatment of colorectal cancer.

The Colorectal Adenoma/Carcinoma Prevention Program (CAPP) has examined the potential of aspirin to reduce colorectal neoplasia in Lynch syndrome carriers. The initial CAPP report concluded that 4-year exposure to aspirin did not significantly reduce the incidence of neoplasia [182], although mouse studies clearly suggested that long-term exposure to aspirin was required for chemopreventive benefits. Moreover, a recent clinical analysis reported that regular aspirin use was associated with a lower risk of cancer-specific mortality in individuals already diagnosed with colorectal cancer [183]. Similar observations have been reported for the chemopreventive role of aspirin in breast cancer [184, 185]. Together, these results suggested that the chemopreventive benefits of aspirin might only manifest after long-term continuous administration. The updated report from the CAPP trial indicates that, perhaps not unexpectedly, the benefits of aspirin for Lynch syndrome patients only begin to appear after 5 years of exposure [186]. The end-point for these studies was Lynch syndrome cancers detected during yearly colonoscopy screens. Analyses suggest that the proportion of patients with Lynch syndrome tumors dramatically decreases in the aspirin-treated cohort. On consideration of the combined cellular, mouse, and clinical studies it appears that aspirin presents a particularly promising chemopreventive agent for colorectal cancer. Indeed, The United States Preventive Services Task Force (USPSTF) originally recommended against the use of aspirin for the prevention of colorectal cancer [187]. However, this assessment has been recently updated to include low-dose aspirin as a chemopreventive option for colorectal cancer (and cardiovascular disease) among adults aged between 50 and 69 [188].

11. Conclusion

Insights from *in vivo* modeling studies have had and will continue to have great impact on understanding the genetics of human colorectal tumors and the mechanisms that initiate and lead to their progression. They translate directly to understanding risk for colorectal cancer, showing us how we can exploit tumor mechanisms and personalize therapeutic interventions. Current modalities for colorectal cancer include therapies that target the VEGF (bevacizumab) and EGFR (cetuximab) pathways. Other druggable pathways are those for BRAF (vemurafenib) and of course Wnt/β-catenin signaling (OMP-18R5). Immunobased therapies, including those targeting CTLA4 and PD1, are also the focus of clinical trials for colorectal cancer. Adequate consideration of these regimes lies beyond the scope of this paper; they have been comprehensively reviewed elsewhere [189]. Chemopreventive trials in Lynch syndrome use high dose aspirin, while polyposis patients are treated prophylactically with celecoxib. Most therapies for colorectal tumors rely on leucovorin, 5-fluorouracil, and topoisomerase inhibitors (FOLFIRI) to treat locally and distantly invasive disease. However, other approaches are needed for improving the standard of care and for stratifying these approaches. Mouse models have been instrumental in demonstrating the fact that it is possible to modulate HR-dependent DNA double-strand break repair capacity *in vivo* to alter tumor susceptibility. Furthermore, it is conceivable that levels of specific DNA repair proteins may be titrated to achieve positive therapeutic outcomes in the context of specific hereditary cancer syndromes, exemplified by FAP. Whether this becomes eventually achievable in clinical settings remains a matter for speculation. However, development of these types of systems to target tumors more effectively may make it possible to augment the success of our current treatments for colorectal cancer.

Disclosure

The content is solely the responsibility of the authors. The funders had no role in study design, data collection and analysis, decision to publish, or preparation of the paper.

Competing Interests

The authors declare that they have no competing interests.

Acknowledgments

The authors would like to acknowledge the support from the Bloom Syndrome Foundation (Joanna Groden), The Solid Tumor Biology Program in the OSU Comprehensive Cancer Center, and NIH Grants CA117898 (Joanna Groden) and CA63507 (Joanna Groden).

References

[1] L. Ding, M. C. Wendl, D. C. Koboldt, and E. R. Mardis, "Analysis of next-generation genomic data in cancer: accomplishments and challenges," *Human Molecular Genetics*, vol. 19, no. 2, pp. R188–R196, 2010.

[2] T. Stricker, D. V. T. Catenacci, and T. Y. Seiwert, "Molecular profiling of cancer—the future of personalized cancer medicine: a primer on cancer biology and the tools necessary to bring molecular testing to the clinic," *Seminars in Oncology*, vol. 38, no. 2, pp. 173–185, 2011.

[3] D.-J. Cheon and S. Orsulic, "Mouse models of cancer," *Annual Review of Pathology: Mechanisms of Disease*, vol. 6, pp. 95–119, 2011.

[4] N. E. Sharpless and R. A. Depinho, "The mighty mouse: genetically engineered mouse models in cancer drug development," *Nature Reviews Drug Discovery*, vol. 5, no. 9, pp. 741–754, 2006.

[5] A. T. Chinwalla, L. L. Cook, and K. D. Delehaunty, "Initial sequencing and comparative analysis of the mouse genome," *Nature*, vol. 420, pp. 520–562, 2002.

[6] A. F. Peery, S. D. Crockett, A. S. Barritt et al., "Burden of gastrointestinal, liver, and pancreatic diseases in the United States," *Gastroenterology*, vol. 149, no. 7, pp. 1731–1741.e3, 2015.

[7] P. Lichtenstein, N. V. Holm, P. K. Verkasalo et al., "Environmental and heritable factors in the causation of cancer: analyses of cohorts of twins from Sweden, Denmark, and Finland," *The New England Journal of Medicine*, vol. 343, no. 2, pp. 78–85, 2000.

[8] K. Czene, P. Lichtenstein, and K. Hemminki, "Environmental and heritable causes of cancer among 9.6 million individuals in the Swedish Family-Cancer database," *International Journal of Cancer*, vol. 99, no. 2, pp. 260–266, 2002.

[9] S. Jiao, U. Peters, S. Berndt et al., "Estimating the heritability of colorectal cancer," *Human Molecular Genetics*, vol. 23, no. 14, pp. 3898–3905, 2014.

[10] A. Tenesa and M. G. Dunlop, "New insights into the aetiology of colorectal cancer from genome-wide association studies," *Nature Reviews Genetics*, vol. 10, no. 6, pp. 353–358, 2009.

[11] I. P. M. Tomlinson, L. G. Carvajal-Carmona, S. E. Dobbins et al., "Multiple common susceptibility variants near BMP pathway loci *GREM1*, *BMP4*, and *BMP2* explain part of the missing heritability of colorectal cancer," *PLoS Genetics*, vol. 7, no. 6, Article ID e1002105, 2011.

[12] U. Peters, C. M. Hutter, L. Hsu et al., "Meta-analysis of new genome-wide association studies of colorectal cancer risk," *Human Genetics*, vol. 131, no. 2, pp. 217–234, 2012.

[13] J. K. Kundu and Y.-J. Surh, "Inflammation: gearing the journey to cancer," *Mutation Research—Reviews in Mutation Research*, vol. 659, no. 1-2, pp. 15–30, 2008.

[14] G. Rogler, "Chronic ulcerative colitis and colorectal cancer," *Cancer Letters*, vol. 345, no. 2, pp. 235–241, 2014.

[15] L. Klampfer, "Cytokines, inflammation and colon cancer," *Current Cancer Drug Targets*, vol. 11, no. 4, pp. 451–464, 2011.

[16] H. Gordon, F. Trier Moller, V. Andersen, and M. Harbord, "Heritability in inflammatory bowel disease: from the first twin study to genome-wide association studies," *Inflammatory Bowel Diseases*, vol. 21, no. 6, pp. 1428–1434, 2015.

[17] J. Satsangi, N. A. Kennedy, P. Henderson, D. C. Wilson, and E. R. Nimmo, "Exploring the hidden heritability of inflammatory bowel disease," *Gut*, vol. 60, no. 11, pp. 1447–1448, 2011.

[18] D. Ellinghaus, J. Bethune, B.-S. Petersen, and A. Franke, "The genetics of Crohn's disease and ulcerative colitis-status quo and beyond," *Scandinavian Journal of Gastroenterology*, vol. 50, no. 1, pp. 13–23, 2015.

[19] A. Franke, D. P. McGovern, J. C. Barrett et al. et al., "Genome-wide meta-analysis increases to 71 the number of confirmed Crohn's disease susceptibility loci," *Nature Genetics*, vol. 42, no. 12, pp. 1118–1125, 2010.

[20] K. Fransen, M. Mitrovic, C. C. Van Diemen, and R. K. Weersma, "The quest for genetic risk factors for Crohn's disease in the post-GWAS era," *Genome Medicine*, vol. 3, article 13, 2011.

[21] A. M. Bianco, "Genetics of inflammatory bowel disease from multifactorial to monogenic forms," *World Journal of Gastroenterology*, vol. 21, no. 43, pp. 12296–12310, 2015.

[22] J. A. Eaden, K. R. Abrams, and J. F. Mayberry, "The risk of colorectal cancer in ulcerative colitis: a meta-analysis," *Gut*, vol. 48, no. 4, pp. 526–535, 2001.

[23] G. P. Boivin, K. Washington, K. Yang et al., "Pathology of mouse models of intestinal cancer: consensus report and recommendations," *Gastroenterology*, vol. 124, no. 3, pp. 762–777, 2003.

[24] M. M. Taketo and W. Edelmann, "Mouse models of colon cancer," *Gastroenterology*, vol. 136, no. 3, pp. 780–798, 2009.

[25] S. Kaiser, Y.-K. Park, J. L. Franklin et al., "Transcriptional recapitulation and subversion of embryonic colon development by mouse colon tumor models and human colon cancer," *Genome Biology*, vol. 8, no. 7, article no. R131, 2007.

[26] A. R. Moser, H. C. Pitot, and W. F. Dove, "A dominant mutation that predisposes to multiple intestinal neoplasia in the mouse," *Science*, vol. 247, no. 4940, pp. 322–324, 1990.

[27] A. F. Cheung, A. M. Carter, K. K. Kostova et al., "Complete deletion of Apc results in severe polyposis in mice," *Oncogene*, vol. 29, no. 12, pp. 1857–1864, 2010.

[28] E. C. Robanus-Maandag, P. J. Koelink, C. Breukel et al., "A new conditional Apc-mutant mouse model for colorectal cancer," *Carcinogenesis*, vol. 31, no. 5, pp. 946–952, 2010.

[29] P. Pollard, M. Deheragoda, S. Segditsas et al., "The Apc1322T mouse develops severe polyposis associated with submaximal nuclear β-catenin expression," *Gastroenterology*, vol. 136, no. 7, pp. 2204–2213, 2009.

[30] H. Shibata, K. Toyama, H. Shioya et al., "Rapid colorectal adenoma formation initiated by conditional targeting of the APC gene," *Science*, vol. 278, no. 5335, pp. 120–133, 1997.

[31] S. Colnot, M. Niwa-Kawakita, G. Hamard et al., "Colorectal cancers in a new mouse model of familial adenomatous polyposis: influence of genetic and environmental modifiers," *Laboratory Investigation*, vol. 84, no. 12, pp. 1619–1630, 2004.

[32] M. Kuraguchi, X.-P. Wang, R. T. Bronson et al., "Adenomatous polyposis coli *(APC)* is required for normal development of skin and thymus," *PLoS Genetics*, vol. 2, no. 9, article e146, 2006.

[33] R. Fodde, W. Edelmann, K. Yang et al., "A targeted chain-termination mutation in the mouse Apc gene results in multiple intestinal tumors," *Proceedings of the National Academy of Sciences of the United States of America*, vol. 91, no. 19, pp. 8969–8973, 1994.

[34] R. Smits, M. F. Kielman, C. Breukel et al., "Apc1638T: a mouse model delineating critical domains of the adenomatous polyposis coli protein involved in tumorigenesis and development," *Genes & Development*, vol. 13, no. 10, pp. 1309–1321, 1999.

[35] M. Oshima, H. Oshima, K. Kitagawa, M. Kobayashi, C. Itakura, and M. Taketo, "Loss of Apc heterozygosity and abnormal tissue building in nascent intestinal polyps in mice carrying a truncated Apc gene," *Proceedings of the National Academy of Sciences of the United States of America*, vol. 92, no. 10, pp. 4482–4486, 1995.

[36] C. F. Quesada, H. Kimata, M. Mori, M. Nishimura, T. Tsuneyoshi, and S. Baba, "Piroxicam and acarbose as chemopreventive agents for spontaneous intestinal adenomas in APC gene 1309 knockout mice," *Japanese Journal of Cancer Research*, vol. 89, no. 4, pp. 392–396, 1998.

[37] H. Sasai, M. Masaki, and K. Wakitani, "Suppression of polypogenesis in a new mouse strain with a truncated $ApC^{\Delta 474}$ by a novel COX-2 inhibitor, JTE-522," *Carcinogenesis*, vol. 21, no. 5, pp. 953–958, 2000.

[38] Q. Li, T.-O. Ishikawa, M. Oshima, and M. M. Taketo, "The threshold level of adenomatous polyposis coli protein for mouse intestinal tumorigenesis," *Cancer Research*, vol. 65, no. 19, pp. 8622–8627, 2005.

[39] E. R. Fearon, "Molecular genetics of colorectal cancer," *Annual Review of Pathology: Mechanisms of Disease*, vol. 6, pp. 479–507, 2011.

[40] P. Peltomäki, "Lynch syndrome genes," *Familial Cancer*, vol. 4, no. 3, pp. 227–232, 2005.

[41] Y. Ionov, M. A. Peinado, S. Malkhosyan, D. Shibata, and M. Perucho, "Ubiquitous somatic mutations in simple repeated sequences reveal a new mechanism for colonic carcinogenesis," *Nature*, vol. 363, no. 6429, pp. 558–561, 1993.

[42] L. A. Aaltonen, P. Peltomäki, F. S. Leach et al., "Clues to the pathogenesis of familial colorectal cancer," *Science*, vol. 260, no. 5109, pp. 812–816, 1993.

[43] K. H. Goss and J. Groden, "Biology of the adenomatous polyposis coli tumor suppressor," *Journal of Clinical Oncology*, vol. 18, no. 9, pp. 1967–1979, 2000.

[44] J. Groden, A. Thliveris, W. Samowitz et al., "Identification and characterization of the familial adenomatous polyposis coli gene," *Cell*, vol. 66, no. 3, pp. 589–600, 1991.

[45] C. Albuquerque, C. Breukel, R. Van Der Luijt et al., "The 'just-right' signaling model: APC somatic mutations are selected based on a specific level of activation of the β-catenin signaling cascade," *Human Molecular Genetics*, vol. 11, no. 13, pp. 1549–1560, 2002.

[46] R. Smits, N. Hofland, W. Edelmann et al., "Somatic Apc mutations are selected upon their capacity to inactivate the β-catenin downregulating activity," *Genes Chromosomes and Cancer*, vol. 29, no. 3, pp. 229–239, 2000.

[47] J. P. Cheadle, M. Krawczak, M. W. Thomas et al., "Different combinations of biallelic APC mutation confer different growth advantages in colorectal tumours," *Cancer Research*, vol. 62, no. 2, pp. 363–366, 2002.

[48] M. H. Nieuwenhuis and H. F. A. Vasen, "Correlations between mutation site in APC and phenotype of familial adenomatous polyposis (FAP): a review of the literature," *Critical Reviews in Oncology/Hematology*, vol. 61, no. 2, pp. 153–161, 2007.

[49] E. M. Kohler, A. Derungs, G. Daum, J. Behrens, and J. Schneikert, "Functional definition of the mutation cluster region of adenomatous polyposis coli in colorectal tumours," *Human Molecular Genetics*, vol. 17, no. 13, pp. 1978–1987, 2008.

[50] P. J. Morin, A. B. Sparks, V. Korinek et al., "Activation of β-catenin-Tcf signaling in colon cancer by mutations in β-catenin or APC," *Science*, vol. 275, no. 5307, pp. 1787–1790, 1997.

[51] Y. Shimizu, S. Ikeda, M. Fujimori et al., "Frequent alterations in the Wnt signaling pathway in colorectal cancer with microsatellite instability," *Genes, Chromosomes and Cancer*, vol. 33, no. 1, pp. 73–81, 2002.

[52] A. R. Shoemaker, K. M. Haigis, S. M. Baker, S. Dudley, R. M. Liskay, and W. F. Dove, "Mlh1 deficiency enhances several phenotypes of $APC^{Min/+}$ mice," *Oncogene*, vol. 19, no. 23, pp. 2774–2779, 2000.

[53] A. H. Reitmair, J.-C. Cai, M. Bjerknes et al., "MSH2 deficiency contributes to accelerated APC-mediated intestinal tumorigenesis," *Cancer Research*, vol. 56, no. 13, pp. 2922–2926, 1996.

[54] A. R. Moser, L. F. Hegge, and R. D. Cardiff, "Genetic background affects susceptibility to mammary hyperplasias and carcinomas in $Apc^{(min)/+}$ mice," *Cancer Research*, vol. 61, no. 8, pp. 3480–3485, 2001.

[55] V. Mai, L. H. Colbert, D. Berrigan et al., "Calorie restriction and diet composition modulate spontaneous intestinal tumorigenesis in ApcMin mice through different mechanisms," *Cancer Research*, vol. 63, no. 8, pp. 1752–1755, 2003.

[56] L. Fini, G. Piazzi, Y. Daoud et al., "Chemoprevention of intestinal polyps in ApcMin/+ mice fed with western or balanced diets by drinking annurca apple polyphenol extract," *Cancer Prevention Research*, vol. 4, no. 6, pp. 907–915, 2011.

[57] S. Beyaz, M. D. Mana, J. Roper et al., "High-fat diet enhances stemness and tumorigenicity of intestinal progenitors," *Nature*, vol. 531, no. 7592, pp. 53–58, 2016.

[58] Y. Li, P. Kundu, S. W. Seow et al., "Gut microbiota accelerate tumor growth via c-jun and STAT3 phosphorylation in $APC^{Min/+}$ mice," *Carcinogenesis*, vol. 33, no. 6, pp. 1231–1238, 2012.

[59] A. Belcheva, T. Irrazabal, S. J. Robertson et al., "Gut microbial metabolism drives transformation of MSH2-deficient colon epithelial cells," *Cell*, vol. 158, no. 2, pp. 288–299, 2014.

[60] K. A. Gould, C. Luongo, A. R. Moser et al., "Genetic evaluation of candidate genes for the Mom1 modifier of intestinal neoplasia in mice," *Genetics*, vol. 144, no. 4, pp. 1777–1785, 1996.

[61] R. C. Crist, J. J. Roth, M. P. Lisanti, L. D. Siracusa, and A. M. Buchberg, "Identification of Mom12 and Mom13, two novel modifier loci of Apc Min-mediated intestinal tumorigenesis," *Cell Cycle*, vol. 10, no. 7, pp. 1092–1099, 2011.

[62] A. R. Moser, W. F. Dove, K. A. Roth, and J. I. Gordon, "The Min (multiple intestinal neoplasia) mutation: its effect on gut epithelial cell differentiation and interaction with a modifier system," *Journal of Cell Biology*, vol. 116, no. 6, pp. 1517–1526, 1992.

[63] W. F. Dietrich, E. S. Lander, J. S. Smith et al., "Genetic identification of Mom-1, a major modifier locus affecting Min-induced intestinal neoplasia in the mouse," *Cell*, vol. 75, no. 4, pp. 631–639, 1993.

[64] K. A. Gould, W. F. Dietrich, N. Borenstein, E. S. Lander, and W. F. Dove, "Mom1 is a semi-dominant modifier of intestinal adenoma size and multiplicity in Min/+ mice," *Genetics*, vol. 144, no. 4, pp. 1769–1776, 1996.

[65] M. MacPhee, K. P. Chepenik, R. A. Liddell, K. K. Nelson, L. D. Siracusa, and A. M. Buchberg, "The secretory phospholipase A2 gene is a candidate for the Mom1 locus, a major modifier of ApcMin-induced intestinal neoplasia," *Cell*, vol. 81, no. 6, pp. 957–966, 1995.

[66] A. E. McCart, N. K. Vickaryous, and A. Silver, "Apc mice: models, modifiers and mutants," *Pathology Research and Practice*, vol. 204, no. 7, pp. 479–490, 2008.

[67] K. M. Kokolus, M. L. Capitano, C.-T. Lee et al., "Baseline tumor growth and immune control in laboratory mice are significantly influenced by subthermoneutral housing temperature," *Proceedings of the National Academy of Sciences of the United States of America*, vol. 110, no. 50, pp. 20176–20181, 2013.

[68] J. M. Amos-Landgraf, L. N. Kwong, C. M. Kendziorski et al., "A target-selected Apc-mutant rat kindred enhances the modeling of familial human colon cancer," *Proceedings of the National Academy of Sciences of the United States of America*, vol. 104, no. 10, pp. 4036–4041, 2007.

[69] K. Yoshimi, T. Tanaka, A. Takizawa et al., "Enhanced colitis-associated colon carcinogenesis in a novel Apc mutant rat," *Cancer Science*, vol. 100, no. 11, pp. 2022–2027, 2009.

[70] T. Flisikowska, C. Merkl, M. Landmann et al., "A porcine model of familial adenomatous polyposis," *Gastroenterology*, vol. 143, no. 5, pp. 1173–1175, 2012.

[71] D. Hanahan and R. A. Weinberg, "Hallmarks of cancer: the next generation," *Cell*, vol. 144, no. 5, pp. 646–674, 2011.

[72] K. Takaku, M. Oshima, H. Miyoshi, M. Matsui, M. F. Seldin, and M. M. Taketo, "Intestinal tumorigenesis in compound mutant mice of both *Dpc4* (*Smad4*) and *Apc* genes," *Cell*, vol. 92, no. 5, pp. 645–656, 1998.

[73] K. Aoki, Y. Tamai, S. Horiike, M. Oshima, and M. M. Taketo, "Colonic polyposis caused by mTOR-mediated chromosomal instability in $APC^{+/}\Delta^{716}Cdx2^{+/-}$ compound mutant mice," *Nature Genetics*, vol. 35, no. 4, pp. 323–330, 2003.

[74] C. V. Rao, Y.-M. Yang, M. V. Swamy et al., "Colonic tumorigenesis n $BubR1^{+/-}$ $Apc^{Min/+}$ compound mutant mice is linked to premature separation of sister chromatids and enhanced genomic instability," *Proceedings of the National Academy of Sciences of the United States of America*, vol. 102, no. 12, pp. 4365–4370, 2005.

[75] O. J. Sansom, V. S. Meniel, V. Muncan et al., "Myc deletion rescues Apc deficiency in the small intestine," *Nature*, vol. 446, no. 7136, pp. 676–679, 2007.

[76] K. H. Goss, M. A. Risinger, J. J. Kordich et al., "Enhanced tumor formation in mice heterozygous for Blm mutation," *Science*, vol. 297, no. 5589, pp. 2051–2053, 2002.

[77] S. B. Gruber, N. A. Ellis, G. Rennert et al., "BLM heterozygosity and the risk of colorectal cancer," *Science*, vol. 297, no. 5589, p. 2013, 2002.

[78] A. S. Warthin, "Heredity with reference to carcinoma: as shown by the study of the cases examined in the pathological laboratory of the University of Michigan 1895–1913," *Archives of Internal Medicine*, vol. 12, pp. 546–555, 1913.

[79] H. T. Lynch, M. W. Shaw, C. W. Magnuson, A. L. Larsen, and A. J. Krush, "Hereditary factors in cancer. Study of two large midwestern kindreds," *Archives of Internal Medicine*, vol. 117, no. 2, pp. 206–212, 1966.

[80] H. T. Lynch and A. J. Krush, "Cancer family 'G' revisited: 1895–1970," *Cancer*, vol. 27, no. 6, pp. 1505–1511, 1971.

[81] A. de la Chapelle, "The incidence of Lynch syndrome," *Familial Cancer*, vol. 4, no. 3, pp. 233–237, 2005.

[82] H. F. A. Vasen, J.-P. Mecklin, P. M. Khan, and H. T. Lynch, "The international collaborative group on hereditary non-polyposis colorectal cancer (ICG-HNPCC)," *Diseases of the Colon & Rectum*, vol. 34, no. 5, pp. 424–425, 1991.

[83] C. R. Boland, S. N. Thibodeau, S. R. Hamilton et al., "A National Cancer Institute Workshop on microsatellite instability for cancer detection and familial predisposition: development of international criteria for the determination of microsatellite instability in colorectal cancer," *Cancer Research*, vol. 58, no. 22, pp. 5248–5257, 1998.

[84] H. F. A. Vasen, P. Watson, J.-P. Mecklin, and H. T. Lynch, "New clinical criteria for hereditary nonpolyposis colorectal cancer (HNPCC, Lynch syndrome) proposed by the International Collaborative Group on HNPCC," *Gastroenterology*, vol. 116, no. 6, pp. 1453–1456, 1999.

[85] A. Umar, C. R. Boland, J. P. Terdiman et al., "Revised Bethesda guidelines for hereditary nonpolyposis colorectal cancer (Lynch syndrome) and microsatellite instability," *Journal of the National Cancer Institute*, vol. 96, no. 4, pp. 261–268, 2004.

[86] J. R. Jass, "HNPCC and sporadic MSI-H colorectal cancer: a review of the morphological similarities and differences," *Familial Cancer*, vol. 3, no. 2, pp. 93–100, 2004.

[87] R. R. Lyer, A. Pluciennik, V. Burdett, and P. L. Modrich, "DNA mismatch repair: functions and mechanisms," *Chemical Reviews*, vol. 106, no. 2, pp. 302–323, 2006.

[88] N. de Wind, M. Dekker, A. Berns, M. Radman, and H. te Riele, "Inactivation of the mouse *Msh2* gene results in mismatch repair deficiency, methylation tolerance, hyperrecombination, and predisposition to cancer," *Cell*, vol. 82, no. 2, pp. 321–330, 1995.

[89] N. De Wind, M. Dekker, N. Claij et al., "HNPCC-like cancer predisposition in mice through simultaneous loss of Msh3 and Msh6 mismatch-repair protein functions," *Nature Genetics*, vol. 23, no. 3, pp. 359–362, 1999.

[90] W. Edelmann, K. Yang, A. Umar et al., "Mutation in the mismatch repair gene Msh6 causes cancer susceptibility," *Cell*, vol. 91, no. 4, pp. 467–477, 1997.

[91] S. M. Baker, A. W. Plug, T. A. Prolla et al., "Involvement of mouse Mlh1 in DNA mismatch repair and meiotic crossing over," *Nature Genetics*, vol. 13, no. 3, pp. 336–342, 1996.

[92] W. Edelmann, K. Yang, M. Kuraguchi et al., "Tumorigenesis in Mlh1 and $Mlh1/Apc^{1638N}$ mutant mice," *Cancer Research*, vol. 59, no. 6, pp. 1301–1307, 1999.

[93] T. A. Prolla, S. M. Baker, A. C. Harris et al., "Tumour susceptibility and spontaneous mutation in mice deficient in Mlh1, Pms1 and Pms2 DNA mismatch repair," *Nature Genetics*, vol. 18, no. 3, pp. 276–279, 1998.

[94] S. M. Lipkin, P. B. Moens, V. Wang et al., "Meiotic arrest and aneuploidy in MLH3-deficient mice," *Nature Genetics*, vol. 31, no. 4, pp. 385–390, 2002.

[95] K. Wei, A. B. Clark, E. Wong et al., "Inactivation of exonuclease I in mice results in DNA mismatch repair defects, increased cancer susceptibility, and male and female sterility," *Genes and Development*, vol. 17, no. 5, pp. 603–614, 2003.

[96] http://www.informatics.jax.org/allele/summary?markerId=MGI:101816.

[97] B. Kneitz, P. E. Cohen, E. Avdievich et al., "MutS homolog 4 localization to meiotic chromosomes is required for chromosome pairing during meiosis in male and female mice," *Genes and Development*, vol. 14, no. 9, pp. 1085–1097, 2000.

[98] W. Edelmann, P. E. Cohen, B. Kneitz et al., "Mammalian MutS homologue 5 is required for chromosome pairing in meiosis," *Nature Genetics*, vol. 21, no. 1, pp. 123–127, 1999.

[99] K. E. A. Felton, D. M. Gilchrist, and S. E. Andrew, "Constitutive deficiency in DNA mismatch repair," *Clinical Genetics*, vol. 71, no. 6, pp. 483–498, 2007.

[100] M. H. Kucherlapati, K. Lee, A. A. Nguyen et al., "An Msh2 conditional knockout mouse for studying intestinal cancer and testing anticancer agents," *Gastroenterology*, vol. 138, no. 3, pp. 993–1002, 2010.

[101] C. Reiss, T. Haneke, H.-U. Völker et al., "Conditional inactivation of MLH1 in thymic and naive T-cells in mice leads to a limited incidence of lymphoblastic T-cell lymphomas," *Leukemia and Lymphoma*, vol. 51, no. 10, pp. 1875–1886, 2010.

[102] K. Wojciechowicz, E. Cantelli, B. Van Gerwen et al., "Temozolomide increases the number of mismatch repair-deficient intestinal crypts and accelerates tumorigenesis in a mouse model of Lynch syndrome," *Gastroenterology*, vol. 147, no. 5, pp. 1064–1072, 2014.

[103] N. Barker, J. H. van Es, J. Kuipers et al., "Identification of stem cells in small intestine and colon by marker gene *Lgr5*," *Nature*, vol. 449, no. 7165, pp. 1003–1007, 2007.

[104] J. Jonkers and A. Berns, "Conditional mouse models of sporadic cancer," *Nature Reviews Cancer*, vol. 2, no. 4, pp. 251–265, 2002.

[105] A. Akyol, T. Hinoi, Y. Feng, G. T. Bommer, T. M. Glaser, and E. R. Fearon, "Generating somatic mosaicism with a Cre recombinase-microsatellite sequence transgene," *Nature Methods*, vol. 5, no. 3, pp. 231–233, 2008.

[106] A. J. Miller, S. D. Dudley, J.-L. Tsao, D. Shibata, and R. M. Liskay, "Tractable Cre-lox system for stochastic alteration of genes in mice," *Nature Methods*, vol. 5, no. 3, pp. 227–229, 2008.

[107] L. Johnson, K. Mercer, D. Greenbaum et al., "Somatic activation of the K-ras oncogene causes early onset lung cancer in mice," *Nature*, vol. 410, no. 6832, pp. 1111–1116, 2001.

[108] N. Shivapurkar, L. Huang, B. Ruggeri et al., "K-ras and p53 mutations in aberrant crypt foci and colonic tumors from colon cancer patients," *Cancer Letters*, vol. 115, no. 1, pp. 39–46, 1997.

[109] I. Coste, J.-N. Freund, S. Spaderna, T. Brabletz, and T. Renno, "Precancerous lesions upon sporadic activation of β-catenin in mice," *Gastroenterology*, vol. 132, no. 4, pp. 1299–1308, 2007.

[110] B. Romagnolo, D. Berrebi, S. Saadi-Keddoucci et al., "Intestinal dysplasia and adenoma in transgenic mice after overexpression of an activated β-catenin," *Cancer Research*, vol. 59, no. 16, pp. 3875–3879, 1999.

[111] N. Harada, Y. Tamai, T.-O. Ishikawa et al., "Intestinal polyposis in mice with a dominant stable mutation of the β-catenin gene," *EMBO Journal*, vol. 18, no. 21, pp. 5931–5942, 1999.

[112] E. L. Jackson, N. Willis, K. Mercer et al., "Analysis of lung tumor initiation and progression using conditional expression of oncogenic K-ras," *Genes and Development*, vol. 15, no. 24, pp. 3243–3248, 2001.

[113] B. S. Braun, D. A. Tuveson, N. Kong et al., "Somatic activation of oncogenic Kras in hematopoietic cells initiates a rapidly fatal myeloproliferative disorder," *Proceedings of the National Academy of Sciences of the United States of America*, vol. 101, no. 2, pp. 597–602, 2004.

[114] L. Vitale-Cross, P. Amornphimoltham, G. Fisher, A. A. Molinolo, and J. S. Gutkind, "Conditional expression of K-ras in an epithelial compartment that includes the stem cells is sufficient to promote squamous cell carcinogenesis," *Cancer Research*, vol. 64, no. 24, pp. 8804–8807, 2004.

[115] S. R. Calcagno, S. Li, M. Colon et al., "Oncogenic K-ras promotes early carcinogenesis in the mouse proximal colon," *International Journal of Cancer*, vol. 122, no. 11, pp. 2462–2470, 2008.

[116] K. M. Haigis, K. R. Kendall, Y. Wang et al., "Differential effects of oncogenic K-Ras and N-Ras on proliferation, differentiation and tumor progression in the colon," *Nature Genetics*, vol. 40, no. 5, pp. 600–608, 2008.

[117] K. E. Hung, M. A. Maricevich, L. G. Richard et al., "Development of a mouse model for sporadic and metastatic colon tumors and its use in assessing drug treatment," *Proceedings of the National Academy of Sciences of the United States of America*, vol. 107, no. 4, pp. 1565–1570, 2010.

[118] D. K. Singh, B. Ahn, and V. A. Bohr, "Roles of RECQ helicases in recombination based DNA repair, genomic stability and aging," *Biogerontology*, vol. 10, no. 3, pp. 235–252, 2009.

[119] D. L. Croteau, V. Popuri, P. L. Opresko, and V. A. Bohr, "Human RecQ helicases in DNA repair, recombination, and replication," *Annual Review of Biochemistry*, vol. 83, pp. 519–552, 2014.

[120] M. A. Risinger and J. Groden, "Crosslinks and crosstalk: human cancer syndromes and DNA repair defects," *Cancer Cell*, vol. 6, no. 6, pp. 539–545, 2004.

[121] J. German, "Bloom's syndrome. XX. The first 100 cancers," *Cancer Genetics and Cytogenetics*, vol. 93, no. 1, pp. 100–106, 1997.

[122] A. Diaz, M. G. Vogiatzi, M. M. Sanz, and J. German, "Evaluation of short stature, carbohydrate metabolism and other endocrinopathies in Bloom's syndrome," *Hormone Research*, vol. 66, no. 3, pp. 111–117, 2006.

[123] N. A. Ellis, J. Groden, T.-Z. Ye et al., "The Bloom's syndrome gene product is homologous to *RecQ* helicases," *Cell*, vol. 83, no. 4, pp. 655–666, 1995.

[124] D. J. Stavropoulos, P. S. Bradshaw, X. Li et al., "The Bloom syndrome helicase BLM interacts with TRF2 in ALT cells and promotes telomeric DNA synthesis," *Human Molecular Genetics*, vol. 11, no. 25, pp. 3135–3144, 2002.

[125] S. Bhattacharyya, J. Keirsey, B. Russell et al., "Telomerase-associated protein 1, HSP90, and topoisomerase IIα associate directly with the BLM helicase in immortalized cells using ALT and modulate its helicase activity using telomeric DNA substrates," *The Journal of Biological Chemistry*, vol. 284, no. 22, pp. 14966–14977, 2009.

[126] S. Acharya, Z. Kaul, A. S. Gocha et al., "Association of BLM and BRCA1 during telomere maintenance in ALT cells," *PLoS ONE*, vol. 9, no. 8, Article ID e103819, 2014.

[127] P. M. Grierson, S. Acharya, and J. Groden, "Collaborating functions of BLM and DNA topoisomerase I in regulating human rDNA transcription," *Mutation Research/Fundamental and Molecular Mechanisms of Mutagenesis*, vol. 743-744, pp. 89–96, 2013.

[128] P. M. Grierson, K. Lillard-Wetherell, G. K. Behbehani et al., "BLM helicase facilitates RNA polymerase I-mediated ribosomal RNA transcription," *Human Molecular Genetics*, vol. 21, no. 5, Article ID ddr545, pp. 1172–1183, 2012.

[129] K. Lillard-Wetherell, A. Machwe, G. T. Langland et al., "Association and regulation of the BLM helicase by the telomere proteins TRF1 and TRF2," *Human Molecular Genetics*, vol. 13, no. 17, pp. 1919–1932, 2004.

[130] P. Mohaghegh and I. D. Hickson, "DNA helicase deficiencies associated with cancer predisposition and premature ageing disorders," *Human Molecular Genetics*, vol. 10, no. 7, pp. 741–746, 2001.

[131] A. N. Suhasini and R. M. J. Brosh, "Fanconi anemia and Bloom's syndrome crosstalk through FANCJ-BLM helicase interaction," *Trends in Genetics*, vol. 28, no. 1, pp. 7–13, 2012.

[132] W. Wang, "Emergence of a DNA-damage response network consisting of Fanconi anaemia and BRCA proteins," *Nature Reviews Genetics*, vol. 8, no. 10, pp. 735–748, 2007.

[133] Y. Wang, D. Cortez, P. Yazdi, N. Neff, S. J. Elledge, and J. Qin, "BASC, a super complex of BRCA1-associated proteins involved in the recognition and repair of aberrant DNA structures," *Genes and Development*, vol. 14, no. 8, pp. 927–939, 2000.

[134] B. Russell, S. Bhattacharyya, J. Keirsey et al., "Chromosome breakage is regulated by the interaction of the BLM helicase and topoisomerase IIα," *Cancer Research*, vol. 71, no. 2, pp. 561–571, 2011.

[135] A. R. S. Gocha, S. Acharya, and J. Groden, "WRN loss induces switching of telomerase-independent mechanisms of telomere elongation," *PLoS ONE*, vol. 9, no. 4, Article ID e93991, 2014.

[136] J. S. Andersen, C. E. Lyon, A. H. Fox et al., "Directed proteomic analysis of the human nucleolus," *Current Biology*, vol. 12, no. 1, pp. 1–11, 2002.

[137] A. K. L. Leung, J. S. Andersen, M. Mann, and A. I. Lamond, "Bioinformatic analysis of the nucleolus," *Biochemical Journal*, vol. 376, no. 3, pp. 553–569, 2003.

[138] E. Therman, P. G. Otto, and N. T. Shahidi, "Mitotic recombination and segregation of satellites in Bloom's syndrome," *Chromosoma*, vol. 82, no. 5, pp. 627–636, 1981.

[139] L. M. Starita and J. D. Parvin, "The multiple nuclear functions of BRCA1: transcription, ubiquitination and DNA repair," *Current Opinion in Cell Biology*, vol. 15, no. 3, pp. 345–350, 2003.

[140] B. A. A. Weaver and D. W. Cleveland, "The role of aneuploidy in promoting and suppressing tumors," *Journal of Cell Biology*, vol. 185, no. 6, pp. 935–937, 2009.

[141] M. A. McIlhatton, K. Murnan, D. Carson, G. P. Boivin, C. M. Croce, and J. Groden, "Genetic manipulation of homologous recombination in vivo attenuates intestinal tumorigenesis," *Cancer Prevention Research*, vol. 8, no. 7, pp. 650–656, 2015.

[142] N. Chester, F. Kuo, C. Kozak, C. D. O'Hara, and P. Leder, "Stage-specific apoptosis, developmental delay, and embryonic lethality in mice homozygous for a targeted disruption in the murine Bloom's syndrome gene," *Genes and Development*, vol. 12, no. 21, pp. 3382–3393, 1998.

[143] G. Luo, I. M. Santoro, L. D. McDaniel et al., "Cancer predisposition caused by elevated mitotic recombination Bloom mice," *Nature Genetics*, vol. 26, no. 4, pp. 424–429, 2000.

[144] L. D. McDaniel, N. Chester, M. Watson, A. D. Borowsky, P. Leder, and R. A. Schultz, "Chromosome instability and tumor predisposition inversely correlate with BLM protein levels," *DNA Repair*, vol. 2, no. 12, pp. 1387–1404, 2003.

[145] N. Chester, H. Babbe, J. Pinkas, C. Manning, and P. Leder, "Mutation of the murine Bloom's syndrome gene produces global genome destabilization," *Molecular and Cellular Biology*, vol. 26, no. 17, pp. 6713–6726, 2006.

[146] H. Babbe, N. Chester, P. Leder, and B. Reizis, "The Bloom's syndrome helicase is critical for development and function of the $\alpha\beta$ T-cell lineage," *Molecular and Cellular Biology*, vol. 27, no. 5, pp. 1947–1959, 2007.

[147] M. Goto, "Hierarchical deterioration of body systems in Werner's syndrome: implications for normal ageing," *Mechanisms of Ageing and Development*, vol. 98, no. 3, pp. 239–254, 1997.

[148] S. Huang, L. Lee, N. B. Hanson et al., "The spectrum of WRN mutations in Werner syndrome patients," *Human Mutation*, vol. 27, no. 6, pp. 558–567, 2006.

[149] J. M. Lauper, A. Krause, T. L. Vaughan, and R. J. Monnat Jr., "Spectrum and risk of neoplasia in werner syndrome: a systematic review," *PLoS ONE*, vol. 8, no. 4, Article ID e59709, 2013.

[150] J. J. Rahn, M. P. Lowery, L. Della-Coletta, G. M. Adair, and R. S. Nairn, "Depletion of Werner helicase results in mitotic hyperrecombination and pleiotropic homologous and nonhomologous recombination phenotypes," *Mechanisms of Ageing and Development*, vol. 131, no. 9, pp. 562–573, 2010.

[151] R. Agrelo, W.-H. Cheng, F. Setien et al., "Epigenetic inactivation of the premature aging Werner syndrome gene in human cancer," *Proceedings of the National Academy of Sciences of the United States of America*, vol. 103, no. 23, pp. 8822–8827, 2006.

[152] T. Kawasaki, M. Ohnishi, Y. Suemoto et al., "WRN promoter methylation possibly connects mucinous differentiation, microsatellite instability and CpG island methylator phenotype in colorectal cancer," *Modern Pathology*, vol. 21, no. 2, pp. 150–158, 2008.

[153] B. Frank, M. Hoffmeister, N. Klopp, T. Illig, J. Chang-Claude, and H. Brenner, "Colorectal cancer and polymorphisms in DNA repair genes WRN, RMI1 and BLM," *Carcinogenesis*, vol. 31, no. 3, pp. 442–445, 2010.

[154] K. Sun, A. Gong, and P. Liang, "Predictive impact of genetic polymorphisms in DNA repair genes on susceptibility and therapeutic outcomes to colorectal cancer patients," *Tumor Biology*, vol. 36, no. 3, pp. 1549–1559, 2015.

[155] M. Lebel and P. Leder, "A deletion within the murine Werner syndrome helicase induces sensitivity to inhibitors of topoisomerase and loss of cellular proliferative capacity," *Proceedings of the National Academy of Sciences of the United States of America*, vol. 95, no. 22, pp. 13097–13102, 1998.

[156] D. B. Lombard, C. Beard, B. Johnson et al., "Mutations in the WRN gene in mice accelerate mortality in a p53-null background," *Molecular and Cellular Biology*, vol. 20, no. 9, pp. 3286–3291, 2000.

[157] X. Du, J. Shen, N. Kugan et al., "Telomere shortening exposes functions for the mouse Werner and Bloom syndrome genes," *Molecular and Cellular Biology*, vol. 24, no. 19, pp. 8437–8446, 2004.

[158] Y. Hu, X. Lu, and G. Luo, "Effect of Recql5 deficiency on the intestinal tumor susceptibility of Apcmin mice," *World Journal of Gastroenterology*, vol. 16, no. 12, pp. 1482–1486, 2010.

[159] I. García-Cao, M. García-Cao, J. Martín-Caballero et al., "'Super p53' mice exhibit enhanced DNA damage response, are tumor resistant and age normally," *The EMBO Journal*, vol. 21, no. 22, pp. 6225–6235, 2002.

[160] A. Tomás-Loba, I. Flores, P. J. Fernández-Marcos et al., "Telomerase reverse transcriptase delays aging in cancer-resistant mice," *Cell*, vol. 135, no. 4, pp. 609–622, 2008.

[161] Z.-Q. Zhou, D. Manguino, K. Kewitt et al., "Spontaneous hepatocellular carcinoma is reduced in transgenic mice overexpressing human O6methylguanine-DNA methyltransferase," *Proceedings of the National Academy of Sciences of the United States of America*, vol. 98, no. 22, pp. 12566–12571, 2001.

[162] J. Jans, W. Schul, Y.-G. Sert et al., "Powerful skin cancer protection by a CPD-photolyase transgene," *Current Biology*, vol. 15, no. 2, pp. 105–115, 2005.

[163] A. R. Shoemaker, K. A. Gould, C. Luongo, A. R. Moser, and W. F. Dove, "Studies of neoplasia in the Min mouse," *Biochimica et Biophysica Acta*, vol. 1332, no. 2, pp. F25–F48, 1997.

[164] M. H. Brilliant, Y. Gondo, and E. M. Eicher, "Direct molecular identification of the mouse pink-eyed unstable mutation by genome scanning," *Science*, vol. 252, no. 5005, pp. 566–569, 1991.

[165] A. D. Brown, A. B. Claybon, and A. J. R. Bishop, "A conditional mouse model for measuring the frequency of homologous recombination events in vivo in the absence of essential genes," *Molecular and Cellular Biology*, vol. 31, no. 17, pp. 3593–3602, 2011.

[166] K. Broberg, E. Huynh, K. S. Engström et al., "Association between polymorphisms in RMI1, TOP3A, and BLM and risk of cancer, a case-control study," *BMC Cancer*, vol. 9, article 140, 2009.

[167] V. M. Shastri and K. H. Schmidt, "Cellular defects caused by hypomorphic variants of the Bloom syndrome helicase gene BLM," *Molecular Genetics & Genomic Medicine*, vol. 4, no. 1, pp. 106–119, 2016.

[168] A. B. Newman, S. Walter, K. L. Lunetta et al., "A Meta-analysis of four genome-wide association studies of survival to age 90 years or older: the cohorts for heart and aging research in genomic epidemiology consortium," *Journals of Gerontology—Series A: Biological Sciences and Medical Sciences*, vol. 65, no. 5, pp. 478–487, 2010.

[169] D. P. Lin, Y. Wang, S. J. Scherer et al., "An Msh2 point mutation uncouples DNA mismatch repair and apoptosis," *Cancer Research*, vol. 64, no. 2, pp. 517–522, 2004.

[170] E. Avdievich, C. Reiss, S. J. Scherer et al., "Distinct effects of the recurrent $Mlh1^{G67R}$ mutation on MMR functions, cancer, and meiosis," *Proceedings of the National Academy of Sciences of the United States of America*, vol. 105, no. 11, pp. 4247–4252, 2008.

[171] G. Yang, S. J. Scherer, S. S. Shell et al., "Dominant effects of an Msh6 missense mutation on DNA repair and cancer susceptibility," *Cancer Cell*, vol. 6, no. 2, pp. 139–150, 2004.

[172] H. Houlleberghs, M. Dekker, H. Lantermans et al., "Oligonucleotide-directed mutagenesis screen to identify pathogenic Lynch syndrome-associated MSH2 DNA mismatch repair gene variants," *Proceedings of the National Academy of Sciences of the United States of America*, vol. 113, no. 15, pp. 4128–4133, 2016.

[173] L. Vermeulen, E. Morrissey, M. van der Heijden et al., "Defining stem cell dynamics in models of intestinal tumor initiation," *Science*, vol. 342, no. 6161, pp. 995–998, 2013.

[174] D. E. Corpet and F. Pierre, "Point: from animal models to prevention of colon cancer. Systematic review of chemoprevention in min mice and choice of the model system," *Cancer Epidemiology Biomarkers and Prevention*, vol. 12, no. 5, pp. 391–400, 2003.

[175] D. E. Corpet and S. Taché, "Most effective colon cancer chemopreventive agents in rats: a systematic review of aberrant crypt foci and tumor data, ranked by potency," *Nutrition and Cancer*, vol. 43, no. 1, pp. 1–21, 2002.

[176] N. Arber and B. Levin, "Chemoprevention of colorectal neoplasia: the potential for personalized medicine," *Gastroenterology*, vol. 134, no. 4, pp. 1224–1237, 2008.

[177] J. Cuzick, F. Otto, J. A. Baron et al., "Aspirin and non-steroidal anti-inflammatory drugs for cancer prevention: an international consensus statement," *The Lancet Oncology*, vol. 10, no. 5, pp. 501–507, 2009.

[178] C. M. Ulrich, J. Bigler, and J. D. Potter, "Non-steroidal anti-inflammatory drugs for cancer prevention: promise, perils and pharmacogenetics," *Nature Reviews Cancer*, vol. 6, no. 2, pp. 130–140, 2006.

[179] J. Rüschoff, S. Wallinger, W. Dietmaier et al., "Aspirin suppresses the mutator phenotype associated with hereditary nonpolyposis colorectal cancer by genetic selection," *Proceedings of the National Academy of Sciences of the United States of America*, vol. 95, no. 19, pp. 11301–11306, 1998.

[180] M. A. McIlhatton, J. Tyler, S. Burkholder et al., "Nitric oxide-donating aspirin derivatives suppress microsatellite instability in mismatch repair-deficient and hereditary nonpolyposis colorectal cancer cells," *Cancer Research*, vol. 67, no. 22, pp. 10966–10975, 2007.

[181] M. A. Mcilhatton, J. Tyler, L. A. Kerepesi et al., "Aspirin and low-dose nitric oxide-donating aspirin increase life span in a Lynch syndrome mouse model," *Cancer Prevention Research*, vol. 4, no. 5, pp. 684–693, 2011.

[182] J. Burn, D. T. Bishop, J.-P. Mecklin et al., "Effect of aspirin or resistant starch on colorectal neoplasia in the Lynch syndrome," *The New England Journal of Medicine*, vol. 359, no. 24, pp. 2567–2578, 2008.

[183] A. T. Chan, S. Ogino, and C. S. Fuchs, "Aspirin use and survival after diagnosis of colorectal cancer," *The Journal of the American Medical Association*, vol. 302, no. 6, pp. 649–658, 2009.

[184] M. D. Holmes, W. Y. Chen, L. Li, E. Hertzmark, D. Spiegelman, and S. E. Hankinson, "Aspirin intake and survival after breast cancer," *Journal of Clinical Oncology*, vol. 28, no. 9, pp. 1467–1472, 2010.

[185] N. J. Jacobo-Herrera, C. Pérez-Plasencia, E. Camacho-Zavala et al., "Clinical evidence of the relationship between aspirin and breast cancer risk (review)," *Oncology Reports*, vol. 32, no. 2, pp. 451–461, 2014.

[186] J. Burn, A.-M. Gerdes, F. Macrae et al., "Long-term effect of aspirin on cancer risk in carriers of hereditary colorectal cancer: an analysis from the CAPP2 randomised controlled trial," *The Lancet*, vol. 378, no. 9809, pp. 2081–2087, 2011.

[187] U.S. Preventive Services Task Force, "Routine aspirin or non-steroidal anti-inflammatory drugs for the primary prevention of colorectal cancer: U. S. preventive services task force recommendation statement," *Annals of Internal Medicine*, vol. 146, no. 5, pp. 361–364, 2007.

[188] U.S. Preventive Services Task Force, *Draft Recommendation Statement: Aspirin to Prevent Cardiovascular Disease and Cancer*, U.S. Preventive Services Task Force, 2015, http://www.uspreventiveservicestaskforce.org/Page/Document/draft-recommendation-statement/aspirin-to-prevent-cardiovascular-disease-and-cancer.

[189] H. Seow, W. K. Yip, and T. Fifis, "Advances in targeted and immunobased therapies for colorectal cancer in the genomic era," *OncoTargets and Therapy*, vol. 9, pp. 1899–1920, 2016.

Hindawi Publishing Corporation
BioMed Research International
Volume 2016, Article ID 9704607, 14 pages
http://dx.doi.org/10.1155/2016/9704607

Research Article

Animal Model of Gestational Diabetes Mellitus with Pathophysiological Resemblance to the Human Condition Induced by Multiple Factors (Nutritional, Pharmacological, and Stress) in Rats

Siti Hajar Abdul Aziz,[1] Cini Mathew John,[1,2] Nur Intan Saidaah Mohamed Yusof,[1] Massita Nordin,[3] Rajesh Ramasamy,[4] Aishah Adam,[1] and Fazlin Mohd Fauzi[1]

[1]*Department of Pharmacology and Chemistry, Faculty of Pharmacy, Universiti Teknologi MARA, 42300 Bandar Puncak Alam, Selangor Darul Ehsan, Malaysia*
[2]*Department of Physiology and Pharmacology, Faculty of Medicine, University of Calgary, 3330 Hospital Drive NW, Calgary, AB, Canada T2N 4N1*
[3]*Department of Pharmaceutical and Life Sciences, Faculty of Pharmacy, Universiti Teknologi MARA, 42300 Bandar Puncak Alam, Selangor Darul Ehsan, Malaysia*
[4]*Immunology Unit, Department of Pathology, Faculty of Medicine and Health Sciences, Universiti Putra Malaysia (UPM), 43400 Serdang, Selangor Darul Ehsan, Malaysia*

Correspondence should be addressed to Fazlin Mohd Fauzi; fazlin5465@puncakalam.uitm.edu.my

Received 16 March 2016; Accepted 8 May 2016

Academic Editor: Monica Fedele

This study attempts to develop an experimental gestational diabetes mellitus (GDM) animal model in female Sprague-Dawley rats. Rats were fed with high fat sucrose diet, impregnated, and induced with Streptozotocin and Nicotinamide on gestational day 0 (D0). Sleeping patterns of the rats were also manipulated to induce stress, a lifestyle factor that contributes to GDM. Rats were tested for glycemic parameters (glucose, C-peptide, and insulin), lipid profiles (total cholesterol, triglycerides, HDL, and LDL), genes affecting insulin signaling (IRS-2, AKT-1, and PCK-1), glucose transporters (GLUT-2 and GLUT-4), proinflammatory cytokines (IL-6, TNF-α), and antioxidants (SOD, CAT, and GPX) on D6 and D21. GDM rats showed possible insulin resistance as evidenced by high expression of proinflammatory cytokines, PCK-1 and CRP. Furthermore, low levels of IRS-2 and AKT-1 genes and downregulation of GLUT-4 from the initial to final phases indicate possible defect of insulin signaling. GDM rats also showed an impairment of antioxidant status and a hyperlipidemic state. Additionally, GDM rats exhibited significantly higher body weight and blood glucose and lower plasma insulin level and C-peptide than control. Based on the findings outlined, the current GDM animal model closely replicates the disease state in human and can serve as a reference for future investigations.

1. Introduction

Gestational diabetes mellitus (GDM), a common pregnancy complication, is defined by the American Diabetes Association as diabetes that is not clearly apparent diabetes, diagnosed in the second or third trimester of pregnancy [1]. During pregnancy, mothers undergo several metabolic changes to meet the energy demands of the fetus [2]. Resistance to insulin escalates to increase the glucose supply to the fetus. Pancreatic beta cells then compensate for the increased demand in glucose, and a normoglycemic state is maintained. However, women who develop GDM have deficits in beta cells response leading to insufficient insulin secretion, consequently leading to a state of hyperglycemia [2, 3]. This insulin resistance seen in GDM is similar to that observed in Type 2 diabetes mellitus (T2DM). When beta cells are no longer able to compensate for the insulin resistance, this then leads to glucose intolerance. A large

percentage (over 25%) of women developed an abnormal glucose tolerance in pregnancy, but their glucose tolerance is most likely to return to normal postpartum [4, 5]. Decrease of insulin receptors on cell surfaces has also been associated with insulin resistance. The number of insulin receptors on monocytes has been found to be decreased in GDM [6]. Insulin receptor binding to monocytes increases in pregnancy and in midpregnancy but is significantly decreased in late pregnancy [6]. The insulin concentration necessary to reduce insulin binding by 50% (ID50) is lower in GDM diagnosed in late pregnancy [7]. Women diagnosed with diabetes during gestation have an increased incidence of complications during pregnancy as well as an increased risk of developing Type 2 diabetes mellitus (T2DM) later in life [8]. Additionally, offspring born to GDM mothers have an increased incidence of perinatal complications and an increased risk of obesity and T2DM later in life [9].

Observations of tissues and organs from pregnant women with and without GDM would expand our understanding of the disease. Yet, the scarcity of the samples and the lack of modalities make understanding the molecular mechanism and finding possible therapeutics for GDM difficult. For these reasons, animal models deliver an attractive alternative in studying the molecular mechanisms and treatment options for GDM. Initially, GDM animal models were induced solely by injecting diabetogenic agents such as Streptozotocin (STZ) and alloxan in low and high dosages [10–12]. However, it has been reported that those substances cause a complete or partial ablation of pancreatic beta cells and insulin deficiency instead of the consequences of insulin resistance [13]. In addition, the appropriateness of this model for GDM has been questioned as mean glucose exceeded 350 mg/dL, and diabetes of such severity rarely occurs in humans [14]. Meanwhile, complete or partial ablation of pancreatic beta cells results in a low rate of fetal malformations, which is not desirable [15]. In T2DM animal model, Nicotinamide (NA) is injected just before STZ to protect the pancreas from damage [16]. The combination of STZ + NA was then adopted in GDM animal model [17]. Diet also plays an important role in developing GDM animal models as fat intake affects glucose intolerance and elicits insulin resistance [14, 18]. Rats fed with high fat diet develop obesity and hyperinsulinemia but do not cause frank or effective diabetes [19]. However, diet high in fat and sucrose induced rapid obesity-related metabolic syndrome [20–23]. Abdel-Reheim et al. [24] proposed the combination of minimal dose of STZ with high fat sucrose diet (HFSD) in developing GDM animal model and proved that this combination was successful. Srinivisan et al. [25] highlighted the combination of low dose STZ-treated rats and high fat diet in inducing insulin resistance. In our previous study [26], we used the combination of STZ, NA, and high fat sucrose diet in our GDM animal model and evaluated the effect on Tregs, proliferation of splenocytes, production of reactive oxygen species (ROS) by neutrophils, and serum glucose levels [27].

In addition to the combination of STZ, NA, and HFSD in our previous GDM animal model, we now include stress in the current model. GDM pregnancies are linked with a heightened level of oxidative stress, where sleeplessness or disturbance in sleep increases stressand consequently impairs antioxidant defense system [28]. Mothers' oxidative balance imposes a great impact on fetus development, in addition to the mother's health.

Hence, the current study investigates whether the combination of nutritional manipulation, pharmacological treatment, and stress induction can create appropriate immunometabolic changes in pregnant rat, which can be developed as a model for understanding the consequences of GDM as well as providing insights into potential treatments and preventative measures. To the authors' knowledge, GDM animal model induced with the previously mentioned factors has not been published in the scientific literature and hence recorded as a pilot study. Changes on glycemic and lipid parameters along with proinflammatory cytokines level and oxidative stress in the rats were observed in this study to evaluate the appropriateness of our animal model.

2. Materials and Methods

2.1. Experimental Animals. Female Sprague-Dawley rats aged 8-9 weeks were procured from the Laboratory Animal Facility and Management (LAFAM), UiTM Puncak Alam Campus, Malaysia. A total of 45 female rats were randomly taken for the study, where 10 rats were assigned as control and the rest were assigned as GDM group. Animals were maintained in an experimental room under the following conditions: (a) temperature of $22 \pm 2^{\circ}$C, (b) humidity of $50 \pm 10\%$, and (c) illumination of a 12-hour light/dark cycle for control and 18-hour light/4-hour dark cycle for GDM group. Changes in sleeping cycle and environmental status have been shown to induce abnormally high levels of oxidant stress [29]. All experimental procedures presented in this study were approved by the Research Ethics Committee (Ethics Number: 133/2015) of Universiti Teknologi MARA (UiTM).

2.2. Dietary Intake. Standard diet (Gold Coin, Malaysia) was given to control rats. Meanwhile, GDM group rats were fed with HFSD (SP-11032, Australia) from Week 10 onwards. HFSD consist of 25% sucrose, 40% beef tallow, and 20% of casein protein.

2.3. Smearing and Breeding of Animals. After one week of acclimatization, animals were examined for estrous cycles for 2 consecutive weeks. Rats follow a 4-day pattern of estrous cycle, namely, estrous (E), metaestrous (M), diestrous (D), and proestrous (P). Rats in estrous stage (Figure 1(b)) were allowed to mate overnight with resident males from the same strain at a source ratio of 2 males per 1 female. Pregnancy was confirmed through vaginal smear as shown in Figure 2, whereby copulation was confirmed by detection of sperm. All tests were initiated when pregnancy was confirmed, denoted as D0.

2.4. Pipette Smear Technique. In this technique, vaginal secretion from each rat was collected using a plastic pipette containing ~1-2 mL of normal saline (NaCl 0.9%) every morning. Vaginal secretion was collected by inserting the pipette tip

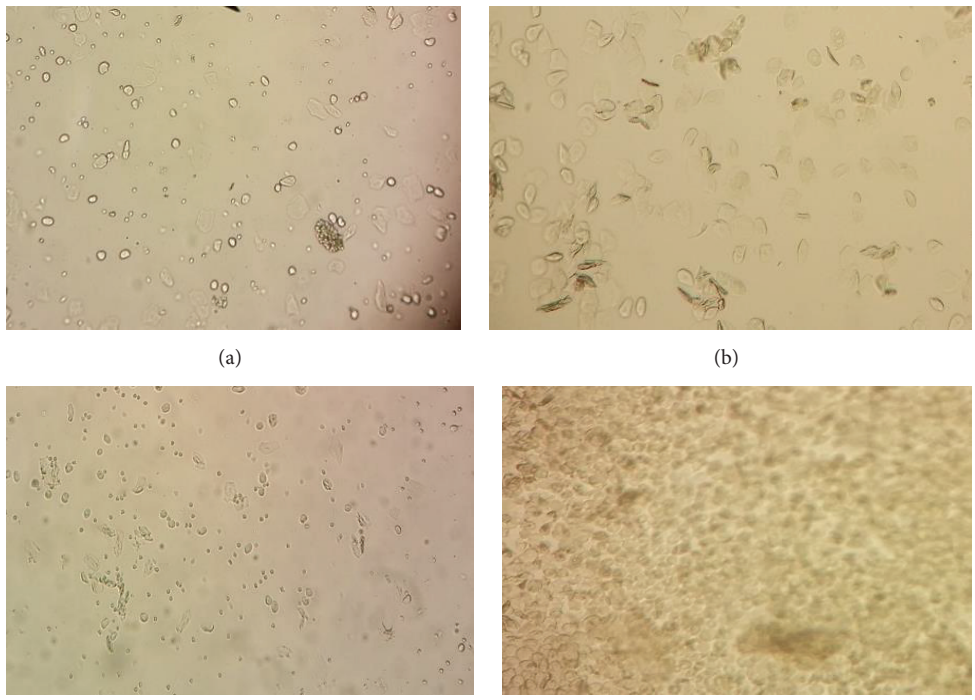

Figure 1: Photomicrograph of the vaginal smears of rat showing estrous cycle stages. (a) Proestrous stage (round nucleated epithelial cells); (b) estrous stage (cornified or irregular shape of epithelial cells); (c) metaestrous stage (low number of round cells); and (d) diestrous stage with mostly small and round cells.

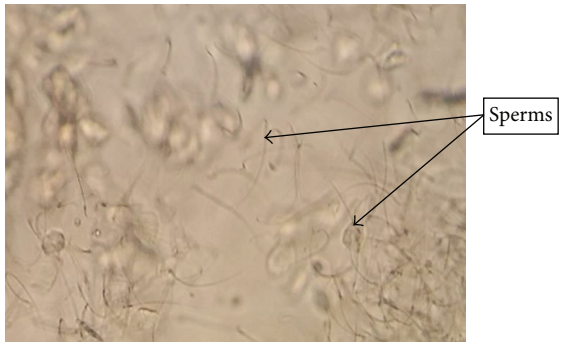

Figure 2: Photomicrograph of the vaginal smears of rat showing the existence of sperms. Sperms were visible and observed during vaginal smears after successful mating.

into the rat's vagina and flushing the cells from the vaginal lining. One or two drops of vaginal secretion were placed onto a clean glass slide. Separate glass slides were used for each cage of animals. Unstained vaginal secretions were directly viewed under a light microscope at 40x magnification. Three types of cells were observed, which were round and nucleated epithelial cells, nonnucleated irregular cornified cells, and small round cells (Figure 1). These characteristics of cells were used for the determination of estrous cycle phases [30]. Rats that do not follow a 4-day pattern of estrous cycle were excluded from the study.

2.5. Induction of Experimental GDM. Streptozotocin (STZ) (Sigma Aldrich, USA) was induced on D0 by a single intraperitoneal (ip) injection at a dose of 35 mg/kg bw in 0.1 mol/L citrate buffer (pH 4.5). Nicotinamide (NA) (Sigma Aldrich, USA) 120 mg/kg bw was induced ip 15 minutes prior to STZ. Control rats received an equal volume of citrate buffer only. The rats were returned to their respective cages and blood glucose levels were analysed 72 hours after STZ administration. Rats with stable hyperglycemia were selected for further study where on D6 half of the animals were euthanized after initial results were collected and the rest were sacrificed after the final results were collected.

2.6. Blood Samples. Blood samples were collected through cardiac puncture for biochemical and hematological analysis on D6 and D21. Serum was collected into plain tubes while plasma was collected into heparin tubes. Collected blood in plain tube was left to clot for half an hour. Subsequently, heparin tubes were kept cold in an ice box to prevent clotting. Both tubes were centrifuged at 2500 rpm for 12 min at −4°C. Serum and plasma were collected in microcentrifuge tubes and kept at −80°C for further analysis.

2.7. Food Intake and Body Weight Changes. Food intake was calculated daily by calculating the difference between the amount of food given and the amount of residual food at the end of each day.

2.8. Laparohysterectomy. Six animals were sacrificed on D6 to acquire the initial results, and the rest was sacrificed on D21. Rats were anesthetized with diethyl ether and thoracic, abdominal, and pelvic regions were dissected. Abnormalities in the internal organs were examined. Uterus and ovaries were excised and exposed. The number of corpora lutea on each ovary was identified and total gravid weight was noted prior to opening the uterus. To find out the implantation loss, uterus was kept in ammonium sulphide (10%) solution for 5 minutes [31]. The weight, number, sex, and location of fetus and implantation sites along with placenta were recorded.

2.9. Measurement of Glucose Level. Tail incision method was used to measure weekly fasting glucose level using hemoglucometer (Lifescan, Johnson and Johnson, USA) and glycemic levels were monitored throughout the experiment. Serum glucose was measured upon sacrifice using commercially available reagent kits (ILab Chemistry Analyzer 300 PLUS; Instrumentation Laboratory, USA).

2.10. Measurement of Insulin Level. Insulin level was assayed using Mercodia Rat Insulin ELISA kit (Sweden). The optical densities of the samples were read at 450 nm. The concentration of insulin level was obtained by computerized data reduction of the absorbance for the calibrators, except for calibrator 0, versus the concentration using cubic spline regression.

2.11. Measurement of C-Peptide. Plasma C-peptide level was assayed by Mercodia Rat C-peptide ELISA kit (Sweden). The optical densities of the samples were read at 450 nm. The concentration of C-peptide was obtained by using cubic spline regression the same way as the Insulin ELISA kit mentioned above.

2.12. Measurement of C-Reactive Protein. Blood plasma was used for the determination of C-reactive protein, using full range CRP (frCRP) commercial kit purchased from Randox (All Eight (M) Sdn. Bhd). Liquid assayed specific protein control levels 1 and 2 were used as control. After preparation of blood samples, 500 μL plasma was transferred to each Selectra tube, and the results were obtained using a Vita lab Selectra machine.

2.13. Biochemical Measurements. Serum levels of triglycerides, total cholesterol, LDL-cholesterol, and HDL-cholesterol were measured using ILab Chemistry Analyzer 300 PLUS (Instrumentation Laboratory, USA).

2.14. Measurement of Gene Expression. Organs for gene expression studies were harvested upon sacrifice and were immediately stored in liquid nitrogen for further investigations. Total RNA of tissues of glucose related genes (GLUT-2, GLUT-4, AKT-1, IRS-2, and PCK-1) and antioxidant genes (SOD, CAT, and GPX) was isolated from the liver while tissues of inflammatory genes (IL-6 and TNF-α) were isolated from spleens RNase Mini Kit (Qiagen, USA) according to the manufacturer's instructions. Purity of the extracted RNA was determined by measuring the ratio of the optical density at 260 and 280 nm using a spectrophotometer (BioRad, USA), which ranged between 1.8 and 2.0. mRNA expressions of the genes were determined by qPCR as described in our previous study, John et al. [26]. Primers specific for respective genes and beta-actin genes (housekeeping gene) were designed from the gene sequence of rat (*Rattus norvegicus*) adapted from NCBI (National Center for Biotechnology Information) GenBank Database [32]. The oligonucleotide sequences of primers used for qPCR, QuantiTect Primer Assay, were purchased from Qiagen USA. Accession numbers of each gene are IRS-1 (NM_012969), Akt-1 (NM_033230), Slc2a2_1 (NM_012879), Rn_Slc2a4_1 (NM_012751), TNF-α-_1 (NM_012675), IL-6 (NM_012589), GPX (NC_005107.4), SOD (NM_017050.1), CAT (NM_012520.1), and ACTB (NM_031144.2) as housekeeping gene. The expression for each sample was measured according to the quantity of β-actin expressed, while the number of fold expressions was calculated using $2^{-\Delta\Delta Ct}$.

2.15. Histology Study. Histology of the pancreas was done to observe the morphological changes. Pancreas tissues were extracted from the rats upon sacrifice on D21 from each group. Pancreas harvested was stored in 10% formalin solution before proceeding with histology study. Haematoxylin and Eosin staining procedure was employed in this experiment.

2.16. Statistical Analysis. GraphPad Prism software was used for statistical analysis using t-test, which compares the different parameters between control and GDM group. Value $P < 0.05$ was considered significant. Data collected for glycemic and lipid parameters were subjected to Hierarchical Clustering and Principal Component Analysis [33] to visualize the variation between control and GDM group. However, parameters which involve gene expressions could not be performed using hierarchical clustering and PCA as control is set and normalized to 1. Hence, this could give a misleading result. Both hierarchical clustering and PCA were performed in R.

3. Results

3.1. Glycemic Parameters (Glucose, Insulin, and C-Peptide) and Body Weight. Weekly fasting serum glucose levels are shown in Figure 3. Glucose level in GDM groups was significantly higher ($P < 0.05$) than control, confirming the hyperglycemic state at both initial (D6) and final (D22) phases of pregnancy. Additionally, insulin and C-peptide levels of GDM group showed a significant increase from the initial phase to the final phase of pregnancy, indicating increase of insulin production in the final phase of pregnancy. A slight decrease in body weight was observed from Week 1 to Week 2 and from Week 2 to Week 3 of GDM group as shown in Figure 3. Rats in control group experienced a slow increase of body weight. From both hierarchical clustering and PCA (see Figure 4), it can be seen that there is a clear separation between control and GDM for all glycemic parameters. There

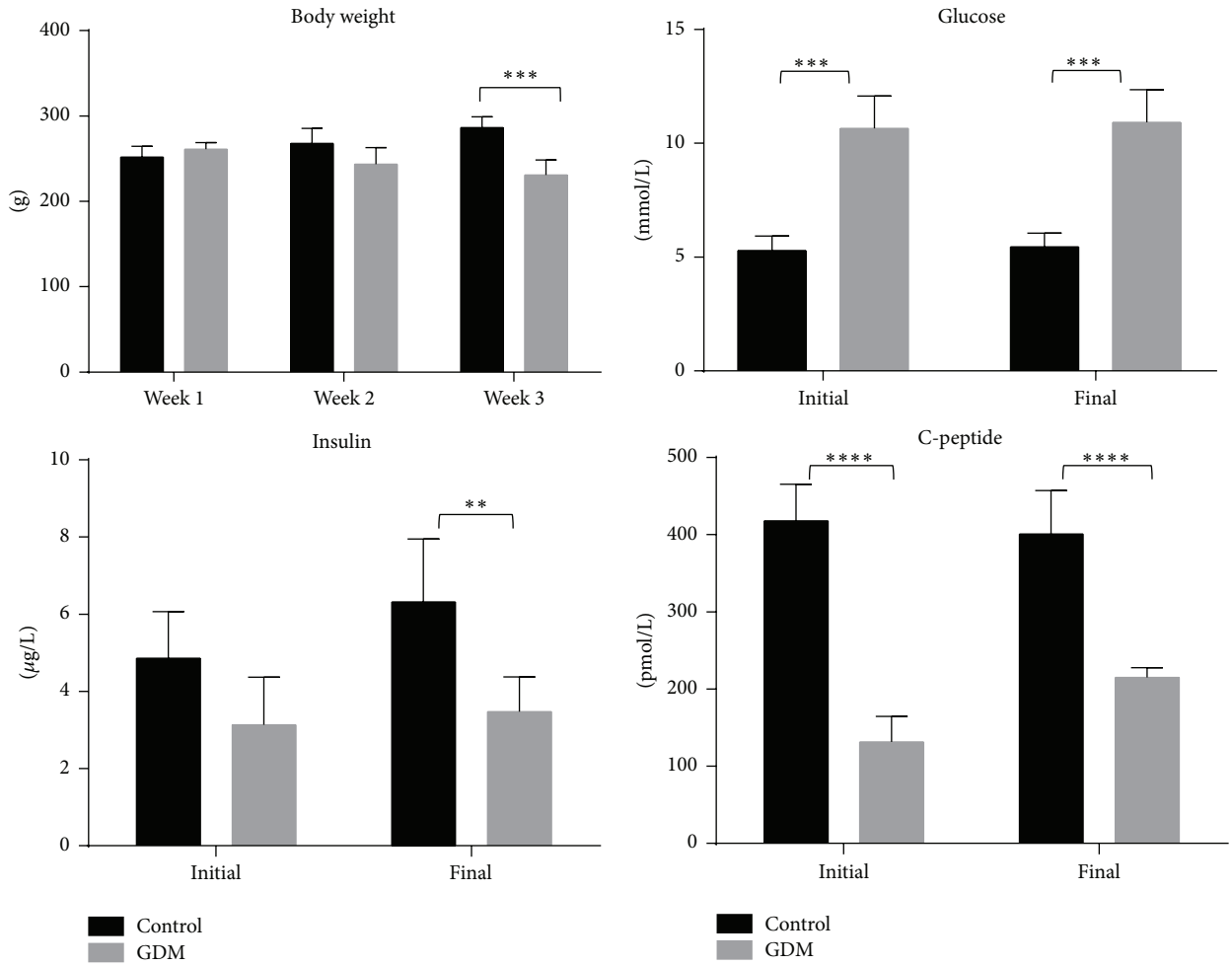

Figure 3: Body weight, glucose level, insulin level, and C-peptide of both control and GDM group. Body weight of GDM-induced rat was decreased from Week 1 to Week 3 compared to control rat, where the body weight was increased significantly. Glucose level was higher in GDM group compared to control. Levels of insulin and C-peptide were higher in control compared to GDM group. Data shown as mean ± SD of four rats. For each parameter, a value with the asterisk signifies $P < 0.05$ and the absence of asterisk indicates otherwise. P value less than 0.01 was designated with two (∗∗) asterisks, P value less than 0.001 was designated with three (∗ ∗ ∗) asterisks, and P value less than 0.0001 was designated with four (∗ ∗ ∗∗) asterisks.

were no notable changes in food intakes for both control and GDM groups (data not shown).

3.2. The Lipid Parameters. The data in Figure 5 shows the changes of lipid profile of both control and GDM groups at the initial and final phases of pregnancy. It can be seen from Figure 4 that there was an increase in total cholesterol, triglyceride, and LDL-cholesterol ($P < 0.001$) from the initial to the final phases of pregnancy in the GDM group compared to the control group. Additionally, HDL-cholesterol was significantly decreased in the GDM group compared to the control group. From both hierarchical clustering and PCA (see Figure 4), it can be seen that there is a clear separation between control and GDM for all lipid parameters, with the exception of HDL.

3.3. Plasma CRP and Proinflammatory Genes. Figure 5 shows the level of plasma CRP and both inflammatory genes (IL-6 and TNF-α) at the initial and final phases of pregnancy in GDM and control groups. The level of plasma CRP is higher in GDM group compared to control group at both phases of pregnancy which stimulates the acute phase inflammatory response (see Figure 6(a)). As shown in Figures 6(b) and 6(c), both IL-6 and TNF-α levels increase ($P < 0.001$) from the initial and final phases of pregnancy in GDM group, but no significant changes were observed in the control group. In addition, in both phases, the level of IL-6 and TNF-α in GDM groups was higher than control.

3.4. Expression of Genes Related to Glucose Metabolism. Genes involved in glucose transporter (GLUT-2 and GLUT-4) and insulin signaling pathway (IRS-2, PCK-1, and AKT-1) at the initial and final phases of pregnancy in the control and GDM group are shown in Figures 7(a)–7(e). GLUT-2, GLUT-4, AKT-1, and IRS-2 levels were lower in the GDM group than control.

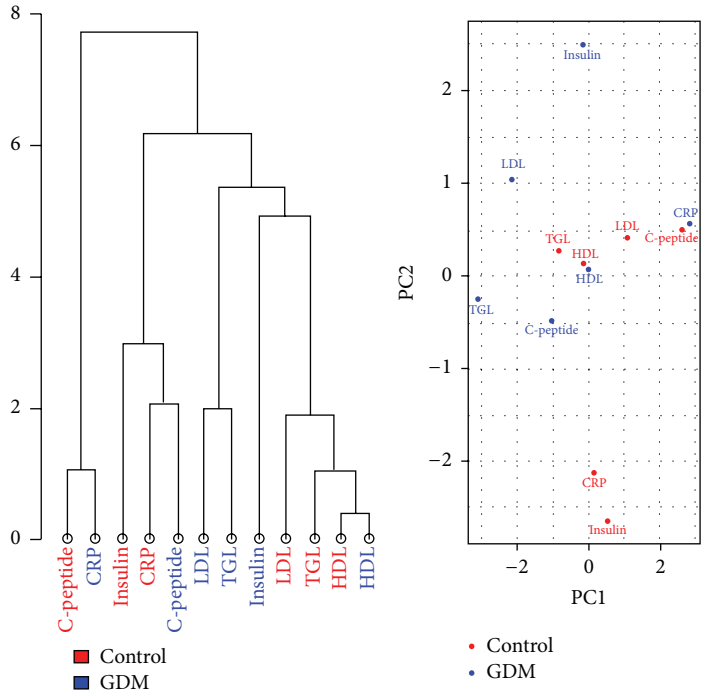

FIGURE 4: Hierarchical Clustering and Principal Component Analysis for both glycemic and lipid parameters. Both graphs showa clear separation between the glycemic and lipid parameters in both GDM group and control. However, there is an exception to this in the case of HDL.

3.5. Expression of Antioxidant Genes. The expressions of antioxidant genes for SOD, CAT, and GPX were shown in Figure 8. All the genes were lower ($P < 0.001$) in the GDM group compared to control, in both initial and final phases.

3.6. Histology of Pancreas. Histology section of pancreas was shown in Figure 9. Pancreas of control group shows an unaffected structure of endocrine gland while pancreas of GDM group shows deteriorated endocrine glands, which confirmed the protective effect of NA on the damage to beta cells within the Islet of Langerhans caused by STZ.

3.7. The Maternal Reproductive Status. Table 1 shows the maternal reproductive status of both control and GDM groups. The average number of live fetuses, number of dead fetuses, gravid weight, empty weight, number of implantations, and sex ratio were significantly lower in the GDM group compared to control. The lower average number of live fetuses in the GDM group confirmed the restriction in the intrauterine growth. GDM groups showed a higher number of postimplantation loss sites, preimplantation loss, placental weight, fetal weight, fetal length, and number of corpora lutea than control. The fetal weight of the GDM group was higher than control, which confirms the macrosomia (large for gestational age) status of the fetuses.

TABLE 1: Data shown below is the reproductive performances of control group and GDM group. Data shown as mean ± SD of four rats. For each parameter, a value with the asterisk signifies $P < 0.05$ and the absence of asterisk indicates otherwise. P value less than 0.05 was designated with one (∗) asterisk, P value less than 0.01 was designated with two (∗∗) asterisks, P value less than 0.001 was designated with three (∗ ∗ ∗) asterisks, P value less than 0.0001 was designated with four (∗ ∗ ∗ ∗) asterisks, and P value less than 0.00001 was designated with five (∗ ∗ ∗ ∗ ∗) asterisks.

Group	Control	GDM
Live fetus	8.57 ± 0.23	5.23 ± 0.12****
Number of dead fetuses	0.32 ± 0.18	0.22 ± 0.13
Gravid wt.	67.23 ± 1.30	65 ± 1.73
Empty uterus weight	6.23 ± 0.12	4.32 ± 0.02*****
Placental wt.	4.02 ± 0.13	4.82 ± 0.04****
Fetal wt.	3.08 ± 0.11	3.42 ± 0.11**
Fetal length	2.89 ± 0.11	4.85 ± 0.11****
Number of corpora lutea	11 ± 0.32	11.23 ± 0.21
Number of implantations	10 ± 0.23	6.56 ± 0.8***
Pre IMP loss%	4.20 ± 1.32	7.51 ± 0.8**
Post IMP loss%	1.22 ± 0.83	3.16 ± 1.12*
Sex ratio (M/F)	1 ± 0.05	0.7 ± 0.02****

4. Discussion

Current animal model combines multiple factors that cause insulin resistance in gestation. This study provides data associated with glycemic parameters, lipid parameters, glucose transporters parameters, genes affecting insulin signaling, proinflammatory cytokines parameters, and oxidative parameters on the initial and final phases of pregnancy in both control and GDM groups. In our study, body weight of

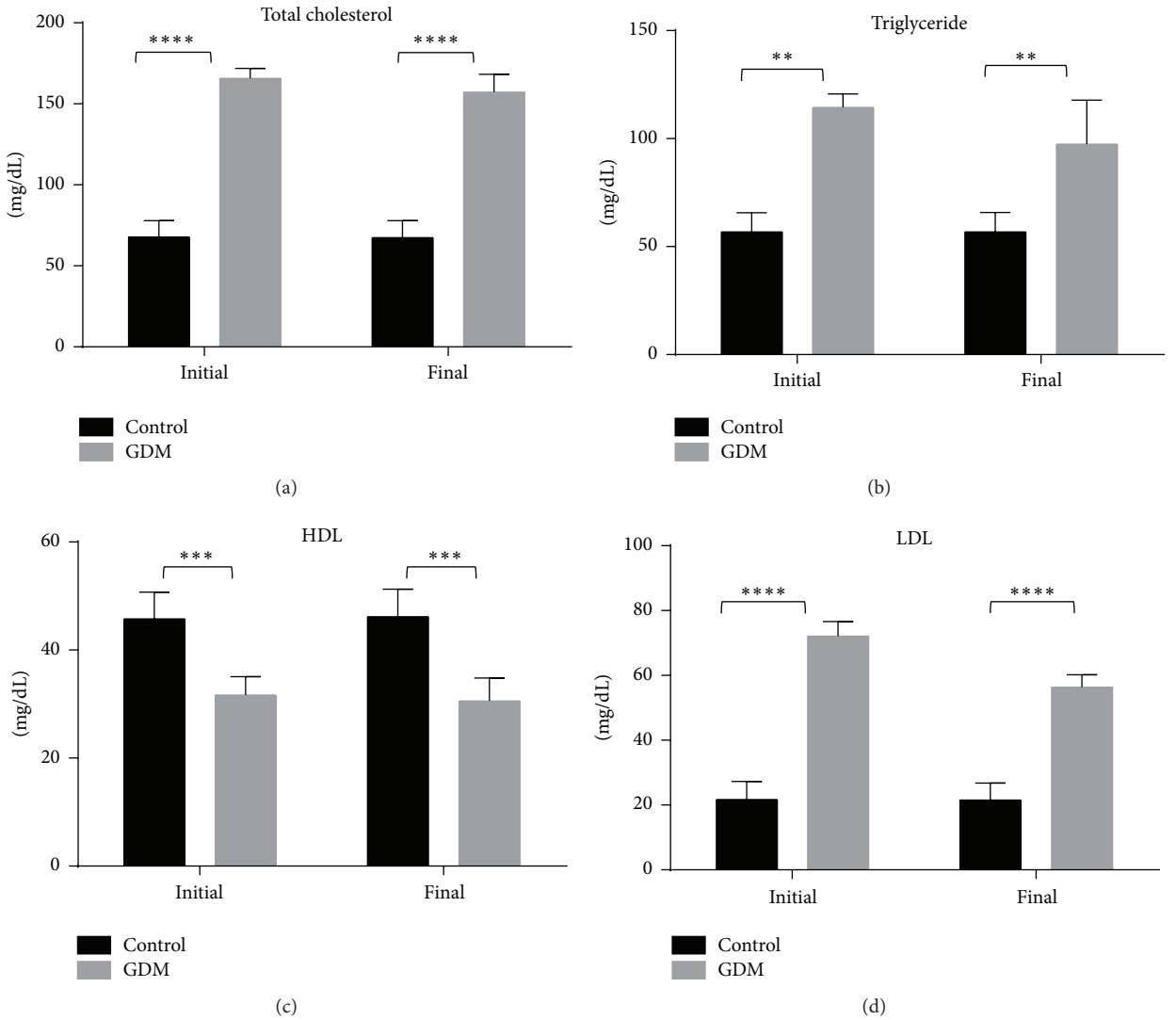

Figure 5: Lipid profile of both control and GDM group. Levels of total cholesterol, triglyceride, and LDL were higher in GDM group compared to control while level of HDL was higher in control compared to GDM group. Data shown as mean ± SD of four rats. For each parameter, a value with the asterisk signifies $P < 0.05$ and the absence of asterisk indicates otherwise. P value less than 0.01 was designated with two (∗∗) asterisks, P value less than 0.001 was designated with three (∗ ∗ ∗) asterisks, and P value less than 0.0001 was designated with four (∗ ∗ ∗∗) asterisks.

rats on first week in the GDM group was higher compared to the control group, which can be attributed to consumption of high fat sucrose diet [34]. A decrease in body weight of rats was observed on the following weeks in the GDM group (Figure 3), despite no notable changes in food intake. It should be noted that a decrease in body weight is not usually seen in human GDM. This decrease in body weight of GDM rats may be due to insulin resistance induced by STZ, due to the partial damage inflicted on the pancreatic beta cells [35]. This then promotes the catabolism of fats and proteins, resulting in weight loss [36]. This decreasing trend of the weight of GDM rats was also seen in the study by Abdel-Reheim et al., [24] where the same dose of STZ (35 mg/kg) was also used in this study. It was noted by Abdel-Reheim et al. [24] that this trend was not seen when a dose of 20 mg/kg STZ was used. Meanwhile, average glucose level was higher in GDM group compared to control group, confirming the glycemic state of rats. Insulin level was lower in GDM group compared to the control group, which is also supported by the low level of C-peptide (measuring insulin production). These results suggest that rats with GDM experienced a higher rate of insulin resistance compared to the control rats, which leads to decrease in insulin secretion. If beta cells are not able to compensate for the increase in insulin resistance, this can lead to GDM [37]. It can be noted that insulin and C-peptide levels were significantly lower than usual (>300 pmol/L) [37]. One possible reason for this is the additional stress factor induced in this animal model. Stress has been linked to

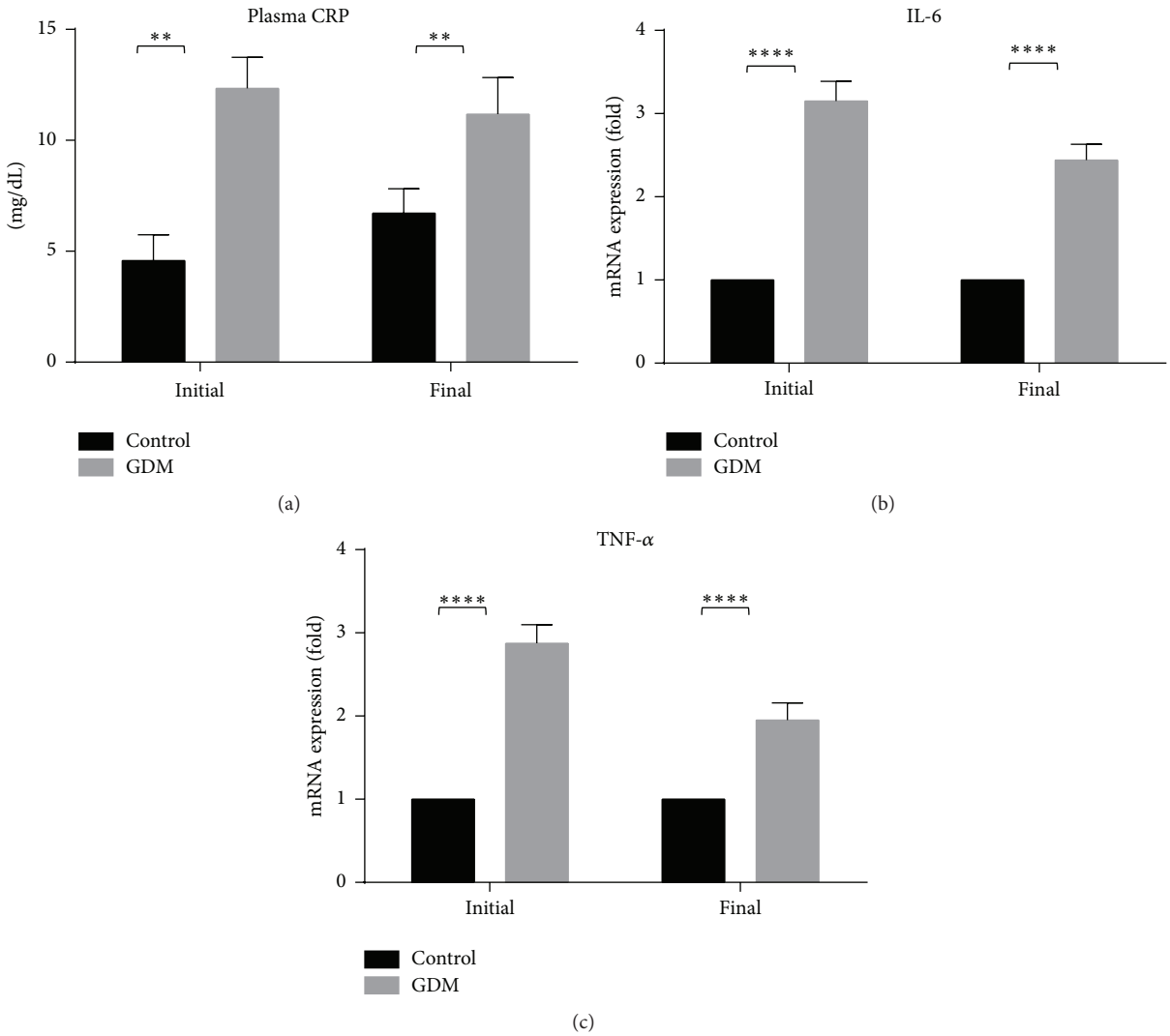

Figure 6: Plasma CRP and expression of inflammatory genes of control and GDM rats. Level of plasma CRP at initial and final stages was high in GDM group compared to control group. mRNA expressions of IL-6 and TNF-α are shown. mRNA levels of inflammatory genes show that both IL-6 and TNF-α were higher in GDM group compared to control. Data shown as mean ± SD of four rats. For each parameter, a value with the asterisk signifies $P < 0.05$ and the absence of asterisk indicates otherwise. P value less than 0.01 was designated with two (∗∗) asterisks, and P value less than 0.0001 was designated with four (∗ ∗ ∗∗) asterisks.

low insulin level due to the production of free radicals. Further explanation of this can be found in the discussion of antioxidant levels of GDM rats later.

A state of hyperlipidemia is commonly observed in GDM [38]. This was also observed in the GDM groups where level of total cholesterol, triglyceride, and LDL were increased from the initial to the final phases whereas level of HDL was decreased (Figure 4). Increase in triglycerides level may be due to the absorption of fat from small intestine due to HFSD intake, where fatty food leads to increase in visceral fat deposition in the early stage of pregnancy. These events can lead to GDM [39]. In addition, HFSD feeding increases plasma free fatty acid (FFA) concentrations and causes insulin resistance by inhibiting insulin-stimulated glucose uptake, glycogen synthesis, and/or phosphorylation activity [40]. In line with this, a downregulation of GLUT-4 was also observed in this study, indicating low glucose translocation and hence low glucose uptake in the skeletal muscles.

In the evaluation of proinflammatory cytokines, our results show that TNF-α level and IL-6 levels are higher in the GDM group compared to control (see Figure 5). Obesity and T2DM, which are associated with insulin resistance, have been shown to have fat cell dysfunction that results in the production of an excessive amount of proinflammatory adipokines such as IL-6 and TNF-α [41]. This excessive production of IL-6 and TNF-α may also be a result of oxidative stress and inflammatory changes caused by hyperglycemia [42, 43]. TNF-α is believed to induce insulin resistance by a number of mechanisms such as increase in serine phosphorylation of IRS-1, which disrupts the insulin signaling cascade [44]. In addition, several studies have shown that there is an inverse correlation between IL-6 concentration and insulin

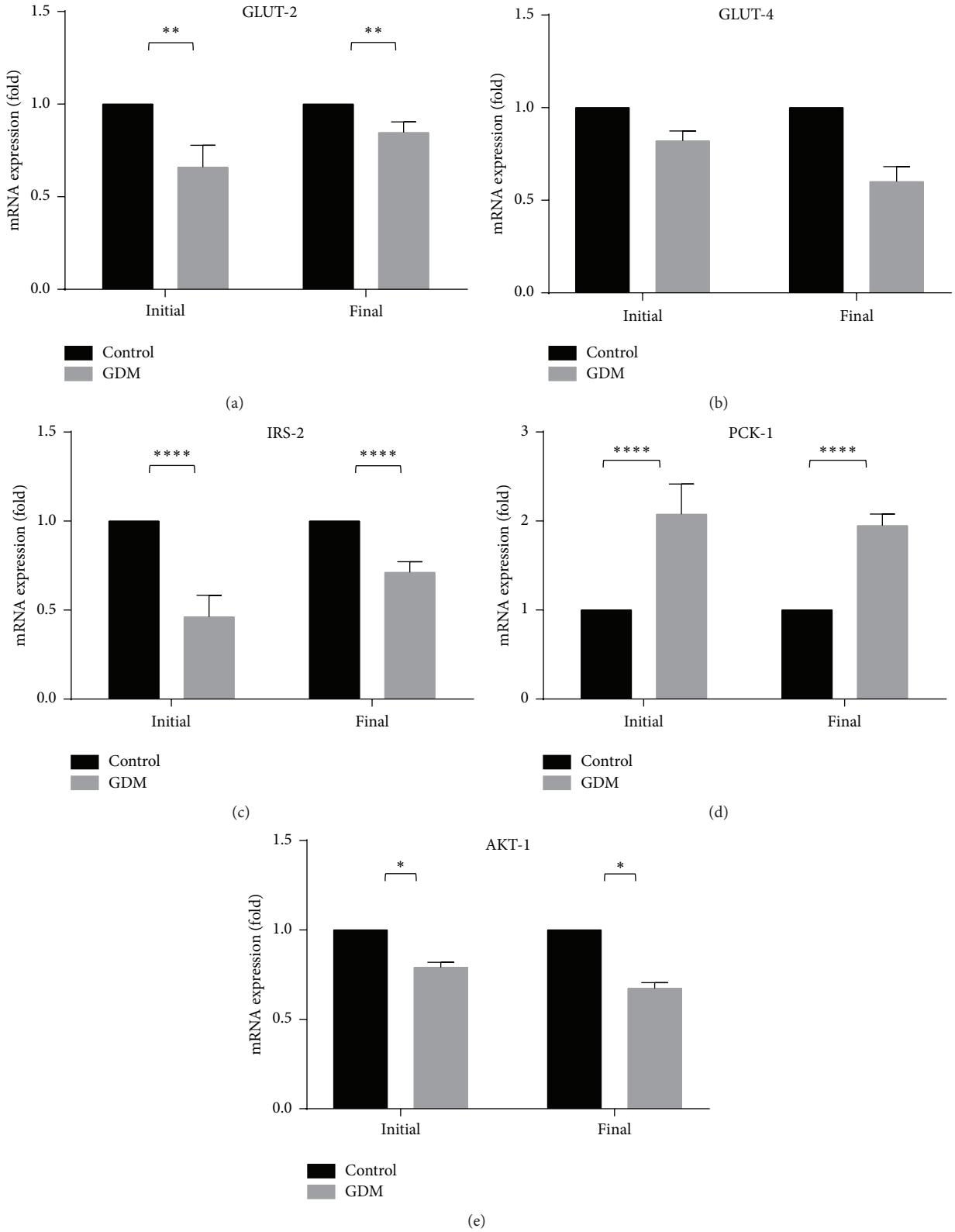

Figure 7: Expression of glucose related genes of control and GDM rats. GLUT-2, GLUT-4, IRS-2, and AKT-1 levels were lower in the GDM group than control. The opposite was true for PCK-1. Data shown as mean ± SD of four rats. For each parameter, a value with the asterisk signifies $P < 0.05$ and the absence of asterisk indicates otherwise. P value less than 0.05 was designated with one (∗) asterisk, P value less than 0.01 was designated with two (∗∗) asterisks, and P value less than 0.0001 was designated with four (∗ ∗ ∗∗) asterisks.

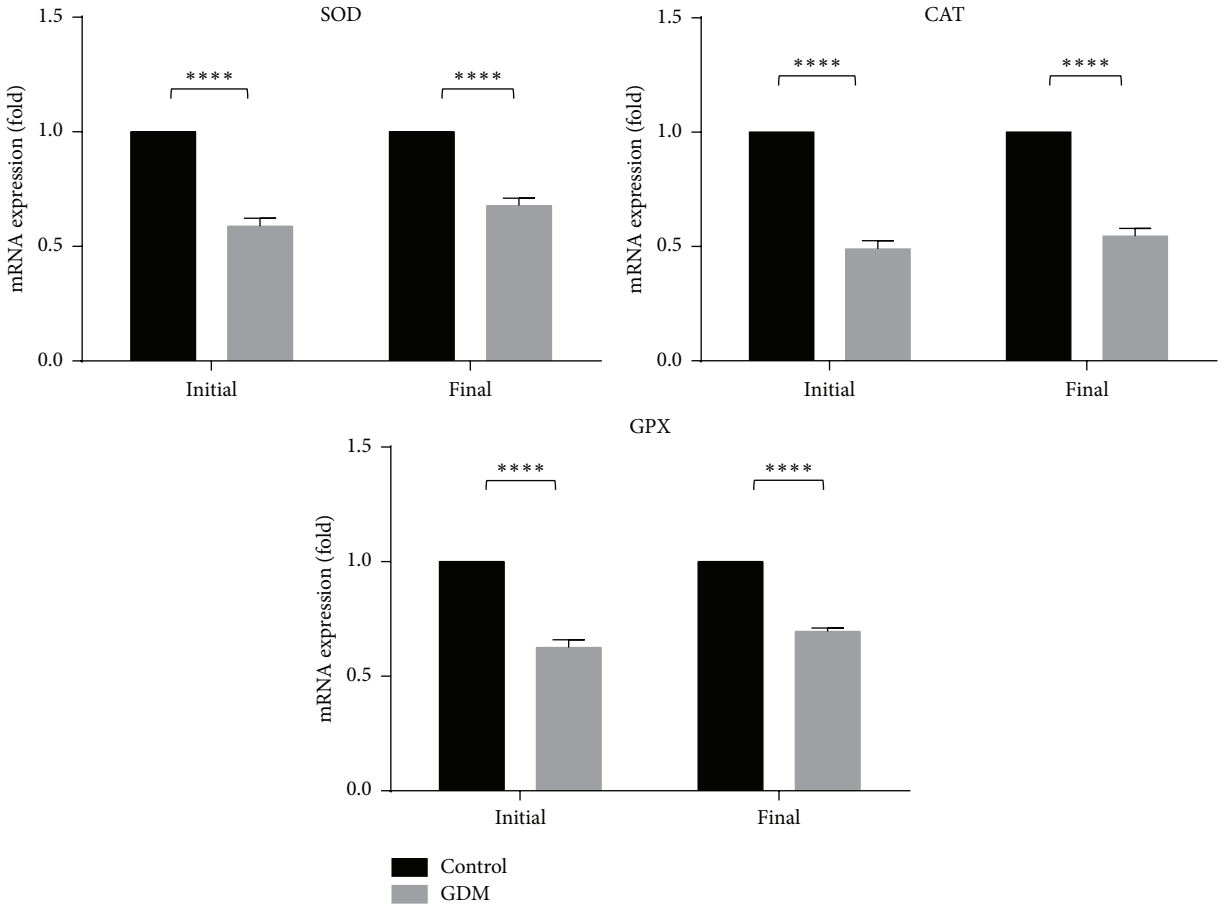

Figure 8: Expression of antioxidant genes of control and GDM rats. SOD, CAT, and GPX genes were lower in the GDM group compared to control, in both initial and final phases at final phase of GDM compared to the initial phase. Data shown as mean ± SD of four rats. For each parameter, a value with the asterisk signifies $P < 0.05$ and the absence of asterisk indicates otherwise. P value less than 0.0001 was designated with four (∗ ∗ ∗∗) asterisks.

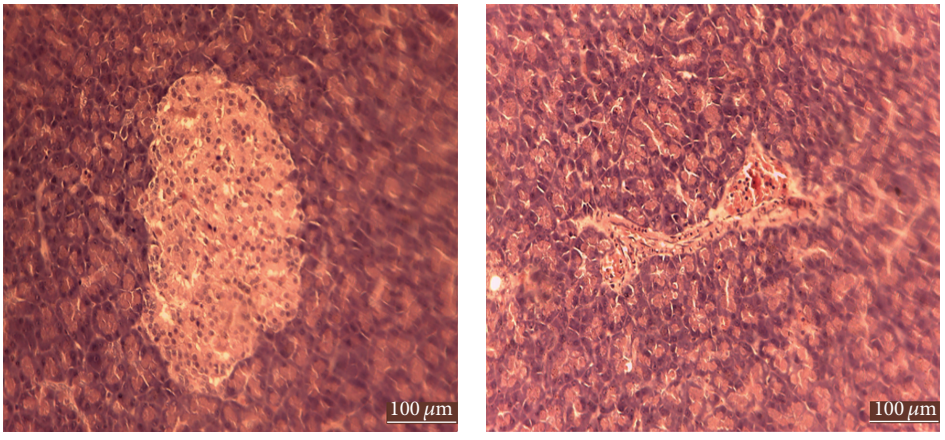

(a) (b)

Figure 9: Histology of pancreas of control and GDM group. (a) H & E staining on normal pancreas showing undestroyed endocrine and exocrine gland. (b) H & E staining on STZ-treated pancreas showing slightly destroyed Islet of Langerhans.

response [45], although the mechanism behind it has not been elucidated. In line with the higher level of IL-6 and TNF-α, serum CRP level (inflammatory marker) was also higher in GDM than control (see Figure 5(a)). Elevated levels of plasma CRP have been reported to enhance the development of diabetes [46] by interacting with cytokines (IL-6 and TNF-α) in stimulating the acute phase inflammatory response [47, 48]. The higher level of proinflammatory cytokines and plasma CRP thus indicates the likelihood of insulin resistance in our GDM model.

In the evaluation of genes affecting insulin signaling pathway, GLUT-2, GLUT-4, AKT-1, and IRS-2 levels were lower in the GDM group than control. The opposite was true for PCK-1. In GDM, fatty-sucrose diet promotes serine phosphorylation of IRS-1, reducing its ability to act as an insulin receptor substrate [49–52], thereby reducing GLUT-4 translocation to the plasma membrane. Serine phosphorylation of IRS also deactivates AKT signaling cascade, which inhibits glycogen synthesis, suppressing the gluconeogenesis in liver of GDM rat [53]. AKT have a secondary role in the production of glycerol which releases FFA into the blood stream [54]. As mentioned previously, elevated FFA is associated with insulin resistance. The lower concentration of IRS-2 genes and AKT-1 in GDM group and reduced level of GLUT-4 from the initial to final phases indicate the possible defect of insulin signaling in our GDM model. Furthermore, the higher level of PCK-1 in the GDM model compared to control indicates that lipid metabolism and glucose homeostasis are compromised, leading to insulin resistance [55].

Antioxidant levels, SOD, GPX, and CAT (Figure 7), were evaluated in this study to analyze the effect of stress on GDM rats. It can be seen that all antioxidant genes were significantly lower in the GDM group than control, indicating that GDM rats were under stress. This result is also in line with the findings of Sindhu et al., [41] where diabetic rats showed reduced activity of the same antioxidant enzymes. Ornoy [56] also observed a significant decrease in endogenous antioxidant enzymes when oxidative stress was induced on embryos under diabetic condition. Both studies also highlight that impaired antioxidant status can be linked to oxidative stress associated with diabetes stress due to an overproduction of reactive oxygen species (ROS) [57]. ROS modulates the insulin signaling pathway *via* two mechanisms. The first mechanism involves the production of ROS in response to insulin where ROS is involved in physiological functions such as vascular homeostasis [58]. In the second mechanism, ROS negatively regulates the insulin pathway, consequently leading to reduced insulin secretion and consequently insulin resistance [59–61]. Hence, this underlines the link between stress and the pathophysiology of GDM.

Pancreas of the control group was undestroyed whereas in the GDM group, there was a slight destruction of the Islet of Langerhans (Figure 8). Effect of GDM on pancreas can be observed clearly after the process of staining. The partially destroyed Islets of Langerhans show the cytotoxic effect of STZ [62]. STZ causes the alkylation of DNA via GLUT-2 which later induces the activation of poly ADP-ribosylation (PARP), leading to depletion of cellular NAD+ and ATP [35]. Necrotic death of beta cells was partially prevented by action of NA in lowering the PARP activity, thus ensuring enough NAD and ATP to be used [63].

Maternal reproductive status (Table 1) was also evaluated in our study where one of the statuses observed was the weight of the fetus. It can be seen from Table 1 that GDM group showed a higher fetal weight than control. Macrosomia, or large gestational size, is caused by hyperinsulinemia to which insulin is one of the main growth factors during fetal life [64]. In addition, hyperglycemia of intrauterine milieu of GDM mother may cause the fetal endocrine pancreas to promote hyperinsulinemia. As previously shown, GDM rats showed a higher insulin and average glucose level than control. Another status observed was the number of live fetuses where GDM group had a lower number than the control. In a retrospective analysis done by Gunther et al., [65] intrauterine fetal death was more prevalent in pregnant women with diabetes (preconceptional diabetes mellitus and GDM) than women without diabetes. Additionally, the number of postimplantation loss sites was higher in GDM group which indicates that rats with GDM had newborns with intrauterine growth restriction.

5. Conclusion

In this study, we administered STZ and NA to pregnant rats, along with feeding them with HFSD and altering sleep patterns to induce GDM. The GDM animal model showed signs of insulin resistance where expressions of both proinflammatory cytokines (IL-6 and TNF-α), PCK-1, and serum CRP level were higher than control. Furthermore, low concentration of IRS-2 genes and AKT-1 and reduced level of GLUT-4 from the initial to final phases indicate the possible defect of insulin signaling in our GDM animal model. The impaired antioxidant status in our GDM model showed that inducing stress through changing sleeping cycle could induce oxidative stress, which is associated with diabetes. Our GDM animal model showed a higher body weight than control during Week 1, which was due to HFSD feeding. The GDM animal then showed a decrease in body weight from Week 1 to Week 3, due to the destruction of beta cells by STZ. Blood glucose level was also higher in GDM group than control, indicating the hyperglycemic state of the GDM rats. Higher level of lipid parameters (triglycerides, total cholesterol, and LDL-cholesterol) in GDM group then confirms the state of hyperlipidemia in GDM rats. Based on these results, it can be concluded that suitable GDM animal model can be created through nutritional, pharmacological, and lifestyle manipulations. This model can then be used to further understand the pathophysiology of GDM and consequently finding novel therapies for GDM.

Competing Interests

The authors confirm that this paper content has no conflict of interests.

Authors' Contributions

Siti Hajar Abdul Aziz and Cini Mathew John contributed equally to this work.

Acknowledgments

This work was supported by Malaysian Ministry of Higher Education's Fundamental Research Grant Scheme (FRGS/1/2014/SKK02/UITM/03/1) through Universiti Teknologi MARA (UiTM).

References

[1] American Diabete Association, "2. Classification and Diagnosis of Diabetes," *Diabetes Care*, vol. 38, supplement 1, pp. S8–S16, 2015.

[2] L. A. Barbour, C. E. McCurdy, T. L. Hernandez, J. P. Kirwan, P. M. Catalano, and J. E. Friedman, "Cellular mechanisms for insulin resistance in normal pregnancy and gestational diabetes," *Diabetes Care*, vol. 30, supplement 2, pp. S112–S119, 2007.

[3] T. A. Buchanan, A. H. Xiang, and K. A. Page, "Gestational diabetes mellitus: risks and management during and after pregnancy," *Nature Reviews Endocrinology*, vol. 8, no. 11, pp. 639–649, 2012.

[4] C. Capula, E. Chiefari, A. Vero et al., "Gestational diabetes mellitus: screening and outcomes in southern Italian pregnant women," *ISRN Endocrinology*, vol. 2013, Article ID 387495, 8 pages, 2013.

[5] R. á Rogvi, J. L. Forman, P. Damm, and G. Greisen, "Women born preterm or with inappropriate weight for gestational age are at risk of subsequent gestational diabetes and pre-eclampsia," *PLoS ONE*, vol. 7, no. 3, Article ID e34001, 2012.

[6] B. He, D. Piao, C. Yu, Y. Wang, and P. Han, "Amelioration in hepatic insulin sensitivity by reduced hepatic lipid accumulation at short-term after Roux-en-Y gastric bypass surgery in type 2 diabetic rats," *Obesity Surgery*, vol. 23, no. 12, pp. 2033–2041, 2013.

[7] C. Kühl, P. J. Hornnes, and O. Andersen, "Review: etiology and pathophysiology of gestational diabetes mellitus," *Diabetes*, vol. 34, no. 2, pp. 66–70, 1985.

[8] L. Bellamy, J.-P. Casas, A. D. Hingorani, and D. Williams, "Type 2 diabetes mellitus after gestational diabetes: a systematic review and meta-analysis," *The Lancet*, vol. 373, no. 9677, pp. 1773–1779, 2009.

[9] B. E. Metzger, T. A. Buchanan, D. R. Coustan et al., "Summary and recommendations of the fifth international workshop-conference on gestational diabetes mellitus," *Diabetes Care*, vol. 30, supplement 2, pp. S251–S260, 2007.

[10] M. Koulmanda, A. Qipo, S. Chebrolu, J. O'Neil, H. Auchincloss Jr., and R. N. Smith, "The effect of low versus high dose of streptozotocin in cynomolgus monkeys (*Macaca fascilularis*)," *American Journal of Transplantation*, vol. 3, no. 3, pp. 267–272, 2003.

[11] F. A. Van Assche, L. Aerts, and K. Holemans, "Metabolic alterations in adulthood after intrauterine development in mothers with mild diabetes," *Diabetes*, vol. 40, supplement 2, pp. 106–108, 1991.

[12] E. Shafrir and G. Desoye, "Pregnancy in diabetic animals," in *Textbook of Diabetes and Pregnancy*, M. Hod, L. Jovanovic, G. C. Di Renzo, A. Leiva, and O. Langer, Eds., pp. 96–97, Informa, London, UK, 2003.

[13] S. Caluwaerts, K. Holemans, R. Van Bree, J. Verhaeghe, and F. A. Van Assche, "Is low-dose streptozotocin in rats an adequate model for gestational diabetes mellitus?" *Journal of the Society for Gynecologic Investigation*, vol. 10, no. 4, pp. 216–221, 2003.

[14] K. Holemans, S. Caluwaerts, L. Poston, and F. A. Van Assche, "Diet-induced obesity in the rat: a model for gestational diabetes mellitus," *American Journal of Obstetrics and Gynecology*, vol. 190, no. 3, pp. 858–865, 2004.

[15] I. López-Soldado and E. Herrera, "Different diabetogenic response to moderate doses of streptozotocin in pregnant rats, and its long-term consequences in the offspring," *Experimental Diabesity Research*, vol. 4, no. 2, pp. 107–118, 2003.

[16] J. Yoshino, K. F. Mills, M. J. Yoon, and S.-I. Imai, "Nicotinamide mononucleotide, a key NAD+ intermediate, treats the pathophysiology of diet- and age-induced diabetes in mice," *Cell Metabolism*, vol. 14, no. 4, pp. 528–536, 2011.

[17] P. Masiello, C. Broca, R. Gross et al., "Experimental NIDDM: development of a new model in adult rats administered streptozotocin and nicotinamide," *Diabetes*, vol. 47, no. 2, pp. 224–229, 1998.

[18] L. H. Storlien, A. B. Jenkins, D. J. Chisholm, W. S. Pascoe, S. Khouri, and E. W. Kraegen, "Influence of dietary fat composition on development of insulin resistance in rats: relationship to muscle triglyceride and ω-3 fatty acids in muscle phospholipid," *Diabetes*, vol. 40, no. 2, pp. 280–289, 1991.

[19] K. Srinivasan, P. S. Patole, C. L. Kaul, and P. Ramarao, "Reversal of glucose intolerance by pioglitazone in high fat diet-fed rats," *Methods and Findings in Experimental and Clinical Pharmacology*, vol. 26, no. 5, pp. 327–333, 2004.

[20] Z.-H. Yang, H. Miyahara, J. Takeo, and M. Katayama, "Diet high in fat and sucrose induces rapid onset of obesity-related metabolic syndrome partly through rapid response of genes involved in lipogenesis, insulin signalling and inflammation in mice," *Diabetology and Metabolic Syndrome*, vol. 4, article 32, 2012.

[21] C. L. Ogden, S. Z. Yanovski, M. D. Carroll, and K. M. Flegal, "The epidemiology of obesity," *Gastroenterology*, vol. 132, no. 6, pp. 2087–2102, 2007.

[22] R. T. Hurt, C. Kulisek, L. A. Buchanan, and S. A. McClave, "The obesity epidemic: challenges, health initiatives, and implications for gastroenterologists," *Gastroenterology and Hepatology*, vol. 6, no. 12, pp. 780–792, 2010.

[23] L. S. Aucott, "Influences of weight loss on long-term diabetes outcomes," *Proceedings of the Nutrition Society*, vol. 67, no. 1, pp. 54–59, 2008.

[24] E. S. Abdel-Reheim, A. A. Abd-Elmoneim, and A. A. Hosni, "Fatty-sucrosed diet/minimal dose of streptozotocin-treated rat: a novel model of gestational diabetes mellitus, metabolic and inflammatory insight," *Journal of Diabetes & Metabolism*, vol. 5, p. 430, 2014.

[25] K. Srinivasan, B. Viswanad, L. Asrat, C. L. Kaul, and P. Ramarao, "Combination of high-fat diet-fed and low-dose streptozotocin-treated rat: a model for type 2 diabetes and pharmacological screening," *Pharmacological Research*, vol. 52, no. 4, pp. 313–320, 2005.

[26] C. M. John, R. Ramasamy, G. Al Naqeeb, A. H. Dhiab Al-Nuaimi, and A. Adam, "Enhanced CD4+CD25+ regulatory T cells with splenic proliferation and protection against oxidative stress by nicotinamide in gestational diabetes," *Current Medicinal Chemistry*, In press.

[27] C. M. John, R. Ramasamy, G. Al Naqeeb, A. H. D. Al-Nuaimi, and A. Adam, "Nicotinamide supplementation protects gestational diabetic rats by reducing oxidative stress and enhancing immune responses," *Current Medicinal Chemistry*, vol. 19, no. 30, pp. 5181–5186, 2012.

[28] A. Gumieniczek, H. Hopkała, Z. Wójtowicz, and J. Nikołajuk, "Changes in antioxidant status of heart muscle tissue in experimental diabetes in rabbits," *Acta Biochimica Polonica*, vol. 49, no. 2, pp. 529–535, 2002.

[29] Y. J. Suzuki, V. Jain, A.-M. Park, and R. M. Day, "Oxidative stress and oxidant signaling in obstructive sleep apnea and associated cardiovascular diseases," *Free Radical Biology and Medicine*, vol. 40, no. 10, pp. 1683–1692, 2006.

[30] F. K. Marcondes, F. J. Bianchi, and A. P. Tanno, "Determination of the estrous cycle phases of rats: some helpful considerations," *Brazilian Journal of Biology*, vol. 62, no. 4, pp. 609–614, 2002.

[31] R. Kopf, D. Lorenz, and E. Salewski, "Procedure for staining implantation sites of fresh rat uteri," *Naunyn-Schmiedebergs Archiv für experimentelle Pathologie und Pharmakologie*, vol. 247, no. 2, pp. 121–135, 1964.

[32] D. A. Benson, I. Karsch-Mizrachi, D. J. Lipman, J. Ostell, B. A. Rapp, and D. L. Wheeler, "GenBank," *Nucleic Acids Research*, vol. 30, no. 1, pp. 17–20, 2002.

[33] I. M. B. Francischetti, E. Gordon, B. Bizzarro et al., "Tempol, an intracellular antioxidant, inhibits tissue factor expression, attenuates dendritic cell function, and is partially protective in a murine model of cerebral malaria," *PLoS ONE*, vol. 9, no. 2, Article ID e87140, 2014.

[34] C. Liang, K. DeCourcy, and M. R. Prater, "High-saturated-fat diet induces gestational diabetes and placental vasculopathy in C57BL/6 mice," *Metabolism: Clinical and Experimental*, vol. 59, no. 7, pp. 943–950, 2010.

[35] T. Szkudelski, "The mechanism of alloxan and streptozotocin action in B cells of the rat pancreas," *Physiological Research*, vol. 50, no. 6, pp. 537–546, 2001.

[36] M. Chatterjea and R. Shinde, *Textbook of Medical Biochemistry*, 2011.

[37] C. Homko, E. Sivan, X. Chen, E. A. Reece, and G. Boden, "Insulin secretion during and after pregnancy in patients with gestational diabetes mellitus," *The Journal of Clinical Endocrinology & Metabolism*, vol. 86, no. 2, pp. 568–573, 2001.

[38] E. Herrera and H. Ortega-Senovilla, "Disturbances in lipid metabolism in diabetic pregnancy—are these the cause of the problem?" *Best Practice and Research: Clinical Endocrinology and Metabolism*, vol. 24, no. 4, pp. 515–525, 2010.

[39] J. Ghalami, H. Zardooz, F. Rostamkhani, B. Farrokhi, and M. Hedayati, "High-fat diet did not change metabolic response to acute stress in rats," *EXCLI Journal*, vol. 10, pp. 205–217, 2011.

[40] A. Dresner, D. Laurent, M. Marcucci et al., "Effects of free fatty acids on glucose transport and IRS-1-associated phosphatidylinositol 3-kinase activity," *The Journal of Clinical Investigation*, vol. 103, no. 2, pp. 253–259, 1999.

[41] H. Bays, L. Mandarino, and R. A. Defronzo, "Role of the adipocyte, free fatty acids, and ectopic fat in pathogenesis of type 2 diabetes mellitus: peroxisomal proliferator-activated receptor agonists provide a rational therapeutic approach," *The Journal of Clinical Endocrinology & Metabolism*, vol. 89, no. 2, pp. 463–478, 2004.

[42] E. M. Sternberg, G. P. Chrousos, R. L. Wilder, and P. W. Gold, "The stress response and the regulation of inflammatory disease," *Annals of Internal Medicine*, vol. 117, no. 10, pp. 854–866, 1992.

[43] M. Lappas, A. Mittion, and M. Permezel, "In response to oxidative stress, the expression of inflammatory cytokines and antioxidant enzymes are impaired in placenta, but not adipose tissue, of women with gestational diabetes," *Journal of Endocrinology*, vol. 204, no. 1, pp. 75–84, 2010.

[44] L. Rui, V. Aguirre, J. K. Kim et al., "Insulin/IGF-1 and TNF-α stimulate phosphorylation of IRS-1 at inhibitory Ser307 via distinct pathways," *The Journal of Clinical Investigation*, vol. 107, no. 2, pp. 181–189, 2001.

[45] J.-P. Bastard, M. Maachi, J. T. Van Nhieu et al., "Adipose tissue IL-6 content correlates with resistance to insulin activation of glucose uptake both in vivo and in vitro," *Journal of Clinical Endocrinology & Metabolism*, vol. 87, no. 5, pp. 2084–2089, 2002.

[46] A. Dehghan, I. Kardys, M. P. M. De Maat et al., "Genetic variation, C-reactive protein levels, and incidence of diabetes," *Diabetes*, vol. 56, no. 3, pp. 872–878, 2007.

[47] B. Vozarova, C. Weyer, K. Hanson, P. A. Tataranni, C. Bogardus, and R. E. Pratley, "Circulating interleukin-6 in relation to adiposity, insulin action, and insulin secretion," *Obesity Research*, vol. 9, no. 7, pp. 414–417, 2001.

[48] P. A. Kern, S. Ranganathan, C. Li, L. Wood, and G. Ranganathan, "Adipose tissue tumor necrosis factor and interleukin-6 expression in human obesity and insulin resistance," *American Journal of Physiology—Endocrinology and Metabolism*, vol. 280, no. 5, pp. E745–E751, 2001.

[49] P. Bevan, "Insulin signalling," *Journal of Cell Science*, vol. 114, no. 8, pp. 1429–1430, 2001.

[50] A. D. Kohn, F. Takeuchi, and R. A. Roth, "Akt, a pleckstrin homology domain containing kinase, is activated primarily by phosphorylation," *The Journal of Biological Chemistry*, vol. 271, no. 36, pp. 21920–21926, 1996.

[51] M. R. Calera, C. Martinez, H. Liu, A. K. El Jack, M. J. Birnbaum, and P. F. Pilch, "Insulin increases the association of Akt-2 with Glut4-containing vesicles," *The Journal of Biological Chemistry*, vol. 273, no. 13, pp. 7201–7204, 1998.

[52] L.-N. Cong, H. Chen, Y. Li et al., "Physiological role of AKT in insulin-stimulated translocation of GLUT4 in transfected rat adipose cells," *Molecular Endocrinology*, vol. 11, no. 13, pp. 1881–1890, 1997.

[53] C. Kim and A. Ferrara, *Gestational Diabetes during and after Pregnancy*, Springer, New York, NY, USA, 2010.

[54] T. Holyoak, S. M. Sullivan, and T. Nowak, "Structural insights into the mechanism of PEPCK catalysis," *Biochemistry*, vol. 45, no. 27, pp. 8254–8263, 2006.

[55] A. Méndez-Lucas, J. A. G. Duarte, N. E. Sunny et al., "PEPCK-M expression in mouse liver potentiates, not replaces, PEPCK-C mediated gluconeogenesis," *Journal of Hepatology*, vol. 59, no. 1, pp. 105–113, 2013.

[56] A. Ornoy, "Embryonic oxidative stress as a mechanism of teratogenesis with special emphasis on diabetic embryopathy," *Reproductive Toxicology*, vol. 24, no. 1, pp. 31–41, 2007.

[57] M. Valko, C. J. Rhodes, J. Moncol, M. Izakovic, and M. Mazur, "Free radicals, metals and antioxidants in oxidative stress-induced cancer," *Chemico-Biological Interactions*, vol. 160, no. 1, pp. 1–40, 2006.

[58] D. Vara and G. Pula, "Reactive oxygen species: physiological roles in the regulation of vascular cells," *Current Molecular Medicine*, vol. 14, no. 9, pp. 1103–1125, 2014.

[59] U. Asmat, K. Abad, and K. Ismail, "Diabetes mellitus andoxidative stress—a concise review," *Saudi Pharmaceutical Journal*, 2015.

[60] H. Zardooz, S. Z. Asl, and M. G. Naseri, "Effect of chronic psychological stress on insulin release from rat isolated pancreatic islets," *Life Sciences*, vol. 79, no. 1, pp. 57–62, 2006.

[61] K. Sakai, K. Matsumoto, T. Nishikawa et al., "Mitochondrial reactive oxygen species reduce insulin secretion by pancreatic

β-cells," *Biochemical and Biophysical Research Communications*, vol. 300, no. 1, pp. 216–222, 2003.

[62] S. Lenzen, "The mechanisms of alloxan- and streptozotocin-induced diabetes," *Diabetologia*, vol. 51, no. 2, pp. 216–226, 2008.

[63] L. I. Rachek, N. P. Thornley, V. I. Grishko, S. P. LeDoux, and G. L. Wilson, "Protection of INS-1 cells from free fatty acid-induced apoptosis by targeting hOGG1 to mitochondria," *Diabetes*, vol. 55, no. 4, pp. 1022–1028, 2006.

[64] R. Schwartz, P. A. Gruppuso, K. Petzold, D. Brambilla, V. Hiilesmaa, and K. A. Teramo, "Hyperinsulinemia and macrosomia in the fetus of the diabetic mother," *Diabetes Care*, vol. 17, no. 7, pp. 640–648, 1994.

[65] H. H. Günter, I. Tzialidou, A. Scharf, P. Wenzlaff, H. Maul, and P. Hillemanns, "Intrauterine fetal death in pregnancies of women with preconceptional and gestational diabetes mellitus and of women without glucose tolerance disorders. Results of the Perinatal Registry of Lower Saxony, Germany," *Zeitschrift fur Geburtshilfe und Neonatologie*, vol. 210, no. 6, pp. 193–199, 2006.

Hindawi Publishing Corporation
BioMed Research International
Volume 2016, Article ID 4521807, 9 pages
http://dx.doi.org/10.1155/2016/4521807

Review Article

Animal Models of Uveal Melanoma: Methods, Applicability, and Limitations

Marta M. Stei, Karin U. Loeffler, Frank G. Holz, and Martina C. Herwig

Department of Ophthalmology, University of Bonn, Ernst-Abbe-Straße 2, 53127 Bonn, Germany

Correspondence should be addressed to Marta M. Stei; marta.kilian@ukb.uni-bonn.de

Received 29 February 2016; Accepted 8 May 2016

Academic Editor: Monica Fedele

Animal models serve as powerful tools for investigating the pathobiology of cancer, identifying relevant pathways, and developing novel therapeutic agents. They have facilitated rapid scientific progress in many tumor entities. However, for establishing a powerful animal model of uveal melanoma fundamental challenges remain. To date, no animal model offers specific genetic attributes as well as histologic, immunologic, and metastatic features of uveal melanoma. Syngeneic models with intraocular injection of cutaneous melanoma cells may suit best for investigating immunologic/tumor biology aspects. However, differences between cutaneous and uveal melanoma regarding genetics and metastasis remain problematic. Human xenograft models are widely used for evaluating novel therapeutics but require immunosuppression to allow tumor growth. New approaches aim to establish transgenic mouse models of spontaneous uveal melanoma which recently provided preliminary promising results. Each model provides certain benefits and may render them suitable for answering a respective scientific question. However, all existing models also exhibit relevant limitations which may have led to delayed research progress. Despite refined therapeutic options for the primary ocular tumor, patients' prognosis has not improved since the 1970s. Basic research needs to further focus on a refinement of a potent animal model which mimics uveal melanoma specific mechanisms of progression and metastasis. This review will summarise and interpret existing animal models of uveal melanoma including recent advances in the field.

1. Introduction

Animal models of human cancer can contribute to the understanding of cancer pathobiology and the development of novel therapeutic agents. The ultimate goal is to translate scientific progress from basic research (*in vitro* and *in vivo*) through preclinical animal studies finally into human clinical trials to demonstrate both efficacy and safety. However, the absence of effective *in vivo* systems that accurately mimic the human disease condition and reliably predict clinical efficacy has hindered therapy and drug development in oncology [1]. Despite a poor rate of successful translation from animal models to clinical cancer trials [2], *in vivo* models have revolutionized options to study tumor biology and better understand molecular and genetic pathways. Cancer xenografts and genetically engineered mice are the most commonly used cancer models of several tumor entities [3]. In skin melanoma, genetically engineered mouse models revealed to be an improved prediction model of anticancer therapeutics and patients' response [4]. Such transgenic mouse models have been developed for many different tumor entities allowing for detailed and diverse studies for basic research purposes as well as preclinical drug screening. However, in some tumor entities like uveal melanoma fundamental challenges in establishing an animal model which meets the tumor's specific characteristics have not been overcome yet.

Uveal melanoma is the second most common type of melanoma after cutaneous and has, compared to skin melanoma, a relatively low incidence (6 per million per year, in the US [5]). However, it represents the most frequent primary intraocular tumor in the adult Caucasian population [6–8]. It arises from intraocular melanocytes of the choroid, the ciliary body, and/or the iris. Treatment strategies comprise brachytherapy, surgical excision, and removal of the entire globe. Even if fresh tumor material is available, establishing cell lines from uveal melanoma remains difficult and is often unsuccessful. There are only a limited number of

permanent cell lines for uveal melanoma research available. Most of these were established some time ago which may have led to alterations in biologic and genetic properties. Thus, there is an urgent need for an effective animal model of uveal melanoma. Such a model should accurately mimic different characteristics of uveal melanoma such as genetics (monosomy 3, GNAQ/GNA11, and BAP1 mutations), hematogenous spread to the liver, (as the eye lacks lymphatics), an inflammatory tumor microenvironment, and other tumor growth characteristics. Intraocular melanomas have rarely been described in companion animals like dogs [9–11] and cats [12–15] or in other animals like horses [16], cattle [17], or others. Despite arising naturally, these intraocular melanomas occurred sporadically and unpredictably and mostly did not metastasize to distant organs. Thus, they do not qualify as an animal model for experimental uveal melanoma. Unfortunately, no spontaneous uveal melanoma has been observed in wild type mice to date. However, mice are the most commonly employed animal model in uveal melanoma studies due to the uncomplicated housing, availability, and genetic manipulation options. It is commonly accepted that, besides transgenic models, iatrogenically induced tumor models represent the best option for oncology research. This includes implantation of animal and human uveal melanoma cell lines into animals to model the behavior of this tumor. Since advanced age is associated with changes in immunologic constitution and inoculated tumors arising in old mice better resemble tumors of their human counterpart, generally, old mice should preferably be used for studies on tumor biology (Stei et al., unpublished data).

To generate and study intraocular melanoma in mice, basically four types of models have been developed including (1) intraocular inoculation with cutaneous melanoma cells into wild type mice, (2) injection of human uveal melanoma cells into mice which requires immunosuppression to allow tumor growth, (3) new approaches aiming to crossbreed or generate genetically engineered mice which spontaneously develop intraocular melanomas, and (4) induction of uveal proliferation by chemicals, radiation, or viruses [18]. Further, in order to study metastatic uveal melanoma, different models of hepatic metastases have been established. Animal models of uveal melanoma other than mice include chick embryos, drosophila, zebrafish, rats, and rabbits. However, as no optimal animal model that faithfully replicates the behavior of the human disease (spontaneously occurring and concurrently metastasizing) has been described yet, all established animal models represent compromises and are facing certain limitations.

This review will summarise and interpret the different types of existing animal models of uveal melanoma including recent advances in the field.

2. Animal Models of Uveal Melanoma

2.1. Intraocular Injection of Cutaneous Melanoma Cells. Syngeneic transplantation models are useful, especially for experiments designed to study or modulate immune responses which require an intact immune system. For cutaneous melanoma, the most frequently used syngeneic murine model is the B16 melanoma which was derived from a spontaneously arising melanoma in a C57Bl/6J mouse and was then established as a permanent cell line [19]. Accordingly, an initial approach to create a model of intraocular melanoma was to inject B16 cutaneous melanoma cells into the eyes of C57Bl/6 mice by a microinjection technique. Different sublines of B16 cells (F10, LS9, etc.) with different metastatic rates and other cutaneous melanoma cell lines such as HCmel12 have been employed for this purpose [20–23]. These cell lines form solid intraocular melanomas with characteristic tumor growth properties which would qualify as a model of intraocular melanoma. Further, the B16LS9 cell line has been selectively developed after serial passages for liver specific metastasis leading to the only model with an ocular tumor metastasizing to the liver [22]. These syngeneic mouse models have since been used in numerous studies mainly to investigate immunologic and angiogenic aspects but also to investigate tumor progression and imaging methodology [20, 21, 24–37]. Besides in mice models, inoculation with cutaneous melanoma cells has also been established in other rodents. Early oncologic experiments have been performed in hamsters by implanting the Greene (actually of rabbit origin) and later the Bomirski melanoma cell line into the anterior chamber [38–41]. Rabbit models provide the advantage of larger eyes and thus allow for an easier examination of experimental intraocular melanoma. The Greene melanoma cell line was implanted into the anterior or posterior chamber as well as into the subchoroidal space of rabbits and was formerly more commonly used for evaluation of treatment effects on intraocular melanomas [18, 42, 43]. However, rapid tumor growth and other complications have repelled this model. Approaches of grafting murine B16F10 cells into rabbit eyes resulted indeed in solid ocular tumors but metastases were not reliably observed and immune suppression was necessary which represented a disadvantage of this model [44, 45].

However, advantages of these syngeneic models include an apparent resemblance of the intraocular cutaneous melanoma compared to human uveal melanomas and the reliable reproducibility of this technique. The melanoma inside the unique intraocular microenvironment can be investigated in an immunologically intact mouse or other hosts. However, the application of different cell lines and different inoculation sites (anterior chamber, posterior chamber, intravitreal, subretinal, or retroorbital injection) complicates the comparability of the reported results. Furthermore and most importantly, one needs to keep in mind underlying genetic differences between cutaneous and uveal melanoma cells. Unlike cutaneous or conjunctival melanoma, mutations in B-RAF, RAS, or KIT genes occur rarely in uveal melanoma [46]. Characteristic mutations differ between uveal and cutaneous melanoma and even among tumors itself, accounting for different progression and metastatic behavior [47]. Although results from these models are suitable to describe immune responses and intraocular tumor behavior they need to be interpreted with caution when translating respective findings into treatment efficacy in human uveal melanoma.

2.2. Injections of Human Uveal Melanoma Cells. The development of xenograft models was an important step in improving animal models of clinical efficacy [95]. In cutaneous melanoma as well as in other tumor entities, human tumor xenograft models are widely used for drug screening, to evaluate targeted therapies or to test combinatorial efficacy of therapeutic agents [96]. For evaluation of intraocular melanoma growth and treatment strategies human xenografts (human uveal melanoma cell lines or primary tumor fragments) are commonly examined and several models have been described. Permanent cells lines grown from human uveal melanomas can be characterized histologically and by genetic profiling. They offer the opportunity to investigate biological and pharmacological aspects *in vitro* or in an animal model. Generally, these xenografts are inoculated into the eye of an immunosuppressed animal or in few cases they are injected retroorbitally. Unfortunately, relatively few permanent uveal melanoma cell lines are available for research and there has been some substantial misidentification [97, 98]. Particularly, C918 and other cell lines are most likely derived from cutaneous but uveal origin [98, 99]. This should be taken into account when interpreting and analyzing past and current data obtained with these cell lines. Further, the diverse molecular landscape of human uveal melanoma can barely be reflected by permanent cell lines. However, recently, novel established permanent cell lines from primary and metastatic uveal melanomas exhibiting a characteristic genetic profile (including GNAQ, GNA11, or BAP1 mutations) allow for further investigations on genetic pathways and their influence on tumor progression and metastasis [100]. Selecting a cell line which phenotypically and genetically reflects desired characteristics is of high importance.

Niederkorn and coworkers investigated multiple human uveal melanoma cell lines in an intraocular model in athymic mice [48–51]. Human xenograft models in immunodeficient mice were frequently used in several studies, for example, on treatment efficacy, on agents or genetic pathways affecting tumor progression, on transcription factors, or on studying immunologic and histologic tumor characteristics [35, 52–58]. Further, labelling human cell lines by bioluminescence allows advanced imaging procedures in the animal. The primary tumor as well as liver and lung metastases are more easily traceable [59–61].

To assess efficacy of treatments on the basis of tumor growth human xenograft models have also been established in nude rats [58], rabbits, and zebrafish. Xenografts were frequently implanted into the eyes of immunosuppressed or nude rabbits with intraocular solid tumor growth, mostly accompanied by metastatic disease, and promising results [62–67]. Rabbits with intraocularly inoculated human uveal melanoma cells were mainly used for basic research [68–71]. Other and upcoming animal models include the injection of human primary and metastatic cell lines into the yolk of zebrafish for screening large libraries of new compounds [72].

Recently, individual patient-derived xenograft (PDX) models have emerged as an important tool for translational research, with the promise of a more personalized approach to patient care. Tumors are obtained from the patient and directly implanted into the model animal. Thus, these models maintain several characteristics of the parental tumor regarding histologic and genetic attributes [101]. First studies with primary and metastatic uveal melanoma transplants into the subcutis or the interscapular fat pad of immunosuppressed mice showed moderate take rates [73–75]. PDX modelling enables tracking of tumor progression and metastasis as well as screening of different (combinatorial) drug strategies to help choose the best and most effective therapy for each individual patient [101, 102]. For uveal melanoma, this approach needs to be further evaluated and established intraocularly in order to achieve methodological advances and increased applicability in research. PDX models of uveal melanoma may help to better understand the complex cascade of uveal melanoma metastasis, to further refine therapy regimes in order to prevent metastasis, or to develop a treatment option once the tumor has metastasized.

However, a major disadvantage of all xenograft animal models is the necessity of immunosuppression. In many malignancies including those derived in immunoprivileged sites like uveal melanoma, tumor progression and the tumor microenvironment are strongly influenced by immune cells [103]. Thus, successful drug screening in xenograft models does not necessarily predict similar effects in humans.

2.3. Transgenic Mice. During the last 30 years novel technologies specifically modifying the genome allowed for the generation of transgenic mouse strains. Several criteria have been suggested for such models; for example, mice must carry the same mutation that occurs in the human tumor and mutations should be engineered within the endogenous locus [104]. Such genetically engineered mice are now considered ideal tools to study molecular and genetic pathways in cancer and other diseases. However, these techniques also can be used to generate mouse strains which spontaneously develop certain forms of malignancies. For skin melanoma, for example, RET transgenic mice with spontaneous melanomas are available since 1998 [105]. In the meantime, numerous transgenic mouse models of cutaneous melanoma have been established which closely resembles human skin malignant melanoma with regard to etiology, histopathology, and clinical progression [96].

For uveal melanoma, unfortunately, no such transgenic mouse model is available to date. Many attempts have been undertaken and numerous transgenic skin melanoma models have been investigated for the proliferation of ocular melanocytes. However, in some models no melanocytic proliferation was observed [76]; in others, pigmented intraocular tumors arising in transgenic mice were identified to be of retinal pigment epithelium origin [77, 78] or the small uveal tumors failed to metastasize to the lungs [79–81]. RET.AAD transgenic mice exhibit hyperplastic lesions within all melanocyte-containing sites (skin, eye, meninges, etc.) with early tumor cell dissemination to local and distant organs [82]. As initial melanocytic lesions are mostly found within the uvea, this model was used for investigations on early local and distant tumor growth as well as dissemination [83, 84]. Schiffner and coworkers described a Tg(Grm1)

transgenic mouse breed, with spontaneous skin melanoma, which exhibited pigmented choroidal proliferation mimicking spontaneous uveal melanoma [85]. However, applicability as a model for studying intraocular melanoma remains questionable and further studies need to be awaited. Overall, most attempts of finding primary and metastatic uveal melanoma in models of cutaneous melanoma were unsuccessful.

Recently, a GNAQ mutated mouse strain was described which showed neoplastic proliferation not only in choroidal structures but also in dermal nevi and other melanocytic neoplasms. Furthermore and more importantly, a vast majority of these mice exhibited distant metastasis, though exclusively in the lungs [86]. This breed represents the first transgenic mouse model of uveal melanocytic proliferation which is driven by a GNAQ gene alteration. By this means it genetically resembles human uveal melanomas, as about 80% of patients carry a G-protein (GNAQ and/or GNA11) mutation as an early event in tumorigenesis [106, 107]. This may be a first basis for a transgenic mouse model of uveal melanoma and further results need to be awaited. To our knowledge, a new animal model of spontaneous uveal melanoma was established in transgenic zebrafish. Oncogenic resemblance with human uveal melanoma is given as uveal tumorigenesis is driven by an inserted plasmid with a *mitfa*:GNA11 Q209L overexpression (Rose, unpublished data). Publication of this new transgenic model needs to be awaited.

2.4. Models of Metastatic Uveal Melanoma. Between 10 and 40% of uveal melanoma patients develop metastatic disease within 10 years after the initial diagnosis [108–110]. Metastases disseminate predominantly hematogenously to the liver and rarely to the lungs or other organs [111]. Liver metastases occur in 95% of patients with metastatic uveal melanoma and result in death in almost all cases [112, 113]. Thus, liver metastases represent a main focus in research. Early detection of uveal melanoma reduces the risk of metastasis and can be lifesaving [114]. Currently, no effective treatment for hepatic or other metastases is available; thus, patients' prognosis worsens dramatically when metastatic disease occurs [108]. As no liver metastasizing primary uveal melanoma model has been established yet, designing a suitable animal model of liver metastasis represents an additional challenge. Different approaches of liver metastatic tumor cell application exist, direct intrahepatic dissemination, splenic implantation with following hematogenous dissemination into the liver, or direct intravenous/intracardiac injection with hematogenous dissemination. By this means the tumor cells reach the liver directly or gain access via the blood stream in order to proliferate at this secondary site. Primary human uveal melanoma cells can be injected into immunosuppressed mice resulting in metastatic disease in most cases [49–51, 59, 60, 90–92] and into immunosuppressed rabbits [64, 67]. On the other hand, murine cutaneous melanoma cells can be orthotopically inoculated into immunocompetent mice [37, 115]. Further, ocular injection of B16LS9 cutaneous melanoma cells leads to hepatic and lung metastases; thus this model mimics the metastatic process from an ocular tumor to secondary sites [20, 33].

However, the generation of metastatic cell clones within a primary tumor requires genetic alterations and subsequent selection of such clones is heavily influenced by interactions with the surrounding microenvironment. Thus, when modelling hepatic metastasis, cell lines generated from a confirmed metastatic origin represent a more appropriate option than cells from the primary ocular tumor. Such models have been investigated and applied for studies in immunodeficient mice [50, 59, 61, 90, 93]. New approaches also use zebrafish or chick embryos for studies on the metastatic behavior of human metastatic uveal melanoma cell lines [72, 94]. Since some uveal "metastatic" cell lines which were thought to originate from metastases turned out to be most likely of primary origin [97], obtained data with these cell lines needs to be interpreted carefully.

Overall, these animal models of metastasis may offer a more detailed investigation of the biological behavior of metastatic uveal melanoma cells in the liver or allow for screening of novel antimetastatic compounds [93]. According to a specific research aspect the adequate cell line and model animal need to be carefully selected. However, a potent model which resembles the dissemination process from an intraocular uveal melanoma into the blood stream in an immunocompetent animal is still missing.

2.5. Induced Models. Animals may characteristically develop neoplastic proliferation or tumors after exposure to a given carcinogen or a cancer-causing agent. The agent may be of chemical, radiational, physical, or biological origin and the impact may result in alterations and mutations that lead to uncontrolled cell growth. Certain intraocularly injected oncogenic viruses are capable of inducing neoplasms including melanomas [87, 88]. Two-stage carcinogenesis by chemicals or radiation in pigmented rabbits [89] and other early attempts of induced ocular melanoma resulted in intraocular tumors but did not lead to reproducible animal models [18]. Due to uncontrolled and undirected carcinogenesis this approach barely offers controllability and reproducibility and subsequently does not qualify as a useful animal model. However, treating transgenic mice which harbor a predisposing genetic alteration in an oncogene responsible for uveal melanocytic proliferation might provide an opportunity of a new animal model. By intraocular application of a carcinogenic agent like 7,12-dimethylbenz[a]anthracene (DMBA) uveal tumorigenesis might be accelerated in a controlled manner. Such models already exist for other tumor entities like cutaneous melanoma [116] but have not been examined with respect to uveal melanoma, yet.

3. Conclusions

The development of animal models that recapitulate characteristics of human cancers and their clinical response to therapy are a major prerequisite for efficient bench-to-bedside translation and improvement of patients' prognosis, which overall is currently dismal. Research in this area for uveal melanoma has been seriously hampered by a lack of potent experimental *in vivo* models. Unlike other tumor

Table 1: Animal models of uveal melanoma.

	Strength	Limitation	Comment	References
Intraocular injection of syngeneic cutaneous melanoma cells	Intraocular melanoma in an immunocompetent animal, reliable reproducibility	Different genetic background, difficulties to achieve hematogenously spread metastasis	Qualifies for studies on the microenvironment (immunologic or angiogenic aspects)	In mice, [20–37] In rabbits, [18, 42–45]
Intraocular injection of human uveal melanoma cells	Human uveal melanoma: its progression and behavior can be investigated	Necessity of immunosuppression, equivocal permanent cell lines	Frequently used for evaluating treatment options or screening therapeutic agents	In mice, [35, 48–61] In rats, [58] In rabbits, [62–71] In zebrafish, [72]
Patient-derived xenografts (PDX)	Individualized investigation of tumor progression and screening of therapeutic compounds	Necessity of immunosuppression, fresh material not constantly available for research	To date, only preliminary studies for uveal melanoma, further research and refinement needed	In mice, [73–75]
Transgenic models of cutaneous melanoma	Spontaneous uveal proliferation in an immunocompetent animal	Different genetic background, no reliable metastasis	Spontaneous skin melanoma does not necessarily guarantee uveal proliferations	In mice, [76–85]
Transgenic models of uveal melanoma	Spontaneous uveal melanoma in an immunocompetent animal with a genetic background similar to human uveal melanoma	No reliable hematogenous metastasis to the liver yet	Promising basis which demands further research	In mice, [86] In zebrafish, [Rose, unpublished]
Induced models	Easy to induce	In wild type animals uncontrolled, undirected tumorigenesis	If performed in transgenic animals potentially a promising approach	Viruses, [87, 88] Chemicals/radiation [89], reviewed in [18]
Models of liver metastasis	Investigation of behavior of metastatic uveal/cutaneous melanoma cells	No "true" metastatic process from a primary tumor, partially in immunosuppressed animals	If using metastatic cell lines, screening of novel antimetastatic compounds is possible	Primary human cell lines in mice, [49–51, 59, 60, 90–92] Primary human cell lines in rabbits, [64, 67] Metastatic human cell lines in mice, [50, 59, 61, 90, 93] Metastatic human cell lines in others, [72, 94]

entities, to date, all existing animal models of uveal melanoma exhibit limitations. However, these models represent the best available *in vivo* options and each model has its advantages, which may render it more suitable to address a respective scientific question (Table 1). In essence, syngeneic models suit best for immunologic and tumor biology aspects whereas human xenograft models are commonly used for evaluating treatment strategies. Most importantly, many efforts have been made on establishing transgenic mouse models of spontaneous and metastasizing uveal melanoma which recently provided first promising results.

These limitations in the availability of an integral animal model of uveal melanoma may have fundamentally contributed to delayed research progress. Despite enhanced and refined treatment procedures of the primary tumor, unfortunately, patients' prognosis has not improved significantly since the 1970s [8]. To move forward, it is necessary to better understand and adequately model the unique characteristics of uveal melanoma. Besides genetic attributes, this includes specific features of the ocular immune system leading to a characteristic intraocular tumor microenvironment, the hematogenous dissemination, and colonisation of the liver as well as finally dormancy and the angiogenic switch of hepatic micrometastases. Prevention of metastasis will be the key to improved prognosis. Basic research needs to further focus on the intraocular tumor characteristics and metastatic process of uveal melanoma in order to successfully generate a powerful animal model. This may lead to accelerated research progress on new therapeutic targets. Meanwhile, a better understanding of underlying genetic and molecular abnormalities of uveal melanoma may provide a great opportunity for further development of targeted and individualized

therapy regimes in order to improve the prognosis of patients with metastatic disease.

Recent advances in immunotherapy have been followed by a large number of clinical trials in different tumor entities. These new therapeutic strategies are now also being tested in uveal melanoma patients. However, many of these trials are based on results obtained from models of or patients with cutaneous melanoma or other tumor entities. The agents have rarely been tested in animal models of uveal melanoma because a powerful model does not exist and in the case of immunotherapeutics preclinical safety testing was accomplished earlier in other tumor entities. Hence, clinical efficacy of such new therapeutic strategies in uveal melanoma patients might be very variable or even disappointing.

Overall, in order to achieve an improvement in patients' outcomes a better understanding of the pathogenesis of uveal melanoma is required which may be accomplished by using effective *in vitro* methods like 3D tumor cultures or powerful animal models of intraocular melanoma. Established models may be further refined (improved injection techniques, authenticated or new cell lines) and based on existing limitations they need to be carefully selected for a respective scientific question. Basic research may further focus on the generation and establishment of a transgenic animal model as this type of model offers strong advantages regarding immunologic, genetic, and histopathologic aspects. To reliably test novel therapeutic regimes and accurately identify therapy responses a personalized approach seems to be most promising. Therefore, PDX models for testing compounds or combinatorial therapy regimes (including targeted gene therapy and immunotherapy) may offer the best option. Further research on this type of model is strongly needed in uveal melanoma. Hence, in future these different animal models should be the basis for both biological and pharmacological testing and for rational clinical trials, thereby guiding treatment decisions and eventually improving the prognosis in patients with uveal melanoma.

Competing Interests

The authors declare that there are no competing interests regarding the publication of this paper.

References

[1] I. W. Y. Mak, N. Evaniew, and M. Ghert, "Lost in translation: animal models and clinical trials in cancer treatment," *American Journal of Translational Research*, vol. 6, no. 2, pp. 114–118, 2014.

[2] D. G. Hackam and D. A. Redelmeier, "Translation of research evidence from animals to humans," *The Journal of the American Medical Association*, vol. 296, no. 14, pp. 1731–1732, 2006.

[3] G. Damia and M. D'Incalci, "Contemporary pre-clinical development of anticancer agents—what are the optimal preclinical models?" *European Journal of Cancer*, vol. 45, no. 16, pp. 2768–2781, 2009.

[4] A. J. Combest, P. J. Roberts, P. M. Dillon et al., "Genetically engineered cancer models, but not xenografts, faithfully predict anticancer drug exposure in melanoma tumors," *Oncologist*, vol. 17, no. 10, pp. 1303–1316, 2012.

[5] C. C. McLaughlin, X.-C. Wu, A. Jemal, H. J. Martin, L. M. Roche, and V. W. Chen, "Incidence of noncutaneous melanomas in the U.S," *Cancer*, vol. 103, no. 5, pp. 1000–1007, 2005.

[6] S. Mallone, E. De Vries, M. Guzzo et al., "Descriptive epidemiology of malignant mucosal and uveal melanomas and adnexal skin carcinomas in Europe," *European Journal of Cancer*, vol. 48, no. 8, pp. 1167–1175, 2012.

[7] G. Virgili, G. Gatta, L. Ciccolallo et al., "Incidence of uveal melanoma in Europe," *Ophthalmology*, vol. 114, no. 12, pp. 2309–2315.e2, 2007.

[8] A. D. Singh, M. E. Turell, and A. K. Topham, "Uveal melanoma: trends in incidence, treatment, and survival," *Ophthalmology*, vol. 118, no. 9, pp. 1881–1885, 2011.

[9] N.-Y. Yi, S.-A. Park, S.-W. Park et al., "Malignant ocular melanoma in a dog," *Journal of Veterinary Science*, vol. 7, no. 1, pp. 89–90, 2006.

[10] B. P. Wilcock and R. L. Peiffer Jr., "Morphology and behavior of primary ocular melanomas in 91 dogs," *Veterinary Pathology*, vol. 23, no. 4, pp. 418–424, 1986.

[11] H. H. Dietz, O. A. Jensen, and J. B. Jørgensen, "Malignant melanoma of the uvea in the dog," *Nordisk Veterinaermedicin*, vol. 38, no. 2, pp. 68–73, 1986.

[12] A. Bourguet, V. Piccicuto, E. Donzel, M. Carlus, and S. Chahory, "A case of primary choroidal malignant melanoma in a cat," *Veterinary Ophthalmology*, vol. 18, no. 4, pp. 345–349, 2015.

[13] R. W. Bellhorn and P. Henkind, "Intra-ocular malignant melanoma in domestic cats," *Transactions of the Ophthalmological Societies of the United Kingdom*, vol. 89, pp. 321–333, 1970.

[14] M. Planellas, J. Pastor, M. D. Torres, T. Peña, and M. Leiva, "Unusual presentation of a metastatic uveal melanoma in a cat," *Veterinary Ophthalmology*, vol. 13, no. 6, pp. 391–394, 2010.

[15] R. W. Bertoy, A. H. Brightman, and K. Regan, "Intraocular melanoma with multiple metastases in a cat," *Journal of the American Veterinary Medical Association*, vol. 192, no. 1, pp. 87–89, 1988.

[16] H. J. Davidson, G. L. Blanchard, C. A. Wheeler, and J. A. Render, "Anterior uveal melanoma, with secondary keratitis, cataract, and glaucoma, in a horse," *Journal of the American Veterinary Medical Association*, vol. 199, no. 8, pp. 1049–1050, 1991.

[17] J. C. L. Schuh, "Congenital intraocular melanoma in a calf," *Journal of Comparative Pathology*, vol. 101, no. 1, pp. 113–116, 1989.

[18] H. E. Grossniklaus, S. Dithmar, and D. M. Albert, "Animal models of uveal melanoma," *Melanoma Research*, vol. 10, no. 3, pp. 195–211, 2000.

[19] I. J. Fidler and G. L. Nicolson, "Organ selectivity for implantation survival and growth of B16 melanoma variant tumor lines," *Journal of the National Cancer Institute*, vol. 57, no. 5, pp. 1199–1202, 1976.

[20] H. E. Grossniklaus, B. C. Barron, and M. W. Wilson, "Murine model of anterior and posterior ocular melanoma," *Current Eye Research*, vol. 14, no. 5, pp. 399–404, 1995.

[21] M. M. Kilian, K. U. Loeffler, C. Pfarrer, F. G. Holz, C. Kurts, and M. C. Herwig, "Intravitreally injected HCmel12 melanoma cells serve as a mouse model of tumor biology of intraocular melanoma," *Current Eye Research*, vol. 41, no. 1, pp. 121–128, 2016.

[22] C. E. Diaz, D. Rusciano, S. Dithmar, and H. E. Grossniklaus, "B16LS9 melanoma cells spread to the liver from the murine ocular posterior compartment (PC)," *Current Eye Research*, vol. 18, no. 2, pp. 125–129, 1999.

[23] J. Y. Niederkorn, "Enucleation in consort with immunologic impairment promotes metastasis of intraocular melanomas in mice," *Investigative Ophthalmology and Visual Science*, vol. 25, no. 9, pp. 1080–1086, 1984.

[24] J. De Lange, L. V. Ly, K. Lodder et al., "Synergistic growth inhibition based on small-molecule p53 activation as treatment for intraocular melanoma," *Oncogene*, vol. 31, no. 9, pp. 1105–1116, 2012.

[25] Q. Zhang, H. Yang, S. J. Kang et al., "In vivo high-frequency, contrast-enhanced ultrasonography of uveal melanoma in mice: imaging features and histopathologic correlations," *Investigative Ophthalmology and Visual Science*, vol. 52, no. 5, pp. 2662–2668, 2011.

[26] T. L. Knisely and J. Y. Niederkorn, "Immunologic evaluation of spontaneous regression of an intraocular murine melanoma," *Investigative Ophthalmology and Visual Science*, vol. 31, no. 2, pp. 247–257, 1990.

[27] L. V. Ly, A. Baghat, M. Versluis et al., "In aged mice, outgrowth of intraocular melanoma depends on proangiogenic M2-type macrophages," *Journal of Immunology*, vol. 185, no. 6, pp. 3481–3488, 2010.

[28] H. Yang and H. E. Grossniklaus, "Combined immunologic and anti-angiogenic therapy reduces hepatic micrometastases in a murine ocular melanoma model," *Current Eye Research*, vol. 31, no. 6, pp. 557–562, 2006.

[29] J. M. Lattier, H. Yang, S. Crawford, and H. E. Grossniklaus, "Host pigment epithelium-derived factor (PEDF) prevents progression of liver metastasis in a mouse model of uveal melanoma," *Clinical and Experimental Metastasis*, vol. 30, no. 8, pp. 969–976, 2013.

[30] L. Chen, S. Zhang, X. Li et al., "A pilot study of vasculogenic mimicry immunohistochemical expression in intraocular melanoma model," *Oncology Reports*, vol. 21, no. 4, pp. 989–994, 2009.

[31] M. el Filali, L. V. Ly, G. P. M. Luyten et al., "Bevacizumab and intraocular tumors: an intriguing paradox," *Molecular Vision*, vol. 18, pp. 2454–2467, 2012.

[32] H. Yang and H. E. Grossniklaus, "Constitutive overexpression of pigment epithelium-derived factor inhibition of ocular melanoma growth and metastasis," *Investigative Ophthalmology and Visual Science*, vol. 51, no. 1, pp. 28–34, 2010.

[33] S. Dithmar, D. Rusciano, and H. E. Grossniklaus, "A new technique for implantation of tissue culture melanoma cells in a murine model of metastatic ocular melanoma," *Melanoma Research*, vol. 10, no. 1, pp. 2–8, 2000.

[34] I. D. Fabian, M. Rosner, I. Fabian et al., "Low thyroid hormone levels improve survival in murine model for ocular melanoma," *Oncotarget*, vol. 6, no. 13, pp. 11038–11046, 2015.

[35] H. Yang, M. J. Jager, and H. E. Grossniklaus, "Bevacizumab suppression of establishment of micrometastases in experimental ocular melanoma," *Investigative Ophthalmology and Visual Science*, vol. 51, no. 6, pp. 2835–2842, 2010.

[36] J. Niederkorn, G. E. Sanborn, and E. E. Scarbrough, "Mouse model of brachytherapy in consort with enucleation for treatment of malignant intraocular melanoma," *Archives of Ophthalmology*, vol. 108, no. 6, pp. 865–868, 1990.

[37] S. Xue, H. Yang, J. Qiao et al., "Protein MRI contrast agent with unprecedented metal selectivity and sensitivity for liver cancer imaging," *Proceedings of the National Academy of Sciences of the United States of America*, vol. 112, no. 21, pp. 6607–6612, 2015.

[38] H. S. Greene and E. K. Harvey, "The growth and metastasis of amelanotic melanomas in heterologous hosts," *Cancer Research*, vol. 26, no. 4, pp. 706–714, 1966.

[39] A. Bomirski, A. Słominski, and J. Bigda, "The natural history of a family of transplantable melanomas in hamsters," *Cancer and Metastasis Review*, vol. 7, no. 2, pp. 95–118, 1988.

[40] B. Romanowska-Dixon, K. Urbanska, M. Elas, S. Pajak, H. Zygulska-Mach, and A. Miodonski, "Angiomorphology of the pigmented Bomirski melanoma growing in hamster eye," *Annals of Anatomy*, vol. 183, no. 6, pp. 559–565, 2001.

[41] R. P. Burns and F. T. Fraunfelder, "Experimental intraocular malignant melanoma in the Syrian Golden hamster," *American Journal of Ophthalmology*, vol. 51, no. 5, pp. 977–993, 1961.

[42] D. L. Krohn, R. Brandt, D. A. Morris, and A. S. Keston, "Subchoroidal transplantation of experimental malignant melanoma," *American Journal of Ophthalmology*, vol. 70, no. 5, pp. 753–756, 1970.

[43] F. H. Lambrou, M. Chilbert, W. F. Mieler, G. A. Williams, and K. Olsen, "A new technique for subchoroidal implantation of experimental malignant melanoma," *Investigative Ophthalmology and Visual Science*, vol. 29, no. 6, pp. 995–998, 1988.

[44] M. Krause, K. K. Kwong, J. Xiong, E. S. Gragoudas, and L. H. Y. Young, "MRI of blood volume and cellular uptake of superparamagnetic iron in an animal model of choroidal melanoma," *Ophthalmic Research*, vol. 34, no. 4, pp. 241–250, 2002.

[45] L. K. Hu, K. Huh, E. S. Gragoudas, and L. H. Y. Young, "Establishment of pigmented choroidal melanomas in a rabbit model," *Retina*, vol. 14, no. 3, pp. 264–269, 1994.

[46] K. G. Griewank, H. Westekemper, R. Murali et al., "Conjunctival melanomas harbor BRAF and NRAS mutations and copy number changes similar to cutaneous and mucosal melanomas," *Clinical Cancer Research*, vol. 19, no. 12, pp. 3143–3152, 2013.

[47] J. M. Mehnert and H. M. Kluger, "Driver mutations in melanoma: lessons learned from bench-to-bedside studies," *Current Oncology Reports*, vol. 14, no. 5, pp. 449–457, 2012.

[48] D. Ma, R. D. Gerard, X.-Y. Li, H. Alizadeh, and J. Y. Niederkorn, "Inhibition of metastasis of intraocular melanomas by adenovirus-mediated gene transfer of plasminogen activator inhibitor type 1 (PAI-1) in an athymic mouse model," *Blood*, vol. 90, no. 7, pp. 2738–2746, 1997.

[49] D. Ma, G. P. Luyten, T. M. Luider, M. J. Jager, and J. Y. Niederkorn, "Association between NM23-H1 gene expression and metastasis of human uveal melanoma in an animal model," *Investigative Ophthalmology and Visual Science*, vol. 37, no. 11, pp. 2293–2301, 1996.

[50] D. Ma and J. Y. Niederkorn, "Role of epidermal growth factor receptor in the metastasis of intraocular melanomas," *Investigative Ophthalmology and Visual Science*, vol. 39, no. 7, pp. 1067–1075, 1998.

[51] J. Y. Niederkorn, J. Mellon, M. Pidherney, E. Mayhew, and R. Anand, "Effect of anti-ganglioside antibodies on the metastatic spread of intraocular melanomas in a nude mouse model of human uveal melanoma," *Current Eye Research*, vol. 12, no. 4, pp. 347–358, 1993.

[52] A. J. Mueller, A. J. Maniotis, W. R. Freeman et al., "An orthotopic model for human uveal melanoma in SCID mice," *Microvascular Research*, vol. 64, no. 2, pp. 207–213, 2002.

[53] X. L. Xu, D.-N. Hu, C. Iacob et al., "Effects of zeaxanthin on growth and invasion of human uveal melanoma in nude mouse model," *Journal of Ophthalmology*, vol. 2015, Article ID 392305, 8 pages, 2015.

[54] M. R. Miller, J. B. Mandell, K. M. Beatty et al., "Splenectomy promotes indirect elimination of intraocular tumors by $CD8^+$ T cells that is associated with IFNgamma- and Fas/FasL-dependent activation of intratumoral macrophages," *Cancer Immunology Research*, vol. 2, no. 12, pp. 1175–1185, 2014.

[55] K. Hu, S. Babapoor-Farrokhran, M. Rodrigues et al., "Hypoxia-inducible factor 1 upregulation of both VEGF and ANGPTL4 is required to promote the angiogenic phenotype in uveal melanoma," *Oncotarget*, vol. 7, no. 7, pp. 7816–7828, 2016.

[56] F.-X. Yu, J. Luo, J.-S. Mo et al., "Mutant Gq/11 promote uveal melanoma tumorigenesis by activating YAP," *Cancer Cell*, vol. 25, no. 6, pp. 822–830, 2014.

[57] K. A. Matatall, O. A. Agapova, M. D. Onken, L. A. Worley, A. M. Bowcock, and J. W. Harbour, "BAP1 deficiency causes loss of melanocytic cell identity in uveal melanoma," *BMC Cancer*, vol. 13, article 371, 2013.

[58] R. D. Braun and K. S. Vistisen, "Modeling human choroidal melanoma xenograft growth in immunocompromised rodents to assess treatment efficacy," *Investigative Ophthalmology and Visual Science*, vol. 53, no. 6, pp. 2693–2701, 2012.

[59] O. Surriga, V. K. Rajasekhar, G. Ambrosini, Y. Dogan, R. Huang, and G. K. Schwartz, "Crizotinib, a c-met inhibitor, prevents metastasis in a metastatic uveal melanoma model," *Molecular Cancer Therapeutics*, vol. 12, no. 12, pp. 2817–2826, 2013.

[60] H. Yang, G. Fang, X. Huang, J. Yu, C.-L. Hsieh, and H. E. Grossniklaus, "In-vivo xenograft murine human uveal melanoma model develops hepatic micrometastases," *Melanoma Research*, vol. 18, no. 2, pp. 95–103, 2008.

[61] G. Barisione, M. Fabbi, A. Gino et al., "Potential role of soluble c-Met as a new Candidate biomarker of metastatic uveal melanoma," *JAMA Ophthalmology*, vol. 133, no. 9, pp. 1013–1021, 2015.

[62] P. E. Liggett, G. Lo, K. J. Pince, N. A. Rao, S. G. Pascal, and J. Kan-Mitchel, "Heterotransplantation of human uveal melanoma," *Graefe's Archive for Clinical and Experimental Ophthalmology*, vol. 231, no. 1, pp. 15–20, 1993.

[63] A. J. Mueller, R. Folberg, W. R. Freeman et al., "Evaluation of the human choroidal melanoma rabbit model for studying microcirculation patterns with confocal ICG and histology," *Experimental Eye Research*, vol. 68, no. 6, pp. 671–678, 1999.

[64] G. Blanco, M. A. Saornil, E. Domingo et al., "Uveal melanoma model with metastasis in rabbit: effects of different doses of cyclosporine A," *Current Eye Research*, vol. 21, no. 3, pp. 740–747, 2000.

[65] P. Bonicel, J. Michelot, F. Bacin et al., "Establishment of IPC 227 cells as human xenografts in rabbits: a model of uveal melanoma," *Melanoma Research*, vol. 10, no. 5, pp. 445–450, 2000.

[66] R. López-Velasco, A. Morilla-Grasa, M. A. Saornil-Álvarez et al., "Efficacy of five human melanocytic cell lines in experimental rabbit choroidal melanoma," *Melanoma Research*, vol. 15, no. 1, pp. 29–37, 2005.

[67] P. L. Blanco, J. C. A. Marshall, E. Antecka et al., "Characterization of ocular and metastatic uveal melanoma in an animal model," *Investigative Ophthalmology and Visual Science*, vol. 46, no. 12, pp. 4376–4382, 2005.

[68] S. J. Kang, Q. Zhang, S. R. Patel et al., "In vivo high-frequency contrast-enhanced ultrasonography of choroidal melanoma in rabbits: imaging features and histopathologic correlations," *British Journal of Ophthalmology*, vol. 97, no. 7, pp. 929–933, 2013.

[69] S. Di Cesare, S. Maloney, B. F. Fernandes et al., "The effect of blue light exposure in an ocular melanoma animal model," *Journal of Experimental and Clinical Cancer Research*, vol. 28, article 48, 2009.

[70] J.-C. A. Marshall, B. F. Fernandes, S. Di cesare et al., "The use of a cyclooxygenase-2 inhibitor (Nepafenac) in an ocular and metastatic animal model of uveal melanoma," *Carcinogenesis*, vol. 28, no. 9, pp. 2053–2058, 2007.

[71] J.-C. Marshall, A. Nantel, P. Blanco, J. Ash, S. R. Cruess, and M. N. Burnier Jr., "Transcriptional profiling of human uveal melanoma from cell lines to intraocular tumors to metastasis," *Clinical and Experimental Metastasis*, vol. 24, no. 5, pp. 353–362, 2007.

[72] W. van der Ent, C. Burrello, A. F. A. S. Teunisse et al., "Modeling of human uveal melanoma in zebrafish xenograft embryos," *Investigative Ophthalmology & Visual Science*, vol. 55, no. 10, pp. 6612–6622, 2014.

[73] S. Heegaard, M. Spang-Thomsen, and J. U. Prause, "Establishment and characterization of human uveal malignant melanoma xenografts in nude mice," *Melanoma Research*, vol. 13, no. 3, pp. 247–251, 2003.

[74] F. Némati, C. de Montrion, G. Lang et al., "Targeting Bcl-2/Bcl-XL induces antitumor activity in uveal melanoma patient-derived xenografts," *PLoS ONE*, vol. 9, no. 1, Article ID e80836, 2014.

[75] F. Némati, X. Sastre-Garau, C. Laurent et al., "Establishment and characterization of a panel of human uveal melanoma xenografts derived from primary and/or metastatic tumors," *Clinical Cancer Research*, vol. 16, no. 8, pp. 2352–2362, 2010.

[76] M. M. Kilian, M. C. Herwig, F. G. Holz, T. Tüting, and K. U. Loeffler, "Overexpression of hepatocyte growth factor and an oncogenic CDK4 variant in mice alters corneal stroma morphology but does not lead to spontaneous ocular melanoma," *Melanoma Research*, vol. 26, no. 1, pp. 89–91, 2016.

[77] N. A. Syed, J. J. Windle, S. R. Darjatmoko et al., "Transgenic mice with pigmented intraocular tumors: tissue of origin and treatment," *Investigative Ophthalmology & Visual Science*, vol. 39, no. 13, pp. 2800–2805, 1998.

[78] D. M. Albert, A. Kumar, S. A. Strugnell et al., "Effectiveness of 1α-hydroxyvitamin D2 in inhibiting tumor growth in a murine transgenic pigmented ocular tumor model," *Archives of Ophthalmology*, vol. 122, no. 9, pp. 1365–1369, 2004.

[79] T. R. Kramer, M. B. Powell, M. M. Wilson, J. Salvatore, and H. E. Grossniklaus, "Pigmented uveal tumours in a transgenic mouse model," *British Journal of Ophthalmology*, vol. 82, no. 8, pp. 953–960, 1998.

[80] W. H. Tolleson, J. C. Doss, J. Latendresse et al., "Spontaneous uveal amelanotic melanoma in transgenic Tyr-RAS+ Ink4a/Arf−/− mice," *Archives of Ophthalmology*, vol. 123, no. 8, pp. 1088–1094, 2005.

[81] J. R. Latendresse, L. Muskhelishvili, A. Warbritton, and W. H. Tolleson, "Two cases of uveal amelanotic melanoma in transgenic Tyr-HRAS+ Ink4a/Arf heterozygous mice," *Toxicologic Pathology*, vol. 35, no. 6, pp. 827–832, 2007.

[82] J. Eyles, A.-L. Puaux, X. Wang et al., "Tumor cells disseminate early, but immunosurveillance limits metastatic outgrowth, in a mouse model of melanoma," *The Journal of Clinical Investigation*, vol. 120, no. 6, pp. 2030–2039, 2010.

[83] Y. K. Pin, K. Khoo, M. Tham et al., "Lymphadenectomy promotes tumor growth and cancer cell dissemination in the spontaneous RET mouse model of human uveal melanoma," *Oncotarget*, vol. 6, no. 42, pp. 44806–44818, 2015.

[84] M. Tham, K. Khoo, K. P. Yeo et al., "Macrophage depletion reduces postsurgical tumor recurrence and metastatic growth in a spontaneous murine model of melanoma," *Oncotarget*, vol. 6, no. 26, pp. 22857–22868, 2015.

[85] S. Schiffner, B. M. Braunger, M. M. de Jel, S. E. Coupland, E. R. Tamm, and A. K. Bosserhoff, "Tg(*Grm1*) transgenic mice: a murine model that mimics spontaneous uveal melanoma in humans?" *Experimental Eye Research*, vol. 127, pp. 59–68, 2014.

[86] J. L.-Y. Huang, O. Urtatiz, and C. D. Van Raamsdonk, "Oncogenic G protein GNAQ induces uveal melanoma and intravasation in mice," *Cancer Research*, vol. 75, no. 16, pp. 3384–3397, 2015.

[87] D. M. Albert, J. A. Shadduck, J. L. Craft, and J. Y. Niederkorn, "Feline uveal melanoma model induced with feline sarcoma virus," *Investigative Ophthalmology & Visual Science*, vol. 20, no. 5, pp. 606–624, 1981.

[88] D. M. Albert, A. S. Rabson, and A. J. Dalton, "In vitro neoplastic transformation of uveal and retinal tissue by oncogenic DNA viruses," *Investigative Ophthalmology*, vol. 7, no. 4, pp. 357–365, 1968.

[89] J. Pe'er, R. Folberg, S. J. Massicotte et al., "Clinicopathologic spectrum of primary uveal melanocytic lesions in an animal model," *Ophthalmology*, vol. 99, no. 6, pp. 977–986, 1992.

[90] R. Folberg, L. Leach, K. Valyi-Nagy et al., "Modeling the behavior of uveal melanoma in the liver," *Investigative Ophthalmology & Visual Science*, vol. 48, no. 7, pp. 2967–2974, 2007.

[91] H. Li, H. Alizadeh, and J. Y. Niederkorn, "Differential expression of chemokine receptors on uveal melanoma cells and their metastases," *Investigative Ophthalmology & Visual Science*, vol. 49, no. 2, pp. 636–643, 2008.

[92] I. C. Notting, J. T. Buijs, I. Que et al., "Whole-body bioluminescent imaging of human uveal melanoma in a new mouse model of local tumor growth and metastasis," *Investigative Ophthalmology and Visual Science*, vol. 46, no. 5, pp. 1581–1587, 2005.

[93] S. Ozaki, R. Vuyyuru, K. Kageyama et al., "Establishment and characterization of orthotopic mouse models for human uveal melanoma hepatic colonization," *The American Journal of Pathology*, vol. 186, no. 1, pp. 43–56, 2016.

[94] H. Shahidipour, S. E. Coupland, D. Moss, B. E. Damato, and H. Kalirai, "Chick embryo model systems to study uveal melanoma metastasis," *Investigative Ophthalmology & Visual Science*, vol. 55, no. 13, article 5075, 2014.

[95] L. R. Kelland, "Of mice and men: values and liabilities of the athymic nude mouse model in anticancer drug development," *European Journal of Cancer*, vol. 40, no. 6, pp. 827–836, 2004.

[96] O. F. Kuzu, F. D. Nguyen, M. A. Noory, and A. Sharma, "Current state of animal (mouse) modeling in melanoma research," *Cancer Growth and Metastasis*, vol. 8, supplement 1, pp. 81–94, 2015.

[97] R. Folberg, S. S. Kadkol, S. Frenkel et al., "Authenticating cell lines in ophthalmic research laboratories," *Investigative Ophthalmology and Visual Science*, vol. 49, no. 11, pp. 4697–4701, 2008.

[98] K. G. Griewank, X. Yu, J. Khalili et al., "Genetic and molecular characterization of uveal melanoma cell lines," *Pigment Cell and Melanoma Research*, vol. 25, no. 2, pp. 182–187, 2012.

[99] X. Yu, G. Ambrosini, J. Roszik et al., "Genetic analysis of the 'uveal melanoma' C918 cell line reveals atypical BRAF and common KRAS mutations and single tandem repeat profile identical to the cutaneous melanoma C8161 cell line," *Pigment Cell and Melanoma Research*, vol. 28, no. 3, pp. 357–359, 2015.

[100] N. Amirouchene-Angelozzi, F. Nemati, D. Gentien et al., "Establishment of novel cell lines recapitulating the genetic landscape of uveal melanoma and preclinical validation of mTOR as a therapeutic target," *Molecular Oncology*, vol. 8, no. 8, pp. 1508–1520, 2014.

[101] D. Siolas and G. J. Hannon, "Patient-derived tumor xenografts: transforming clinical samples into mouse models," *Cancer Research*, vol. 73, no. 17, pp. 5315–5319, 2013.

[102] M. Hidalgo, F. Amant, A. V. Biankin et al., "Patient-derived xenograft models: an emerging platform for translational cancer research," *Cancer Discovery*, vol. 4, no. 9, pp. 998–1013, 2014.

[103] I. H. Bronkhorst and M. J. Jager, "Inflammation in uveal melanoma," *Eye*, vol. 27, no. 2, pp. 217–223, 2013.

[104] A. Richmond and S. Yingjun, "Mouse xenograft models vs GEM models for human cancer therapeutics," *Disease Models & Mechanisms*, vol. 1, no. 2-3, pp. 78–82, 2008.

[105] M. Kato, M. Takahashi, A. A. Akhand et al., "Transgenic mouse model for skin malignant melanoma," *Oncogene*, vol. 17, no. 14, pp. 1885–1888, 1998.

[106] C. D. Van Raamsdonk, V. Bezrookove, G. Green et al., "Frequent somatic mutations of GNAQ in uveal melanoma and blue naevi," *Nature*, vol. 457, no. 7229, pp. 599–602, 2009.

[107] C. D. Van Raamsdonk, K. G. Griewank, M. B. Crosby et al., "Mutations in GNA11 in uveal melanoma," *The New England Journal of Medicine*, vol. 363, no. 23, pp. 2191–2199, 2010.

[108] AJCC, "International validation of the American Joint Committee on Cancer's 7th edition classification of uveal melanoma," *JAMA Ophthalmology*, vol. 133, no. 4, pp. 376–383, 2015.

[109] J. A. Shields, C. L. Shields, and L. A. Donoso, "Management of posterior uveal melanoma," *Survey of Ophthalmology*, vol. 36, no. 3, pp. 161–195, 1991.

[110] E. Kujala, T. Mäkitie, and T. Kivelä, "Very long-term prognosis of patients with malignant uveal melanoma," *Investigative Ophthalmology & Visual Science*, vol. 44, no. 11, pp. 4651–4659, 2003.

[111] M. Diener-West, S. M. Reynolds, D. J. Agugliaro et al., "Development of metastatic disease after enrollment in the COMS trials for treatment of choroidal melanoma: Collaborative Ocular Melanoma Study Group Report No. 26," *Archives of Ophthalmology*, vol. 123, no. 12, pp. 1639–1643, 2005.

[112] J. J. Augsburger, Z. M. Corrêa, and A. H. Shaikh, "Effectiveness of treatments for metastatic uveal melanoma," *American Journal of Ophthalmology*, vol. 148, no. 1, pp. 119–127, 2009.

[113] J. K. V. Willson, D. M. Albert, M. Diener-West et al., "Assessment of metastatic disease status at death in 435 patients with large choroidal melanoma in the collaborative ocular melanoma study (coms) coms report no. 15," *Archives of Ophthalmology*, vol. 119, no. 5, pp. 670–676, 2001.

[114] C. L. Shields, S. Kaliki, M. Furuta, E. Fulco, C. Alarcon, and J. A. Shields, "American joint committee on cancer classification of uveal melanoma (anatomic stage) predicts prognosis in 7731 patients: the 2013 zimmerman lecture," *Ophthalmology*, vol. 122, no. 6, pp. 1180–1186, 2015.

[115] W. Yang, H. Li, E. Mayhew, J. Mellon, P. W. Chen, and J. Y. Niederkorn, "NKT cell exacerbation of liver metastases arising from melanomas transplanted into either the eyes or spleens of mice," *Investigative Ophthalmology & Visual Science*, vol. 52, no. 6, pp. 3094–3102, 2011.

[116] D. Tormo, A. Ferrer, E. Gaffal et al., "Rapid growth of invasive metastatic melanoma in carcinogen-treated hepatocyte growth factor/scatter factor-transgenic mice carrying an oncogenic CDK4 mutation," *The American Journal of Pathology*, vol. 169, no. 2, pp. 665–672, 2006.

Hindawi Publishing Corporation
BioMed Research International
Volume 2016, Article ID 5258727, 14 pages
http://dx.doi.org/10.1155/2016/5258727

Review Article

Animal Models of Cystic Fibrosis Pathology: Phenotypic Parallels and Divergences

Gillian M. Lavelle, Michelle M. White, Niall Browne, Noel G. McElvaney, and Emer P. Reeves

Respiratory Research Division, Department of Medicine, Royal College of Surgeons in Ireland, Beaumont Hospital, Dublin 9, Ireland

Correspondence should be addressed to Emer P. Reeves; emerreeves@rcsi.ie

Received 18 February 2016; Accepted 8 May 2016

Academic Editor: Oreste Gualillo

Cystic fibrosis (CF) is caused by mutations in the cystic fibrosis transmembrane conductance regulator (CFTR) gene. The resultant characteristic ion transport defect results in decreased mucociliary clearance, bacterial colonisation, and chronic neutrophil-dominated inflammation. Much knowledge surrounding the pathophysiology of the disease has been gained through the generation of animal models, despite inherent limitations in each. The failure of certain mouse models to recapitulate the phenotypic manifestations of human disease has initiated the generation of larger animals in which to study CF, including the pig and the ferret. This review will summarise the basic phenotypes of three animal models and describe the contributions of such animal studies to our current understanding of CF.

1. Introduction

The Multiorgan Pathology of Cystic Fibrosis. In 1989 the CFTR gene was identified and isolated from epithelial cells of the pancreas, lungs, colon, sweat glands, and nasal polyps of healthy control individuals [1, 2]. By facilitating ion transport into and out of the cell, CFTR function results in hydration of the airways and normal airway surface liquid (ASL) volume. Adequate ASL permits optimal movement of airway cilia, whose function is to remove mucus containing proinflammatory mediators, immune cells, and inhaled pathogens from the lung. CF is an autosomal recessive inherited disorder caused by mutations within the CFTR gene [2], leading to increased morbidity at a young age [3]. CF affects 70,000 people worldwide [4] and is characterised by defective CFTR function, resulting in decreased chloride (Cl^-) secretion and hyperabsorption of sodium (Na^+). Reduced ion transport significantly dehydrates the airway mucus leading to reduced ASL, preventing adequate removal of mucus *via* the mucociliary escalator [5]. Mucus-laden cilia become dyskinetic with the resultant pathological triad that hallmarks CF: chronic airway mucus build-up, microbe trapping, and sustained inflammation involving persistent inflammatory cell influx to the lungs, leading to pulmonary function loss and poorer clinical outcome [6, 7].

Although the chronic pathology of the lung represents the most serious clinical manifestation [8, 9], CF is a multiorgan disease. Extrapulmonary clinical manifestations of CF include impairment of the gastrointestinal (GI) tract. For example, meconium ileus (MI), a condition caused by increased viscosity of the intestinal mucus within hours of birth, occurs in 13% to 17% of infants with CF [10]. The CFTR protein is also expressed on the apical membrane of pancreatic epithelial cells. Here, it modulates Cl^- absorption and secretion of bicarbonate, an important buffer for maintaining optimum pH. Inspissated mucus obstruction, secondary to dysfunctional CFTR in the pancreas, perpetuates localised inflammation and pancreatic scarring. Common pathologies associated with this organ in CF include pancreatic insufficiency, pancreatitis, glucose intolerance, and CF-related diabetes mellitus [11]. In this regard, CFTR plays an important

role in the secretion of pancreatic proenzymes (e.g., zymogen) into the duodenum and poor endocrine function, as occurs in CF, results in malabsorption of nutrients including fat-soluble vitamins, cholesterol, and proteins, leading to poor weight gain and nutritional deficiency. CF can also affect the hepatobiliary system. Liver disease is caused by biliary obstruction and progressive periportal fibrosis, resulting in biliary cirrhosis. Although only 3.9% of children and 5.4% of adults with CF suffer from liver disease, it can be a fatal condition, with 4% of the CF population succumbing to liver disease in 2013 [12]. CF also impairs fertility, with 97% of males affected by sterility and a reduced likelihood of successful pregnancy in females [13, 14].

Animal models of CF are important as they have served to further our understanding of the mechanisms associated with CF disease progression and disease pathology and also assist in the development of new therapies to treat patients with CF. Until recently, many studies have centred on the mouse model. However, its use in understanding CF pathology is becoming less popular for a number of reasons. Firstly, mice have a short life span; therefore the progression of CF lung disease cannot be adequately studied in these animals. Of major importance, CF mice fail to develop spontaneous lung disease or chronic bacterial infections [15], unlike patients with CF. CF mice also express a CFTR-independent alternative Cl^- channel meaning that CFTR-deficient mice still secrete Cl^-, thereby compensating for dysfunctional CFTR.

In light of this, researchers have moved towards animals that have similar pathological outcomes to humans in terms of CF. A CFTR knockout pig model and a pig harbouring the Δ*F508* mutation were developed in 2008 [16]. This animal is favoured for many reasons; firstly, pigs have a long life span, therefore allowing researchers to study CF disease progression over time and the efficacy of long-term therapeutics. Interestingly, even though newborn CFTR-deficient pigs have similar numbers of airway neutrophils and IL-8 levels compared to wild type (WT) pigs, they still develop spontaneous lung disease. The lungs of newborn CF piglets infected with *Staphylococcus aureus* (*S. aureus*) failed to eradicate infection, stimulating the debate as to whether airway inflammation or infection occurs first [17].

The ferret is another well-characterised animal model that is now being routinely used for CF research. CFTR expression in ferrets is identical to humans and, like pigs, they have a long life span. CFTR-deficient neonatal ferrets exhibit similar phenotypic characteristics to humans, including liver disease, pancreatic disease, and spontaneous lung infections [18]. CFTR-deficient ferrets also have lower BMI and demonstrate impaired mucus clearance [19]. Furthermore, CF ferrets fail to successfully eradicate lung infections [20] although bronchoalveolar lavage fluid (BALF) of newborn ferrets have increased levels of IL-8 and tumor necrosis factor- (TNF-) α, as described for humans with CF [20].

In this review we will discuss how the CF mouse, pig, and ferret models have enhanced our knowledge of CF pathology and have furthered our understanding of CF disease. This review of the literature was carried out using the MEDLINE database, Google Scholar, and The Cochrane Library databases using several appropriate generic terms.

2. The Effect of CFTR Mutations on Membrane Channel Abundance and Activity

An understanding of CFTR function, and CFTR mutations impacting on channel activity, is required prior to the description of animal models of CF-related disease. Under normal conditions the CFTR protein functions as a Cl^- channel pumping Cl^- ions out of the cell. CFTR also functions as a regulator of other ions, including Na^+, by negatively regulating the epithelial Na^+ channel (ENaC) [21, 22]. ENaC, also known as sodium channel nonneuronal 1 (Scnn1), is an amiloride-sensitive ion channel responsible for the transepithelial transport of Na^+ ions. Structurally, the ENaC protein comprises three distinct α, β, and γ subunits encoded by the *Scnn1a*, *Scnn1b*, and *Scnn1c* genes, respectively [23]. Each subunit contains two transmembrane domains, an extracellular loop, and short N and C termini. A fourth (δ) subunit of ENaC has been described but remains comparably underexplored [24, 25]. Dysfunctional CFTR combined with increased ENaC activity in CF results in the inhibition of normal Cl^- secretion to the apical surface of airway epithelium and significant Na^+ hyperabsorption, followed by an osmotically driven efflux of water to the basolateral membrane. The resultant dehydrated ASL volume significantly impairs mucociliary clearance [26]. In line with this, CF neutrophils have been shown to contain increased concentrations of both Na^+ and Cl^- ions, secondary to impaired CFTR function [27]. ENaC impairment has also been linked to diseases beyond CF, including Liddle disease and pseudohyperaldosteronism [28]. CFTR also controls potassium (K^+) transport by regulating the renal outer medullar potassium channel (ROMK) (Figure 1) [29].

Over 2000 CFTR mutations have been identified to date [30] and are divided into 6 categories based on their loss-of-function effect on protein translation, cellular processing, or channel gating of CFTR (Figure 2). Missense (single amino acid change) mutations account for 39.71% of all CFTR mutations, frameshift mutations (insertions or deletions) account for 15.66%, splicing mutations (affecting the splicing of introns) account for 11.45%, and nonsense (insertion of a premature stop codon) mutations account for 8.28% of CFTR mutations worldwide [30]. Class I mutations impair protein synthesis. Premature stop codons encountered by ribosomes give rise to the early termination of CFTR protein translation. The resultant truncated CFTR, a result of a frameshift or nonsense mutation, is degraded within the endoplasmic reticulum (ER) and does not reach the cell surface [12, 31]. Class II mutations affect the maturation of the CFTR protein and are characterised by missense mutations. Improper processing of the CFTR protein causes protein misfolding. Misfolded CFTR is targeted for degradation within the ER, and thus the unstable protein does not reach the apical cell membrane. The Δ*F508* mutation is Class II mutation and is caused by deletion of a phenylalanine residue at position 508 within the CFTR gene [31]. The Δ*F508* mutation is a severe mutation and is the most common mutation with over 90% of people with CF heterozygous for the Δ*F508* mutation [12]. Class III mutations are known as gating defects and affect the opening of the CFTR channel by controlling adenosine triphosphate- (ATP-)

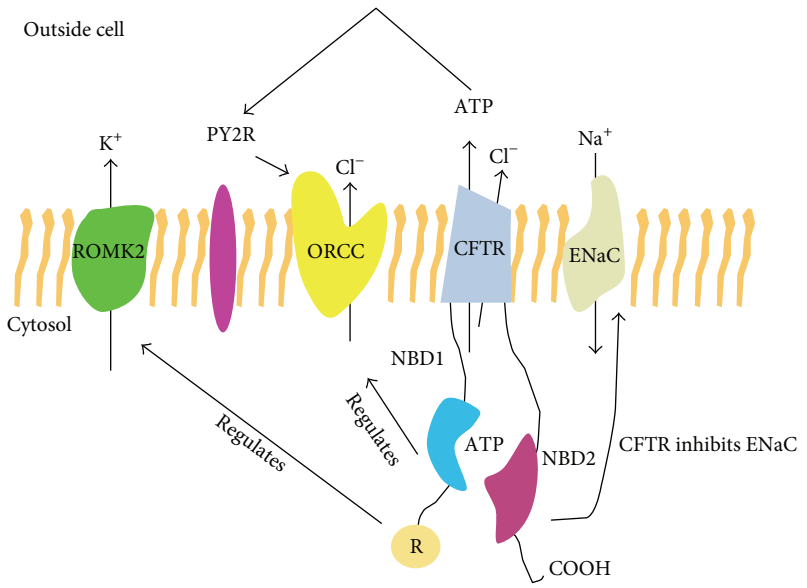

Figure 1: The role of CFTR in regulating additional ion channels. CFTR regulates many ion channels. CFTR primarily functions as a Cl^- channel. However, it also has a role in regulating the transport of K^+ through renal outer medullar potassium channel (ROMK2). ROMK2 interacts with the intracellular cytoplasmic nucleotide-binding domains 1 (NBD1) and the regulatory (R) domain. CFTR can regulate the activity of outwardly rectified Cl^- channel (ORCC) through the binding of ATP to the purinergic receptor (PY2R). CFTR can also inhibit ENaC, therefore regulating Na^+ transport into the cell.

binding and hydrolysis [31]. Although CFTR is processed correctly and is stably expressed on the cell membrane, the gating performance of this mutant is heavily impaired. The *G551D* mutation is a Class III mutation and is caused by a missense mutation at nucleotide 1784, resulting in a change from a glycine to an aspartate residue. Due to this mutation, the channel is held in the closed conformation, thus blocking Cl^- transport.

Classes IV, V, and VI mutations are relatively less severe than the first three classes because they still retain residual CFTR function at the cell surface. As a result of these mutations, Cl^- conductance may be reduced (Class IV), CFTR splicing may reduce protein function at the cell surface (Class V), or accelerated protein turnover may reduce CFTR half-life at the cell surface [12, 31, 32] (Figure 2).

3. CF Treatment Options

The treatment of CF involves therapeutics for management of the symptoms and potential correction of the CFTR protein. For symptomatic management of the disease, current mainstay treatments include hypertonic saline (HTS) which can be used to improve mucociliary airway clearance in patients with CF [33]. HTS consisting of 3–7% sodium chloride (NaCl) rehydrates the airways, reduces the mucosal load [34], and increases the clearance of the lung. HTS dilutes the mucus, by causing the airway cells to release water, thus restoring the moisture layer, facilitating easier removal of mucus by coughing, and reducing levels of proinflammatory mediators [35, 36]. Other treatments are also available to alleviate mucus build-up. The aerosolised mucolytic enzyme recombinant DNase (rhDNase) or its trade name Pulmozyme® cleaves the extracellular DNA that is released from cells in biofilms during necrosis, therefore reducing the viscosity of the mucus. Reducing the viscoelasticity of airway mucus allows better access of antibiotics to targeted microbes buried deep within the mucus. It is currently the third most common long-term treatment for CF patients with 46% of children and 50% of adults with CF prescribed rhDNase in 2013 [12] and has been shown to improve lung function and reduce exacerbations within 6 months [3, 37]. Maintaining good nutritional status is important for patients with CF to maximise clinical outcomes. Supplementary pancreatic enzymes, vitamins, and minerals all form part of the symptomatic control of the disease [12]. If patient health continues to decline despite all available therapeutic avenues being explored, transplantation may be considered as the next intervention. It has been shown that lung transplants increase survival compared to predicted survival for those without transplant [38].

For many years, therapies for CF have involved symptomatic control of the secondary effects of CFTR dysfunction rather than curative treatment of the primary defect. Since the discovery of the CFTR gene in 1989, considerable focus has been directed towards the development of drugs such as correctors and potentiators to address the genetic defect in CF. To this end, high throughput screening has facilitated the development of therapeutics that treat the cause of the genetic disorder rather than the symptoms. Ion channel correctors and potentiators facilitate the correction and function of the defective CFTR protein. Ivacaftor (VX-770), or its registered name Kalydeco®, is an example of a potentiator drug produced by Vertex Pharmaceuticals (MA, USA) and is currently administered orally in patients with the *G551D* mutation. Ivacaftor addressed the issues associated

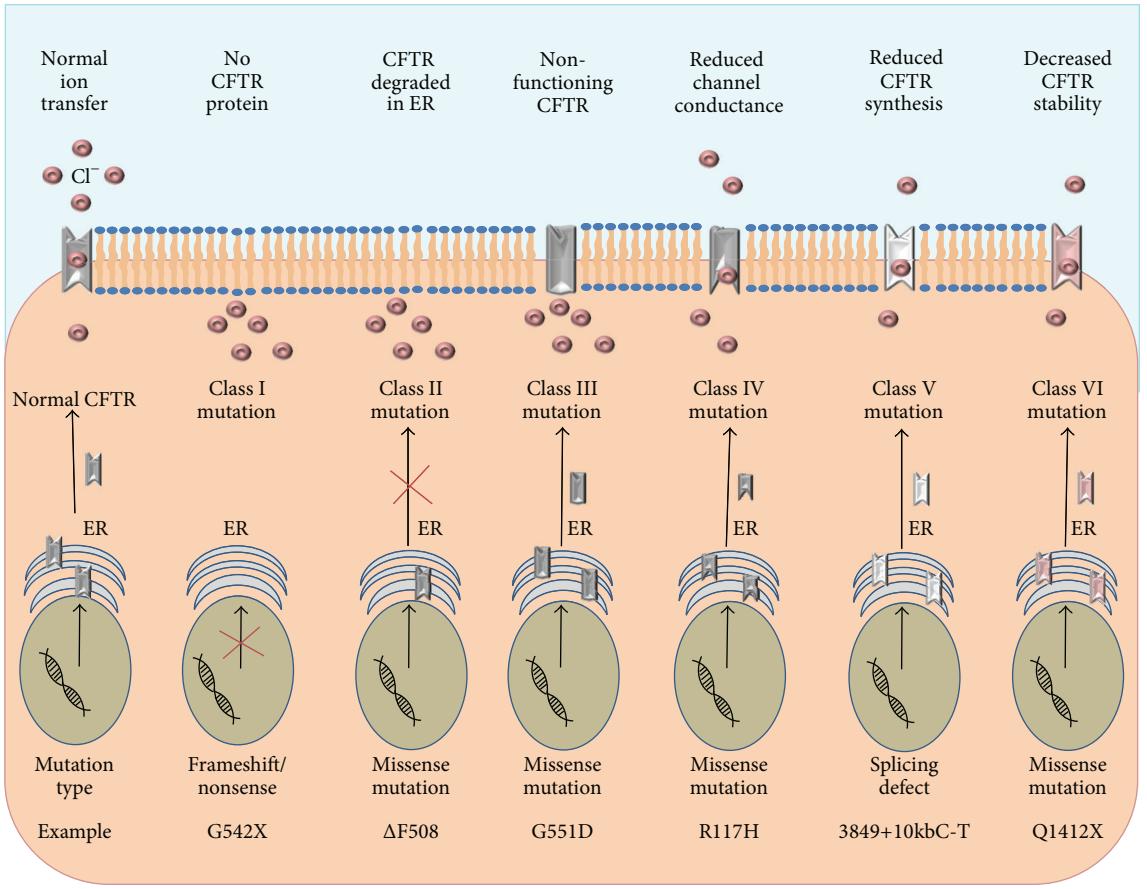

Figure 2: Classification of CFTR mutations. In healthy CFTR sufficient cells, the functional CFTR protein is correctly trafficked to the plasma membrane. Class I mutations result in a lack of CFTR protein synthesis. Class II mutations block CFTR processing, where misfolded protein is degraded in the ER. Class III mutations affect the regulation of the CFTR, where the CFTR channel is less functional. Class IV mutations alter the CFTR conductance of Cl^-. Class V mutations lead to reduced synthesis of functional CFTR. Class VI mutations result in accelerated turnover of CFTR protein on the cell surface.

with the gating defects of the mutated CFTR protein. In patients with the *G551D* mutation, the CFTR is present on the cell surface but is nonfunctional; therefore ivacaftor has been designed to increase the time for which the CFTR channel remains open, allowing for the transfer of ions into and out of the cell [39]. The CFTR potentiator increased FEV_1 by 10%, improved weight gain, reduced sweat Cl^-, and reduced exacerbations [40]. Reports are now emerging of the potential indirect benefits of ivacaftor as an anti-inflammatory. Rowe et al. reported that CF patients treated with ivacaftor had a marked increase in mucosal bacterial clearance [41]. In support of this, Reznikov et al. demonstrated a dose-dependent reduction of *S. aureus* with ivacaftor therapy *in vitro* [42]. Furthermore, Pohl et al. highlighted the importance of ivacaftor treatment for improved neutrophil degranulation [27]. Finally, Bratcher et al. identified the potential of ivacaftor to reduce CD11b expression on isolated neutrophils from patients on treatment [43].

The Δ*F508* mutation is the most common and severe CF mutation worldwide [30]. Ivacaftor administered to patients harbouring the Δ*F508* mutation did not induce improvements in FEV_1 or sweat Cl^- when compared to patients receiving placebo. Unlike the results observed for the *G551D* mutation, the potentiator did not directly repair the specific underlying defect of Class II mutations [44]. In contrast, corrector-type therapies enable the trafficking of the CFTR to the plasma membrane and have the potential to treat patients with the Δ*F508* mutation. Lumacaftor (VX-809) is an approved investigational corrector aimed at targeting the defective Δ*F508* mutation. A combination approach of the corrector VX-809 and potentiator VX-770 drug in phase 3 clinical trials demonstrated marginally improved lung function, reduced pulmonary exacerbations, and increased BMI in patients homozygous for the Δ*F508* mutation [45, 46]. This is a promising result and could improve the quality of life for the majority of patients with CF worldwide. On July 2, 2015, the Food and Drug Administration approved the combined lumacaftor/ivacaftor approach, known as Orkambi®, to treat Δ*F508* homozygote patients. This was a major breakthrough for CF patients, and although studies have demonstrated

marginal effects, the minimal positive clinical outcomes will no doubt improve the quality of life of patients [47].

4. The Use of Murine Models in the Study of CF

The characterisation of the CFTR gene in 1989 by positional cloning [2, 48] heralded new insights into the pathophysiology of CF disease and, merely three years after its discovery, the very first murine models of CF disease were described [49]. With an overall amino acid sequence homology of 78% between murine and human CFTR, these models have facilitated significant strides in our understanding of this complex and life-limiting disease [50]. The loss-of-function null murine model was first proposed as a model for CF by Snouwaert et al. at the University of North Carolina, in which they successfully generated a CFTR knockout ($CFTR^{tm1UNC}$) mouse from embryonic stem cells by insertion of a stop codon in exon 10 of the CFTR coding sequence, termed the *S489X* mutation [49]. These models were further developed upon by others to generate many knockout models on various genetic backgrounds including the $CFTR^{tm1CAM}$, $CFTR^{tm1HSC}$, $CFTR^{tm1BAY}$, and $CFTR^{tm3BAY}$ models [51–54]. In addition to the knockout model of CF, various knock-in mutants were also developed. Specific CF-causing mutations were introduced to the endogenous mouse CFTR gene to bear mice carrying the Class II Δ*F508* ($CFTR^{tm1EUR}$, $CFTR^{tm1KTH}$, and $CFTR^{tm2CAM}$) and *G480C* ($CFTR^{tm2HGU}$) mutations [55–58], followed by mutants carrying the Class III *G551D* mutation ($CFTR^{tm1G551D}$) [59]. However, intramutant variations in the survival, disease severity, and pathology of these animals have been reported. A list of CF mouse models is outlined in Table 1.

Although not a typical CFTR murine model, the "β-ENaC" mouse model has also been considered. As previously mentioned, the channel, in concert with CFTR-mediated Cl^- secretion, plays an important role in the proper regulation of ASL volume and in the adequate clearance of inhaled microorganisms and environmental particulates by the mucociliary escalator [65, 66].

4.1. Respiratory Tract Disease-Related Changes. As previously mentioned, CF airway disease in humans is characterised by dehydrated mucus, inflammation, and infection; and, accordingly, any mouse models used to study the disease should be representative of this [9, 67]. Where data is available, the nasal epithelium of most mouse models, including $CFTR^{tm1EUR}$, $CFTR^{tm2HGU}$, $CFTR^{tm1HGU}$, $CFTR^{tm1HSC}$, $CFTR^{tm1KTH}$, and $CFTR^{tm1G551D}$, mirrors the abnormal nasal electrophysiological profile seen in humans with CF with significant Na^+ hyperabsorption and increased amiloride-sensitive basal nasal potential difference (PD) compared to non-CF littermate mice [54–56, 58–60].

While the upper respiratory tract of the murine models is representative of the upper airways of humans with CF, the lower airways represent an entirely different picture. No CFTR mouse model developed spontaneous lung inflammation without challenge, limiting their usefulness in the study of pulmonary disease progression in CF. No lower airway epithelial abnormalities were reported for knockout models including $CFTR^{tm1UNC}$, $CFTR^{tm1CAM}$, $CFTR^{tm1BAY}$, and $CFTR^{tm1HGU}$ or in models carrying Δ*F508* and *G551D* alleles such as $CFTR^{tm1KTH}$, $CFTR^{tm1EUR}$, or $CFTR^{tm1G551D}$ [49, 51, 52, 55, 56, 59, 60]. The lack of severe spontaneous lung pathology in these mouse models has been partially attributed to the expression of a non-CFTR calcium-activated Cl^- channel (CACC) in certain mouse tissues and the fact that this expression serves to rectify the ion imbalance underlying CF lung disease. Of note, a congenic strain of the $CFTR^{tm1UNC}$ mouse model, termed B6-$CFTR^{tm1UNC}$, in which the murine-expressed alternative Cl^- channel was absent, did develop spontaneous lung disease including impaired mucociliary clearance and tissue fibrosis even when bred in a pathogen-free environment. These congenic mice also displayed impaired control of *Pseudomonas aeruginosa* (*P. aeruginosa*) infection [62, 68, 69]. The development of chronic pulmonary inflammation and bacterial persistence has been reported in the $CFTR^{tm1UNC}$ model following intranasal challenge with *Burkholderia cepacia* (*B. cepacia*; BC7), with increased neutrophil counts and cytokine levels in BC7-challenged mice compared to control animals [70]. Using a different approach, significant pulmonary inflammation and associated pathology were also induced in S489X mice following transtracheal delivery of *P. aeruginosa*-embodied agarose beads [71]. Furthermore, low ATP12A proton-pump expression levels in CF mice may allow for normal ASL pH and unimpaired airway host defences. Such findings may explain why CF mice exhibit increased protection from pulmonary infection [72]. Interestingly, in the β-ENaC mouse model, excessive ENaC activity, specifically an overexpression of the β-subunit of ENaC (β-ENaC), accelerated Na^+ absorption and induced a CF-like pulmonary clinical phenotype, including ASL depletion, significant airway mucus obstruction, and neutrophil-dominated inflammation, rendering it an important and relevant model for the study of CF lung disease. The β-ENaC mouse model not only demonstrated the critical importance of the β-subunit for optimal ENaC activity but also highlighted the mechanism between abnormal ion transport and ASL height and impaired mucociliary clearance in CF [23, 73].

4.2. Development of Intestinal Disease in CF Murine Models. As mentioned, CF encompasses many extrapulmonary manifestations in humans, including GI tract complications. Studies have documented significant CFTR expression throughout the GI tract, suggesting an important role for the ion channel in this milieu. Indeed, dysfunctional CFTR in the GI tract can lead to retained mucus secretions, MI, distal intestinal obstruction syndrome, intestinal dysmotility and dysbiosis, pancreatic insufficiency, and gastric reflux [11, 49, 74]. MI can develop *in utero* but is rarely life-threatening with vigilant screening and prompt surgical intervention available. Similarly, severe intestinal obstruction has been reported in many CF mouse models but unlike, in humans, develops postnatally and is associated with significant mortality. In fact, the intestinal complications exhibited by the CF murine

Table 1: Mouse models of cystic fibrosis.

Identifier	Mutation	Detectable CFTR mRNA	Salient features	Reference
CFTR^{tm1UNC}	Exon 10 replacement	No detectable WT CFTR mRNA	Severe intestinal complications	[49]
CFTR^{tm1CAM}	Exon 10 replacement	No detectable WT CFTR mRNA	Pancreatic ductal blockage Severe intestinal pathology	[51]
CFTR^{tm2CAM}	Δ*F508* Exon 10 replacement	Mutant mRNA 30% of WT CFTR levels	No pancreatic abnormalities Longer survival than null models	[57]
CFTR^{tm1BAY}	Exon 3 insertional duplication	<2% of WT CFTR mRNA	Severe intestinal complications	[52]
CFTR^{tm3BAY}	Exon 2 replacement	No detectable WT CFTR mRNA	Severe intestinal complications	[53]
CFTR^{tm1EUR}	Δ*F508* Exon 10 insertion (hit and run)	Mutant mRNA at normal WT levels	Nonlethal intestinal abnormalities; no pancreatic or liver abnormalities	[55]
CFTR^{tm1KTH}	Δ*F508* Exon 10 replacement	Decreased mutant mRNA in intestine	Impaired sperm transport within the female reproductive tract; no gallbladder pathology	[56]
CFTR^{tm1HGU}	Exon 10 insertion	10% of WT CFTR mRNA	Mild intestinal complications; longer survival	[60, 61]
CFTR^{tm2HGU}	*G480C* Exon 10 insertion (hit and run)	Mutant mRNA at normal WT levels	Nonlethal intestinal abnormalities	[58]
CFTR^{tm1HSC}	Exon 1 replacement	No detectable WT CFTR mRNA	Severe intestinal complications	[54]
CFTR^{tm1G551D}	*G551D* Exon 11 replacement	Mutant mRNA 53% of WT CFTR levels	Absent or mild (nonlethal) intestinal obstruction	[59]

CFTR: cystic fibrosis transmembrane conductance regulator; WT: *wild type*.
Adapted from [62–64].

models represent the most pronounced pathology of this model, rendering it an appropriate model in which to study CF intestinal disease [75, 76].

While variation in the degree of severity of intestinal disease exists, most models mirror the pathology reported for CFTR^{tm1UNC} and CFTR^{tm1BAY}, with severe intestinal complications including runting, goblet cell hyperplasia, mucus impaction, obstruction, crypt dilation, and death a common theme [49, 52–54, 63]. Interestingly, the CFTR^{tm1EUR} and CFTR^{tm2HGU} models (carrying the Class II Δ*F508* and *G480C* mutations, resp.) display intestinal abnormalities; however the mice do not suffer the same lethal intestinal obstruction observed in humans or in the knockout mice [55, 58]. Similarly, the CFTR^{tm1HGU} mouse model displays a considerably mild intestinal phenotype which is likely explained by the "leaky" nature of the exon 10 insertional mutation resulting in residual CFTR function [77]. A second Δ*F508* model, CFTR^{tm2CAM}, develops significant mucus impaction in the small intestine, jejunum, and colon with a mortality rate similar to that of the knockout models [57]. While the *G551D* model did portray some intestinal abnormalities, including obstruction, abnormal or absent villi, and necrotic and faecal material deposition in the small intestine, mortality rates were significantly lower than in the knockout murine model [59]. The survival and phenotypic differences observed between models likely result from variations in genetic background, pathogen exposure, and husbandry conditions used during the respective studies [50].

4.3. Pancreatic Disease in the CF Mouse Model. Another important facet of CF disease is severe structural and functional abnormalities of the pancreas, where CFTR plays a role in pancreatic duct secretion. However, murine models fail to develop pancreatic dysfunction with the same severity that humans do [11, 67]. The null knockout models such as CFTR^{tm1UNC} and CFTR^{tm1CAM} were reported to have only mild to moderate pathological changes to the pancreas, including slightly enlarged acini, luminal dilatation, or blockage of some pancreatic ducts compared to WT [49, 51]. Of note, Δ*F508* and *G551D* mouse models (CFTR^{tm2CAM}, CFTR^{tm1EUR}, CFTR^{tm1KTH}, and CFTR^{tm1G551D}) lack any pancreatic abnormalities at all [55–57, 59]. The significant disparity between the severe CF pancreatic phenotype observed in humans and the milder presentation in mice may be explained by very low levels of residual CFTR activity, sufficient to maintain ion secretion, in the pancreas of mice. Furthermore, the action of the alternative CFTR-independent CACC in the murine pancreas may result in more normalised Cl^- conductance and an improved pancreatic pathology [63, 67, 68].

4.4. Hepatobiliary Disease Development in Murine Models of CF. Liver disease has not been studied extensively in mouse models of CF disease. While liver abnormalities such as biliary cirrhosis were seen in some CFTR^{tm1G551D} mice [59], other models including CFTR^{tm1UNC} and CFTR^{tm1EUR} report no remarkable liver abnormalities [49, 55]. In humans, however, the onset of liver disease presents later in life, so, despite most mouse models displaying little or no obvious liver pathology, studies in older mice are warranted to elucidate the potential progression of this disease [62, 64]. Interestingly, two mouse models, CFTR^{tm1UNC} and CFTR^{tm1G551D}, were found to have distended/ruptured and bile-laden gallbladders with concurrent neutrophil-dominated localised inflammation, suggesting a potential role for these models in investigations into the formation and potential treatment of gallstones, which present frequently in humans with CF [49, 59, 62]. This is in contrast to the CFTR^{tm1KTH} in which no obvious gallbladder pathology was described [56].

4.5. Fertility and Reproductive Problems in the CF Mouse. Infertility is a common characteristic of CF affecting approximately 97% of males due to a congenital absence of the vas deferens resulting in azoospermia [14, 78]. However, many mouse models, including CFTR^{tm1CAM} and CFTR^{tm2HGU}, fail to recapitulate this infertility [49, 51, 52, 55, 58, 59]. The lack of observed corollary between mouse models and humans is speculated to again involve the expression of the aforementioned alternative Cl^- channel in murine seminal vesicles and epididymides [79]. Although some females with CF are also affected by infertility, studies are far less numerous. Mouse models have been useful in the past to study reproductive patterns in females. A knockout model, CFTR^{tm1UNC}, and the Δ*F508* mouse model, CFTR^{tm1KTH}, have been used to demonstrate impaired sperm transport within the CF female mouse reproductive tract, due to inadequate fluid control. This study also reported delayed puberty, smaller reproductive organs, and decreased oocyte numbers during ovulation, which may all contribute to female infertility in humans [67, 80].

4.6. The Use of the CF Murine Model for Evaluating New Treatment Options. The development of murine models birthed a new avenue in which to test experimental compounds for their efficacy in targeting the dysfunctional CFTR gene. Du et al. generated a mouse model carrying the Class I mutation *G542X* in which they demonstrated the ability of the orally bioavailable PTC124 compound to read through premature stop codons, a key feature of Class I CFTR mutations, resulting in partial restoration of the CFTR protein in the mouse intestinal tract [81]. More recently, a similar read-through compound, NB124, was shown to suppress nonsense mutations and partly restore CFTR function in a *G542X* transgenic mouse model [82]. Other drugs and gene therapy approaches have also been described in murine models [83–85].

Aside from the CFTR modulator approach, ENaC channel antagonists are also being investigated using the β-ENaC mouse model for their efficacy in restoring normal Na^+ flux and their downstream effects on mucus clearance and inflammation [86].

5. The Use of Pig Models to Study CF Pathology

Although the field of CF research has been much advanced through the use of murine models over the past two decades,

the manifestations seen in mice do not fully mirror the normal clinical phenotype of CF in humans, particularly in relation to pulmonary disease progression. Consequently, researchers have turned their attention to the porcine model of CF disease as a more robust representation of the human CF phenotype [75]. Indeed, the pig shares 92% CFTR sequence homology with human CFTR [87]. In 2008, Rogers and colleagues generated a pig model of CF in domestic animals (*Sus scrofa*) using recombinant adenoassociated virus-mediated (AAV-mediated) gene targeting in foetal pig fibroblast. This process involved the generation of two different CFTR defects including the null allele, which lacked production of CFTR protein, and the heterozygous Δ*F508* mutation [16]. Furthermore, in 2011, Ostedgaard and coworkers employed the heterozygous $CFTR^{\Delta F508/\Delta F508}$ pig previously generated by Rogers et al. (2008) [16] to generate homozygous $CFTR^{\Delta F508/\Delta F508}$ animals. Maintenance of these animals involves initial surgery to alleviate intestinal obstruction [88]. CF piglets also require pancreatic enzyme replacement therapy, vitamins and H2 blockers, and/or proton-pump inhibitors to improve gastric acid control [87, 89].

5.1. Respiratory Tract Disease-Related Changes in the Porcine CF Model. The pig model was a suitable candidate to study CF lung disease due to anatomical and physiological similarities between the human and porcine lung [90, 91]. Interestingly, as far back as 1976 the respiratory tract of pigs was used to mimic the cycle of infection and inflammation of humans [92]. Phenotypically, Meyerholz et al. demonstrated that the trachea and bronchi of CF piglets were smaller than WT piglets [93], although the lung volume was reportedly similar to their non-CF littermates. CF piglets ($CFTR^{-/-}$ and $CFTR^{-/\Delta F508}$) have also been shown to have increased airway resistance, indicating airway obstruction [94] and airway wall thickening, similarly to children with CF [17]. Additionally, Ostedgaard et al. reported that $CFTR^{\Delta F508/\Delta F508}$ piglets had airways disease from as young as 2 days old, with the development of mucopurulent material causing airway obstruction [87].

In recent years in the CF field, a debate has developed as to whether inflammation or infection occurs first in the CF airways, with some authors agreeing that inflammation precedes infection in children with CF [95, 96] and others providing evidence to the contrary [97]. The pig model of CF provided scientists with a strong platform to study this important conundrum in detail. Studies employing the $CFTR^{-/-}$ pig demonstrated similar numbers of immune cells and cytokine IL-8 concentrations in WT and CF piglets [89]. Building on this foundation of knowledge and because $CFTR^{-/-}$ pigs lack inflammation at birth, Chen et al. concluded that this was an ideal model to study electrolyte transport defects. Results demonstrated that c-AMP-stimulated Cl^- transport was impaired in nasal and tracheal transepithelial airways of CF piglets with the $CFTR^{-/-}$ mutation [98], similar to humans with CF [99, 100]. Moreover, hyperabsorption of Na^+ in nasal cells of CF piglets was increased when compared to WT piglets.

Of major importance, BALF from $CFTR^{-/-}$ piglets contained greater numbers of bacteria, including *S. aureus*, which was not present in the WT piglets [17]. Interestingly, this data reflects reports in children with CF, where the main bacterium isolated from airway samples was *S. aureus* [4]. Moreover, bacteria were isolated from the lungs of $CFTR^{\Delta F508/\Delta F508}$ piglets, in contrast to WT piglets, which lacked culturable bacterial colonies [87]. This data provided the first line of evidence that inflammation occurs after infection in CF piglets and demonstrates that an inherited defect associated with a lack of CFTR protein and function results in impaired bacterial clearance and development of inflammation. Collectively, these reports indicate that $CFTR^{-/-}$ and $CFTR^{\Delta F508/\Delta F508}$ pig models resemble similar lung pathological outcomes as their genotypically identical human counterparts and facilitate our understanding of lung disease in CF, providing evidence on the origins of inflammation and infection within the lungs.

5.2. Intestinal Disease Development in the CF Pig Model. MI is classified as either simple or complex. Simple MI is the failure to remove the meconium within the first 48 hours of birth and complex MI represents intestinal atresia, necrosis, and perforation [11]. Interestingly, using the $CFTR^{-/-}$ pig, Rogers et al. demonstrated that the earliest manifestation of CF was MI [89]. Studies have shown that 100% of $CFTR^{-/-}$ and $CFTR^{\Delta F508/\Delta F508}$ pigs develop complex MI [87, 89, 101]. This is in agreement with the increased occurrence of MI in humans carrying the Δ*F508* mutation [102].

No inflammation was noted in the intestines of $CFTR^{-/-}$ piglets; however the spiral colon of the $CFTR^{-/-}$ pig contained microcellular accumulations and high levels of mucus [87]. $CFTR^{-/-}$ piglets also had intestinal atresia, a complication that occurs at birth resulting in the narrowing of the intestine. Interestingly this also commonly occurs in CF infants [101]. Ostedgaard et al. reported that $CFTR^{\Delta F508/\Delta F508}$ pigs had similar GI tract pathology to the $CFTR^{-/-}$ pigs [87]. Additionally, diverticulitis a condition caused by the formation of a sac within the colon wall commonly occurs in CF individuals and was also reported in $CFTR^{-/-}$ piglets [103]. These findings indicate that the GI pathologies of $CFTR^{-/-}$ and $CFTR^{\Delta F508/\Delta F508}$ are similar, indicating a CFTR-related defect affecting pathological outcomes in piglets, not dissimilar to their human counterparts.

5.3. Pancreatic Disease in the CF Pig Model. Data has shown that $CFTR^{-/-}$ piglets fail to gain weight [89]. Pancreatic insufficiency is another characteristic associated with CF piglets and is phenotypically similar to CF infants [104]. Studying pancreatic disorder in adult CF individuals is difficult, as it involves sampling the fluid of the jejunum which contains a mixture of bile and pancreatic fluid, as the common bile duct and pancreas duct intervene. Interestingly, pigs have a separate common bile and pancreas duct, allowing researchers to study bile and pancreatic fluid separately [105]. $CFTR^{\Delta F508/\Delta F508}$ pigs presented with decreased pancreatic fluid secretions of altered pH and protein content [105]. In $CFTR^{-/-}$ pigs, the number of acinar cells and cytoplasmic

zymogen granules decreased, with increased zymogen secretions found in the interstitium and within pancreatic ducts; this is similar to what is described in adults with CF [101]. Of interest, histology of the pancreas of $CFTR^{\Delta F508/\Delta F508}$ pigs was less severe than the $CFTR^{-/-}$ pigs [87] indicating that minimal CFTR presence/function in Δ*F508* pigs may reduce pancreatic disease progression, an important finding which may facilitate researchers in understanding pancreatic disease development and progression in CF individuals.

5.4. Hepatobiliary Disease in the Pig Model of CF. Within the hepatobiliary system, the CFTR is located on the apical membrane of cholangiocytes [106] and plays a role in regulating fluid and electrolyte stability in bile. Gallbladder abnormalities, including a noticeably smaller gallbladder, occur in approximately 10% to 30% of all patients with CF [107]. Indeed, congealed bile and mucus have been found in smaller gallbladders of $CFTR^{-/-}$ and $CFTR^{\Delta F508/\Delta F508}$ pigs compared to WT pigs [87, 89]. It was shown that the $CFTR^{-/-}$ pig had mild to moderate hepatic lesions [89] and elevated bile protein compared to the WT pigs [105]. Moreover, the $CFTR^{-/-}$ pig had increased cellular inflammation, ductal hyperplasia, and mild fibrosis. In concurrence, the $CFTR^{\Delta F508/\Delta F508}$ pig model presented with inflammation and exhibited common symptoms of biliary cirrhosis [87].

5.5. The Potential Use of the CF Pig Model for Development of Novel Therapeutics. Cook et al. demonstrated, using pig epithelial cells, that ivacaftor therapy functions to potentiate the CFTR channel, similar to human epithelial cells [108]. This provides researchers with the opportunity to study the longevity of ivacaftor therapy on pig models and further opens the research to other potentiators and correctors.

6. Disease Phenotype of the CF Ferret

The ferret model has been extensively used in the assessment of lung infections including severe acute respiratory syndrome [109] and influenza virus [110] due to the similarity in lung cell biology and anatomy to humans, thus making it an ideal candidate for CF research. The extent of lung similarities between humans and ferrets includes comparable submucosal gland expression of CFTR within the serous tubules, important for the secretion of fluids and mucus into the lung [111] and for protection of the airways from infection [112]. Moreover, CFTR pharmacologic and bioelectric functionality in ferret epithelia is similar to that of human epithelia [113]. The ferret's short gestation period and time to reach adolescence within 4–6 months along with its smaller size compared to the pig may make it a more cost-effective model to maintain. The development of the CF ferret model has utilised recombinant adenovirus gene targeting of the CFTR gene to introduce partial disruption of exon 10 or complete deletion of the CFTR gene [114]. This process has generated $CFTR^{+/-}$ breeding pairs for the production of CFTR-deficient ferrets [18].

6.1. Respiratory Tract Disease-Specific Changes in the Ferret Model of CF. Of the $CFTR^{-/-}$ ferret kits that avoid MI-induced death, lung infections in the form of pneumonia and poor nutritional status are the main causes of mortality. Even with improved weight gain, $CFTR^{-/-}$ ferrets demonstrate increased levels of enteric bacteria in their lungs, with *Staphylococcus* spp. and *Streptococcus* spp. isolates found. CFTR-deficient ferrets demonstrated improved survival with the administration of antibiotics. Consistent with CF individuals, the $CFTR^{-/-}$ ferret presents with dysfunction of the proximal airways including impaired submucosal gland fluid secretion and c-AMP-induced Cl^- permeability [18].

6.2. Intestinal Disease Studied in the CF Ferret Model. In CF ferrets, intestinal obstruction in the form of MI is found in approximately 75% of $CFTR^{-/-}$ ferret kits [18], compared to 13%–17% observed in human CF neonates [10]. $CFTR^{-/-}$ ferrets show greater morbidity after 48 h as they fail to thrive with half of the MI-positive ferret kits succumbing to intestinal lesions of the colon or ileum [18]. Of approximately 25% of newborn kits that survive MI, none thrive or live longer than 4 days. The ferret intestinal tract demonstrates a more severe form of MI compared to humans, mice, and pigs [18] due to the ferret's faster intestinal transit time which results from the lack of a cecum seen in omnivores or herbivores [115].

6.3. Pancreatic and Hepatobiliary Disease and Fertility. The pancreas of the $CFTR^{-/-}$ ferret demonstrates a similar histopathology to that of human neonates where lesions and dilation of acini and ductules occur [18, 116]. CF ferrets that survived MI demonstrated increased pancreatic inflammation with exocrine tissue loss similar to that observed in humans with CF. Sun and colleagues administered a proton-pump inhibitor, omeprazole, to $CFTR^{-/-}$ ferrets to counter the lower-than-normal gut pH as a result of impaired pancreatic secretions of bicarbonate. This improved fat absorption and resulted in weight gain comparable to the $CFTR^{+/+}$ ferrets [18].

The gallbladder and liver of $CFTR^{-/-}$ ferret kits demonstrated no histological differences between the $CFTR^{+/+}$ or $CFTR^{+/-}$ kits. Through blood analyses the liver function of $CFTR^{-/-}$ ferret kits demonstrated low levels of cholesterol and high levels of plasma alanine aminotransferase (ALT) and bilirubin, which highlights an early onset of liver disease, although no liver lesions were found in $CFTR^{-/-}$ ferrets. CF infants that present with liver disease demonstrate a similar pathology to that observed in ferret neonates although it commonly resolves within humans [117].

$CFTR^{-/-}$ ferrets also demonstrate reduced bile acid absorption by the GI tract, causing poor fat absorption leading to reduced nutritional status [18]. The $CFTR^{-/-}$ ferrets poor nutritional condition results from poor absorption of nutrients which is corrected by supplementation of ursodeoxycholic acid (UDCA) which normalises the levels of liver ALT and bilirubin. However, even in combination with antibiotics to stop infections of the lung, mortality still occurs within 5–9 days [18].

Table 2: Phenotypic manifestations of cystic fibrosis in humans and animal models.

	Spontaneous lung infection	Pancreatic disease	Intestinal disease	Liver and gallbladder disease	Reproduction
Human	Yes	PI	MI	Biliary cirrhosis	Severe vas deferens defect
Mouse*	No	No	Intestinal obstruction, often fatal	No	Reduced fertility in females
Pig	Yes	PI	100% MI	Biliary cirrhosis	Severe vas deferens defect
Ferret	Yes	PI	75% MI	Liver disease	Severe vas deferens defect

*The phenotypic manifestations outlined above may differ between mouse models. PI: *pancreatic insufficiency*; MI: *meconium ileus*.

Absent or degenerate vas deferens was found in $CFTR^{-/-}$ ferrets similar to that of humans [118]. In CF humans, the vas deferens is degenerated due to mucoid blockage and a progressive degeneration [119]. Ferrets kits with either $CFTR^{+/+}$ or $CFTR^{+/-}$ demonstrated intact normal vas deferens in the same study.

7. Concluding Remarks

The generation of CF animal models has greatly advanced our knowledge of the disease and will continue to inform upon the complexity of this disease for many years to come. Inherent weaknesses lie in some earlier models but the generation of larger models endeavoured to address these deficiencies. The phenotypic characterisations of the three models discussed herein are outlined in Table 2.

There are many advantages to the use of mice to study the pathology of CF disease, including the ease with which they can be genetically manipulated, short gestation times, and low cost of animal upkeep [62]. However, there are also a number of limitations to their use. Firstly, phenotypic variations exist between models and, indeed, the degree of severity of such manifestations also differs greatly between models. While the mouse model certainly displays severe intestinal obstruction and altered nasal electrophysiology similar to that seen in humans, the mouse models fail to initiate spontaneous lung infection without pathogen challenge. Most models only display mild complications in the pancreas, liver, and vas deferens, which is in contrast to the severe abnormalities in human tissues. It is suggested that low levels of residual CFTR expression may induce sufficient ion transport to alleviate the severity of the disease in the mouse model. Also, in mice, the epithelial expression of a second Cl^- ion channel with an alternative signalling pathway to CFTR may compensate for dysfunctional CFTR and may account for the phenotypic disparities between the human and murine manifestations of CF disease [64, 68].

Pigs are ideal models for the study of CF for a number of reasons; they have perfect reproductive characteristics with a large number of offspring. Furthermore, they have a fast maturation rate and have a long life span, thus allowing researchers to study the pathological outcomes and prognosis of CF. A lack of CFTR protein and function in $CFTR^{-/-}$ piglets impacts on the lungs, liver, pancreas, and GI tract, all organs which are similarly affected in humans with CF [87, 89, 98]. However, MI presents in 100% of $CFTR^{-/-}$ piglets (in contrast to its prevalence of 15% in infants with CF) and is fatal without early surgical intervention [89]. This burden may limit the usefulness of the porcine model in some institutions. The potential risks involved in surgery and complications associated with MI, including intestinal atresia, demand great understanding and commitment to the use of these animals in the study of CF.

The ferret model does demonstrate a large number of similarities to CF pathology in humans, particularly neonates. Ongoing steps to generate a $CFTR^{-/-}$ ferret that overcomes the GI pathology to enable animals to reach adolescence are needed to establish whether ferret lung pathology mirrors that of humans with CF. Nevertheless, it must be mentioned that the appearance of lung infections at both the start and end of the $CFTR^{-/-}$ ferret life span mirrors human disease, highlighting the potential benefits of this model. The development of $\Delta F508$ and *G551D* specific mutant is required to establish the ferret as an exemplary animal model for CF.

In summary, it is certain that animal models have significantly contributed to our understanding of this complex disease. The animal models now available will continue to be modified and improved to provide an even greater depth to our knowledge. Importantly, animal models will not only provide information on the pathology of disease but also provide an invaluable canvas on which to test new compounds and therapies for use in CF disease management.

Competing Interests

The authors declare that they have no competing interests.

Authors' Contributions

Gillian M. Lavelle and Michelle M. White contributed equally to this work.

Acknowledgments

The authors would like to acknowledge their funding sources, including the Health Research Board, Ireland, Science Foundation Ireland (Grant nos. 11/RFP/BMT/3094 and SFI/08/US/B1676), The Charitable Infirmary Charitable Trust, Ireland, and the Programme for Research in Third Level Institutes (PRTLI) administered by the Higher Education Authority.

References

[1] K. Yoshimura, H. Nakamura, B. C. Trapnell et al., "Expression of the cystic fibrosis transmembrane conductance regulator gene in cells of non-epithelial origin," *Nucleic Acids Research*, vol. 19, no. 19, pp. 5417–5423, 1991.

[2] J. R. Riordan, J. M. Rommens, B.-S. Kerem et al., "Identification of the cystic fibrosis gene: cloning and characterization of complementary DNA," *Science*, vol. 245, no. 4922, pp. 1066–1073, 1989.

[3] The Cystic Fibrosis Registry of Ireland, *2012 Annual Report*, The Cystic Fibrosis Registry of Ireland, Dublin, Ireland, 2012.

[4] Cystic Fibrosis Foundation, *Patient Registry—Annual Data Report 2012*, Cystic Fibrosis Foundation, Bethesda, Md, USA, 2012.

[5] L. Zhang, B. Button, S. E. Gabriel et al., "CFTR delivery to 25% of surface epithelial cells restores normal rates of mucus transport to human cystic fibrosis airway epithelium," *PLoS Biology*, vol. 7, no. 7, Article ID e1000155, 2009.

[6] D. S. Armstrong, K. Grimwood, J. B. Carlin et al., "Lower airway inflammation in infants and young children with cystic fibrosis," *American Journal of Respiratory and Critical Care Medicine*, vol. 156, no. 4, pp. 1197–1204, 1997.

[7] M. W. Konstan, K. A. Hilliard, T. M. Norvell, and M. Berger, "Bronchoalveolar lavage findings in cystic fibrosis patients with stable, clinically mild lung disease suggest ongoing infection and inflammation," *American Journal of Respiratory and Critical Care Medicine*, vol. 150, no. 2, pp. 448–454, 1994.

[8] R. C. Boucher, "New concepts of the pathogenesis of cystic fibrosis lung disease," *European Respiratory Journal*, vol. 23, no. 1, pp. 146–158, 2004.

[9] Y. Gernez, C. E. Dunn, C. Everson et al., "Blood basophils from cystic fibrosis patients with allergic bronchopulmonary aspergillosis are primed and hyper-responsive to stimulation by aspergillus allergens," *Journal of Cystic Fibrosis*, vol. 11, no. 6, pp. 502–510, 2012.

[10] H. P. J. van der Doef, F. T. M. Kokke, C. K. van der Ent, and R. H. J. Houwen, "Intestinal obstruction syndromes in cystic fibrosis: meconium ileus, distal intestinal obstruction syndrome, and constipation," *Current Gastroenterology Reports*, vol. 13, no. 3, pp. 265–270, 2011.

[11] T. Kelly and J. Buxbaum, "Gastrointestinal manifestations of cystic fibrosis," *Digestive Diseases and Sciences*, vol. 60, no. 7, pp. 1903–1913, 2015.

[12] The Cystic Fibrosis Registry of Ireland, *2013 Annual Report*, The Cystic Fibrosis Registry of Ireland, Dublin, Ireland, 2013.

[13] S. M. Moskowitz, J. F. Chmiel, D. L. Sternen et al., "Clinical practice and genetic counseling for cystic fibrosis and CFTR-related disorders," *Genetics in Medicine*, vol. 10, no. 12, pp. 851–868, 2008.

[14] P. Y. D. Wong, "CFTR gene and male fertility," *Molecular Human Reproduction*, vol. 4, no. 2, pp. 107–110, 1998.

[15] J. T. Fisher, Y. Zhang, and J. F. Engelhardt, "Comparative biology of cystic fibrosis animal models," *Methods in Molecular Biology*, vol. 742, pp. 311–334, 2011.

[16] C. S. Rogers, Y. Hao, T. Rokhlina et al., "Production of CFTR-null and CFTR-ΔF508 heterozygous pigs by adeno-associated virus–mediated gene targeting and somatic cell nuclear transfer," *The Journal of Clinical Investigation*, vol. 118, no. 4, pp. 1571–1577, 2008.

[17] D. A. Stoltz, D. K. Meyerholz, A. A. Pezzulo et al., "Cystic fibrosis pigs develop lung disease and exhibit defective bacterial eradication at birth," *Science Translational Medicine*, vol. 2, no. 29, Article ID 29ra31, 18 pages, 2010.

[18] X. Sun, H. Sui, J. T. Fisher et al., "Disease phenotype of a ferret CFTR-knockout model of cystic fibrosis," *The Journal of Clinical Investigation*, vol. 120, no. 9, pp. 3149–3160, 2010.

[19] X. Sun, A. K. Olivier, B. Liang et al., "Lung phenotype of juvenile and adult cystic fibrosis transmembrane conductance regulator-knockout ferrets," *American Journal of Respiratory Cell and Molecular Biology*, vol. 50, no. 3, pp. 502–512, 2014.

[20] N. W. Keiser, S. E. Birket, I. A. Evans et al., "Defective innate immunity and hyperinflammation in newborn cystic fibrosis transmembrane conductance regulator-knockout ferret lungs," *American Journal of Respiratory Cell and Molecular Biology*, vol. 52, no. 6, pp. 683–694, 2015.

[21] J. J. Smith, P. H. Karp, and M. J. Welsh, "Defective fluid transport by cystic fibrosis airway epithelia," *The Journal of Clinical Investigation*, vol. 93, no. 3, pp. 1307–1311, 1994.

[22] J. B. Lyczak, C. L. Cannon, and G. B. Pier, "Lung infections associated with cystic fibrosis," *Clinical Microbiology Reviews*, vol. 15, no. 2, pp. 194–222, 2002.

[23] M. Mall, B. R. Grubb, J. R. Harkema, W. K. O'Neal, and R. C. Boucher, "Increased airway epithelial Na^+ absorption produces cystic fibrosis-like lung disease in mice," *Nature Medicine*, vol. 10, no. 5, pp. 487–493, 2004.

[24] S. Haerteis, B. Krueger, C. Korbmacher, and R. Rauh, "The δ-subunit of the epithelial sodium channel (ENaC) enhances channel activity and alters proteolytic ENaC activation," *The Journal of Biological Chemistry*, vol. 284, no. 42, pp. 29024–29040, 2009.

[25] R. Waldmann, G. Champigny, F. Bassilana, N. Voilley, and M. Lazdunski, "Molecular cloning and functional expression of a novel amiloride-sensitive Na+ channel," *Journal of Biological Chemistry*, vol. 270, no. 46, pp. 27411–27414, 1995.

[26] M. Althaus, "ENaC inhibitors and airway re-hydration in cystic fibrosis: state of the art," *Current Molecular Pharmacology*, vol. 6, no. 1, pp. 3–12, 2013.

[27] K. Pohl, E. Hayes, J. Keenan et al., "A neutrophil intrinsic impairment affecting Rab27a and degranulation in cystic fibrosis is corrected by CFTR potentiator therapy," *Blood*, vol. 124, no. 7, pp. 999–1009, 2014.

[28] M. B. Butterworth, "Regulation of the epithelial sodium channel (ENaC) by membrane trafficking," *Biochimica et Biophysica Acta (BBA)—Molecular Basis of Disease*, vol. 1802, no. 12, pp. 1166–1177, 2010.

[29] M. Lu, Q. Leng, M. E. Egan et al., "CFTR is required for PKA-regulated ATP sensitivity of Kir1.1 potassium channels in mouse kidney," *Journal of Clinical Investigation*, vol. 116, no. 3, pp. 797–807, 2006.

[30] D. J. M. Rommens, "Cystic Fibrosis Mutation Database," http://www.genet.sickkids.on.ca/Home.html.

[31] E. Hayes, K. Pohl, N. G. McElvaney, and E. P. Reeves, "The cystic fibrosis neutrophil: a specialized yet potentially defective cell," *Archivum Immunologiae et Therapiae Experimentalis*, vol. 59, no. 2, pp. 97–112, 2011.

[32] G. L. Lukacs, X.-B. Chang, C. Bear et al., "The ΔF508 mutation decreases the stability of cystic fibrosis transmembrane conductance regulator in the plasma membrane: determination of functional half-lives on transfected cells," *Journal of Biological Chemistry*, vol. 268, no. 29, pp. 21592–21598, 1993.

[33] J. Bott, S. Blumenthal, M. Buxton et al., "Guidelines for the physiotherapy management of the adult, medical, spontaneously breathing patient," *Thorax*, vol. 64, no. 1, pp. i1–i52, 2009.

[34] M. Robinson, A. L. Hemming, J. A. Regnis et al., "Effect of increasing doses of hypertonic saline on mucociliary clearance in patients with cystic fibrosis," *Thorax*, vol. 52, no. 10, pp. 900–903, 1997.

[35] P. Wark and V. M. McDonald, "Nebulised hypertonic saline for cystic fibrosis," *Cochrane Database of Systematic Reviews*, vol. 2, Article ID CD001506, 2009.

[36] E. P. Reeves, M. Williamson, S. J. O'Neill, P. Greally, and N. G. McElvaney, "Nebulized hypertonic saline decreases IL-8 in sputum of patients with cystic fibrosis," *American Journal of Respiratory and Critical Care Medicine*, vol. 183, no. 11, pp. 1517–1523, 2011.

[37] F. Christopher, D. Chase, K. Stein, and R. Milne, "rhDNase therapy for the treatment of cystic fibrosis patients with mild to moderate lung disease," *Journal of Clinical Pharmacy and Therapeutics*, vol. 24, no. 6, pp. 415–426, 1999.

[38] M. Hofer, C. Benden, I. Inci et al., "True survival benefit of lung transplantation for cystic fibrosis patients: the Zurich experience," *The Journal of Heart and Lung Transplantation*, vol. 28, no. 4, pp. 334–339, 2009.

[39] F. J. Accurso, S. M. Rowe, J. P. Clancy et al., "Effect of VX-770 in persons with cystic fibrosis and the G551D-CFTR mutation," *The New England Journal of Medicine*, vol. 363, no. 21, pp. 1991–2003, 2010.

[40] B. W. Ramsey, J. Davies, N. G. McElvaney et al., "A CFTR potentiator in patients with cystic fibrosis and the G551D mutation," *The New England Journal of Medicine*, vol. 365, no. 18, pp. 1663–1672, 2011.

[41] S. M. Rowe, S. L. Heltshe, T. Gonska et al., "Clinical mechanism of the cystic fibrosis transmembrane conductance regulator potentiator ivacaftor in G551D-mediated cystic fibrosis," *American Journal of Respiratory and Critical Care Medicine*, vol. 190, no. 2, pp. 175–184, 2014.

[42] L. R. Reznikov, M. H. Abou Alaiwa, C. L. Dohrn et al., "Antibacterial properties of the CFTR potentiator ivacaftor," *Journal of Cystic Fibrosis*, vol. 13, no. 5, pp. 515–519, 2014.

[43] P. E. Bratcher, S. M. Rowe, G. Reeves et al., "Alterations in blood leukocytes of G551D-bearing cystic fibrosis patients undergoing treatment with ivacaftor," *Journal of Cystic Fibrosis*, vol. 15, no. 1, pp. 67–73, 2016.

[44] P. A. Flume, T. G. Liou, D. S. Borowitz et al., "Ivacaftor in subjects with cystic fibrosis who are homozygous for the F508del-CFTR mutation," *Chest*, vol. 142, no. 3, pp. 718–724, 2012.

[45] Vertex Pharmaceuticals Incorporated Report, "Two 24-Week Phase 3 Studies of Lumacaftor in Combination with Ivacaftor Met Primary Endpoint with Statistically Significant Improvements in Lung Function (FEV1) in People with Cystic Fibrosis Who Have Two Copies of the F508del Mutation," 2014.

[46] C. E. Wainwright, J. S. Elborn, B. W. Ramsey et al., "Lumacaftor-ivacaftor in patients with cystic fibrosis homozygous for Phe508del CFTR," *The New England Journal of Medicine*, vol. 373, no. 3, pp. 220–231, 2015.

[47] FDA, "FDA approves new treatment for cystic fibrosis," http://www.fda.gov/NewsEvents/Newsroom/PressAnnouncements/ucm453565.htm.

[48] B.-S. Kerem, J. M. Rommens, J. A. Buchanan et al., "Identification of the cystic fibrosis gene: genetic analysis," *Science*, vol. 245, no. 4922, pp. 1073–1080, 1989.

[49] J. N. Snouwaert, K. K. Brigman, A. M. Latour et al., "An animal model for cystic fibrosis made by gene targeting," *Science*, vol. 257, no. 5073, pp. 1083–1088, 1992.

[50] D. J. Davidson and J. R. Dorin, "The CF mouse: an important tool for studying cystic fibrosis," *Expert Reviews in Molecular Medicine*, vol. 3, pp. 1–27, 2004.

[51] R. Ratcliff, M. J. Evans, A. W. Cuthbert et al., "Production of a severe cystic fibrosis mutation in mice by gene targeting," *Nature Genetics*, vol. 4, no. 1, pp. 35–41, 1993.

[52] W. K. O'Neal, P. Hasty, P. B. McCray Jr. et al., "A severe phenotype in mice with a duplication of exon 3 in the cystic fibrosis locus," *Human Molecular Genetics*, vol. 2, no. 10, pp. 1561–1569, 1993.

[53] P. Hasty, W. K. O'Neal, K.-Q. Liu et al., "Severe phenotype in mice with termination mutation in exon 2 of cystic fibrosis gene," *Somatic Cell and Molecular Genetics*, vol. 21, no. 3, pp. 177–187, 1995.

[54] R. Rozmahel, M. Wilschanski, A. Matin et al., "Modulation of disease severity in cystic fibrosis transmembrane conductance regulator deficient mice by a secondary genetic factor," *Nature Genetics*, vol. 12, no. 3, pp. 280–287, 1996.

[55] J. H. van Doorninck, P. J. French, E. Verbeek et al., "A mouse model for the cystic fibrosis ΔF508 mutation," *The EMBO Journal*, vol. 14, no. 18, pp. 4403–4411, 1995.

[56] B. G. Zeiher, E. Eichwald, J. Zabner et al., "A mouse model for the delta F508 allele of cystic fibrosis," *The Journal of Clinical Investigation*, vol. 96, no. 4, pp. 2051–2064, 1995.

[57] W. H. Colledge, B. S. Abella, K. W. Southern et al., "Generation and characterization of a ΔF508 cystic fibrosis mouse model," *Nature Genetics*, vol. 10, no. 4, pp. 445–452, 1995.

[58] P. Dickinson, S. N. Smith, S. Webb et al., "The severe G480C cystic fibrosis mutation, when replicated in the mouse, demonstrates mistrafficking, normal survival and organ-specific bioelectrics," *Human Molecular Genetics*, vol. 11, no. 3, pp. 243–251, 2002.

[59] S. J. Delaney, E. W. F. W. Alton, S. N. Smith et al., "Cystic fibrosis mice carrying the missense mutation G551D replicate human genotype-phenotype correlations," *The EMBO Journal*, vol. 15, no. 5, pp. 955–963, 1996.

[60] J. R. Dorin, P. Dickinson, E. W. F. W. Alton et al., "Cystic fibrosis in the mouse by targeted insertional mutagenesis," *Nature*, vol. 359, no. 6392, pp. 211–215, 1992.

[61] J. R. Dorin, P. Dickinson, E. Emslie et al., "Successful targeting of the mouse cystic fibrosis transmembrane conductance regulator gene in embryonal stem cells," *Transgenic Research*, vol. 1, no. 2, pp. 101–105, 1992.

[62] C. Guilbault, Z. Saeed, G. P. Downey, and D. Radzioch, "Cystic fibrosis mouse models," *American Journal of Respiratory Cell and Molecular Biology*, vol. 36, no. 1, pp. 1–7, 2007.

[63] D. J. Davidson and M. Rolfe, "Mouse models of cystic fibrosis," *Trends in Genetics*, vol. 17, no. 10, pp. S29–S37, 2001.

[64] M. Wilke, R. M. Buijs-Offerman, J. Aarbiou et al., "Mouse models of cystic fibrosis: phenotypic analysis and research applications," *Journal of Cystic Fibrosis*, vol. 10, no. 2, pp. S152–S171, 2011.

[65] B. Johannesson, S. Hirtz, J. Schatterny, C. Schultz, and M. A. Mall, "CFTR regulates early pathogenesis of chronic obstructive lung disease in βenac-overexpressing mice," *PLoS ONE*, vol. 7, no. 8, article e44059, 2012.

[66] H. Ma and Y. Yang, "Epithelial sodium channel (ENaC)," *Journal of American Science*, vol. 5, no. 6, pp. 62–69, 2009.

[67] M. E. Egan, "How useful are cystic fibrosis mouse models?" *Drug Discovery Today: Disease Models*, vol. 6, no. 2, pp. 35–41, 2009.

[68] L. L. Clarke, B. R. Grubb, J. R. Yankaskas, C. U. Cotton, A. McKenzie, and R. C. Boucher, "Relationship of a non-cystic fibrosis transmembrane conductance regulator-mediated chloride conductance to organ-level disease in Cftr(−/−) mice," *Proceedings of the National Academy of Sciences of the United States of America*, vol. 91, no. 2, pp. 479–483, 1994.

[69] D. Gosselin, M. M. Stevenson, E. A. Cowley et al., "Impaired ability of Cftr knockout mice to control lung infection with *Pseudomonas aeruginosa*," *American Journal of Respiratory and Critical Care Medicine*, vol. 157, no. 4, part 1, pp. 1253–1262, 1998.

[70] U. Sajjan, G. Thanassoulis, V. Cherapanov et al., "Enhanced susceptibility to pulmonary infection with *Burkholderia cepacia* in *Cftr*$^{-/-}$ mice," *Infection and Immunity*, vol. 69, no. 8, pp. 5138–5150, 2001.

[71] A. Van Heeckeren, R. Walenga, M. W. Konstan, T. Bonfield, P. B. Davis, and T. Ferkol, "Excessive inflammatory response of cystic fibrosis mice to bronchopulmonary infection with *Pseudomonas aeruginosa*," *The Journal of Clinical Investigation*, vol. 100, no. 11, pp. 2810–2815, 1997.

[72] V. S. Shah, D. K. Meyerholz, X. X. Tang et al., "Airway acidification initiates host defense abnormalities in cystic fibrosis mice," *Science*, vol. 351, no. 6272, pp. 503–507, 2016.

[73] S. Gehrig, J. Duerr, M. Weitnauer et al., "Lack of neutrophil elastase reduces inflammation, mucus hypersecretion, and emphysema, but not mucus obstruction, in mice with cystic fibrosislike lung disease," *American Journal of Respiratory and Critical Care Medicine*, vol. 189, no. 9, pp. 1082–1092, 2014.

[74] D. Borowitz and D. Gelfond, "Intestinal complications of cystic fibrosis," *Current Opinion in Pulmonary Medicine*, vol. 19, no. 6, pp. 676–680, 2013.

[75] N. W. Keiser and J. F. Engelhardt, "New animal models of cystic fibrosis: what are they teaching us?" *Current Opinion in Pulmonary Medicine*, vol. 17, no. 6, pp. 478–483, 2011.

[76] S. M. Rowe, S. Miller, and E. J. Sorscher, "Cystic fibrosis," *The New England Journal of Medicine*, vol. 352, no. 19, pp. 1992–2001, 2005.

[77] J. R. Dorin, B. J. Stevenson, S. Fleming, E. W. F. W. Alton, P. Dickinson, and D. J. Porteous, "Long-term survival of the exon 10 insertional cystic fibrosis mutant mouse is a consequence of low level residual wild-type Cftr gene expression," *Mammalian Genome*, vol. 5, no. 8, pp. 465–472, 1994.

[78] P. G. Noone and M. R. Knowles, "'CFTR-opathies': disease phenotypes associated with cystic fibrosis transmembrane regulator gene mutations," *Respiratory Research*, vol. 2, no. 6, pp. 328–332, 2001.

[79] A. Y. H. Leung, P. Y. D. Wong, J. R. Yankaskas, and R. C. Boucher, "cAMP- but not Ca(2+)-regulated Cl- conductance is lacking in cystic fibrosis mice epididymides and seminal vesicles," *American Journal of Physiology—Cell Physiology*, vol. 271, no. 1, part 1, pp. C188–C193, 1996.

[80] C. A. Hodges, M. R. Palmert, and M. L. Drumm, "Infertility in females with cystic fibrosis is multifactorial: evidence from mouse models," *Endocrinology*, vol. 149, no. 6, pp. 2790–2797, 2008.

[81] M. Du, X. Liu, E. M. Welch, S. Hirawat, S. W. Peltz, and D. M. Bedwell, "PTC124 is an orally bioavailable compound that promotes suppression of the human CFTR-G542X nonsense allele in a CF mouse model," *Proceedings of the National Academy of Sciences of the United States of America*, vol. 105, no. 6, pp. 2064–2069, 2008.

[82] X. Xue, V. Mutyam, L. Tang et al., "Synthetic aminoglycosides efficiently suppress cystic fibrosis transmembrane conductance regulator nonsense mutations and are enhanced by ivacaftor," *American Journal of Respiratory Cell and Molecular Biology*, vol. 50, no. 4, pp. 805–816, 2014.

[83] R. Robert, G. W. Carlile, J. Liao et al., "Correction of the ΔPhe508 cystic fibrosis transmembrane conductance regulator trafficking defect by the bioavailable compound glafenine," *Molecular Pharmacology*, vol. 77, no. 6, pp. 922–930, 2010.

[84] S. Noël, M. Wilke, A. G. M. Bot, H. R. De Jonge, and F. Becq, "Parallel improvement of sodium and chloride transport defects by miglustat (n-butyldeoxynojyrimicin) in cystic fibrosis epithelial cells," *Journal of Pharmacology and Experimental Therapeutics*, vol. 325, no. 3, pp. 1016–1023, 2008.

[85] D. Vidović, M. S. Carlon, M. F. da Cunha et al., "rAAV-CFTRΔR rescues the cystic fibrosis phenotype in human intestinal organoids and cystic fibrosis mice," *American Journal of Respiratory and Critical Care Medicine*, vol. 193, no. 3, pp. 288–298, 2016.

[86] M. A. Mall and L. J. V. Galietta, "Targeting ion channels in cystic fibrosis," *Journal of Cystic Fibrosis*, vol. 14, no. 5, pp. 561–570, 2015.

[87] L. S. Ostedgaard, D. K. Meyerholz, J.-H. Chen et al., "The ΔF508 mutation causes CFTR misprocessing and cystic fibrosis-like disease in pigs," *Science Translational Medicine*, vol. 3, no. 74, Article ID 74ra24, pp. 1–24, 2011.

[88] D. A. Stoltz, T. Rokhlina, S. E. Ernst et al., "Intestinal CFTR expression alleviates meconium ileus in cystic fibrosis pigs," *The Journal of Clinical Investigation*, vol. 123, no. 6, pp. 2685–2693, 2013.

[89] C. S. Rogers, D. A. Stoltz, D. K. Meyerholz et al., "Disruption of the CFTR gene produces a model of cystic fibrosis in newborn pigs," *Science*, vol. 321, no. 5897, pp. 1837–1841, 2008.

[90] K. O. McKay, B. R. Wiggs, P. D. Paré, and R. D. Kamm, "Zero-stress state of intra- and extraparenchymal airways from human, pig, rabbit, and sheep lung," *Journal of Applied Physiology*, vol. 92, no. 3, pp. 1261–1266, 2002.

[91] J. N. Maina and P. Van Gils, "Morphometric characterization of the airway and vascular systems of the lung of the domestic pig, Sus scrofa: comparison of the airway, arterial and venous systems," *Comparative Biochemistry and Physiology—A Molecular and Integrative Physiology*, vol. 130, no. 4, pp. 781–798, 2001.

[92] P. Bradley, F. J. Bourne, and P. Brown, "The respiratory tract immune system in the pig," *Veterinary Pathology*, vol. 13, no. 2, pp. 90–97, 1976.

[93] D. K. Meyerholz, D. A. Stoltz, E. Namati et al., "Loss of cystic fibrosis transmembrane conductance regulator function produces abnormalities in tracheal development in neonatal pigs and young children," *American Journal of Respiratory and Critical Care Medicine*, vol. 182, no. 10, pp. 1251–1261, 2010.

[94] R. J. Adam, A. S. Michalski, C. Bauer et al., "Air trapping and airflow obstruction in newborn cystic fibrosis piglets," *American Journal of Respiratory and Critical Care Medicine*, vol. 188, no. 12, pp. 1434–1441, 2013.

[95] M. Rosenfeld, R. L. Gibson, S. McNamara et al., "Early pulmonary infection, inflammation, and clinical outcomes in infants with cystic fibrosis," *Pediatric Pulmonology*, vol. 32, no. 5, pp. 356–366, 2001.

[96] J. L. Burns, R. L. Gibson, S. McNamara et al., "Longitudinal assessment of Pseudomonas aeruginosa in young children with cystic fibrosis," *Journal of Infectious Diseases*, vol. 183, no. 3, pp. 444–452, 2001.

[97] T. Z. Khan, J. S. Wagener, T. Bost, J. Martinez, F. J. Accurso, and D. W. H. Riches, "Early pulmonary inflammation in infants with

cystic fibrosis," *American Journal of Respiratory and Critical Care Medicine*, vol. 151, no. 4, pp. 1075–1082, 1995.

[98] J.-H. Chen, D. A. Stoltz, P. H. Karp et al., "Loss of anion transport without increased sodium absorption characterizes newborn porcine cystic fibrosis airway epithelia," *Cell*, vol. 143, no. 6, pp. 911–923, 2010.

[99] T. A. Standaert, L. Boitano, J. Emerson et al., "Standardized procedure for measurement of nasal potential difference: an outcome measure in multicenter cystic fibrosis clinical trials," *Pediatric Pulmonology*, vol. 37, no. 5, pp. 385–392, 2004.

[100] J. C. Davies, M. Davies, D. McShane et al., "Potential difference measurements in the lower airway of children with and without cystic fibrosis," *American Journal of Respiratory and Critical Care Medicine*, vol. 171, no. 9, pp. 1015–1019, 2005.

[101] D. K. Meyerholz, D. A. Stoltz, A. A. Pezzulo, and M. J. Welsh, "Pathology of gastrointestinal organs in a porcine model of cystic fibrosis," *American Journal of Pathology*, vol. 176, no. 3, pp. 1377–1389, 2010.

[102] S. M. Blackman, R. Deering-Brose, R. McWilliams et al., "Relative contribution of genetic and nongenetic modifiers to intestinal obstruction in cystic fibrosis," *Gastroenterology*, vol. 131, no. 4, pp. 1030–1039, 2006.

[103] E. C. Benya, A. R. Nussbaum-Blask, and D. M. Selby, "Colonic diverticulitis causing partial bowel obstruction in a child with cystic fibrosis," *Pediatric Radiology*, vol. 27, no. 12, pp. 918–919, 1997.

[104] B. P. O'Sullivan, D. Baker, K. G. Leung, G. Reed, S. S. Baker, and D. Borowitz, "Evolution of pancreatic function during the first year in infants with cystic fibrosis," *Journal of Pediatrics*, vol. 162, no. 4, pp. 808–812.e1, 2013.

[105] A. Uc, R. Giriyappa, D. K. Meyerholz et al., "Pancreatic and biliary secretion are both altered in cystic fibrosis pigs," *American Journal of Physiology—Gastrointestinal and Liver Physiology*, vol. 303, no. 8, pp. G961–G968, 2012.

[106] K. N. Lazaridis, M. Strazzabosco, and N. F. Larusso, "The cholangiopathies: disorders of biliary epithelia," *Gastroenterology*, vol. 127, no. 5, pp. 1565–1577, 2004.

[107] L. Vítek and M. C. Carey, "Enterohepatic cycling of bilirubin as a cause of 'black' pigment gallstones in adult life," *European Journal of Clinical Investigation*, vol. 33, no. 9, pp. 799–810, 2003.

[108] D. P. Cook, M. V. Rector, D. C. Bouzek et al., "Cystic fibrosis transmembrane conductance regulator in sarcoplasmic reticulum of airway smooth muscle. Implications for airway contractility," *American Journal of Respiratory and Critical Care Medicine*, vol. 193, no. 4, pp. 417–426, 2016.

[109] M. E. R. Darnell, E. P. Plant, H. Watanabe et al., "Severe acute respiratory syndrome coronavirus infection in vaccinated ferrets," *The Journal of Infectious Diseases*, vol. 196, no. 9, pp. 1329–1338, 2007.

[110] F. Krammer, R. Hai, M. Yondola et al., "Assessment of influenza virus hemagglutinin stalk-based immunity in ferrets," *Journal of Virology*, vol. 88, no. 6, pp. 3432–3442, 2014.

[111] J. F. Engelhardt, J. R. Yankaskas, S. A. Ernst et al., "Submucosal glands are the predominant site of CFTR expression in the human bronchus," *Nature Genetics*, vol. 2, no. 3, pp. 240–248, 1992.

[112] R. Dajani, Y. Zhang, P. J. Taft et al., "Lysozyme secretion by submucosal glands protects the airway from bacterial infection," *American Journal of Respiratory Cell and Molecular Biology*, vol. 32, no. 6, pp. 548–552, 2005.

[113] X. Liu, M. Luo, L. Zhang, W. Ding, Z. Yan, and J. F. Engelhardt, "Bioelectric properties of chloride channels in human, pig, ferret, and mouse airway epithelia," *American Journal of Respiratory Cell and Molecular Biology*, vol. 36, no. 3, pp. 313–323, 2007.

[114] X. Sun, Z. Yan, Y. Yi et al., "Adeno-associated virus—targeted disruption of the CFTR gene in cloned ferrets," *Journal of Clinical Investigation*, vol. 118, no. 4, pp. 1578–1583, 2008.

[115] C. A. Johnson-Delaney, "Ferret nutrition," *Veterinary Clinics of North America: Exotic Animal Practice*, vol. 17, no. 3, pp. 449–470, 2014.

[116] D. H. Andersen, "Cystic fibrosis of the pancreas and its relation to celiac disease: a clinical and pathologic study," *American Journal of Diseases of Children*, vol. 56, no. 2, pp. 344–399, 1938.

[117] R. W. Shepherd and G. J. Cleghorn, *Cystic Fibrosis: Nutritional and Intestinal Disorders*, CRC Press, New York, NY, USA, 1989.

[118] W. Lissens, B. Mercier, H. Tournaye et al., "Cystic fibrosis and infertility caused by congenital bilateral absence of the vas deferens and related clinical entities," *Human Reproduction*, vol. 11, no. 4, pp. 55–80, 1996.

[119] D. A. Gaillard, F. Carre-Pigeon, and A. Lallemand, "Normal vas deferens in fetuses with cystic fibrosis," *Journal of Urology*, vol. 158, no. 4, pp. 1549–1552, 1997.

Hindawi Publishing Corporation
BioMed Research International
Volume 2016, Article ID 3938523, 8 pages
http://dx.doi.org/10.1155/2016/3938523

Research Article

Comparison of Neuroprotective Effect of Bevacizumab and Sildenafil following Induction of Stroke in a Mouse Model

Ivan Novitzky,[1] Neelan J. Marianayagam,[1,2] Shirel Weiss,[2,3] Orkun Muhsinoglu,[4] Moran Fridman,[2,3] Tamar Azrad Leibovitch,[2,3] Nitza Goldenberg-Cohen,[2,3,4] and Shalom Michowiz[1,3]

[1]*Department of Neurosurgery, Rabin Medical Center-Beilinson Hospital, 49100 Petach Tikva, Israel*
[2]*Krieger Eye Research Laboratory, Felsenstein Medical Research Center, 49202 Petach Tikva, Israel*
[3]*Sackler Faculty of Medicine, Tel Aviv University, 6997801 Tel Aviv, Israel*
[4]*Pediatric Ophthalmology Unit, Schneider Children's Medical Center of Israel, 49100 Petach Tikva, Israel*

Correspondence should be addressed to Nitza Goldenberg-Cohen; ncohen1@gmail.com

Received 9 January 2016; Revised 11 April 2016; Accepted 21 April 2016

Academic Editor: Monica Fedele

To evaluate the effect of bevacizumab and sildenafil on stroke parameters in a mouse model, middle cerebral artery occlusion was induced in male C57Bl/6 mice using an intra-arterial filament method. The filament was removed after 60 minutes, and the mice were immediately given a single intraperitoneal injection of saline, bevacizumab, or sildenafil. An additional group of mice ($n = 7$) received bevacizumab 6 h after MCAO induction. The mice were euthanized 24 hours later and evaluated for infarct area and brain edema using triphenyltetrazolium chloride staining and ImageJ. In the saline-treated mice ($n = 16$), total stroke volume was $19.20 \pm 6.38\,mm^3$, mean penumbra area was $4.5 \pm 2.03\,mm^3$, and hemispheric asymmetry was 106.5%. Corresponding values in the bevacizumab group ($n = 19$) were $17.79 \pm 5.80\,mm^3$, $7.3 \pm 3.5\,mm^3$, and 108.6%; in the delayed (6 h) bevacizumab injected mice ($n = 7$) they were $9.80 \pm 8.00\,mm^3$, $2.4 \pm 2.0\,mm^3$, and 98.2%; and in the sildenafil group ($n = 16$) they were $18.42 \pm 5.41\,mm^3$, $5.7 \pm 2.02\,mm^3$, and 109.9%. The bevacizumab group had a significantly larger mean penumbra area when given immediately and smaller total stroke area in both groups than the saline- ($p = 0.03$) and sildenafil-treated ($p = 0.003$) groups. Only delayed bevacizumab group had reduced edema. Bevacizumab, injected immediately or delayed after injury, exerts a neuroprotective/salvage effect, whereas immediate treatment with sildenafil does not. Inflammation may play a role in the neuroprotective effect.

1. Introduction

Bevacizumab is an inhibitor of vascular endothelial growth factor (VEGF) that targets VEGF-A, an isoform of VEGF that stimulates endothelial cell proliferation and migration. By specifically binding the VEGF-A protein, it reduces the VEGF protein levels and restricts the growth of abnormal blood vessels, thus reducing their leakage. In addition, it has an anti-inflammatory role that reduces macrophage activity and inhibits infiltration of inflammatory materials causing neuronal damage [1]. Bevacizumab has been found to exert an antiangiogenic effect in tumors and a neuroprotective effect in the brain by reducing leakage and edema [1]. It is used in the treatment of colon cancer [2] and gliomas (low and high grade) [3] and age-related macular degeneration [4]. It was also recently found to be effective in reducing macular edema in the sensory retina of patients with diabetes [5]. However, some studies suggest that bevacizumab may play a role in causing cerebral ischemia [6, 7].

Sildenafil citrate is a potent vasodilator which inhibits the action of phosphodiesterase 5 (PDE 5). Sildenafil competes with cyclic guanosine monophosphate (cGMP), responsible for smooth muscle relaxation, for the substrate-binding site on PDE 5, thereby increasing the concentration of cGMP in the tissue [8]. Sildenafil is used mainly in the treatment of erectile dysfunction. It is beneficial for the treatment of

pulmonary hypertension as well, as PDE 5 is also distributed in the smooth muscle arterial walls of the lungs [9]. It was also found to induce retinal artery and vein dilatation in healthy subjects [10]. Recent studies have shown that sildenafil may exert a protective effect against ischemic injury in various organ systems such as the heart and kidney [11–13]. In cardiac tissue, it acts as a mimetic for super oxide dismutase, preventing the generation of hydrogen peroxide (H_2O_2) [11]. This reduces the formation of oxygen-free radicals, the driving force behind ischemia reperfusion injury and consequent mitochondrial dysfunction and cardiac myocyte injury. Sildenafil also protects the heart by activating the ATP-sensitive potassium channels on the mitochondrial walls [12], thereby helping to maintain the mitochondrial membrane potential during ischemia reperfusion injury. Furthermore, sildenafil has at least a partial anti-inflammatory effect through iNOS inhibition [14]. It was found to reduce the expression of cytokines, COX-2, and GFAP (glial fibrillary acidic protein) in a demyelinating model induced in wild type mice, and in $iNOS^{-/-}$ mice, sildenafil reduced Iba-1, IFN-γ, and IL-1β levels following cuprizone induced myelin damage, and increased glutathione S-transferase pi, improving the myelin structure/ultrastructure [14]. Prompted by findings that sildenafil citrate is protective against ischemia reperfusion injury in neonatal rats, researchers postulated that it may be helpful in the treatment of neonatal cerebral ischemia [15]. At the same time, several reports have described sildenafil as a stroke inducer in the presence of preexisting conditions or a history of stroke [16].

The aim of the present study was to determine if bevacizumab and sildenafil have a protective influence on cerebral ischemic events using a mouse model of stroke.

2. Methods

2.1. Animals. All protocols were conducted in accordance with the ARVO Statement for the Use of Animals in Ophthalmic and Visual Research and were approved and monitored by the Animal Care Committee of Rabin Medical Center (Permit Number 030813, 022-b6640-2). Adult male C57Bl/6 mice (wild type) were purchased from Harlan Laboratories (Jerusalem, Israel). Animals were maintained in our animal colony at 22°C on a 12-hour light/12-hour dark cycle. All procedures and analyses were performed by the same researcher (Ivan Novitzky) to reduce variability.

2.2. Induction of Middle Cerebral Artery Occlusion. Our middle cerebral artery occlusion (MCAO) model is based on previously published protocols [17, 18]. In brief, mice were anesthetized with ketamine/xylazine (80 mg/kg and 8 mg/kg, resp.), and the neck was incised to expose the left common carotid artery (LCCA). Two separate LCCA ligatures were made using 6.0 surgical sutures. The left internal carotid artery (LICA) and the left pterygopalatine artery were clipped. The LCCA was perforated with a 27-gauge needle, and a sterile 5.0-nylon monofilament with cautery-enlarged tip was inserted through the hole and pushed up to the clip in the LICA. Both microvascular clips were then removed. The filament was advanced and inserted about 10 mm into the middle cerebral artery. After 60 minutes of occlusion, a third ligature was placed around the LCCA, the filament was removed, and the LCCA was permanently ligated.

2.3. Treatment. Immediately after removal of the filament and wound closure with nylon suture, the mice were allocated to one of three groups: 0.3 mL (300 μL) saline treatment (0.9% sterile NaCl solution, sham injection), single peritoneal injection of bevacizumab (Avastin, Genentech/Roche, 75 μg/300 μL), or single peritoneal injection of sildenafil (Revatio 0.8 mg/mL solution for injection, Pfizer Limited, Sandwich, United Kingdom; 24 μg/300 μL). An additional group of 7 mice received a single bevacizumab injection 6 h after induction. All mice were given fluid replenishment (0.5 mL sterile saline) postoperatively, and topical lidocaine gel was placed on the incision site for pain relief.

2.4. Triphenyltetrazolium Chloride Staining. At 24 hours after MCAO induction, the animals were euthanized with carbon dioxide. The brains were removed, incubated in 0.5% 2,3,5-triphenyltetrazolium chloride (TTC) solution in 0.9% saline for 10 minutes at 37°C, and cut coronally.

2.5. Fluorescent Gelatin Perfusion for Brain Vascular Imaging. Vascular imaging was performed by transcardial perfusion of gelatin containing fluorescently labeled bovine serum albumin (BSA), as previously reported [18, 19]. Briefly, the mice were terminally anesthetized with pentobarbital overdose, and a series of solutions was perfused transcardially as follows: 20 mL heparinized 0.9% saline, 10 mL 2% type A gelatin in saline with fluorescein-conjugated BSA (approximately 0.01 mg/mL), and 2 mL 4% type A gelatin in saline with cyanin-conjugated BSA. Thereafter, the ascending aorta was clamped with a hemostat while under pressure, and the animal was immersed in an ice-water bath to congeal the gelatin. Perfusion of both hemispheres (unaffected and injured) was compared.

2.6. Immunostaining. Cryosections of untreated (saline) MCAO induced brain sections were taken at 24 h, washed with phosphate buffer saline ×1, blocked with 2% BSA in phosphate buffer saline with 0.5% Triton X-100 for 15 min, and incubated at 4°C overnight with the primary antibody: rat anti-CD45 (1 : 100, Millipore, Temecula, CA). The sections were washed with 0.2% PBS with 0.5% Triton X-100 and incubated at room temperature for 1 h with the secondary antibody: goat anti-rat IgG Alexa Fluor 488 (1 : 200) (Molecular Probes, Invitrogen Corporation, Carlsbad, CA, USA). The brain sections underwent nuclear counterstaining with DAPI (Invitrogen). Images were generated using a conventional fluorescence microscope (Fluoview X; Olympus, Tokyo, Japan). Excitation wavelengths were 405 nm for DAPI and 488 nm for Alexa Fluor.

2.7. Calculation of Lesion Volume and Hemispheric Asymmetry. Digital images of the TTC-stained coronal sections were analyzed for lesion volume and edema using Fiji imaging

Table 1: List of primers.

Gene	Forward primer sequence (5′-3′)	Reverse primer sequence (5′-3′)
Mouse ACTB	TAGGCACCAGGGTGTGATGGT	CATGTCGTCCCAGTTGGTAACA
Mouse SOD-1	GCCCGGCGGATGAAGA	CGTCCTTTCCAGCAGTCACA
Mouse HO-1	CAGGTGTCCAGAGAAGCTTT	TCTTCCAGGGCCGTGTAGAT
Mouse CD45	GAACATGCTGCCAATGG	TGTCCCACATGACTCCTT
Mouse BAX	CTGAGCTGACCTTGGA	GACTCCAGCCACAAAG
Mouse BCL-2	CCTGTGGATGACTGAG	GAGCAGGGTCTTCAGA
Mouse TNF-α	TCT CAA AAT TCG AGT GAC AAG C	ACT CCA GCT GCT CCT CCA C
Mouse GFAP	CCAGCTTCGAGCCAAGG	GAAGCTCCGCCTGGTAG
Mouse MIP-2	CAGGGTGTGATGGTGGGAAT	TGCTCTGGGCCTCGTCA

processing software (ImageJ, National Institutes of Health, USA). Stroke area and penumbra and hemispheric volume were calculated. The stroke lesions were identified as white areas completely devoid of TTC staining, and the penumbra was segmented by any color noticeably lighter than healthy tissue, which appears bright red [20]. Total stroke area was defined as the sum of the stroke and penumbra region. Brain edema was defined by hemispheric asymmetry, calculated as the ratio of infarcted hemisphere to normal healthy hemisphere.

2.8. Molecular Analysis

2.8.1. RNA Extraction. Brain tissues from 11 mice after MCAO induction, 6 treated 6 hours after induction by bevacizumab, were dissected and frozen in RNAlater (Life Science Division, Sigma-Aldrich, St. Louis, MO, USA). The middle third of each hemisphere was used. The mRNA samples were analyzed in pairs per mice (injured and uninjured hemisphere) and also pooled (normal unaffected hemispheres versus stroke hemispheres, for treated and untreated groups). Total RNA was isolated using TRIzol™ reagent (Life Technologies, Invitrogen) according to the manufacturer's protocol and then reverse-transcribed into cDNA using random hexamers (Amersham Biosciences, Buckinghamshire, UK) and Moloney murine leukemia virus reverse transcriptase (Promega, Madison, WI, USA).

2.8.2. Real-Time Quantitative PCR. Real-time quantitative PCR (RT-qPCR) was applied to study gene expression of apoptosis-related BAX and BCL-2 genes, inflammatory-related CD45 and MIP-2 (IL-8), and stress-related HO-1 genes in the brain using gene-specific primers (Table 1). The reaction efficiency was tested using a standard curve. Gene expression was normalized to mouse beta actin, a housekeeping gene. StepOne™ Software v2.2.2 (Applied Biosystems, Foster City, CA, USA) was used for RT-qPCR. Reactions were performed in a 10 μL volume containing 1 μL cDNA, 0.5 μM of each of the forward and reverse primers, and buffer included in the Master Mix (SYBR® Green I; Applied Biosystems).

Cycling conditions consisted of an initial denaturation step of 95°C for 10 min followed by 50 cycles of 1 min at 95°C and 1 min of annealing and extension at 60°C. Duplicate RT-qPCR reactions were performed for each gene to minimize individual tube variability, and an average was taken for each time point. Threshold cycle efficiency corrections were calculated, and melting curves were obtained using cDNA for each individual-gene PCR assay. The results were quantified by the comparative threshold cycle (Ct) method, where $\Delta\Delta$Ct = ΔCt (sample) − ΔCt (reference gene) (Data Assist™ Software v2.2.2, Applied Biosystems).

2.9. Statistical Analysis. Experimental data are expressed as mean ± standard error. Student's t-test was used to determine the significance of differences between groups. $p < 0.05$ was considered significant.

3. Results

Mean values of the stroke and edema parameters after MCAO induction in the mice treated with saline, bevacizumab, or sildenafil are shown in Table 2 and Figure 1. The early bevacizumab-treated animals had a significantly greater mean penumbra area (salvageable tissue surrounding the infarct) than both the control mice ($p = 0.03$) and the sildenafil-treated mice ($p = 0.003$) and both groups of bevacizumab had smaller total stroke area than the other groups. The percentage of injured brain hemisphere relative to total healthy hemispheric tissue was lower in the bevacizumab-treated mice than in the sildenafil-treated mice ($p = 0.34$). The saline-treated animals had the lowest hemispheric asymmetry. There was no decrease in brain edema after ischemic injury in either the bevacizumab- or sildenafil-immediately treated group.

Figure 2 shows the lack of perfusion in the injured hemisphere as compared to the unaffected hemisphere of untreated mice (control). Immunostaining for inflammation (CD45) of the same brains (Figure 3) shows the extravascular infiltration of inflammatory cells into the damaged area, where the vascular perfusion was interrupted. Figure 4 shows infiltration of CD45 into the stroke area, in the delayed bevacizumab-treated brain.

Table 3 shows the MCAO-related morbidity and mortality in the three groups. Mortality was categorized as either perioperative (traumatic bleeding during the procedure or anesthesia related) or postoperative (death after surgery).

Table 2: Penumbra, stroke, and brain edema in sildenafil-, bevacizumab- (immediate and 6 h), and saline-treated MCAO induced mice.

Treatment	N	Mean penumbra area (mm^3)	Mean stroke area (mm^3)	Total stroke area (mm^3)	Total injured hemisphere (mm^3)	% of injured hemisphere	Normal hemisphere	Hemispheric asymmetry (ratio)
Sildenafil	16	5.7 ± 2.02	12.72 ± 6.76	18.42 ± 5.41	32.63 ± 1.60*	56.10 ± 15.31	29.68 ± 3.13	1.099
Bevacizumab	19	7.3 ± 3.5	10.50 ± 5.53	17.79 ± 5.80	34.67 ± 2.04*	51.0 ± 15.52	31.89 ± 3.25	1.086
	7	2.4 ± 2.0	7.40 ± 5.42	9.80 ± 8.00	32.90 ± 2.93	29.00 ± 22.3	33.51 ± 2.23	0.982
Saline	16	4.5 ± 2.03	14.70 ± 6.75	19.20 ± 6.38	32.72 ± 2.95	58.09 ± 16.7	30.70 ± 3.20	1.065

* $p = 0.03$ versus saline and $p = 0.003$ versus sildenafil.

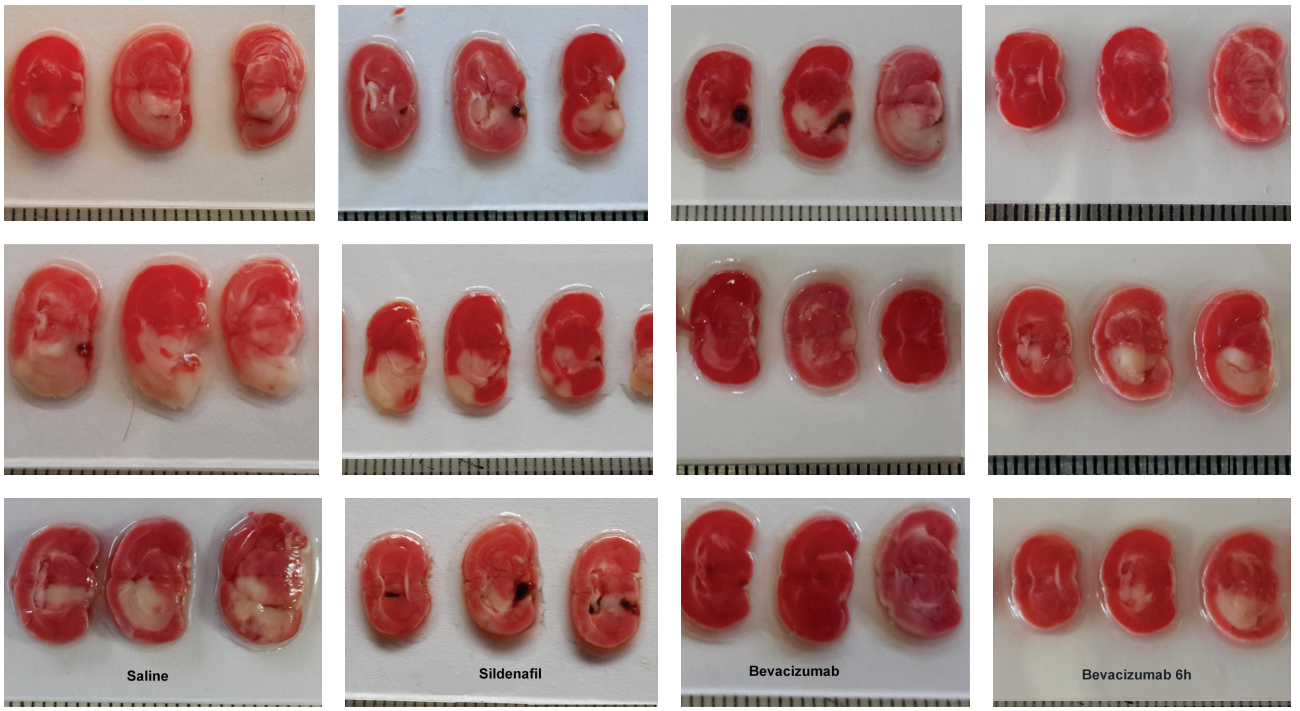

Figure 1: TTC (2,3,5-triphenyltetrazolium chloride) staining of MCAO infarcted brain tissue from mice treated with saline (control, first column), sildenafil (2nd column), and bevacizumab (3rd and 4th columns). Infarcted tissue is pale while healthy tissue is pink. It is evident that the mice treated with bevacizumab (immediate and late) have the largest amount of healthy tissue, indicating a neuroprotective effect. Each line represents different animal.

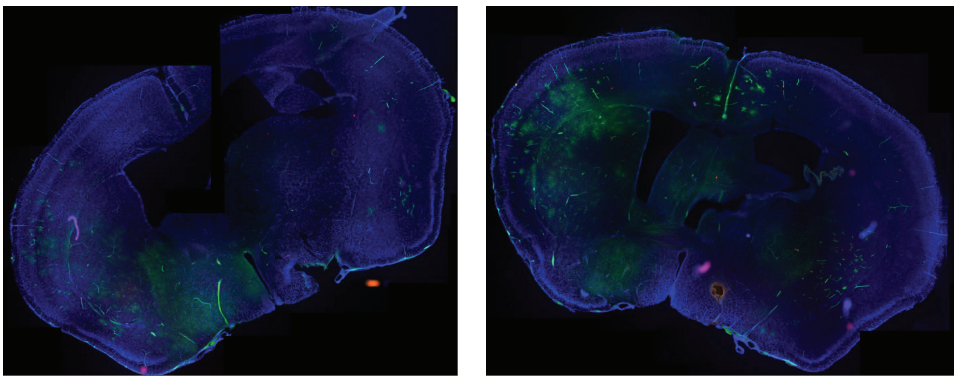

(a) (b)

Figure 2: Perfusion studies of injured hemisphere versus control. Two brain sections following fluorescent perfusion of MCAO induced brains without treatment (saline group). Note the good vascularization on the healthy side, with infarct and lack of perfusion in the infarcted area. (Low magnification ×5, panoramic view).

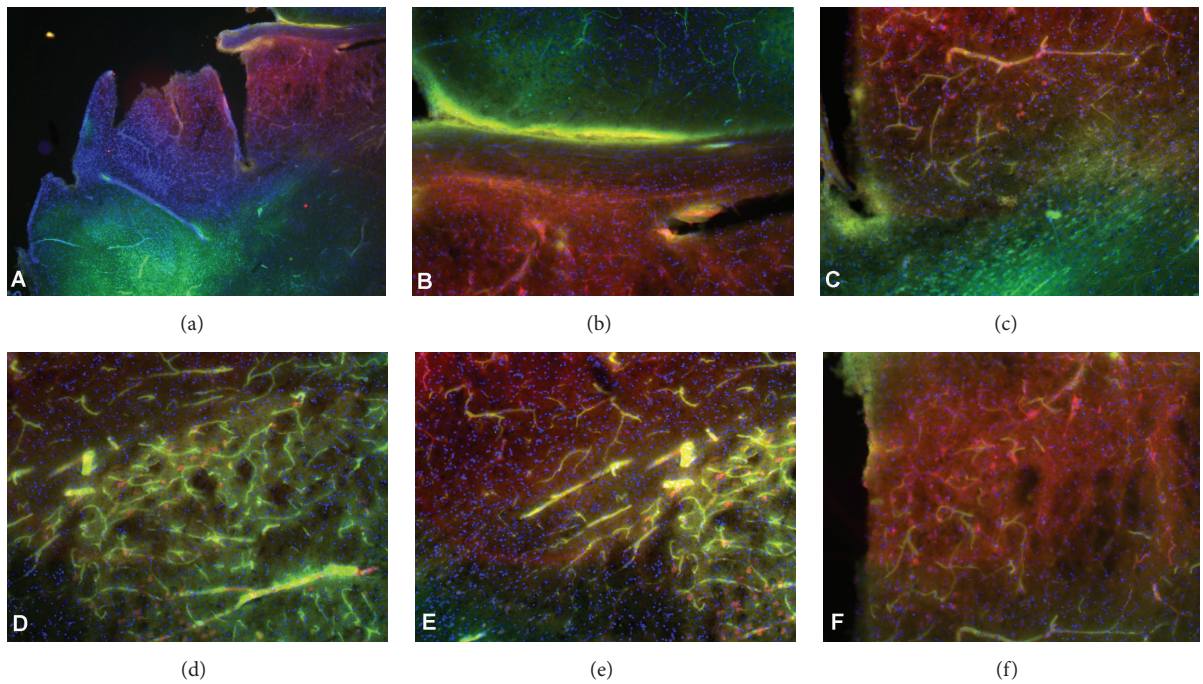

Figure 3: CD45 staining (red) of brains section of mice following MCAO induction without treatment (saline injected, controls) and perfusion with fluorescent gelatin (green). The nuclei are stained with DAPI (blue). (a) CD45 immunostaining (red) showing infiltration of the inflammatory cells to the injured hemisphere and increased cellularity (DAPI, blue) (×5), while the unaffected hemisphere is well perfused (green). (b) Higher magnification of the injured versus unaffected brain (×20). (c) Incomplete perfusion of the vessels in the infarct area, with extravasation of inflammatory cells to the tissue, as compared to the unaffected brain (green) without inflammatory cells. (d–f) Incomplete vascularization with intra- and extracellular inflammatory cells (×40).

Morbidity was defined as visible neurological deficit after surgery and/or treatment. The highest mortality (75%) was detected in the late bevacizumab injection, followed by 60% in the saline group, probably due to three experiments where none of the mice survived the anesthesia. Following the MCAO induction, the bevacizumab-treated mice had lower morbidity and mortality rates than controls. The sildenafil-treated group had lower mortality than controls but higher morbidity.

The molecular analysis of the untreated group versus the bevacizumab 6 h treated group showed significantly increased BAX levels and BAX/BCL-2 ratio (5.07-fold versus 0.90-fold for BAX and BAX/Bcl-2 ratio 3.84 versus 0.51) and increased CD45 levels in the bevacizumab 6 h treated group (2.04-fold) versus untreated group (0.84-fold). SOD1 and GFAP levels remained at baseline in the untreated group and mildly reduced (0.82 fold, NS) in the 6 h bevacizumab-treated group; MIP-2 remained at baseline in both groups.

4. Discussion

This study shows that bevacizumab, a VEGF inhibitor, has a neuroprotective effect on mice after MCAO induction. The bevacizumab-treated mice had a lower volume of injured brain and a larger penumbra, meaning more salvageable tissue than the untreated mice. Furthermore, injection 6 h after MCAO induction still showed a neuroprotective effect with reduced brain edema. However, there was no between-group difference in brain edema in the early treated groups. We did not provide any evidence to support the assumption that bevacizumab decreases the leakage and therefore protects the brain. However, the neuroprotective effect might be exerted through the reduced inflammatory cell infiltration into the injured area. Inhibition of the inflammatory reaction plays a role in the neuroprotective effect. We hypothesize that this neuroprotective effect of bevacizumab is directly related to the anti-inflammatory properties of the drug. It is of note that the mortality was highest in the group treated only 6 hours after MCAO induction (Table 2). This warrants further investigation.

Molecular analysis showed a neuroprotective effect in reducing apoptosis reaction. While CD45 was elevated in the 6 h bevacizumab-treated group, the untreated group showed a trend to receding inflammatory reaction, which is not significant to discuss protection or destruction. MIP-2 and GFAP levels were similar near baseline in both groups. Previous studies from our laboratory have demonstrated protective effect in reducing acute inflammation in stroke model in TLR4 knockout mice in brain [20] and optic nerve [21].

We have demonstrated here the increased infiltration of inflammatory cells to the damage area in the brain (using immunohistochemistry) in untreated mice but showed increased molecular gene expression levels of CD45 but not MIP-2 in the 6 h treated brain. We assume that the CD45 represent inflammatory reaction that can be protective

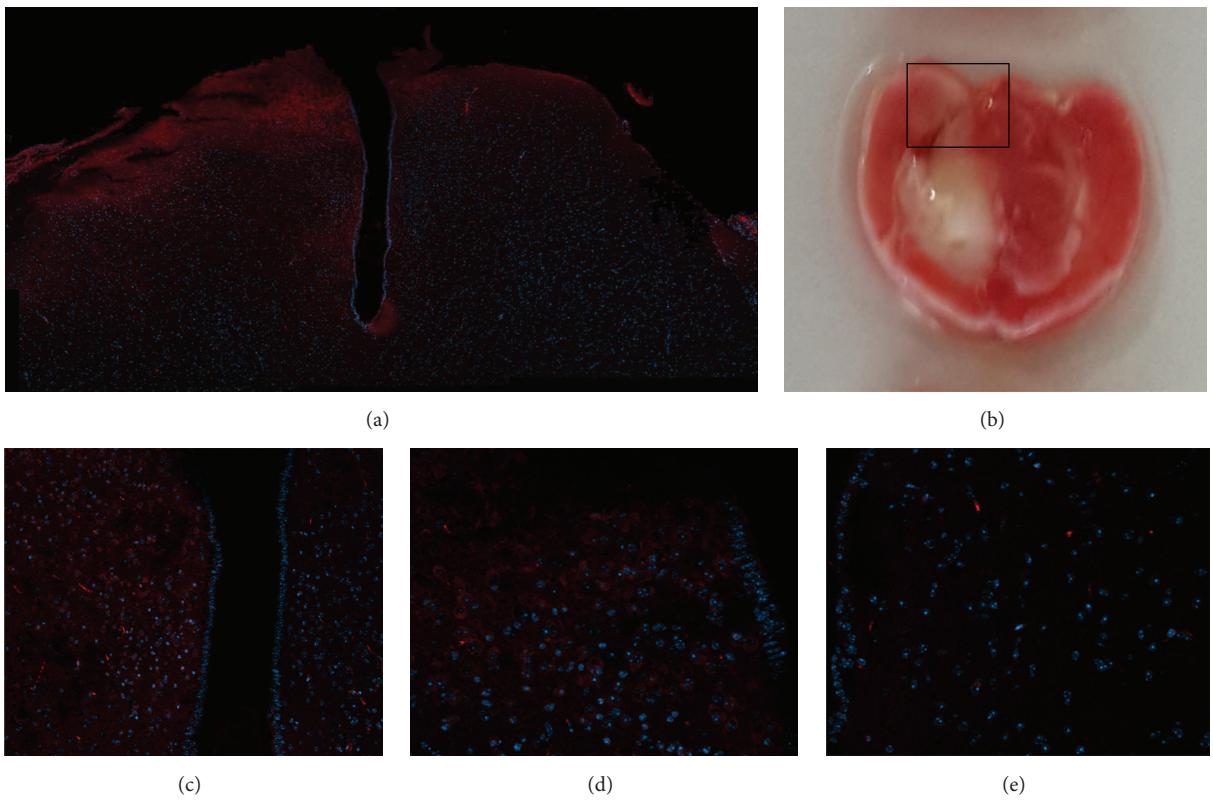

Figure 4: Immunohistochemistry staining for inflammatory cells using CD45 marker, demonstrating Inflammatory infiltration to the infarct area. (a) Inflammatory cells in the injured hemisphere but not in the other side (×20). (b) The location of the area immunostained in (a) is demonstrated in TTC staining (×5). (c) Higher magnification of (a) (×40). (d) The injured hemisphere with positive staining for inflammatory cells. (e) The unaffected hemisphere, negative for CD45 staining.

Table 3: Mortality and morbidity in treated rats after MCAO induction.

	Saline	Bevacizumab		Sildenafil
	Imm.	Imm.	6 h	Imm.
Total number of mice at study onset	58	32	35	27
Mortality				
After surgery	15	5	14	1
After anesthesia	20	4	9	1
Total	35 (60%)	9 (28%)	23 (68%)	2 (0.74%)
Morbidity				
After surgery	3 (13%)	0	0	6 (24%)
Survived procedure	20	23	12	19
Included in study	*16*	*19*	*12*[*]	*16*
No stroke	4 (20%)	3 (13%)	0 (0%)	1 (6.3%)
Extreme damage	0	1 (4.3%)	0 (0%)	2 (10.5%)

Imm.: immediately injected after MCAO induction. [*]7 of 11 for histology (TTC) and immunohistochemistry and 5 for molecular analysis.

or destructive, depending on its expression levels. Further analysis of IL-8/MIP-2 and GFAP did not show differences between the groups.

It has been postulated that there might be a connection between hypoxia and inflammations [22]. This relationship could be explained by the fact that the hypoxic endothelium expresses inflammatory chemokine receptors, such as CXCR4 and CXCR7, as well as the angiogenic chemokines (such as CXCL8 and CXCL1) [22]. These are all regulated by the transcription factor hypoxia inducible factor and serve

as potential future drug targets for anti-inflammatory drugs. We measured the inflammatory-related gene expression and confirmed the increased inflammatory effect after stroke induction. Immunostaining for CD45 and molecular expression levels confirmed its effect.

Unlike bevacizumab, sildenafil did not exert a significant generalized neuroprotective effect. Although sildenafil was found to reduce the inflammatory reaction in models of demyelinating brain injury [14], it was not effective in the MCAO model. There was no significant difference in poststroke brain edema between sildenafil- and saline-treated mice.

These findings contrast with earlier clinical studies. Bevacizumab has been shown to induce cerebral ischemic events in patients being treated for glioma and to reduce brain edema in patients with brain tumor [3, 7]. We attribute its protective effect to the restriction of proinflammatory activities. Sildenafil has been found to protect against cerebral edema [15, 16] and to serve as an appropriate therapy for patients with stroke [23]. Accordingly, in an experimental study of the poststroke effects of bevacizumab [24], researchers treated Sprague-Dawley rats with bevacizumab or saline following induction of MCAO and analyzed the findings with positron emission tomography in conjunction with behavioral analysis. Their results suggested that bevacizumab has no effect on functional recovery after stroke [24]. However, positron emission tomography showed a decreased metabolic demand for glucose and inhibition of vascular formation, which could explain our finding of a neuroprotective effect. In an analogous study of sildenafil, rats in the study group had consistently better behavioral scores than controls and a reduced cerebral infarction volume [25]. Transmission electron microscopy showed a significant decrease in the number of degenerated neurons in the sildenafil group, and molecular analysis showed a significant decrease in the extent of synapse damage via the cGMP-dependent Nogo-R pathway.

The difference between similar studies in the brain [24, 25] and our study has several explanations. These experimental studies used rat models of stroke instead of a mouse model which we utilized. A much smaller number of animals (n = 8–12) were used in these studies compared to our work (bevacizumab 19/51 and sildenafil 16/51) with much higher doses of the study drugs (up to 32 mg/kg ×3) [24, 25]. The time course of our experiments was also different. Our animals were investigated only 24 hours after MCAO induction, whereas other studies used varying time points [24, 25]. Also, the neuroprotective effect of bevacizumab was observed in the context of solid tumors, where it could be due to a decrease in glucose demand in neural tissue, as shown on positron emission tomography [24].

Sildenafil was also found to have a protective effect in various organ systems, such as heart and kidney [13], probably via a reduction in oxidative stress in ischemia reperfusion injury. Specifically, sildenafil induced mitochondrial biogenesis in the injured cells in the renal cortex. Mitochondrial dysfunction/disruption of mitochondrial biogenesis is one of the mechanisms underlying ischemia/reperfusion injury in the kidney and apparently plays a role in acute kidney injury and renal tubular dysfunction [13]. It has also been implicated in ischemia reperfusion injury in the brain. Sildenafil was found to induce mitochondrial biogenesis in the mouse renal cortex [12], and a postmortem analysis of brain tissue from patients after ischemic events showed that mitochondrial oxidative stress was responsible for neuronal cell death [23]. Therefore, sildenafil is considered a promising therapeutic agent for patients with acute kidney injury or stroke.

However, it must be mentioned that the fundamental physiology of neural tissue is different to other tissues, making it less forgiving to ischemic injury. It has been shown that mitochondrial dysfunction due to oxidative stress after ischemic injury is most likely the mechanism of neuronal damage in stroke [23]. It is likely, however, that sildenafil has a less protective effect in neural tissue compared to other tissues in the body due to the less forgiving nature of the central nervous system to ischemic injury.

5. Conclusions

This study demonstrated that bevacizumab has a slight neuroprotective effect after ischemic stroke, whereas sildenafil does not. This is in contradiction to previous studies [24, 25]. However, we have utilized a larger sample size. Caution should be used in attempting to identify neuroprotective drugs. Neural tissue is complex, and a large amount of animals/samples are needed before meaningful results can be obtained.

Disclosure

The authors alone are responsible for the content and writing of the paper. This work was presented in part at the International Symposium on Ocular Pharmacology and Therapeutics (ISOPT), Berlin, Germany, in July 2015.

Competing Interests

The authors declare no competing financial interests.

Authors' Contributions

Ivan Novitzky conducted the study, analyzed the results, and edited the figures. Neelan J. Marianayagam analyzed the results and wrote the paper draft. Shirel Weiss analyzed the results. Orkun Muhsinoglu performed the study. Moran Fridman performed the immunohistochemistry studies and microscopy. Tamar Azrad Leibovitch performed the molecular analysis and analyzed the results. Nitza Goldenberg-Cohen designed, analyzed, and wrote the paper. Shalom Michowiz designed, performed, analyzed the results and critically revised the paper. All authors discussed the results and implications and commented on the paper at all stages. Ivan Novitzky and Neelan J. Marianayagam contributed equally to this paper.

Acknowledgments

This study was partially supported by the Zanvyl and Isabelle Krieger Fund, Baltimore, Maryland, USA; Israel Scientific Foundation (Grant no. 1189/12); and Rabin Young Investigator Award (Ivan Novitzky).

References

[1] Y. Sun, K. Jin, L. Xie et al., "VEGF-induced neuroprotection, neurogenesis, and angiogenesis after focal cerebral ischemia," *The Journal of Clinical Investigation*, vol. 111, no. 12, pp. 1843–1851, 2003.

[2] J. H. Strickler and H. I. Hurwitz, "Bevacizumab-based therapies in the first-line treatment of metastatic colorectal cancer," *The Oncologist*, vol. 17, no. 4, pp. 513–524, 2012.

[3] S. J. Peak and V. A. Levin, "Role of bevacizumab therapy in the management of glioblastoma," *Cancer Management and Research*, vol. 2, no. 1, pp. 97–104, 2010.

[4] J. M. Pitlick, K. F. Vecera, K. N. Barnes, J. W. Reski, and A. B. Forinash, "Bevacizumab for the treatment of neovascular age-related macular degeneration," *Annals of Pharmacotherapy*, vol. 46, no. 2, pp. 290–296, 2012.

[5] J. A. Wells, A. R. Glassman, A. R. Ayala et al., "Aflibercept, bevacizumab, or ranibizumab for diabetic macular edema," *The New England Journal of Medicine*, vol. 372, no. 13, pp. 1193–1203, 2015.

[6] A. A. Grivas, D. T. Trafalis, and A. E. Athanassiou, "Implication of bevacizumab in fatal arterial thromboembolic incidents," *Journal of B.U.ON.*, vol. 14, no. 1, pp. 115–117, 2009.

[7] T. J. Fraum, T. N. Kreisl, J. Sul, H. A. Fine, and F. M. Iwamoto, "Ischemic stroke and intracranial hemorrhage in glioma patients on antiangiogenic therapy," *Journal of Neuro-Oncology*, vol. 105, no. 2, pp. 281–289, 2011.

[8] J. D. Corbin, "Mechanisms of action of PDE5 inhibition in erectile dysfunction," *International Journal of Impotence Research*, vol. 16, supplement 1, pp. S4–S7, 2004.

[9] C. F. Barnett and R. F. Machado, "Sildenafil in the treatment of pulmonary hypertension," *Vascular Health and Risk Management*, vol. 2, no. 4, pp. 411–422, 2006.

[10] M. Pache, P. Meyer, C. Prünte, S. Orgül, I. Nuttli, and J. Flammer, "Sildenafil induces retinal vasodilatation in healthy subjects," *The British Journal of Ophthalmology*, vol. 86, no. 2, pp. 156–158, 2002.

[11] M. A. S. Fernandes, R. J. F. Marques, J. A. F. Vicente et al., "Sildenafil citrate concentrations not affecting oxidative phosphorylation depress H_2O_2 generation by rat heart mitochondria," *Molecular and Cellular Biochemistry*, vol. 309, no. 1-2, pp. 77–85, 2008.

[12] X. Wang, P. W. Fisher, L. Xi, and R. C. Kukreja, "Essential role of mitochondrial Ca^{2+}-activated and ATP-sensitive K^+ channels in sildenafil-induced late cardioprotection," *Journal of Molecular and Cellular Cardiology*, vol. 44, no. 1, pp. 105–113, 2008.

[13] R. M. Whitaker, L. P. Wills, L. J. Stallons, and R. G. Schnellmann, "CGMP-selective phosphodiesterase inhibitors stimulate mitochondrial biogenesis and promote recovery from acute kidney injury," *The Journal of Pharmacology and Experimental Therapeutics*, vol. 347, no. 3, pp. 626–634, 2013.

[14] C. Raposo, A. K. D. S. Nunes, R. L. D. A. Luna, S. M. D. R. Araújo, M. A. da Cruz-Höfling, and C. A. Peixoto, "Sildenafil (Viagra) protective effects on neuroinflammation: the role of iNOS/NO system in an inflammatory demyelination model," *Mediators of Inflammation*, vol. 2013, Article ID 321460, 11 pages, 2013.

[15] C. Charriaut-Marlangue, T. Nguyen, P. Bonnin et al., "Sildenafil mediates blood-flow redistribution and neuroprotection after neonatal hypoxia-ischemia," *Stroke*, vol. 45, no. 3, pp. 850–856, 2014.

[16] M. Lorberboym, I. Mena, J. Wainstein, M. Boaz, and Y. Lampl, "The effect of sildenafil citrate (Viagra) on cerebral blood flow in patients with cerebrovascular risk factors," *Acta Neurologica Scandinavica*, vol. 121, no. 6, pp. 370–376, 2010.

[17] O. Engel, S. Kolodziej, U. Dirnagl, and V. Prinz, "Modeling stroke in mice—middle cerebral artery occlusion with the filament model," *Journal of Visualized Experiments*, no. 47, article 2423, 2011.

[18] D. Rappoport, D. Morzaev, S. Weiss et al., "Effect of intravitreal injection of bevacizumab on optic nerve head leakage and retinal ganglion cell survival in a mouse model of optic nerve crush," *Investigative Ophthalmology & Visual Science*, vol. 54, no. 13, pp. 8160–8171, 2013.

[19] J. D. Nicholson, A. C. Puche, Y. Guo, D. Weinreich, B. J. Slater, and S. L. Bernstein, "PGJ_2 provides prolonged CNS stroke protection by reducing white matter edema," *PLoS ONE*, vol. 7, no. 12, Article ID e50021, 2012.

[20] D. Pushkov, J. D. Nicholson, S. Michowiz et al., "Relative neuroprotective effects hyperbaric oxygen treatment and TLR4 knockout in a mouse model of temporary middle cerebral artery occlusion," *International Journal of Neuroscience*, vol. 126, no. 2, pp. 174–181, 2016.

[21] D. Morzaev, J. D. Nicholson, T. Caspi, S. Weiss, E. Hochhauser, and N. Goldenberg-Cohen, "Toll-like receptor-4 knockout mice are more resistant to optic nerve crush damage than wild-type mice," *Clinical and Experimental Ophthalmology*, vol. 43, no. 7, pp. 655–665, 2015.

[22] C. R. Mackay, "Moving targets: cell migration inhibitors as new anti-inflammatory therapies," *Nature Immunology*, vol. 9, no. 9, pp. 988–998, 2008.

[23] L. T. Watts, R. Lloyd, R. J. Garling, and T. Duong, "Stroke neuroprotection: targeting mitochondria," *Brain Sciences*, vol. 3, no. 2, pp. 540–560, 2013.

[24] Y. Dong, F. Song, J. Ma et al., "Small-animal PET demonstrates brain metabolic change after using bevacizumab in a rat model of cerebral ischemic injury," *Neuroscience Bulletin*, vol. 30, no. 5, pp. 838–844, 2014.

[25] X.-M. Chen, N.-N. Wang, T.-Y. Zhang, F. Wang, C.-F. Wu, and J.-Y. Yang, "Neuroprotection by sildenafil: neuronal networks potentiation in acute experimental stroke," *CNS Neuroscience and Therapeutics*, vol. 20, no. 1, pp. 40–49, 2014.

Hindawi Publishing Corporation
BioMed Research International
Volume 2016, Article ID 4601532, 11 pages
http://dx.doi.org/10.1155/2016/4601532

Research Article

The Influence of Bone Marrow-Secreted IL-10 in a Mouse Model of Cerulein-Induced Pancreatic Fibrosis

Wey-Ran Lin,[1] Siew-Na Lim,[2] Tzung-Hai Yen,[3] and Malcolm R. Alison[4]

[1]*Department of Gastroenterology and Hepatology, Chang Gung Memorial Hospital, Chang Gung University College of Medicine, Taoyuan 333, Taiwan*
[2]*Department of Neurology, Chang Gung Memorial Hospital, Chang Gung University College of Medicine, Taoyuan 333, Taiwan*
[3]*Department of Nephrology, Chang Gung Memorial Hospital, Chang Gung University College of Medicine, Taoyuan 333, Taiwan*
[4]*Centre for Tumour Biology, Barts and The London School of Medicine and Dentistry, London EC1M 6BQ, UK*

Correspondence should be addressed to Wey-Ran Lin; t12360@adm.cgmh.org.tw

Received 24 February 2016; Accepted 3 May 2016

Academic Editor: Monica Fedele

This study aimed to understand the role of IL-10 secreted from bone marrow (BM) in a mouse model of pancreatic fibrosis. The severity of cerulein-induced inflammation, fibrosis, and the frequency of BM-derived myofibroblasts were evaluated in the pancreas of mice receiving either a wild-type (WT) BM or an IL-10 knockout (KO) BM transplantation. The area of collagen deposition increased significantly in the 3 weeks after cerulein cessation in mice with an IL-10 KO BM transplant ($13.7 \pm 0.6\%$ and $18.4 \pm 1.1\%$, $p < 0.05$), but no further increase was seen in WT BM recipients over this time. The percentage of BM-derived myofibroblasts also increased in the pancreas of the IL-10 KO BM recipients after cessation of cerulein ($6.7 \pm 1.1\%$ and $11.9 \pm 1.3\%$, $p < 0.05$), while this figure fell in WT BM recipients after cerulein withdrawal. Furthermore, macrophages were more numerous in the IL-10 KO BM recipients than the WT BM recipients after cerulein cessation (23.2 ± 2.3 versus 15.3 ± 1.7 per HPF, $p < 0.05$). In conclusion, the degree of fibrosis, inflammatory cell infiltration, and the number of BM-derived myofibroblasts were significantly different between IL-10 KO BM and WT BM transplanted mice, highlighting a likely role of IL-10 in pancreatitis.

1. Introduction

Interleukin-10 (IL-10), an anti-inflammatory cytokine, is mainly expressed and secreted by a variety of cell types derived from bone marrow (BM) such as T cells, monocytes/macrophages, dendritic cells, B cells, and natural killer cells. The anti-inflammatory effect of IL-10 is through the inhibition of proinflammatory cytokines from monocytes/macrophages, which are involved in the recruitment of additional inflammatory cells to sites of injury or infection [1]. In the pancreas, IL-10 has also been shown to play an anti-inflammatory role. The pretreatment of IL-10 could decrease the severity of cerulein-induced acute pancreatitis in mice by inhibiting cellular necrosis [2]. This effect is not directly related to a decrease of pancreatic inflammation but most likely due to the inhibition of proinflammatory cytokines from local inflammatory cells. Moreover, the level of IL-10 in serum and *IL-10* mRNA expression in lung, liver, and pancreas have been found to increase during acute pancreatic inflammation. Blocking endogenous IL-10 production by pretreatment with an anti-IL-10 monoclonal antibody increased the severity of acute inflammation suggesting a protective role of endogenous IL-10 in acute pancreatitis [3]. In chronic pancreatitis, using IL-10 knockout (KO) mice, Demols et al. have demonstrated that IL-10 could modulate proliferation and fibrosis in a cerulein-induced chronic pancreatitis mouse model [4], while in a nonalcoholic fatty pancreas disease mouse model, IL-10 secreted from spleen can downregulate the severity of inflammation [5].

BM-derived cells have been shown to be involved in pathogenesis of human pancreatic diseases. In patients with pancreatic cancer, BM-derived stem cells traffic more extensively in the peripheral blood [6]. Moreover, these increased numbers of BM-derived cells are associated with raised levels of various interleukins, including IL-10 [7]. Among the various types of BM-derived cells, BM-derived myofibroblasts

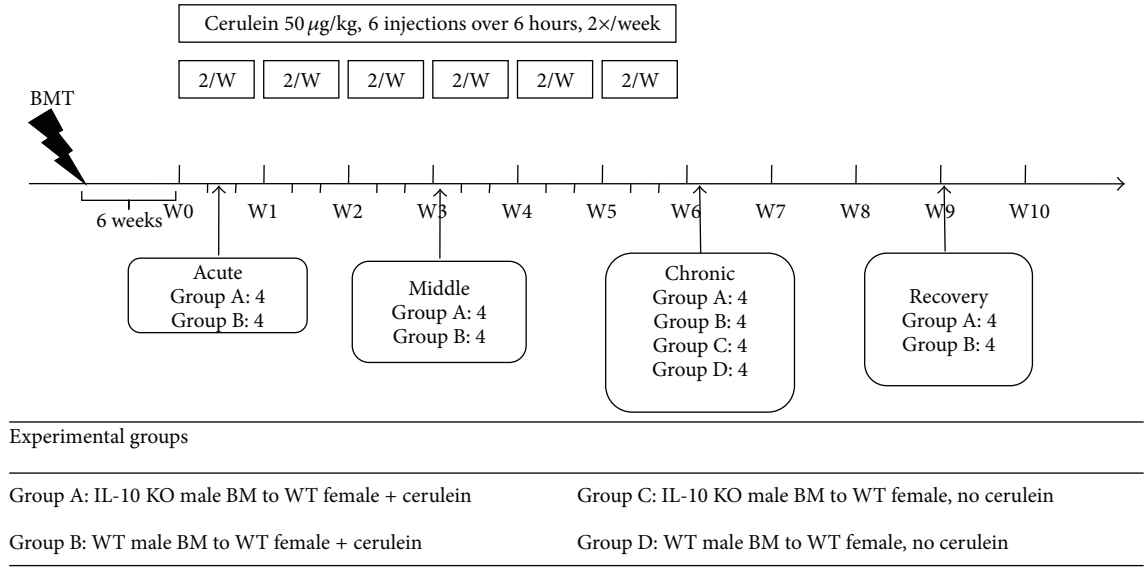

Experimental groups	
Group A: IL-10 KO male BM to WT female + cerulein	Group C: IL-10 KO male BM to WT female, no cerulein
Group B: WT male BM to WT female + cerulein	Group D: WT male BM to WT female, no cerulein

Figure 1: The study design for determining the role of bone marrow-secreted IL-10 in the cerulein-induced acute pancreatitis and pancreatic fibrosis mouse model. Bone marrow transplantation (BMT).

have been shown to participate in pancreatic fibrosis [8, 9]. However, whether BM-derived myofibroblasts are affected by endogenous cytokines of BM origin, that is, can BM-secreted cytokines influence the number of myofibroblasts derived from BM, is not clear. In an IL-10 KO inflammatory bowel disease mouse model, it has been demonstrated that wild-type (WT) BM transplantation can ameliorate the severity of inflammation in the intestine, suggesting that BM-secreted IL-10 plays an anti-inflammatory role [10]. Similarly, IL-10 KO mice have an increased degree of inflammation and fibrosis in chronic pancreatitis [4]; however, this study was performed on an IL-10 KO background, and the role of BM-secreted IL-10 in pancreatic fibrosis is not well explored. Whether BM-secreted IL-10 can attenuate inflammation and fibrosis in pancreatitis and, furthermore, can change the number of myofibroblasts derived from BM is still not known. The aim of this study was to examine the inflammation, fibrosis, and recruitment of BM-derived myofibroblasts in the context of an absence of IL-10 secreted by BM cells.

2. Material and Methods

2.1. Experimental Design. The procedures for animal experiments were performed under British Home Office procedural and ethical guidelines (Figure 1). Six-to-eight-week-old BALB/C WT female recipient mice (The Charles River Laboratory, Wilmington, Maine, USA) underwent whole body lethal gamma irradiation with 10 Gy in a divided dose four hours apart, to ablate their BM, followed immediately by tail vein injection of either WT (groups B and D) or IL-10 KO (groups A and C) male whole BM (2×10^6 cells), resuspended in 0.1 mL sterile PBS with 2% FCS. After six weeks, the mice received either cerulein or vehicle (saline) injections to induce pancreatitis. There were four mice in each group. Acute pancreatitis was induced by 6 intraperitoneal injections of cerulein (50 μg/kg) given at hourly intervals for 1 day. Pancreatic fibrosis was induced by the same protocol of cerulein injections being repeated twice a week for 3 and 6 consecutive weeks. Blood and tissues were harvested at 24 hours after the first injection on day 1 (acute groups), week 3 (middle groups), week 6 (chronic groups), and week 9 (recovery groups) for further analysis.

2.2. Scoring of Acute and Chronic Pancreatitis. The severity of acute pancreatitis was graded as previously reported by Van Laethem et al. [3]. The severity of chronic pancreatitis was graded as previously reported by Demols et al. [4]. The assessments were performed by two specialists independently in a blind manner.

2.3. Immunohistochemical Analyses. A mouse monoclonal anti-α-SMA antibody (A-2547, Sigma-Aldrich) and a mouse monoclonal anti-F4/80 antibody (MCA497, Serotec) were used to detect myofibroblasts and macrophages, respectively. Sections cut at 4 μm were dewaxed, incubated in 1.8% v/v hydrogen peroxide in methanol for 15 min to block endogenous peroxidases, and then taken through graded alcohols to PBS. The sections were then incubated in 20% v/v acetic acid in methanol to block endogenous alkaline phosphatases.

Antigen retrieval treatment was performed by microwaving sections in BD Retrievagen A solution (550524, BD Pharmagen) for 10 minutes. To reduce nonspecific background staining, sections were next preincubated with 1% bovine serum albumin (A4503, Sigma-Aldrich) for 30 minutes. Primary antibodies were used at dilutions of 1 : 4000 for α-SMA and 1 : 100 for F4/80. The secondary antibody for α-SMA and F4/80 was a biotinylated polyclonal rabbit anti-mouse immunoglobulin used at a dilution of 1 : 300 (E0464, Dako). The tertiary layer was alkaline phosphatase-conjugated streptavidin (D0396; Dako) used at a 1 : 50 dilution. Slides were further developed in DAB and counterstained lightly with haematoxylin, dehydrated and mounted in DPX-type mount.

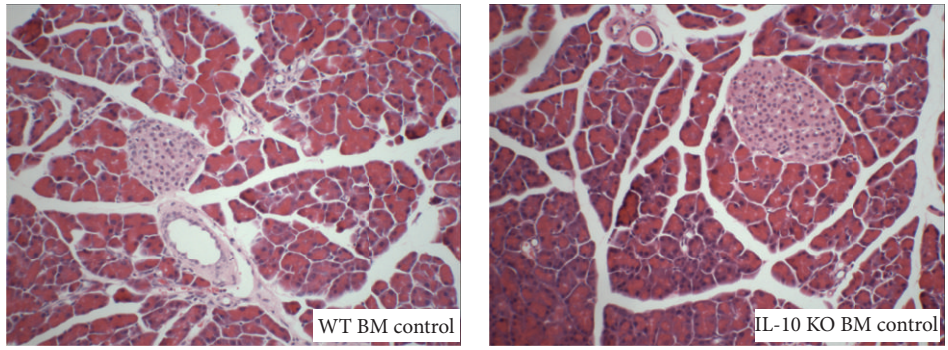

(a) (b)

Figure 2: Histology of the pancreas from saline (control groups) treated female mice that received either wild-type (a) or IL-10 knock out (b) male BM transplants. H&E staining of the pancreas from the control group showed normal pancreatic structure.

2.4. In Situ Hybridisation for Y Chromosome Detection. *In situ* hybridisation for Y chromosome-specific sequences in combination with immunostaining for α-SMA was performed to detect BM-derived myofibroblasts as previously reported [11] with slight modification. Briefly, sections were cut at 4 μm and incubated in 1 M sodium thiocyanate (S7757; Sigma-Aldrich) to improve access of the probe to DNA. Following PBS washing, sections were digested in 0.4% w/v pepsin (P6887; Sigma-Aldrich) in 0.1 M hydrochloric acid to improve further access of the Y chromosome probe. The protease reaction was quenched in 0.2% w/v glycine (G4392; Sigma-Aldrich) in double concentration PBS and sections were then rinsed in PBS, postfixed in 4% w/v PFA (P6148; Sigma-Aldrich) in PBS, dehydrated through graded alcohols, and lastly air dried. A fluorescein isothiocyanate-labelled Y chromosome paint (1189-YMF-01; Cambio, Cambridge, UK) was used in the supplier's hybridisation mix. The probe mixture was added to the sections, sealed under glass with rubber cement, heated to 60°C for 10 minutes, and then incubated overnight at 37°C in a humidified chamber.

The next day, all slides were washed in 0.5x Standard Saline Citrate. The anti-FITC antibody (ab6656, Abcam) was applied in a dilution of 1 : 100 and slides further developed in DAB and counterstained lightly with haematoxylin, dehydrated and mounted in DPX-type mount.

2.5. Collagen Staining. Picrosirius red (VWR International) staining was used for intrapancreatic collagen detection. Quantitative analysis of collagen deposition was performed by digitized image analysis with NIH-Image J software [12]. The total pancreatic tissue area was distinguished from the background according to a difference in light density. The total amount of collagen (stained in red) was measured and expressed as a percentage of the total pancreatic surface.

2.6. Cell Counting. For each mouse pancreas, sections were analyzed by digitally photographing 10 consecutive microscope fields at ×400 total magnification. The numbers of myofibroblasts (α-SMA positive) and macrophages (F4/80 positive) were quantified and the proportion of BM-derived (Y chromosome positive) myofibroblasts was expressed as a percentage.

2.7. Statistics. Results are expressed as mean ± standard error of the mean (SEM). Mean values of the experimental groups were compared by Student's unpaired t-tests. p values of less than 0.05 were considered to be statistically significant.

3. Results

3.1. The Histological Changes in WT BM and IL-10 KO BM Transplanted Mice. In the saline-treated mice, the morphology of the pancreas was normal in mice receiving either WT BM or IL-10 KO BM (Figure 2). However, at 12 weeks after BMTx and 6-week saline injection, IHC staining with the F4/80 anti-macrophage antibody showed more infiltrated macrophages in the pancreas of mice receiving IL-10 KO BM (4.2 ± 0.3 per high power field (HPF, 400x)) compared to the mice receiving WT BM (1.9 ± 0.3 per HPF, $p < 0.05$) (Figures 7(a), 7(b), and 7(h)). This suggests that the lack of IL-10 secreted from the BM causes subtle inflammatory cell infiltration without any obvious histological changes.

After cerulein injection for 1 day, the morphology of the pancreas from the mice in both groups showed very mild focal oedema between lobules, inflammatory cell infiltration in the parenchyma but without collagen deposition, acinar atrophy, or structural change, which are the characteristic features of acute pancreatitis (Figures 3(a) and 3(b)). The acute pancreatitis histological score showed no significant differences between WT BM (2.3 ± 1.0) and IL-10 KO BM (3.0 ± 1.5, $p > 0.05$) groups (Figure 4(a)).

The atrophy of acinar cells, deformed architecture, pseudotubular complex formation, intralobular collagen deposition, and severe fibrotic change, which are the characteristic features of chronic pancreatitis were found not only in the pancreas of mice receiving 3 and 6 weeks of cerulein treatment, but also in the pancreas of mice that had 3 weeks rest after 6 weeks of cerulein (Figures 3(c)–3(h)). The histological scores of chronic pancreatitis including architectural changes, glandular atrophy, and pseudotubular complexes showed no significant differences between mice receiving WT BM and IL-10 KO BM, indicating that the lack of IL-10 secreted from the BM did not affect the severity of chronic pancreatitis, but there was a distinct trend for lower scores in the IL-10 KO BM administered mice (Figures 4(b)–4(d)).

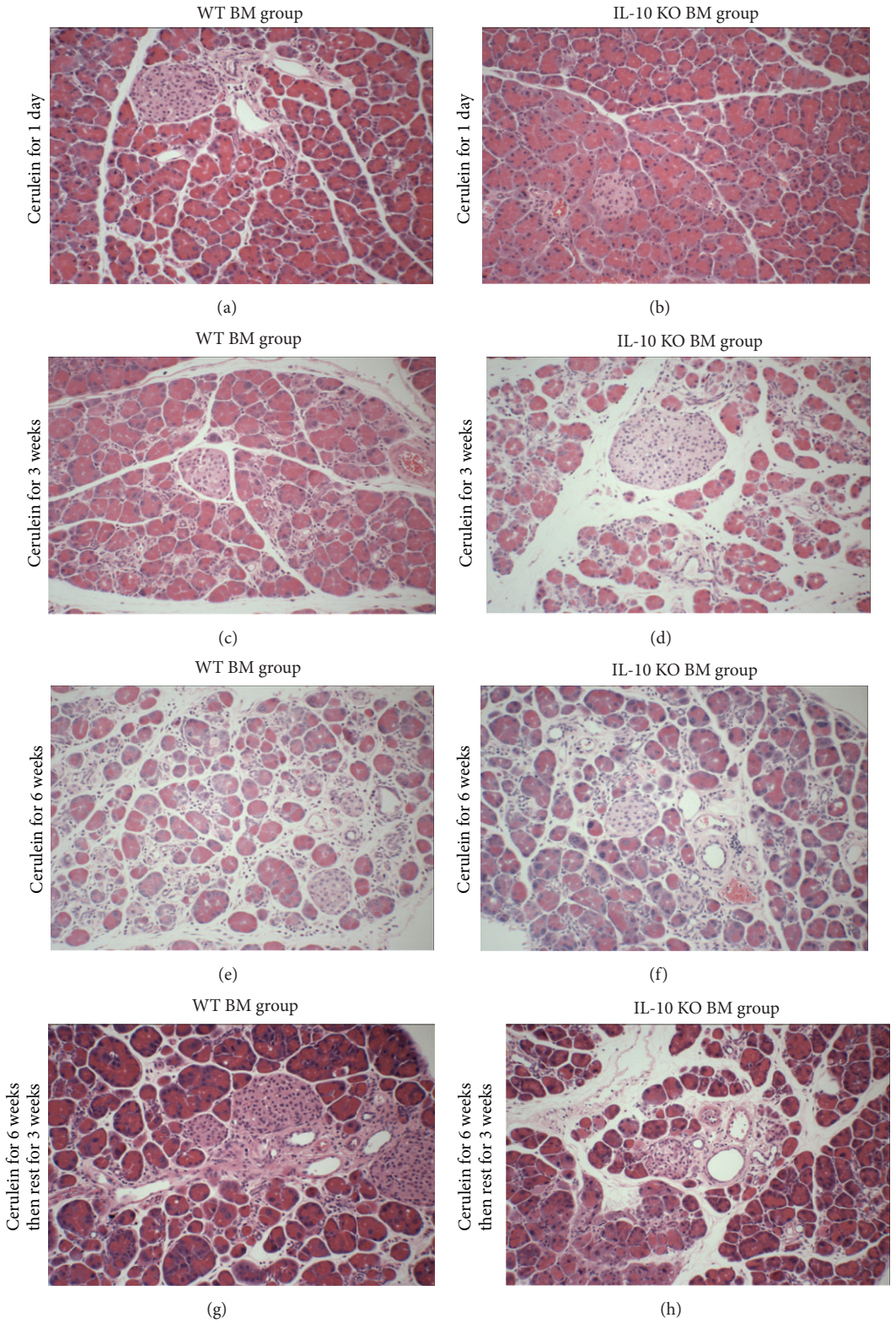

FIGURE 3: Histology of the pancreas from cerulein treated female mice that received either wild-type or IL-10 knocked out male bone marrow transplants. The development of mild acute pancreatic inflammation from 1-day cerulein treated mice ((a) and (b), 200x). Acinar atrophy, architectural changes, and pseudotubular complexes were found in mice receiving cerulein for 3 and 6 weeks and persisted for a further 3 weeks after cerulein injections ((c)–(h), 200x).

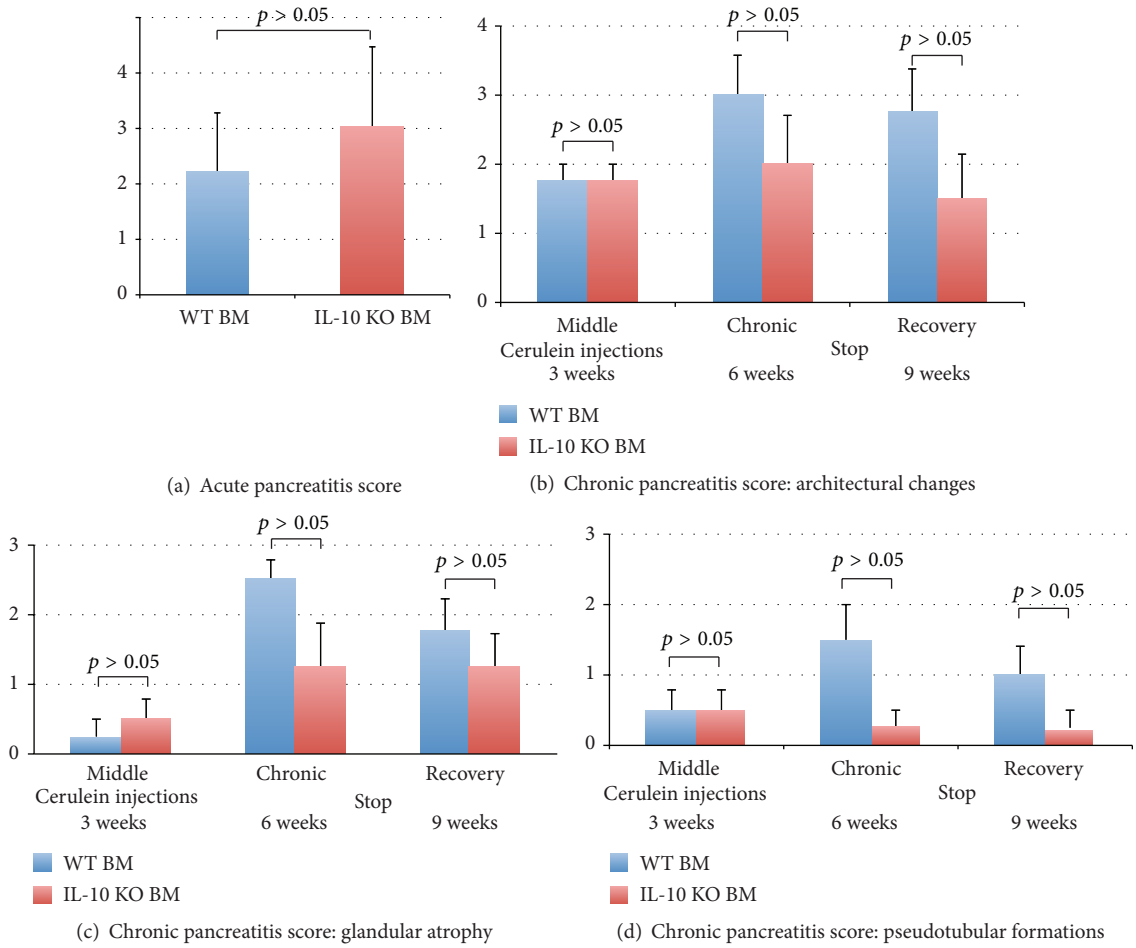

Figure 4: Histological scoring of acute pancreatitis (a) and chronic pancreatitis ((b)–(d)) in mice that received either a wild-type (blue bar) bone marrow or IL-10 knockout bone marrow (red bar) transplantation. Values represent the mean of scores ± standard error of mean ($n = 4$ mice per group).

3.2. Collagen Deposition in WT BM and IL-10 KO BM Transplanted Mice. One of characteristic features of chronic pancreatitis is collagen deposition. In the control groups, the percentage of collagen deposition (defined by Sirius red positive staining) to the total pancreatic area was 1.7 ± 0.2% and 1.8 ± 0.1% in mice that received a WT BM or an IL-10 KO BM transplant, respectively ($p > 0.05$). This result suggests that the lack of BM IL-10 does not affect normal collagen deposition.

Sirius red staining was also performed on all experimental groups (Figure 5). The 1-day cerulein injection did not cause further collagen deposition in either WT BM or IL-10 KO BM groups (Figures 5(a) and 5(b)), while continuous cerulein injections for 3 and 6 weeks induced progressive intralobular collagen deposition (Figures 5(c)–5(f)). Even following 3-week rest, the excessive intralobular collagen deposition remained (Figures 5(g) and 5(h)). In mice receiving a WT BM transplant, the areas occupied by collagen in the acute, middle, chronic, and recovery groups were 1.2 ± 0.2%, 7.6 ± 0.3%, 12.4 ± 0.2%, and 12.5 ± 0.4%, respectively. In mice receiving a IL-10 KO BM transplant, the areas were 1.4 ± 0.1%, 7.4 ± 0.4%, 13.7 ± 0.6%, and 18.4 ± 1.1%, respectively (Figure 5(i)). Similar degrees of collagen deposition were observed in mice with WT BM after 6 weeks of cerulein and following a further 3 weeks of recovery (12.4 ± 0.2% and 12.5 ± 0.4%, $p > 0.05$), suggesting that there was no immediate resolution of collagen deposition. On the other hand, the area occupied by collagen increased significantly in the 3 weeks after cerulein cessation in the mice with a IL-10 KO BM transplant (13.7 ± 0.6% and 18.4 ± 1.1%, $p < 0.05$), suggesting that the lack of IL-10 secreted from the BM results in further collagen deposition.

3.3. BM-Derived Myofibroblasts in the Pancreas of WT BM and IL-10 KO BM Transplanted Mice. Because increased collagen deposition was found in the IL-10 KO BM transplanted mice 3 weeks after the last cerulein injections, we wanted to know whether active myofibroblasts, the major collagen-producing cells in the pancreas, are also increased in number and are of BM derivation. Active myofibroblasts were identified by IHC for α-SMA in both WT BM and IL-10 KO BM transplanted mice in both the chronic and recovery groups. In order to detect BM-derived myofibroblasts, ISH for Y chromosome detection was then performed after the IHC for α-SMA

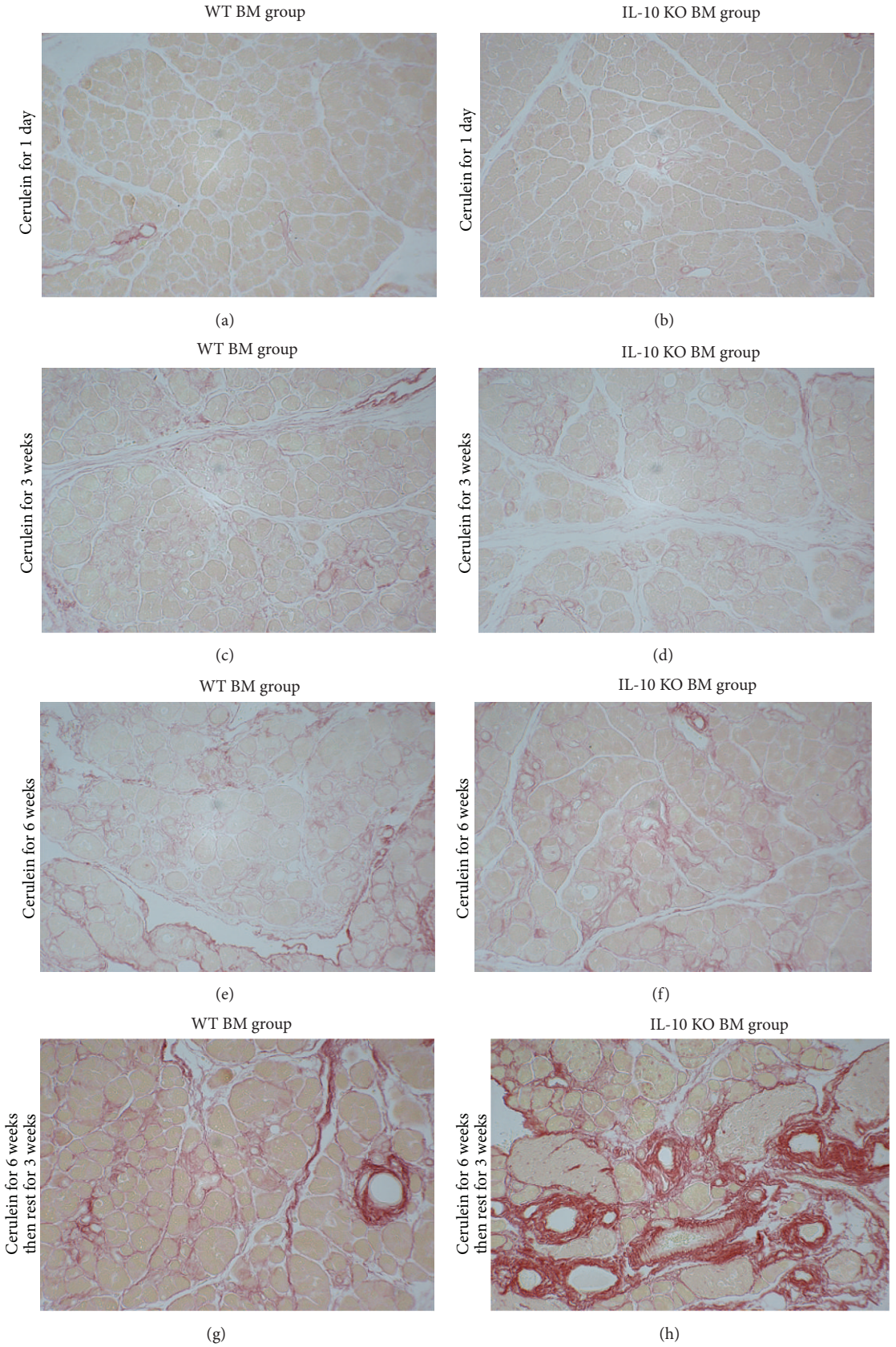

Figure 5: Continued.

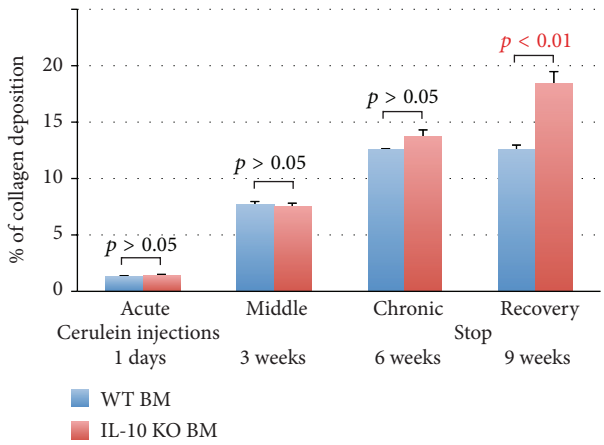

(i) Collagen deposition

FIGURE 5: ((a)–(h)) Sirius red staining of the pancreas from cerulein treated female mice that received either a wild-type male bone marrow or an IL-10 knock out male bone marrow transplant. (a) and (b) show normal collagen deposition between lobules after cerulein injection for 1 day. (c)–(h) show progressive collagen deposition with time. (i) Sirius red positive areas to the total area. Only in the recovery group is collagen deposition in the IL-10 knock out group significantly higher than that in the wild-type bone marrow group ($p < 0.01$).

(Figures 6(b)–6(d)). The spleen was used as a positive control of ISH for Y chromosome detection (Figure 6(a)), and the total number of myofibroblasts per high power field (HPF, 400x) was calculated. In mice receiving a WT BM transplant, the numbers of myofibroblasts per HPF in the chronic and recovery groups were 10.1 ± 1.1 and 11.6 ± 1.0, respectively. In mice receiving a IL-10 KO BM transplant, the numbers were 10.1 ± 0.2 and 11.7 ± 0.9, respectively (Figure 6(e)); thus, there were no differences between WT BM and IL-10 KO BM transplanted mice in the number of active myofibroblasts.

BM-derived myofibroblasts were readily recognised (Figures 6(b)–6(d)), and percentages were counted (Figure 6(f)). In mice receiving a WT BM transplant, the percentages of BM-derived myofibroblasts in the chronic and recovery groups were 9.3 ± 2.2% and 6.7 ± 1.1%, respectively. In the IL-10 KO BM recipients, the percentages were 9.2 ± 1.0% and 11.9 ± 1.3% (Figure 6(f)). Interestingly among the recovery groups, the percentage of BM-derived myofibroblasts was increased in the pancreas of the IL-10 KO BM recipients compared to those with WT BM (11.9 ± 1.3% versus 6.7 ± 1.1%, $p < 0.05$). This finding might suggest that BM-secreted IL-10 plays a role in suppressing BM cell transdifferentiation into myofibroblasts.

3.4. The Inflammatory Cell Response in the Pancreas of WT BM and IL-10 KO BM Transplanted Mice. IL-10 is considered as an anti-inflammatory cytokine; therefore it is reasonable to think that a lack of IL-10 secreted by the BM would result in a more severe pancreatitis. To investigate this, the numbers of macrophages were counted.

Macrophages (F4/80-positive cells) are considered as chronic inflammatory cells contributing to tissue destruction, infiltrating the pancreas once acute pancreatitis is induced by cerulein. Staining with F4/80 in the spleen was used as a positive control (Figure 7(g)). Macrophages were very rare in the control pancreas of mice receiving WT male BM (1.9 ± 0.3 per HPF; Figures 7(a) and 7(h)), while in the controls with IL-10 KO male BM they were increased (4.2 ± 0.3 per HPF, $p < 0.05$; Figures 7(b) and 7(h)). In the mice with a WT BM transplant, the numbers of macrophages in the chronic and recovery groups were 26.8 ± 3.1 and 15.3 ± 1.7 per HPF, respectively (Figures 7(c), 7(e), and 7(h)), clearly a large decrease. In the mice with an IL-10 KO BM transplant, the number of macrophages in the chronic group was 20.8 ± 1.3 per HPF increasing to 23.2 ± 2.3 per HPF in the recovery group (Figures 7(d), 7(f), and 7(h)). Comparing the recovery groups, macrophage infiltration was significantly increased in the IL-10 KO BM recipients compared to the WT BM transplanted group ($p < 0.05$).

4. Discussion

The participation of BM-derived myofibroblasts has been well documented in pancreatic fibrosis using the experimental cerulein-induced pancreatitis mouse model [8, 9]. However, the influence of cytokines on these BM-derived fibrogenic cells has not been well clarified. Here we demonstrate for the first time that the lack of IL-10 secreted by BM cells is associated with progressive collagen deposition combined with increased numbers of BM-derived myofibroblasts and persistent infiltration of macrophages, all at 3 weeks after the cessation of cerulein treatment.

Pancreatic fibrosis is defined by the overgrowth and excess deposition of extracellular matrix components including collagen. It is caused by recurrent episodes of pancreatic parenchymal cell necrosis followed by fibrosis and is considered to be the end result of chronic pancreatitis induced by insults such as alcohol abuse, genetic disorders, pancreatic duct obstruction, recurrent acute pancreatitis, autoimmune pancreatitis, and unknown mechanisms [13]. Activated myofibroblasts serve as the primary collagen-producing cells and are believed to be the key cellular mediators of fibrosis in various organs [14]. Previous studies have also suggested that pancreatic myofibroblasts play

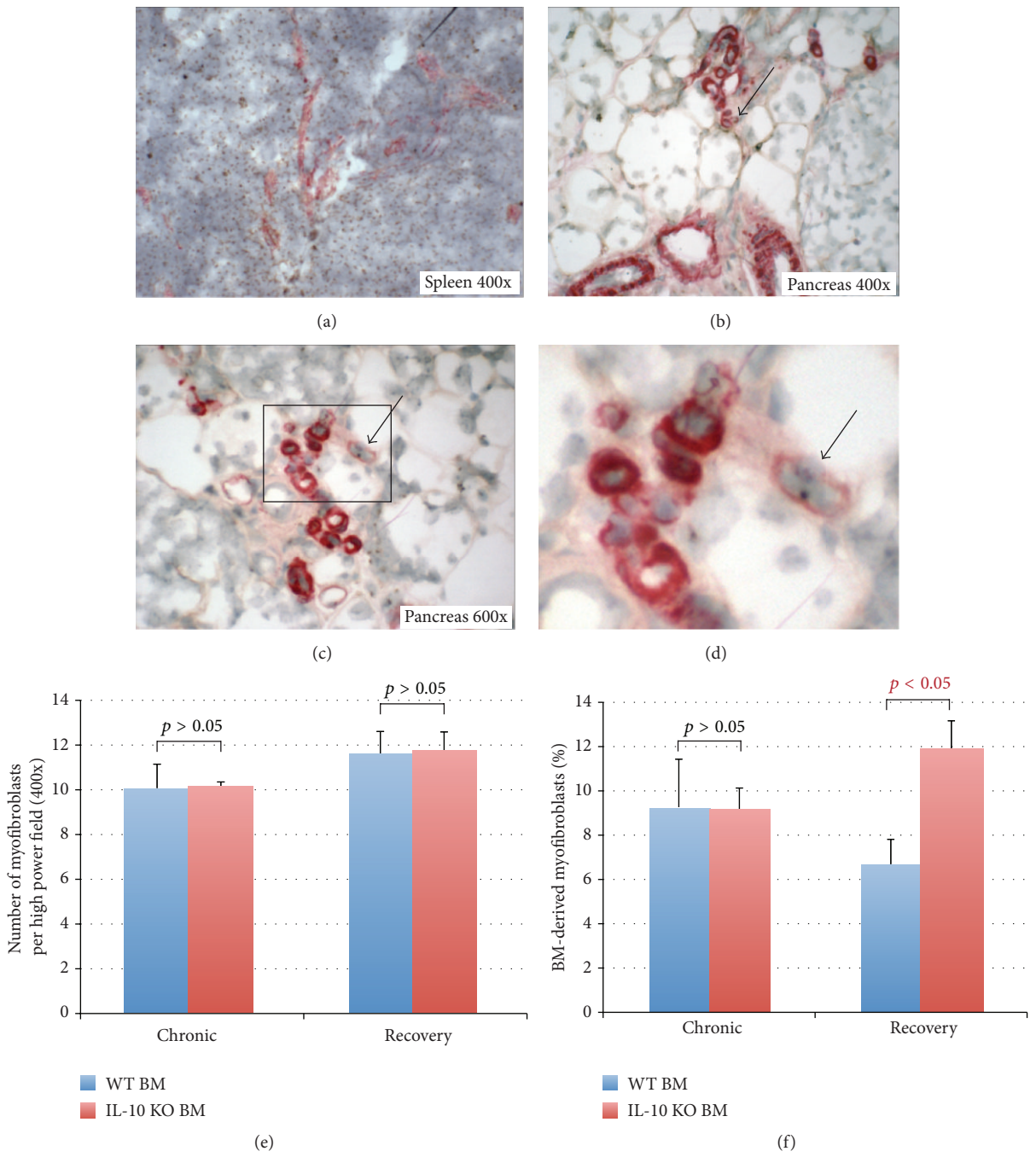

Figure 6: Bone marrow-derived α-SMA-positive cells in the pancreas from cerulein treated female mice that received either a wild-type (WT) or an IL-10 knock out (KO) male bone marrow (BM) transplant. (a) ISH for the Y chromosome in the spleen of female mice that received a WT male BM transplant. (b) IHC for α-SMA (red) and ISH for the Y chromosome shows BM-derived myofibroblasts in the pancreas from a mouse that received a WT male BM transplant (arrow, 400x) ((c) and (d)). Active myofibroblasts illustrated by α-SMA expression (red), while a small brown dot in the nucleus indicates this is a BM-derived myofibroblast in the pancreas from a mouse that received an IL-10 KO BM transplant (arrow). (e) The number of myofibroblasts per high power field (HPF) in mice receiving either a WT BM (blue bars) or IL-10 KO BM (red bars) in both the chronic and recovery groups. (f) The percentage of BM-derived myofibroblasts in the same groups.

an important role in the progression of pancreatic fibrosis [13, 15–18]. In the pancreas, multiple origins are considered as the source of activated myofibroblasts including pancreatic stellate cells [19], BM [8, 9], and fibrocytes [11]. Other studies have shown that BM-derived myofibroblasts contribute to the total population of activated myofibroblasts in the pancreas, with estimates varying from 6% to 20% in cerulein-induced chronic pancreatitis [8, 9]. Our experiments have also confirmed this finding since ~9% of myofibroblasts in the mice treated with cerulein for 6 weeks were derived from

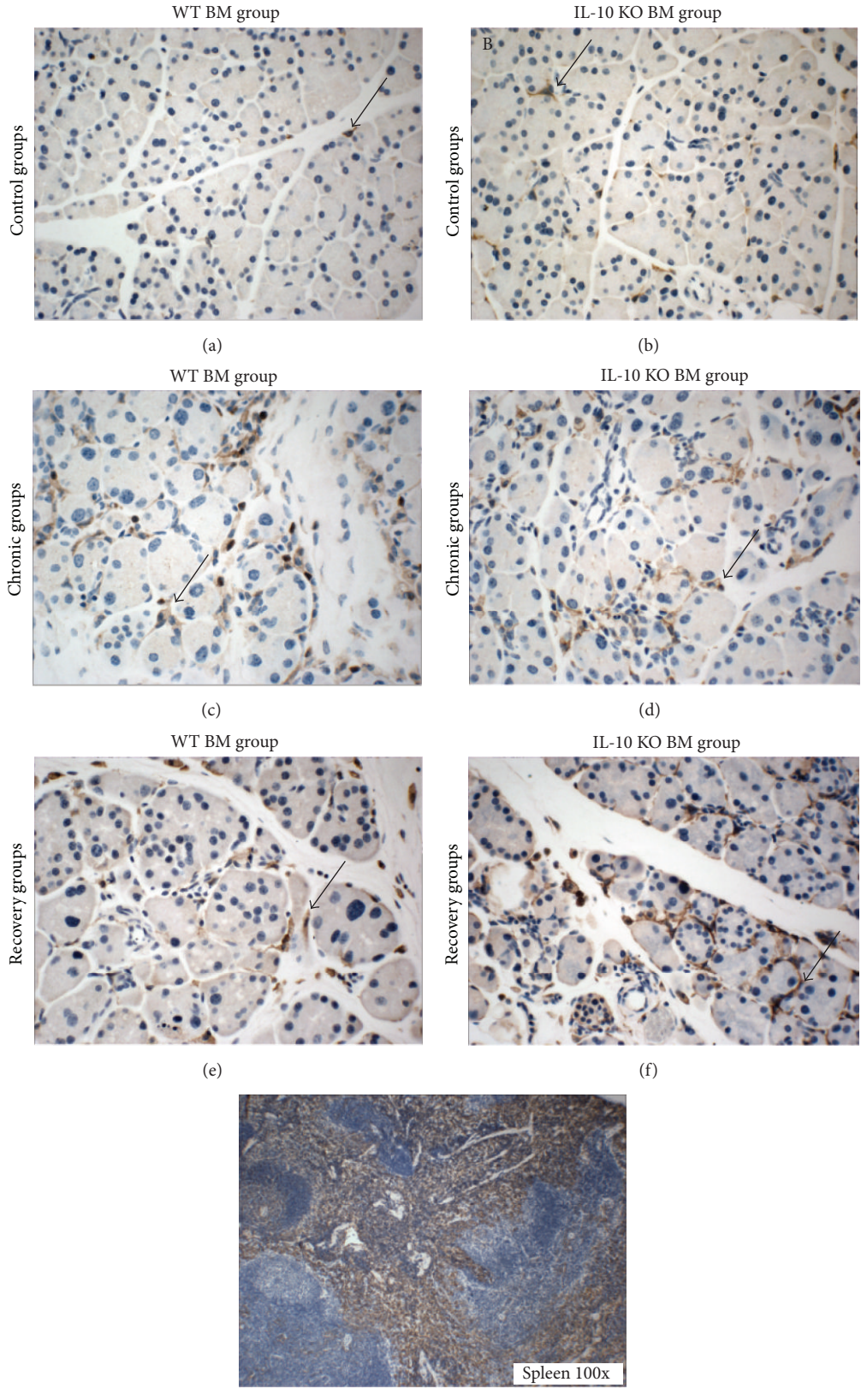

Figure 7: Continued.

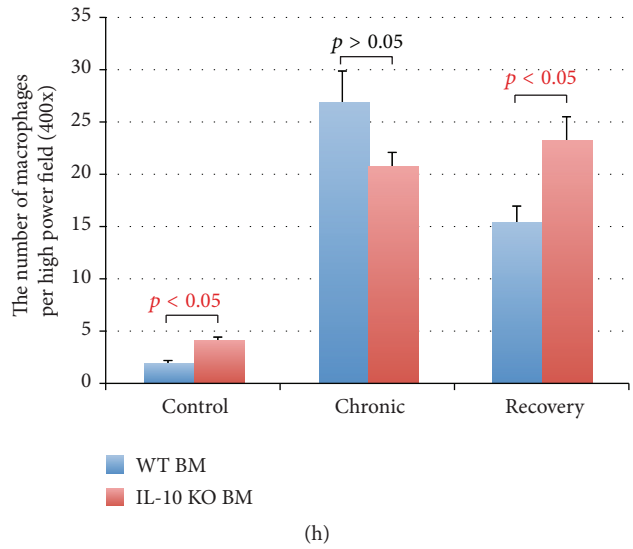

(h)

Figure 7: Immunohistochemical staining with F4/80 for macrophages in the pancreas from cerulein treated female mice that received either a wild-type (WT) male bone marrow (BM) or an IL-10 knock out (KO) male BM transplant. (a) and (b) show that in saline-treated mice (control groups), the F4/80 positive cells are rare in the pancreas of WT male BM transplanted mice (a), while the infiltration of F4/80-positive cells is increased in the pancreas of IL-10 KO male BM transplanted mice (b). (c) and (d) show that macrophage infiltration is significantly increased in the pancreas of both WT BM transplanted (c) and IL-10 KO BM (d) transplanted mice after receiving 6 weeks of cerulein injections (chronic groups). (e) and (f) show that macrophage infiltration was less in the WT BM transplanted mice after a 3-week recovery (e) but was unaltered in the IL-10 KO BM transplanted mice (f). (g) shows F4/80 staining in the spleen from a mouse that received a WT BM transplant but no cerulein. (h) shows the number of macrophages per HPF in mice receiving either a WT BM (blue bars) or an IL-10 KO BM (red bars).

the BM. However, our results also showed that the percentage of BM-derived myofibroblasts increased in the IL-10 KO BM transplanted mice treated with cerulein for 6 weeks followed by a gap of 3 weeks, suggesting that IL-10 may play a role in the suppression of BM cells' transdifferentiation. Furthermore, the degree of fibrosis was also increased significantly in the IL-10 KO BM transplanted after the 3-week gap, suggesting that the increased number of BM-derived myofibroblasts may functionally contribute to pancreatic fibrosis. How IL-10 acts to suppress BM transdifferentiation into myofibroblasts is not answered in these experiments.

IL-10 has been shown to be a potent anti-inflammatory cytokine released during the course of experimental pancreatitis by decreasing the release of proinflammatory factors [2, 3, 20]. IL-10 levels were shown to be upregulated by Sonic hedgehog expression in the mouse model of cerulein-induced acute pancreatitis [21]. In this study, we further showed that a lack of IL-10 secreting BM cells could affect the inflammatory cell response during the recovery phase of cerulein-induced pancreatic fibrosis. The increased number of macrophages in the pancreas from the IL-10 KO BM transplanted mice is compatible with similar findings in skin wounds created on IL-10 KO mice [22].

Apart from an anti-inflammatory effect, IL-10 is also considered as an antifibrotic cytokine. It has been shown that the severity of fibrosis is increased in carbon tetrachloride-induced liver fibrosis in IL-10 KO mice [23]. Furthermore, the wound healing process is accelerated in IL-10 KO mice [22]. Increased numbers of α-SMA-positive myofibroblasts as well as macrophages were found in the skin wounds of IL-10 KO mice, suggesting that these two cell types enhance the contraction of wounds and mediate the accelerated tissue repair. In the cerulein-induced pancreatic fibrosis model, IL-10 KO mice have more severe histological lesions and fibrosis (intrapancreatic collagen content) than controls [4]. The plasma level of TGF-β1, a key stimulatory factor for myofibroblast activation, and the number of activated myofibroblasts were significantly higher in IL-10 KO mice, suggesting that the lack of IL-10 causes myofibroblast activation by increasing TGF-β1 that in turn increases the severity of fibrosis [4]. However, the results from this study were that the severity of fibrosis, the number of activated myofibroblasts, and inflammatory cells were the same in the IL-10 KO BM and WT BM transplanted mice after 6 weeks of cerulein. Differences were only revealed after a gap of 3 weeks from the last cerulein injection. A possible explanation is that IL-10 could be secreted from other cell types apart from BM cells during the episodes of acute pancreatitis induced by cerulein, and this is sufficient to maintain basic IL-10 levels during the acute inflammatory response. Indeed, although IL-10 is mainly secreted by BM-derived haematopoietic cells, it has been shown that IL-10 can also be detected in rodent hepatic stellate cells during the course of activation *in vitro* [24]. During the time without cerulein injection, the secretion of IL-10 from other cell types may decrease because of lack of inflammatory stimulation, and BM-secreted IL-10 may become predominant. The hypothesis that IL-10 secreted by other cell types can function well enough during acute inflammation is also supported by a previous study of IBD in IL-10 KO mice [10]; spontaneous colitis did not occur in WT mice that received the IL-10 KO BM transplantation, suggesting the IL-10 secreted from other cell types has

a protective effect. Further experiments will be needed to clarify the significance of IL-10 secreted by other cell types.

5. Conclusions

The degree of fibrosis, the inflammatory cell response, and the number of BM-derived myofibroblasts were altered in the IL-10 KO BM transplanted mice in the recovery phase of pancreatic fibrosis after cerulein. These findings highlight a potential role of IL-10 on BM-derived myofibroblast behaviour and fibrosis in the pancreas.

Competing Interests

No competing interests were declared.

Acknowledgments

This study was funded by a grant from Chang Gung Memorial Hospital, Taiwan (CMRPG3E1461).

References

[1] K. W. Moore, R. de Waal Malefyt, R. L. Coffman, and A. O'Garra, "Interleukin-10 and the interleukin-10 receptor," *Annual Review of Immunology*, vol. 19, pp. 683–765, 2001.

[2] J.-L. Van Laethem, A. Marchant, A. Delvaux et al., "Interleukin 10 prevents necrosis in murine experimental acute pancreatitis," *Gastroenterology*, vol. 108, no. 6, pp. 1917–1922, 1995.

[3] J.-L. Van Laethem, R. Eskinazi, H. Louis, F. Rickaert, P. Robberecht, and J. Devière, "Multisystemic production of interleukin 10 limits the severity of acute pancreatitis in mice," *Gut*, vol. 43, no. 3, pp. 408–413, 1998.

[4] A. Demols, J.-L. Van Laethem, E. Quertinmont et al., "Endogenous interleukin-10 modulates fibrosis and regeneration in experimental chronic pancreatitis," *American Journal of Physiology—Gastrointestinal and Liver Physiology*, vol. 282, no. 6, pp. G1105–G1112, 2002.

[5] K. Gotoh, M. Inoue, K. Shiraishi et al., "Spleen-derived interleukin-10 downregulates the severity of high-fat diet-induced non-alcoholic fatty pancreas disease," *PLoS ONE*, vol. 7, no. 12, article e53154, 2012.

[6] T. Starzyńska, K. Dabkowski, W. Błogowski et al., "An intensified systemic trafficking of bone marrow-derived stem/progenitor cells in patients with pancreatic cancer," *Journal of Cellular and Molecular Medicine*, vol. 17, no. 6, pp. 792–799, 2013.

[7] W. Błogowski, A. Deskur, M. Budkowska et al., "Selected cytokines in patients with pancreatic cancer: a preliminary report," *PLoS ONE*, vol. 9, no. 5, Article ID e97613, 2014.

[8] F. Marrache, S. Pendyala, G. Bhagat, K. S. Betz, Z. Song, and T. C. Wang, "Role of bone marrow-derived cells in experimental chronic pancreatitis," *Gut*, vol. 57, no. 8, pp. 1113–1120, 2008.

[9] T. Watanabe, A. Masamune, K. Kikuta et al., "Bone marrow contributes to the population of pancreatic stellate cells in mice," *American Journal of Physiology—Gastrointestinal and Liver Physiology*, vol. 297, no. 6, pp. G1138–G1146, 2009.

[10] S. Bamba, C.-Y. Lee, M. Brittan et al., "Bone marrow transplantation ameliorates pathology in interleukin-10 knockout colitic mice," *The Journal of Pathology*, vol. 209, no. 2, pp. 265–273, 2006.

[11] W.-R. Lin, O. Inatomi, C. Y. Lee et al., "Bone marrow-derived cells contribute to cerulein-induced pancreatic fibrosis in the mouse," *International Journal of Experimental Pathology*, vol. 93, no. 2, pp. 130–138, 2012.

[12] G. K. Rangan and G. H. Tesch, "Quantification of renal pathology by image analysis (Methods in Renal Research)," *Nephrology*, vol. 12, no. 6, pp. 553–558, 2007.

[13] K. Shimizu, "Mechanisms of pancreatic fibrosis and applications to the treatment of chronic pancreatitis," *Journal of Gastroenterology*, vol. 43, no. 11, pp. 823–832, 2008.

[14] T. A. Wynn, "Cellular and molecular mechanisms of fibrosis," *Journal of Pathology*, vol. 214, no. 2, pp. 199–210, 2008.

[15] A. Masamune and T. Shimosegawa, "Signal transduction in pancreatic stellate cells," *Journal of Gastroenterology*, vol. 44, no. 4, pp. 249–260, 2009.

[16] A. Nishida, A. Andoh, O. Inatomi, and Y. Fujiyama, "Interleukin-32 expression in the pancreas," *The Journal of Biological Chemistry*, vol. 284, no. 26, pp. 17868–17876, 2009.

[17] T. Saotome, H. Inoue, M. Fujimiya, Y. Fujiyama, and T. Bamba, "Morphological and immunocytochemical identification of periacinar fibroblast-like cells derived from human pancreatic acini," *Pancreas*, vol. 14, no. 4, pp. 373–382, 1997.

[18] K. Suda, H. Shiotsu, T. Nakamura, J. Akai, and T. Nakamura, "Pancreatic fibrosis in patients with chronic alcohol abuse: correlation with alcoholic pancreatitis," *American Journal of Gastroenterology*, vol. 89, no. 11, pp. 2060–2062, 1994.

[19] M. B. Omary, A. Lugea, A. W. Lowe, and S. J. Pandol, "The pancreatic stellate cell: a star on the rise in pancreatic diseases," *The Journal of Clinical Investigation*, vol. 117, no. 1, pp. 50–59, 2007.

[20] A. J. Rongione, A. M. Kusske, K. Kwan, S. W. Ashley, H. A. Reber, and D. W. McFadden, "Interleukin 10 reduces the severity of acute pancreatitis in rats," *Gastroenterology*, vol. 112, no. 3, pp. 960–967, 1997.

[21] X. Zhou, Z. Liu, F. Jang, C. Xiang, Y. Li, and Y. He, "Autocrine Sonic hedgehog attenuates inflammation in cerulein-induced acute pancreatitis in mice via upregulation of IL-10," *PLoS ONE*, vol. 7, no. 8, Article ID e44121, 2012.

[22] S. A. Eming, S. Werner, P. Bugnon et al., "Accelerated wound closure in mice deficient for interleukin-10," *American Journal of Pathology*, vol. 170, no. 1, pp. 188–202, 2007.

[23] H. Louis, J.-L. Van Laethem, W. Wu et al., "Interleukin-10 controls neutrophilic infiltration, hepatocyte proliferation, and liver fibrosis induced by carbon tetrachloride in mice," *Hepatology*, vol. 28, no. 6, pp. 1607–1615, 1998.

[24] K. C. Thompson, A. Trowern, A. Fowell et al., "Primary rat and mouse hepatic stellate cells express the macrophage inhibitor cytokine interleukin-10 during the course of activation in vitro," *Hepatology*, vol. 28, no. 6, pp. 1518–1524, 1998.

Hindawi Publishing Corporation
BioMed Research International
Volume 2016, Article ID 5952165, 14 pages
http://dx.doi.org/10.1155/2016/5952165

Review Article

A Review of Animal Models of Intervertebral Disc Degeneration: Pathophysiology, Regeneration, and Translation to the Clinic

Chris Daly,[1,2,3] Peter Ghosh,[1,4] Graham Jenkin,[1] David Oehme,[1,5] and Tony Goldschlager[1,2,3]

[1] *The Ritchie Centre, Hudson Institute of Medical Research, Clayton, VIC 3168, Australia*
[2] *Department of Neurosurgery, Monash Medical Centre, Clayton, VIC 3168, Australia*
[3] *Department of Surgery, Monash University, Clayton, VIC 3168, Australia*
[4] *Proteobioactives, Pty. Ltd., Balgowlah, NSW 2093, Australia*
[5] *Department of Neurosurgery, St Vincent's Private Hospital, Fitzroy, VIC 3065, Australia*

Correspondence should be addressed to Chris Daly; christopher.daly@monash.edu

Received 18 March 2016; Accepted 3 May 2016

Academic Editor: Oreste Gualillo

Lower back pain is the leading cause of disability worldwide. Discogenic pain secondary to intervertebral disc degeneration is a significant cause of low back pain. Disc degeneration is a complex multifactorial process. Animal models are essential to furthering understanding of the degenerative process and testing potential therapies. The adult human lumbar intervertebral disc is characterized by the loss of notochordal cells, relatively large size, essentially avascular nature, and exposure to biomechanical stresses influenced by bipedalism. Animal models are compared with regard to the above characteristics. Numerous methods of inducing disc degeneration are reported. Broadly these can be considered under the categories of spontaneous degeneration, mechanical and structural models. The purpose of such animal models is to further our understanding and, ultimately, improve treatment of disc degeneration. The role of animal models of disc degeneration in translational research leading to clinical trials of novel cellular therapies is explored.

1. Introduction

Lower back pain causes more global disability than any other condition worldwide [1] and is an enormous financial burden due to costs related to loss in working hours as well as for its medical treatment. Up to 80% of people may experience lower back pain at some stage in their life, with prevalence ranging from 15 to 45%. Chronic lower back pain can be caused by degenerative lumbar disc disease which produces discogenic pain [2]. This needs to be distinguished from radicular pain, which is pain resulting from nerve root compression, often due to a disc prolapse. Lumbar disc degeneration is a complex process manifested by changes in cellular, matrix, endplate, and the neurovascular components of the intervertebral disc. Given the significant contribution of disc degeneration to the enormous disease burden of lower back pain numerous animal models have been developed in an effort to further understanding and treatment of this condition. In order to compare and contrast the merits of different models a basic appreciation of the structure of the intervertebral disc and underlying pathophysiology is a prerequisite.

2. The Intervertebral Disc

The intervertebral disc is a complex multicomponent structural tissue consisting of an outer fibrous ring, the annulus fibrosus (AF), and an inner hydrated gel-like substance, the nucleus pulposus (NP) [3]. It is the largest avascular structure in the body. Nutrition of the intervertebral disc is provided by diffusion through the cartilaginous endplates (CEP). The CEP are specialized interfaces that connect the intervertebral disc with the adjacent vertebral bodies. The AF is a fibrocartilaginous tissue rich in type I and II collagen and assembled as lamellae fibres oriented at varying degrees to adjacent lamella in different locations and species. The AF connects the caudal and cranial vertebral bodies of the spinal

column [4]. The main cell types of the AF are fibroblasts that synthesize not only the lamellar collagen, but also proteoglycan (PGs), elastin, and other noncollagenous proteins [5]. The tough fibrous composite structure of the AF encapsulates the gelatinous NP and provides the necessary mechanical strength and resilience to allow the disc to recover from deformation arising from axial, rotational, and bending loading. In healthy discs the NP consists of a hydrated gel composed of predominantly type II collagen and large amounts of PGs. Aggrecan is the most abundant PG type in the NP. Due to its high anionic charge aggrecan attracts and retains high levels of water molecules within the NP thereby maintaining a high hydrostatic swelling pressure that confers resistance to disc deformation and maintenance of disc height [3, 6].

Cells of the disc NP are derived from the notochord. In man these cells are retained throughout childhood but with maturity disappear and are replaced by chondrocyte-like cells [5]. The loss of notochordal cells from the NP represents an important early step along the path to degenerative disc disease and in this regard it should be noted that apart from a limited number of animal species (chondrodystrophoid dogs, old sheep, and cattle) NP notochord cells are retained throughout their life.

3. Intervertebral Disc Degeneration

Human intervertebral disc degeneration is a complex and incompletely understood multifactorial process with contributions from genes, mechanical stresses, cellular senescence, and alterations in nutrition via the limited vascular supply [7]. With respect to mechanically loading the intervertebral disc there is a delicate balance between "normal" mechanical loading, which is required for maintenance of an optimal disc cellular phenotype [8, 9], and excessive mechanical loading that causes damage. Excessive loading can result from excessive bodyweight [10] or trauma and produces many of the features of degeneration that can be visualized by histological and radiological methods.

Studies comparing degenerate discs with nondegenerate controls have demonstrated increased evidence of senescent cells in degenerate intervertebral discs [11]. Such cells lose the ability to divide, thus potentially contributing to the decreased cellularity of the diseased degenerate intervertebral discs. Moreover, the senescent cells have a reduced ability to function. Thus they produce less matrix which, in turn, further compromises the structure of the intervertebral discs.

Intervertebral discs comprise the largest essentially avascular tissue in the human body. Only the outermost layers of the AF contain blood vessels. The cells of NP are dependent on diffusion of nutrients from capillary buds in the cartilaginous endplate to meet their metabolic needs [12]. The cells in the NP are therefore metabolically compromised by this limited vascular and nutritional supply and may promulgate intervertebral disc degeneration. Causes of impaired nutrition to the intervertebral disc include endplate calcification, microvascular disease, and smoking and have all been associated with early disc degeneration.

Ultimately there is an imbalance between the rates of production and breakdown of the matrix components leading

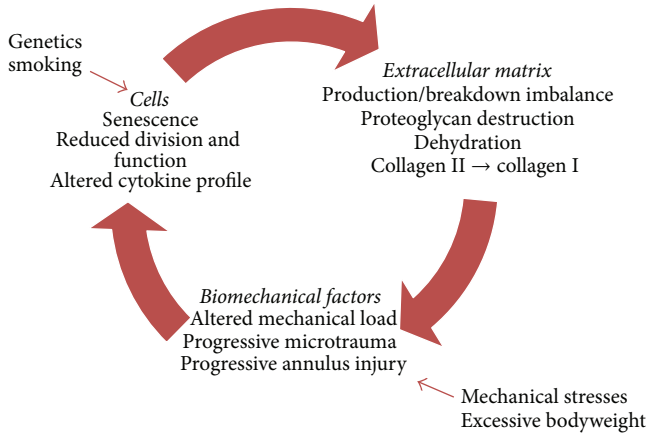

Figure 1: Schematic of the process of disc degeneration demonstrating multifactorial pathophysiology and interplay of cellular, matrix, and biomechanical factors. Modification of figure from Vergroesen et al. [17].

to a cascade of events (see Figure 1) consisting of alterations in matrix synthesis, reduced aggrecan synthesis, and a transition from type II to type I collagen production [13], reduction in cellular viability and activity, and alterations in cytokine profile upregulating the breakdown of proteoglycans, all leading to dehydration and loss of mechanical integrity of the intervertebral disc [6, 12]. The dehydration of the intervertebral disc reduces the mechanical support provided by the swelling pressure of the previously hydrated NP. This alters the mechanical load to which the AF is exposed and thus the tension in the AF collagen fibres. This leads to subsequent progressive microtrauma of these fibres [6]. The degeneration of the AF and subsequent tears in this structure predispose patients to disc herniation, wherein fragments of disc tissue herniate through this annular defect causing neural compression and radicular pain [14]. As the mechanical and structural integrity of the disc progressively deteriorates neurovascular invasion may occur via annular tears. Neurovascular invasion extending to the NP via annular fissures has been demonstrated in painful discs in clinical studies [15]. In contrast, control (nonpainful) discs demonstrated restriction of vascular and neural supply to the outer annulus [15]. This process of neoinnervation of the degenerate intervertebral discs is hypothesized to be a significant contributor to the development of back pain [16].

3.1. Animal Models of Disc Degeneration. The development of appropriate animal models of intervertebral disc disease is necessary to gain insight into the pathophysiology and to develop and test potential therapies. In vitro and in silico (computer based) systems can be helpful to investigate specific components of intervertebral disc degeneration. However, given the complexity inherent in the intervertebral disc with biochemical, biomechanical, nutritional, and metabolic factors acting simultaneously, in vivo animals are able to more faithfully replicate this environment. A range of animal models and mechanisms of replicating the process of degeneration have been investigated and utilized in efforts to

develop appropriate models of intervertebral disc degeneration. However, given the extreme complexity of this system no perfect model currently exists.

Initial discussion will focus on the merits and inadequacies of particular species as models for human intervertebral disc degeneration. This will be followed by a discussion of the comparative merits of the various methods of inducing disc degeneration.

3.1.1. Comparison of Various Animal Models. Animal models range from small rodents such as mice knockout models [18] to rats [19], rabbits [20], dogs [21], goats [22], sheep [23], and primates [24, 25]. Various mechanisms of inducing degeneration have been described for these animal models which are summarized in Table 1. When considering the potential suitability of an animal model several important characteristics must be taken into account and these are discussed in Table 1.

3.1.2. Persistence of Notochordal Cells. The vertebral column and thus intervertebral discs of all mammals arise from aggregation of the mesenchyme around the notochord and subsequent segmentation during development [26]. Notochordal cells persist in the NP of the majority of species (e.g., mice, rats, rabbits, and pigs) into adulthood. However, the number of these cells decreases rapidly following birth in humans and notochordal cells are completely absent from the NP by early adulthood [26]. Sheep and goats are among the few animals to also lose the notochordal cells rapidly from the NP following birth. Dogs are divided into two populations with regard to notochordal persistence into adulthood. Chondrodystrophoid (CD) dogs rapidly lose the notochordal cells following birth and as such are predisposed to intervertebral disc degeneration in later life. Nonchondrodystrophoid (NCD) dogs have persistent notochordal cells and are far less inclined to disc degeneration. The persistence of notochordal cells is an important consideration as these cells have a significant influence on the intervertebral disc by influencing proteoglycan metabolism [27, 28], hyaluronan production [29], and possible progenitor cell function [26].

Loss of intervertebral disc notochordal cells may be observed in animal models with otherwise persistent notochordal cells following adequate stimulus [30, 31]. Apoptotic processes have been demonstrated to play a significant role in this process of notochordal cells loss [31, 32] and are also observed in human aged and degenerate discs [33]. Thus such animal models may have greater relevance following the loss of notochordal cells than otherwise.

However, given the use of animal models to investigate cellular regenerative therapies for the treatment of disc degeneration the potential presence of a preexisting precursor cell population may complicate investigation of the regenerative potential of such therapies. For instance, in cell transplantation therapies, one cannot be sure that it is not the resident notochordal cells which are responsible for the regenerative effects, instead of, or in combination with, the transplanted cells.

3.1.3. Disc Size and Geometry. Intervertebral discs vary markedly across species and according to location within the spine. The discs of most animal models are smaller than human intervertebral discs. Disc size affects solute diffusion in the intervertebral disc. Given the largely avascular nature of the intervertebral disc and dependence on diffusion to meet nutritional requirements this is of particular significance to the clinical relevance of animal models. Given the size discrepancies between common animal models and humans investigators have analyzed disc geometry hoping to better determine the relevance of particular models to the human intervertebral disc. In a study by O'Connell et al. [34] the geometries of intervertebral discs of commonly used animal models were analyzed with regard to their similarity to the human intervertebral discs as measured by relative proportions (e.g., disc height, width, and NP size). Interestingly, the authors ranked mouse lumbar intervertebral disc as the animal model most geometrically analogous to the human intervertebral disc.

3.1.4. Disc Mechanical Forces. The vast majority of animal models of intervertebral disc disease are quadrupedal. The only bipedal models available, certain primates to varying extents (e.g., rhesus monkey [35]) and the bipedal mouse and rat [36], present ethical dilemmas that preclude their usage in most institutions. Given that the mechanical loading to which human intervertebral lumbar discs are exposed is significantly influenced by the upright posture it may be thought that this precludes usage of quadrupedal animal models. However, muscle contraction and ligament tension is a significant contributor to the load to which intervertebral discs are exposed [37]. It has been hypothesized that the load exerted on the lumbar intervertebral discs of large animals by these structures may be even greater than that observed in humans resulting from the bipedal stance due to the increased complexity of stabilizing a horizontally aligned spine versus a vertically balanced spine [26].

3.2. Animal Models. Taking the above general considerations into account the following models are those most commonly described for use as in vivo models of intervertebral disc degeneration.

3.2.1. Rodent Models. Mice and rat models, despite the obvious difference in intervertebral disc size, have significant advantages with regard to ease of use and application of technology. Genetic knockout and mutation mice models have enabled the investigation of the effects of the elimination of particular proteins, for example, collagen II [18], on disc function. Bipedal mouse and rat models were created through bilateral mid-humeral surgical and tail amputations [36]. Bipedal mice were observed to demonstrate accelerated NP degeneration with frequent NP herniation [40]. However, more recent studies have indicated that bipedal rats do not assume a more erect posture than their quadrupedal peers [69] calling into question the cause of the observed increased disc degeneration.

The mouse and rat tail provide a readily accessible model for intervertebral disc degeneration through mechanical injury, asymmetrical compression, or administration of digestive enzymes [39, 70].

Table 1: Summary of animal models of disc degeneration.

Animal	Notochordal cells in adult intervertebral disc	Mechanism	References
Mouse	Present	*Spontaneous*	
		Knockout: Col2a1 gene/type II collagen	Sahlman et al. [18]
		Collagen IX mutation	Kimura et al. [38]
		Mechanical	
		Tail bending	Court et al. [39]
		Bipedal mouse	Higuchi et al. [40], Goff and Landmesser [36]
		Instability: resection of posterior elements	Miyamoto et al. [41]
Rat	Present	*Spontaneous*	
		HLA-B27 and human β_2-microglobulin gene transgenic	Hammer et al. [42]
		Mechanical	
		Tail bending	Lindblom [43]
		Bipedal rat	Goff and Landmesser [36]
		Ilizarov-type apparatus	Iatridis et al. [44]
		Cyclical compression	Ching et al. [45]
		Structural	
		Stab incision	Rousseau et al. [46] and Jeong et al. [47]
Sand rat	Present	*Spontaneous*	
		Laboratory diet	Silberberg et al. [48], Gruber et al. [49], Moskowitz et al. [50]
Rabbit	Present	*Mechanical*	
		External loading device	Kroeber et al. [51]
		Adjacent segment fusion	Phillips et al. [52]
		Structural	
		Annulus puncture	Masuda et al. [20]
		Chemonucleolysis: chondroitinase ABC	Kiester et al. [53]
		NP aspiration	Sakai et al. [54]
Canine			
Nonchondrodystrophoid dog	Present	*Spontaneous*	Bergknut et al. [21]
		Structural	
		Annular injury with scalpel/drill	Keyes and Compere [55]
		Subtotal discectomy	Hohaus et al. [56]
Chondrodystrophoid dog	Absent	*Spontaneous*	Gillett et al. [57] and Bergknut et al. [21]
		Structural	
		Needle aspiration of NP	Serigano et al. [58]
		Chemonucleolysis: chymopapain	Melrose et al. [59]
Goat	Absent	*Structural*	
		Chondroitinase ABC	Hoogendoorn et al. [60]
		Drill bit injury/annulotomy	Zhang et al. [22]

Table 1: Continued.

Animal	Notochordal cells in adult intervertebral disc	Mechanism	References
Pig	Present	*Structural* Nucleotomy	Acosta et al. [61]
Sheep	Absent	*Structural* Partial thickness annulotomy Annular incision and partial nucleotomy (simulated microdiscectomy) Chondroitinase ABC	Osti et al. [62], Oehme et al. [63], Melrose et al. [64] Oehme et al. [23] Ghosh et al. [65]
Macaque	Present	*Spontaneous* Age related degeneration	Nuckley et al. [66]
Baboon	Present	*Spontaneous* Age related degeneration	Lauerman et al. [24] and Platenberg et al. [25]
Rhesus monkey	Present	*Structural* Annulotomy ± collagenase Bleomycin injection of subchondral bone	Stern and Coulson [67] Wei et al. [68]

NP indicates nucleus pulposus.

However significant limitations exist for such models:

(1) Persistent notochordal cells: limiting the potential relevance of such models to the clinical environment particularly with regard to testing potential therapeutics.

(2) Differing mechanical loading: rodent tail models: the tail may have significantly different mechanical loading to the human lumbar spine although this has been disputed by some authors.

(3) Significantly smaller disc size reducing the nutritional challenge.

(4) Ethical concerns regarding the bipedal mouse.

3.2.2. Rabbit Models. The rabbit model of intervertebral disc degeneration has been utilized by several authors for investigation of disc degeneration and of potential therapeutic agents [20, 71]. Major advantages of this model are the higher degree of homology to the human intervertebral disc with the presence of facet joints and paravertebral muscles and ligaments in comparison to the rodent tail models [51], the larger size of the animal and intervertebral discs, and the cost-effectiveness as a model relative to large animals. Limitations relate to the persistence of notochordal cells and the significant variation from human geometry [72].

3.2.3. Canine Models. As discussed previously CD dogs demonstrate a decrease of notochordal cells from birth onwards with complete loss by early adulthood predisposing the animal to intervertebral disc degeneration. The CD dogs, among which beagles and dachshunds number, are well-characterized models of spontaneous intervertebral disc degeneration [57]. The larger size of the disc space relative to rodents makes administration of intradiscal therapeutic agents technically less challenging [58]. Similarities exist with regard to the gross pathology, histopathology, and glycosaminoglycan content among humans and canines in intervertebral disc disease [21]. Differences exist with regard to the thicker cartilaginous endplates in humans, the presence of growth plates within the vertebrae of the canine [21], and intervertebral disc size. Additional ethical concerns exist with regard to the use of dogs for experimental research in many parts of the world.

3.2.4. Goat Models. Goats have previously been used as models for intervertebral disc degeneration [22, 60]. Advantages of the use of this species include anatomical similarities with regard to size and shape with respect to the human intervertebral disc, comparable mechanical load [73], absence of notochordal cells in the adult [74], and the pragmatic benefits of a hardy, economical animal model that tolerates surgery well [22].

3.2.5. Sheep Models. The sheep model has proven to have particular merit for several major reasons. Firstly, the sheep, similar to humans, suffers from a loss of notochordal cells in early adulthood, predisposing the sheep intervertebral discs to degeneration [75]. The sheep is of a roughly similar size to humans and, despite its quadrupedal stature, is exposed to very similar mechanical stresses to the human intervertebral disc [76]. The ovine spine has previously been used to model disc degeneration [62–64] and test implant devices and in the preclinical investigation of cellular therapies [23, 77–79]. Similar to the goat the sheep is a hardy animal with demonstrated ability to tolerate surgical intervention.

3.2.6. Porcine Models. Porcine models have been utilized in models of intervertebral disc degeneration and in the preclinical assessment of biological therapies such as mesenchymal stem cells [61, 80]. Major advantages attributed to the porcine model include the similarity in size of the disc to the human intervertebral disc and overall size of the animal. However, this advantage is significantly offset by the persistence of notochordal cells into adult life in the porcine model [80], potentially confounding interpretation of investigations of disc degeneration and regenerative therapies.

3.2.7. Primate Models. Spontaneous disc degeneration has been demonstrated in baboon and macaque models [24, 25, 66]. Both species are quadrupedal for locomotion but spend large amounts of time in semierect and erect positions. Rhesus monkeys have also been used as models of disc degeneration following annulotomy ± intradiscal administration of collagenase [67] and subchondral administration of bleomycin [68]. The advantages of such nonhuman primate animal models include intervertebral disc size closer to humans, comparable anatomy, spontaneous disc degeneration, and exposure to mechanical stresses compatible with erect posture. However major ethical and practical considerations (e.g., expense and housing) are associated with the use of nonhuman primate animal models significantly restricting their use for such studies in many institutions.

3.3. Comparison of Mechanisms. Given the complexity of human disc degeneration no animal model can perfectly mimic the entire pathophysiological process. Disc degeneration in animal models is typically initiated by various chemical (e.g., chondroitinase ABC injection [81]) or mechanical (e.g., surgical incision [63], nucleotomy-NP aspiration [82], and drill bit injury [22]) stimuli though it can develop spontaneously in some animals [83].

3.3.1. Spontaneous Models. Spontaneous disc degeneration occurs in a limited number of species, with inconsistent onset and development over a long time frame. The most well-studied species with regard to spontaneous disc degeneration are the sand rat and the chondrodystrophoid dog species. As described above spontaneous disc degeneration has also been observed in nonhuman primates.

Sand Rat. The sand rat is native to east Mediterranean deserts [84] and was first described to undergo spontaneous disc degeneration by Silberberg et al. [48]. When fed a standard laboratory diet the sand rat develops diabetes and widespread disc degeneration [85]. The degenerative changes consist of loss of notochordal cells, annular disorganization, cellular

metaplasia, endplate sclerosis, and the formation of peripheral osteophytes [50]. In a longitudinal study conducted by Gruber et al. [49] radiographic evidence of degeneration was evident by two months with older animals demonstrating disc space wedging, narrowing, irregular disc margins, and endplate calcification. The degenerative process commenced in the NP with subsequent degeneration of the facets and endplates occurring only after disc herniation had developed [48]. Additionally the sand rat has been successfully used in studies of cellular therapy of disc degeneration despite the significant technical challenges this entailed [86].

Genetically Modified Mice. Genetically modified mice models have been developed to investigate the contribution of specific proteins to disc degeneration. Genetically modified mice with collagen IX mutations demonstrated increased cervical degeneration [38]. Similarly mice with collagen II mutations underwent premature endplate calcification and subsequent disc degeneration [18].

Canines. As detailed previously CD dogs demonstrate loss of notochordal cells from birth onwards and progress to demonstrate gross pathology and histopathological and glycosaminoglycan content changes similar to humans in intervertebral disc degeneration [21]. There are also marked similarities between magnetic resonance images of intervertebral disc degeneration in different stages of progression in canines and humans [87, 88]. Canines (both CD and NCD) also undergo routine clinical treatment for degenerative disc disease including decompressive surgery [21]. The chondrodystrophoid dog has long served as an animal model of intervertebral disc degeneration and will continue to do so into the future.

Primates. Baboons and macaques have both been demonstrated to undergo spontaneous disc degeneration [25, 66]. As nonhuman primates that spend a significant proportion of time in erect and semierect postures such animal models demonstrate significant potential for modeling human disc degeneration. However, ethical and pragmatic consideration will likely limit their usage.

Spontaneous models of disc disease can be particularly useful in providing models of disc degeneration. However, the long and at times unpredictable course of spontaneous degeneration often limits their utilization in studies of potential therapies.

3.3.2. Mechanical Animal Models of Disc Degeneration. Mechanical models afford the advantage of initiating the degenerative cascade at a defined time point in a replicable fashion. Epidemiological studies have suggested the association between exposure of the spine to force and disc degeneration [89]. Mechanical models of disc degeneration can be broadly divided into two groups: compression and instability, although there is overlap between the two groups [83].

Compression. Compression involves the application of altered mechanical stresses to the intervertebral disc through mechanism such as bending [43], postural change [90] (i.e., the bipedal rat), or cyclical compression [45].

(1) Bending. Bending of the rat tail is one of the earliest reported methods of inducing disc degeneration [43]. In pioneering studies by Lindblom [43] rat tails fixed into bent shapes demonstrated annulus degeneration on the concave side with connective tissue injury and reduced cellularity. In a more recent study Court et al. [39] were able to demonstrate increased cell death and decreased aggrecan gene expression in the concave side of a disc compressed by forceful fixed mouse tail bending. Such differences were not observed in mice tails exposed to only slight bending.

(2) Postural Change. The bipedal rat and mouse models, as described above, are based on the hypothesis that surgically modified animals will spend more time in an erect posture thus exposing the intervertebral discs to increased mechanicals stress. Given the more recent findings indicating bipedal rats do not spend an increased time in an erect posture and, in fact, possibly less time than their quadrupedal counterparts [69] it is interesting to reflect as to the aetiology of the underlying degenerative changes observed in the primary studies.

(3) Chronic and Cyclical Compression. Researchers have investigated the application of static and cyclical compression to the intervertebral disc. Iatridis et al. [44] described a rat tail compression model to apply chronic compression. This consisted of an Ilizarov-type apparatus (an external fixation device enabling application of mechanical force across the intervertebral disc) applied to the tail of rats. Rats were assigned to sham, immobilization, or compression groups. The immobilization and compression groups demonstrated decreased disc thickness, axial compliance, and angular laxity with the compression group demonstrating these changes more quickly and with greater magnitude. Interestingly the discs demonstrated increased proteoglycan content in contrast to human disc degeneration, in which reduced proteoglycan content is observed during the degenerative process.

Kroeber et al. [51] developed a novel model that enabled the application of compressive force to the intervertebral discs of rabbits via attachment of an external loading device. Rabbit intervertebral discs were exposed to up to 28 days of loading of a disc compressive force equivalent to five times bodyweight. After 14 and 28 days of loading discs demonstrated significantly reduced disc space with annulus disorganization observed histologically. Increased dead cells were observed in the annulus and endplate. These changes were not reversible after an equivalent period of unloading.

Cyclical compression has also been investigated. In a rat tail model Ching et al. [45] investigated the effects of static and cyclical loading at 0.5, 1.5, or 2.5 Hz. Pins were inserted into the caudal 4th and 5th vertebrae. A compression device was applied to these pins. The greatest loss of interpin distance (a measure of intervertebral disc height and thus disc degeneration) was observed in rat tails subjected to static compression with the least loss of interpin distance, other than the sham control, observed in the 1.5 Hz group, suggesting disc response varies with the frequency of loading.

Instability. Various animal models of disc disease exist in which the intervertebral disc is exposed to increased instability at the motion segment promoting intervertebral disc degeneration. Approaches to produce instability include surgical resection of posterior elements such as facet joint and spinous processes [41] and the fusion of an adjacent level [52]. Miyamoto et al. [41] demonstrated that resection of spinous processes, supraspinous and interspinous ligament, with paravertebral muscle detachment accelerated cervical disc degeneration in a mouse model. At 12 months following surgical intervention the experimental group demonstrated advanced disc degeneration with intervertebral disc material herniation, AF disorganization, metaplasia of fibroblastic cells in the AF into chondrocytes, loss of disc height, and osteophyte formation.

Phillips et al. [52] reported a novel method of modeling intervertebral disc degeneration in the rabbit by performing simulated surgical spinal fusion at the lumbar L5–L7 level in rabbits. Spinal fusion eliminates movement at the index level but induces altered stresses at the adjacent mobile segments [91, 92]. The adjacent level intervertebral discs L4-L5 and L7-S1 demonstrated progressive disc degeneration. Annular disorganization with loss of normal collagen bundle arrangement was observed at three months. This was increased at six months and by nine months the normal structure of the disc had been replaced by disorganized fibrous tissue, annular tears, and loss of chondrocytes and notochordal cells in the NP were observed as was decreased monomeric size of the proteoglycans. Furthermore disc space narrowing, endplate sclerosis, and osteophyte formation were also observed in keeping with the clinical condition.

Instability studies allow an inducible method of progressive disc degeneration with many of the features observed in the clinical condition. The time course of progression of these models, requiring 9–12 months for the establishment of severe disc degeneration, may preclude their usage in studies of regenerative therapies given cost concerns.

3.3.3. Structural Models. An alternate mechanism of inducing disc degeneration is directly compromising the structural integrity of the intervertebral disc. This task can be accomplished by chemical or direct physical methods.

Chemonucleolysis. Various chemical agents have been investigated as potential stimuli to induce the pathophysiological process of disc degeneration. The best described such agent, chymopapain, was first reported in clinical use in 1964 for the treatment of sciatica secondary to presumed disc protrusion [93]. Chymopapain is a proteolytic enzyme derived from the papaya latex [94] that produces disc degeneration by inducing proteolytic digestion or removal of glycosaminoglycan chains. Proteoglycan loss leads to disc height loss and altered biomechanical stability [26]. The enzyme selectively degrades intervertebral disc proteoglycan in a dose dependent fashion [59]. Inadequate doses may be followed by NP proteoglycan restoration [95]. High doses have also been demonstrated to directly produce annulus destruction in animal models [53].

Chondroitinase ABC is another enzyme demonstrated to produce disc degeneration in animal models [96]. Chondroitinase causes its effect by producing degradation of the polysaccharide side chains of the proteoglycans of the intervertebral disc [97]. Chondroitinase ABC injection was demonstrated to produce dose dependent intervertebral disc degeneration in a caprine model by Hoogendoorn et al. [98]. Chondroitinase ABC injection has also been used in an ovine model to induce intervertebral disc degeneration to enable assessment of regenerative therapies [65].

As described above injection of enzymes leads to proteoglycan loss, an essential component of the pathophysiological process of disc degeneration observed clinically. A criticism of the chondroitinase ABC for inducing disc degeneration is that the viability of native disc cells is largely preserved, enabling regeneration of the extracellular matrix [99].

Physical Methods. Surgical injury to the intervertebral disc is a well-established method of inducing disc degeneration. Injury can be performed to the endplate, the annulus, or the annulus and nucleus.

Endplate injury has been demonstrated in a porcine model to produce changes consistent with disc degeneration. Following lumbar endplate injury with a drill bit porcine intervertebral discs were observed over a 3-month period to demonstrate annular delamination, with reduction in nucleus proteoglycan content, cellularity and loss of gel-like structure [100]. Evidence of degeneration of varying degrees of magnitude was observed seven months following injury in a similar porcine model of endplate injury induced disc degeneration [101].

Annular injury models were first described in the 1930s by Keyes and Compere [55]. Keyes and Compere demonstrated that annular injury with subsequent NP expulsion leads to loss of disc height and degenerative changes at the index level. Following these pioneering studies multiple intervertebral disc injury methods have been investigated for their potential to induce disc degeneration. Broadly such methods can be considered under the categories of partial thickness annular injury and full thickness annular injury with nucleus involvement (see Figure 2). Full thickness annular injuries have the advantage of producing nuclear avulsion with relatively rapid degeneration. Partial thickness injuries produce a slower degenerative process.

Stab injuries and annulotomies have been performed in a variety of animal models including rats [46], rabbits [20], sheep [62], and pigs [61]. Osti et al. [62] demonstrated in an ovine model that partial thickness annular injury, consisting of a 5 mm depth incision that left the inner annulus and NP intact at the time of injury, would lead to progressive failure of the inner annulus with progressive disc degeneration over several months. Oehme et al. [63, 102] demonstrated in an ovine model that after three months a larger (20 mm × 6 mm) partial thickness annular injury resulted in significant increased disc height loss, increased MRI Pfirrmann degeneration scores, increased histological injury scores, and decreased NP glycosaminoglycans in the injured discs.

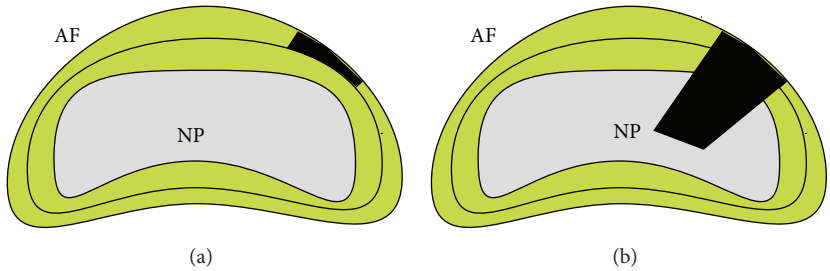

Figure 2: (a) Partial thickness annular injury. (b) Full thickness annular injury with NP involvement. AF indicates annulus fibrosus; NP indicates nucleus pulposus.

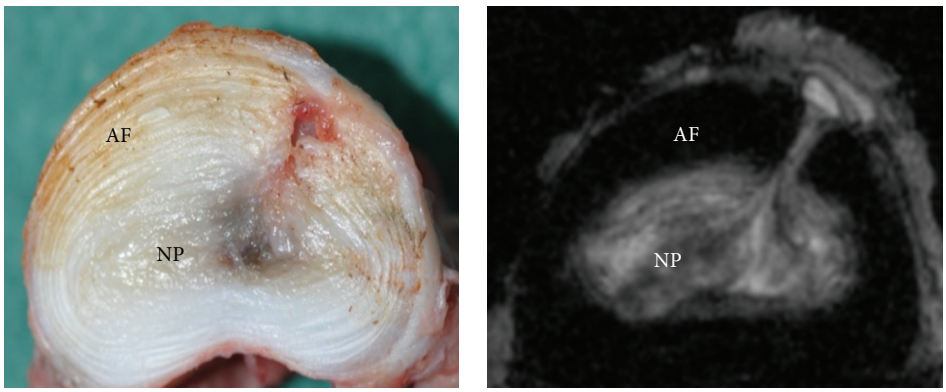

Figure 3: (a) Ovine drill bit injured intervertebral disc demonstrating injury penetrating through the annulus into the nucleus. (b) 9.4 T axial MRI T2 sequence demonstrating drill bit injury tract extending through AF to NP. AF indicates annulus fibrosus; NP indicates nucleus pulposus.

Full thickness intervertebral disc injury is demonstrated in the approach of Oehme et al. [23]. In this injury model a simulated partial lumbar microdiscectomy was performed by creating a 3 × 5 mm annular incision in ovine discs followed by removal of 0.2 g of intervertebral disc tissue, including NP. 24 weeks following performance of the partial-microdiscectomy injured and otherwise untreated intervertebral discs demonstrated increased disc height loss, increased MRI Pfirrmann degeneration scores, and reduced NP proteoglycan content relative to controls.

A novel full thickness intervertebral disc injury caprine model utilizing a drill bit has recently been described by Zhang et al. [22]. The authors compared scalpel blade annulotomy with insertion of a 4.5 mm drill bit to a depth of 15 mm. At two months the drill bit injured intervertebral discs demonstrated significantly increased histological injury scores relative to controls. This injury model has served as the stimulus for investigation in our laboratory utilizing an ovine model. The drill bit injury model has the advantage of producing a highly replicable injury demonstrated in the goat to produce disc degeneration over a two-month period. Drill bit injury was performed by insertion of a 3.5 mm drill bit 12 mm in depth in two adjacent ovine lumbar intervertebral discs. Sheep underwent necropsy at two months. Gross morphology and 9.4-tesla MRI demonstrated significantly increased injury scores in injured versus control discs (see Figure 3).

4. Involvement in Preclinical Trials

Despite the limitations of the animal models described above such models play an integral role in increasing our knowledge and understanding of the process of disc degeneration and in the development of novel therapies for clinical application. Given the complex pathophysiological process of disc degeneration with the interplay of cellular, biomechanical, and matrix components cellular therapy is considered by many to demonstrate the greatest potential in the treatment of this condition.

A recent review by Oehme et al. [103] comprehensively details the variety of preclinical and clinical trials of novel cell-based therapies for the treatment of lumbar intervertebral disc degeneration. Animal models used in preclinical trials of novel therapies include rat [47], rabbit [54], canine [56], porcine [61], ovine [23, 78, 79], and rhesus monkeys [104]. The vast majority of animal models described utilized full thickness annular injury with nuclear involvement to induce disc degeneration. As detailed above, the advantage of this injury model is the ability to consistently induce degeneration at a specified time point. Cell types investigated for regenerative potential include NP chondrocytes [56], bone marrow derived mesenchymal stem cells [54], and bone marrow derived mesenchymal precursor cells [23]. The three cell types detailed are notable for having demonstrated the ability

to promote intervertebral disc regeneration in preclinical trials with subsequent progression to clinical trials/series.

4.1. Clinical Translation. The EuroDISC clinical trial [105] investigated the transplantation of expanded autologous disc chondrocytes in patients undergoing single level discectomy. Interim analysis of 28 patients at 24 months revealed those patients who received chondrocyte transplantation reported greater pain reduction and demonstrated increased disc fluid content on MRI compared to controls. Percutaneous injection of expanded autologous mesenchymal stem cells in two small noncontrolled clinical trials leads to improved MRI T2 signal and clinical improvement [106, 107].

Autologous bone marrow mesenchymal stem cell administration has been investigated in two small series of patients [106, 107]. The trial of Orozco et al. [106] reported clinical improvement in 9 of 10 patients who received expanded autologous MSCs for treatment of low back pain with degenerative disc disease and failure of conservative treatment. The series of Yoshikawa et al. [107] consisted of two patients who at two years both reported significant improvement with improved disc hydration on MRI.

The administration of allogeneic mesenchymal precursor cells for the treatment of back pain has been investigated in a Phase II study [108]. A significantly greater proportion of MPC treated patients achieved minimal residual back pain and at least a 50% reduction in back pain. Phase III trials are now underway.

4.2. Pain. The discussion of clinical translation raises one of the most important considerations regarding the translation of findings from animal models of disc degeneration, that of pain. Disc degeneration causes the majority of its morbidity and disability through back pain—a subjective phenomenon. Pain is a symptom experienced by patients and is multifactorial in nature. The clinical observation of significant radiological disc degeneration in the absence of significant back pain in many patients is suggestive of the notion that the two are not necessarily well correlated at all times. Thus the measures of disc degeneration employed in animal models of disc disease such as histology and radiological degeneration scores and macroscopic and biochemical analysis can serve as useful markers of underlying disc degeneration but can inform the observer to only a limited degree of the likely disability associated with such findings.

The assessment of intervertebral disc degeneration related pain in animal models is still in its relative infancy. The majority of such research has been conducted in rodent models [109, 110]. Pain in rodents can be assessed in three ways [110]: observation of pain-related behaviours (e.g., increased grooming and "wet-dog shakes" [111]), measuring functional performance (e.g., locomotor ability assessment in mice [109]), or determining response to mechanical or thermal stimuli (e.g., grip strength in response to axial stretch, a possible measure of axial low back pain). A recent study comparing sensitivities of different pain assessment methods in a rat model suggested hind paw mechanical sensitivity and duration of grooming as the most sensitive measures of degeneration induced pain [110]. Hind paw mechanical sensitivity offers the advantage of enabling analysis of threshold changes whereas spontaneous behavioural change may better relate to the presence of pain and general condition of an animal [111, 112]. Performance on functional assessments, such as the rotarod test, also declines following lumbar intervertebral disc injury [46].

The assessment of pain in small animal models is imperfect but greatly increases our power to investigate the underlying pathophysiology of intervertebral disc degeneration related pain.

5. Conclusions

The complexity of the human intervertebral disc bares repetition. Given this inherent complexity no animal model will perfectly replicate the clinical condition. The best that can be hoped for is to mimic as closely as possible the clinical condition of degenerative disc disease. Important considerations in choosing an appropriate animal model are the absence of notochordal cells, animal and intervertebral disc size relative to humans, biomechanical forces acting upon the intervertebral disc, mechanistic concerns (i.e., mechanical injury versus chemical injury), and ethical considerations. Nonhuman primates closely match the clinical condition with regard to many of the physical and mechanistic criteria, particularly given the demonstration of spontaneous intervertebral disc degeneration in baboons and macaques. However, ethical considerations should preclude their widespread utilization.

The ovine model of disc disease possesses many desirable characteristics when considering the ideal intervertebral discs model: absence of notochordal cells, similar body mass to humans, and similar biomechanical forces acting upon the intervertebral disc. A major potential criticism of this model is the quadrupedal rather than bipedal nature of sheep. As discussed previously biomechanical studies have indicated that the ovine and human lumbar spines have good comparability in many biomechanical properties [113] in spite of the quadrupedal/bipedal dichotomy.

Certain questions will remain unanswerable in large animal models without significant advances in technology. As such, a role for small animal models will continue, particularly in the investigation of the action of specific gene products in disc degeneration through the use of genetically modified/knockout mice.

The variety of methods of inducing disc degeneration is even broader than the variation in animal models. Spontaneous models of disc degeneration, such as the chondrodystrophic dog and primate, are most likely to parallel the clinical condition in terms of underlying mechanism and time frame. However, the variability of onset and prolonged time course of the degenerative process renders such models difficult to utilize in many contexts. Investigation of regenerative therapies, for example, would be rendered exceptionally difficult if an investigator were to wait for all animals scheduled for investigation to spontaneously develop an appropriate degree of degeneration. For investigations of regenerative therapies it is thus likely that methods of inducing structural injury will be the most utilized as these enable instantaneous production of a replicable injury at a defined time point.

In conclusion no animal model will mimic the clinical condition of disc degeneration with complete fidelity. This is due to the complexity of clinical intervertebral disc degeneration and the immense influence of the subjective phenomena of pain in determining patient outcomes. Animal models will continue to play an essential role in refining our understanding of the pathophysiology of disc degeneration, developing novel therapies for this condition, and ultimately translating such therapies to the clinic.

Competing Interests

The authors have no competing interests to disclose with regard to this paper.

Acknowledgments

Dr. Chris Daly is the recipient of the Foundation for Surgery Richard Jepson Research Scholarship.

References

[1] D. Hoy, L. March, P. Brooks et al., "The global burden of low back pain: estimates from the Global Burden of Disease 2010 study," *Annals of the Rheumatic Diseases*, vol. 73, no. 6, pp. 968–974, 2014.

[2] K. Luoma, H. Riihimäki, R. Luukkonen, R. Raininko, E. Viikari-Juntura, and A. Lamminen, "Low back pain in relation to lumbar disc degeneration," *Spine*, vol. 25, no. 4, pp. 487–492, 2000.

[3] M. D. Humzah and R. W. Soames, "Human intervertebral disc: structure and function," *Anatomical Record*, vol. 220, no. 4, pp. 337–356, 1988.

[4] F. Marchand and A. M. Ahmed, "Investigation of the laminate structure of lumbar disc anulus fibrosus," *Spine*, vol. 15, no. 5, pp. 402–410, 1990.

[5] P. Colombier, J. Clouet, O. Hamel, L. Lescaudron, and J. Guicheux, "The lumbar intervertebral disc: from embryonic development to degeneration," *Joint Bone Spine*, vol. 81, no. 2, pp. 125–129, 2014.

[6] A. J. Freemont, "The cellular pathobiology of the degenerate intervertebral disc and discogenic back pain," *Rheumatology*, vol. 48, no. 1, pp. 5–10, 2009.

[7] M. A. Adams and P. J. Roughley, "What is intervertebral disc degeneration, and what causes it?" *Spine*, vol. 31, no. 18, pp. 2151–2161, 2006.

[8] L. A. Setton and J. Chen, "Mechanobiology of the intervertebral disc and relevance to disc degeneration," *The Journal of Bone & Joint Surgery—American Volume*, vol. 88, supplement 2, pp. 52–57, 2006.

[9] W. Johannessen, E. J. Vresilovic, A. C. Wright, and D. M. Elliott, "Intervertebral disc mechanics are restored following cyclic loading and unloaded recovery," *Annals of Biomedical Engineering*, vol. 32, no. 1, pp. 70–76, 2004.

[10] S. R. Pye, D. M. Reid, J. E. Adams, A. J. Silman, and T. W. O'Neill, "Influence of weight, body mass index and lifestyle factors on radiographic features of lumbar disc degeneration," *Annals of the Rheumatic Diseases*, vol. 66, no. 3, pp. 426–427, 2007.

[11] C. L. Le Maitre, A. J. Freemont, and J. A. Hoyland, "Accelerated cellular senescence in degenerate intervertebral discs: a possible role in the pathogenesis of intervertebral disc degeneration," *Arthritis Research and Therapy*, vol. 9, no. 3, article R45, 2007.

[12] J. P. G. Urban and S. Roberts, "Degeneration of the intervertebral disc," *Arthritis Research and Therapy*, vol. 5, no. 3, pp. 120–130, 2003.

[13] C. L. Le Maitre, A. Pockert, D. J. Buttle, A. J. Freemont, and J. A. Hoyland, "Matrix synthesis and degradation in human intervertebral disc degeneration," *Biochemical Society Transactions*, vol. 35, part 4, pp. 652–655, 2007.

[14] R. J. Moore, B. Vernon-Roberts, R. D. Fraser, O. L. Osti, and M. Schembri, "The origin and fate of herniated lumbar intervertebral disc tissue," *Spine*, vol. 21, no. 18, pp. 2149–2155, 1996.

[15] B. Peng, W. Wu, S. Hou, P. Li, C. Zhang, and Y. Yang, "The pathogenesis of discogenic low back pain," *The Journal of Bone & Joint Surgery—British Volume*, vol. 87, no. 1, pp. 62–67, 2005.

[16] C. Liang, H. Li, Y. Tao et al., "New hypothesis of chronic back pain: low pH promotes nerve ingrowth into damaged intervertebral disks," *Acta Anaesthesiologica Scandinavica*, vol. 57, no. 3, pp. 271–277, 2013.

[17] P.-P. A. Vergroesen, I. Kingma, K. S. Emanuel et al., "Mechanics and biology in intervertebral disc degeneration: a vicious circle," *Osteoarthritis and Cartilage*, vol. 23, no. 7, pp. 1057–1070, 2015.

[18] J. Sahlman, R. Inkinen, T. Hirvonen et al., "Premature vertebral endplate ossification and mild disc degeneration in mice after inactivation of one allele belonging to the Col2a1 gene for type II collagen," *Spine*, vol. 26, no. 23, pp. 2558–2565, 2001.

[19] J. H. Jeong, J. H. Lee, E. S. Jin, J. K. Min, S. R. Jeon, and K. H. Choi, "Regeneration of intervertebral discs in a rat disc degeneration model by implanted adipose-tissue-derived stromal cells," *Acta Neurochirurgica*, vol. 152, no. 10, pp. 1771–1777, 2010.

[20] K. Masuda, Y. Aota, C. Muehleman et al., "A novel rabbit model of mild, reproducible disc degeneration by an anulus needle puncture: Correlation between the degree of disc injury and radiological and histological appearances of disc degeneration," *Spine*, vol. 30, no. 1, pp. 5–14, 2005.

[21] N. Bergknut, J. P. H. J. Rutges, H.-J. C. Kranenburg et al., "The dog as an animal model for intervertebral disc degeneration?" *Spine*, vol. 37, no. 5, pp. 351–358, 2012.

[22] Y. Zhang, S. Drapeau, H. S. An, D. Markova, B. A. Lenart, and D. G. Anderson, "Histological features of the degenerating intervertebral disc in a goat disc-injury model," *Spine*, vol. 36, no. 19, pp. 1519–1527, 2011.

[23] D. Oehme, P. Ghosh, S. Shimmon et al., "Mesenchymal progenitor cells combined with pentosan polysulfate mediating disc regeneration at the time of microdiscectomy: a preliminary study in an ovine model," *Journal of Neurosurgery Spine*, vol. 20, no. 6, pp. 657–669, 2014.

[24] W. C. Lauerman, R. C. Platenberg, J. E. Cain, and V. F. X. Deeney, "Age-related disk degeneration: preliminary report of a naturally occurring baboon model," *Journal of Spinal Disorders*, vol. 5, no. 2, pp. 170–174, 1992.

[25] R. C. Platenberg, G. B. Hubbard, W. J. Ehler, and C. J. Hixson, "Spontaneous disc degeneration in the baboon model: magnetic resonance imaging and histopathologic correlation," *Journal of Medical Primatology*, vol. 30, no. 5, pp. 268–272, 2001.

[26] M. Alini, S. M. Eisenstein, K. Ito et al., "Are animal models useful for studying human disc disorders/degeneration?," *European Spine Journal*, vol. 17, no. 1, pp. 2–19, 2008.

[27] D. J. Aguiar, S. L. Johnson, and T. R. Oegema Jr., "Notochordal cells interact with nucleus pulposus cells: Regulation of proteoglycan synthesis," *Experimental Cell Research*, vol. 246, no. 1, pp. 129–137, 1999.

[28] T. R. Oegema, S. L. Johnson, D. J. Aguiar, and J. W. Ogilvie, "Fibronectin and its fragments increase with degeneration in the human intervertebral disc," *Spine*, vol. 25, no. 21, pp. 2742–2747, 2000.

[29] J. W. Stevens, G. L. Kurriger, A. S. Carter, and J. A. Maynard, "CD44 expression in the developing and growing rat intervertebral disc," *Developmental Dynamics*, vol. 219, no. 3, pp. 381–390, 2000.

[30] S. Sobajima, J. F. Kompel, J. S. Kim et al., "A slowly progressive and reproducible animal model of intervertebral disc degeneration characterized by MRI, X-ray, and histology," *Spine*, vol. 30, no. 1, pp. 15–24, 2005.

[31] J. C. Lotz and J. R. Chin, "Intervertebral disc cell death is dependent on the magnitude and duration of spinal loading," *Spine*, vol. 25, no. 12, pp. 1477–1483, 2000.

[32] T. Yurube, H. Hirata, K. Kakutani et al., "Notochordal cell disappearance and modes of apoptotic cell death in a rat tail static compression-induced disc degeneration model," *Arthritis Research and Therapy*, vol. 16, article R31, 2014.

[33] H. E. Gruber and E. N. Hanley, "Analysis of aging and degeneration of the human intervertebral disc. Comparison of surgical specimens with normal controls," *Spine*, vol. 23, no. 7, pp. 751–757, 1998.

[34] G. D. O'Connell, E. J. Vresilovic, and D. M. Elliott, "Comparison of animals used in disc research to human lumbar disc geometry," *Spine*, vol. 32, no. 3, pp. 328–333, 2007.

[35] K. D. K. Luk, D. K. Ruan, D. H. K. Chow, and J. C. Y. Leong, "Intervertebral disc autografting in a bipedal animal model," *Clinical Orthopaedics and Related Research*, no. 337, pp. 13–26, 1997.

[36] C. W. Goff and W. Landmesser, "Bipedal rats and mice," *The Journal of Bone & Joint Surgery—American Volume*, vol. 39, no. 3, pp. 616–622, 1957.

[37] H.-J. Wilke, A. Rohlmann, S. Neller, F. Graichen, L. Claes, and G. Bergmannt, "ISSLS prize winner: a novel approach to determine trunk muscle forces during flexion and extension: a comparison of data from an in vitro experiment and in vivo measurements," *Spine*, vol. 28, no. 23, pp. 2585–2593, 2003.

[38] T. Kimura, K. Nakata, N. Tsumaki et al., "Progressive degeneration of articular cartilage and intervertebral discs: an experimental study in transgenic mice bearing a type IX collagen mutation," *International Orthopaedics*, vol. 20, no. 3, pp. 177–181, 1996.

[39] C. Court, O. K. Colliou, J. R. Chin, E. Liebenberg, D. S. Bradford, and J. C. Lotz, "The effect of static in vivo bending on the murine intervertebral disc," *Spine Journal*, vol. 1, no. 4, pp. 239–245, 2001.

[40] M. Higuchi, K. abe, and K. Kaneda, "Changes in the nucleus pulposus of the intervertebral disc in bipedal mice: a light and electron microscopic study," *Clinical Orthopaedics and Related Research*, vol. 175, article 251, 1983.

[41] S. Miyamoto, K. Yonenobu, and K. Ono, "Experimental cervical spondylosis in the mouse," *Spine*, vol. 16, pp. S495–S500, 1991.

[42] R. E. Hammer, S. D. Maika, J. A. Richardson, J.-P. Tang, and J. D. Taurog, "Spontaneous inflammatory disease in transgenic rats expressing HLA-B27 and human β2m: an animal model of HLA-B27-associated human disorders," *Cell*, vol. 63, no. 5, pp. 1099–1112, 1990.

[43] K. Lindblom, "Intervertebral-disc degeneration considered as a pressure atrophy," *The Journal of Bone and Joint Surgery. American*, vol. 39, no. 4, pp. 933–945, 1957.

[44] J. C. Iatridis, P. L. Mente, I. A. F. Stokes, D. D. Aronsson, and M. Alini, "Compression-induced changes in intervertebral disc properties in a rat tail model," *Spine*, vol. 24, no. 10, pp. 996–1002, 1999.

[45] C. T. S. Ching, D. H. K. Chow, F. Y. D. Yao, and A. D. Holmes, "The effect of cyclic compression on the mechanical properties of the inter-vertebral disc: an in vivo study in a rat tail model," *Clinical Biomechanics*, vol. 18, no. 3, pp. 182–189, 2003.

[46] M.-A. A. Rousseau, J. A. Ulrich, E. C. Bass, A. G. Rodriguez, J. J. Liu, and J. C. Lotz, "Stab incision for inducing intervertebral disc degeneration in the rat," *Spine*, vol. 32, no. 1, pp. 17–24, 2007.

[47] J. H. Jeong, E. S. Jin, J. K. Min et al., "Human mesenchymal stem cells implantation into the degenerated coccygeal disc of the rat," *Cytotechnology*, vol. 59, no. 1, pp. 55–64, 2009.

[48] R. Silberberg, M. Aufdermaur, and J. H. Adler, "Degeneration of the intervertebral disks and spondylosis in aging sand rats," *Archives of Pathology and Laboratory Medicine*, vol. 103, no. 5, pp. 231–235, 1979.

[49] H. E. Gruber, T. Johnson, H. J. Norton, and E. N. Hanley Jr., "The sand rat model for disc degeneration: radiologic characterization of age-related changes: cross-sectional and prospective analyses," *Spine*, vol. 27, no. 3, pp. 230–234, 2002.

[50] R. W. Moskowitz, I. Ziv, C. W. Denko, B. Boja, P. K. Jones, and J. H. Adler, "Spondylosis in sand rats: a model of intervertebral disc degeneration and hyperostosis," *Journal of Orthopaedic Research*, vol. 8, no. 3, pp. 401–411, 1990.

[51] M. W. Kroeber, F. Unglaub, H. Wang et al., "New in vivo animal model to create intervertebral disc degeneration and to investigate the effects of therapeutic strategies to stimulate disc regeneration," *Spine*, vol. 27, no. 23, pp. 2684–2690, 2002.

[52] F. M. Phillips, J. Reuben, and F. T. Wetzel, "Intervertebral disc degeneration adjacent to a lumbar fusion," *Journal of Bone and Joint Surgery B*, vol. 84, no. 2, pp. 289–294, 2002.

[53] D. P. Kiester, J. M. Williams, G. B. J. Andersson, E. J. M. A. Thonar, and T. W. McNeill, "The dose-related effect of intradiscal chymopapain on rabbit intervertebral discs," *Spine*, vol. 19, no. 7, pp. 747–751, 1994.

[54] D. Sakai, J. Mochida, T. Iwashina et al., "Differentiation of mesenchymal stem cells transplanted to a rabbit degenerative disc model: potential and limitations for stem cell therapy in disc regeneration," *Spine*, vol. 30, no. 21, pp. 2379–2387, 2005.

[55] D. C. Keyes and E. L. Compere, "The normal and pathological physiology of the nucleus pulposus of the intervertebral disc," *The Journal of Bone & Joint Surgery—American Volume*, vol. 14, no. 4, pp. 897–938, 1932.

[56] C. Hohaus, T. M. Ganey, Y. Minkus, and H. J. Meisel, "Cell transplantation in lumbar spine disc degeneration disease," *European Spine Journal*, vol. 17, supplement 4, pp. 492–503, 2008.

[57] N. A. Gillett, R. Gerlach, J. J. Cassidy, and S. A. Brown, "Age-related changes in the beagle spine," *Acta Orthopaedica*, vol. 59, no. 5, pp. 503–507, 1988.

[58] K. Serigano, D. Sakai, A. Hiyama, F. Tamura, M. Tanaka, and J. Mochida, "Effect of cell number on mesenchymal stem cell transplantation in a canine disc degeneration model," *Journal of Orthopaedic Research*, vol. 28, no. 10, pp. 1267–1275, 2010.

[59] J. Melrose, T. K. F. Taylor, P. Ghosh, C. Holbert, C. Macpherson, and C. R. Bellenger, "Intervertebral disc reconstitution after

chemonucleolysis with chymopapain is dependent on dosage: an experimental study in beagle dogs," *Spine*, vol. 21, no. 1, pp. 9–17, 1996.

[60] R. J. W. Hoogendoorn, M. N. Helder, R. J. Kroeze, R. A. Bank, T. H. Smit, and P. I. J. M. Wuisman, "Reproducible long-term disc degeneration in a large animal model," *Spine*, vol. 33, no. 9, pp. 949–954, 2008.

[61] F. L. Acosta Jr., L. Metz, H. D. Adkisson et al., "Porcine intervertebral disc repair using allogeneic juvenile articular chondrocytes or mesenchymal stem cells," *Tissue Engineering—Part A*, vol. 17, no. 23-24, pp. 3045–3055, 2011.

[62] O. L. Osti, B. Vernon-Roberts, and R. D. Fraser, "Anulus tears and intervertebral disc degeneration: an experimental study using an animal model," *Spine*, vol. 15, no. 8, pp. 762–767, 1990.

[63] D. Oehme, T. Goldschlager, S. Shimon, and J. Wu, "Radiological, morphological, histological and biochemical changes of lumbar discs in an animal model of disc degeneration suitable for evaluating the potential regenerative capacity of novel biological agents," *Journal of Tissue Science & Engineering*, vol. 6, article 153, 2015.

[64] J. Melrose, C. Shu, C. Young et al., "Mechanical destabilization induced by controlled annular incision of the intervertebral disc dysregulates metalloproteinase expression and induces disc degeneration," *Spine*, vol. 37, no. 1, pp. 18–25, 2012.

[65] P. Ghosh, R. Moore, B. Vernon-Roberts et al., "Immunoselected STRO-3^+ mesenchymal precursor cells and restoration of the extracellular matrix of degenerate intervertebral discs: laboratory investigation," *Journal of Neurosurgery: Spine*, vol. 16, no. 5, pp. 479–488, 2012.

[66] D. J. Nuckley, P. A. Kramer, A. Del Rosario, N. Fabro, S. Baran, and R. P. Ching, "Intervertebral disc degeneration in a naturally occurring primate model: radiographic and biomechanical evidence," *Journal of Orthopaedic Research*, vol. 26, no. 9, pp. 1283–1288, 2008.

[67] W. E. Stern and W. F. Coulson, "Effects of collagenase upon the intervertebral disc in monkeys," *Journal of Neurosurgery*, vol. 44, no. 1, pp. 32–44, 1976.

[68] F. Wei, R. Zhong, Z. Zhou et al., "In vivo experimental intervertebral disc degeneration induced by bleomycin in the rhesus monkey," *BMC Musculoskeletal Disorders*, vol. 15, article 340, 2014.

[69] A. S. Bailey, F. Adler, S. Min Lai, and M. A. Asher, "A comparison between bipedal and quadrupedal rats: do bipedal rats actually assume an upright posture?" *Spine*, vol. 26, no. 14, pp. E308–E313, 2001.

[70] J. P. Norcross, G. E. Lester, P. Weinhold, and L. E. Dahners, "An in vivo model of degenerative disc disease," *Journal of Orthopaedic Research*, vol. 21, no. 1, pp. 183–188, 2003.

[71] T. Miyamoto, T. Muneta, T. Tabuchi et al., "Intradiscal transplantation of synovial mesenchymal stem cells prevents intervertebral disc degeneration through suppression of matrix metalloproteinase-related genes in nucleus pulposus cells in rabbits," *Arthritis Research and Therapy*, vol. 12, no. 6, article R206, 2010.

[72] H.-J. Wilke, A. Kettler, K. H. Wenger, and L. E. Claes, "Anatomy of the sheep spine and its comparison to the human spine," *Anatomical Record*, vol. 247, no. 4, pp. 542–555, 1997.

[73] T. H. Smit, "The use of a quadruped as an in vivo model for the study of the spine—biomechanical considerations," *European Spine Journal*, vol. 11, no. 2, pp. 137–144, 2002.

[74] R. J. W. Hoogendoorn, M. N. Helder, T. H. Smit, and P. I. J. M. Wuisman, "Notochordal cells in mature caprine intervertebral discs," *European Cells and Materials*, vol. 10, no. 3, p. 59, 2005.

[75] C. J. Hunter, J. R. Matyas, and N. A. Duncan, "Cytomorphology of notochordal and chondrocytic cells from the nucleus pulposus: a species comparison," *Journal of Anatomy*, vol. 205, no. 5, pp. 357–362, 2004.

[76] H. J. Wilke, A. Kettler, and L. E. Claes, "Are sheep spines a valid biomechanical model for human spines?" *Spine*, vol. 22, no. 20, pp. 2365–2374, 1997.

[77] T. Goldschlager, J. V. Rosenfeld, P. Ghosh et al., "Cervical interbody fusion is enhanced by allogeneic mesenchymal precursor cells in an ovine model," *Spine*, vol. 36, no. 8, pp. 615–623, 2011.

[78] T. Goldschlager, P. Ghosh, A. Zannettino et al., "A comparison of mesenchymal precursor cells and amnion epithelial cells for enhancing cervical interbody fusion in an ovine model," *Neurosurgery*, vol. 68, no. 4, pp. 1025–1035, 2011.

[79] T. Goldschlager, P. Ghosh, A. Zannettino et al., "Cervical motion preservation using mesenchymal progenitor cells and pentosan polysulfate, a novel chondrogenic agent: preliminary study in an ovine model," *Neurosurgical Focus*, vol. 28, no. 6, article E4, 2010.

[80] G. W. Omlor, A. G. Nerlich, H.-J. Wilke et al., "A new porcine in vivo animal model of disc degeneration: response of anulus fibrosus cells, chondrocyte-like nucleus pulposus cells, and notochordal nucleus pulposus cells to partial nucleotomy," *Spine*, vol. 34, no. 25, pp. 2730–2739, 2009.

[81] P. Ghosh, R. Moore, B. Vernon-Roberts et al., "Immunoselected STRO-3+ mesenchymal precursor cells and restoration of the extracellular matrix of degenerate intervertebral discs," *Journal of Neurosurgery: Spine*, vol. 16, no. 5, pp. 479–488, 2012.

[82] D. Sakai, J. Mochida, T. Iwashina et al., "Regenerative effects of transplanting mesenchymal stem cells embedded in atelocollagen to the degenerated intervertebral disc," *Biomaterials*, vol. 27, no. 3, pp. 335–345, 2006.

[83] J. C. Lotz, "Animal models of intervertebral disc degeneration: lessons learned," *Spine*, vol. 29, no. 23, pp. 2742–2750, 2004.

[84] K. Singh, K. Masuda, and H. S. An, "Animal models for human disc degeneration," *The Spine Journal*, vol. 5, no. 6, 2005.

[85] R. Silberberg, "Histologic and morphometric observations on vertebral bone of aging sand rats," *Spine*, vol. 13, no. 2, pp. 202–208, 1988.

[86] H. E. Gruber, T. L. Johnson, K. Leslie et al., "Autologous intervertebral disc cell implantation: a model using *Psammomys obesus*, the sand rat," *Spine*, vol. 27, no. 15, pp. 1626–1633, 2002.

[87] C. W. A. Pfirrmann, A. Metzdorf, M. Zanetti, J. Hodler, and N. Boos, "Magnetic resonance classification of lumbar intervertebral disc degeneration," *Spine*, vol. 26, no. 17, pp. 1873–1878, 2001.

[88] N. Bergknut, E. Auriemma, S. Wijsman et al., "Evaluation of intervertebral disk degeneration in chondrodystrophic and nonchondrodystrophic dogs by use of Pfirrmann grading of images obtained with low-field magnetic resonance imaging," *American Journal of Veterinary Research*, vol. 72, no. 7, pp. 893–898, 2011.

[89] J. L. Kelsey, P. B. Githens, T. O'Conner et al., "Acute prolapsed lumbar intervertebral disc. An epidemiologic study with special reference to driving automobiles and cigarette smoking," *Spine*, vol. 9, no. 6, pp. 608–613, 1984.

[90] K. Yamada, "The dynamics of experimental posture. Experimental study of intervertebral disk herniation in bipedal animals," *Clinical Orthopaedics*, vol. 25, pp. 20–31, 1962.

[91] C. K. Lee and N. A. Langrana, "Lumbosacral spinal fusion a biomechanical study," *Spine*, vol. 9, no. 6, pp. 574–581, 1984.

[92] R. C. Quinnell and H. R. Stockdale, "Some experimental observations of the influence of a single lumbar floating fusion on the remaining lumbar spine," *Spine*, vol. 6, no. 3, pp. 263–267, 1981.

[93] L. Smith, "Enzyme dissolution of the nucleus pulposus in humans," *The Journal of the American Medical Association*, vol. 187, no. 2, pp. 137–140, 1964.

[94] L. Smith and J. E. Brown, "Treatment of lumbar intervertebral disc lesions by direct injection of chymopapain," *The Journal of Bone & Joint Surgery—British Volume*, vol. 49, no. 3, pp. 502–519, 1967.

[95] D. S. Bradford, T. R. Oegema Jr., K. M. Cooper, K. Wakano, and E. Y. Chao, "Chymopapain, chemonucleolysis, and nucleus pulposus regeneration. A biochemical and biomechanical study," *Spine*, vol. 9, no. 2, pp. 135–147, 1984.

[96] M. Sakuma, N. Fujii, T. Takahashi, J. Hoshino, S. Miyauchi, and H. Iwata, "Effect of chondroitinase ABC on matrix metalloproteinases and inflammatory mediators produced by intervertebral disc of rabbit in vitro," *Spine*, vol. 27, no. 6, pp. 576–580, 2002.

[97] NC-IUBMB, *Enzyme Nomenclature 1992: Recommendations of the Nomenclature Committee of the International Union of Biochemistry and Molecular Biology on the Nomenclature and Classification of Enzymes*, Academic Press, San Diego, Calif, USA, 1992.

[98] R. J. Hoogendoorn, P. I. Wuisman, T. H. Smit, V. E. Everts, and M. N. Helder, "Experimental intervertebral disc degeneration induced by chondroitinase ABC in the goat," *Spine*, vol. 32, no. 17, pp. 1816–1825, 2007.

[99] D. Oehme, P. Ghosh, T. Goldschlager et al., "Reconstitution of degenerated ovine lumbar discs by STRO-3–positive allogeneic mesenchymal precursor cells combined with pentosan polysulfate," *Journal of Neurosurgery: Spine*, vol. 24, no. 5, pp. 715–726, 2016.

[100] S. Holm, A. K. Holm, L. Ekström, A. Karladani, and T. Hansson, "Experimental disc degeneration due to endplate injury," *Journal of Spinal Disorders and Techniques*, vol. 17, no. 1, pp. 64–71, 2004.

[101] G. Cinotti, C. D. Rocca, S. Romeo, F. Vittur, R. Toffanin, and G. Trasimeni, "Degenerative changes of porcine intervertebral disc induced by vertebral endplate injuries," *Spine*, vol. 30, no. 2, pp. 174–180, 2005.

[102] D. Oehme, T. Goldschlager, J. Rosenfeld et al., "Lateral surgical approach to lumbar intervertebral discs in an ovine model," *ScientificWorldJournal*, vol. 2012, Article ID 873726, 8 pages, 2012.

[103] D. Oehme, T. Goldschlager, P. Ghosh, J. V. Rosenfeld, and G. Jenkin, "Cell-based therapies used to treat lumbar degenerative disc disease: a systematic review of animal studies and human clinical trials," *Stem Cells International*, vol. 2015, no. 2, pp. 946031–946016, 2015.

[104] K. D. K. Luk, D. K. Ruan, D. S. Lu, and Z. Q. Fei, "Fresh frozen intervertebral disc allografting in a bipedal animal model," *Spine*, vol. 28, no. 9, pp. 864–870, 2003.

[105] H. J. Meisel, V. Siodla, T. Ganey, Y. Minkus, W. C. Hutton, and O. J. Alasevic, "Clinical experience in cell-based therapeutics: disc chondrocyte transplantation: a treatment for degenerated or damaged intervertebral disc," *Biomolecular Engineering*, vol. 24, no. 1, pp. 5–21, 2007.

[106] L. Orozco, R. Soler, C. Morera, M. Alberca, A. Sánchez, and J. García-Sancho, "Intervertebral disc repair by autologous mesenchymal bone marrow cells: a pilot study," *Transplantation*, vol. 92, no. 7, pp. 822–828, 2011.

[107] T. Yoshikawa, Y. Ueda, K. Miyazaki, M. Koizumi, and Y. Takakura, "Disc regeneration therapy using marrow mesenchymal cell transplantation: a report of two case studies," *Spine*, vol. 35, no. 11, pp. E475–E480, 2010.

[108] H. W. Bae, K. Amirdelfan, D. Coric et al., "A phase II study demonstrating efficacy and safety of mesenchymal precursor cells in low back pain due to disc degeneration," *The Spine Journal*, vol. 14, no. 11, pp. S31–S32, 2014.

[109] M. Millecamps, J. T. Czerminski, A. P. Mathieu, and L. S. Stone, "Behavioral signs of axial low back pain and motor impairment correlate with the severity of intervertebral disc degeneration in a mouse model," *The Spine Journal*, vol. 15, no. 12, pp. 2524–2537, 2015.

[110] A. Lai, A. Moon, D. Purmessur et al., "Assessment of functional and behavioral changes sensitive to painful disc degeneration," *Journal of Orthopaedic Research*, vol. 33, no. 5, pp. 755–764, 2015.

[111] K. Olmarker, "Puncture of a lumbar intervertebral disc induces changes in spontaneous pain behavior: an experimental study in rats," *Spine*, vol. 33, no. 8, pp. 850–855, 2008.

[112] K. Omarker and R. R. Myers, "Pathogenesis of sciatic pain: role of herniated nucleus pulposus and deformation of spinal nerve root and dorsal root ganglion," *Pain*, vol. 78, no. 2, pp. 99–105, 1998.

[113] N. E. Easley, M. Wang, L. M. McGrady, and J. M. Toth, "Biomechanical and radiographic evaluation of an ovine model for the human lumbar spine," *Proceedings of the Institution of Mechanical Engineers, Part H: Journal of Engineering in Medicine*, vol. 222, no. 6, pp. 915–922, 2008.

Hindawi Publishing Corporation
BioMed Research International
Volume 2016, Article ID 9549036, 13 pages
http://dx.doi.org/10.1155/2016/9549036

Research Article

A New Transgenic Mouse Model of Heart Failure and Cardiac Cachexia Raised by Sustained Activation of Met Tyrosine Kinase in the Heart

Valentina Sala,[1,2] Stefano Gatti,[1] Simona Gallo,[1] Enzo Medico,[1,3] Daniela Cantarella,[3] James Cimino,[4] Antonio Ponzetto,[2] and Tiziana Crepaldi[1]

[1]*Department of Oncology, University of Turin, 10126 Turin, Italy*
[2]*Department of Medical Sciences, University of Turin, 10126 Turin, Italy*
[3]*FPO-IRCCS, 10060 Candiolo, Italy*
[4]*Department of Molecular Biotechnology and Health Sciences, University of Turin, 10126 Turin, Italy*

Correspondence should be addressed to Tiziana Crepaldi; tiziana.crepaldi@unito.it

Received 22 January 2016; Accepted 5 April 2016

Academic Editor: Oreste Gualillo

Among other diseases characterized by the onset of cachexia, congestive heart failure takes a place of relevance, considering the high prevalence of this pathology in most European countries and in the United States, and is undergoing a rapid increase in developing countries. Actually, only few models of cardiac cachexia exist. Difficulties in the recruitment and follow-up of clinical trials implicate that new reproducible and well-characterized animal models are pivotal in developing therapeutic strategies for cachexia. We generated a new model of cardiac cachexia: a transgenic mouse expressing Tpr-Met receptor, the activated form of c-Met receptor of hepatocyte growth factor, specifically in the heart. We showed that the cardiac-specific induction of Tpr-Met raises a cardiac hypertrophic remodelling, which progresses into concentric hypertrophy with concomitant increase in Gdf15 mRNA levels. Hypertrophy progresses to congestive heart failure with preserved ejection fraction, characterized by reduced body weight gain and food intake and skeletal muscle wasting. Prevention trial by suppressing Tpr-Met showed that loss of body weight could be prevented. Skeletal muscle wasting was also associated with altered gene expression profiling. We propose transgenic Tpr-Met mice as a new model of cardiac cachexia, which will constitute a powerful tool to understand such complex pathology and test new drugs/approaches at the preclinical level.

1. Introduction

Cachexia has been defined as a "a complex metabolic syndrome associated with underlying illness and characterized by loss of muscle" [1]. Cardiologists have a clear interest in the matter, since 10–15% of chronic heart failure (CHF) patients experience weight loss and wasting of muscle [2], a phenomenon described as cardiac cachexia [3, 4]. The treatment of CHF has made significant advances over the last two decades. Despite this, the clinical perspective remains poor. The situation worsens considerably once muscle wasting is diagnosed [2, 5]. The factors that trigger the progression from clinically and body weight-stable CHF to cardiac cachexia, however, remain poorly understood.

Cachectic patients have significantly reduced fat and bone tissue [6]. However, the major site of protein loss in cachexia is skeletal muscle [7]: skeletal muscle is an important repository of muscle proteins which are mobilized to provide energy substrates and to sustain protein synthesis in other vital organs.

While cancer patients are known to be prone to develop cachexia, cardiac cachexia due to chronic heart failure takes the lead in terms of absolute patient numbers [8]. Despite this, although a large number of animal studies were performed to investigate novel treatments for heart failure, few studies concentrated on cardiac cachexia [3].

Animal models which replicate the clinical findings of cardiac cachexia mainly rely on surgical techniques including

myocardial infarction and aortic banding [9]. Two other models of cardiac cachexia have been developed so far [10]. Li et al. demonstrated that cardiac-specific overexpression of calsequestrin, a sarcoplasmic reticulum Ca^{2+} storage protein, resulted in chronic heart failure as evidenced by decreased fractional shortening and cachexia [11]. Kato et al. used the Dahl salt-sensitive rat as a model of cardiac cachexia; these rats showed impaired growth and reduced food intake in comparison with controls [12].

c-Met tyrosine kinase has been identified as the receptor of the hepatocyte growth factor (HGF) [13]. In our previous studies, we aimed at investigating Met's role in the heart, by constitutively activating the HGF/Met system through the expression of Tpr-Met [14]. In the Tpr-Met oncoprotein, the N-terminal region of Tpr, which includes two dimerization motifs, is fused to the tyrosine kinase of Met, which is, thus, constitutively active in the absence of the ligand [15]. By postnatal cardiac-specific expression of Tpr-Met, we generated a model of congestive HF leading to cardiac cachexia.

2. Materials and Methods

2.1. Ethics Statement. The use of mice for this study and all animal procedures were approved by the Ethical Commission of the University of Turin and by the Italian Ministry of Health.

2.2. Conditional Cardiac Tpr-Met Mice. The single transgenics (α-MHC-tTA mouse and Tpr-Met-TRE-GFP responder mouse) and bitransgenics were described in [14, 16, 17]. All animals were in FVB 100% background. For genotyping of mouse tail DNA extract, tTa-α-MHC and eGFP primers were used. Bitransgenic and control mice were conceived and delivered in the presence of 0.01% Doxycycline Hydrochloride (DOX, MP Biomedicals) in drinking water, in order to maintain suppressing the transgene, during *in utero* development. The day following birth, DOX was removed from drinking water to allow Tpr-Met expression in the postnatal age. All animals were fed standard diet and water *ad libitum* and were maintained on a 12 h light-dark cycle at 23 ± 2°C room temperature. Environmental enrichment was provided.

2.3. Echocardiography. Size and function of the left ventricle were evaluated by high-resolution transthoracic m-mode and two-dimensional echocardiography with Vevo 2100 echocardiograph (Visualsonics), as previously described in detail [14, 18]. Fractional shortening and h/r ratio were calculated using standard formulas. Cardiac function was assessed when the heart rate was 350 to 450 bpm.

2.4. Sample Collection. Animals were sacrificed by cervical dislocation and organs were immediately rinsed in ice-cold PBS, grossly dried, weighted and immersed in RNAlater (Qiagen) overnight at 4°C, and then deposited at −80°C for long-term storage, to preserve total mRNA/proteins. Hindlimbs were excised and digested overnight with Proteinase K (Euroclone). Tibias were scanned and measured using Image J. The mean of weights of left and right muscles was calculated and used for subsequent statistics. After excision of muscles, tibias were excised and digested with proteases. The mean tibia length was used for normalization.

2.5. Western Blot and RT-PCR. Protein and total RNA extracts were prepared and analysed as described [14, 16, 17]. Proteins were separated by 8–10% SDS-PAGE and transferred to Hybond C-Extra membranes (Amersham). Equal protein loading was verified by PonceauS (Euroclone) staining. Membranes were blocked in 10% BSA (Sigma Aldrich), incubated overnight at 4° with the primary antibody diluted in 5% BSA, and probed with horseradish peroxidase- (HRP-) conjugated IgGs. Bands were detected using Supersignal West Pico (Thermo Scientific) by Chemidoc XRS (Biorad). Unsaturated images were used for quantification with Imagelab (Biorad). Gapdh was used for normalization of MF20 protein bands in the same gel [16]; Spectra Multicolor Broad Range or Page Ruler reference protein ladder (Thermo Scientific) was used. All the protein samples compared were loaded on the same gel. $n = 6$ ctrls and $n = 5$ TM for WB.

2.6. Histology: Cross-Sectional Area (CSA). PBS-rinsed muscles were fixed in freshly made 4% paraformaldehyde (Sigma Aldrich) 4–8 hours at room temperature or overnight at 4° and then embedded in paraffin. Transversal 10 μm thick sections of the middle were prepared and stained with hematoxylin and eosin. Images were taken with Leica DMRE microscope. ImageProPlus 5.1 software was used for acquisition. Fiber CSA delimited was measured using Image J as described [14]. At least 250 CSA from nonoverlapping fields were measured. $n = 7$ TM and $n = 9$ ctrls.

2.7. Illumina Gene Expression Profiling and Bioinformatical Analysis. Processing of tissue and RNA and Illumina technology were described in [17]. Wild-type and single transgenics were used as controls. Cubic spline-normalized probe intensity data and detection p values were obtained using GenomeStudio (Illumina). Subsequent data processing included Log_2 and Log_2 Ratio transformation. Expander [19] was used to merge redundant probes by Gene ID and generate the heat map from Log_2 Ratio values, after standardization (mean 0 and std 1) and using complete linkage type and Pearson correlation similarity measurement. Only genes showing a fold change of more than 1.7 and a p value of less than 0.05 were included in the analysis. Expander unsupervised hierarchical clustering was used to identify clusters of up- and downregulated genes.

2.8. Statistics. Data are expressed as relative values (mean ± SD). In relative measures, controls are set at 1. Differences between groups were determined by independent two-tailed Student's t-test.

3. Results and Discussion

3.1. Cardiac Concentric Hypertrophy Progresses to Marked Heart Failure with Preserved Ejection Function at P27. To obtain transgenic mice in which expression of Tpr-Met can be specifically induced in cardiac muscle in a regulated

manner, we adopted the Tet-Off technology [20]. The Tpr-Met-TRE-GFP responder (Tpr-Met responder) construct was assembled by inserting the cDNAs of Tpr-Met and GFP reporter into the bidirectional plasmid pBI. We thus generated a gain-of-function transgenic model with tetracycline-suppressible expression of Tpr-Met under control of the α-myosin heavy chain (α-MHC) promoter, for specific expression of the transgene in the heart [14]. Tpr-Met mice were conceived and delivered in the presence of DOX, in order to suppress Tpr-Met expression during *in utero* development. The day following birth, DOX was removed from drinking water to allow permanent Met activation in postnatal cardiomyocytes. We have previously shown that cardiac-specific postnatal expression of Tpr-Met oncoprotein leads to cardiac hypertrophy and Tpr-Met mice die at ~4 weeks after birth (between P25 and P27) with signs of congestive heart failure, lung edema, alopecia, ascites, dyspnea, cyanosis, and lethargy [14].

At P27, Tpr-Met hearts displayed marked features of cardiac hypertrophy [14], which was also shown by echocardiographic analysis putting in evidence significantly reduced LV Volumes, in both diastole and systole, compared to controls (Figure 1(a)). A pattern fitting in the human classification of concentric hypertrophy [21] was further underlined by the concomitant significant increase in thickness/radius ratio (h/r) (Figure 1(b)), LV mass (Figure 1(c)), and LV mass normalized on body weight (LV mass/BW) in Tpr-Met mice, compared to controls (Figure 1(d)). Plotting relative wall thickness (RWT) and normalized LV mass (Figure 1(e)) showed an important shift of Tpr-Met hearts towards the upper-right corner of the plot, further confirming the diagnosis of concentric hypertrophy. Notably, at the age of P27, Tpr-Met mice did not show systolic dysfunction as assessed by ejection fraction (EF) measurement, but rather a phenotype resembling heart failure with preserved ejection fraction (HFpEF, Figure 1(f)). Indeed, HFpEF is more frequently associated with concentric remodelling and concentric hypertrophy, compared to normal or eccentric geometry [22].

3.2. The Progression of Cardiac Hypertrophy to Heart Failure Is Associated with a Progressive Increase in Cardiac Gdf15 Levels. With the massive progressive increase in cardiac hypertrophy from P21 to P27 (Figure 1(g)), also a corresponding dramatic increase in cardiac growth differentiation factor 15 (Gdf15) mRNA levels was observed (Figures 1(h) and 1(i)). Gdf15, also referred to as macrophage-inhibitory cytokine 1 (Mic1), a member of the transforming growth factor-β (TGF-β) family (Bootcov PNAS 1997), is not expressed in the heart under physiological conditions but increases in response to cardiovascular injuries (i.e., pressure overload, heart failure, and ischemia/reperfusion) and is associated with cardiac remodelling [23]. Higher circulating levels of Gdf15 have been reported in CVDs [24, 25], and such elevations were correlated with disease progression [26]. Notably, Gdf15 has been suggested as a promising diagnostic and prognostic tool for HFpEF [25, 27]. Consistently, we report that, in our model, cardiac levels of Gdf15 increase progressively with the severity of cardiac hypertrophy (Figures 1(g)–1(i)).

Elevated Gdf15 concentrations may be the result of compensating protective mechanisms for tissue repair. Indeed, Gdf15 has shown antihypertrophic and cardioprotective functions [28, 29]. However, beneficial adaptative effects may be detrimental in the long-term. This molecule is overexpressed in cachexia-associated diseases and is capable of modulating appetite [30]. Increased circulating levels of Gdf15 have been reported in patients with several types of cancer [31]. Mice xenografted with tumours overexpressing Gdf15 showed a degree of weight loss proportional to the elevation of serum Gdf15 levels [32]. A direct action of the circulating cytokine on feeding centres in the brain has been also reported [32].

Gdf15 emerges, therefore, as a potential new target for anticachectic therapies. So far, however, no therapies have been identified that decrease the circulating levels of Gdf15 in patients with cardiovascular disease.

3.3. Heart Failure Leads to Cardiac Cachexia Syndrome, Characterized by Loss of Body Weight, Reduced Body Weight Gain, and Skeletal Muscle Wasting. Increased heart-to-body weight ratio (cardiac hypertrophy) and enhanced lung-to-body weight ratio (pulmonary congestion) were the most impressive signs of cardiac failure at P27, as we have previously described [14].

To investigate such progression from body-weight stable to failing conditions, each animal was placed in a single case starting from P21. Body weight gain and food intake of Tpr-Met mice and control littermates were evaluated starting from the age of P14 and P22, respectively. At P27, Tpr-Met mice showed marked (>27%) decrease in body weight (Figure 2(a); $n = 18$ controls and $n = 9$ Tpr-Met). According to Anker and Coats, when weight loss higher than 7.5% of the previous normal weight is observed in heart failure patients (for at least six months and without signs of other primary cachectic states), cachexia should be diagnosed [33]. Decreased body weight at P27 resulted from a reduction in body weight gain, which started from postnatal day P20 (Figure 2(b); $n = 8$ controls and $n = 5$ Tpr-Met). Cardiac cachexia involves similar features of other forms of cachexia, including anorexia. Food intake of Tpr-Met mice was still normal at P22 but diminished significantly starting from postnatal day 23 (Figure 2(c); $n = 8$ controls and $n = 5$ Tpr-Met).

According to its definition, cachexia is characterized by loss of muscle. Hence, when signs of congestive heart failure were clear, Tpr-Met mice were sacrificed and tissues were collected and weighed. Muscle weights were normalized to the respective tibia lengths. Cachectic Tpr-Met mice showed wasted hindlimb muscles (Figure 3(a)) and had significantly reduced skeletal muscle weight with respect to controls (TA, SOL, and GSN; $n = 10$ Tpr-Met and $n = 26$ controls; Figure 3(b)). Accordingly, the mean Cross-Sectional Area of TA, SOL, and GSN muscle fibers of Tpr-Met mice was reduced, with respect to controls ($n = 9$ controls and $n = 7$ Tpr-Met for CSA; Figures 3(c)–3(e), left and middle graph). The maximum value of fiber CSA was also significantly reduced in TA and GSN muscles (Figures 3(c)–3(e), right graphs).

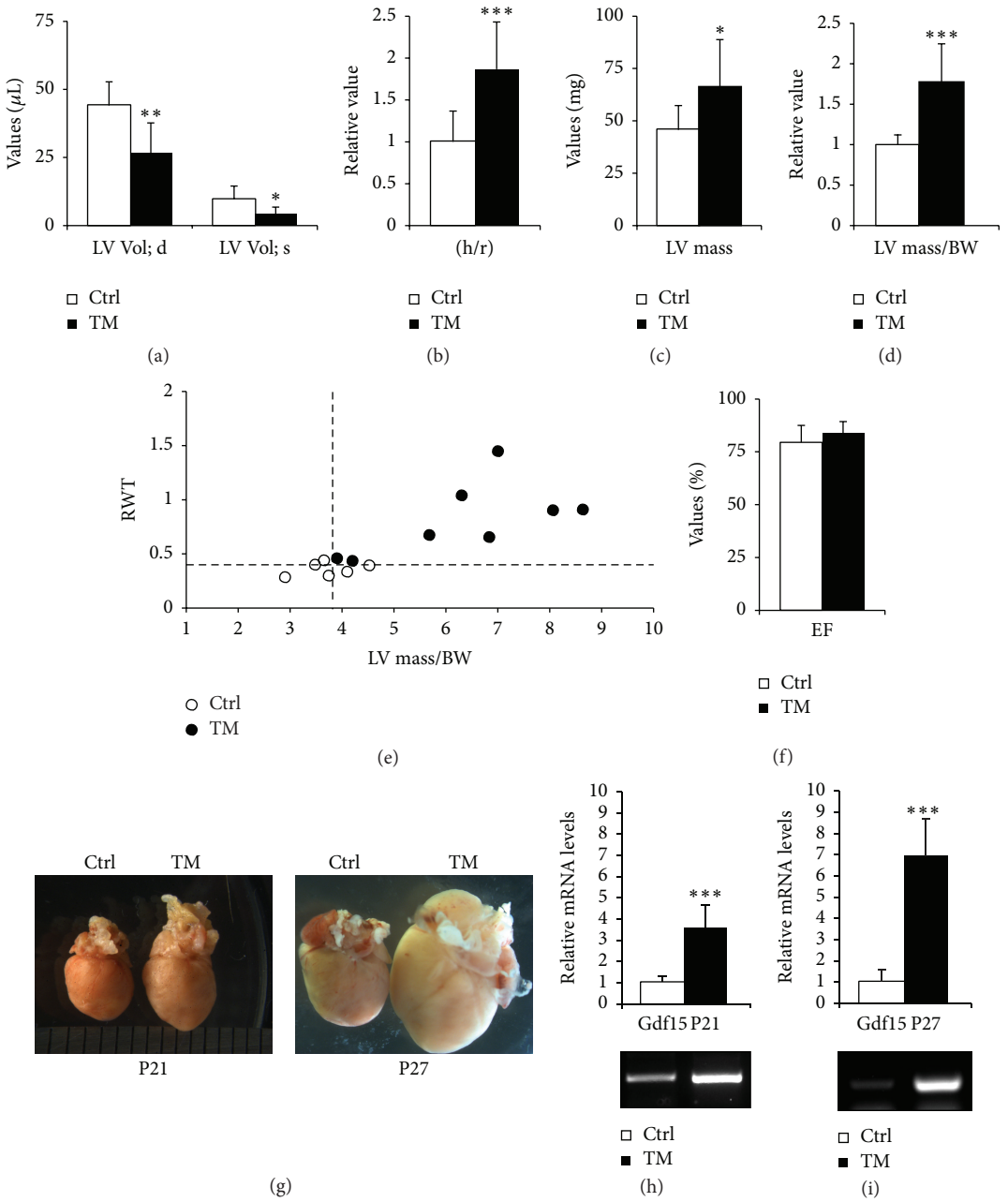

Figure 1: Progressive concentric hypertrophy is accompanied by increased Gdf15 expression in Tpr-Met expressing hearts. (a) At P27, Tpr-Met hearts displayed echocardiographic features of cardiac hypertrophy, including significantly reduced LV Volumes, in both diastole and systole, compared to controls. Hypertrophy was further underlined by a significant increase in thickness/radius ratio (h/r) (b), LV mass (c) and LV mass normalized on body weight (LV mass/BW) (d), and relative wall thickness (RWT) (e) in Tpr-Met mice, compared to controls. (f) At the age of P27, Tpr-Met mice showed preserved ejection fraction (EF). With the increase in the extent of cardiac hypertrophy from P21 to P27, as shown by stereomicroscopy (g), a progressive increase in cardiac Gdf15 mRNA levels was observed from P21 (h) to P27 (i). $^{*}p < 0.05$; $^{**}p < 0.01$; $^{***}p < 0.005$.

In the sum, Tpr-Met mice suffering from heart failure showed a marked decrease in body weight, body weight gain, and food intake and showed skeletal muscle loss due to muscle fiber atrophy, hence recapitulating the phenotype of cardiac cachexia syndrome.

3.4. Suppressing Tpr-Met Expression at P21 Rescues Cardiac Hypertrophy and Loss of Muscular Weight. The extent to which hypertrophic remodelling is reversible is poorly known. To this aim, at birth, Doxycycline (DOX) was withdrawn from a group of Tpr-Met mice for 21 days in order to

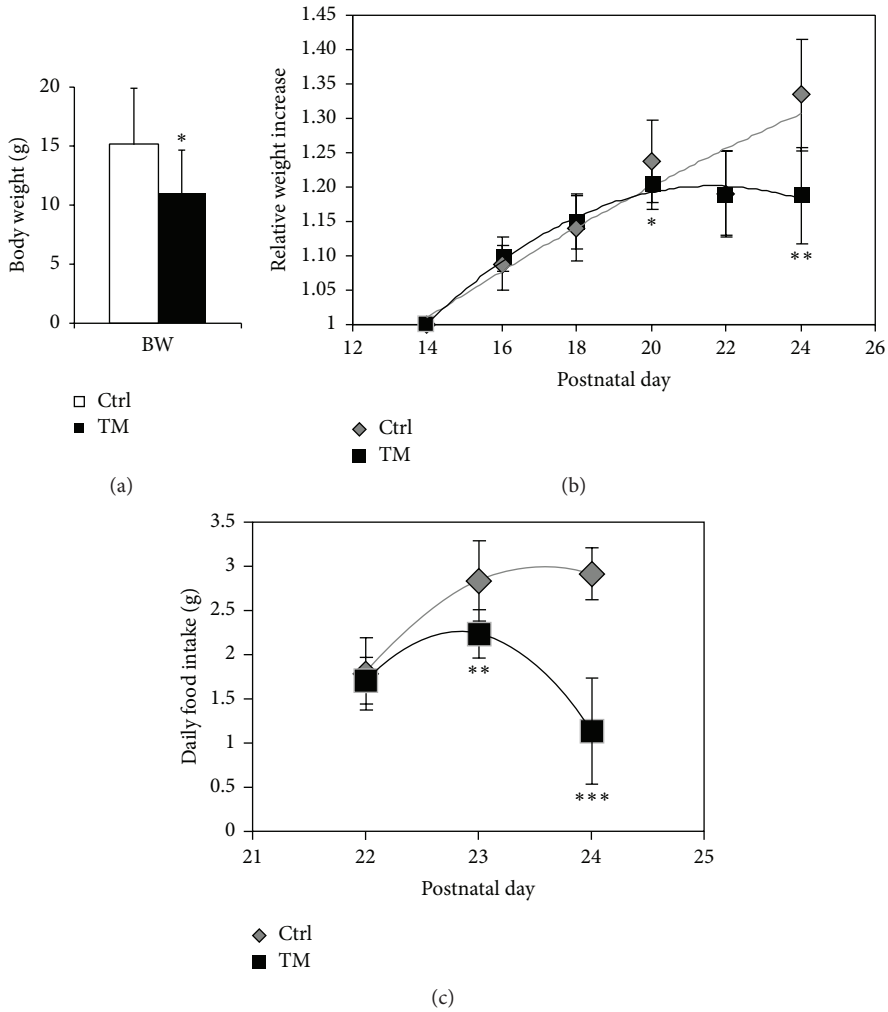

Figure 2: In Tpr-Met mice, progressive concentric hypertrophy leads to reduced body weight and food intake. Tpr-Met mice showed a significant decrease in body weight (BW) (a), body weight gain (b), and daily food intake (c). Tpr-Met mice showed marked decrease in body weight starting from postnatal day 20 (P20) and food intake starting from postnatal day 22 (P22). $^{*}p < 0.05$; $^{**}p < 0.01$; $^{***}p < 0.005$.

activate Tpr-Met signaling; DOX was subsequently restored to stop Tpr-Met expression. At study completion (P27), a complete rescue of heart hypertrophy and lung edema was obtained when suppressing Tpr-Met expression at P21, since Tpr-Met mice showed normal heart and lung weights [34].

It has been demonstrated that the use of ACE inhibitors and β-blockers can potentially delay (and eventually prevent) the onset of cardiac cachexia [3]. Notably, the reduction in body weight gain was completely rescued when Tpr-Met transgene expression was suppressed by DOX administration from P21 (Tpr-Met + DOX P27; $n = 4$), perfectly overlapping with values from littermate controls ($n = 6$) (Figure 4(a)). After such prevention trial, Tpr-Met mice showed normal body weight at P27 (Figure 4(b)), and, consistently, the weight of TA, SOL, and GSN muscles was increased to values comparable with those of controls ($n = 10$ Tpr-Met, $n = 6$ Tpr-Met + DOX P27, and $n = 26$ controls; Figure 4(c)).

These data put in evidence the fact that solving the hypertrophic phenotype, before the appearance of skeletal muscle wasting, can prevent the onset of cardiac cachexia in an effective way, even if cardiac hypertrophy is already manifest.

3.5. Gene Expression Profiling of Wasting Gastrocnemius Muscle. For the molecular analysis of wasting skeletal muscle, we concentrated on gastrocnemius (GSN) muscle. In GSN muscle, a marked decrease of MF20 protein level normalized on Gapdh was shown (Figure 5), in accordance with the loss of muscle fiber detected in terms of weight and Cross-Sectional Area.

Then, we performed gene expression profiling with Illumina technology on GSN muscle samples. Total RNA from three cachectic Tpr-Met mice was compared to three littermate controls. Standardization was applied to Log_2 absolute intensities and all subsequent analysis was performed using Expander software. A cut-off of $p < 0.05$ and fold change >1.7 was used. Unsupervised hierarchical clustering was performed and the corresponding heat map

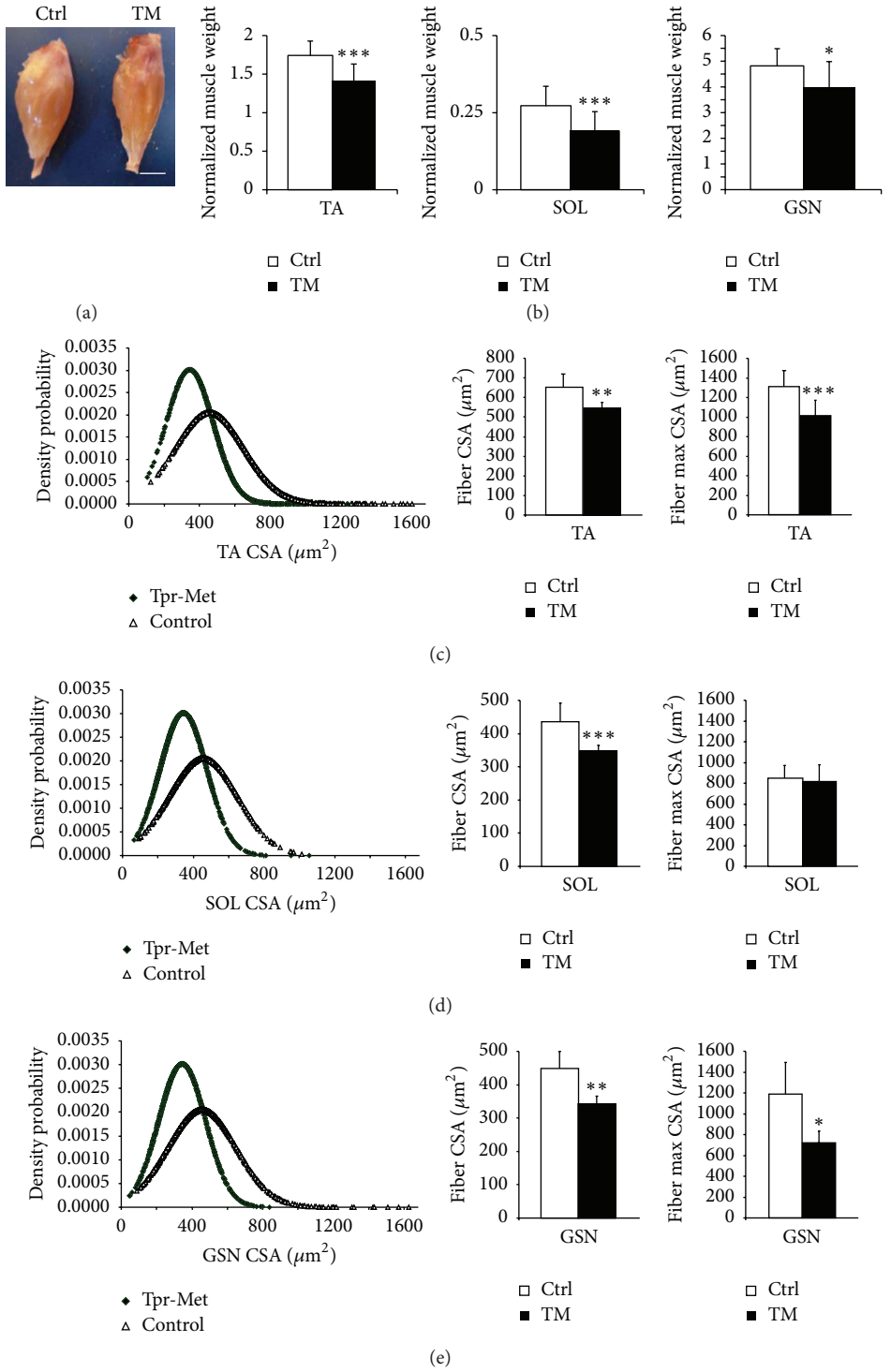

FIGURE 3: At P27, heart failure in Tpr-Met mice is associated with skeletal muscle wasting. Cachectic Tpr-Met mice had significantly reduced skeletal muscle (a) mass and (b) weight with respect to controls (tibialis anterior: TA, soleus: SOL, and gastrocnemius: GSN). A shift towards smaller fibers was recognized in all three muscles ((c)–(e), left graphs). Accordingly, the mean Cross-Sectional Area (CSA) of TA (c), SOL (d), and GSN (e) muscle fibers of Tpr-Met mice was reduced with respect to controls (middle graphs). The maximum value of CSA was also significantly reduced in TA (c) and GSN (e) muscles (right graphs). Consistently, muscles from Tpr-Met mice showed reduced areas and mass. $^{*}p < 0.05$; $^{**}p < 0.01$; $^{***}p < 0.005$.

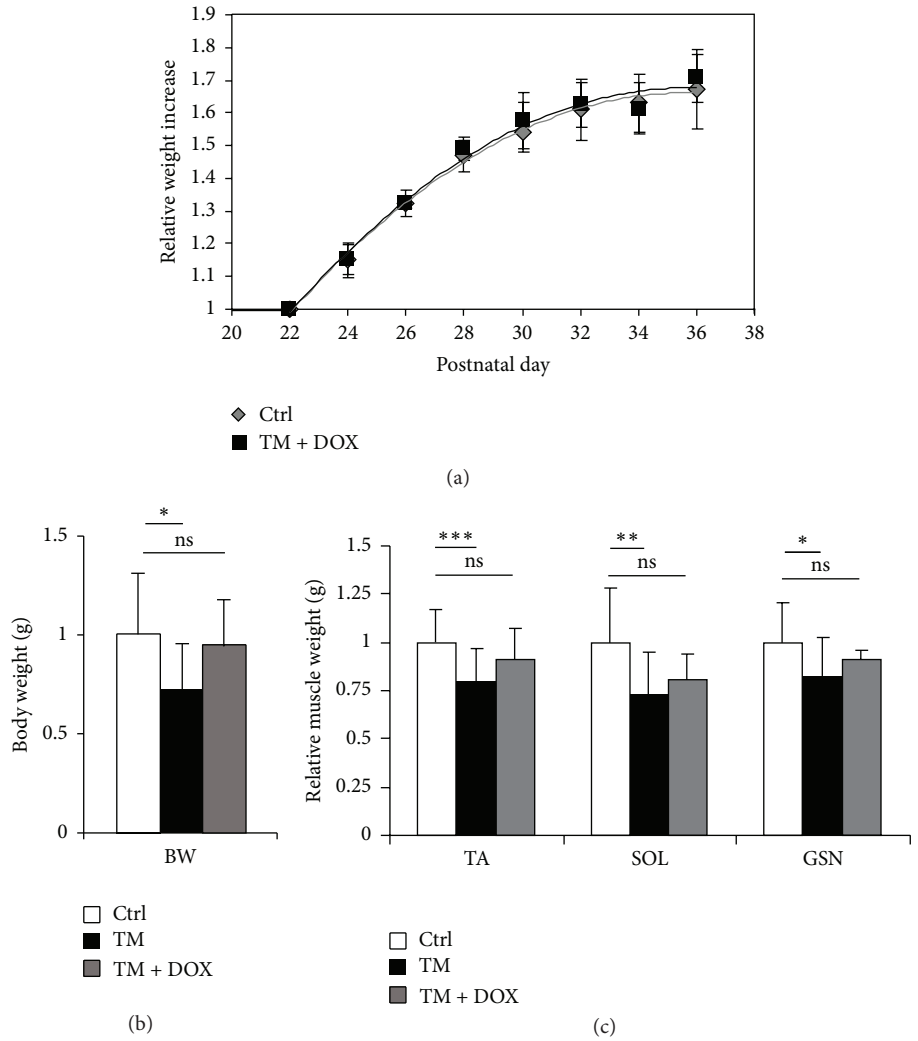

Figure 4: Suppressing Tpr-Met expression at P21 prevents loss of muscular weight at P27. Doxycycline (DOX) was withdrawn from a group of Tpr-Met mice for 21 days in order to activate Tpr-Met signaling; DOX was subsequently restored. The reduction in body weight gain (a) and (b) body weight (BW) was completely rescued when Tpr-Met transgene expression was suppressed by DOX administration (Tpr-Met + DOX) from P21, perfectly overlapping with values from controls for the whole follow-up. (c) When suppressing Tpr-Met expression at P21, the weight of tibialis anterior (TA), soleus (SOL), and gastrocnemius (GSN) muscles was normalized to values overlapping those of controls. $^{*}p < 0.05$; $^{**}p < 0.01$; $^{***}p < 0.005$.

was generated (Figure 6). 120 differentially expressed probes were identified and then reduced to 107 unique genes. Among these, 63 were downregulated and 44 genes were upregulated (Supplementary Tables 1 and 2 in Supplementary Material available online at http://dx.doi.org/10.1155/2016/9549036).

A number of genes were downregulated (Supplementary Table 1), including those controlling energy metabolism: muscle glycogen phosphorylase (Pygm) and phosphofructokinase (Pfkm), pyruvate dehydrogenase kinase 2 (Pdk2), NADH dehydrogenase (ubiquinone) 1 alpha subcomplex 10 (Ndufa10), aldo-keto reductase family 7a5 (Akr7a5), and isocitrate dehydrogenase 3 (NAD+) alpha (Idh3a). Also genes regulating protein synthesis were downregulated: eukaryotic translation initiation factor 2, subunit 3 (Eif2s3y), eukaryotic translation elongation factor 1a2 (Eef1a2), and E2F transcription factor 2 (E2f2) as well as myosin XVIIIa (Myo18a) and heat shock protein 90b1 (Hsp90ab1).

We then performed classification of downregulated genes into functional GO categories (Table 1) and KEGG pathways (Table 2). Among the downregulated GO categories, we found translation factor activity, nucleic acid and nucleotide binding, regulation of metabolic process and phosphate metabolic process, muscle system process, generation of precursor metabolites and energy, and cellular protein metabolic and biosynthetic processes. Among the downregulated KEGG pathways, we found tight and gap junctions, galactose metabolism, metabolic pathways, oxidative phosphorylation, and insulin signaling pathway. Altogether, these

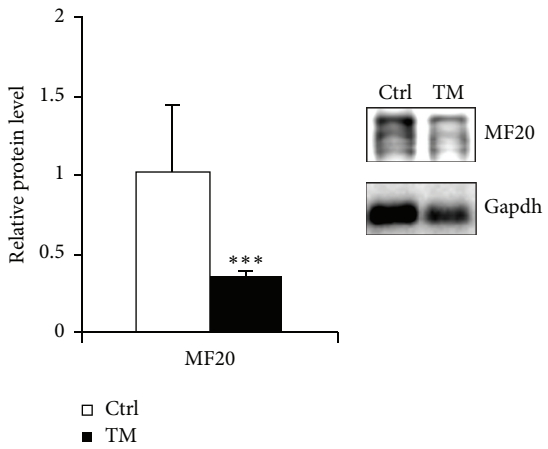

Figure 5: Reduced myosin heavy chain content in gastrocnemius muscle from cachectic Tpr-Met mice. Myosin heavy chain content was quantified in the gastrocnemius muscle (GSN) of cachectic Tpr-Met mice and normalized on Gapdh levels. $^{***}p < 0.005$.

data suggest an alteration in metabolic activities and growth processes.

On the other hand, among the upregulated genes (Supplementary Table 2), we found tumour necrosis factor receptor superfamily 12a (Tnfrsf12a), also known as the Tweak-receptor (TweakR), as well as a number of cytokines and chemokines. Accordingly with data shown in [35], our work suggests the presence of an inflammatory response in the muscle milieu. Indeed, among the upregulated GO categories and KEGG pathways, there were immune and defense response, chemokine activity, and chemokine signaling pathway cytokine-cytokine receptor interaction.

Finally, several genes regulating ion trafficking, homeostasis, and signaling were either upregulated (S100 calcium binding protein A10 (S100a10), gap junction membrane channel protein alpha 1 (Gja1), cytochrome P450, and family 2e1 (Cyp2e1)) or downregulated (ryanodine receptor 1 (Ryr1), cAMP dependent protein kinase alpha (Prkaca), potassium voltage gated channel, Shaw-related subfamily 1 (Kcnc1), calmodulin binding transcription activator 2 (Camta2), and calcium/calmodulin-dependent protein kinase 2b (Camk2b)). Cation transport GO category and calcium signaling pathway, long-term depression, and long-term potentiation KEGG pathways were enriched in the list of downregulated genes. Indeed, disruptions in calcium signaling have been implicated in cytokine-mediated disruptions in skeletal muscle and function, at least in cancer cachexia [36, 37].

By gene expression profiling and bioinformatical analysis, we found that genes and TFs associated with muscle metabolism, growth, and protein synthesis were negatively modulated. Indeed, the overall net catabolic dominance in heart failure provokes systemic tissue wasting [38], and such downregulation may have contributed to the suppression of growth in wasting muscle.

On the other hand, genes associated with inflammation were increased. Indeed, cytokines may play a significant role in the progression of cardiac cachexia since they may directly

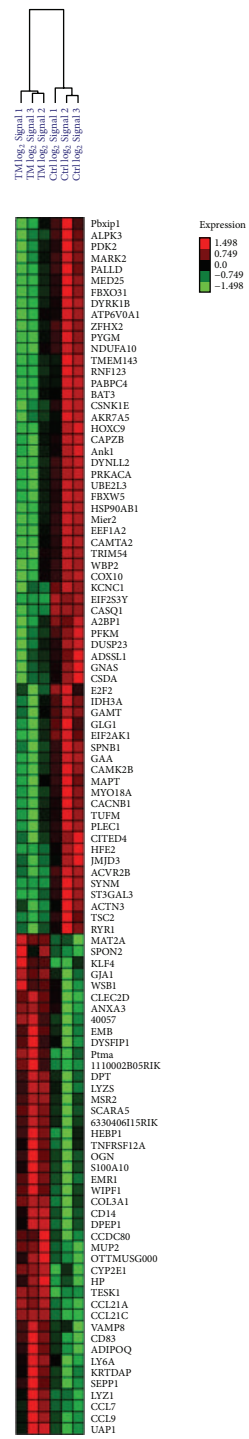

Figure 6: Heat map of the gene expression profiling of wasting gastrocnemius muscle from cachectic Tpr-Met mice. Total RNA from gastrocnemius muscle (GSN) of cachectic Tpr-Met mice was compared to littermate controls. Standardization was applied to Log_2 absolute intensities. A cut-off of $p < 0.05$ and fold change >1.7 was used. Unsupervised hierarchical clustering was performed and the corresponding heat map was generated. 107 unique genes differentially expressed were identified.

affect peripheral skeletal muscle metabolism. A possible underlying pathogenic mechanism for such effect might be

Table 1: Enriched GO molecular function (MF) and biological process (BP) categories in down- and upregulated genes (fold change > 1.7; $p < 0.05$). Only categories significantly associated (p value < 0.05) are considered. The name and number of gene ontology (GO) categories, number of enriched genes, raw and corrected p values, frequency in the gene set, and the corresponding gene list are reported.

GO category	Number of genes	Raw p value	Correct p value	Frequency in set (%)	Gene list
Gene set: downregulated genes					
Translation factor activity, nucleic acid binding, GO:0008135	4	$1.98E-5$	0.008	6.3	*Tufm*, *Eif2ak1*, *Eif2s3y*, and *Eef1a2*
Transferase activity, GO:0016740	15	$7.49E-8$	0.001	24.0	*Pdk2*, *St3gal3*, *Acvr2b*, *Eif2ak1*, *Alpk3*, *Pygm*, *Cox10*, *Csnk1e*, *Dyrk1b*, *Camk2b*, *Gamt*, *Prkaca*, *Pfkm*, *Ndufa10*, and *Mark2*
Regulation of system process, GO:0044057	4	$1.61E-4$	0.04	6.3	*Ryr1*, *Gaa*, *Prkaca*, and *Casq1*
Regulation of multicellular organismal process, GO:0051239	7	$1.65E-4$	0.04	11.0	*Ryr1*, *Gaa*, *Gnas*, *Gamt*, *Prkaca*, *Csda*, and *Casq1*
Regulation of metabolic process, GO:0019222	17	$7.73E-7$	0.002	27.0	*E2f2*, *Camta2*, *Med25*, *Csda*, *Ube2l3*, *Cited4*, *Capzb*, *Acvr2b*, *Hoxc9*, *Eif2ak1*, *Trim54*, *Mapt*, *Tsc2*, *Spnb1*, *Mier2*, *Gnas*, and *Jmjd3*
Regulation of biological quality, GO:0065008	8	$1.88E-4$	0.046	13.0	*Ank1*, *ACVR2B*, *TSC2*, *SPNB1*, *RYR1*, *GAA*, *PFKM*, and *CAPZB*
Porphyrin metabolic process, GO:0006778	4	$1.22E-7$	0.001	6.3	*Ank1*, *EIF2AK1*, *COX10*, and *SPNB1*
Phosphotransferase activity, alcohol group as acceptor, GO:0016773	11	$1.42E-8$	0.001	17.0	*Pdk2*, *Acvr2b*, *Eif2ak1*, *Alpk3*, *Csnk1e*, *Dyrk1b*, *Camk2b*, *Prkaca*, *Pfkm*, *Ndufa10*, and *Mark2*
Phosphate metabolic process, GO:0006796	11	$1.01E-7$	0.001	17.0	*Pdk2*, *Acvr2b*, *Eif2ak1*, *Alpk3*, *Csnk1e*, *Dyrk1b*, *Dusp23*, *Atp6v0a1*, *Camk2b*, *Prkaca*, and *Mark2*
Organ development, GO:0048513	12	$1.0E-5$	0.007	19.0	*Hsp90ab1*, *Ank1*, *Acvr2b*, *Hoxc9*, *Alpk3*, *Dyrk1b*, *Tsc2*, *Gaa*, *Gnas*, *Gamt*, *Prkaca*, and *Csda*
Nucleotide binding, GO:0000166	22	$1.08E-12$	0.001	35.0	*Hsp90ab1*, *Tufm*, *Pdk2*, *Adssl1*, *Eif2s3y*, *Alpk3*, *Eef1a2*, *Pfkm*, *Ndufa10*, *Ube2l3*, *Idh3a*, *Mark2*, *Acvr2b*, *Eif2ak1*, *Pygm*, *Csnk1e*, *Dyrk1b*, *A2bp1*, *Gnas*, *Camk2b*, *Prkaca*, and *Myo18a*
Nitrogen compound metabolic process, GO:0006807	16	$3.13E-5$	0.012	25.0	*E2f2*, *Camta2*, *Adssl1*, *Cox10*, *Med25*, *Csda*, *Ndufa10*, *Cited4*, *Ank1*, *Eif2ak1*, *Hoxc9*, *A2bp1*, *Spnb1*, *Mier2*, *Atp6v0a1*, and *Gamt*
Negative regulation of protein complex disassembly, GO:0043242	4	$2.58E-7$	0.001	6.3	*Trim54*, *Mapt*, *Spnb1*, and *Capzb*
Negative regulation of biological process, GO:0048519	10	$2.38E-5$	0.009	16.0	*Eif2ak1*, *Trim54*, *Mapt*, *Eef1a2*, *Tsc2*, *Spnb1*, *Ryr1*, *Jmjd3*, *Csda*, and *Capzb*
Muscle system process, GO:0003012	4	$3.79E-6$	0.005	6.3	*Camta2*, *Ryr1*, *Gaa*, and *Actn3*
Heterocycle metabolic process, GO:0046483	6	$5.44E-6$	0.006	9.5	*Ank1*, *ADSSL1*, *EIF2AK1*, *COX10*, *SPNB1*, and *ATP6V0A1*
Generation of precursor metabolites and energy, GO:0006091	8	$1.13E-8$	0.001	13.0	*Pygm*, *Cox10*, *Gaa*, *Atp6v0a1*, *Gnas*, *Pfkm*, *Ndufa10*, and *Idh3a*
Cytoskeletal protein binding, GO:0008092	6	$3.77E-5$	0.014	9.5	*Trim54*, *Spnb1*, *Actn3*, *Palld*, *Plec1*, and *Capzb*
Cellular protein metabolic process, GO:0044267	21	$2.52E-12$	0.001	33.0	*Hsp90ab1*, *Tufm*, *Pdk2*, *Eif2s3y*, *Alpk3*, *Cox10*, *Eef1a2*, *Dusp23*, *Ube2l3*, *Mark2*, *Acvr2b*, *Rnfl23*, *St3gal3*, *Eif2ak1*, *Fbxw5*, *Csnk1e*, *Dyrk1b*, *Fbxo31*, *Camk2b*, *Jmjd3*, and *Prkaca*
Cellular macromolecule catabolic process, GO:0044265	7	$7.08E-5$	0.025	11.0	*Rnfl23*, *Pygm*, *Fbxw5*, *Gaa*, *Fbxo31*, *Pfkm*, and *Ube2l3*
Cellular biosynthetic process, GO:0044249	17	$4.59E-6$	0.005	27.0	*Tufm*, *E2f2*, *Camta2*, *Adssl1*, *Eif2s3y*, *Cox10*, *Eef1a2*, *Med25*, *Csda*, *Cited4*, *St3gal3*, *Ank1*, *Hoxc9*, *Spnb1*, *Mier2*, *Atp6v0a1*, and *Gamt*
Cation transport, GO:0006812	6	$1.69E-4$	0.04	9.5	*Kcnc1*, *Ank1*, *Ryr1*, *Cacnb1*, *Atp6v0a1*, and *Camk2b*
Anatomical structure morphogenesis, GO:0009653	9	$5.54E-5$	0.021	14.0	*Acvr2b*, *Hoxc9*, *Cox10*, *Dyrk1b*, *Tsc2*, *Gaa*, *Gnas*, *Gamt*, and *Prkaca*
GTPase activity, GO:0003924	4	$4.34E-5$	0.015	6.3	*Tufm*, *Eif2s3y*, *Eef1a2*, *Gnas*

Table 1: Continued.

GO category	Number of genes	Raw p value	Correct p value	Frequency in set (%)	Gene list
Gene set: upregulated genes					
Response to stimulus, GO:0050896	15	$1.16E-8$	0.001	34.0	*Lyz1, Ccl21c, Ccl21a, Ccl9, Gja1, Adipoq, Ccl7, Lyzs, Cd83, Clec2d, Sepp1, Spon2, Scara5, Cd14,* and *Klf4*
Response to external stimulus, GO:0009605	7	$3.16E-6$	0.003	16.0	*Ccl21c, Ccl21a, Ccl9, Gja1, Klf4, Cd14,* and *Ccl7*
Receptor binding, GO:0005102	8	$5.33E-7$	0.002	18.0	*Ogn, Ccl21c, Ccl21a, Clec2d, Ccl9, Gja1, Adipoq,* and *Ccl7*
Positive regulation of biological process, GO:0048518	8	$9.25E-5$	0.03	18.0	*Cd83, Tnfrsf12a, Ccl21a, Ccdc80, Gja1, Adipoq, Klf4,* and *Cd14*
Locomotion, GO:0040011	6	$3.15E-6$	0.003	14.0	*Tnfrsf12a, Ccl21c, Ccl21a, Ccl9, Gja1,* and *Ccl7*
Immune response, GO:0006955	6	$6.88E-6$	0.007	14.0	*Ccl21c, Ccl21a, Ccl9, Spon2, Cd14,* and *Ccl7*
Defense response, GO:0006952	7	$5.33E-7$	0.002	16.0	*Lyz1, Ccl21c, Ccl21a, Clec2d, Lyzs, Cd14,* and *Ccl7*
Chemokine activity, GO:0008009	4	$1.1E-7$	0.001	9.1	*Ccl21c, Ccl21a, Ccl9,* and *Ccl7*

Table 2: Enriched KEGG pathways in down- and upregulated genes (fold change > 1.7; $p < 0.05$).Only categories significantly associated (p value < 0.05) are considered. Kyoto Encyclopedia of Genes and Genomes (KEGG) pathways, number of enriched genes, p value, enrichment factor, and list of the genes enriched in each pathway are reported.

KEGG pathway	Number of genes	p value	Enrichment factor	Gene list
Gene set: downregulated genes				
Tight junction	2	0.0261	8.0	*Actn3, Csda*
Melanogenesis	3	$8.18E-4$	16.5	*Camk2b, Gnas,* and *Prkaca*
Long-term depression	2	0.00871	14.3	*Ryr1, Gnas*
Arrhythmogenic right ventricular cardiomyopathy (ARVC)	2	0.00789	15.0	*Cacnb1, Actn3*
GnRH signaling pathway	3	$7.52E-4$	17.0	*Camk2b, Gnas,* and *Prkaca*
Prostate cancer	2	0.0119	12.2	*Hsp90ab1, E2f2*
Gap junction	2	0.0119	12.2	*Gnas, Prkaca*
Galactose metabolism	2	0.00103	42.4	*Gaa, Pfkm*
Glioma	2	0.00692	16.1	*E2f2, Camk2b*
Dilated cardiomyopathy	3	$5.91E-4$	18.4	*Cacnb1, Gnas,* and *Prkaca*
Metabolic pathways	9	$2.11E-4$	4.34	*Adssl1, St3gal3, Cox10, Gaa, Atp6v0a1, Gamt, Pfkm, Ndufa10,* and *Idh3a*
Oxidative phosphorylation	3	0.00266	10.9	*Cox10, Atp6v0a1,* and *Ndufa10*
Calcium signaling pathway	4	$3.64E-4$	11.9	*Ryr1, Camk2b, Gnas,* and *Prkaca*
Insulin signaling pathway	3	0.00196	12.2	*Pygm, Tsc2,* and *Prkaca*
Lysosome	2	0.0185	9.61	*Gaa, Atp6v0a1*
Taste transduction	2	0.00499	19.1	*Gnas, Prkaca*
Progesterone-mediated oocyte maturation	2	0.0157	10.5	*Hsp90ab1, Prkaca*
Parkinson's disease	2	0.0343	6.89	*Ube2l3, Ndufa10*
Long-term potentiation	2	0.00809	14.9	*Camk2b, Prkaca*
Hedgehog signaling pathway	2	0.00421	20.8	*Csnk1e, Prkaca*
Wnt signaling pathway	3	0.00276	10.8	*Csnk1e, Camk2b,* and *Prkaca*
Vascular smooth muscle contraction	2	0.0212	8.94	*Gnas, Prkaca*
MAPK signaling pathway	3	0.0132	6.11	*Mapt, Cacnb1,* and *Prkaca*
Starch and sucrose metabolism	2	0.00284	25.4	*Pygm, Gaa*
Gene set: upregulated genes				
Chemokine signaling pathway	4	$1.09E-4$	16.2	*Ccl21c, Ccl21a, Ccl9,* and *Ccl7*
Cytokine-cytokine receptor interaction	5	$1.43E-5$	16.2	*Tnfrsf12a, Ccl21c, Ccl21a, Ccl9,* and *Ccl7*

found in enhanced activation of the transcription factor NF-κB [39]. In fact, chronic activation of this TF results in skeletal muscle wasting resembling clinical cachexia [40]. Increased expression of proinflammatory cytokines in the skeletal muscle has been demonstrated in cancer [37] and chronic heart failure [35, 41]. Notably, circulating cytokine levels do not correctly reflect tissue levels [35].

4. Conclusions

Only a few animal models which replicate the clinical findings of cardiac cachexia have been generated [10]. However, some of these mainly rely on surgical techniques [9]; following these procedures, an increase in resources is required, due to delay in cachexia onset and to the costs due to surgery itself. Moreover, technical issues are still important in limiting the preciseness and reproducibility of heart failure models. This criticism has been overcome by means of transgenic mice and Dahl salt-sensitive rats models. In the present study, we propose a new animal model for research on cardiac cachexia, characterized by high reproducibility and very fast timing.

Some pharmacological treatments for cardiac cachexia have been suggested [42]. Notably, using short-term models of cardiac cachexia could be the best choice for testing the efficacy of a wide range of compounds, from those which have already passed early tests for the development of tolerance to the treatment to new innovative drugs. Notably, in experimental animals, weight loss has been reversed by

neutralisation of tumour-produced Gdf15 with a monoclonal antibody [30], encouraging further research to provide a new effective therapy to patients suffering from cardiac cachexia.

Competing Interests

The authors declare that they have no conflict of interests.

Authors' Contributions

Project conception, study design, and paper writing were done by Valentina Sala and Tiziana Crepaldi. Biochemical/histological experiments and data analysis were done by Valentina Sala, Stefano Gatti, and Simona Gallo. Echocardiography was carried out by Valentina Sala, Stefano Gatti, Simona Gallo, and James Cimino. Illumina array and bioinformatics analysis were carried out by Enzo Medico, Daniela Cantarella, and Valentina Sala. Supervision and paper preparation were done by Antonio Ponzetto and Tiziana Crepaldi. Stefano Gatti and Simona Gallo contributed equally to the work.

Acknowledgments

The authors gratefully acknowledge Marcello Raspa for transgenic mice repository service. This work was granted by Association Francaise contre les Myopathies (AFM) nos. 14901 and 15816 to Tiziana Crepaldi. Fellowship to VS was provided by FP7-2010-ICT-GC Project no. 265772.

References

[1] W. J. Evans, J. E. Morley, J. Argilés et al., "Cachexia: a new definition," *Clinical Nutrition*, vol. 27, no. 6, pp. 793–799, 2008.

[2] S. D. Anker, P. Ponikowski, S. Varney et al., "Wasting as independent risk factor for mortality in chronic heart failure," *The Lancet*, vol. 349, no. 9058, pp. 1050–1053, 1997.

[3] S. von Haehling, M. Lainscak, J. Springer, and S. D. Anker, "Cardiac cachexia: a systematic overview," *Pharmacology and Therapeutics*, vol. 121, no. 3, pp. 227–252, 2009.

[4] S. von Haehling, R. Stepney, and S. D. Anker, "Advances in understanding and treating cardiac cachexia: highlights from the 5th Cachexia Conference," *International Journal of Cardiology*, vol. 144, no. 3, pp. 347–349, 2010.

[5] S. D. Anker, T. P. Chua, P. Ponikowski et al., "Hormonal changes and catabolic/anabolic imbalance in chronic heart failure and their importance for cardiac cachexia," *Circulation*, vol. 96, no. 2, pp. 526–534, 1997.

[6] S. D. Anker, P. P. Ponikowski, A. L. Clark et al., "Cytokines and neurohormones relating to body composition alterations in the wasting syndrome of chronic heart failure," *European Heart Journal*, vol. 20, no. 9, pp. 683–693, 1999.

[7] D. C. McMillan, T. Preston, W. S. Watson et al., "Relationship between weight loss, reduction of body cell mass and inflammatory response in patients with cancer," *British Journal of Surgery*, vol. 81, no. 7, pp. 1011–1014, 1994.

[8] J. Farkas, S. von Haehling, K. Kalantar-Zadeh, J. E. Morley, S. D. Anker, and M. Lainscak, "Cachexia as a major public health problem: frequent, costly, and deadly," *Journal of Cachexia, Sarcopenia and Muscle*, vol. 4, no. 3, pp. 173–178, 2013.

[9] M. D. Deboer, "Animal models of anorexia and cachexia," *Expert Opinion on Drug Discovery*, vol. 4, no. 11, pp. 1145–1155, 2009.

[10] M. Konishi, N. Ebner, S. Von Haehling, S. D. Anker, and J. Springer, "Developing models for cachexia and their implications in drug discovery," *Expert Opinion on Drug Discovery*, vol. 10, no. 7, pp. 743–752, 2015.

[11] P. Li, R. E. Waters, S. I. Redfern et al., "Oxidative phenotype protects myofibers from pathological insults induced by chronic heart failure in mice," *The American Journal of Pathology*, vol. 170, no. 2, pp. 599–608, 2007.

[12] T. Kato, S. Niizuma, Y. Inuzuka et al., "Analysis of liver metabolism in a rat model of heart failure," *International Journal of Cardiology*, vol. 161, no. 3, pp. 130–136, 2012.

[13] C. Birchmeier, W. Birchmeier, E. Gherardi, and G. F. Vande Woude, "Met, metastasis, motility and more," *Nature Reviews Molecular Cell Biology*, vol. 4, no. 12, pp. 915–925, 2003.

[14] C. Leo, V. Sala, M. Morello et al., "Activated met signalling in the developing mouse heart leads to cardiac disease," *PLoS ONE*, vol. 6, no. 2, Article ID e14675, 2011.

[15] P. Peschard and M. Park, "From Tpr-Met to Met, tumorigenesis and tubes," *Oncogene*, vol. 26, no. 9, pp. 1276–1285, 2007.

[16] T. Crepaldi, F. Bersani, C. Scuoppo et al., "Conditional activation of MET in differentiated skeletal muscle induces atrophy," *The Journal of Biological Chemistry*, vol. 282, no. 9, pp. 6812–6822, 2007.

[17] S. Gatti, C. Leo, S. Gallo et al., "Gene expression profiling of HGF/Met activation in neonatal mouse heart," *Transgenic Research*, vol. 22, no. 3, pp. 579–593, 2013.

[18] F. Vinchi, L. De Franceschi, A. Ghigo et al., "Hemopexin therapy improves cardiovascular function by preventing heme-induced endothelial toxicity in mouse models of hemolytic diseases," *Circulation*, vol. 127, no. 12, pp. 1317–1329, 2013.

[19] I. Ulitsky, A. Maron-Katz, S. Shavit et al., "Expander: from expression microarrays to networks and functions," *Nature Protocols*, vol. 5, no. 2, pp. 303–322, 2010.

[20] M. Gossen and H. Bujard, "Tight control of gene expression in mammalian cells by tetracycline-responsive promoters," *Proceedings of the National Academy of Sciences of the United States of America*, vol. 89, no. 12, pp. 5547–5551, 1992.

[21] K. J. Harjai, "Potential new cardiovascular risk factors: left ventricular hypertrophy, homocysteine, lipoprotein(a), triglycerides, oxidative stress, and fibrinogen," *Annals of Internal Medicine*, vol. 131, no. 5, pp. 376–386, 1999.

[22] A. M. Shah, "Ventricular remodeling in heart failure with preserved ejection fraction," *Current Heart Failure Reports*, vol. 10, no. 4, pp. 341–349, 2013.

[23] M. Shimano, N. Ouchi, and K. Walsh, "Cardiokines: recent progress in elucidating the cardiac secretome," *Circulation*, vol. 126, no. 21, pp. e327–e332, 2012.

[24] R. Adela and S. K. Banerjee, "GDF-15 as a target and biomarker for diabetes and cardiovascular diseases: a translational prospective," *Journal of Diabetes Research*, vol. 2015, Article ID 490842, 14 pages, 2015.

[25] J. M. Cheng, K. M. Akkerhuis, L. C. Battes et al., "Biomarkers of heart failure with normal ejection fraction: a systematic review," *European Journal of Heart Failure*, vol. 15, no. 12, pp. 1350–1362, 2013.

[26] I. S. Anand, T. Kempf, T. S. Rector et al., "Serial measurement of growth-differentiation factor-15 in heart failure: relation to disease severity and prognosis in the valsartan heart failure trial," *Circulation*, vol. 122, no. 14, pp. 1387–1395, 2010.

[27] R. Santhanakrishnan, J. P. Chong, T. P. Ng, L. H. Ling, D. Sim, K. T. Leong et al., "Growth differentiation factor 15, ST2, high-sensitivity troponin T, and N-terminal pro brain natriuretic peptide in heart failure with preserved vs. Reduced ejection fraction," *European Journal of Heart Failure*, vol. 14, no. 12, pp. 1338–1347, 2012.

[28] J. Xu, T. R. Kimball, J. N. Lorenz et al., "GDF15/MIC-1 functions as a protective and antihypertrophic factor released from the myocardium in association with SMAD protein activation," *Circulation Research*, vol. 98, no. 3, pp. 342–350, 2006.

[29] S. Q. Khan, K. Ng, O. Dhillon et al., "Growth differentiation factor-15 as a prognostic marker in patients with acute myocardial infarction," *European Heart Journal*, vol. 30, no. 9, pp. 1057–1065, 2009.

[30] V. W. W. Tsai, Y. Husaini, R. Manandhar et al., "Anorexia/cachexia of chronic diseases: a role for the TGF-β family cytokine MIC-1/GDF15," *Journal of Cachexia, Sarcopenia and Muscle*, vol. 3, no. 4, pp. 239–243, 2012.

[31] J. B. Welsh, L. M. Sapinoso, S. G. Kern et al., "Large-scale delineation of secreted protein biomarkers overexpressed in cancer tissue and serum," *Proceedings of the National Academy of Sciences of the United States of America*, vol. 100, no. 6, pp. 3410–3415, 2003.

[32] H. Johnen, S. Lin, T. Kuffner et al., "Tumor-induced anorexia and weight loss are mediated by the TGF-β superfamily cytokine MIC-1," *Nature Medicine*, vol. 13, no. 11, pp. 1333–1340, 2007.

[33] S. D. Anker and A. J. S. Coats, "Cardiac cachexia: a syndrome with impaired survival and immune and neuroendocrine activation," *Chest*, vol. 115, no. 3, pp. 836–847, 1999.

[34] V. Sala, S. Gallo, S. Gatti et al., "Cardiac concentric hypertrophy promoted by activated Met receptor is mitigated in vivo by inhibition of Erk1,2 signalling with Pimasertib," *Journal of Molecular and Cellular Cardiology*, vol. 93, pp. 84–97, 2016.

[35] P. C. Schulze, S. Gielen, V. Adams et al., "Muscular levels of proinflammatory cytokines correlate with a reduced expression of insulin-like growth factor-I in chronic heart failure," *Basic Research in Cardiology*, vol. 98, no. 4, pp. 267–274, 2003.

[36] S. T. Isaac, T. C. Tan, and P. Polly, "Endoplasmic reticulum stress, calcium dysregulation and altered protein translation: intersection of processes that contribute to cancer cachexia induced skeletal muscle wasting," *Current Drug Targets*, 2015.

[37] P. Costelli, R. D. Tullio, F. M. Baccino, and E. Melloni, "Activation of Ca^{2+}-dependent proteolysis in skeletal muscle and heart in cancer cachexia," *British Journal of Cancer*, vol. 84, no. 7, pp. 946–950, 2001.

[38] W. Doehner, M. Frenneaux, and S. D. Anker, "Metabolic impairment in heart failure: the myocardial and systemic perspective," *Journal of the American College of Cardiology*, vol. 64, no. 13, pp. 1388–1400, 2014.

[39] V. Adams, U. Späte, N. Kränkel et al., "Nuclear factor-kappa B activation in skeletal muscle of patients with chronic heart failure: correlation with the expression of inducible nitric oxide synthase," *European Journal of Cardiovascular Prevention and Rehabilitation*, vol. 10, no. 4, pp. 273–277, 2003.

[40] D. Cai, J. D. Frantz, N. E. Tawa Jr. et al., "IKKβ/NF-κB activation causes severe muscle wasting in mice," *Cell*, vol. 119, no. 2, pp. 285–298, 2004.

[41] P. C. Schulze, S. Gielen, G. Schuler, and R. Hambrecht, "Chronic heart failure and skeletal muscle catabolism: effects of exercise training," *International Journal of Cardiology*, vol. 85, no. 1, pp. 141–149, 2002.

[42] T. Martins, R. Vitorino, D. Moreira-Gonçalves, F. Amado, J. A. Duarte, and R. Ferreira, "Recent insights on the molecular mechanisms and therapeutic approaches for cardiac cachexia," *Clinical Biochemistry*, vol. 47, no. 1-2, pp. 8–15, 2014.

Hindawi Publishing Corporation
BioMed Research International
Volume 2016, Article ID 4874809, 11 pages
http://dx.doi.org/10.1155/2016/4874809

Research Article

Vitamin A Inhibits Development of Dextran Sulfate Sodium-Induced Colitis and Colon Cancer in a Mouse Model

Isao Okayasu,[1] Kiyomi Hana,[1] Noriko Nemoto,[2] Tsutomu Yoshida,[1] Makoto Saegusa,[1] Aya Yokota-Nakatsuma,[3] Si-Young Song,[4] and Makoto Iwata[3]

[1]*Department of Pathology, School of Medicine, Kitasato University, Sagamihara, Kanagawa 252-0374, Japan*
[2]*Research Center for Biological Imaging, School of Medicine, Kitasato University, Sagamihara, Kanagawa 252-0374, Japan*
[3]*Laboratory of Immunology, Kagawa School of Pharmaceutical Sciences, Tokushima Bunri University, Sanuki, Kagawa 769-2193, Japan*
[4]*Institute of Neuroscience, Kagawa School of Pharmaceutical Sciences, Tokushima Bunri University, Sanuki, Kagawa 769-2193, Japan*

Correspondence should be addressed to Isao Okayasu; isaokaya@gmail.com

Received 25 January 2016; Revised 30 March 2016; Accepted 12 April 2016

Academic Editor: Andrea Vecchione

Vitamin A is essential to mucosal immunity and cell differentiation. The fact that lack of it might involve chronic inflammation and increased risk of cancer has been reported. Little is known about the mechanism of vitamin A deficiency in the development of colitis and its influence on development of colorectal cancer. To determine the influence of vitamin A deficiency on colitis and colorectal cancer development, an experimental study using a colitis mouse model was performed. Dextran sulfate sodium (DSS) colitis was induced in vitamin A-deficient and vitamin A-supplemented mice. Further, colorectal carcinoma was induced by a combination of azoxymethane preinjection and DSS colitis. Results were compared between the two groups mainly by immunohistochemical analysis. Colitis was more severe and recovery from colitis was slower in vitamin A-deficient mice than in vitamin A-supplemented mice. Compared with vitamin A-supplemented mice, vitamin A-deficient mice had decreases in colonic subepithelial myofibroblasts and the ratio of mucosal IgA^+/IgG^+ cells, increases in $CD11c^+$ dendritic cells, and a higher rate of development of colorectal carcinoma with colitis following azoxymethane. Vitamin A lipid droplets in subepithelial myofibroblasts were decreased in vitamin A-deficient mice, suggesting alterations in colonic crypt niche function. Thus, vitamin A inhibited colitis and the development of colorectal cancer.

1. Introduction

The influence of vitamin A and its deficiency on mucosal immunity and cell differentiation has been widely explored and lack of it has been reported to involve chronic inflammation and increased risk of cancer. Through a retrospective chart review it was revealed that deficiencies of vitamins D and A and zinc were relatively common in children and young adults with newly developed inflammatory bowel diseases [1]. Also, low levels of serum vitamins A and E were shown in children and young adults with active inflammatory bowel disease [2].

Further, vitamin A deficiency enhanced the T-helper type 1 (Th1) response and elevated levels of proinflammatory cytokines in obese individuals, suggesting an increased inflammatory response [3]. In rats with vitamin A deficiency downregulation of Retinoic Acid Receptor- (RAR-) α mRNA, increased dendritic cells, and increased protein secretion of IL-12 in the intestinal mucosa were shown. Inversely, supplemental vitamin A in an in vitro culture system of Peyer's patches promoted maturation of dendritic cells and upregulation of RAR-α mRNA, suggesting the possibility of a reduction in intestinal inflammation [4]. Kang et al. reported that a high vitamin A level induced a $CCR9^+$ $\alpha 4\beta 7^+$ $FoxP3^+$ T cell subset, suppressive of intestinal inflammation in SAMP1/YP mice, which had the characteristic of developing spontaneous transmural ileitis like Crohn's disease [5]. These findings suggest that vitamin A is important in maintaining appropriate mucosal immunity and in regulating intestinal inflammation. Considering the above findings, there may be an association of vitamin A levels with intestinal inflammation.

Retinoids, vitamin A metabolites, are essential for epithelial differentiation and control of epithelial and mesenchymal interaction through *Ret* expression [6]. Concerning carcinogenesis, retinoids are effective in chemoprevention and differentiation therapy for cancers of various organs [7]. Further, an association of vitamin A deficiency with cervical intraepithelial neoplasia in HIV-infected women was reported [8] as was chemically induced nephroblastoma in rats [9]. CYP26A1, the gene encoding the cytochrome P450 enzyme which is a major retinoic acid-catabolic enzyme, was highly expressed in cancers of various organs [10–13]. Decreased intracellular retinoic acid or a deficiency due to high CYP26A1 expression induced cells into highly proliferative and invasive states [13] and promoted significant resistance to apoptosis, possibly contributing to the carcinogenic process [14]. These findings may indicate that vitamin A deficiency promotes carcinogenesis [15]. Regarding nutrition, inverse associations were shown between the risk of colon cancer and the use of multivitamin and calcium supplements, although direct associations between colon cancer risk and supplemental vitamin A and vitamin C were inconsistent [16].

Previously we revealed that subepithelial myofibroblasts corresponded to colonic stellate cells containing vitamin A lipid droplets, which are thought to play an important role in the maintenance of the niche function of colonic stem cells [17–20]. For this report, we examined whether vitamin A inhibits intestinal inflammation and the development of inflammation-associated colon cancer using our previously developed DSS colitis mouse model [21, 22].

2. Materials and Methods

2.1. Mice. BALB/c mice were purchased from CLEA Japan (Tokyo, Japan) and maintained under specific pathogen-free conditions in our animal center. Vitamin A-deficient and vitamin A-supplemented BALB/c female mice were produced according to a previously described method [23, 24]. Briefly, mice were bred, and gravid females received either a chemically defined diet that lacked vitamin A (modified AIN-93M feed, Oriental Yeast, Tokyo, Japan) or a vitamin A-supplemented control diet containing retinyl acetate (5,000 IU/kg in the modified AIN-93M feed). This concentration is appropriate as a supplement considering the natural oxidative degradation of vitamin A [24, 25]. These diets were started before gestation. The mouse pups were weaned at 4 weeks of age and maintained on the same diet until the experiment finished.

2.2. Induction and Assessment of Colitis. Colitis was induced with administration of synthetic dextran sulfate sodium (DSS, mol wt 54,000, Ensuikou Sugar Refining Co., Ltd., Chuo-ku, Tokyo, Japan), a procedure that we originally developed [21]. Briefly, mice were divided into two groups, vitamin A-deficient and vitamin A-supplemented groups, and given distilled drinking water containing 0% or 1% (wt/vol) DSS ad libitum under the regimen established for the experiment. After drinking 0% or 1% DSS for 7 or 12 days, mice were killed. The removed colon was put on thick qualitative filter paper, exposed inside out by cutting longitudinally, and fixed in 10% formalin solution. Longitude of each colon was measured. Histological examinations were performed with H&E staining of paraffin sections of the longitudinal sections of the colons [21]. Total colon was equally divided into three segments, the proximal, middle, and distal segments, to assess the distribution of colitis. Severity of colitis at each part was graded on a scale from 0 to 3 and expressed as the pathological index according to the standard scoring system: 0, normal; 1, focal inflammatory cell infiltration including polymorphonuclear leukocytes; 2, inflammatory cell infiltration with gland dropout and/or crypt abscess; and 3, mucosal ulceration. The sum of each colitis score at three segments was shown as total colitis score.

2.3. Induction of Colonic Tumors. For induction of colonic tumors, mice were administered an intraperitoneal injection of azoxymethane (7.4 mg/kg, Sigma-Aldrich Corp., St. Louis, MO, USA), which was followed beginning two weeks later by administration of 1% DSS for 7 days. After drinking distilled water for 3 weeks, the mice were killed. All polypoid or flat elevated lesions that developed were histopathologically counted by observation of a longitudinal paraffin section with H&E staining [22].

2.4. Electron Microscopic Examination. For electron microscopic observation, the colonic wall was fixed by 2.5% (vol/vol) glutaraldehyde in a solution of phosphate buffer (pH 7.2) and by 2% (wt/vol) osmium tetroxide in a similar phosphate buffer solution (pH 7.2). After Epon embedding, ultrathin sections were stained with uranyl acetate and lead citrate followed by electron microscopic examination.

2.5. Immunohistochemical Analysis. Immunohistochemical staining was performed as shown in Table 1. Frozen sections of colonic mucosa after 2% paraformaldehyde fixation were supplied for examination of $CD11c^+$ dendritic cells. Formalin-fixed paraffin sections were used for analysis of α-SMA^+, IgM^+, IgG^+, and IgA^+ cells. Sections were incubated with the primary antibodies at the given dilution overnight at 4°C. 3,3′-Diaminobenzidine was applied as the final chromogen, and nuclei were counterstained with methyl green solution to facilitate histopathological assessment.

2.6. Statistical Analysis. Results are summarized as means ± standard deviation (SD). Data were statistically analyzed by the Mann-Whitney U test and Chi-squared test using Stat View ver. 5.0 for Windows (SAS Institute Inc., Cary, NC, USA). All p values < 0.05 were considered statistically significant.

3. Results

3.1. Modifications of Intestinal Homeostasis in Vitamin A-Deficient Mice

3.1.1. Decrease in Lipid Droplets in Subepithelial Myofibroblasts in Vitamin A-Deficient Mice. Lipid droplets identified by electron microscopy in subepithelial myofibroblasts that were

Table 1: Antibodies and immunohistochemical examination.

Antibody	Clone	Source	Fixation	Dilution	Antigen retrieval	2nd step and colorization	Interpretation
CD11c	Hamster anti-mouse CD11c	BD Pharmingen 550283	2% paraformaldehyde, frozen sections	×10	Not applied	Streptavidin Biotin/HRP kit (Jackson ImmunoResearch, West Grove, PA)	Dendritic cells
α-SMA	Monoclonal mouse anti-α-SMA	DAKO M851 (DakoCytomation, Glostrup, Denmark)	10% buffered formalin, paraffin sections	×1000	Not applied	Histofine mouse staining kit (Nichirei, Tokyo, Japan)	Smooth muscle actin
IgM	Goat polyclonal	Abcam ab98673 (Abcam, Cambridge, MA)	10% buffered formalin, paraffin sections	×500	Microwave 5 min × 3 times	Streptavidin Biotin/HRP kit (Jackson ImmunoResearch)	IgM^+ lymphocytes
IgG	Goat polyclonal	Abcam ab98802 (Abcam, Cambridge, MA)	10% buffered formalin, paraffin sections	×500	Microwave 5 min × 3 times	Streptavidin Biotin/HRP kit (Jackson ImmunoResearch)	IgG^+ lymphocytes
IgA	Goat polyclonal	Abcam ab97233 (Abcam, Cambridge, MA)	10% buffered formalin, paraffin sections	×500	Microwave 5 min × 3 times	Streptavidin Biotin/HRP kit (Jackson ImmunoResearch)	IgA^+ lymphocytes

α-SMA: α-smooth muscle antigen.

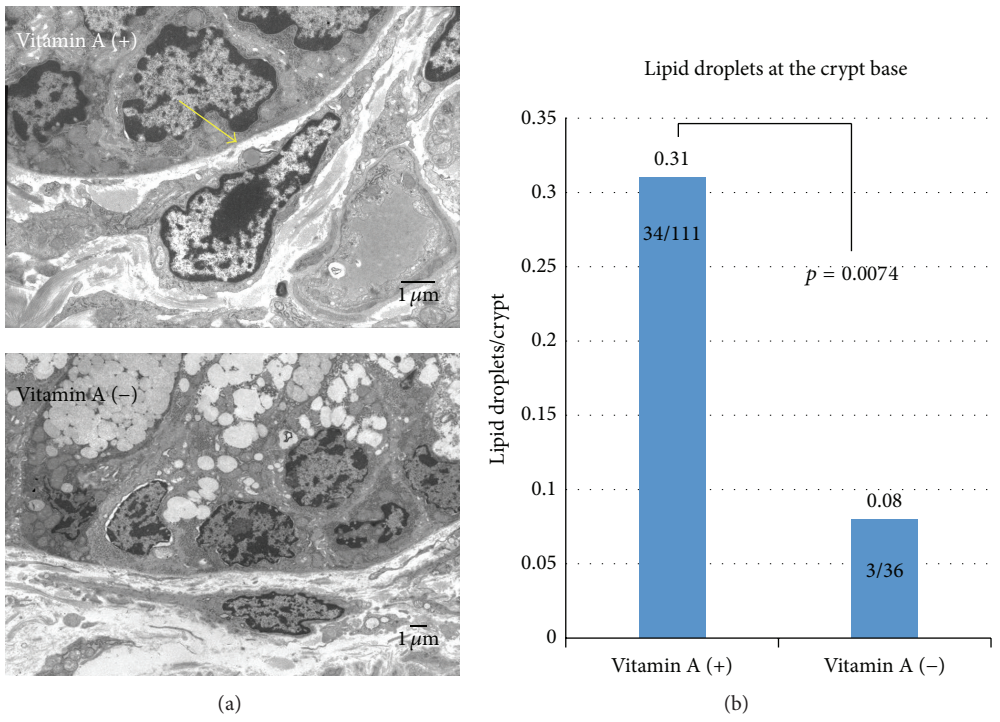

Figure 1: (a) Intracellular lipid droplets in mucosal subepithelial myofibroblasts of the distal segment of the colon. No lipid droplets were observed in a subepithelial myofibroblast from the colonic crypt base of a vitamin A-deficient mouse (upper) in contrast to detection of lipid droplets (arrow) in that of a vitamin A-supplemented mouse (lower) as assessed by electron microscopy. (b) Significant difference of intracellular lipid droplets in mucosal subepithelial myofibroblasts at the crypt base between two groups (Chi-squared test).

located in crypt bases were significantly decreased ($p = 0.0074$) in vitamin A-deficient mice (3 lipid droplets/36 crypts, 8.3%) compared to vitamin A-supplemented mice (34/111, 30.1%) (Figure 1). Representative figures of stellate cell in the liver were shown in a vitamin A-supplemented mouse and a vitamin A-deficient mouse for the reference (see Supplementary Figure 1 in Supplementary Material available online at http://dx.doi.org/10.1155/2016/4874809).

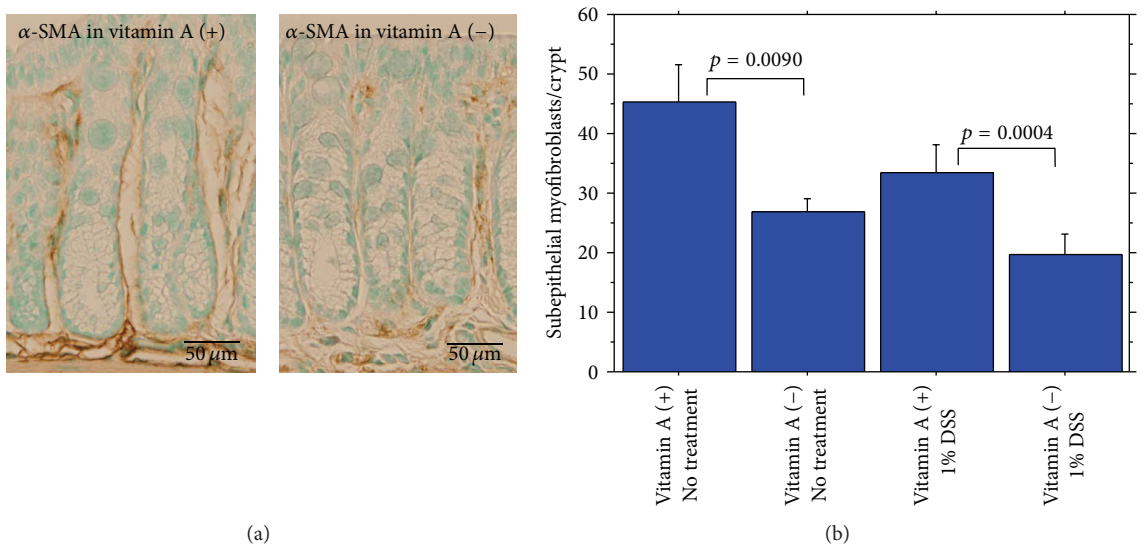

Figure 2: (a) Immunohistochemical α-smooth muscle actin (α-SMA)$^+$ subepithelial myofibroblasts (brown) in the colonic mucosa (left, vitamin A-supplemented mouse, and right, vitamin A-deficient mouse). (b) Summary of α-SMA$^+$ subepithelial myofibroblasts in the colonic mucosa.

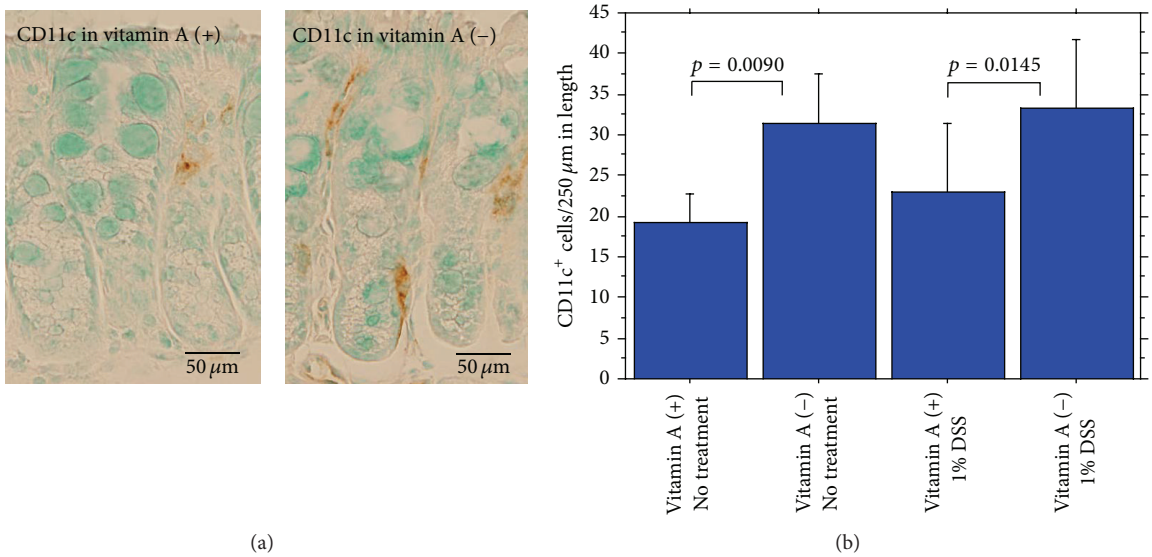

Figure 3: (a) Immunohistochemical CD11c$^+$ dendritic cells (brown) in the colonic mucosa (left, vitamin A-supplemented mouse, and right, vitamin A-deficient mouse). (b) Summary of CD11c$^+$ dendritic cells in the colonic mucosa.

3.1.2. Increase in CD11c$^+$ Dendritic Cells and Decrease in Subepithelial Myofibroblasts and Ratio of Mucosal IgA$^+$/IgG$^+$ Cells in Vitamin A-Deficient Mice. α-smooth muscle actin-positive (α-SMA$^+$) subepithelial myofibroblasts were significantly decreased (Figure 2). On the contrary, CD11c-immunoreactive dendritic cells (CD11c$^+$ cells/250 μm of colonic length) in colonic mucosa were significantly increased in vitamin A-deficient mice compared with vitamin A-supplemented mice (Figure 3). The ratio of IgA$^+$ cells (/250 μm of colonic length)/IgG$^+$ cells (/250 μm of colonic length) in mucosa of the proximal segment was significantly lower in vitamin A-deficient mice than in vitamin A-supplemented mice but not significantly lower in mucosa of the distal segment (Figure 4). IgA$^+$ cells were rather less in vitamin A-deficient mice, compared to vitamin A-supplemented mice in both proximal and distal segments, the difference being not significant.

3.2. Acceleration of Acute Colitis in Vitamin A-Deficient Mice. Acute colitis induced by oral intake of 1% DSS for 7 days was significantly more severe in vitamin A-deficient mice than in vitamin A-supplemented mice as assessed by shortening of colon length and the colitis score (Figure 5) (Supplementary Table 1a).

Colons of vitamin A-deficient mice were shown histologically to have undergone shortening, mild dilatation due

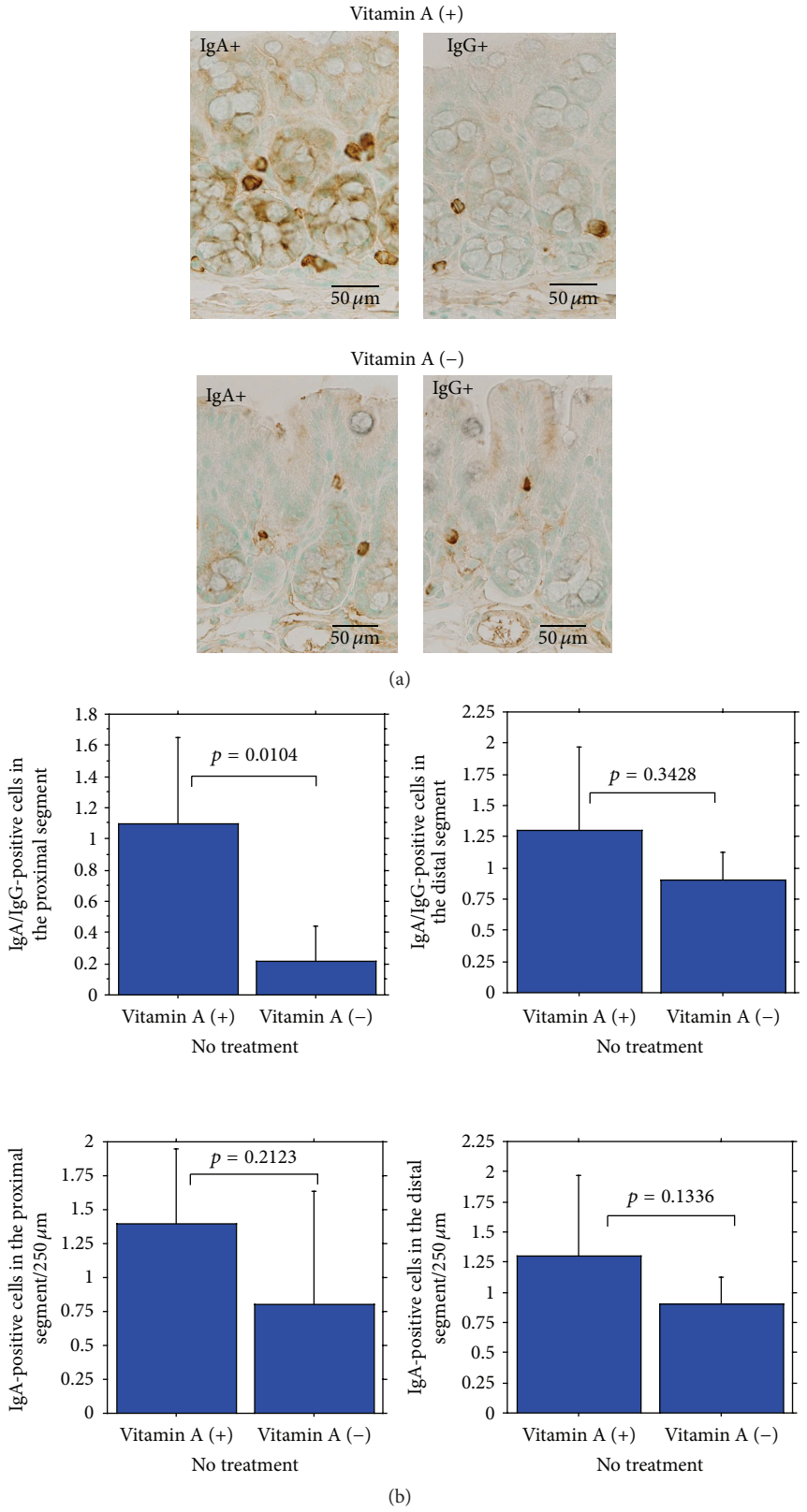

FIGURE 4: (a) Immunohistochemical IgA^+ or IgG^+ cells (brown) in the colonic mucosa (upper, vitamin A-supplemented mouse, and lower, vitamin A-deficient mouse). (b) Summary of the ratio of IgA^+/IgG^+ cells in the mucosa of the proximal (upper left) and distal segments (upper right) and IgA^+ cells in the mucosa of the proximal (lower left) and distal (lower right) segments.

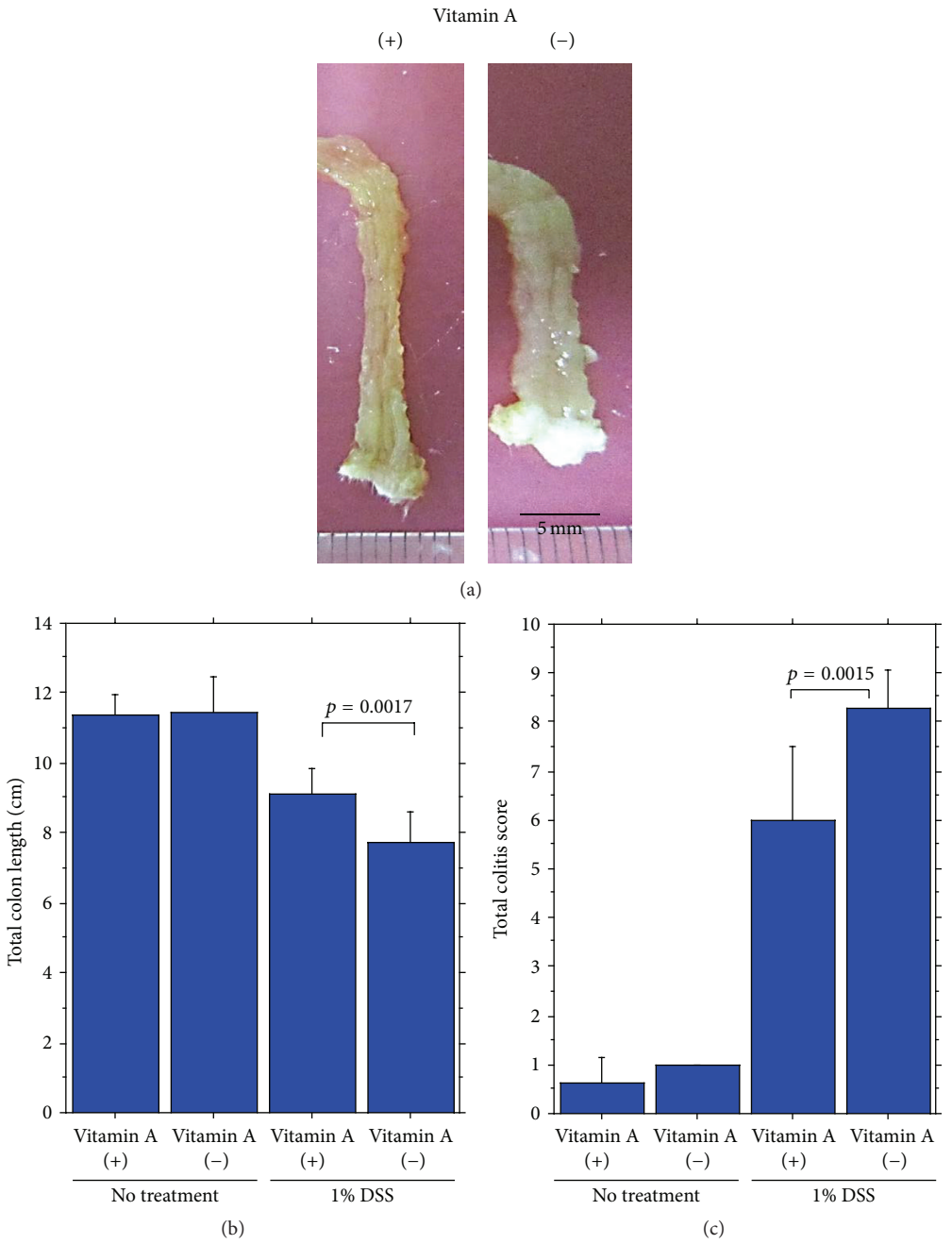

Figure 5: (a) Gross appearance of acute DSS colitis of the distal segment of the colon in vitamin A-supplemented mice (left) and vitamin A-deficient mice (right). In the latter there were shortening and dilatation of the colon. Colitis was induced with intake of 1% DSS for 7 days. Significant difference of (b) total colon length and (c) total colitis score between vitamin A-supplemented mice and vitamin A-deficient mice.

to inflammation, gross and inflammatory granulation, and erosion (Figure 6) (Supplementary Figure 2). Differences in the degree of acute colitis induced by intake of 1% DSS for 12 days between vitamin A-deficient and vitamin A-supplemented mice were again confirmed by increased shortening of colon length, histological colitis score, and ulcer length (Figure 6) (Supplementary Table 1b).

3.3. Slow Recovery from Acute Colitis in Vitamin A-Deficient Mice. Long-term observation of colitis after induction by intake of 1% DSS for 7 days revealed extensive differences between vitamin A-deficient and vitamin A-supplemented mice on experimental day 43. Vitamin A-deficient mice had much more severe colitis, including increased shortening of colon length, increased histological colitis score, and increased total ulcer length compared to vitamin A-supplemented mice (Figure 7) (Supplementary Table 1c). These findings indicate that not only the development of DSS colitis is worse with vitamin A deficiency but also recovery from DSS colitis is much slower.

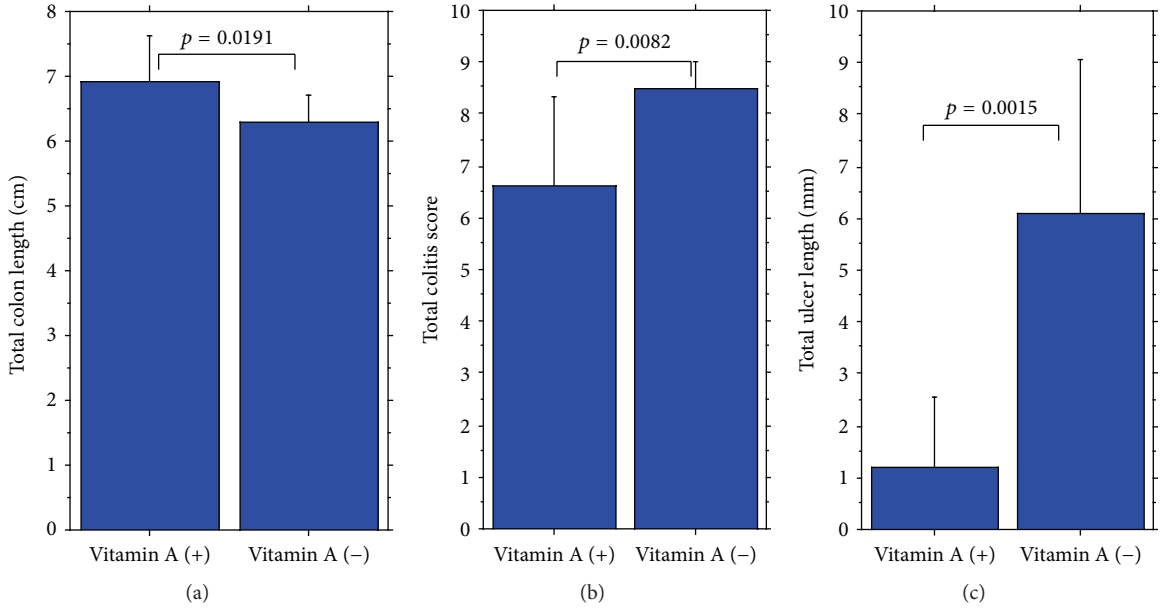

Figure 6: Significant difference of (a) total colon length, (b) total colitis score, and (c) total ulcer length between vitamin A-supplemented mice (left) and vitamin A-deficient mice (right). Colitis was induced with intake of 1% DSS for 12 days.

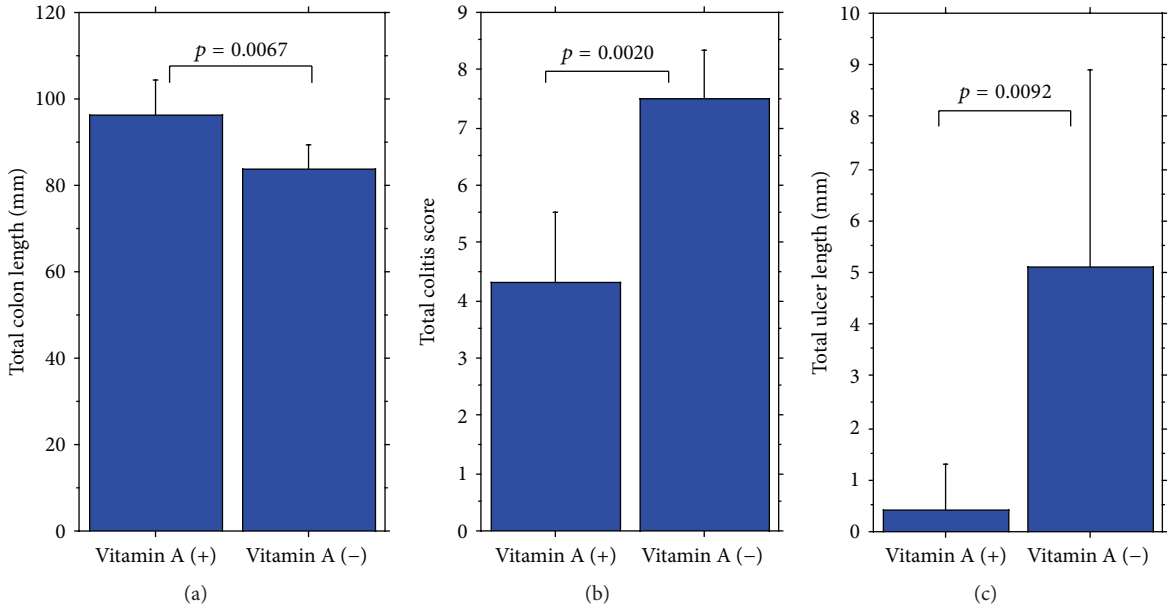

Figure 7: Recovery from acute colitis. Significant difference of (a) total colon length, (b) total colitis score, and (c) total ulcer length between vitamin A-supplemented mice (left) and vitamin A-deficient mice (right). Colitis was induced with intake of 1% DSS for 7 days. After that, mice were given distilled drinking water for 36 days.

3.4. Development of Colonic Tumors in Vitamin A-Deficient Mice. A single intraperitoneal injection of azoxymethane (7.4 mg/kg) 14 days prior to intake of 1% DSS for 7 subsequent days [7] induced multiple types of colorectal neoplasia, including low grade dysplasia, high grade dysplasia, and invasive carcinoma as well as severe colitis in vitamin A-deficient mice (Figures 8, 9, and 10). In contrast, only a few neoplastic lesions developed in vitamin A-supplemented mice in addition to mild colitis (Supplementary Table 2).

4. Discussion

Our results demonstrated that vitamin A inhibits development of DSS colitis and the subsequent development of colonic neoplasia and prolonged the recovery from colitis in a mouse model of DSS colitis.

Dietary vitamin A is essential for production of the precursor of tissue retinol, which participates in immunity and cell differentiation. First, in immunity, vitamin A deficiency

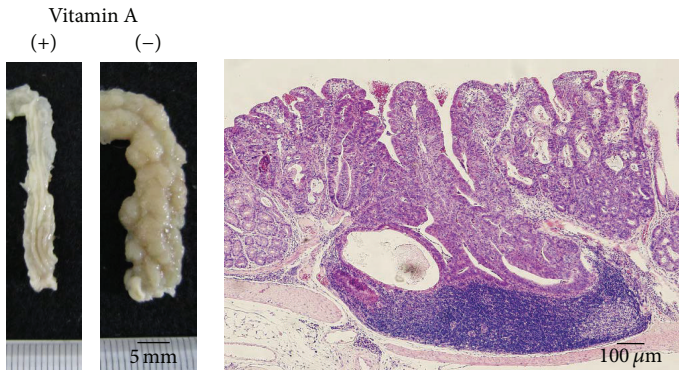

Figure 8: (a) Colonic neoplasia induced by a single preinjection of azoxymethane (7.4 mg/kg) 14 days prior to intake of 1% DSS for 7 subsequent days (left, no neoplasia in a vitamin A-supplemented mouse, and right, neoplasia in a vitamin A-deficient mouse). (b) Invasive adenocarcinoma.

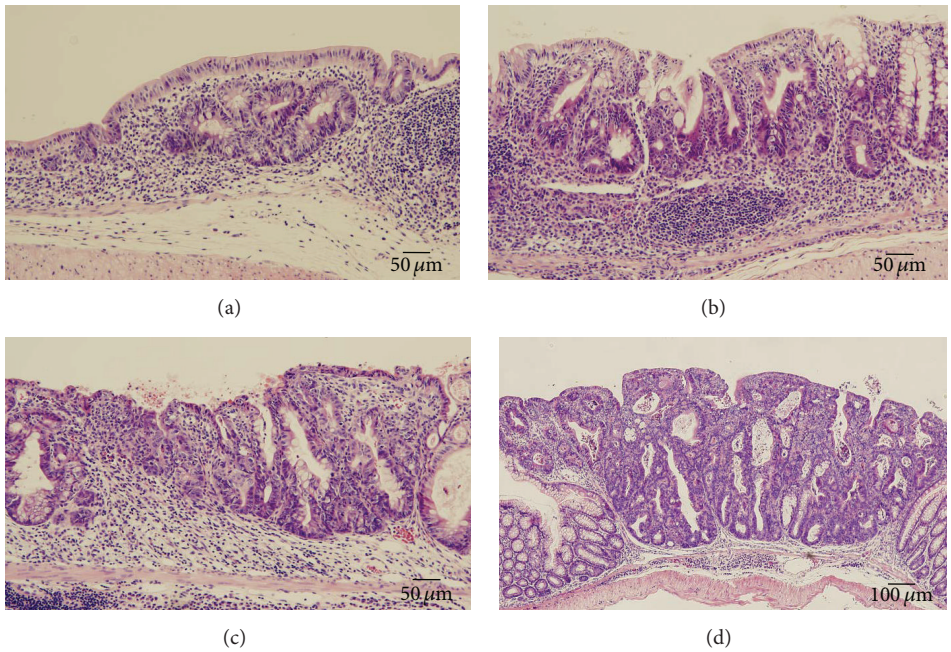

Figure 9: Representative dysplasia induced by a single preinjection of azoxymethane (7.4 mg/kg) 14 days prior to intake of 1% DSS for 7 subsequent days. (a) Depressed low grade dysplasia, (b) flat low grade dysplasia, (c) flat high grade dysplasia, and (d) elevated high grade dysplasia.

causes a helper T cell imbalance with excess Th1 and insufficient Th2 function and a reduction in $\alpha 4\beta 7^+$ memory/activated T cell generation [23]. In contrast, retinoic acid, a vitamin A metabolite, enhances IL-22 production by $\gamma\delta$ T cells in vitro and inhibits DSS-induced colitis [24]. We demonstrated an increase in $CD11c^+$ dendritic cells in the colonic mucosa of vitamin A-deficient mice in line with results of both in vivo and in vitro studies using vitamin A-deficient rats performed by Dong et al. [4]. It can be suggested that this was a compensatory increase because vitamin A deficiency induces dendritic cell malfunction in the activation of T lymphocytes [25, 26] since vitamin A supplementation was shown to induce maturation of dendritic cells [4, 25, 27]. Further, vitamin A is necessary for generation of gut-homing IgA-secreting B cells by intestinal dendritic cells [28]. In the present study, a decrease in the ratio of IgA^+ cells/IgG^+ cells in the mucosa of the proximal segment of colon indicates an aspect of disorganization of mucosal immunity in vitamin A deficiency [23, 28, 29]. On the other hand, present experimental results were obtained in BALB/c mice, which had higher intestinal epithelial expression of retinaldehyde dehydrogenase 1 (RALDH1), leading to an increased activity to induce IgA class switching from B cells [24]. According to this, the results might be different in another strain with low expression of RALDH1, suggesting the possibility of differences in susceptibility of ulcerative colitis in humans. This remains to be clarified.

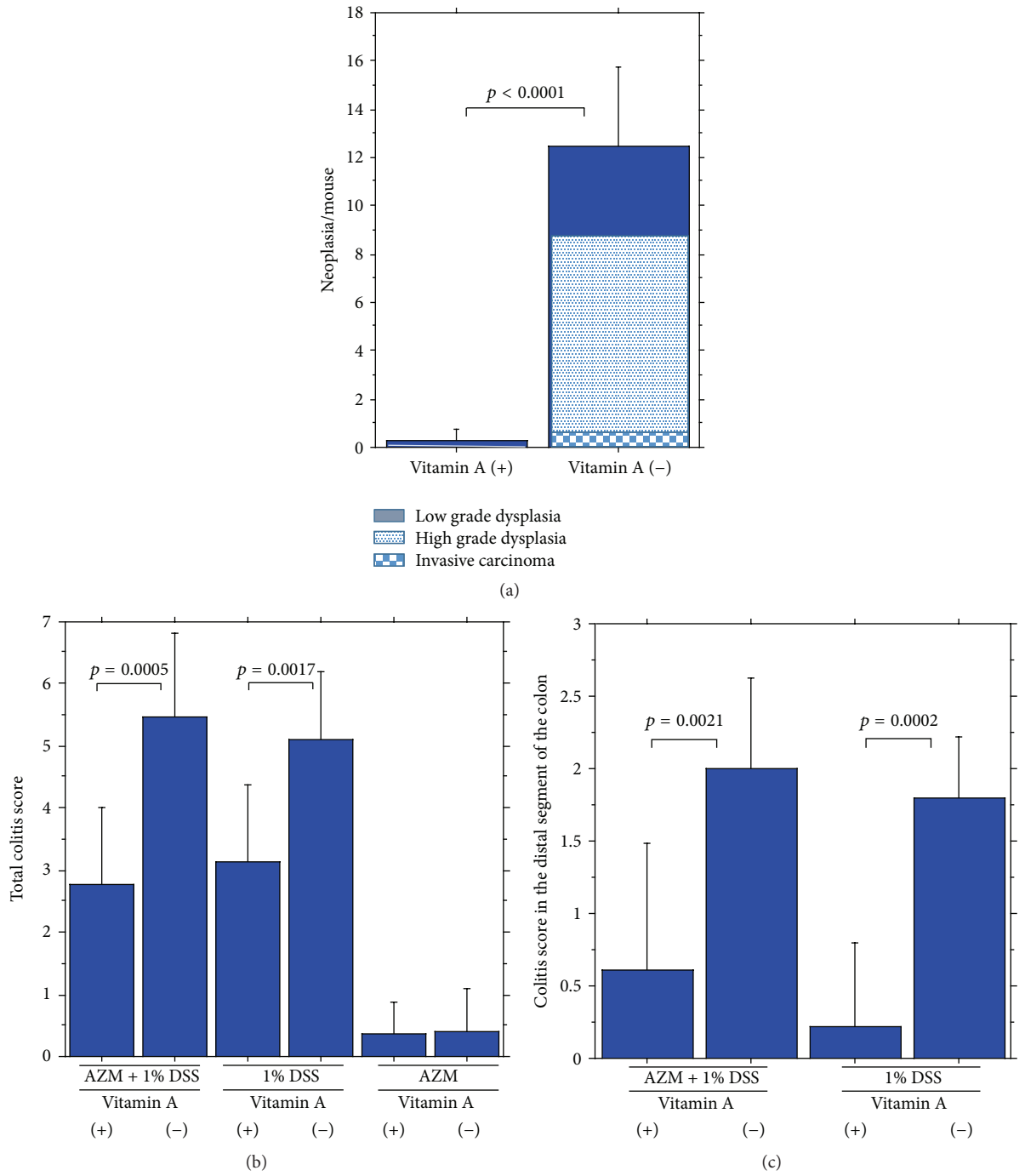

Figure 10: Significant difference of (a) appearing neoplasia including invasive carcinoma, high grade dysplasia, and low grade dysplasia, (b) total colitis score, and (c) colitis score of the distal segment between vitamin A-supplemented mice and vitamin A-deficient mice induced by a single preinjection of azoxymethane (7.4 mg/kg) 14 days prior to intake of 1% DSS for 7 subsequent days.

Second, in addition, hepatic stellate cells and intestinal subepithelial myofibroblasts participate in niche function for epithelial cell stem cells and progenitor cells in the liver and intestinal crypts, respectively [17, 19, 30–34]. Hepatic stellate cells need vitamin A-rich lipids to maintain their niche function. We found a decrease in subepithelial myofibroblasts in the crypt base of vitamin A-deficient mice as well as a reduction in cytoplasmic vitamin A lipids in subepithelial myofibroblasts. The decrease in α-SMA$^+$ subepithelial myofibroblasts may indicate an alteration of the niche function for protection of colonic mucosal stem cells or progenitor cells based on the concept that α-SMA$^+$ subepithelial myofibroblasts correspond to colonic stellate cells [17, 19, 34]. Thus, our findings might suggest that dysfunction of dendritic cells and subepithelial myofibroblasts caused by vitamin A deficiency accelerated DSS colitis, which resulted in the

development of colorectal cancer in our DSS colitis mouse model.

Third, with regard to cell differentiation, it is well known that vitamin A and its metabolite, retinoids, play an important role [6, 35]. Retinoids perform effective chemoprevention against cancers in various organs and are used for differentiation therapy against acute promyelocytic leukemia [7]. Further, it was suggested clinically and experimentally that vitamin A deficiency promotes cancer development and progression [8, 9, 36–39]. Particularly, CYP26A1, the gene encoding the cytochrome P450 enzyme specifically involved in metabolic inactivation of retinoic acid, was highly expressed in breast cancers and showed oncogenic characteristics suggesting a link between intracellular retinoic acid status and tumorigenesis [15, 40, 41]. Our results that showed severe DSS colitis, prolonged recovery of DSS colitis, and the development of colonic tumors following DSS colitis in vitamin A-deficient mice are in line with previous reports of promotion of cancer development.

Although it is suggested that dietary and nutritional factors, including vitamin A, have an intimate relationship to development or exacerbation of inflammatory bowel diseases [42, 43], there are no any definite clinical indications of vitamin A administration. Our present basic research results may help us to know the possibility that vitamin A administration might inhibit colitis and subsequent cancer development, depending on unknown phenotypes of clinical cases of ulcerative colitis, if they are present. Further studies should be conducted to find the possible underlying mechanisms on inhibition of colitis and subsequent colonic neoplasia development by vitamin A supplementation.

5. Conclusion

Vitamin A inhibited development of DSS colitis and colorectal cancer in the DSS colitis mouse model. Therefore, vitamin A supplementation might help to improve diarrhea and enteritis in inflammatory bowel disease and could possibly inhibit insidious colonic inflammation and cancer development. These effects of vitamin A remain to be examined in a future study.

Ethical Approval

This experimental study using mice was approved by the Animal Experiment Committee, Kitasato University School of Medicine (2010-184).

Competing Interests

The authors declare that they have no competing interests.

Acknowledgments

This work was supported in part by a Grant-in-Aid for Japan Science and Technology Agency (no. 23659190).

References

[1] R. H. Alkhouri, H. Hashmi, R. D. Baker, D. Gelfond, and S. S. Baker, "Vitamin and mineral status in patients with inflammatory bowel disease," *Journal of Pediatric Gastroenterology and Nutrition*, vol. 56, no. 1, pp. 89–92, 2013.

[2] A. Bousvaros, D. Zurakowski, C. Duggan et al., "Vitamins A and E serum levels in children and young adults with inflammatory bowel disease: effect of disease activity," *Journal of Pediatric Gastroenterology and Nutrition*, vol. 26, no. 2, pp. 129–135, 1998.

[3] O. P. Garcia, "Effect of vitamin A deficiency on the immune response in obesity," *Proceedings of the Nutrition Society*, vol. 71, no. 2, pp. 290–297, 2012.

[4] P. Dong, Y. Tao, Y. Yang, and W. Wang, "Expression of retinoic acid receptors in intestinal mucosa and the effect of vitamin A on mucosal immunity," *Nutrition*, vol. 26, no. 7-8, pp. 740–745, 2010.

[5] S. G. Kang, C. Wang, S. Matsumoto, and C. H. Kim, "High and low vitamin A therapies induce distinct FoxP3$^+$ T-cell subsets and effectively control intestinal inflammation," *Gastroenterology*, vol. 137, no. 4, pp. 1391–1402, 2009.

[6] E. Batourina, S. Gim, N. Bello et al., "Vitamin A controls epithelial/mesenchymal interactions through *Ret* expression," *Nature Genetics*, vol. 27, no. 1, pp. 74–78, 2001.

[7] L. A. Hansen, C. C. Sigman, F. Andreola, S. A. Ross, G. J. Kelloff, and L. M. De Luca, "Retinoids in chemoprevention and differentiation therapy," *Carcinogenesis*, vol. 21, no. 7, pp. 1271–1279, 2000.

[8] A. L. French, L. M. Kirstein, L. S. Massad et al., "Association of vitamin A deficiency with cervical squamous intraepithelial lesions in human immunodeficiency virus-infected women," *Journal of Infectious Diseases*, vol. 182, no. 4, pp. 1084–1089, 2000.

[9] K. Li, J. Gao, X. Xiao, L. Chen, and L. Zhang, "The enhancing role of vitamin A deficiency on chemically induced nephroblastoma in rats," *Journal of Pediatric Surgery*, vol. 40, no. 12, pp. 1951–1956, 2005.

[10] E. Sonneveld, C. E. van den Brink, B.-J. M. van der Leede et al., "Human retinoic acid (RA) 4-hydroxylase (CYP26) is highly specific for all-trans-RA and can be induced through RA receptors in human breast and colon carcinoma cells," *Cell Growth and Differentiation*, vol. 9, no. 8, pp. 629–637, 1998.

[11] J. Van Heusden, W. Wouters, F. C. S. Ramaekers et al., "The antiproliferative activity of all-*trans*-retinoic acid catabolites and isomers is differentially modulated by liarozole-fumarate in MCF-7 human breast cancer cells," *British Journal of Cancer*, vol. 77, no. 8, pp. 1229–1235, 1998.

[12] D. N. Shelton, I. T. Sandoval, A. Eisinger et al., "Up-regulation of CYP26A1 in adenomatous polyposis coli-deficient vertebrates via a WNT-dependent mechanism: implications for intestinal cell differentiation and colon tumor development," *Cancer Research*, vol. 66, no. 15, pp. 7571–7577, 2006.

[13] C.-L. Chang, E. Hong, P. Lao-Sirieix, and R. C. Fitzgerald, "A novel role for the retinoic acid-catabolizing enzyme CYP26A1 in Barrett's associated adenocarcinoma," *Oncogene*, vol. 27, no. 21, pp. 2951–2960, 2008.

[14] M. Osanai and M. Petkovich, "Expression of the retinoic acid-metabolizing enzyme CYP26A1 limits programmed cell death," *Molecular Pharmacology*, vol. 67, no. 5, pp. 1808–1817, 2005.

[15] M. Osanai, N. Sawada, and G.-H. Lee, "Oncogenic and cell survival properties of the retinoic acid metabolizing enzyme, CYP26A1," *Oncogene*, vol. 29, no. 8, pp. 1135–1144, 2010.

[16] R. C. Heine-Bröring, R. M. Winkels, J. M. S. Renkema et al., "Dietary supplement use and colorectal cancer risk: a systematic review and meta-analyses of prospective cohort studies," *International Journal of Cancer*, vol. 136, no. 10, pp. 2388–2401, 2015.

[17] I. Okayasu, T. Yoshida, T. Mikami et al., "Mucosal remodeling in long-standing ulcerative colitis with colorectal neoplasia: significant alterations of $NCAM^+$ or α-SMA^+ subepithelial myofibroblasts and interstitial cells," *Pathology International*, vol. 59, no. 10, pp. 701–711, 2009.

[18] N. Lahar, N. Y. Lei, J. Wang et al., "Intestinal subepithelial myofibroblasts support in vitro and in vivo growth of human small intestinal epithelium," *PLoS ONE*, vol. 6, no. 11, Article ID e26898, 2011.

[19] I. Okayasu, T. Mikami, T. Yoshida et al., "Cytoglobin expression of rectal subepithelial myofibroblasts: significant alterations of $cytoglobin^+$ stromal cells in long-standing ulcerative colitis," *Histology and Histopathology*, vol. 26, no. 6, pp. 679–688, 2011.

[20] I. Okayasu, "Development of ulcerative colitis and its associated colorectal neoplasia as a model of the organ-specific chronic inflammation-carcinoma sequence," *Pathology International*, vol. 62, no. 6, pp. 368–380, 2012.

[21] I. Okayasu, S. Hatakeyama, M. Yamada, T. Ohkusa, Y. Inagaki, and R. Nakaya, "A novel method in the induction of reliable experimental acute and chronic ulcerative colitis in mice," *Gastroenterology*, vol. 98, no. 3, pp. 694–702, 1990.

[22] I. Okayasu, T. Ohkusa, K. Kajiura, J. Kanno, and S. Sakamoto, "Promotion of colorectal neoplasia in experimental murine ulcerative colitis," *Gut*, vol. 39, no. 1, pp. 87–92, 1996.

[23] M. Iwata, A. Hirakiyama, Y. Eshima, H. Kagechika, C. Kato, and S.-Y. Song, "Retinoic acid imprints gut-homing specificity on T cells," *Immunity*, vol. 21, no. 4, pp. 527–538, 2004.

[24] G. Goverse, B. J. Olivier, R. Molenaar et al., "Vitamin A metabolism and mucosal immune function are distinct between BALB/c and C57BL/6 mice," *European Journal of Immunology*, vol. 45, no. 1, pp. 89–100, 2015.

[25] A. Yokota, H. Takeuchi, N. Maeda et al., "GM-CSF and IL-4 synergistically trigger dendritic cells to acquire retinoic acid-producing capacity," *International Immunology*, vol. 21, no. 4, pp. 361–377, 2009.

[26] A. Yokota-Nakatsuma, H. Takeuchi, Y. Ohoka et al., "Retinoic acid prevents mesenteric lymph node dendritic cells from inducing IL-13-producing inflammatory Th2 cells," *Mucosal Immunology*, vol. 7, no. 4, pp. 786–801, 2014.

[27] M. Iwata, "Retinoic acid production by intestinal dendritic cells and its role in T-cell trafficking," *Seminars in Immunology*, vol. 21, no. 1, pp. 8–13, 2009.

[28] J. R. Mora, M. Iwata, B. Eksteen et al., "Generation of gut-homing IgA-secreting B cells by intestinal dendritic cells," *Science*, vol. 314, no. 5802, pp. 1157–1160, 2006.

[29] J. L. Bjersing, E. Telemo, U. Dahlgren, and L. Å. Hanson, "Loss of ileal IgA^+ plasma cells and of $CD4^+$ lymphocytes in ileal Peyer's patches of vitamin A deficient rats," *Clinical and Experimental Immunology*, vol. 130, no. 3, pp. 404–408, 2002.

[30] T.-H. Yen and N. A. Wright, "The gastrointestinal tract stem cell niche," *Stem Cell Reviews*, vol. 2, no. 3, pp. 203–212, 2006.

[31] C. Kosinski, V. S. W. Li, A. S. Y. Chan et al., "Gene expression patterns of human colon tops and basal crypts and BMP antagonists as intestinal stem cell niche factors," *Proceedings of the National Academy of Sciences of the United States of America*, vol. 104, no. 39, pp. 15418–15423, 2007.

[32] I. Sawitza, C. Kordes, S. Reister, and D. Häussinger, "The niche of stellate cells within rat liver," *Hepatology*, vol. 50, no. 5, pp. 1617–1624, 2009.

[33] C. Kordes, I. Sawitza, and D. Häussinger, "Hepatic and pancreatic stellate cells in focus," *Biological Chemistry*, vol. 390, no. 10, pp. 1003–1012, 2009.

[34] M. Plateroti, D. C. Rubin, I. Duluc et al., "Subepithelial fibroblast cell lines from different levels of gut axis display regional characteristics," *The American Journal of Physiology*, vol. 274, no. 5, part 1, pp. G945–G954, 1998.

[35] A. Janesick, S. C. Wu, and B. Blumberg, "Retinoic acid signaling and neuronal differentiation," *Cellular and Molecular Life Sciences*, vol. 72, no. 8, pp. 1559–1576, 2015.

[36] A. Bernstein and B. Harris, "The relationship of dietary and serum vitamin A to the occurrence of cervical intraepithelial neoplasia in sexually active women," *American Journal of Obstetrics and Gynecology*, vol. 148, no. 3, pp. 309–312, 1984.

[37] P. A. Stehr, M. F. Gloninger, L. H. Kuller, G. M. Marsh, E. P. Radford, and G. B. Weinberg, "Dietary vitamin A deficiencies and stomach cancer," *American Journal of Epidemiology*, vol. 121, no. 1, pp. 65–70, 1985.

[38] C.-P. Zou, J. L. Clifford, X.-C. Xu et al., "Modulation by retinoic acid (RA) of squamous cell differentiation, cellular RA-binding proteins, and nuclear RA receptors in human head and neck squamous cell carcinoma cell lines," *Cancer Research*, vol. 54, no. 20, pp. 5479–5487, 1994.

[39] L. A. Hansen, D. Brown, V. Virador et al., "A PMLRARA transgene results in a retinoid-deficient phenotype associated with enhanced susceptibility to skin tumorigenesis," *Cancer Research*, vol. 63, no. 17, pp. 5257–5265, 2003.

[40] M. Osanai and G.-H. Lee, "Enhanced expression of retinoic acid-metabolizing enzyme CYP26A1 in sunlight-damaged human skin," *Medical Molecular Morphology*, vol. 44, no. 4, pp. 200–206, 2011.

[41] M. Osanai and G.-H. Lee, "Increased expression of the retinoic acid-metabolizing enzyme CYP26A1 during the progression of cervical squamous neoplasia and head and neck cancer," *BMC Research Notes*, vol. 7, article 697, 2014.

[42] A. Lan, F. Blachier, R. Benamouzig et al., "Mucosal healing in inflammatory bowel diseases: is there a place for nutritional supplementation?" *Inflammatory Bowel Diseases*, vol. 21, no. 1, pp. 198–207, 2015.

[43] D. Owczarek, T. Rodacki, R. Domagala-Rodacka et al., "Diet and nutritional factors in inflammatory bowel diseases," *World Journal of Gastroenterology*, vol. 22, no. 3, pp. 895–905, 2016.

Hindawi Publishing Corporation
BioMed Research International
Volume 2016, Article ID 9750795, 11 pages
http://dx.doi.org/10.1155/2016/9750795

Review Article

Mouse Models in Prostate Cancer Translational Research: From Xenograft to PDX

Domenica Rea,[1] Vitale del Vecchio,[1] Giuseppe Palma,[1] Antonio Barbieri,[1] Michela Falco,[1] Antonio Luciano,[1] Davide De Biase,[2] Sisto Perdonà,[3] Gaetano Facchini,[4] and Claudio Arra[1]

[1]*Animal Facility Unit, Department of Experimental Oncology, Istituto Nazionale per lo Studio e la Cura dei Tumori "Fondazione G. Pascale", IRCCS, 80131 Naples, Italy*
[2]*Department of Veterinary Medicine and Animal Productions, Università di Napoli Federico II, Via Delpino 1, 80137 Naples, Italy*
[3]*Department of Urology, Istituto Nazionale per lo Studio e la Cura dei Tumori "Fondazione G. Pascale", IRCCS, 80131 Naples, Italy*
[4]*Division of Medical Oncology, Department of Uro-Gynaecological Oncology, Istituto Nazionale per lo Studio e la Cura dei Tumori "Fondazione G. Pascale", IRCCS, 80131 Naples, Italy*

Correspondence should be addressed to Domenica Rea; d.rea@istitutotumori.na.it

Received 17 March 2016; Accepted 21 April 2016

Academic Editor: Oreste Gualillo

Despite the advancement of clinical and preclinical research on PCa, which resulted in the last five years in a decrement of disease incidence by 3-4%, it remains the most frequent cancer in men and the second for mortality rate. Based on this evidence we present a brief dissertation on numerous preclinical models, comparing their advantages and disadvantages; among this we report the PDX mouse models that show greater fidelity to the disease, in terms of histopathologic features of implanted tumor, gene and miRNA expression, and metastatic pattern, well describing all tumor progression stages; this characteristic encourages the translation of preclinical results. These models become particularly useful in meeting the need of new treatments identification that eradicate PCa bone metastases growing, clarifying pathway of angiogenesis, identifying castration-resistant stem-like cells, and studying the antiandrogen therapies. Also of considerable interest are the studies of 3D cell cultures derived from PDX, which have the ability to maintain PDX cell viability with continued native androgen receptor expression, also showing a differential sensitivity to drugs. 3D PDX PCa may represent a diagnostic platform for the rapid assessment of drugs and push personalized medicine. Today the development of preclinical models in vitro and in vivo is necessary in order to obtain increasingly reliable answers before reaching phase III of the drug discovery.

1. Introduction

Despite the many scientific advances in pharmacological, clinical, and preclinical settings, prostate cancer (PCa) remains to be the first most common cancer in men [1]; it represents a major cause of cancer-related morbidity and mortality [2, 3]. In the United States there were estimated 233,000 (27%) new cancer prostate cases diagnosed in 2014, with an incidence of death valued at 29,480 (10%) patients annually [4]. Currently the radical prostatectomy is one of the gold standards for the treatment of PCa [5], despite the recent pharmacological approach with novel antineoplastic developed and approved drugs (enzalutamide and abiraterone) that target the androgen receptor axis [6, 7], and also immunologic therapies with antiangiogenic molecules used in patients with progression of disease [8]. The lethal cases generally have a high Gleason score and can be metastatic and/or refractory to androgen deprivation therapy (castration-resistant prostate cancer mCRPC); these have a short survival of 1–3 years, depending on context. Skeletal metastasis is the most significant cause of morbidity and mortality in PCa; it is found in approximately 90% of patients who die because of PCa [9]; this one indicates that the bone microenvironment may promote the growth of PCa cells. The majority of bone lesions in PCa usually show a greater proportion of active osteoblasts than active osteoclasts, resulting in the net formation of bone [10]. On the other hand, despite the many new therapies for patients with advanced CRPC,

the overall survival is still relatively short [11] due to an endocrine therapy resistance development in a part of patients. These mechanisms include interference of androgen receptor (AR) axis and inhibition of androgens biosynthesis [1, 12, 13]. Malignant cells derived from prostate epithelial layers of PCa, which include secretory luminal, basal, and rare neuroendocrine cells, lend to disease a high grade of heterogeneity [9]. A question is pending about which type of epithelial cell represents the origin of PCa: luminal stem cells, basal stem cells, or both [14]; this point still remains unclear, but it is likely that there is a complex explanation of the heterogeneity of the disease and the many genetic pathways that are involved [15]. Despite the incidence rate trend in PCa, which continues to fall by 3-4% each year, and a large amount of prostate cancer studies, only very few findings have influenced the clinical management of the disease.

Innovative mouse models of prostate cancer have been developed to overcome the well-known limits and difficulties in PCa research [4]. For instance, the heterotopic models show some advantages like an easier tumor cells inoculation and in vivo tumor growth monitoring. While the heterotopic models mimic human prostate cancer in a more realistic way, the orthotopic implantation of tumor cells in the host more likely resembles the different tumor stages, dealing with native environment of tumor cells [16]. Independently from the advantages of these models in preclinical research, most studies are additionally hampered by a lack of standardization. Especially in orthotopic tumor cell application, the quality and number of inoculated tumor cells, as well as the addition of extracellular factors, have never been investigated in detail.

A major limitation in prostate cancer research is the lack of relevant preclinical models, which allow studying the molecular mechanisms of tumorigenesis. In fact, advanced in vitro and in vivo models are an indispensable requirement for the development of effective prevention and therapeutic intervention strategies [3]. To address and overcome the limitations of traditional models, reaching a greater loyalty compared to PCa human, currently patient-derived models (PDX) are used for preclinical research. Their use permits highlighting various aspects of PCa biology including angiogenesis, the identification of resistant castrate stem-like cells, and the effect of antiandrogen therapies [17]. PDX models are generated by using tumor tissues surgically removed from patient and plugged directly into the immune-compromised mice, without any manipulation in vitro. The tumors are subsequently maintained in vivo by mouse-to-mouse passages. Therefore we expect that PDX tumors models, which remain biologically stable and retain much of molecular, genetic, and histological characteristics, heterogeneity of original tumor, and response to treatment, become largely used in studies; instead, given the high costs of animal maintenance, lengthy latency period following engraftment, variable engraftment rates, and rare access to patient tissue specimens, PDX in vivo models are generally not yet widely employed in cancer research [18–20]. Mouse models can answer many questions about the etiology of cancer and help in screening new drugs and the development of more effective treatments. This work aims to collect and summarize data from research studies in order to identify, evaluate, and critically analyse in vivo models of PCa. Our ultimate goal was to obtain a systematic treatise about the progress as well as the advantages and disadvantages of these models in preclinical translational research.

2. Prostate Cancer Mouse Models

To date, preclinical prostate cancer mouse models still represent an essential tool to improve our understanding of PCa development, progression, and metastatic pattern. Spontaneous PCa transformation in different mouse strains is really uncommon [21]; therefore in the last years there have been created different generations of new manipulated mouse models of PCa to simulate all the stages of pathology, from the hyperplasia to HGPIN (high-grade prostatic intraepithelial neoplasia), until metastasis dissemination [21]; these transformation steps are slightly different from a histopathological point of view between human and mouse [22].

Xenograft mouse models (Table 1) represent a common "recipient" of human PCa, generated through orthotopic or heterotopic implantation of human tumor tissues, cell lines, or primary cell cultures, in nude mice [23], SCID [24], NOD-SCID [25], NOG/NSG [26], or RAG [27]. Different human prostate cancer cell lines have been used to perform various xenograft mouse models that, in this way, exhibit different features of the prostatic neoplasia. For instance LNCaP-LN3 cells, derived from androgen receptor mutated LNCaP [28], promote a high regional lymph node metastatic pattern after prostatic implantation, with castration-resistance features [29]. Instead PC3 cell lines, derived from bone metastasis of human PCa, are androgen-independent [30]; the PC-3M variant shows a higher ability to produce regional lymph node and distant organ metastasis [29].

Allograft mouse models (Table 1) represent a mouse tumor system that can be generated by using tumor cell lines/tissues derived from the same genetic background. In this way transplanted material and the host share the strain. TRAMP-C1/2/3 [31, 32] prostate cancer cell lines, derived from the prostatic epithelium of TRAMP mouse, and PTEN-CaP8 [33], from Pten-null transgenic mouse model of PCa, are both in strain C57BL/6; instead PNEC30, originated from neuroendocrine cell population in mouse prostate cancer, is in strain BALB/c [34].

Genetically engineered mouse models (GEMMs) (Table 2) reproduce in depth the different stages of PCa associated with typical human genetic mutation that allow tumor progression. We recognize two generations of PCa GEMMs, the first one is characterized by the ectopic expression of Simian virus 40 (SV40) Large Antigen T (Tag) in prostate; this effector acts as an oncoprotein that negatively regulates p53 [35, 36]. In 1994 the C3(1)-Tag model was generated, the first GEMM under the expression of SV40 large Tag; this model showed prostatic epithelial hyperplasia about 3 months of age and local adenocarcinoma by 7–11 months of age [37]. Also the TRAMP model (transgenic adenocarcinoma of the mouse prostate) is based on the SV40 Tag activity, under the prostate-specific rat Probasin promoter [38]; these mice develop epithelial hyperplasia, after 8 weeks of age, PIN

Table 1: Prostatic mouse models of engraftment.

Type	Background strain	Year	Features	Disadvantages	Reference
Xenograft	Nude, SCID, NOD-SCID, NOG/NSG, RAG	1996–2006	High take rate, low costs, LNCaP, LNCaP-LN3, PC-3, PC-3M cell lines and human prostatic tissues implanted	Immune-compromised mice tested	[23–27]
Allograft	C57BL/6	1997–1994	High take rate, low costs, use of immune-competent mice; TRAMP-C1/2/3, PTEN-CaP8 cell lines implanted	Low translational potential	[31, 32, 38]
Allograft	BALBC/c	2004	High take rate, low costs, use of immune-competent mice; use of PNEC30 cell lines	Low translational potential Neuroendocrine originated cells	[34]

Table 2: Genetically engineered mouse models (GEMM) of prostate cancer.

Name	Background strain	Year	Features	Disadvantages	Reference
C3(1)-Tag	FVB/N	1994	PHH (3 mths) PCa (7–11 mths)	Sporadic metastases, aspecific breast cancer in female (12 wks)	[37]
TRAMP	C57BL/6	1994	PHH (8 wks), PIN (18 wks) Lymph. metastases (28 wks)	Neuroendocrine originated tumors	[38]
FG-Tag	C57BL/6	1996	Accurate model of castration-resistant PCa	Aspecific adrenocortical tumors in 50% of female mice	[39]
LPB-Tag (LADY)	CD-1	1997	Accurate model for all stages of PCa studies	Neuroendocrine originated foci in liver, lymph., and lung metastases	[40]
LPB-Tag/ARR$_2$PB hepsin	C57BL/6JxCBA	2004	Increased migratory ability	Neuroendocrine originated cells forming liver metastases	[41]
Mt-PRL	C57BL/6JxCBA-f2	1997	Appropriate model to study BPH	Rare PCa progression, no metastases	[42]
BK5-IGF1	FVB × ICR	2000	PIN (6 mths), PCa (9 mths)	Not metastases, off-target effects	[43]
PB-mAR	FVB	2001	Microinvasive HGPIN, useful in PCa studies about androgens	Rare metastases	[44]
ARR$_2$PB-Myc	FVB	1999	From PIN to PCa in 2 mths Regression after castration (8 mths)	Not metastases observed	[45]
ARR$_2$PB-FGFR1	FVB	2003	Hyperproliferation and PIN	Failed in the later stages of disease	[46]
PB-Ras	FVB/N	2004	Did not progress further than PIN	Intestinal metaplasia Thickened fibromuscular stroma	[47]
PB-Neu	C57BL/6JxCBA	2006	Similar to human acinar type	Low translational potential (rare cases of Neu alteration in human PCa)	[48]
ARR$_2$PB-ERG	FVB	2008	PIN (12–14 wks)	Take rate of 38%	[49]

PHH: prostatic epithelial hyperplasia; PIN: prostatic intraepithelial neoplasia; BPH: benign prostatic hyperplasia.

(prostatic intraepithelial neoplasia) by 18 weeks, and lymph node metastasis by 28 weeks; this model has been the first that showed distant organ metastasis. The FG-Tag (fetal globin-γ/T-antigen) [39], LPB-Tag (LADY) [40], and LPB-Tag/ARR$_2$PB-hepsin [41] chronologically represent the last example of first generation GEMM with a typical neuroendocrine cell transformation.

The second-generation GEMMs were born in 1997 with the Mt-PRL [42], a mouse model created to further study the role of prolactin (PRL) in prostate hyperplasia; the PRL ectopic expression has been inducted by Metallothionein-1 (Mt-1) promoter. Subsequently the BK5-IGF1 mouse models [43] were created which overexpressed the insulin-like growth factor 1, a molecule that resulted as an indicator of PCa in some patients that showed normal levels of PSA [62]. From 2001 there have been developed some other models using the Probasin (PB) promoter, among which are the following: PB-mAR [44], to further understand the role of androgen receptor on the disease progression; ARR$_2$PB-Myc that shows high levels of Myc, with a PIN progression and then invasive carcinoma, by the third month of age [45]; ARR$_2$PB-FGFR1 models that show the physiological role of

Fibroblast growth factor receptors 1 and 2 (FGFR1-2) that become upregulated in 40% of poorly differentiated PCa [46]; PB-Ras [47], PB-Neu [48], and ARR_2PB-ERG [49] instead were generated inducing an overexpression of any oncogenes that have an important role in different human tumor disease, as Neu in breast cancer [63] or Ras in any other [64].

Knockout models (Table 3) have been carried out by a different strategy that led to induce silencing of any tumor suppressor genes through deletion of whole sequences or part of them, essential for their activities. In 1993 RARγ, the first KO mouse model of prostate cancer, was born; it was not able to develop PCa but only squamous metaplasia in mouse prostate and seminal vesicles [50]. Kip1 knockout mouse instead was generated through the loss of p27 [51]; this model showed hyperplasia of some organs among which is prostate. For these reasons it represents a very good model of BPH (benign prostatic hyperplasia). In 1999 Nkx3.1 KO model [52] that showed several prostatic phenotype as hyperplasia and dysplasia was generated but no tumor lesions have been detected. Finally we report the Pten KO, probably the best model to study PIN progression [53], without metastatic proliferation. The Pten-null background has been intercrossed with other KO to generate a more confident mouse model of PCa, for instance, Pten-null × p27 [54] that showed the prostatic adenocarcinoma features or Pten-null × p53 that instead displays HGPIN [55]. Different conditional knockout models of PCa have been developed, during last years, using the Cre-loxP recombination system to excise specific DNA regions in somatic cells, through the gene regulation by tissue specific promoter as Probasin or PSA. Also these models are generated by specific gene silencing of PTEN [56], pRB [57], p53 [58], Apc [59], IGF-1 [60], and Brca2 [61].

3. Prostate Tumor PDX Mouse Models

Preclinical prostate cancer mouse models described so far fail to reproduce with high fidelity the different stages of tumorigenesis and the progression of disease observed in the clinic. Normally the xenograft cell lines lose the original tissue architecture of the site of origin, with related impaired physical and biochemical pattern of interaction with the environment, different gene expression, and altered response to pharmacological treatments [65, 66]. Because of the issues described so far, PDX seems to be a good preclinical model to reproduce tumor features, maintaining more similarities; in this way many studies have shown the quality of PDX models highlighting histological compatibilities [67, 68], saved tumor cells heterogeneity [69], similar gene expression [70], gene variants [71], and miRNA pattern [72]. On the contrary there are no other limitations that suggest why these models are not still widely used, such as the more difficult tissue implantation procedures, especially in orthotopic mouse models [73, 74]; the site of implantation choice, in order to provide a good vascularization and cytokines/growth factors supply [73]; an average graft latency period from two to twelve months [75]; an average value of 23–75% of engraftment rates, strictly dependent on tumor aggressiveness [70]. We found studies that demonstrate a strong correlation between poor diagnosis and engraftment rates [68]. More authors suggest making some different serial engraftments (<10) to increase the rates of mouse models, preserving the genetic integrity of parental tumor [76].

The human prostatic tumor xenotransplantation has been firstly described by Gittes in 1980 that reported high take rates (TR = 50%) with the maintenance of many histological human tumor features in athymic nude mice [77]. Subsequently other studies showed a discouraging TR = 0–2% obtained using moderate/well-differentiated carcinomas [78] that poorly increase transplanting pelvic lymph node metastatic tumors supplemented with T-pellets (TR = 10%) [23]; all of the experiments described so far have carried out choosing, as a preferred strategy, the subcutaneous way of implantation, on the mice flank. Reid et al. have increased the TR in their studies, until hundred percent, treating mice with sheep or rabbit anti-mouse interferon serum (globulin fraction) [79]. These latter results have shown that the use of athymic nude mice did not improve the procedure and so the authors decided to change the immunodeficient mice strain, now choosing the NMRI or CB17-NOD athymic nude mice which have a reduced NK activity; Wang et al. [80] described a TR = 58,1% using these strains also supplemented with T-pellet, but in this work the authors decide to investigate also the other way of implantation: subrenal capsule (TR = 93,4%) and orthotopical (TR = 71,9%).

From a histological point of view Gittes [77] showed for the first time a study that demonstrated the development of squamous metaplasia and interstitial fibrosis in the PCa SC xenograft mouse models. They underlined any different modifications in the insert, from the parental carcinoma. Subsequently, for many different tumors, the high cytohistopathological similarity before and after the transplantation has been demonstrated [79, 81, 82]; in addition, both of them had the same Gleason score [83]. Moreover other studies also reported a substantial matching for the PAP and PSA expression in serum, as biomarkers [84, 85]. In most of this work also the metastatic pattern of the different models has been studied in depth; for instance, Hoehn et al. [84] did not find metastasis in any organs during necropsy in PC-82 tumor heterotransplant. On the other hand Lubaroff et al. [86] reported lung metastasis in SCID mice.

According to all of the reported studies so far, it can be affirmed that currently the subrenal capsule (SRC) represents the best way of transplantation because of the high TR; this site represents the gold standard thanks to a high vascularization, a good interstitial fluid pressure, and a high lymphatic flow; those ensure an even nutrients, hormones, oxygen, and growth factors supply [87]; however this site permits the easy placement of an insert with right size [88]. Lin et al. described the SRC grafting procedure using small cutting tumor pieces ($1 \times 3 \times 3\,mm^3$ in size) implanted in male NOD/SCID and supplemented with testosterone. After 3 to 6 months of growth the animals were sacrificed and the masses were harvested and reimplanted in SRC. The xenograft pieces were maintained for up to 3 years, increasing the aggressiveness during each passage. Subsequently, in the last passage, the hosts were sacrificed and examined for

Table 3: Prostatic knockout and conditional knockout mouse models.

Name	Type	Background strain	Year	Features	Disadvantages	Reference
RARγ	KO	C57Bl6F1	1993	Squamous cell metaplasia in prostate and seminal vesicles	PCa not developed; mucosal alteration, inflammation	[50]
Kip1	KO	C57BL/6	1996	Hyperplasia of prostate acinar cells (similar to that seen in PPH)	Hyperplasia of multiple organs; not metastases	[51]
Nkx3.1	KO	129/SvImJ C57Bl/6J	1999	Severe hyperplasia/dysplasia with haploinsufficiency (in heterozygous)	Altered morphogenesis of salivary glands	[52]
PTEN	KO	C57BL6/J	1998	PIN development	Off-target alteration: gonads, lymphoid cells, uterus, thyroid, adrenal glands	[53]
PTEN × p27	KO	C57BL6/J	2001	PCa progression with high take rate	Off-target alteration: endometrium, thyroid, adrenal glands	[54]
PTEN × p53	KO	129 SvJ	2009	HGPIN	Off-target alteration: gonads, lymphoid cells, uterus, thyroid, adrenal glands	[55]
$PSA^{Cre}Pten^{flox}$	Conditional KO	FVB	2005	Various stages of hyper/displasia High translational potential	Rare lymph nodes metastases	[56]
$PB^{Cre}Rb^{flox}$	Conditional KO	C57BL/6	2004	Hyperplasia with loss of basement membrane integrity	Insufficient transformation	[57]
$PB^{Cre4}p53^{flox}Rb^{flox}$	Conditional KO	C57BL/6xDBA2 × FVB/N	2006	Metastatic carcinoma (also with distant metastases)	Rare skeletal metastases	[58]
$PB^{Cre4}Apc^{flox}$	Conditional KO	C57Bl/6J and 129Sv/J	2007	PIN followed by locally adenocarcinoma	Not distant metastases displayed	[59]
$PB^{Cre4}IGF\text{-}1^{flox}$	Conditional KO	FVB/NJ	2008	Hyperplasia	Insufficient transformation	[60]
$PB^{Cre4}Brca2^{flox}p53^{flox}$	Conditional KO	Mixed genetic background	2010	Early HGPIN (from 12 mths) due to high DNA damage	Rare metastasis	[61]

HGPIN: high-grade prostatic intraepithelial neoplasia.

metastasis in lymph nodes, lungs, liver, kidneys, spleen, and femur [89].

This procedure allows preserving the tumor cells heterogeneity; in fact different studies, focused on prostatic cancer but also on many other different tumors, have shown that during the first phases of xenotransplantation the various tumor cells subpopulation are subjected to an anoxia status caused by the total absence of vascularization that make a selective pressure on them and only the most resistant cells variant can tolerate this environment; the SRC implantation attenuates these hard conditions. This statements have been supported by different studies that confirmed the high similarity between SRC xenograft and the parent tumors in terms of androgen sensitivity, histopathology, biomarkers expression, and metastatic potential [90–93]. Furthermore it has been demonstrated that also the subcutaneous reengraftment, in NSG or NOD-SCID mice, is improved after a well SRC establishment of the insert (TR ~ 95%); this procedure is used to better control the tumor growth, therapeutic responsiveness, or metastatic potential [94].

Given this data we can consider the PDX mouse models like a powerful tool to study the biology of cancer from early stages of tumor progression, until the metastatic dissemination, without losing architectural tissue features or molecular and genetic basis of the disease.

4. The "Big Things" in PCa Modelling: PDX 3D Spheroids and Humanized Mice

To date the research on prostate cancer has been hindered not only by the lack of relevant tumor models for clinical use, but also by the heterogeneity of cancer patients. During the last years many studies have investigated the use of PDX derived cell lines to generate disease models; in particular the use of 3D cellular culture was favored with respect to using the 2D monolayer cell lines. 3D spheroids more closely resemble in vivo tissue in terms of cellular communication and the development of extracellular matrices, while standard 2D cell cultures are inadequate representations of this environment, which often makes them unreliable predictors of in vivo drug efficacy and toxicity [18, 95–97]. These evidences reveal that the cell stimulation by environment represents a crucial feature to generate a better disease model; for instance, the bone metastatic PCa cells, whether derived from cell lines or primary PDX tumor tissue, show poor viability and the inability to grow in 2D culture; this is an established phenomenon that indicates the lack of critical components from the bone microenvironment upon which these highly adapted cells depend [98, 99]. To overcome these critical issues, the PDX cancer cells were encapsulated within three-dimensional hyaluronic acid-based hydrogels (HA); such a system has demonstrated that the hydrogel maintains the viability of the cells with the native PDX continuous expression of the androgen receptor [17]. The hydrogel encapsulation provides the means to fully recapitulate the tumor microenvironment with precise, tunable control over architectural and mechanical cues and/or critical cell–extracellular matrix interactions, specifically, as a ubiquitous component of the bone marrow where bone metastatic PCa cells reside. HA plays an active role in regulating several biological processes, including tumorigenesis, strongly justifying its use as an extracellular matrix analogue for culturing bone metastatic tumor cells in vitro [100]. Fong et al. showed that 3D PDX PCa cells exhibited an increased resistance to docetaxel as compared to a standard cell line commonly used in PCa research. The discoveries translation from mouse models to clinical trials has been hampered by the genetic differences between human and inbreed mouse strains and also by the inability to recapitulate human immunological system; for these reasons new and more performing humanized models are required; these tools represent useful ground-breaking platforms for cancer research. To generate humanized mice with functional human immune system, animals with severe immunodeficiency as NOD scid gamma (NSG™) are used; they have a severe combined immune deficiency mutation (scid) and IL2 receptor gamma chain deficiency, resulting in a lack of mature T cells and B cells and impaired NK cells, and are deficient in cytokine signalling [101, 102]. In the last few years, in order to eliminate the remaining adaptive and innate immunity in host mice, the animals are inoculated with Human Peripheral Blood Mononuclear Cells (PBMCs) or hematopoietic stem cells CD34+ (HSCs) to create a stable human immune system. PDX-engrafted humanized-NSG models represent the next step in cancer modelling, because they offer a unique platform to examine human T cell-dependent and B cell-dependent responses against clinically relevant tumors and to induce the immune system action versus specific tumor types. In PCa research these models can be considered as a highly validated instrument in human tumor microenvironment studies, also to test tumor response to both Standard Oncologic Cares treatments and novel compounds. They represent an affordable approach to validate single immune-based as well as preclinical combination therapies and allowing new individualized cancer treatments [102, 103].

5. Conclusion

Major limitation in prostate cancer research is the lack of relevant preclinical models, which allow studying the molecular mechanisms of tumorigenesis. In fact, advanced in vitro and in vivo models represent an indispensable requirement for the development of new therapeutic strategies. Currently there is a continued research for innovative PCa in vivo models with greater fidelity to disease, which try to foster the translation of preclinical findings into the clinic, particularly to satisfy the need to identify new treatments that will eradicate PCa metastases growing in bone.

The xenograft models represent a great tool to study the mechanisms underlying many human tumors, including efficacy of specific treatments, or cancer stem cell-like properties.

Nevertheless they show some limits related to a compromised immune system of the host that instead becomes crucial in human PCa, especially in metastatic dissemination pattern. In addition, using stabilized or primary tumor cell line, in xenograft, the complete bypassing of all the tumor initiation stages as the interaction with microenvironment or angiogenesis process has been observed. Using cell lines

derived from human metastasis, also the metastatic development was impaired [104].

The allograft mouse models results are widely used because they overcome the limits represented by the use of an immunosuppressed host; in this way it is possible to study in depth the interaction between tumor progression and immune system; on the other hand they do not show any limitations linked with the use of not human biological materials.

The GEMMs have been allowed to reproduce the similar genetic alterations that occur in human. So we can divide all the transgenic mouse models discussed in two different categories, on the basis of typical features. The first-generation GEMMs showed an aggressive phenotype, often with metastatic proliferation, castration-resistant PCa, due to the SV40 Tag action on p53 and pRB (not present in human), and a high incidence of neuroendocrine aberrant transformation. Instead the second generation, created through ectopic expression of endogenous oncogenic effectors, seems to not be able to reproduce the different human disease stages of PCa in mouse.

The last generation of preclinical mouse models is represented by PDXs that offer a powerful means for studying biological pathways in cancer and for testing new drugs. Given the data reported, they seem to closely reproduce the progression of PCa, representing a better predictive model compared with all those that are generated by established or primary cell line transplantation, further tracking the various passages of tumor progression, from implantation to metastatic dissemination. Instead, especially in PCa models, we have described the different issues that occur during the procedures, correlated with the choice of the site of implantation; this leads to a less broad availability of prostatic tumor PDX models than others, as breast cancer PDX, that can be developed through transplantation in different sites: interscapular or mammary fat pad and renal capsule.

To date many scientists have developed different tools to overcome the limits of the PDXs; one of the most promising ones seems to be the in vitro PDX 3D cell cultures. This procedure considers all the PDX passages, with the advantage of reducing the number of animal hosts [17], subsequently transferring all the experimental conditions in 3D cell cultures. This technology represents a valid preclinical model that bypasses the issues of 2D monolayer cell cultures; it may be used for a rapid and high throughput platform to assess drug efficacy and to find new predictive biomarkers for novel targeted therapies [91].

The models discussed here have considerable importance to understand the tumor pathogenesis and the complex biology of PCa. They also represent a promising support to enhance development of new approaches to prevention, detection, and treatment of this malignancy. These tools will be useful for a better and faster pharmacological screening in drug discovery and personalized medicine. Furthermore, PDX mouse models will allow a more profound knowledge about a still unexplored area of research in preclinical mouse models generation such as the interaction between human xenogenic stroma and the neoplasm. In the near future, new models for translational research are expected to be generated; they will aim to ameliorate the correlation between results obtained in animal models and human patients. Given the data it could be necessary to generate new preclinical mouse models to enhance understanding of PCa development and progression to metastasis.

Competing Interests

The authors confirm that this paper's content has no potential competing interests.

Authors' Contributions

Domenica Rea and Vitale del Vecchio contributed equally and are co-first authors.

Acknowledgments

This work was supported by Italian Ministry of Health RF-2010-2316780. The authors would like to express their gratitude to Mr. Massimiliano Spinelli, Data Manager of Animal Facility Unit, Department of Experimental Oncology, Istituto Nazionale per lo Studio e la Cura dei Tumori "Fondazione G. Pascale", IRCCS, Naples, Italy, for kind help in providing informatic assistance.

References

[1] A. R. Mehta and A. J. Armstrong, "Tasquinimod in the treatment of castrate-resistant prostate cancer—current status and future prospects," *Therapeutic Advances in Urology*, vol. 8, no. 1, pp. 9–18, 2016.

[2] A. Jemal, R. Siegel, E. Ward et al., "Cancer statistics, 2008," *CA Cancer Journal for Clinicians*, vol. 58, no. 2, pp. 71–96, 2008.

[3] M. Saar, C. Körbel, V. Jung et al., "Experimental orthotopic prostate tumor in nude mice: techniques for local cell inoculation and three-dimensional ultrasound monitoring," *Urologic Oncology: Seminars and Original Investigations*, vol. 30, no. 3, pp. 330–338, 2012.

[4] R. Siegel, J. Ma, Z. Zou, and A. Jemal, "Cancer statistics, 2014," *CA: A Cancer Journal for Clinicians*, vol. 64, no. 1, pp. 9–29, 2014.

[5] Y. I. Lee, H. M. Lee, J. K. Jo et al., "Association between seminal vesicle invasion and prostate cancer detection location after transrectal systemic biopsy among men who underwent radical prostatectomy," *PLoS One*, vol. 11, no. 2, article e0148690, 2016.

[6] T. M. Beer, A. J. Armstrong, D. E. Rathkopf et al., "Enzalutamide in metastatic prostate cancer before chemotherapy," *The New England Journal of Medicine*, vol. 371, no. 5, pp. 424–433, 2014.

[7] J. S. de Bono, C. J. Logothetis, A. Molina et al., "Abiraterone and increased survival in metastatic prostate cancer," *The New England Journal of Medicine*, vol. 364, no. 21, pp. 1995–2005, 2011.

[8] G. R. Thoreson, B. A. Gayed, P. H. Chung, and G. V. Raj, "Emerging therapies in castration resistant prostate cancer," *The Canadian Journal of Urology*, vol. 21, no. 2, supplement 1, pp. 98–105, 2014.

[9] K. C. Valkenburg and B. O. Williams, "Mouse models of prostate cancer," *Prostate Cancer*, vol. 2011, Article ID 895238, 22 pages, 2011.

[10] J. Dai, C. L. Hall, J. Escara-Wilke, A. Mizokami, J. M. Keller, and E. T. Keller, "Prostate cancer induces bone metastasis through Wnt-induced bone morphogenetic protein-dependent and independent mechanisms," *Cancer Research*, vol. 68, no. 14, pp. 5785–5794, 2008.

[11] V. A. DiPippo, H. M. Nguyen, L. G. Brown, W. C. Olson, R. L. Vessella, and E. Corey, "Addition of PSMA ADC to enzalutamide therapy significantly improves survival in in vivo model of castration resistant prostate cancer," *The Prostate*, vol. 76, no. 3, pp. 325–334, 2016.

[12] K. Chi, S. J. Hotte, A. M. Joshua et al., "Treatment of mCRPC in the AR-axis-targeted therapy-resistant state," *Annals of Oncology*, vol. 26, no. 10, Article ID mdv267, pp. 2044–2056, 2015.

[13] Y. N. S. Wong, R. Ferraldeschi, G. Attard, and J. De Bono, "Evolution of androgen receptor targeted therapy for advanced prostate cancer," *Nature Reviews Clinical Oncology*, vol. 11, no. 6, pp. 365–376, 2014.

[14] X. Wang, M. K.-D. Julio, K. D. Economides et al., "A luminal epithelial stem cell that is a cell of origin for prostate cancer," *Nature*, vol. 461, no. 7263, pp. 495–500, 2009.

[15] G. P. Risbridger and R. A. Taylor, "The complexities of identifying a cell of origin for human prostate cancer," *Asian Journal of Andrology*, vol. 13, no. 1, pp. 118–119, 2011.

[16] K. J. Pienta, C. Abate-Shen, D. B. Agus et al., "The current state of preclinical prostate cancer animal models," *Prostate*, vol. 68, no. 6, pp. 629–639, 2008.

[17] E. L. S. Fong, M. Martinez, J. Yang et al., "Hydrogel-based 3D model of patient-derived prostate xenograft tumors suitable for drug screening," *Molecular Pharmaceutics*, vol. 11, no. 7, pp. 2040–2050, 2014.

[18] J. J. Tentler, A. C. Tan, C. D. Weekes et al., "Patient-derived tumour xenografts as models for oncology drug development," *Nature Reviews Clinical Oncology*, vol. 9, no. 6, pp. 338–350, 2012.

[19] D. Siolas and G. J. Hannon, "Patient-derived tumor xenografts: transforming clinical samples into mouse models," *Cancer Research*, vol. 73, no. 17, pp. 5315–5319, 2013.

[20] R. Kirk, "Prostate cancer from basal cells," *Nature Reviews Clinical Oncology*, vol. 7, article 550, 2010.

[21] S. B. Shappell, G. V. Thomas, R. L. Roberts et al., "Prostate pathology of genetically engineered mice: definitions and classification. the consensus report from the bar harbor meeting of the mouse models of human cancer consortium prostate pathology committee," *Cancer Research*, vol. 64, no. 6, pp. 2270–2305, 2004.

[22] R. A. DePinho, "The age of cancer," *Nature*, vol. 408, no. 6809, pp. 248–254, 2000.

[23] W. M. van Weerden, C. M. A. De Ridder, C. L. Verdaasdonk et al., "Development of seven new human prostate tumor xenograft models and their histopathological characterization," *The American Journal of Pathology*, vol. 149, no. 3, pp. 1055–1062, 1996.

[24] N. Craft, Y. Shostak, M. Carey, and C. L. Sawyers, "A mechanism for hormone-independent prostate cancer through modulation of androgen receptor signaling by the HER-2/neu tyrosine kinase," *Nature Medicine*, vol. 5, no. 3, pp. 280–285, 1999.

[25] J. A. Nemeth, J. F. Harb, U. Barroso Jr., Z. He, D. J. Grignon, and M. L. Cher, "Severe combined immunodeficient-hu model of human prostate cancer metastasis to human bone," *Cancer Research*, vol. 59, no. 8, pp. 1987–1993, 1999.

[26] J. M. D'Antonio, D. J. van der Griend, L. Antony et al., "Loss of androgen receptor-dependent growth suppression by prostate cancer cells can occur independently from acquiring oncogenic addiction to androgen receptor signaling," *PLoS ONE*, vol. 5, no. 7, Article ID e11475, 2010.

[27] Q. Zhang, X. J. Yang, S. D. Kundu et al., "Blockade of transforming growth factor-β signaling in tumor-reactive $CD8^+$ T cells activates the antitumor immune response cycle," *Molecular Cancer Therapeutics*, vol. 5, no. 7, pp. 1733–1743, 2006.

[28] J. Veldscholte, C. Ris-Stalpers, G. G. J. M. Kuiper et al., "A mutation in the ligand binding domain of the androgen receptor of human INCaP cells affects steroid binding characteristics and response to anti-androgens," *Biochemical and Biophysical Research Communications*, vol. 173, no. 2, pp. 534–540, 1990.

[29] C. A. Pettaway, S. Pathak, G. Greene et al., "Selection of highly metastatic variants of different human prostatic carcinomas using orthotopic implantation in nude mice," *Clinical Cancer Research*, vol. 2, no. 9, pp. 1627–1636, 1996.

[30] M. E. Kaighn, K. S. Narayan, Y. Ohnuki, J. F. Lechner, and L. W. Jones, "Establishment and characterization of a human prostatic carcinoma cell line (PC-3)," *Investigative Urology*, vol. 17, no. 1, pp. 16–23, 1979.

[31] B. A. Foster, J. R. Gingrich, E. D. Kwon, C. Madias, and N. M. Greenberg, "Characterization of prostatic epithelial cell lines derived from transgenic adenocarcinoma of the mouse prostate (TRAMP) model," *Cancer Research*, vol. 57, no. 16, pp. 3325–3330, 1997.

[32] N. M. Greenberg, F. DeMayo, M. J. Finegold et al., "Prostate cancer in a transgenic mouse," *Proceedings of the National Academy of Sciences of the United States of America*, vol. 92, no. 8, pp. 3439–3443, 1995.

[33] J. Jiao, S. Wang, R. Qiao et al., "Murine cell lines derived from Pten null prostate cancer show the critical role of PTEN in hormone refractory prostate cancer development," *Cancer Research*, vol. 67, no. 13, pp. 6083–6091, 2007.

[34] Y. Hu, T. Wang, G. D. Stormo, and J. I. Gordon, "RNA interference of achaete-scute homolog 1 in mouse prostate neuroendocrine cells reveals its gene targets and DNA binding sites," *Proceedings of the National Academy of Sciences of the United States of America*, vol. 101, no. 15, pp. 5559–5564, 2004.

[35] D. P. Lane and L. V. Crawford, "T antigen is bound to a host protein in SV40-transformed cells," *Nature*, vol. 278, no. 5701, pp. 261–263, 1979.

[36] J. A. DeCaprio, J. W. Ludlow, J. Figge et al., "SV40 large tumor antigen forms a specific complex with the product of the retinoblastoma susceptibility gene," *Cell*, vol. 54, no. 2, pp. 275–283, 1988.

[37] I. G. Maroulakou, M. Anver, L. Garrett, and J. E. Green, "Prostate and mammary adenocarcinoma in transgenic mice carrying a rat C3(1) simian virus 40 large tumor antigen fusion gene," *Proceedings of the National Academy of Sciences of the United States of America*, vol. 91, no. 23, pp. 11236–11240, 1994.

[38] N. M. Greenberg, F. J. DeMayo, P. C. Sheppard et al., "The rat probasin gene promoter directs hormonally and developmentally regulated expression of a heterologous gene specifically to the prostate in transgenic mice," *Molecular Endocrinology*, vol. 8, no. 2, pp. 230–239, 1994.

[39] C. Perez-Stable, N. H. Altman, J. Brown, M. Harbison, C. Cray, and B. A. Roos, "Prostate, adrenocortical, and brown adipose tumors in fetal globin/T antigen transgenic mice," *Laboratory Investigation*, vol. 74, no. 2, pp. 363–373, 1996.

[40] Y. Yan, P. C. Sheppard, S. Kasper et al., "Large fragment of the probasin promoter targets high levels of transgene expression to the prostate of transgenic mice," *Prostate*, vol. 32, no. 2, pp. 129–139, 1997.

[41] O. Klezovitch, J. Chevillet, J. Mirosevich, R. L. Roberts, R. J. Matusik, and V. Vasioukhin, "Hepsin promotes prostate cancer progression and metastasis," *Cancer Cell*, vol. 6, no. 2, pp. 185–195, 2004.

[42] H. Wennbo, J. Kindblom, O. G. P. Ísaksson, and J. Törnell, "Transgenic mice overexpressing the prolactin gene develop dramatic enlargement of the prostate gland," *Endocrinology*, vol. 138, no. 10, pp. 4410–4415, 1997.

[43] J. DiGiovanni, K. Kiguchi, A. Frijhoff et al., "Deregulated expression of insulin-like growth factor 1 in prostate epithelium leads to neoplasia in transgenic mice," *Proceedings of the National Academy of Sciences of the United States of America*, vol. 97, no. 7, pp. 3455–3460, 2000.

[44] M. Stanbrough, I. Leav, P. W. L. Kwan, G. J. Bubley, and S. P. Balk, "Prostatic intraepithelial neoplasia in mice expressing an androgen receptor transgene in prostate epithelium," *Proceedings of the National Academy of Sciences of the United States of America*, vol. 98, no. 19, pp. 10823–10828, 2001.

[45] G. Jenster, "The role of the androgen receptor in the development and progression of prostate cancer," *Seminars in Oncology*, vol. 26, no. 4, pp. 407–421, 1999.

[46] K. W. Freeman, B. E. Welm, R. D. Gangula et al., "Inducible prostate intraepithelial neoplasia with reversible hyperplasia in conditional FGFR1-expressing mice," *Cancer Research*, vol. 63, no. 23, pp. 8256–8263, 2003.

[47] A. Scherl, J.-F. Li, R. D. Cardiff, and N. Schreiber-Agus, "Prostatic intraepithelial neoplasia and intestinal metaplasia in prostates of Probasin-RAS transgenic mice," *Prostate*, vol. 59, no. 4, pp. 448–459, 2004.

[48] Z. Li, M. Szabolcs, J. D. Terwilliger, and A. Efstratiadis, "Prostatic intraepithelial neoplasia and adenocarcinoma in mice expressing a probasin-Neu oncogenic transgene," *Carcinogenesis*, vol. 27, no. 5, pp. 1054–1067, 2006.

[49] S. A. Tomlins, B. Laxman, S. Varambally et al., "Role of the TMPRSS2-ERG gene fusion in prostate cancer," *Neoplasia*, vol. 10, no. 2, pp. 177–188, 2008.

[50] D. Lohnes, P. Kastner, A. Dierich, M. Mark, M. LeMeur, and P. Chambon, "Function of retinoic acid receptor γ in the mouse," *Cell*, vol. 73, no. 4, pp. 643–658, 1993.

[51] K. Nakayama, N. Ishida, M. Shirane et al., "Mice lacking $p27^{Kip1}$ display increased body size, multiple organ hyperplasia, retinal dysplasia, and pituitary tumors," *Cell*, vol. 85, no. 5, pp. 707–720, 1996.

[52] R. Bhatia-Gaur, A. A. Donjacour, P. J. Sciavolino et al., "Roles for Nkx3.1 in prostate development and cancer," *Genes and Development*, vol. 13, no. 8, pp. 966–977, 1999.

[53] A. Di Cristofano, B. Pesce, C. Cordon-Cardo, and P. P. Pandolfi, "Pten is essential for embryonic development and tumour suppression," *Nature Genetics*, vol. 19, no. 4, pp. 348–355, 1998.

[54] C. Abate-Shen, W. A. Banach-Petrosky, X. Sun et al., "Nkx3.1; Pten mutant mice develop invasive prostate adenocarcinoma and lymph node metastases," *Cancer Research*, vol. 63, no. 14, pp. 3886–3890, 2003.

[55] S. S. Couto, M. Cao, P. C. Duarte et al., "Simultaneous haploinsufficiency of Pten and Trp53 tumor suppressor genes accelerates tumorigenesis in a mouse model of prostate cancer," *Differentiation*, vol. 77, no. 1, pp. 103–111, 2009.

[56] S. Wang, J. Gao, Q. Lei et al., "Prostate-specific deletion of the murine Pten tumor suppressor gene leads to metastatic prostate cancer," *Cancer Cell*, vol. 4, no. 3, pp. 209–221, 2003.

[57] L. A. Maddison, B. W. Sutherland, R. J. Barrios, and N. M. Greenberg, "Conditional deletion of Rb causes early stage prostate cancer," *Cancer Research*, vol. 64, no. 17, pp. 6018–6025, 2004.

[58] Z. Zhou, A. Flesken-Nikitin, D. C. Corney et al., "Synergy of p53 and Rb deficiency in a conditional mouse model for metastatic prostate cancer," *Cancer Research*, vol. 66, no. 16, pp. 7889–7898, 2006.

[59] K. J. Bruxvoort, H. M. Charbonneau, T. A. Giambernardi et al., "Inactivation of Apc in the mouse prostate causes prostate carcinoma," *Cancer Research*, vol. 67, no. 6, pp. 2490–2496, 2007.

[60] B. W. Sutherland, S. E. Knoblaugh, P. J. Kaplan-Lefko, F. Wang, M. Holzenberger, and N. M. Greenberg, "Conditional deletion of insulin-like growth factor-I receptor in prostate epithelium," *Cancer Research*, vol. 68, no. 9, pp. 3495–3504, 2008.

[61] J. C. Francis, A. McCarthy, M. K. Thomsen, A. Ashworth, and A. Swain, "Brca2 and Trp53 deficiency cooperate in the progression of mouse prostate tumourigenesis," *PLoS Genetics*, vol. 6, no. 6, pp. 1–9, 2010.

[62] J. M. Chan, M. J. Stampfer, E. Giovannucci et al., "Plasma insulin-like growth factor-I and prostate cancer risk: a prospective study," *Science*, vol. 279, no. 5350, pp. 563–566, 1998.

[63] T. Sorlie, C. M. Perou, R. Tibshirani et al., "Gene expression patterns of breast carcinomas distinguish tumor subclasses with clinical implications," *Proceedings of the National Academy of Sciences of the United States of America*, vol. 98, no. 19, pp. 10869–10874, 2001.

[64] N. Shimizu, M. Ohtsubo, and S. Minoshima, "MutationView/KMcancerDB: a database for cancer gene mutations," *Cancer Science*, vol. 98, no. 3, pp. 259–267, 2007.

[65] A. Goodspeed, L. M. Heiser, J. W. Gray, and J. C. Costello, "Tumor-derived cell lines as molecular models of cancer pharmacogenomics," *Molecular Cancer Research*, vol. 14, no. 1, pp. 3–13, 2016.

[66] S. Domcke, R. Sinha, D. A. Levine, C. Sander, and N. Schultz, "Evaluating cell lines as tumour models by comparison of genomic profiles," *Nature Communications*, vol. 4, article 2126, 2013.

[67] P. Loukopoulos, K. Kanetaka, M. Takamura, T. Shibata, M. Sakamoto, and S. Hirohashi, "Orthotopic transplantation models of pancreatic adenocarcinoma derived from cell lines and primary tumors and displaying varying metastatic activity," *Pancreas*, vol. 29, no. 3, pp. 193–203, 2004.

[68] Y. S. Derose, G. Wang, Y.-C. Lin et al., "Tumor grafts derived from women with breast cancer authentically reflect tumor pathology, growth, metastasis and disease outcomes," *Nature Medicine*, vol. 17, no. 11, pp. 1514–1520, 2011.

[69] C. C. Whiteford, S. Bilke, B. T. Greer et al., "Credentialing preclinical pediatric xenograft models using gene expression and tissue microarray analysis," *Cancer Research*, vol. 67, no. 1, pp. 32–40, 2007.

[70] X. Zhao, Z. Liu, L. Yu et al., "Global gene expression profiling confirms the molecular fidelity of primary tumor-based orthotopic xenograft mouse models of medulloblastoma," *Neuro-Oncology*, vol. 14, no. 5, pp. 574–583, 2012.

[71] C. L. Morton and P. J. Houghton, "Establishment of human tumor xenografts in immunodeficient mice," *Nature Protocols*, vol. 2, no. 2, pp. 247–250, 2007.

[72] P. N. Bogner, S. K. Patnaik, R. Pitoniak et al., "Lung cancer xenografting alters microRNA profile but not immunophenotype," *Biochemical and Biophysical Research Communications*, vol. 386, no. 2, pp. 305–310, 2009.

[73] J. M. Fleming, T. C. Miller, M. J. Meyer, E. Ginsburg, and B. K. Vonderhaar, "Local regulation of human breast xenograft models," *Journal of Cellular Physiology*, vol. 224, no. 3, pp. 795–806, 2010.

[74] J. E. Talmadge, R. K. Singh, I. J. Fidler, and A. Raz, "Murine models to evaluate novel and conventional therapeutic strategies for cancer," *The American Journal of Pathology*, vol. 170, no. 3, pp. 793–804, 2007.

[75] A. Bergamaschi, G. O. Hjortland, T. Triulzi et al., "Molecular profiling and characterization of luminal-like and basal-like in vivo breast cancer xenograft models," *Molecular Oncology*, vol. 3, no. 5-6, pp. 469–482, 2009.

[76] B. Rubio-Viqueira, A. Jimeno, G. Cusatis et al., "An in vivo platform for translational drug development in pancreatic cancer," *Clinical Cancer Research*, vol. 12, no. 15, pp. 4652–4661, 2006.

[77] R. F. Gittes, "The nude mouse—its use as tumor-bearing model of the prostate," *Progress in Clinical and Biological Research*, vol. 37, pp. 31–37, 1980.

[78] M. A. Jones, G. Williams, and A. J. S. Davies, "Value of xenografts in the investigation of prostatic function: preliminary communication," *Journal of the Royal Society of Medicine*, vol. 73, no. 10, pp. 708–712, 1980.

[79] L. M. Reid, N. Minato, I. Gresser, J. Holland, A. Kadish, and B. R. Bloom, "Influence of anti-mouse interferon serum on the growth and metastasis of tumor cells persistently infected with virus and of human prostatic tumors in athymic nude mice," *Proceedings of the National Academy of Sciences of the United States of America*, vol. 78, no. 2, pp. 1171–1175, 1981.

[80] Y. Wang, M. P. Revelo, D. Sudilovsky et al., "Development and characterization of efficient xenograft models for benign and malignant human prostate tissue," *The Prostate*, vol. 64, no. 2, pp. 149–159, 2005.

[81] Y. Shimosato, T. Kameya, K. Nagai et al., "Transplantation of human tumors in nude mice," *Journal of the National Cancer Institute*, vol. 56, no. 6, pp. 1251–1260, 1976.

[82] Z. Csapo, K. Brand, R. Walther, and K. Fokas, "Comparative experimental study of the serum prostate specific antigen and prostatic acid phosphatase in serially transplantable human prostatic carcinoma lines in nude mice," *The Journal of Urology*, vol. 140, no. 5, pp. 1032–1038, 1988.

[83] W. J. Huss, D. R. Gray, E. S. Werdin, W. K. Funkhouser Jr., and G. J. Smith, "Evidence of pluripotent human prostate stem cells in a human prostate primary xenograft model," *Prostate*, vol. 60, no. 2, pp. 77–90, 2004.

[84] W. Hoehn, F. H. Schroeder, J. F. Reimann, A. C. Joebsis, and P. Hermanek, "Human prostatic adenocarcinoma: some characteristics of a serially transplantable line in nude mice (PC 82)," *The Prostate*, vol. 1, no. 1, pp. 95–104, 1980.

[85] D. R. McCulloch, K. Opeskin, E. W. Thompson, and E. D. Williams, "BM18: a novel androgen-dependent human prostate cancer xenograft model derived from a bone metastasis," *Prostate*, vol. 65, no. 1, pp. 35–43, 2005.

[86] D. M. Lubaroff, M. B. Cohen, L. D. Shultz, and W. G. Beamer, "Survival of human prostate carcinoma, benign hyperplastic prostate tissues, and IL-2-activated lymphocytes in SCID mice," *Prostate*, vol. 27, no. 1, pp. 32–41, 1995.

[87] C. E. Ott and F. G. Knox, "Tissue pressures and fluid dynamics in the kidney," *Federation Proceedings*, vol. 35, no. 8, pp. 1872–1875, 1976.

[88] N. J. Robertson, P. J. Fairchild, and H. Waldmann, "Ectopic transplantation of tissues under the kidney capsule," *Methods in Molecular Biology*, vol. 380, pp. 347–353, 2007.

[89] D. Lin, A. W. Wyatt, H. Xue et al., "High fidelity patient-derived xenografts for accelerating prostate cancer discovery and drug development," *Cancer Research*, vol. 74, no. 4, pp. 1272–1283, 2014.

[90] C.-H. Lee, H. Xue, M. Sutcliffe et al., "Establishment of subrenal capsule xenografts of primary human ovarian tumors in SCID mice: potential models," *Gynecologic Oncology*, vol. 96, no. 1, pp. 48–55, 2005.

[91] J.-C. Cutz, J. Guan, J. Bayani et al., "Establishment in severe combined immunodeficiency mice of subrenal capsule xenografts and transplantable tumor lines from a variety of primary human lung cancers: potential models for studying tumor progression-related changes," *Clinical Cancer Research*, vol. 12, no. 13, pp. 4043–4054, 2006.

[92] X. Dong, J. Guan, J. C. English et al., "Patient-derived first generation xenografts of non-small cell lung cancers: promising tools for predicting drug responses for personalized chemotherapy," *Clinical Cancer Research*, vol. 16, no. 5, pp. 1442–1451, 2010.

[93] D. Lin, H. Xue, Y. Wang et al., "Next generation patient-derived prostate cancer xenograft models," *Asian Journal of Andrology*, vol. 16, no. 3, pp. 407–412, 2014.

[94] D. Lin, J. Bayani, Y. Wang et al., "Development of metastatic and non-metastatic tumor lines from a patient's prostate cancer specimen-identification of a small subpopulation with metastatic potential in the primary tumor," *Prostate*, vol. 70, no. 15, pp. 1636–1644, 2010.

[95] J. Kondo, H. Endo, H. Okuyama et al., "Retaining cell-cell contact enables preparation and culture of spheroids composed of pure primary cancer cells from colorectal cancer," *Proceedings of the National Academy of Sciences of the United States of America*, vol. 108, no. 15, pp. 6235–6240, 2011.

[96] V. C. Daniel, L. Marchionni, J. S. Hierman et al., "A primary xenograft model of small-cell lung cancer reveals irreversible changes in gene expression imposed by culture in vitro," *Cancer Research*, vol. 69, no. 8, pp. 3364–3373, 2009.

[97] M. D. Landis, B. D. Lehmann, J. A. Pietenpol, and J. C. Chang, "Patient-derived breast tumor xenografts facilitating personalized cancer therapy," *Breast Cancer Research*, vol. 15, no. 1, article 201, 2013.

[98] L. A. Gurski, A. K. Jha, C. Zhang, X. Jia, and M. C. Farach-Carson, "Hyaluronic acid-based hydrogels as 3D matrices for in vitro evaluation of chemotherapeutic drugs using poorly adherent prostate cancer cells," *Biomaterials*, vol. 30, no. 30, pp. 6076–6085, 2009.

[99] X. Xu, L. A. Gurski, C. Zhang, D. A. Harrington, M. C. Farach-Carson, and X. Jia, "Recreating the tumor microenvironment in a bilayer, hyaluronic acid hydrogel construct for the growth of prostate cancer spheroids," *Biomaterials*, vol. 33, no. 35, pp. 9049–9060, 2012.

[100] E. Burdett, F. K. Kasper, A. G. Mikos, and J. A. Ludwig, "Engineering tumors: a tissue engineering perspective in cancer biology," *Tissue Engineering Part B: Reviews*, vol. 16, no. 3, pp. 351–359, 2010.

[101] M. A. Brehm, N. Jouvet, D. L. Greiner, and L. D. Shultz, "Humanized mice for the study of infectious diseases," *Current Opinion in Immunology*, vol. 25, no. 4, pp. 428–435, 2013.

[102] L. Gonzalez, N. Strbo, and E. R. Podack, "Humanized mice: novel model for studying mechanisms of human immune-based therapies," *Immunologic Research*, vol. 57, no. 1–3, pp. 326–334, 2013.

[103] Q. Zhou, J. Facciponte, M. Jin, Q. Shen, and Q. Lin, "Humanized NOD-SCID IL2rg$^{-/-}$ mice as a preclinical model for cancer research and its potential use for individualized cancer therapies," *Cancer Letters*, vol. 344, no. 1, pp. 13–19, 2014.

[104] J. T. Buijs and G. van der Pluijm, "Osteotropic cancers: from primary tumor to bone," *Cancer Letters*, vol. 273, no. 2, pp. 177–193, 2009.

Hindawi Publishing Corporation
BioMed Research International
Volume 2016, Article ID 5498271, 12 pages
http://dx.doi.org/10.1155/2016/5498271

Research Article

Longitudinal Comparison of Enzyme- and Laser-Treated Intervertebral Disc by MRI, X-Ray, and Histological Analyses Reveals Discrepancies in the Progression of Disc Degeneration: A Rabbit Study

Marion Fusellier,[1,2] Pauline Colombier,[1,3] Julie Lesoeur,[1,3] Samy Youl,[1] Stéphane Madec,[1,2] Olivier Gauthier,[1,4] Olivier Hamel,[1,5] Jérôme Guicheux,[1,3,6] and Johann Clouet[1,7,8]

[1] *Institut National de la Santé et de la Recherche Médicale (INSERM) UMRS 791, Laboratoire d'Ingénierie Ostéo-Articulaire et Dentaire (LIOAD), Group STEP "Skeletal Tissue Engineering and Physiopathology", School of Dental Surgery, 44042 Nantes, France*
[2] *Department of Diagnostic Imaging, CRIP, National Veterinary School (ONIRIS), 44307 Nantes, France*
[3] *Odontology Faculty, University of Nantes, 44093 Nantes, France*
[4] *Department of Experimental Surgery, CRIP, National Veterinary School (ONIRIS), 44307 Nantes, France*
[5] *Medicine Faculty, University of Nantes, 44093 Nantes, France*
[6] *PHU4 OTONN, University Hospital of Nantes, 44093 Nantes, France*
[7] *Department of Pharmacy, University Hospital of Nantes, 44093 Nantes, France*
[8] *Pharmacy Faculty, University of Nantes, 44093 Nantes, France*

Correspondence should be addressed to Jérôme Guicheux; jerome.guicheux@inserm.fr

Received 15 February 2016; Revised 7 April 2016; Accepted 17 April 2016

Academic Editor: Monica Fedele

Regenerative medicine is considered an attractive prospect for the treatment of intervertebral disc (IVD) degeneration. To assess the efficacy of the regenerative approach, animal models of IVD degeneration are needed. Among these animal models, chemonucleolysis based on the enzymatic degradation of the Nucleus Pulposus (NP) is often used, but this technique remains far from the natural physiopathological process of IVD degeneration. Recently, we developed an innovative animal model of IVD degeneration based on the use of a laser beam. In the present study, this laser model was compared with the chemonucleolysis model in a longitudinal study in rabbits. The effects of the treatments were studied by MRI (T2-weighted signal intensity (T2wsi)), radiography (IVD height index), and histology (NP area and Boos' scoring). The results showed that both treatments induced a degeneration of the IVD with a decrease in IVD height and T2wsi as well as NP area and an increase in Boos' scoring. The enzyme treatment leads to a rapid and acute process of IVD degeneration. Conversely, laser radiation induced more progressive and less pronounced degeneration. It can be concluded that laser treatment provides an instrumental in vivo model of slowly evolving IVD degenerative disease that can be of preclinical relevance for assessing new prophylactic biological treatments of disc degeneration.

1. Introduction

Low back pain (LBP) is an extremely frequent symptom that affects up to 20% of individuals aged from 30 to 64 years [1], and 70–85% of all people suffer from back pain at some time in life [2]. It is therefore becoming a major public health concern (approximately 650 million individuals are affected in the world) with an increasing socioeconomic cost in aging populations. In 40% of patients, this low back pain is thought to stem from intervertebral disc degenerative disease (DDD), also called discogenic LBP [3]. DDD is primarily managed by pharmacological treatments and, if unsuccessful, by surgical procedures (spine fusion or disc prosthesis) whose goal is to relieve pain. Nevertheless, these surgical treatments are particularly invasive and have limitations, despite significant improvements, notably the development of new minimally

invasive routes. Given the limitations of these therapies, regenerative medicine has recently been increasingly considered as an attractive prospect for the treatment of DDD [4].

Spontaneous degeneration of the intervertebral disc (IVD) involves mechanical processes and aging that lead to the degradation of the extracellular matrix of the Nucleus Pulposus (NP). This deterioration in turn induces dehydration of the NP that ultimately decreases IVD resistance to mechanical constraints. IVD degeneration is classically investigated, in vivo, using magnetic resonance imaging (MRI) and radiography. A decrease in the T2-weighted signal intensity (T2wsi) and a later decrease in the IVD height index are observed on MRI and X-rays, respectively. At the same time, histological analyses of the degenerated IVD usually show a cell density decrease, the loss of a clearly delimited boundary between NP and annulus fibrosus (AF), and an associated increase in the histological Boos' scoring. This Boos' scoring closely reflects the histological state of the degenerated IVD on the basis of criteria including cell density, granular changes, tear and cleft formation, and mucus degeneration.

To demonstrate the relevance of innovative regenerative medicine approaches, and before transposing the approach to humans, animal models of DDD that closely mimic the slowly evolving IVD degeneration observed in humans are required. In this context, a relevant animal model should include the following features: (1) an animal tall enough to allow introduction of therapeutic agents directly into the disc; (2) an animal that is easy to obtain and inexpensive; (3) DDD developed in a progressive time-dependent manner; and (4) DDD histologically close to spontaneous degeneration. Many models have been developed so far, but none gather the required features. Among animal models described in recent years [5, 6], two subgroups can be defined: models with spontaneous and experimentally induced disease.

The spontaneous disease models are probably among the most relevant models since they are expected to closely mimic the physiopathological process of DDD. Unfortunately, they often take too long to evolve to make them appropriate models for experimental studies.

Numerous experimentally induced DDD animal models have been used in preclinical studies and are commonly categorized in three groups: mechanical, physical, and chemical models. Among the mechanical models, mechanical overload has been induced by multiple procedures [7–14]. Most of the time, while animals used (rabbits or dogs) are large enough to consider regenerative therapies via percutaneous approaches, these models remain time-consuming, painful, ethically debatable, and expensive, particularly the canine models.

Physical models usually combine various methods of inducing disc lesions including AF disruption [15] and NP aspiration [16]. The scalpel-induced disruption of AF presents the disadvantage of being unreliable because it remains difficult to remove the same amount of AF material. NP aspiration consists of needle-assisted removal of the NP content. Although it can be used for biomechanical studies, the aspiration process is far from reflecting the progressivity and complexity of IVD degeneration.

The other commonly used animal model is chemonucleolysis [17–24], based on the intra-NP injections of proteolytic enzymes (hyaluronidase, papain, or chondroitinase ABC). These enzymes induce a chemical degradation of the NP extracellular matrix, particularly proteoglycan and collagens, which are essential for the biomechanical properties of the IVD [17]. The major limitation of chemonucleolysis is that it induces an acute degenerative process, despite the fact that it can be tuned by varying the concentration of enzyme injected into the disc. In addition, deleterious effects caused by the persistence of enzyme and the presence of metabolites could be considered as a limitation to investigate regenerative medicine approaches in these models.

In this context and considering the numerous limitations of currently available animal models, an innovative approach has been proposed using a laser radiation treatment [25]. Our preliminary data [25] demonstrated that laser treatment induced degenerative changes in rabbit IVD, making this model a promising tool to help validate cell-based strategies for the prevention and treatment of early stages of IVD degeneration. However, to further assess the relevance of laser radiation as a model of DDD, we sought to compare this model with the chemonucleolysis model, notably to evaluate the ability of laser to induce slowly evolving DDD.

In the present study, the longitudinal effects of laser and enzyme treatments were assessed for a 3-month period in 1-year-old rabbits. To evaluate the ability of laser to induce progressive DDD, degenerative changes of the IVD were followed using MRI (T2-weighted signal intensity), X-rays (IVD height), and histological Boos' scoring.

2. Materials and Methods

2.1. Ethical Aspects and Animals. All animal handling and surgical procedures were conducted according to European Community guidelines for the care and use of laboratory animals (DE 86/609/CEE). The Pays de la Loire ethics committee approved the animal study protocol (agreement CEEA.2012.16 and CEEA.2012.181).

Thirteen healthy female New Zealand white rabbits (age, 1 year; weight, 2.5–3.5 kg; Grimaud Frères, Roussay, France) were used for the study. Three of the 13 rabbits were used as controls and no surgical treatment was performed on them.

2.2. Surgical Procedure. A preoperative MRI was performed to eliminate spontaneous degenerated IVDs from the study. IVD lesions were induced under general anesthesia and fluoroscopic guidance following two methods: enzyme and laser treatment. The animals were tranquilized with an intramuscular injection of ketamine (15–20 mg/kg) and xylazine (2 mg/kg) and then put under gaseous anesthesia (NO (0.5 L/min)/O_2 (0.5 L/min)/isoflurane (2%)). A longitudinal mid-line skin incision was made from the xiphoid to the pelvic rim. The anterior side of the vertebral column from L1 to L6 was exposed via the transperitoneal approach.

Disc levels were identified under fluoroscopic guidance. Four IVDs (L2-L3, L3-L4, L4-L5, and L5-6) were used for the experiment, and the lesions were randomized according to the protocol summarized in Table 1.

Table 1: Group organization and treatments protocol.

	Group 1					Group 2					Group 3		
	Rabbit number 1	Rabbit number 2	Rabbit number 3	Rabbit number 4	Rabbit number 5	Rabbit number 6	Rabbit number 7	Rabbit number 8	Rabbit number 9	Rabbit number 10	Rabbit number 11	Rabbit number 12	Rabbit number 13
IVD L2-L3	CTRL	CTRL	CTRL	CTRL	Laser	Laser	E	E	CTRL	Laser	Laser	E	E
IVD L3-L4	CTRL	CTRL	CTRL	Laser	Laser	E	CTRL	Laser	Laser	Laser	E	CTRL	Laser
IVD L4-L5	CTRL	CTRL	CTRL	E	E	CTRL	Laser	Laser	E	E	CTRL	Laser	Laser
IVD L5-L6	CTRL	CTRL	CTRL	E	CTRL	E	Laser	E	E	CTRL	E	Laser	E
MRI and X-ray	D0	Rabbit 2: days 0 and 7 Rabbit 3: days 0, 7, 30, 60, and 90				D0 and D7					D0, D7, D30, D60, and D90		
Histology	Sacrifice at day 0	Rabbit 2: sacrifice at day 7 Rabbit 3: sacrifice at day 90				Sacrifice at day 7					Sacrifice at day 90		

CTRL: control; E: enzyme; IVD: intervertebral disc.

The enzyme treatment consists in injecting 20 μL of hyaluronidase (50 μg/μL in PBS 1x; 37.5–150 IU/mL; ref H4272; Sigma-Aldrich, St. Louis, MO, USA), using 25 Ga needle, at the lumbar IVD according to the modalities previously described [17].

Laser treatment was performed using a KaVo GENTLEray 980® diode laser as previously described [25]. Briefly, after AF puncture with a 25-gauge needle to allow the insertion of the 300 μm laser fiber, the end of the fiber was guided into the NP under fluoroscopic guidance. The parameters used were pulse sequence mode with 1.6 W pulse output, pulse length of 200 ms, pulse spacing of 200 ms, and duration of 40 s. These parameters were determined by preliminary studies [25].

The abdominal white line and skin were closed in layers with resorbable sutures.

2.3. MRI and X-Ray Scanning Procedure. For imaging procedures, the rabbits were tranquilized with an intramuscular injection of dexmedetomidine (100 μg/kg) and ketamine (15–20 mg/kg). MRI and X-rays were always performed on each rabbit at day 0 to exclude spontaneously degenerated IVDs from a further surgical procedure and then at days 7, 30, 60, and 90.

An MRI of the entire lumbar spine was performed on a 1.0 T MR scanner (Magnetom Harmony, Siemens Medical Solutions, Erlangen, Germany) using a standard body coil to obtain T2-weighted images (TR, 5000 ms; TE, 111 ms) with the following parameters: matrix, 400 × 200; field of view, 200 × 100 mm; and slice thickness, 3 mm with no interslice gap.

Plain radiographs of the spines were taken using a radiograph machine (Convix 80 generator and Universix 120 table) from Picker International (Uniontown, OH, USA). Coronal and sagittal plain radiographs of the spines were taken with a collimator-to-film distance of 100 cm, exposure of 100 mAs, and penetration power of 48 kVp.

2.4. Image Analysis. The image data were analyzed with Osirix software 3.9 (Osirix Foundation, Geneva, Switzerland).

T2-weighted signal intensity (T2wsi) was determined on MRI images on a midsagittal slice. T2wsi is measured by the ratio of NP mean weighted signal intensity divided by the spinal cord signal measured at each time point.

The index of IVD height was measured on X-rays. This index represents the mean of the ventral and the dorsal height of the disc divided by mean of the ventral and dorsal length of the adjacent vertebra. The results were expressed as relative IVD height decrease.

2.5. Histological Analysis. At days 0, 7, and 90, three rabbits were sacrificed by intramuscular injection of ketamine (15–20 mg/kg) followed by an intravenous injection of sodium pentobarbital (1.2 g/kg). For ethical reasons, we chose to limit the number of animals sacrificed and no sacrifice was performed at days 30 and 60. The lumbar IVDs were then collected from four consecutive levels (L2-L3 to L5-L6). IVDs were dissected and fixed in 10% neutral buffered formalin for 1 week and decalcified for 24 h in Decalcifier II® (Surgipath, Richmond, IL, USA). After dehydration and incubation with Histosol® (Shandom, Brussels, Belgium), specimens were embedded in paraffin and sectioned into 3 μm slices. For histological analysis, 3 μm thick paraffin sections were deparaffinized using toluene, rehydrated through a graded series of ethanol, and rinsed in distilled water. Sections were stained with hematoxylin phloxine safran (HPS) and 0.1% Alcian blue-PAS (Sigma-Aldrich, St. Louis, MO, USA) as previously described [26].

For each IVD, using HPS stainings, NP area measurements were taken using NDP view2 software (Hamamatsu Photonics) and expressed in square millimeters.

Histological sections were also analyzed using a modified Boos' scoring [27] specifically designed to characterize the histomorphology of the IVD and to evaluate the degenerative changes in the extracellular matrix of the NP. Briefly, this Boos' scoring was based on the analysis of four criteria: decrease in cell density, granular changes, tear and cleft formation, and mucus degeneration. Some parameters were ranked from 0 to 4 (granular and mucus degeneration) and others were ranked from 0 to 5 (decrease in cell density, and tear and cleft formation) depending on the intensity of the parameters tested (0, lowest; 4 or 5, highest). Three independent investigators who had expertise in reading histological slides performed a blind evaluation of histological samples.

2.6. Statistical Analysis. Statistical analysis was performed with R software. IVD height, T2wsi, Boos' scoring, and NP area were assessed for statistically significant differences using the Tukey test after an analysis of variance test. The significance level was set at 0.05.

3. Results

3.1. MRI T2-Weighted Signal Intensity Changes. To analyze the degenerative changes of rabbit intervertebral discs, we first measured the T2wsi changes using MRI. For the enzyme-treated discs, the T2wsi image showed an intense and significant decrease from day 7 (35% ± 2.35%) compared to control (2.5% ± 3%) and the laser group (8.5% ± 3.8%). This decrease was more progressive and delayed in the laser group in which it became significant only at day 90 compared with the control group (Figure 1).

3.2. IVD Height Changes. To further analyze the IVD degenerative process, we then measured the changes in disc height using X-rays. The changes observed confirm the modification observed on MRI. Indeed, for both treatments, significant and gradual IVD narrowing as compared with untreated discs was observed (Figure 2). Ninety days after surgery, 45% and 13% (±SEM) decrease in IVD height were observed in enzyme- and laser-treated discs, respectively (Figure 2). A time-course analysis also revealed that the IVD height decrease occurred more quickly with the hyaluronidase treatment compared to with the laser treatment. Indeed, the early decrease in the IVD height was significantly different between controls and enzyme-treated discs as early as day 7, while in laser-treated discs, a significant decrease in IVD height was not observed before day 90.

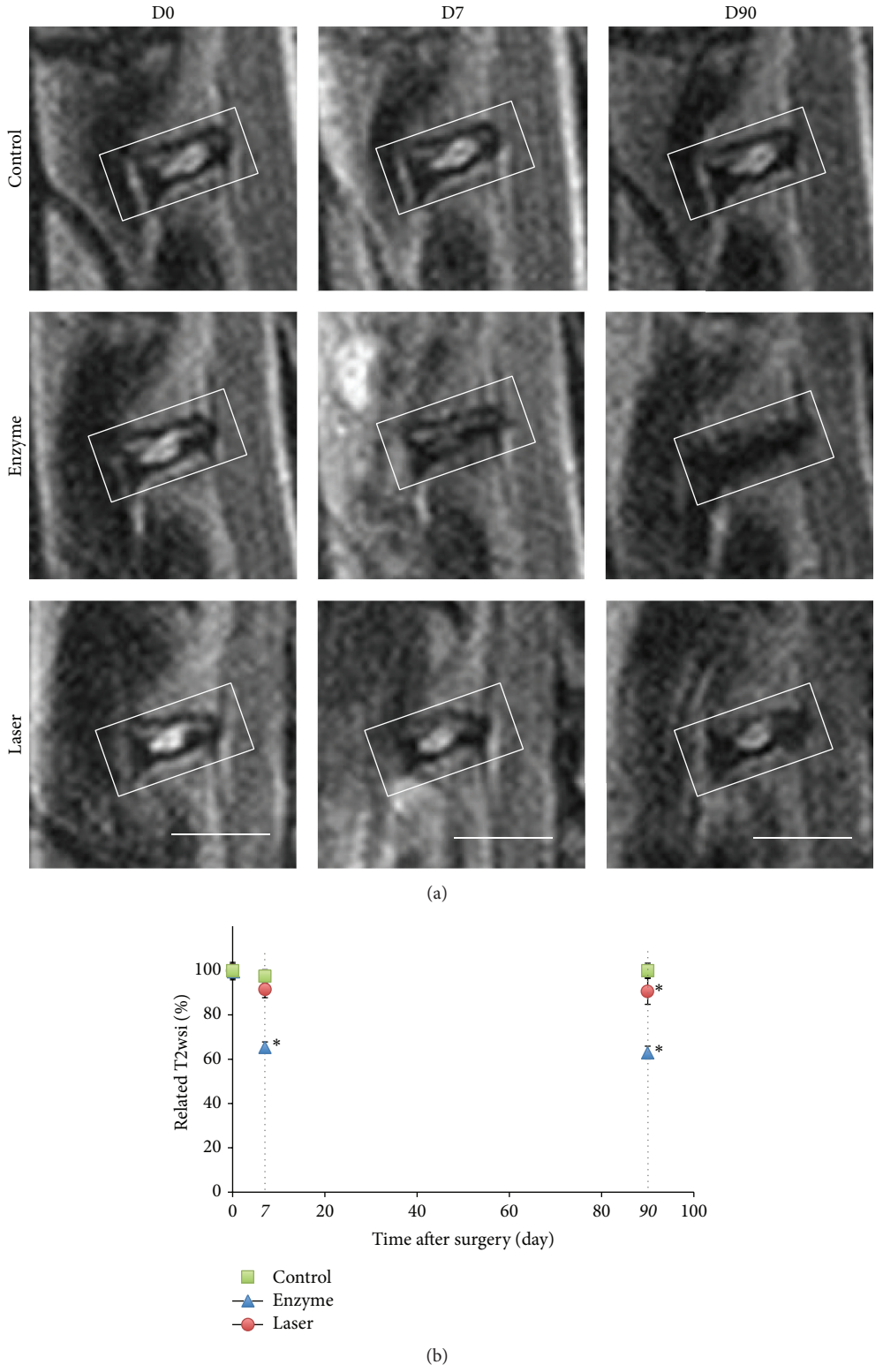

FIGURE 1: MRI images (T2-weighted midsagittal) and analysis of rabbit lumbar spines. Intervertebral discs of 1-year-old rabbits were treated according to either the enzyme technique (enzyme) or the laser procedure (laser) as described in Materials and Methods. Untreated IVDs were used as an internal control. (a) After the indicated times, a magnetic resonance imaging (MRI) scan of the spine was performed. Representative MRI scans are shown. Bar: 1 cm. (b) T2-weighted signal intensity was measured after the indicated times as described in Materials and Methods. $^{*}P < 0.05$ as compared with day 0. Values are expressed as mean ± SEM.

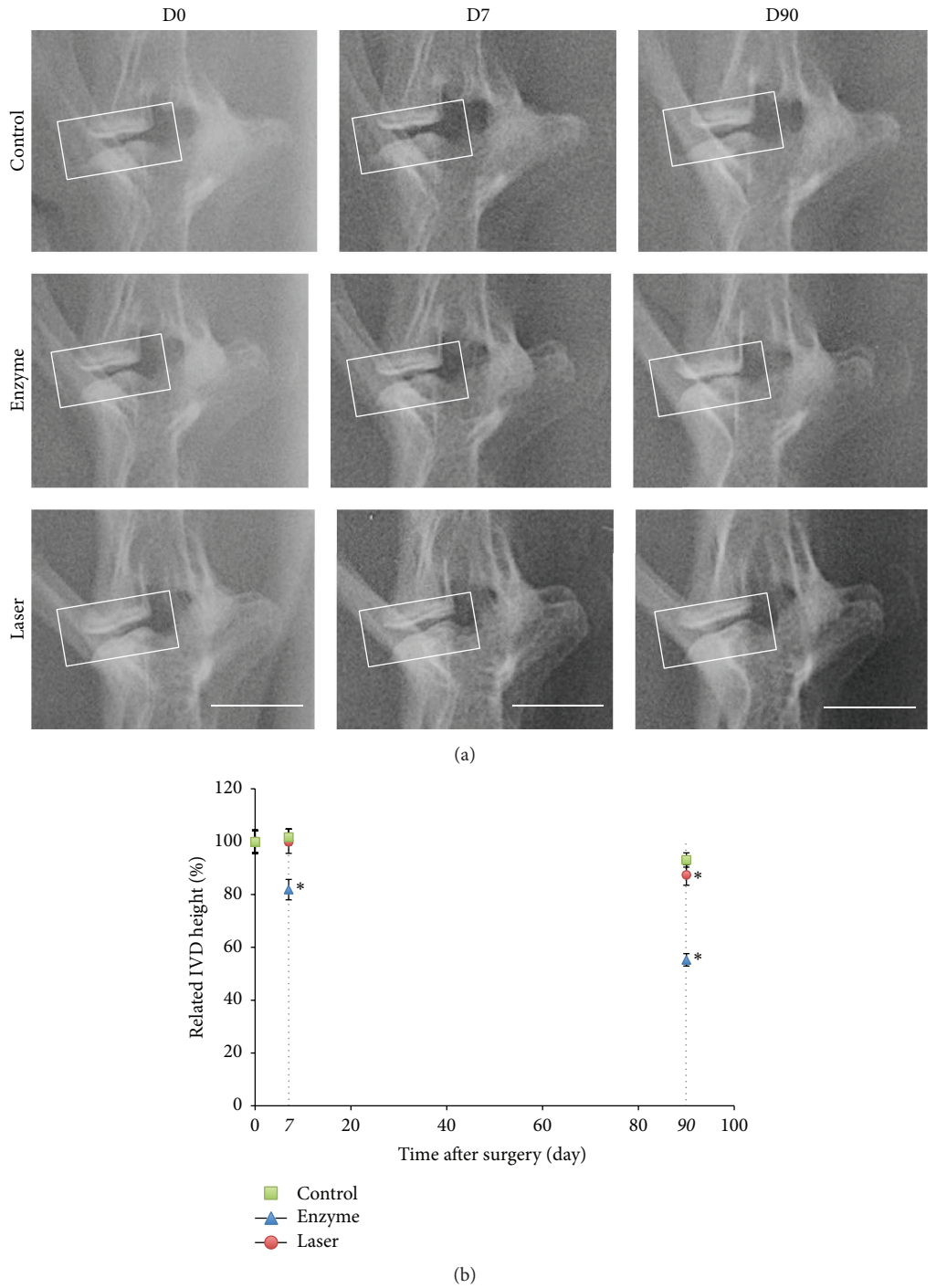

Figure 2: X-ray images and analysis of rabbit lumbar spines. Intervertebral discs of 1-year-old rabbits were treated according to either the enzyme technique (enzyme) or the laser procedure (laser) as described in Materials and Methods. Untreated IVDs (control) were used as an internal control. (a) After the indicated times, X-ray images of spines were taken. Representative X-ray images are shown. Bar: 1 cm. (b) Decrease in IVD height (%) was measured after the indicated times as described in Materials and Methods. $^{*}P < 0.05$ as compared with day 0. Values are expressed as percentage of decrease ± SEM.

3.3. Histological Analysis and Boos' Scoring. To further address whether the experimentally induced degeneration observed on MRI and radiological changes were correlated with tissue changes, we then performed histological analyses on histological stainings (HPS and BA-PAS) (Figures 3 and 4). To quantitatively assess tissue changes, the NP surface was measured and assessed with Boos' scoring (Figure 5).

Regarding HPS stainings, compared to the control condition at day 0 (Figure 3(a)), the injured IVD analysis after enzyme treatment showed a decrease in cell density at days

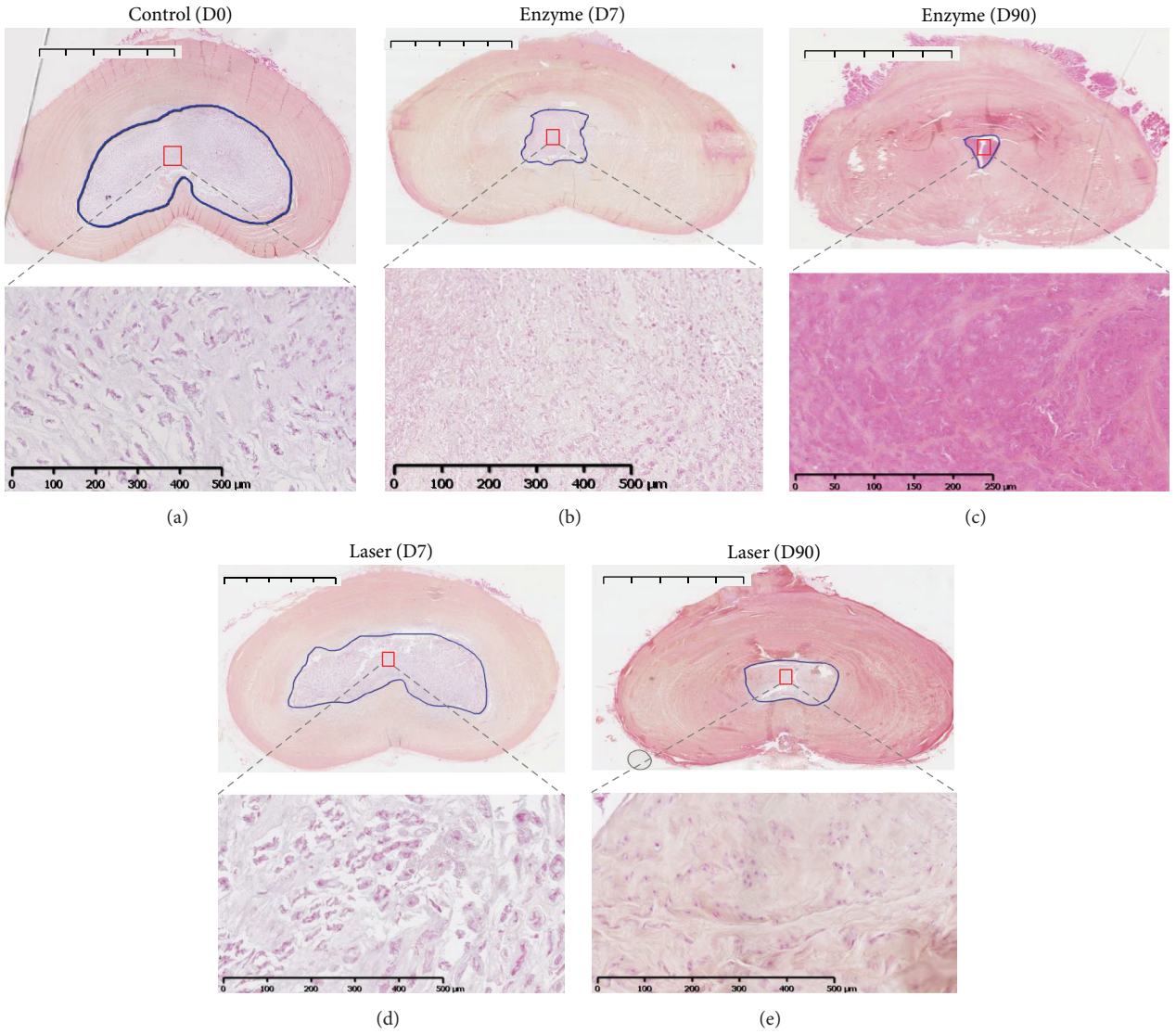

Figure 3: Histological analysis of rabbit intervertebral discs (IVDs) using hematoxylin phloxine safran (HPS) staining. IVDs of 1-year-old rabbits were treated according to either the enzyme technique (enzyme) or the laser procedure (laser) as described in Materials and Methods. IVDs were processed for histological analysis at days 0 (untreated IVD from two rabbits as internal control) and 7 and 90 days after treatment as described in Materials and Methods. Representative hematoxylin phloxine safran is shown at days 0, 7, and 90. For clarity reasons and regarding similarities in follow-up, only the control at day 0 is illustrated. Bar: 5 mm for macroscopic section image and 500 μm for magnification image.

7 and 90 (Figures 3(b) and 3(c)). Interestingly, this decrease occurred early in the enzyme-treated group beginning at day 7 (Figure 3(b)), in contrast to the laser group in which the cell density gradually decreased from day 0 to day 90 (Figures 3(d) and 3(e)). Regarding BA-PAS staining, the extracellular matrix of the NP in the control condition demonstrated no notable changes (Figure 4(a)). Conversely, an alteration of the extracellular matrix was observed in the enzyme (Figures 4(b) and 4(c)) and laser (Figures 4(d) and 4(e)) groups characterized by mucoid and granular changes that reflect extracellular matrix degeneration. Compared with changes observed in the enzyme condition (Figures 4(b) and 4(c)), the mucoid and granular changes in the laser condition (Figures 4(d) and 4(e)) were less pronounced. Moreover, the mucoid and granular changes appeared as early as day 7 in the enzyme condition (Figure 4(b)).

The degenerative changes of the NP induced by enzyme and laser treatments were finally quantitatively assessed by measuring the NP surface from the HPS section (Figure 5(a)). Compared to controls, the enzyme treatment induced a drastic decrease in the NP area as early as day 7, compared with controls (mean, 3.6 versus 20.5) but also compared with laser treatment (mean, 3.6 versus 5.6). Interestingly, no significant decrease was observed with laser treatment at day 7 compared to controls (mean, 18.1 versus 20.5). A significant decrease in the NP area was observed only at day 90 compared to the control condition (mean, 5.6 versus 20.4).

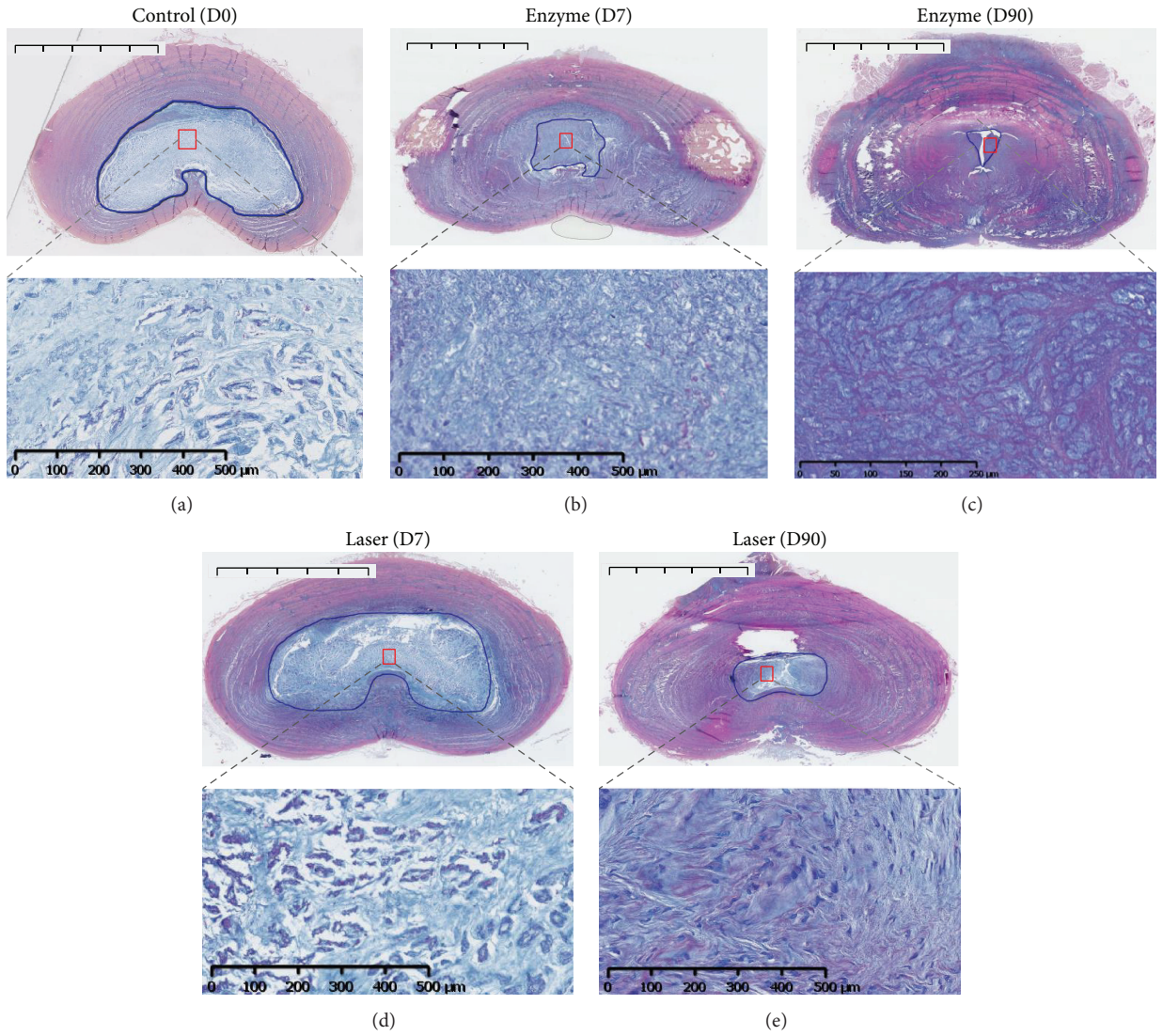

Figure 4: Histological analysis of rabbit intervertebral discs (IVDs) by Alcian blue/PAS staining (BA-PAS). IVDs of 1-year-old rabbits were treated according to either the enzyme technique (enzyme) or the laser procedure (laser) as described in Materials and Methods. IVDs were processed for histological analysis at days 0 (untreated IVD from two rabbits as internal control) and 7 and 90 days after treatment as described in Materials and Methods. Representative Alcian blue/PAS staining is shown at days 0, 7, and 90. For clarity reasons and regarding similarities in follow-up, only the control at day 0 is illustrated. Bar: 5 mm for macroscopic section image and 500 μm for magnification image.

At the same time, Boos' scoring allowed us to compile and quantitatively assess degenerative tissue changes (Figure 5(b)). In the control condition, no significant increase was observed. Conversely, an increase in both enzyme and laser conditions was observed as a function of time. Interestingly, Boos' scoring after laser treatment increased more progressively compared with the enzyme treatment, with values of approximately 9.5 and 13.5 at day 7 and 17.5 at day 90, respectively.

4. Discussion

To clinically address LBP originating from IVD degeneration (discogenic lumbalgia), tissue engineers have sought to develop cell-based approaches to functionally "regenerate" the damaged tissue [4]. To preclinically test the relevance of these cell-based approaches, animal models are required. Numerous models of degenerative disc disease have been developed. Whereas some of them are instrumental for studying the specific aspects of IVD biology or pathology, most of them fail to meet all the criteria required for the preclinical testing of IVD regenerative medicine approaches. These models are either spontaneous or experimentally induced models.

Spontaneous models use sand rat, Chinese hamster, transgenic mice, or rats [28–31] as well as nonchondrodystrophic or chondrodystrophic canine breeds [32–34]. While these models are of considerable value to study the IVD's physiopathological mechanisms, they generally remain too small to develop strategies that could be easily transferred to

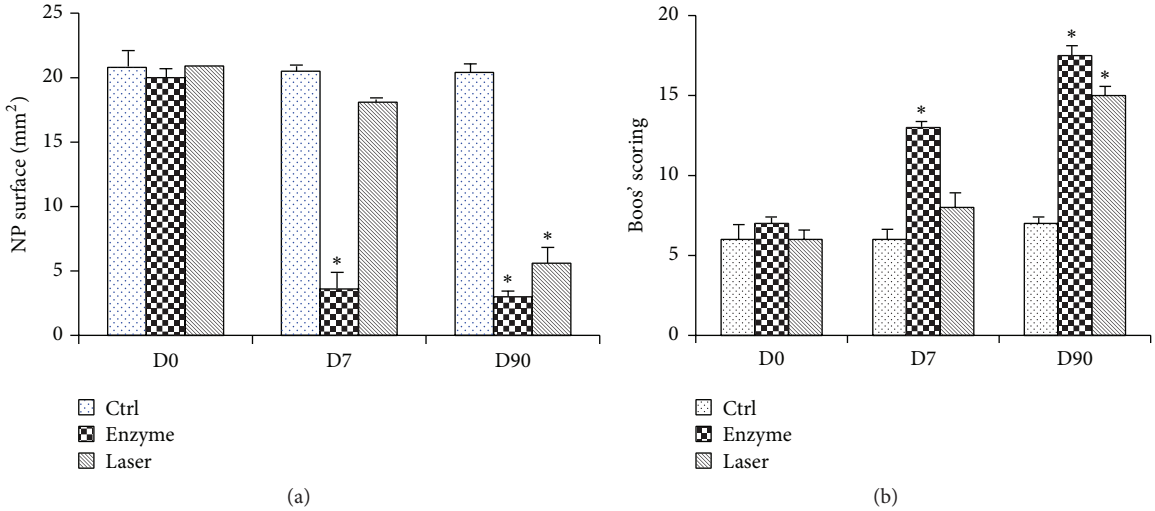

Figure 5: Evaluation of NP area and Boos' scoring for rabbit intervertebral discs (IVDs). IVDs of 1-year-old rabbits were treated according to either the enzyme technique (enzyme) or the laser procedure (laser) as described in Materials and Methods. Untreated IVDs from two rabbits were used as an internal control. NP area (a) and Boos' scoring (b) were determined for the different conditions at 0, 7, and 90 days as described in Materials and Methods. $^*P < 0.05$ compared to control. Values are expressed as mean ± SEM.

the human clinical situation. Back pain is well documented in the dog with a high prevalence of spontaneous disc hernia. However, the veterinary patients are difficult to recruit for large-scale studies in part because of the heterogeneity of the breeds and difficulties to obtain owner consent. In addition, such canine model remains problematic to implement because it implies exogenous (mechanical stress and nutritional effects) and endogenous (genetic predisposition) factors that can be difficult to control. Moreover, nonchondrodystrophic breeds develop DDD quite late in their lifespan making them inappropriate as an experimental model.

Among experimentally induced animal models, three modalities to induce IVD degeneration have been defined. First, mechanical models based on the application of overloading stimuli on the IVD using an axial dynamic loading system [7], lumbar fusion [8], tail suspension [9], torsion [10], compression [6, 11], bipedism [12], muscle stimulation [13], and resection of spinal process or facet joint [14] have been described. As spontaneous models, they are essentially suitable for physiopathological studies. Their reproducibility is generally reported to be low and they often require invasive surgical protocols that remain debatable from an ethical point of view.

Second, physical models (needle puncture [16, 35], scalpel stab of AF [15], end plate injury [36], and nucleus aspiration [16, 37–43]) have been developed in numerous species including rabbit [35], sheep [44], or pig [45, 46]. Unfortunately, aspiration and scalpel lesion have proved to be poorly reliable because of difficulties in inducing accurate and reproducible lesions to the disc. Needle puncture lesion was generally found more gradual and reproducible but tissue lesions were reported to substantially dependent on the gauge size of the needle used.

Moreover, the IVD damage induced by aspiration is quite far from spontaneous degeneration and could instead be considered as a model of disc herniation because of the removal of the cells and extracellular matrix from the center of the disc.

Third, chemical models were widely studied in numerous species such as rats [24], dogs [20, 22, 23], and even cattle [19, 21]. Hyaluronidase [17], chondroitinase ABC [23], and papain [18] were the most widely used enzymes. All of them deteriorated the extracellular matrix components, notably proteoglycans, and they were considered in evaluation of regenerative strategies of the IVD. The reliability of IVD degeneration is widely debated and the main limitation is the persistence of proteolytic enzymes, metabolites, and degradation factors that could be cytotoxic not only for IVD resident cells, but also for the injected regenerative cells. Finally, since the optimal dose of enzyme has not been clearly established, enzyme injection has usually been associated with rapid degenerative changes that fail to completely mimic the naturally occurring DDD.

Considering these animal models, new research has focused on the potential of an innovative laser treatment to induce a reliable, progressive, large, and manageable IVD degeneration model [25]. In a preliminary study, the influence of the laser treatment on IVD degeneration was compared with NP aspiration (a mechanically induced model). The results revealed the consistency of this innovative experimentally induced animal model of IVD degeneration. To provide a model suitable for preclinical assessment of the early stages of IVD degeneration, we now sought to precisely analyze the progressivity of the degeneration induced by laser. The results demonstrated that the enzyme induced a quick degeneration of the IVD with a drastic decrease of the T2wsi and IVD height. Tissue integrity was also altered regarding the decrease of the NP area measurement and a high Boos' scoring value at early times, despite the absence of a clearly delimited boundary between NP and AF. Interestingly, the laser procedure induced a progressive degenerative process characterized by a slow decrease in the T2wsi and IVD height

as shown by MRI and X-ray, respectively. This slow and moderate decrease in IVD height is much closer to that observed in spontaneous degeneration in humans. Indeed, in humans, aging induces an approximately 11% decrease in the lumbar IVD height after 15 years in follow-up studies [47]. The histological data and the elevated Boos' scoring also confirmed the progressive alteration of the NP extracellular matrix. The exact mechanisms by which laser irradiation induces IVD degeneration remain poorly understood but are likely to involve the high temperature resulting from the irradiation, as reported previously to explain the changes in ultrastructure and composition observed in laser-irradiated dentin [48].

Like other models, this one has a number of limitations that deserve consideration. The rabbit NP is populated with notochordal cells rather than the chondrocytic cells found in human IVD and the role of these cells has not yet been clarified. Another animal model should be tested to confirm the results obtained in rabbits in the present study. Nevertheless, this model has several advantages over other existing models. First, it is extremely simple and inexpensive, requiring only percutaneous access and a minimal surgical procedure as well as shorter anesthesia, thus allowing faster recovery. Second, the model is extremely effective, given that several degenerative IVDs can be produced per animal. One of the most promising features of this model is that it yields significant changes in the IVD treated that correlate with the histological changes classically described during DDD in humans. This process seems more progressive and therefore closer to spontaneous aging than the process observed in the nonprogressive tissue damage triggered by enzyme treatment. Therefore, the laser model can be considered as an interesting model to investigate the safety and efficacy of preventive treatment of disc disease because it allows us to intervene early in the course of the disease. Moreover, it allows inducing reproducible tissue lesions without the risk of external remnants and the routes tested on these models could be easily transposed to future human applications.

5. Conclusion

This study shows that progressive IVD degeneration can be induced in the rabbit by a laser procedure. MRI, radiological, and histological data have confirmed the relevance of this experimentally induced animal model of IVD degeneration compared to an enzymatic procedure (chemonucleolysis). This model could be quite instrumental in helping validate a cell-based strategy for the prevention of IVD degeneration.

Disclosure

Jérôme Guicheux and Johann Clouet are co-last authors.

Competing Interests

None of the authors of this paper has a financial or personal relationship with other people or organizations that could inappropriately influence or bias the content of the paper.

Authors' Contributions

Marion Fusellier, Johann Clouet, and Jérôme Guicheux conceived the study. Marion Fusellier and Johann Clouet coordinated the study. Marion Fusellier performed X-ray radiography and MRI and performed data analysis. She also drafted the paper and performed statistical analysis from imaging data. Johann Clouet, Pauline Colombier, and Julie Lesoeur performed histological stainings and Boos' scoring analysis. Stéphane Madec performed X-ray radiography and MRI. Samy Youl participated in the surgery. Olivier Gauthier participated in the design of the study, particularly in the animal management. Olivier Hamel participated in surgery and image analysis. Jérôme Guicheux helped in the writing of the paper and approved final version. Johann Clouet performed the statistical analyses from histological data and participated in the writing of the paper.

Acknowledgments

This study was supported by grants from Société Française de Rhumatologie, Société Française de Neurochirurgie, Agence Nationale de la Recherche AAP TeCSAN (Chondrograft project), Agence de la Biomédecine, Institut National de la Santé Et de la Recherche Médicale (INSERM), Fondation pour la Recherche Médicale-MESCLE (FRM-MESCLE), Région des Pays de la Loire (BIOREGOS project, Gérontopôle LMA), ANR génériques 2013 (REMEDIV project), FRM Bioingénierie (DBS20131128442), and the University Hospital of Nantes, LMA. The authors gratefully acknowledge the technical assistance of Patrice Roy, Dominique Rouleau, and Christian Raphael, as well as Linda Northrup for editing the paper.

References

[1] J. Gourmelen, J.-F. Chastang, A. Ozguler, J.-L. Lanoë, J.-F. Ravaud, and A. Leclerc, "Frequency of low back pain among men and women aged 30 to 64 years in France. Results of two national surveys," *Annales de Réadaptation et de Médecine Physique*, vol. 50, no. 8, pp. 640–644, 2007.

[2] G. B. J. Andersson, "Epidemiological features of chronic low-back pain," *The Lancet*, vol. 354, no. 9178, pp. 581–585, 1999.

[3] K. Luoma, H. Riihimäki, R. Luukkonen, R. Raininko, E. Viikari-Juntura, and A. Lamminen, "Low back pain in relation to lumbar disc degeneration," *Spine*, vol. 25, no. 4, pp. 487–492, 2000.

[4] P. Colombier, A. Camus, L. Lescaudron, J. Clouet, and J. Guicheux, "Intervertebral disc regeneration: a great challenge for tissue engineers," *Trends in Biotechnology*, vol. 32, no. 9, pp. 433–435, 2014.

[5] M. Alini, S. M. Eisenstein, K. Ito et al., "Are animal models useful for studying human disc disorders/degeneration?" *European Spine Journal*, vol. 17, no. 1, pp. 2–19, 2008.

[6] J. C. Lotz, O. K. Colliou, J. R. Chin, N. A. Duncan, and E. Liebenberg, "Compression-induced degeneration of the intervertebral disc: an in vivo mouse model and finite-element study," *Spine*, vol. 23, no. 23, pp. 2493–2506, 1998.

[7] M. W. Kroeber, F. Unglaub, H. Wang et al., "New in vivo animal model to create intervertebral disc degeneration and to

investigate the effects of therapeutic strategies to stimulate disc regeneration," *Spine*, vol. 27, no. 23, pp. 2684–2690, 2002.

[8] F. M. Phillips, J. Reuben, and F. T. Wetzel, "Intervertebral disc degeneration adjacent to a lumbar fusion. An experimental rabbit model," *The Journal of Bone & Joint Surgery—British Volume*, vol. 84, no. 2, pp. 289–294, 2002.

[9] W. C. Hutton, S. T. Yoon, W. A. Elmer et al., "Effect of tail suspension (or simulated weightlessness) on the lumbar intervertebral disc: study of proteoglycans and collagen," *Spine*, vol. 27, no. 12, pp. 1286–1290, 2002.

[10] A. G. Hadjipavlou, J. W. Simmons, J. P. Yang et al., "Torsional injury resulting in disc degeneration: I. An in vivo rabbit model," *Journal of Spinal Disorders*, vol. 11, no. 4, pp. 312–317, 1998.

[11] J. C. Iatridis, P. L. Mente, I. A. F. Stokes, D. D. Aronsson, and M. Alini, "Compression-induced changes in intervertebral disc properties in a rat tail model," *Spine*, vol. 24, no. 10, pp. 996–1002, 1999.

[12] J. D. Cassidy, K. Yong-Hing, W. H. Kirkaldy-Willis, and A. A. Wilkinson, "A study of the effects of bipedism and upright posture on the lumbosacral spine and paravertebral muscles of the Wistar rat," *Spine*, vol. 13, no. 3, pp. 301–308, 1988.

[13] E. Wada, S. Ebara, S. Saito, and K. Ono, "Experimental spondylosis in the rabbit spine. Overuse could accelerate the spondylosis," *Spine*, vol. 17, no. 3, supplement, pp. S1–S6, 1992.

[14] S. Miyamoto, K. Yonenobu, and K. Ono, "Experimental cervical spondylosis in the mouse," *Spine*, vol. 16, no. 10, supplement, pp. S495–S500, 1991.

[15] S. J. Lipson and H. Muir, "Experimental intervertebral disc degeneration: morphologic and proteoglycan changes over time," *Arthritis and Rheumatism*, vol. 24, no. 1, pp. 12–21, 1981.

[16] K. S. Kim, S. T. Yoon, J. Li, J. S. Park, and W. C. Hutton, "Disc degeneration in the rabbit: a biochemical and radiological comparison between four disc injury models," *Spine*, vol. 30, no. 1, pp. 33–37, 2005.

[17] J. Antoniou, F. Mwale, C. N. Demers et al., "Quantitative magnetic resonance imaging of enzymatically induced degradation of the nucleus pulposus of intervertebral discs," *Spine*, vol. 31, no. 14, pp. 1547–1554, 2006.

[18] S. C. W. Chan, A. Bürki, H. M. Bonél, L. M. Benneker, and B. Gantenbein-Ritter, "Papain-induced in vitro disc degeneration model for the study of injectable nucleus pulposus therapy," *Spine Journal*, vol. 13, no. 3, pp. 273–283, 2013.

[19] E. A. Growney Kalaf, S. A. Sell, and J. G. Bledsoe, "Developing a mechanical and chemical model of degeneration in young bovine lumbar intervertebral disks and reversing loss in mechanical function," *Journal of Spinal Disorders and Techniques*, vol. 27, no. 5, pp. E168–E175, 2014.

[20] J. Melrose, T. K. F. Taylor, P. Ghosh, C. Holbert, C. Macpherson, and C. R. Bellenger, "Intervertebral disc reconstitution after chemonucleolysis with chymopapain is dependent on dosage: an experimental study in beagle dogs," *Spine*, vol. 21, no. 1, pp. 9–17, 1996.

[21] S. Roberts, J. Menage, S. Sivan, and J. P. G. Urban, "Bovine explant model of degeneration of the intervertebral disc," *BMC Musculoskeletal Disorders*, vol. 9, article 24, 2008.

[22] T. Suguro, T. R. Oegema Jr., and D. S. Bradford, "Ultrastructural study of the short-term effects of chymopapain on the intervertebral disc," *Journal of Orthopaedic Research*, vol. 4, no. 3, pp. 281–287, 1986.

[23] K. Yamada, S. Tanabe, H. Ueno et al., "Investigation of the short-term effect of chemonucleolysis with chondroitinase ABC," *Journal of Veterinary Medical Science*, vol. 63, no. 5, pp. 521–525, 2001.

[24] J. P. Norcross, G. E. Lester, P. Weinhold, and L. E. Dahners, "An in vivo model of degenerative disc disease," *Journal of Orthopaedic Research*, vol. 21, no. 1, pp. 183–188, 2003.

[25] O. Lucas, O. Hamel, A. Blanchais et al., "Laser-treated Nucleus pulposus as an innovative model of intervertebral disc degeneration," *Experimental Biology and Medicine*, vol. 237, no. 11, pp. 1359–1367, 2012.

[26] C. Vinatier, O. Gauthier, M. Masson et al., "Nasal chondrocytes and fibrin sealant for cartilage tissue engineering," *Journal of Biomedical Materials Research Part A*, vol. 89, no. 1, pp. 176–185, 2009.

[27] N. Boos, S. Weissbach, H. Rohrbach, C. Weiler, K. F. Spratt, and A. G. Nerlich, "Classification of age-related changes in lumbar intervertebral discs: 2002 Volvo award in basic science," *Spine*, vol. 27, no. 23, pp. 2631–2644, 2002.

[28] T. Kimura, K. Nakata, N. Tsumaki et al., "Progressive degeneration of articular cartilage and intervertebral discs," *International Orthopaedics*, vol. 20, no. 3, pp. 177–181, 1996.

[29] J. Sahlman, R. Inkinen, T. Hirvonen et al., "Premature vertebral endplate ossification and mild disc degeneration in mice after inactivation of one allele belonging to the Col2a1 gene for type II collagen," *Spine*, vol. 26, no. 23, pp. 2558–2565, 2001.

[30] J. H. Adler, M. Schoenbaum, and R. Silberberg, "Early onset of disk degeneration and spondylosis in sand rats (*Psammomys obesus*)," *Veterinary Pathology*, vol. 20, no. 1, pp. 13–22, 1983.

[31] R. Silberberg and G. Gerritsen, "Aging changes in intervertebral discs and spondylosis in Chinese hamsters," *Diabetes*, vol. 25, no. 6, pp. 477–483, 1976.

[32] N. Bergknut, J. P. H. J. Rutges, H.-J. C. Kranenburg et al., "The dog as an animal model for intervertebral disc degeneration?" *Spine*, vol. 37, no. 5, pp. 351–358, 2012.

[33] P. Ghosh, T. K. F. Taylor, K. G. Braund, and L. H. Larsen, "A comparative chemical and histochemical study of the chondrodystrophoid and nonchondrodystrophoid canine intervertebral disc," *Veterinary Pathology*, vol. 13, no. 6, pp. 414–427, 1976.

[34] T. C. Cole, P. Ghosh, and T. K. F. Taylor, "Variations of the proteoglycans of the canine intervertebral disc with ageing," *Biochimica et Biophysica Acta (BBA)—General Subjects*, vol. 880, no. 2-3, pp. 209–219, 1986.

[35] S. Sobajima, J. F. Kompel, J. S. Kim et al., "A slowly progressive and reproducible animal model of intervertebral disc degeneration characterized by MRI, X-ray, and histology," *Spine*, vol. 30, no. 1, pp. 15–24, 2005.

[36] S. Holm, A. K. Holm, L. Ekström, A. Karladani, and T. Hansson, "Experimental disc degeneration due to endplate injury," *Journal of Spinal Disorders and Techniques*, vol. 17, no. 1, pp. 64–71, 2004.

[37] T. Nomura, J. Mochida, M. Okuma, K. Nishimura, and K. Sakabe, "Nucleus pulposus allograft retards intervertebral disc degeneration," *Clinical Orthopaedics and Related Research*, no. 389, pp. 94–101, 2001.

[38] M. Gorenšek, Č. Joksimović, N. Kregar-Velikonja et al., "Nucleus pulposus repair with cultured autologous elastic cartilage derived chondrocytes," *Cellular and Molecular Biology Letters*, vol. 9, no. 2, pp. 363–373, 2004.

[39] T. Miyamoto, T. Muneta, T. Tabuchi et al., "Intradiscal transplantation of synovial mesenchymal stem cells prevents intervertebral disc degeneration through suppression of matrix metalloproteinase-related genes in nucleus pulposus cells in rabbits," *Arthritis Research and Therapy*, vol. 12, no. 6, article R206, 2010.

[40] H. B. Henriksson, T. Svanvik, M. Jonsson et al., "Transplantation of human mesenchymal stems cells into intervertebral discs in a xenogeneic porcine model," *Spine*, vol. 34, no. 2, pp. 141–148, 2009.

[41] D. Sakai, J. Mochida, T. Iwashina et al., "Differentiation of mesenchymal stem cells transplanted to a rabbit degenerative disc model: potential and limitations for stem cell therapy in disc regeneration," *Spine*, vol. 30, no. 21, pp. 2379–2387, 2005.

[42] P. A. Revell, E. Damien, L. Di Silvio, N. Gurav, C. Longinotti, and L. Ambrosio, "Tissue engineered intervertebral disc repair in the pig using injectable polymers," *Journal of Materials Science: Materials in Medicine*, vol. 18, no. 2, pp. 303–308, 2007.

[43] M. Okuma, J. Mochida, K. Nishimura, K. Sakabe, and K. Seiki, "Reinsertion of stimulated nucleus pulposus cells retards intervertebral disc degeneration: an in vitro and in vivo experimental study," *Journal of Orthopaedic Research*, vol. 18, no. 6, pp. 988–997, 2000.

[44] O. L. Osti, B. Vernon-Roberts, and R. D. Fraser, "1990 Volvo award in experimental studies: anulus tears and intervertebral disc degeneration: an experimental study using an animal model," *Spine*, vol. 15, no. 8, pp. 762–767, 1990.

[45] E. Kääpä, S. Holm, X. Han, T. Takala, V. Kovanen, and H. Vanharanta, "Collagens in the injured porcine intervertebral disc," *Journal of Orthopaedic Research*, vol. 12, no. 1, pp. 93–102, 1994.

[46] M. Pfeiffer, P. Griss, P. Franke et al., "Degeneration model of the porcine lumbar motion segment: effects of various intradiscal procedures," *European Spine Journal*, vol. 3, no. 1, pp. 8–16, 1994.

[47] T. Videman, M. C. Battié, L. E. Gibbons, and K. Gill, "Aging changes in lumbar discs and vertebrae and their interaction: a 15-year follow-up study," *Spine Journal*, vol. 14, no. 3, pp. 469–478, 2014.

[48] R. Rohanizadeh, R. Z. LeGeros, S. Bohic, P. Pilet, A. Barbier, and G. Daculsi, "Ultrastructural properties of bone mineral of control and tiludronate-treated osteoporotic rat," *Calcified Tissue International*, vol. 67, no. 4, pp. 330–336, 2000.

Hindawi Publishing Corporation
BioMed Research International
Volume 2016, Article ID 3140290, 9 pages
http://dx.doi.org/10.1155/2016/3140290

Research Article

Lycium barbarum Polysaccharide Mediated the Antidiabetic and Antinephritic Effects in Diet-Streptozotocin-Induced Diabetic Sprague Dawley Rats via Regulation of NF-κB

Mingzhao Du,[1] Xinyu Hu,[2] Ling Kou,[1] Baohai Zhang,[1] and Chaopu Zhang[1]

[1]*Affiliated Hospital of Jiangsu University, Jiangsu University, Zhenjiang 212001, China*
[2]*Faculty of Medicine, Changchun Medical College, Changchun 130013, China*

Correspondence should be addressed to Ling Kou; 327196901@qq.com

Received 17 November 2015; Accepted 6 April 2016

Academic Editor: Andrea Vecchione

Lycium barbarum, extensively utilized as a medicinal plant in China for years, exhibits antitumor, immunoregulative, hepatoprotective, and neuroprotective properties. The present study aims to investigate the hyperglycemic and antidiabetic nephritic effects of polysaccharide which is separated from *Lycium barbarum* (LBPS) in high-fat diet-streptozotocin- (STZ-) induced rat models. The reduced bodyweight and enhanced blood glucose concentration in serum were observed in diabetic rats, and they were significantly normalized to the healthy level by 100 mg/kg of metformin (Met) and LBPS at doses of 100, 250, and 500 mg/kg. LBPS inhibited albuminuria and blood urea nitrogen concentration and serum levels of inflammatory factors including IL-2, IL-6, TNF-α, IFN-α, MCP-1, and ICAM-1 compared with diabetic rats, and it indicates the protection on renal damage. Furthermore, the activities of SOD and GSH-Px in serum were enhanced strikingly by LBPS which suggests its antioxidation effects. LBPS, compared with nontreated diabetic rats, inhibited the expression of phosphor-nuclear factors kappa B (NF-κB) and inhibitor kappa B alpha in kidney tissues. Collectively, LBPS possesses antidiabetic and antinephritic effects related to NF-κB-mediated antioxidant and antiinflammatory activities.

1. Introduction

As reported, nearly 2.2% of total death worldwide is caused by diabetes mellitus [1], which is characterized by hyperglycemia and metabolic disturbance including lipids, carbohydrates, and proteins [2]. Type II diabetes, the most common form of diabetes, is related to insulin resistance, and it will affect over 8 billion people till 2025 worldwide [3]. Combining with insulin secretion deficiency, hyperlevel of blood glucose is observed in diabetic patients; what is worse, several complications, such as nephropathy, endanger the patients' lives [3]. Diabetic nephropathy is the major cause of end-stage renal disease, and various pathways are involved during this process [4]. It has been confirmed that the reduction of oxidative stress and the enhancement of host antioxidant defense system are related to diabetic nephropathy therapy [5]. The levels of superoxide dismutase (SOD) are related to human aging and health; meanwhile, glutathione peroxidase (GSH-Px) displays protective effects on cell structure and membrane function [6]. The inflammatory cytokines including interleukin play central roles during diabetic nephropathy attack and treatment [7].

Till now, the traditional treatments only focus on regulating blood glucose levels, which fail to control complications [8]. Insulin injection and some oral antihyperglycemic agents, such as metformin, display undesirable side effects including insulin resistance, hypoglycemia, and gastrointestinal disturbances [9]. Due to the limitation of existing antidiabetic agents, a search for alternative treatment is highly demanded.

As reported previously, natural products turn out to be a valuable reservoir for searching novel drugs [10]. Scientific

evidence has been collected to support *Rhizoma coptidis* being used as an effective agent for the treatment of diabetes mellitus [11]. Danhong injection successfully inhibits diabetic retinopathy and nephropathy via ameliorating glucose metabolism [12]. *Lycium barbarum*, extensively utilized as a medicinal plant in China, exhibits immune enhancing, hepatoprotective, and neuroprotective properties [13]. As one of important bioactive components, *Lycium barbarum* polysaccharide (LBPS) prevents 6-OHDA-caused PC12 cell apoptosis partially via reactive oxygen species- (ROS-) nitric oxide (NO) pathway [14]. In both *in vitro* and *in vivo* experiments, LBPS shows synergistic immunotherapeutic effects with interferon-α2b on renal cell carcinoma [15]. In high-fat diet-induced insulin resistance animal models, LBPS is confirmed to be an antioxidant against insulin resistance via activating phosphatidyl inositol 3-kinase (PI3K)/AKT/nuclear factor erythroid 2 p45 related factor 2 (Nrf2) pathway. Furthermore, LBPS increases insulinogenic index and high density lipoprotein (HDL) levels in patients with type II diabetes [16]. Purified LBPS has significantly inhibited the absorption of glucose in a dose-dependent manner in cell experiments [17]. These encouraging data let us further investigate the antidiabetic and antinephritic effects of LBPS and underlying mechanism systematically.

The present study aims to investigate the hyperglycemic and anti-inflammatory effects of LBPS in high-fat diet-streptozotocin- (STZ-) induced rat models. During the experiments, serum indexes were measured to verify the positive effects of LBPS; meanwhile the activations of nuclear factors kappa B (NF-κB) in kidney were detected via western blot to analyze its possible mechanisms.

2. Materials and Methods

2.1. Lycium barbarum Polysaccharide Preparation. 100 g of *Lycium barbarum* (obtained from pharmacy in Affiliated Hospital of Jiangsu University, Jiangsu, China) was extracted two times in 500 mL hot water at 80°C for 3 h. After centrifuging, the supernatant was sequentially concentrated, and the existing proteins were removed using Sevag reagent [V (n-butanol) : V (chloroform) = 1 : 4, 50 mL]. After adding fourfold ethanol, the supernate was placed at 4°C overnight. The precipitate polysaccharide (LBPS) was collected and freeze-dried for further experiments.

2.2. Diet-STZ-Induced Diabetic Rat Model Establishment. The experimental animal protocol was approved by the Animal Ethics Committee of Jiangsu University. Sprague Dawley rats (male; 8 weeks; 180–220 g) were housed under the standard laboratory conditions of 22°C ± 1°C, relative humidity of 55%, and 12-h : 12-h light/dark cycle (lights on 7:00–19:00 h) during the study. The animals were given standard rat pellets and tap water *ad libitum*.

Rats ($n = 8$) fed with the standard control diet following with normal saline injection served as control group. Another 40 rats were fed with a high-fat diet (HFHSD, 12% protein, 5% fat, 67% carbohydrate, 5% cholesterol, and 5% other additives) for 8 weeks and then injected with 30 mg/kg streptozotocin (STZ; Sigma, USA) dissolved in a citrate buffer (0.1 mol/L sodium citrate and 0.1 mol/L citric acid, pH 4.5) for one week. After the last STZ injection, the blood glucose level was detected, and rats with the value of more than 11.1 mmol/L were defined as with diabetes.

2.3. Animal Treatment Process. Rats ($n = 8$) in control group were given 2.0 mL/kg sterile saline for four weeks. Diabetic rats were divided into five groups randomly and orally treated with 2.0 mL/kg sterile saline (model rats, $n = 8$), 100 mg/kg of metformin hydrochloride (Met; Sigma, USA) (positive control rats, $n = 8$), LBPS at doses of 100 mg/kg (low dose-treated rats, $n = 8$), 250 mg/kg (middle dose-treated rats, $n = 8$), and 500 mg/kg (high dose-treated rats, $n = 8$). The oral administration lasted for four weeks, and the bodyweight and blood glucose level of each rat were recorded every week.

2.4. Oral Glucose Tolerance Test (OGTT) in Rats. OGTT was performed to avoid a false positive result which is obtained from the monitor of blood glucose. The experimental rats were fasted for 12 h after the last administration of LBPS and Met and then orally treated with 2.0 g/kg glucose. The blood glucose levels were analyzed, respectively, at 0, 30, 60, 90, and 120 min. The area under the blood glucose curve (AUC) was calculated [18] according to

$$\begin{aligned} \mathrm{AUC} = {} & (\text{basal glycaemia} + \text{glycaemia } 0.5\,\text{h}) \times 0.25 \\ & + (\text{glycaemia } 0.5\,\text{h} + \text{glycaemia } 1\,\text{h}) \times 0.25 \\ & + (\text{glycaemia } 1\,\text{h} + \text{glycaemia } 2\,\text{h}) \times 0.5. \end{aligned} \quad (1)$$

2.5. Blood Biochemical Indexes Analysis. At the end of the experiment, blood samples were collected from the caudal vein of each rat. The serum levels of insulin (INS), interleukin-2 (IL-2), interleukin-6 (IL-6), tumor necrosis factor-α (TNF-α), interferon-α (IFN-α), monocyte chemoattractant protein 1 (MCP-1), and intercellular adhesion molecule (ICAM-1) were detected by using enzyme-linked immunosorbent assay (ELISA) kits according to operation manual (Calbiotech, USA). The activities of SOD and GSH-Px in serum and the levels of blood urea nitrogen (BUN) and albuminuria in urine were analyzed via commercial kits obtained from Nanjing Biotechnology Co. Ltd. (Nanjing, China).

2.6. Histopathological Examination. Collected kidney tissue was immersed in 4% paraformaldehyde for 48 h and then dehydrated step by step using 50–100% ethanol. Samples were immersed in xylene for 30 min and incubated in paraffin at 65°C overnight. Once embedded in wax, samples were cut serially into 5 μm thick sections using a microtome (Leica, Germany) and spread over microscopy slides. The sections were deparaffinized with fresh xylene for 10 min, rehydrated with a gradient of ethanol (100%, 90%, 80%, and 70%), washed three times with DD water, analyzed via hematoxylin and eosin (H&E) staining, and photographed with a light microscope digital camera (Nikon Instruments, Tokyo, Japan).

Table 1: Results on the body weight gain, food intake, water intake, and urine excretion in each experimental group.

Group	Dose (mg/kg/d)	Bodyweight gain/g	Water intake/mL	Food intake/g
CTRL	—	6.58 ± 1.27	45.00 ± 9.68	10.72 ± 2.60
Model	—	6.69 ± 2.09	89.00 ± 6.42[b]	19.85 ± 1.55[b]
DH-treated	100	30.06 ± 1.87[a]	43.52 ± 7.91[a]	8.97 ± 2.19[a]
LBPS	100	5.87 ± 2.32	94.17 ± 12.31	16.33 ± 2.50
	250	23.13 ± 1.81[a]	67.00 ± 13.11	11.41 ± 1.54[a]
	500	28.67 ± 3.16[a]	47.78 ± 8.14[a]	9.97 ± 1.89[a]

Data are expressed as mean ± SD (n = 8/group) and analyzed using ANOVA followed by Dunn's test.
[a]Statistical significance compared with diabetic model rats ($P < 0.05$).
[b]Statistical significance compared with control rats ($P < 0.05$).

2.7. Western Blot. Collected kidney tissues were homogenized in radioimmunoprecipitation assay buffer (RIPA; Sigma-Aldrich, USA) which contains 1% protease inhibitor cocktail (Sigma-Aldrich, USA) and 2% phenylmethanesulfonyl fluoride (PMSF; Sigma-Aldrich, USA). Protein concentration was analyzed via Bradford method, and 30 μg samples were separated by using a 10% SDS-PAGE gel and transferred electrophoretically onto nitrocellulose membranes (0.45 m; Bio Basic, Inc., USA). After being blocked in 5% bull serum albumin (BSA) for 4 h at 4°C, the membranes were blotted at 4°C overnight with primary antibodies phosphor-nuclear factor-κB (P-NF-κB) receptor, total-NF-κB (T-NF-κB) (1 : 500; Santa Cruz, USA), inhibitor kappa B alpha (IκBα), and glyceraldehyde-3-phosphate dehydrogenase (GAPDH) (Santa Cruz, USA) at dilution of 1 : 500. The membranes were further incubated with horseradish peroxidase-conjugated secondary antibodies (1 : 2000; Santa Cruz, USA). Chemiluminescence was detected by using ECL detection kits (GE Healthcare, UK). The intensity of the bands was quantified by scanning densitometry using software Image J (National Institutes of Health, Bethesda, USA).

2.8. Statistical Analysis. All values were expressed as mean ± SD. A one-way analysis of variance (ANOVA) was used to detect statistical significance followed by *post hoc* multiple comparisons (Dunn's test) via software SPSS 16.0 (IBM corporation, Armonk, USA). A value of $P < 0.05$ was considered to be significant.

3. Results

3.1. The Hypoglycaemic Effect of LBPS in Diet-STZ-Induced Diabetic Rats. Compared with normal controls, the enhanced water and food intake ($P < 0.05$; Table 1), blood glucose levels ($P < 0.01$; Figure 1(a)), and the inhibited growth rate ($P < 0.05$; Table 1) were observed after STZ injection in diabetic rats. Four-week Met (100 mg/kg) treatment relieved the abnormal alternations ($P < 0.05$; Table 1 and Figure 1). Compared with nontreated diabetic rats, LBPS at 500 mg/kg resulted in 40.5% increment of bodyweight ($P < 0.05$; Table 1), 46.1% reduction of water intake ($P < 0.05$; Table 1), 49.8% reduction of food intake ($P < 0.05$; Table 1), and 45.6% reduction of fasting blood glucose levels ($P < 0.05$; Figure 1(a)). Furthermore, a 27.4% enhancement of serum insulin concentration was noted in 500 mg/kg of LBPS-treated diabetic rats compared with nontreated group ($P < 0.05$; Figure 1(b)).

Within 30 minutes of starting OGTT, nearly twofold blood glucose concentration was noted compared with its initial control value. Met and LBPS prevented blood glucose levels from shooting up significantly from 30 min to 120 min ($P < 0.05$, Figure 2(a)). The suppressive effects of Met and LBPS on AUC further confirmed their hypoglycaemic activities ($P < 0.05$, Figure 2(b)).

3.2. The Antioxidative Effects of LBPS in Diabetic Rats. Oxidative stress has been implicated in inflammation which is directly related to the activities of SOD and GSH [19]. Low serum concentrations of SOD and GSH-Px were noted in nontreated diabetic rats ($P < 0.05$; Figure 3). LBPS at dose of 500 mg/kg enhanced 39.2% of SOD level ($P < 0.01$; Figure 3(a)) and 75.1% of GSH-Px level ($P < 0.001$; Figure 3(b)) in serum of diet-STZ-induced diabetic rats compared with model group. Interestingly, Met only enhanced 55.3% SOD serum level in diabetic rats ($P < 0.05$; Figure 3(a)) but failed to regulate GSH-Px levels (Figure 3(b)).

3.3. The Effect of LBPS on Renal Function in Diabetic Rats. BUN is one of the important factors renal dysfunction manifests. Met and LBPS significantly reduced the hyperlevel of BUN in diabetic rats ($P < 0.05$; Figure 4(a)). Albuminuria, considered as the hallmark for diabetic nephropathy [20], strikingly increased in diabetic rats ($P < 0.01$; Figure 4(b)). Both Met and LBPS strikingly reduced the albuminuria levels after four-week treatment in diabetic rats ($P < 0.05$; Figure 4(b)). In diabetic rats, glomerular basement membrane thickening or mesangial proliferation and inflammatory infiltrate injuries were observed, which were strongly ameliorated by Met and LBPS (Figure 4(c)).

3.4. The Anti-Inflammatory Effects of PBPS in Diabetic Rats. Hyperglycemia leads to kidney damage associated with the severe inflammation characterized by the release of multiple inflammatory factors. Diabetic rats have exhibited the significant increase in serum levels of IL-2, IL-6, TNF-α, IFN-α, MCP-1, and ICAM-1 compared with normal rats

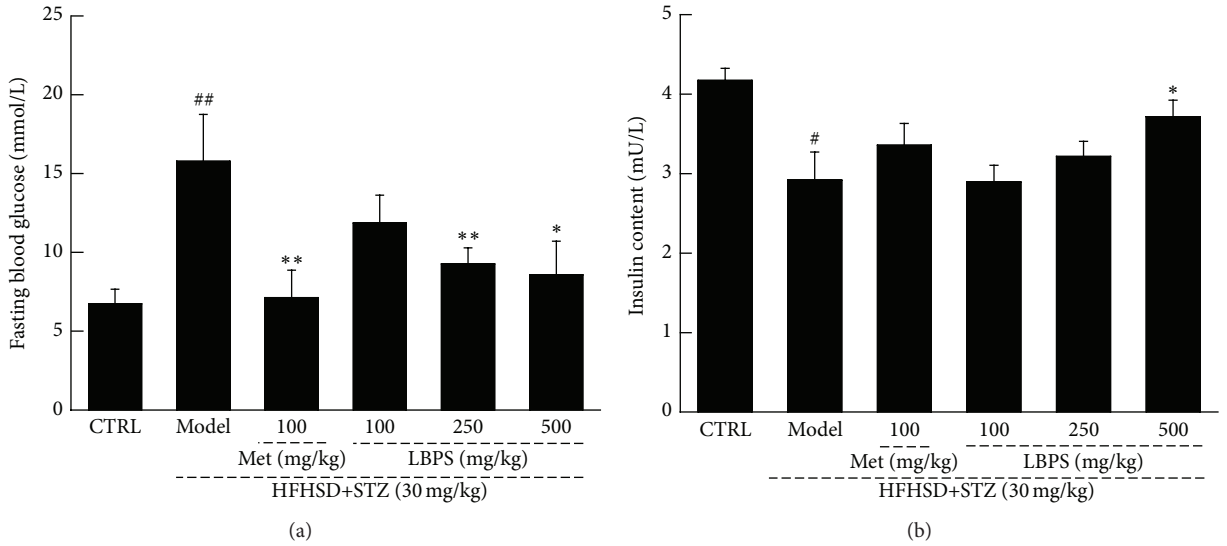

Figure 1: Compared with diabetic rats, four-week 100 mg/kg of metformin (Met) and *Lycium barbarum* polysaccharide (LBPS) at doses of 100, 250, and 500 mg/kg positively regulated the abnormal changes on (a) fasting plasma glucose level and (b) serum insulin concentration. Data are expressed as mean ± SD ($n = 8$) and analyzed by using a one-way ANOVA. $^{\#}P < 0.05$ and $^{\#\#}P < 0.01$ versus normal controls; $^{*}P < 0.05$ and $^{**}P < 0.01$ versus diabetic model rats.

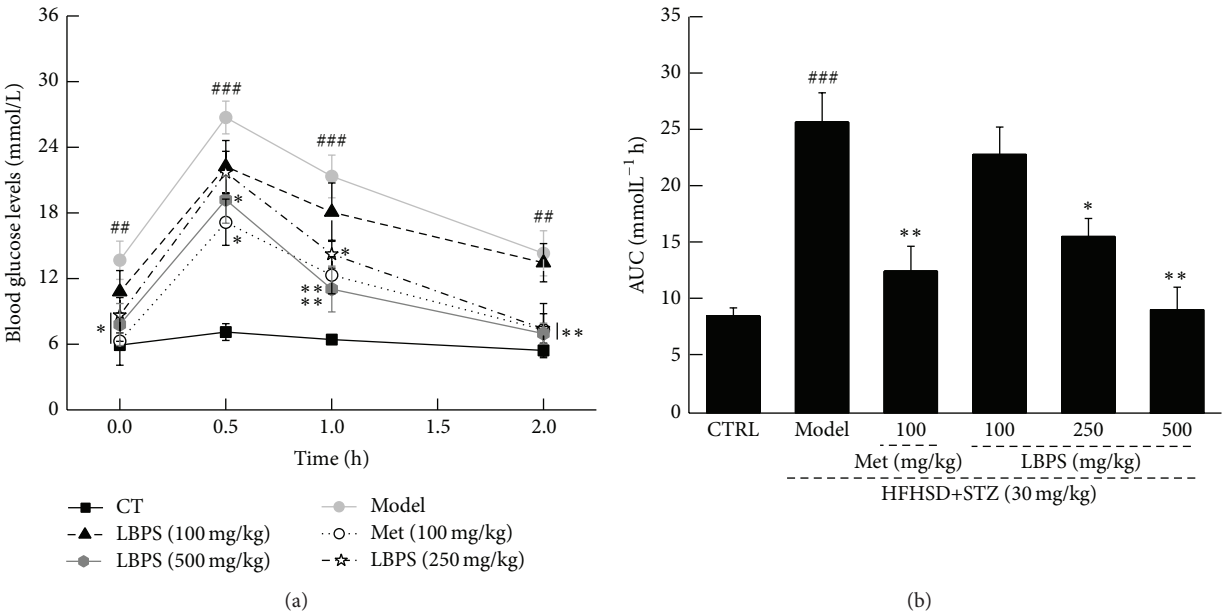

Figure 2: After the final treatment, all rats were orally treated with 2 g/kg of D-glucose; the changes of (a) plasma glucose and (b) area under the curve of glucose were detected. Data are expressed as mean ± SD ($n = 8$). $^{\#\#}P < 0.01$ and $^{\#\#\#}P < 0.001$ versus normal controls; $^{*}P < 0.05$ and $^{**}P < 0.01$ versus diabetic model rats.

($P < 0.05$; Figure 5). Except for ICAM-1 level, Met reduced these hyperlevels of inflammatory factors ($P < 0.05$; Figure 5). LBPS showed similar effects on inflammatory cytokines regulation. Compared with diabetic rats, LBPS at 500 mg/kg caused a significant reduction in the serum levels of IL-2 (28.4% reduction; $P < 0.05$; Figure 5(a)), IL-6 (35.9% reduction; $P < 0.05$; Figure 5(b)), TNF-α (38.8% reduction; $P < 0.05$; Figure 5(c)), IFN-α (34.8% reduction; $P < 0.05$; Figure 5(d)), MCP-1 (36.1% reduction; $P < 0.05$; Figure 5(e)), and ICAM-1 (40.9% reduction; $P < 0.05$; Figure 5(f)).

3.5. LBPS Regulated the Activation of NF-κB. The activation of NF-κB p65 is controlled via the inhibitory protein IκBα, which is considered to regulate multiple inflammatory

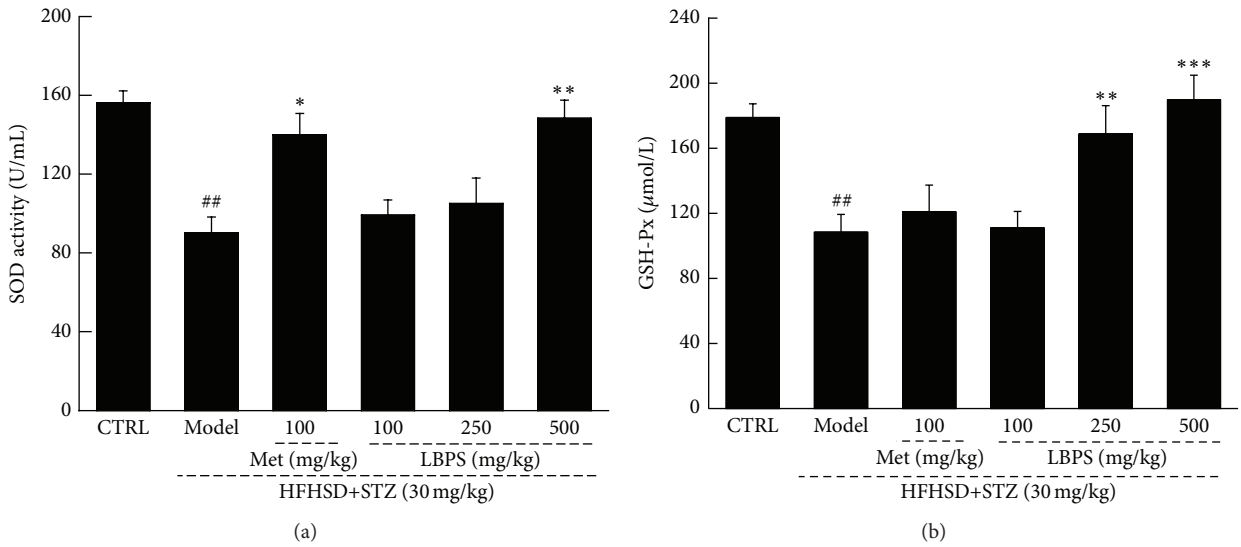

Figure 3: Met and LBPS enhanced the activities of (a) SOD and (b) GSH-Px in serum after four-week treatment in diabetic rats. Data are expressed as mean ± SD ($n = 8$) and analyzed by using a one-way ANOVA. $^{\#\#}P < 0.01$ versus normal controls; $^{*}P < 0.05$, $^{**}P < 0.01$, and $^{***}P < 0.001$ versus model rats.

factors. The strikingly enhanced expression of IκBα and activities of NF-κB were observed in the kidney tissues of diet-STZ-induced diabetic rats ($P < 0.01$; Figure 5). Compared with model group, both Met and LBPS significantly restored these expressions to normal levels ($P < 0.05$; Figure 6).

4. Discussion

Diet-STZ-induced diabetic rat model was successfully established for analysis of LBPS-mediated antidiabetic and antinephritic effects. Compared with diabetes model rats, the improved weight growth and reduced fasting blood glucose level were observed in LBPS-treated rats which indicates its hyperglycemic activity. Due to the more sensitivity of OGTT in glucose disregulation compared to that of fasting plasma glucose [1], the antidiabetic effect of LBPS was verified via OGTT. Hyperglycaemia decreased insulin secretion which is associated with the reduction in β-cell mass and impaired β-cell function [21]. LBPS strongly enhanced insulin secretion in diabetic rats and it indicates the protective activities of LBPS on β-cell damages in hyperglycaemia.

Oxidative stress is recognized as a major cause of diabetic complications. The disequilibrium of physical function in diabetic patients causes accumulation of reactive oxygen species (ROS); meanwhile, SOD and GSH-Px are primary enzymes for elimination of ROS [22]. SOD catalyzes the conversion of superoxide into hydrogen peroxide and oxygen, and GSH-Px scavenges the hydroxyl radical [23]. High blood glucose level leads to the autooxidative glycosylation of proteins [24], which further causes tissue damage. Antioxidant compounds have been recognized as an effective way to rescue the destruction of pancreatic beta-cell caused by alloxan [25]. *Cordyceps militaris* presents excellent antidiabetic and antinephropathic activities via modulating the oxidative system including the enhancement of SOD and GSH-Px levels [18]. LBPS-mediated hyperglycemic activity may be related to the normalization of oxidative system.

Interestingly, oxidative stress in diabetics favors the imbalance of endothelial function, and this is an important step in inflammation [26]. During diabetic nephropathy, the apoptosis of podocyte is controlled by oxidative stress [27]. It has been confirmed that inflammatory and immunosuppressive factors are involved in hyperglycemia which causes glomerular hypertrophy and glomerular basement membrane thickening [28]. The overexpression of IL-2 enhanced the expression of endogenous cytokines, such as INF-g [29], which may be responsible for deteriorating glomerular damages [30]. IL-6 and TNF-α elevation contributed to cell damage and influenced β-cell development [31]. LBPS not only normalized L-2, IL-6, TNF-α, and IFN-α in serum, but also enhanced the serum concentration of ICAM-1 and MCP-1 in diabetic rats. In clinical trials, inflammatory stimuli have caused the disorder expressions of adhesion molecules and chemokines, especially in nephritis patients [32]. Via regulating inflammatory factors, especially for ICAM-1, and lowering uric acid, tubulointerstitial injury is reduced in diabetes [33]. All these data suggest that LBPS possesses antidiabetic nephropathy in diet-STZ-induced rat model via regulating inflammatory factors which may be controlled by oxidative stress. However, more experiments will be performed to find the detail connection between oxidative stress and inflammatory cytokines.

Furthermore, LBPS reduces the expression of phosphor-NF-κB and IκBα in kidney of diabetic rats. NF-κB, a nuclear transcription factor, regulates various genes related

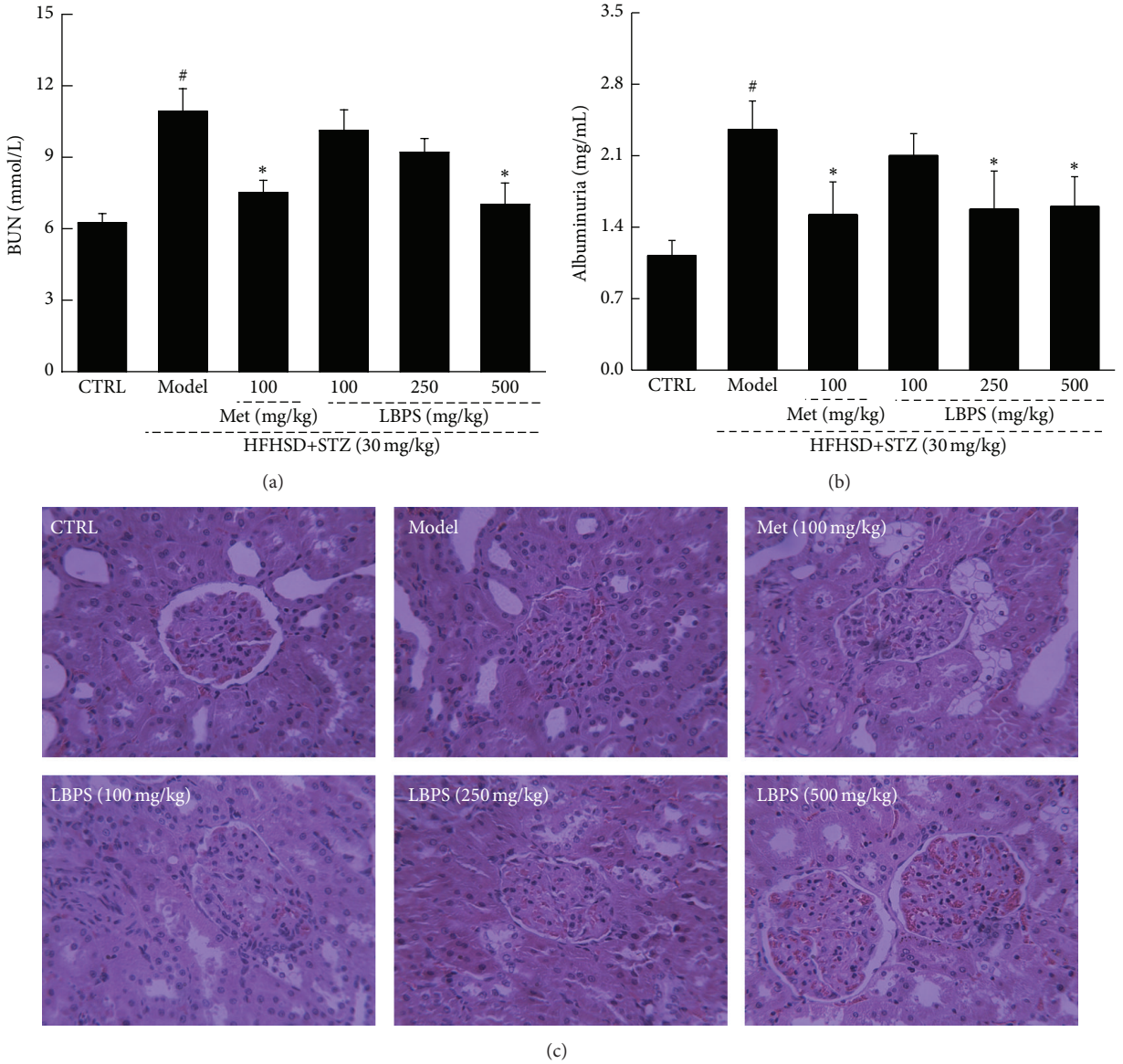

Figure 4: Diet-STZ-induced diabetic rats were orally treated with or without Met and LBPS at indicated doses for four weeks. The levels of (a) BUN and (b) urine albuminuria were detected. (c) Histopathological changes in kidney were analyzed through H&E staining ($n = 6$; ×400). Data are expressed as mean ± SD ($n = 8$) and analyzed by using a one-way ANOVA. $^{\#}P < 0.05$ versus control; $^{*}P < 0.05$ versus model rats.

to inflammation and autoimmune diseases [34]. NF-κB displays the central role in renal protection via modulating proinflammatory cytokine [35]. Overexpression of NF-κB in glomerular cells is responsible for nephritis in rats [36], which is reported to be controlled by protein IκBα. Previous study also proves that the activation of NF-κB is involved in cobalt chloride-mediated oxidative stress and inflammation in human renal proximal tubular epithelial cells [37]. Via modulation of NF-κB, *Cordyceps militaris* fruit body extracts ameliorate cationic bovine serum albumin-induced membranous glomerulonephritis by attenuating oxidative stress and renal inflammation [38]. IκB inhibitor, BAY 11-7082, attenuates hyperglycemia-mediated oxidative stress and renal inflammation in diabetic rat models via downregulating NF-κB activation [39]. Altogether, NF-κB contributes to LBPS-mediated anti-inflammatory and antioxidant properties in diabetes rat models.

In conclusion, via inhibiting the activation of NF-κB, *Lycium barbarum* polysaccharide has attenuated oxidative stress and inflammation to show antidiabetic and antinephritic effects in diet-STZ-induced diabetic rats. *Lycium barbarum* can be a potential Chinese traditional medicine for diabetes mellitus and nephritis complications treatment.

Competing Interests

The authors declare that they have no competing interests.

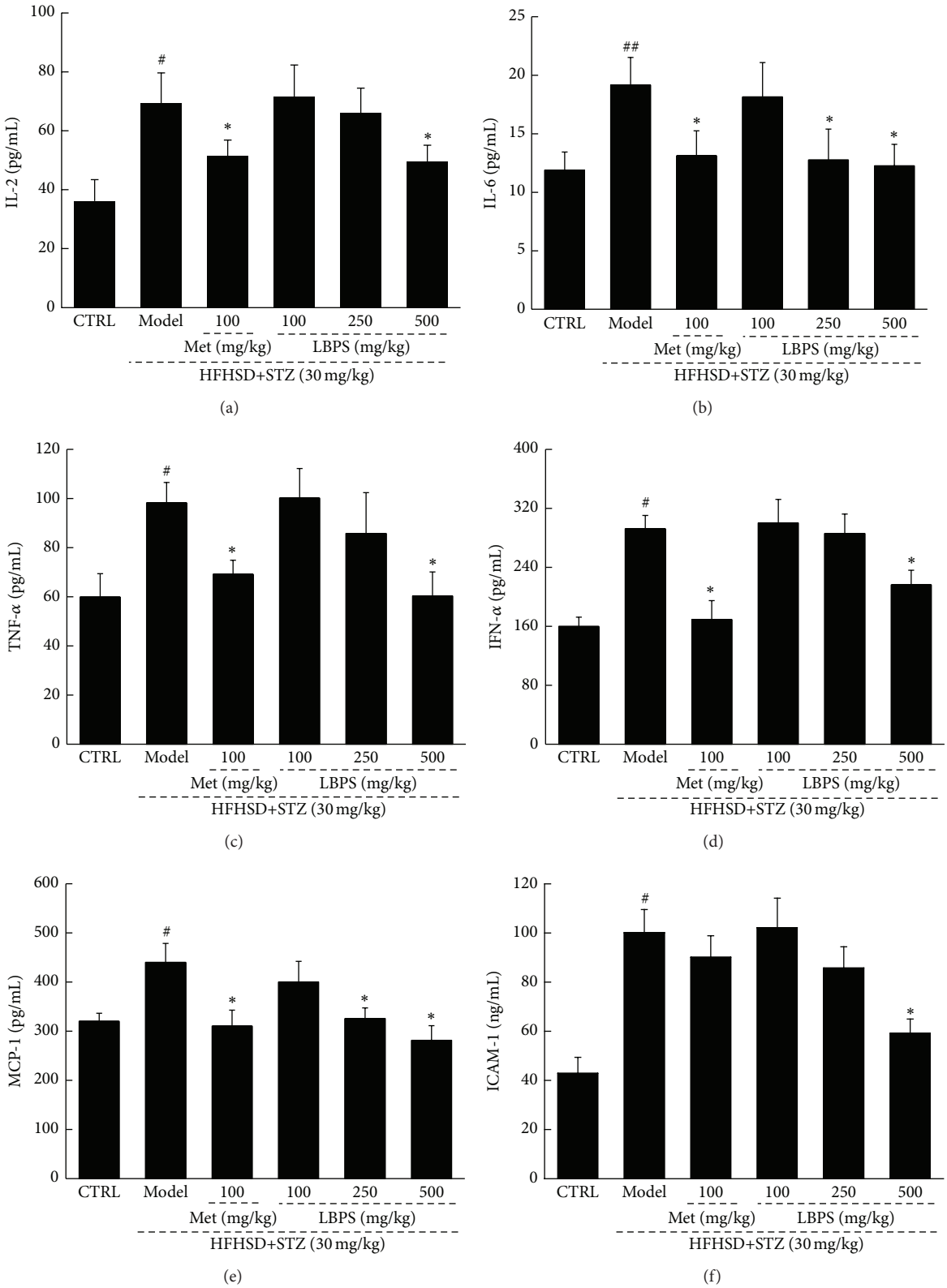

Figure 5: Diet-STZ-induced diabetic rats were orally treated with 100 mg/kg of Met and LBPS at doses of 100, 250, and 500 mg/kg for four weeks. The effects on the serum levels of (a) IL-2, (b) IL-6, (c) TNF-α, (d) IFN-α, (e) MCP-1, and (f) ICAM-1 were analyzed via ELISA method. Data are expressed as mean ± SD ($n = 8$) and analyzed by using a one-way ANOVA. $^{\#}P < 0.05$ and $^{\#\#}P < 0.01$ versus normal controls; $^{*}P < 0.05$ versus diabetic model rats.

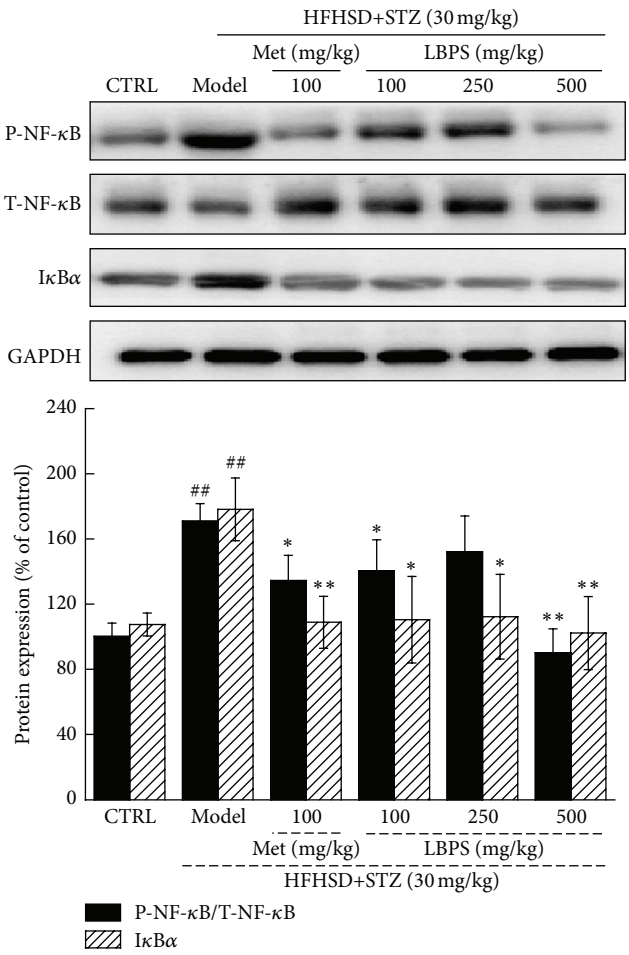

Figure 6: After four-week Met and LBPS treatment, the expression of P-NF-κB, T-NF-κB, and IκBα in kidney was determined using western blot. Quantification data of the expressions of P-NF-κB and IκBα was normalized by T-NF-κB and GAPDH, respectively. Data are expressed as mean ± SD ($n = 4$) and analyzed by using a one-way ANOVA. $^{\#\#}P < 0.01$ versus normal controls; $^{*}P < 0.05$ and $^{**}P < 0.01$ versus diabetic model rats.

Acknowledgments

This work is supported by Research fund for the Doctoral Program of Affiliated Hospital of Jiangsu University in China (no. jdfyRC-2015004), Scientific Research Program of the Affiliated Hospital of Jiangsu University in China (no. jdfyRC-2013003), and the Social Development Project of Zhenjiang Province in China (no. SH2014028).

References

[1] B. A. Sheikh, L. Pari, A. Rathinam, and R. Chandramohan, "Trans-anethole, a terpenoid ameliorates hyperglycemia by regulating key enzymes of carbohydrate metabolism in streptozotocin induced diabetic rats," *Biochimie*, vol. 112, pp. 57–65, 2015.

[2] W. Kerner and J. Brückel, "Definition, classification and diagnosis of diabetes mellitus," *Experimental and Clinical Endocrinology and Diabetes*, vol. 122, no. 7, pp. 384–386, 2014.

[3] G. Winkler, T. Hidvegi, G. Vandorfi et al., "Risk-stratified screening for type 2 diabetes in adult subjects: results from Hungary," *Diabetologia*, vol. 54, p. S119, 2011.

[4] Y. Pan, Y. Huang, Z. Wang et al., "Inhibition of MAPK-mediated ACE expression by compound C66 prevents STZ-induced diabetic nephropathy," *Journal of Cellular and Molecular Medicine*, vol. 18, no. 2, pp. 231–241, 2014.

[5] N. M. Elsherbiny, M. El-Sherbiny, and E. Said, "Amelioration of experimentally induced diabetic nephropathy and renal damage by nilotinib," *Journal of Physiology and Biochemistry*, vol. 71, no. 4, pp. 635–648, 2015.

[6] J. Q. Wu, T. R. Kosten, and X. Y. Zhang, "Free radicals, antioxidant defense systems, and schizophrenia," *Progress in Neuro-Psychopharmacology and Biological Psychiatry*, vol. 46, pp. 200–206, 2013.

[7] D. Yaghobian, A. S. Don, S. Yaghobian, X. Chen, C. A. Pollock, and S. Saad, "Increased sphingosine 1-phosphate mediates inflammation and fibrosis in tubular injury in diabetic nephropathy," *Clinical and Experimental Pharmacology and Physiology*, vol. 43, no. 1, pp. 56–66, 2016.

[8] D. S. Kania, J. D. Gonzalvo, and Z. A. Weber, "Saxagliptin: a clinical review in the treatment of type 2 diabetes mellitus," *Clinical Therapeutics*, vol. 33, no. 8, pp. 1005–1022, 2011.

[9] A. J. Scheen, "Antidiabetic agents in subjects with mild dysglycaemia: prevention or early treatment of type 2 diabetes?" *Diabetes & Metabolism*, vol. 33, no. 1, pp. 3–12, 2007.

[10] T. Salihu Shinkafi, L. Bello, S. Wara Hassan, and S. Ali, "An ethnobotanical survey of antidiabetic plants used by Hausa-Fulani tribes in Sokoto, Northwest Nigeria," *Journal of Ethnopharmacology*, vol. 172, pp. 91–99, 2015.

[11] B. Pang, X.-T. Yu, Q. Zhou et al., "Effect of *Rhizoma coptidis* (Huang Lian) on treating diabetes mellitus," *Evidence-Based Complementary and Alternative Medicine*, vol. 2015, Article ID 921416, 10 pages, 2015.

[12] D. Yin, Y. Y. Liu, T. X. Wang et al., "Paeoniflorin exerts analgesic and hypnotic effects via adenosine A_1 receptors in a mouse neuropathic pain model," *Psychopharmacology*, vol. 233, no. 2, pp. 281–293, 2016.

[13] S. Zareisedehizadeh, C.-H. Tan, and H.-L. Koh, "A review of botanical characteristics, traditional usage, chemical components, pharmacological activities, and safety of Pereskia bleo (Kunth) DC," *Evidence-Based Complementary and Alternative Medicine*, vol. 2014, Article ID 326107, 11 pages, 2014.

[14] K. Gao, M. Liu, J. Cao et al., "Protective effects of lycium barbarum polysaccharide on 6-OHDA-induced apoptosis in PC12 cells through the ROS-NO pathway," *Molecules*, vol. 20, no. 1, pp. 293–308, 2015.

[15] S. Chen, L. Liang, Y. Wang et al., "Synergistic immunotherapeutic effects of Lycium barbarum polysaccharide and interferon-α2b on the murine Renca renal cell carcinoma cell line in vitro and in vivo," *Molecular Medicine Reports*, vol. 12, no. 5, pp. 6727–6737, 2015.

[16] H. Cai, F. Liu, P. Zuo et al., "Practical application of antidiabetic efficacy of *Lycium barbarum* polysaccharide in patients with type 2 diabetes," *Medicinal Chemistry*, vol. 11, no. 4, pp. 383–390, 2015.

[17] H.-L. Tang, C. Chen, S.-K. Wang, and G.-J. Sun, "Biochemical analysis and hypoglycemic activity of a polysaccharide isolated from the fruit of *Lycium barbarum* L," *International Journal of Biological Macromolecules*, vol. 77, pp. 235–242, 2015.

[18] Y. Dong, T. Jing, Q. Meng et al., "Studies on the antidiabetic activities of *Cordyceps militaris* extract in diet-streptozotocin-induced diabetic sprague-dawley rats," *BioMed Research International*, vol. 2014, Article ID 160980, 11 pages, 2014.

[19] S. Rubattu, B. Pagliaro, G. Pierelli et al., "Pathogenesis of target organ damage in hypertension: role of mitochondrial oxidative stress," *International Journal of Molecular Sciences*, vol. 16, no. 1, pp. 823–839, 2015.

[20] M. E. Williams, "Diabetic nephropathy: the proteinuria hypothesis," *American Journal of Nephrology*, vol. 25, no. 2, pp. 77–94, 2005.

[21] H. Yki-Jarvinen, "Glucose toxicity," *Endocrine Reviews*, vol. 13, no. 3, pp. 415–431, 1992.

[22] Z. Tang, H. Gao, S. Wang, S. Wen, and S. Qin, "Hypolipidemic and antioxidant properties of a polysaccharide fraction from *Enteromorpha prolifera*," *International Journal of Biological Macromolecules*, vol. 58, pp. 186–189, 2013.

[23] T.-T. Huang, D. Leu, and Y. Zou, "Oxidative stress and redox regulation on hippocampal-dependent cognitive functions," *Archives of Biochemistry and Biophysics*, vol. 576, pp. 2–7, 2015.

[24] J.-H. Park, N. S. Park, S. M. Lee, and E. Park, "Effect of *Dongchunghacho* rice on blood glucose level, lipid profile, and antioxidant metabolism in streptozotocin-induced diabetic rats," *Food Science and Biotechnology*, vol. 20, no. 4, pp. 933–940, 2011.

[25] H. Sebai, S. Selmi, K. Rtibi, A. Souli, N. Gharbi, and M. Sakly, "Lavender (*Lavandula stoechas* L.) essential oils attenuate hyperglycemia and protect against oxidative stress in alloxan-induced diabetic rats," *Lipids in Health and Disease*, vol. 12, article 189, 2013.

[26] A. Ceriello, A. Novials, E. Ortega et al., "Vitamin C further improves the protective effect of glucagon-like peptide-1 on acute hypoglycemia-induced oxidative stress, inflammation, and endothelial dysfunction in type 1 diabetes," *Diabetes Care*, vol. 36, no. 12, pp. 4104–4108, 2013.

[27] W. Hua, H.-Z. Huang, L.-T. Tan et al., "CD36 mediated fatty acid-induced podocyte apoptosis via oxidative stress," *PLoS ONE*, vol. 10, no. 5, Article ID e0127507, 2015.

[28] E. N. Ellis and B. H. Good, "Prevention of glomerular basement membrane thickening by aminoguanidine in experimental diabetes mellitus," *Metabolism*, vol. 40, no. 10, pp. 1016–1019, 1991.

[29] O. Boyman, A. G. Kolios, and M. E. Raeber, "Modulation of T cell responses by IL-2 and IL-2 complexes," *Clinical and Experimental Rheumatology*, vol. 33, no. 4, supplement 92, pp. 54–57, 2015.

[30] R. Bertelli, A. Di Donato, M. Cioni et al., "LPS nephropathy in mice is ameliorated by IL-2 independently of regulatory T cells activity," *PLoS ONE*, vol. 9, no. 10, Article ID e111285, 2014.

[31] T. Peters, W. Bloch, C. Wickenhauser et al., "Terminal B cell differentiation is skewed by deregulated interleukin-6 secretion in β_2 integrin-deficient mice," *Journal of Leukocyte Biology*, vol. 80, no. 3, pp. 599–607, 2006.

[32] E. Honkanen, E. Von Willebrand, A.-M. Teppo, T. Törnroth, and C. Grönhagen-Riska, "Adhesion molecules and urinary tumor necrosis factor-α in idiopathic membranous glomerulonephritis," *Kidney International*, vol. 53, no. 4, pp. 909–917, 1998.

[33] T. Kosugi, T. Nakayama, M. Heinig et al., "Effect of lowering uric acid on renal disease in the type 2 diabetic db/db mice," *American Journal of Physiology—Renal Physiology*, vol. 297, no. 2, pp. F481–F488, 2009.

[34] T. D. Gilmore, "Introduction to NF-κB: players, pathways, perspectives," *Oncogene*, vol. 25, no. 51, pp. 6680–6684, 2006.

[35] P. Pan, Y.-J. Wang, L. Han, X. Liu, M. Zhao, and Y.-F. Yuan, "Effects of sodium houttuyfonate on expression of NF-kappaB and MCP-1 in membranous glomerulonephritis," *Journal of Ethnopharmacology*, vol. 131, no. 1, pp. 203–209, 2010.

[36] S. Li, Y. Zhang, and J. Zhao, "Preparation and suppressive effect of astragalus polysaccharide in glomerulonephritis rats," *International Immunopharmacology*, vol. 7, no. 1, pp. 23–28, 2007.

[37] S. W. O. Oh, Y.-M. Lee, S. Kim, H. J. U. Chin, D.-W. Chae, and K. Y. O. Na, "Cobalt chloride attenuates oxidative stress and inflammation through NF-κB inhibition in human renal proximal tubular epithelial cells," *Journal of Korean medical science*, vol. 29, supplement 2, pp. S139–S145, 2014.

[38] J. Song, Y. Wang, C. Liu et al., "Cordyceps militaris fruit body extract ameliorates membranous glomerulonephritis by attenuating oxidative stress and renal inflammation via the NF-κB pathway," *Food & Function*, 2016.

[39] S. R. Kolati, E. R. Kasala, L. N. Bodduluru et al., "BAY 11-7082 ameliorates diabetic nephropathy by attenuating hyperglycemia-mediated oxidative stress and renal inflammation via NF-κB pathway," *Environmental Toxicology and Pharmacology*, vol. 39, no. 2, pp. 690–699, 2015.

Hindawi Publishing Corporation
BioMed Research International
Volume 2015, Article ID 562345, 10 pages
http://dx.doi.org/10.1155/2015/562345

Research Article

Antifatigue Activity of Liquid Cultured *Tricholoma matsutake* Mycelium Partially via Regulation of Antioxidant Pathway in Mouse

Quan Li,[1] Yanzhen Wang,[1,2] Guangsheng Cai,[1] Fange Kong,[1] Xiaohan Wang,[1] Yang Liu,[1] Chuanbin Yang,[3] Di Wang,[1] and Lirong Teng[1,2]

[1]*School of Life Sciences, Jilin University, Changchun 130012, China*
[2]*Zhuhai College of Jilin University, Jilin University, Guangzhou 519041, China*
[3]*School of Chinese Medicine, Hong Kong Baptist University, Kowloon, Hong Kong*

Correspondence should be addressed to Di Wang; jluwangdi@gmail.com and Lirong Teng; tenglirong@jlu.edu.cn

Received 16 October 2015; Accepted 3 November 2015

Academic Editor: Oreste Gualillo

Tricholoma matsutake has been popular as food and biopharmaceutical materials in Asian countries for its various pharmacological activities. The present study aims to analyze the antifatigue effects on enhancing exercise performance of *Tricholoma matsutake* fruit body (ABM) and liquid cultured mycelia (TM) in mouse model. Two-week *Tricholoma matsutake* treatment significantly enhances the exercise performance in weight-loaded swimming, rotating rod, and forced running test. In TM- and ABM-treated mice, some factors were observed at 60 min after swimming compared with nontreated mice, such as the increased levels of adenosine triphosphate (ATP), antioxidative enzymes, and glycogen and the reduced levels of malondialdehyde and reactive oxygen species in muscle, liver, and/or serum. Further data obtained from western blot show that CM and ABM have strongly enhanced the activation of 5′-AMP-activated protein kinase (AMPK), and the expressions of peroxisome proliferator have activated receptor γ coactivator-1α (PGC-1α) and phosphofructokinase-1 (PFK-1) in liver. Our data suggest that both *Tricholoma matsutake* fruit body and liquid cultured mycelia possess antifatigue effects related to AMPK-linked antioxidative pathway. The information uncovered in our study may serve as a valuable resource for further identification and provide experimental evidence for clinical trials of *Tricholoma matsutake* as an effective agent against fatigue related diseases.

1. Introduction

Regular exercise has been confirmed to protect and alleviate various diseases; however, strenuous sports are responsible for the accumulation of reactive oxygen and lipid peroxides, which damage organ tissues and further lead to fatigue [1, 2]. Fatigue, caused by intense pressure from physical and mental work [3], affects more than 20% of people worldwide. Sleep disturbance, muscle pain, headache, and impaired concentration always appear in patients suffering from chronic fatigue. Repairing the damage occurring in organs and prompting elimination of metabolites accumulation during exercise are required for its recovery. In molecular level, the activation of 5′-AMP-activated protein kinase (AMPK) inhibits the overproduction of reactive oxygen species (ROS) [4] and suppresses anabolic ATP-consuming [5]. On the other hand, enzymatic and nonenzymatic antioxidants protect tissues from exercise-induced oxidative damage [6] and further reduce metabolite production and physical fatigue [7]. Intense exercise causes an imbalance between the body's oxidation and antioxidation systems; thus overproducing reactive oxide species (ROS) and malondialdehyde (MDA) is responsible for fatigue symptoms [8, 9]. The enhanced activities of superoxide dismutase (SOD) and glutathione peroxidase (GSH-Px) are observed combining with the antifatigue process [10].

Fatigue is becoming a serious public health problem, and what is worse current therapeutic regimen is far away from meeting the needs of patients. Since nutrient supplementation positively enhances exercise capacity, researches

attempt to seek antifatigue herbs to accelerate eliminating fatigue in human beings [11]. *Herba Rhodiolae*, commonly used for hypoxia cure by the Tibetan people [12], also enhances physical ability [13]. *Astragalus membranaceus* has been confirmed to improve exercise performance and reduce exercise-caused accumulation of the byproducts in blood [14]. *Cordyceps sinensis* improves animal exercise endurance via regulating glycogen breakdown and fatty acid oxidation which are accommodated by AMPK phosphorylation [15].

Tricholoma matsutake, which is an ectomycorrhizal symbiotic mushroom, has been popular as food and biopharmaceutical materials in Asian countries [16]. The immunomodulatory activities and anticancer effects of *Tricholoma matsutake* have been well established worldwide [17]. Various polysaccharides have been reported, which are separated from *Tricholoma matsutake* fruit body with antioxidant activity [18], antitumor effect [19], and immune regulation property [20]. However, wild fruiting body resources are scarce, and to cultivate the fruit bodies via artificial culture medium is limited. Submerged fermentation has been verified as an efficient way to produce mycelia and bioactive metabolites for fungus in amount of research groups [21, 22]. In our research group, submerged fermentation has been successfully applied to obtain mycelia of *Paecilomyces tenuipes* [23], *Marasmius androsaceus*, and *Irpex lacteus* [24]. One study shows that beta-glucan separated from liquid cultured mycelia of *Tricholoma matsutake* exerts immunostimulating activities via multiple signaling pathways linked to neural factor-kappa B activation [25].

To our knowledge, the antifatigue activities of both *Tricholoma matsutake* fruit body and liquid cultured mycelia have not been reported yet. Our present study aims to investigate the related biological activates of *Tricholoma matsutake* via mouse model. Antioxidant enzyme activities in serum and organs and AMPK activation in liver were assayed in order to further analyze its underlying mechanism.

2. Materials and Methods

2.1. Tricholoma matsutake Preparation. *Tricholoma matsutake* (CGMCC5.793) was cultured in a hundred-liter full-automatic fermentor (BaoXing Bioscience company, Shanghai, China) by using a defined liquid medium containing: 20 g/L sucrose, 10 g/L peptone, 10 g/L yeast extract powder, 0.5 g/L $MgSO_4 \cdot 7H_2O$, 0.5 g/L $KH_2PO_4 \cdot 3H_2O$, and 0.2 g/L Vitamin B1. The fermentation conditions were as follows: loading volume was 70 L/100 L, initial pH was 6.5, rotate speed was 150 rpm, ventilation volume was 200 L/h, culture temperature was 26°C, inoculum age was 3 days, and inoculum size was 5%. The collected *Tricholoma matsutake* mycelium (TM) was freeze-dried, and it was given directly to experimental mice. All the chemical reagents used in the submerged fermentation were obtained from Sigma-Aldrich, USA.

2.2. Antifatigue Capacity Analysis in Mouse. The experimental animal protocol used in the study was approved by Institution of Animal Ethics Committee in Jilin University. Kunming (KM) mice (6 weeks, 18–22 g; $n = 20$/group; equal numbers of males and females; purchased from Norman Bethune University of Medical Science, Jilin University, Jilin, China) (SCXK(JI)-2011-0003) were put on a 12 h light/dark cycle (lights on 07:00–19:00) at 23 ± 1°C with water and food available ad libitum. After one-week adaptation, the experimental mice were divided into five groups randomly and orally treated with physiological saline (control group), 0.4 g/kg of *Tricholoma matsutake* body fruit micropowder (purchased from Japan) (ABM), and TM powder at doses of 0.3 g/kg, 1.0 g/kg, and 2.0 g/kg once a day for two weeks continuously. After two hours since the last administration, following experiments were performed.

2.2.1. Weight-Loaded Swimming Test. Experimental mice were loaded with lead wire of 15% bodyweight and forced to swim in water of 22 ± 1°C temperature and 30 cm depth. The time from the beginning to the point at which mice failed to return to the water surface within 15 s was recorded as exhaustion time.

2.2.2. Rotating Rod Test. Three independent trainings on turning device at a speed of 15 rpm for 1 min were applied before format detection. During the rotating rod test, the total duration of experimental mice on turning device at 20 rpm was recorded.

2.2.3. Forced Running Test. Three independent trainings on a treadmill at a set speed of 15 rpm for 1 min were performed to all the mice. After practices, animals were put on the treadmill with a set speed of 20 rpm, and the total running time was recorded to evaluate their performance before exhaustion, which was identified as five-time consecutive shocks by the electrode.

2.3. Measurement of Physiological Indices Related to Fatigue. Kunming mice (6 weeks, 18–22 g; $n = 20$/group; equal numbers of males and females) were orally treated with physiological saline, 0.4 g/kg of *Tricholoma matsutake* body fruit powder, and TM powder at doses of 0.3 g/kg, 1.0 g/kg, and 2.0 g/kg once a day for two weeks continuously. After four hours since the last administration, blood samples were collected from caudal vein in all mice. The serum levels of ATP, MDA, SOD, and GSH-Px were determined according to the procedures provided by assay kits.

After 24-hour rest, the experimental mice were forced to swim in water with 22 ± 1°C temperature and 30 cm depth for 60 min. Blood samples were collected from caudal vein after 10 min recess. Further, liver and muscle of sacrificed mice were dissected, and they were homogenized in double distilled water after wash three times in ice-cold physiological saline solution. The levels of ATP, SOD, GSH-Px, ROS, and MDA in liver, muscle, and/or serum were detected. The concentration of glycogen in both muscle and liver was measured. All the assay kits were purchased from Nanjing Biotechnology Co. Ltd., Nanjing, China.

Table 1: The effects of *Tricholoma matsutake* on fatigue and oxidant related factors in serum of mice before swimming.

	Female					Male				
	CTRL	TM (g/kg)			ABM (g/kg)	CTRL	TM (g/kg)			ABM (g/kg)
		0.3	1	2	0.4		0.3	1	2	0.4
ATP (nmol/mL)	2.5 ± 0.1	2.6 ± 0.1	3.1 ± 0.1	2.9 ± 0.1	2.7 ± 0.1	2.6 ± 0.1	2.7 ± 0.1	2.9 ± 0.1	2.8 ± 0.1	2.7 ± 0.1
MDA (nmol/mL)	11.4 ± 0.4	11.2 ± 0.4	10.8 ± 0.3	11.3 ± 0.3	11.3 ± 0.3	12.7 ± 0.4	12.1 ± 0.8	11.7 ± 0.6	11.9 ± 0.3	12.3 ± 0.3
SOD (U/mL)	90.4 ± 5.3	93.0 ± 3.1	101.1 ± 3.3	99.6 ± 3.1	99.7 ± 4.8	93.2 ± 4.4	96.2 ± 3.3	93.4 ± 3.1	100.4 ± 2.5	97.8 ± 5.1
GSH-Px (μmol/mL)	156.7 ± 10.6	172.1 ± 8.3	171.0 ± 10.1	176.2 ± 10.0	174.1 ± 9.4	159.0 ± 16.7	167.6 ± 10.2	168.9 ± 12.3	169.7 ± 7.6	171.5 ± 14.4

Values were expressed as mean ± SEM ($n = 10$).

2.4. Western Blot Analysis. A part of liver tissue of each experimental mouse was homogenized in eight volumes of radioimmunoprecipitation assay (RIPA) buffer (Sigma-Aldrich, USA) which contains 1 mM Phenylmethanesulfonyl fluoride (PMSF) and 1x protease inhibitor cocktail (Sigma-Aldrich, USA). The protein concentration was detected by Bradford method, and 30 μg of sample was separated by 10% SDS-PAGE and then transferred onto a nitrocellulose membrane (0.45 μm, Bio Basic, Inc.) with the Mini-Protean two-gel electrophoresis system (Bio-Rad, USA). The blocked membranes with target strips were incubated with primary antibodies at 4°C overnight at dilution of 1 : 1000 as follows: phosphor-AMPK (P-AMPK), total-AMPK (T-AMPK), peroxisome proliferator activated receptor γ coactivator-1α (PGC-1α), phosphofructokinase-1 (PFK-1), and glyceraldehyde-3-phosphate dehydrogenase (GAPDH) (Cell Signaling Technology, Beverly, MA), followed by blotting with horseradish peroxidase-conjugated secondary antibodies diluted 1 : 2000 (Santa Cruz, USA). After visualizing with ECL detection system (GE Healthcare, UK), the intensity of target bands were quantified by using ImageJ.

2.5. Statistical Analysis. All data were expressed as mean ± SEM. A one-way analysis of variance (ANOVA) was used to detect statistical significance followed by post hoc multiple comparisons (Dunn's test) by using SPSS 16.0 software (IBM corporation, Armonk, USA). A P value < 0.05 was considered to be statistically significant.

3. Results

3.1. The Enhancing Exercise Endurance Ability of Tricholoma matsutake. Behavior tests are commonly applied to evaluate the antifatigue performance of drugs [26, 27]; therefore, weight-loaded swimming, rotating rod, and forced running test were taken in the present experiment. Compared to nontreated mice, both TM and ABM have significantly enhanced the exercise endurance indicated by the longer movement duration in all three behavior tests ($P < 0.05$, Figure 1). 2.0 g/kg of TM administration improved nearly twofold of residence time of both female and male mice in all tests ($P < 0.01$, Figure 1). It seems that TM possesses more sensitive effects on athletic ability of female mice.

3.2. The Regulation Effects of Tricholoma matsutake on ATP and Glycogen. Compared to nontreated mice, no significant changes of serum levels of ATP were observed after 14-day TM and ABM administration (Table 1).

ATP, as a direct energy source for normal physiological activity, shortage leads to a variety of physiological dysfunction [28]. Compared with nontreated mice, and similar to ABM, TM dose-dependently enhanced ATP concentration in serum, muscle, and liver after 60 min of swimming, and up to 30% enhancement was noted in both male and female mice ($P < 0.01$, Figure 2).

Glycogen is the primary intracellular storable form of glucose, and its level in liver and skeletal muscles directly reflects fatigue symptoms [29]. After 60 min exercise, compared with nontreated mice, two-week TM treatment at a dose of 2.0 mg/kg has enhanced 35.6% and 28.5% muscle glycogen levels in male and female mice, respectively ($P < 0.05$, Figure 3(a)). In liver tissue, TM has increased to 48.1% and 52.5% glycogen levels in female and male mice, respectively ($P < 0.05$, Figure 3(b)). The similar improvement activities on glycogen concentration in both muscle and liver were also observed in ABM-treated mice ($P < 0.05$, Figure 3).

3.3. The Antioxidant Effects of Tricholoma matsutake. Antioxidant enzymes, such as SOD and GSH-Px, are responsible for cell damage and muscle fatigue. MDA is one of the end products resulting from degradation of cell membrane by radicals [30]. Before swimming, no significant changes on levels of SOD, GSH-Px, and MDA in serum, muscle, and liver were observed in both TM- and ABM-treated mice (Table 1).

Compared to nontreated group, in both female and male mice, TM significantly enhanced the activities of SOD and GSH-Px and reduced the levels of MDA in serum, muscle, and liver after 60 min swimming ($P < 0.05$, Table 2). Similarly, ABM displayed positive regulatory effects on levels of SOD, GSH-Px, and MDA in serum muscle and liver of exercised male or female mice ($P < 0.05$, Table 2). The reduced ROS levels of muscle and liver were observed in

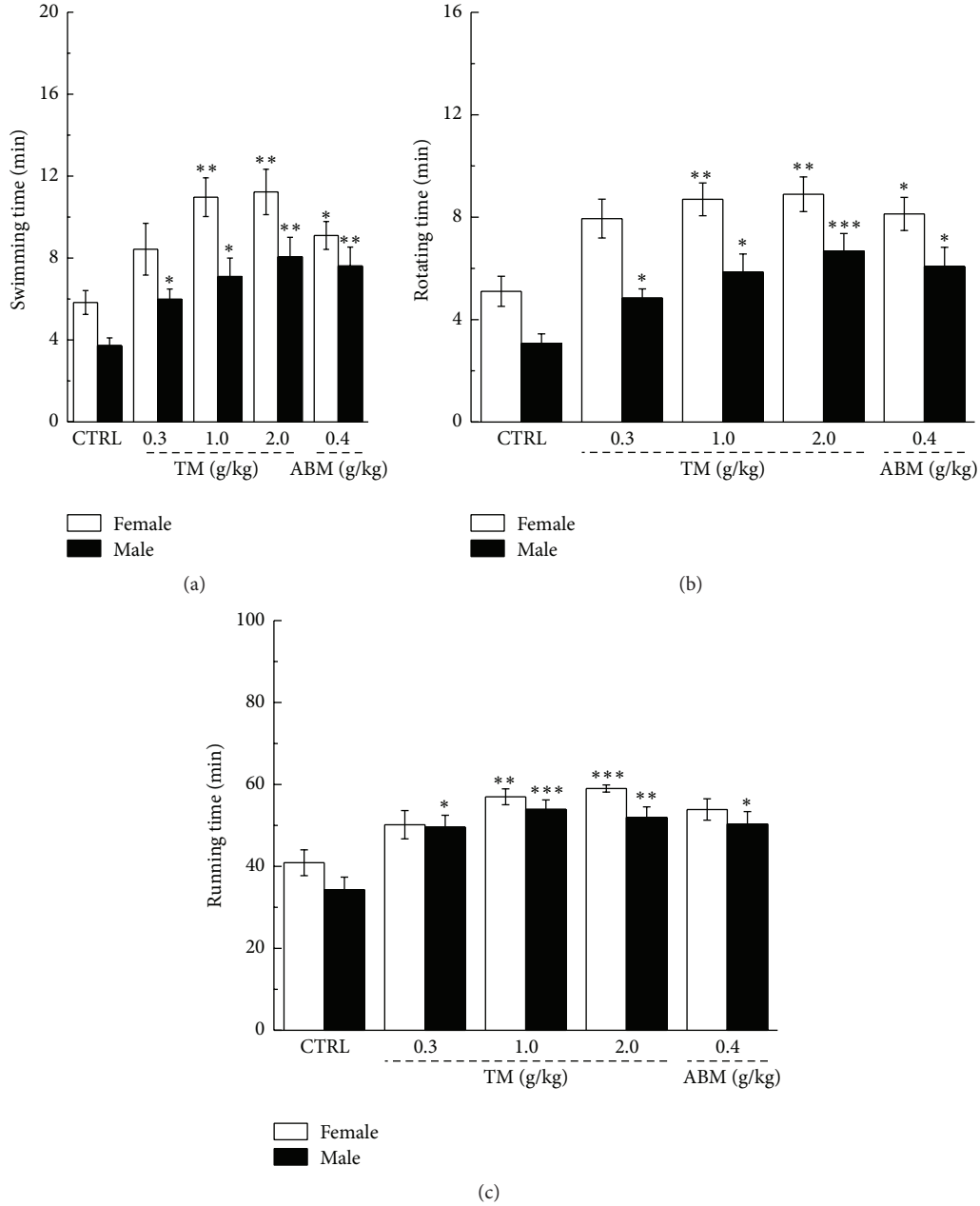

Figure 1: Weight-loaded swimming test (a), rotating rod test (b), and forced running test (c) were performed to verify the antifatigue effects of *Tricholoma matsutake* in mouse model. Data were expressed as mean ± SEM ($n = 10$) and analyzed by using a one-way ANOVA followed by Dunn's test. $^{*}P < 0.05$, $^{**}P < 0.01$, and $^{***}P < 0.001$ versus control group.

TM- and ABM-treated mice after 60 min excise ($P < 0.05$, Table 2).

3.4. The Regulation Effects of Tricholoma matsutake on Protein Expression in Liver. The expressions of P-AMPK, T-AMPK, PFK-1, and PGC-1α were detected to further analyze the preliminary molecular mechanisms under TM-mediated antifatigue effects. After 60 min swimming, over twofold enhancement of P-AMPK expression was observed in liver tissue of TM- or ABM-treated mice ($P < 0.001$, Figure 4). Furthermore, TM dose-dependently enhanced the expressions of PFK-1 and PGC-1α in the liver of exercised mice, and the similar results were noted in ABM-treated group ($P < 0.05$, Figure 4).

4. Discussion

Herbs have become a valuable reservoir for antifatigue agents selection [31]. In our group, the polysaccharides-enriched *Cordyceps militaris* extract exhibiting exercise enhancement

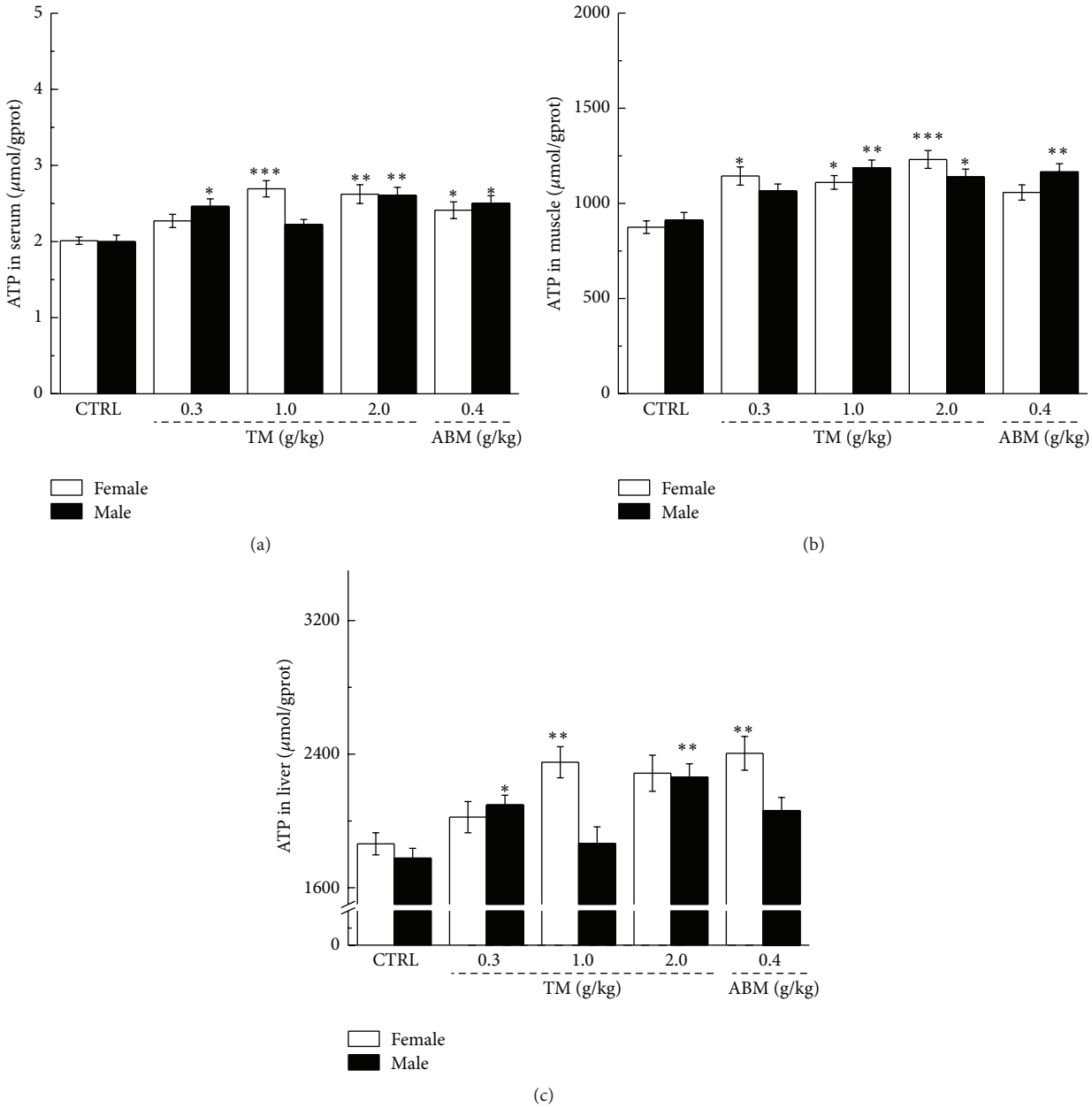

Figure 2: At the end of two-week administration, the levels of ATP in serum (a), muscle (b), and liver (c) in male and female mice were analyzed after 60 min of swimming. Data were expressed as mean ± SEM ($n = 10$) and analyzed by using a one-way ANOVA. $^{*}P < 0.05$, $^{**}P < 0.01$, and $^{***}P < 0.001$ versus control group.

activity has been successfully demonstrated via modulation AMPK-linked pathway [32]. The present study aims to investigate the antifatigue effects of *Tricholoma matsutake* liquid cultured mycelia and fruit body in mouse model. The enhanced exercise endurance of TM- and ABM-treated mice in weigh-loaded swimming, forced running, and rotating rod test revealed the antifatigue activities of *Tricholoma matsutake*. The enhanced levels of ATP and glycogen in serum, muscle, and/or liver of treated mice have contributed to TM-mediate fatigue recovery. ATP, known as a rapid energy source, can be influenced by levels of muscle $[H^{+}]$ and myofibrillar ATPase during exercise [33]. However, the half-life of ATP is <1 second, and it makes glycogen become an indirect energy source for ATP synthesis. Long-term endurance exercise, which is related to muscle mitochondria dysfunction, results in a reduction of muscle glycogen depletion [34]. The regulatory effect of PGC-1α on mitochondrial biogenesis has been well reported, and exercises have influenced the expression of PGC-1α [35]. PGC-1α is involved in exercise-induced downregulation of the expression of glycogenolytic and glycolytic enzymes [34]. Another study reports that fatigue and exhaustion are viewed as a multicomponent biochemical process related to PFK-1 linked glycolytic pathway [36]. Although the enhanced

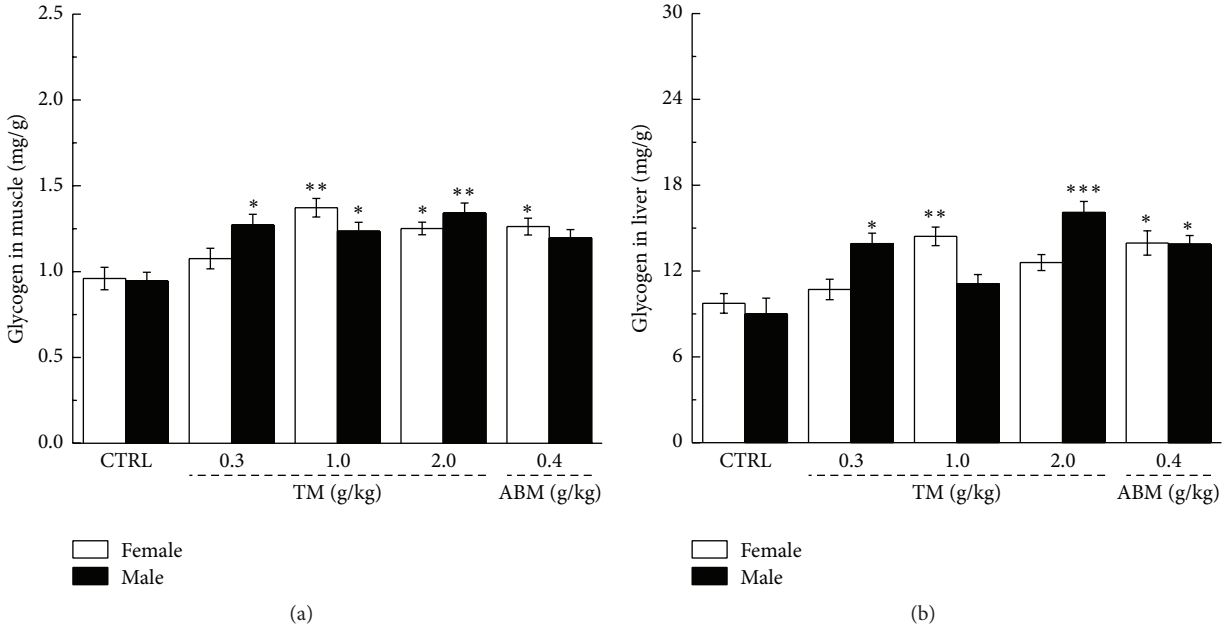

Figure 3: Two-week *Tricholoma matsutake* and ABM administration strikingly enhanced the levels of glycogen in both muscle (a) and liver (b) of exercise fatigue mouse. Data were expressed as mean ± SEM ($n = 10$) and analyzed by using a one-way ANOVA followed by Dunn's test. $^{*}P < 0.05$, $^{**}P < 0.01$, and $^{***}P < 0.001$ versus control group.

expression of both PGC-1α and PFK-1 were observed in the liver of TM- and ABM-treated mice after 60 min exercise, it is hard to conclude that they are involved in the antifatigue effects. Based on our data, the enhanced ATP and glycogen levels in serum and organs by TM and ABM contribute to improve exercise endurance.

The regulatory effects on ROS, MDA, SOD, and GSH-Px in organs and/or serum of TM and ABM in mice after 60 min exercise indicated the important role of oxidative system in preventing exercise-induced fatigue. The accumulation of oxygen free radicals is one of the risk factors which are responsible for oxidative stress and muscle fatigue [37], and they can be cleared by antioxidant enzymes. Antioxidants can successfully prevent or reduce oxidative stress and further improve exercise performance [38]. Proteins, separated from *Panax quinquefolium*, improve behavioural alterations linked to chronic fatigue via inhibition oxidative damage [10]. Meanwhile, *Cordyceps militaris* displays antifatigue property via scavenging ROS and enhancing activities of SOD and GSH-Px [32]. MDA is recognized as the end product of lipid peroxidation, which can be used to assess the degree of the lipid peroxidation for free radical [39]. SOD prevents lipid peroxidation via catalyzing the conversion of superoxide into hydrogen peroxide and oxygen [37]. GSH forms a formidable defense with glutathione peroxidase to prevent lipid peroxides [40]. All these work together to prevent lipid peroxidation and further protect cells from oxidative injury via suppressing hyperlevel of MDA and ROS and enhancing SOD and GSH-Px activities, which are involved in TM- and ABM-mediated antifatigue effect on enhancing exercise endurance.

AMPK serves as the key factor on regulation of glucose and lipid metabolism [41] and helps to maintain the levels of ATP in various conditions [41]. The activated AMPK via falling cellular energy status enhanced ATP generation, whilst inhibiting ATP consumption [42]. AICAR, an AMPK agonist, significantly enhanced running endurance in animals [43]. On the other hand, except for the fatigue situation, during oxidative stress, the activated AMPK successfully promoted cell survival by inhibiting free radical accumulation [44]. Liraglutide reduced oxidative stress by the alteration of AMPK/SREBP1 pathway in Raw264.7 cells [45]. AMPK contributed to the antioxidant activity via regulating the levels of SOD and GSH [46, 47]. Both TM and ABM improved the activities of AMPK by enhancing the expression of its phosphorylated form in liver of 60 min exercised mice. Collectively, the antifatigue effects of *Tricholoma matsutake* may be related to the alteration of AMPK-linked antioxidant pathway.

Although the regulatory effects of TM and ABM on male and female mice were monitored during the experiments, we failed to conclude the different performances on animals of different genders. In the separated experiment, we found that the modulation of sex hormones contribute to the sex differences in response to *Cordyceps militaris*-mediated antifatigue property [32]. Our further study will focus on the regulatory effects of *Tricholoma matsutake* on sex hormones and the relationship between them and antifatigue activities.

In conclusion, our data indicate that TM and ABM elevate the endurance capacity at least in part via activating AMPK-linked antioxidant pathway, which provides experimental

Table 2: The antioxidant effects of *Tricholoma matsutake* in exercise fatigue mice.

	Female					Male				
	CTRL	TM (g/kg) 0.3	TM (g/kg) 1	TM (g/kg) 2	ABM (g/kg) 0.4	CTRL	TM (g/kg) 0.3	TM (g/kg) 1	TM (g/kg) 2	ABM (g/kg) 0.4
Serum										
MDA (nmol/mL)	15.5 ± 0.4	14.3 ± 0.7	13.9 ± 0.3*	13.4 ± 0.4**	13.7 ± 0.4*	17.2 ± 0.5	14.2 ± 0.5*	14.8 ± 0.5*	14.7 ± 0.4**	14.7 ± 0.4**
SOD (U/mL)	105.8 ± 4.0	120.7 ± 2.1*	133.2 ± 6.5**	139.2 ± 5.5	141.4 ± 5.9**	106.7 ± 3.0	118.9 ± 4.9	141.3 ± 3.5**	136.1 ± 3.2**	137.8 ± 3.3***
GSH-Px (μmol/mL)	357.9 ± 8.4	390.3 ± 4.8*	427.5 ± 10.4***	418.1 ± 15.9*	404.5 ± 8.3**	340.1 ± 11.8	417.2 ± 12.5**	397.2 ± 12.1*	415.1 ± 14.3**	401.3 ± 9.1**
Muscle										
MDA (nmol/mgprot)	63.1 ± 4.1	51.04 ± 3.1	46.7 ± 2.1*	41.3 ± 3.4**	48.7 ± 3.4	65.3 ± 2.4	53.1 ± 2.9	49.5 ± 3.5*	44.6 ± 3.9**	50.8 ± 3.2*
SOD (U/mgprot)	87.7 ± 3.1	106.9 ± 5.4	111.5 ± 5.7*	130.9 ± 4.4***	114.1 ± 5.1**	86.6 ± 4.5	104.5 ± 6.8	111.5 ± 5.3*	127.8 ± 6.0***	114.1 ± 4.6**
GSH-Px (μmol/gprot)	369.2 ± 29.2	469.6 ± 48.2	559.8 ± 47.6	550.4 ± 38.8**	514.9 ± 32.1*	371.2 ± 27.8	499.5 ± 42.5	591.6 ± 45.9**	558.6 ± 46.7*	538.9 ± 42.5
ROS (FI/gprot)	15300.7 ± 516.3	14335.0 ± 386.2	12461.6 ± 378.2**	13037.7 ± 527.4*	14277.3 ± 548.6	14294.1 ± 401.6	13532.2 ± 591.9	14396.8 ± 464.7	12162.4 ± 689.7*	11669.1 ± 690.7*
Liver										
MDA (nmol/mgprot)	12.2 ± 0.7	9.8 ± 0.5	8.7 ± 0.4**	8.8 ± 0.5*	9.7 ± 0.6	11.8 ± 0.4	9.6 ± 0.7	9.3 ± 0.6	8.8 ± 0.7*	8.5 ± 0.7*
SOD (U/mgprot)	270.5 ± 17.8	369.8 ± 18.6*	387.5 ± 22.7*	303.9 ± 18.3	317.9 ± 17.6	240.9 ± 19.2	316.7 ± 16.5	365.4 ± 22.6**	296.5 ± 15.6	335.9 ± 17.4*
GSH-Px (μmol/gprot)	1013.5 ± 50.9	1244.7 ± 67.5	1264.0 ± 99.3	1361.5 ± 60.4**	1371.9 ± 74.1*	929.2 ± 32.1	1169.0 ± 55.1*	1098.0 ± 44.4	1365.9 ± 91.8**	1100.8 ± 77.9
ROS (FI/gprot)	1516.2 ± 53.9	1494.2 ± 33.6	1209.1 ± 55.3**	1356.8 ± 46.9	1360.7 ± 30.1	1606.6 ± 75.9	1446.9 ± 46.8	1360.7 ± 62.6	1278.4 ± 51.4*	1286.3 ± 52.7*

After 60 min swimming, the oxidative stress factors in serum, muscle, and liver of all experimental mice were detected. Data were expressed as mean ± SEM ($n = 10$). $^{*}P < 0.05$, $^{**}P < 0.01$, and $^{***}P < 0.001$ versus control group.

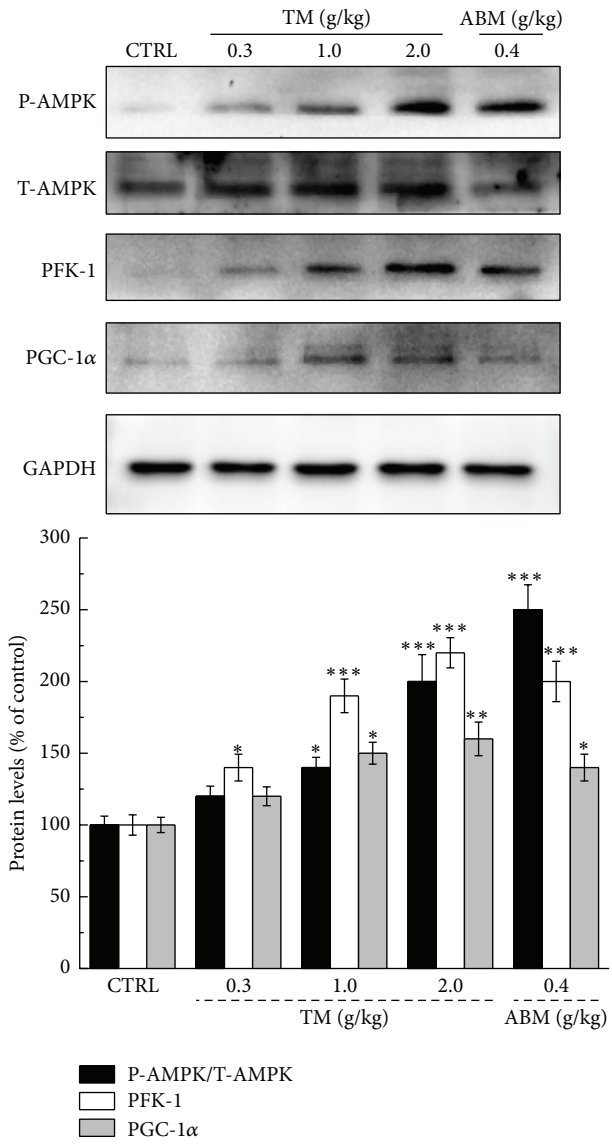

Figure 4: At the end of two-week *Tricholoma matsutake* and ABM administration, a 60 min swimming was performed. After exercise, the levels of P-AMPK, PFK-1, and PGC-1α in liver tissue were detected by western blot. The intensity of target bands was quantified by using ImageJ. Quantification data of P-AMPK, PFK-1, and PGC-1α were normalized by T-AMPK and GAPDH and expressed as a percent of that from corresponding control mice. Data are expressed as mean ± SEM ($n = 4$). $^{*}P < 0.05$, $^{**}P < 0.01$, and $^{***}P < 0.001$ versus control group.

evidence in supporting the clinical use of *Tricholoma matsutake* as an effective agent against fatigue related diseases.

Conflict of Interests

The authors have declared that there is no conflict of interests.

Authors' Contribution

Quan Li and Yanzhen Wang equally contributed to this project.

Acknowledgments

This work was supported by the Natural Science Foundation of China (Grant no. 81402955) and Science and Technology Key Project in Jilin Province of China (Grant no. 20130201006ZY and 20150203002NY).

References

[1] C. K. Roberts and R. J. Barnard, "Effects of exercise and diet on chronic disease," *Journal of Applied Physiology*, vol. 98, no. 1, pp. 3–30, 2005.

[2] R. R. Jenkins, "Exercise, oxidative stress, and antioxidants: a review," *International Journal of Sport Nutrition*, vol. 3, no. 4, pp. 356–375, 1993.

[3] M. Tanaka, Y. Baba, Y. Kataoka et al., "Effects of (−)-epigallocatechin gallate in liver of an animal model of combined (physical and mental) fatigue," *Nutrition*, vol. 24, no. 6, pp. 599–603, 2008.

[4] S. M. Shin and S. G. Kim, "Inhibition of arachidonic acid and iron-induced mitochondrial dysfunction and apoptosis by oltipraz and novel 1,2-dithiole-3-thione congeners," *Molecular Pharmacology*, vol. 75, no. 1, pp. 242–253, 2009.

[5] D. G. Hardie and M. L. J. Ashford, "AMPK: Regulating energy balance at the cellular and whole body levels," *Physiology*, vol. 29, no. 2, pp. 99–107, 2014.

[6] M. Dékány, V. Nemeskéri, I. Györe, I. Harbula, J. Malomsoki, and J. Pucsok, "Antioxidant status of interval-trained athletes in various sports," *International Journal of Sports Medicine*, vol. 27, no. 2, pp. 112–116, 2006.

[7] G. C. Bogdanis, P. Stavrinou, I. G. Fatouros et al., "Short-term high-intensity interval exercise training attenuates oxidative stress responses and improves antioxidant status in healthy humans," *Food and Chemical Toxicology*, vol. 61, pp. 171–177, 2013.

[8] K. P. Skenderi, M. Tsironi, C. Lazaropoulou et al., "Changes in free radical generation and antioxidant capacity during ultra-marathon foot race," *European Journal of Clinical Investigation*, vol. 38, no. 3, pp. 159–165, 2008.

[9] C. Y. Wu, R. Chen, X. S. Wang, B. Shen, W. Yue, and Q. Wu, "Antioxidant and anti-fatigue activities of phenolic extract from the seed coat of *Euryale ferox* Salisb. and identification of three phenolic compounds by LC-ESI-MS/MS," *Molecules*, vol. 18, no. 9, pp. 11003–11021, 2013.

[10] B. Qi, L. Liu, H. Zhang et al., "Anti-fatigue effects of proteins isolated from *Panax quinquefolium*," *Journal of Ethnopharmacology*, vol. 153, no. 2, pp. 430–434, 2014.

[11] C. Xu, J. Lv, Y. M. Lo, S. W. Cui, X. Hu, and M. Fan, "Effects of oat β-glucan on endurance exercise and its anti-fatigue properties in trained rats," *Carbohydrate Polymers*, vol. 92, no. 2, pp. 1159–1165, 2013.

[12] X. Liu, W. Zhu, S. Guan et al., "Metabolomic analysis of anti-hypoxia and anti-anxiety effects of Fu Fang Jin Jing Oral Liquid," *PLoS ONE*, vol. 8, no. 10, Article ID e78281, 2013.

[13] A. Panossian and H. Wagner, "Stimulating effect of adaptogens: an overview with particular reference to their efficacy following single dose administration," *Phytotherapy Research*, vol. 19, no. 10, pp. 819–838, 2005.

[14] T.-S. Yeh, H.-L. Chuang, W.-C. Huang, Y.-M. Chen, C.-C. Huang, and M.-C. Hsu, "*Astragalus membranaceus* improves exercise performance and ameliorates exercise-induced fatigue in trained mice," *Molecules*, vol. 19, no. 3, pp. 2793–2807, 2014.

[15] R. Kumar, P. S. Negi, B. Singh, G. Ilavazhagan, K. Bhargava, and N. K. Sethy, "Cordyceps sinensis promotes exercise endurance capacity of rats by activating skeletal muscle metabolic regulators," *Journal of Ethnopharmacology*, vol. 136, no. 1, pp. 260–266, 2011.

[16] H. Tong, X. Liu, D. Tian, and X. Sun, "Purification, chemical characterization and radical scavenging activities of alkali-extracted polysaccharide fractions isolated from the fruit bodies of *Tricholoma matsutake*," *World Journal of Microbiology & Biotechnology*, vol. 29, no. 5, pp. 775–780, 2013.

[17] A. T. Borchers, A. Krishnamurthy, C. L. Keen, F. J. Meyers, and M. E. Gershwin, "The immunobiology of mushrooms," *Experimental Biology and Medicine*, vol. 233, no. 3, pp. 259–276, 2008.

[18] X. Ding, J. Tang, M. Cao et al., "Structure elucidation and antioxidant activity of a novel polysaccharide isolated from *Tricholoma matsutake*," *International Journal of Biological Macromolecules*, vol. 47, no. 2, pp. 271–275, 2010.

[19] L. You, Q. Gao, M. Feng et al., "Structural characterisation of polysaccharides from *Tricholoma matsutake* and their antioxidant and antitumour activities," *Food Chemistry*, vol. 138, no. 4, pp. 2242–2249, 2013.

[20] H. Hoshi, H. Iijima, Y. Ishihara, T. Yasuhara, and K. Matsunaga, "Absorption and tissue distribution of an immunomodulatory α-D-glucan after oral administration of *Tricholoma matsutake*," *Journal of Agricultural and Food Chemistry*, vol. 56, no. 17, pp. 7715–7720, 2008.

[21] T. Saha, S. Sasmal, S. Alam, and N. Das, "Tamarind kernel powder: a novel agro-residue for the production of cellobiose dehydrogenase under submerged fermentation by *Termitomyces clypeatus*," *Journal of Agricultural and Food Chemistry*, vol. 62, no. 15, pp. 3438–3445, 2014.

[22] Z. Zhou, Z. Yin, and X. Hu, "Corncob hydrolysate, an efficient substrate for *Monascus* pigment production through submerged fermentation," *Biotechnology and Applied Biochemistry*, vol. 61, no. 6, pp. 716–723, 2014.

[23] L. Du, J. Song, H. Wang et al., "Optimization of the fermentation medium for *Paecilomyces tenuipes* N45 using statistical approach," *African Journal of Microbiology Research*, vol. 6, no. 32, pp. 6130–6141, 2012.

[24] Z. Na, L. Quan, W. Juan et al., "Application of near infrared spectroscopy in quality control of Irpex lacteus," *Journal of Food, Agriculture ' Environment*, vol. 12, no. 2, pp. 1213–1219, 2014.

[25] J. Y. Kim, S. E. Byeon, Y. G. Lee et al., "Immunostimulatory activities of polysaccharides from liquid culture of pine-mushroom *Tricholoma matsutake*," *Journal of Microbiology and Biotechnology*, vol. 18, no. 1, pp. 95–103, 2008.

[26] D. Z. Kang, H. D. Hong, K. I. Kim, and S. Y. Choi, "Anti-fatigue effects of fermented *Rhodiola rosea* extract in mice," *Preventive Nutrition and Food Science*, vol. 20, no. 1, pp. 38–42, 2015.

[27] J. A. Mercer, B. T. Bates, J. S. Dufek, and A. Hreljac, "Characteristics of shock attenuation during fatigued running," *Journal of Sports Sciences*, vol. 21, no. 11, pp. 911–919, 2003.

[28] S.-J. Tan, N. Li, F. Zhou et al., "Ginsenoside Rb1 improves energy metabolism in the skeletal muscle of an animal model of postoperative fatigue syndrome," *Journal of Surgical Research*, vol. 191, no. 2, pp. 344–349, 2014.

[29] L. D. Gershen, B. E. Prayson, and R. A. Prayson, "Pathological characteristics of glycogen storage disease III in skeletal muscle," *Journal of Clinical Neuroscience*, vol. 22, no. 10, pp. 1674–1675, 2015.

[30] I. Nallamuthu, A. Tamatam, and F. Khanum, "Effect of hydroalcoholic extract of *Aegle marmelos* fruit on radical scavenging activity and exercise-endurance capacity in mice," *Pharmaceutical Biology*, vol. 52, no. 5, pp. 551–559, 2014.

[31] C. T. Horng, J. K. Huang, H. Y. Wang, C. C. Huang, and F. A. Chen, "Antioxidant and antifatigue activities of polygonatum alte-lobatum hayata rhizomes in rats," *Nutrients*, vol. 6, no. 11, pp. 5327–5337, 2014.

[32] Y. Dong, S. Hu, C. Liu et al., "Purification of polysaccharides from *Cordyceps militaris* and their antihypoxic effect," *Molecular Medicine Reports*, vol. 11, no. 2, pp. 1312–1317, 2015.

[33] L. Zhang and N. Wan, "Advances in the research of sport fatigue caused by the action of free radical lipid oxidation," *Chinese Journal of Laboratory Diagnosis*, vol. 10, pp. 1104–1108, 2006.

[34] S. H. Kim, J. H. Koh, K. Higashida, S. R. Jung, J. O. Holloszy, and D.-H. Han, "PGC-1α mediates a rapid, exercise-induced downregulation of glycogenolysis in rat skeletal muscle," *Journal of Physiology*, vol. 593, no. 3, pp. 635–643, 2015.

[35] K. Baar, A. R. Wende, T. E. Jones et al., "Adaptations of skeletal muscle to exercise: rapid increase in the transcriptional coactivator PGC-1," *The FASEB Journal*, vol. 16, no. 14, pp. 1879–1886, 2002.

[36] G. P. Dobson, W. S. Parkhouse, and P. W. Hochachka, "Regulation of anaerobic ATP-generating pathways in trout fast-twitch skeletal muscle," *American Journal of Physiology—Regulatory Integrative and Comparative Physiology*, vol. 253, no. 1, part 2, pp. R186–R194, 1987.

[37] A. Whaley-Connell, P. A. McCullough, and J. R. Sowers, "The role of oxidative stress in the metabolic syndrome," *Reviews in Cardiovascular Medicine*, vol. 12, no. 1, pp. 21–29, 2011.

[38] T.-T. Peternelj and J. S. Coombes, "Antioxidant supplementation during exercise training: beneficial or detrimental?" *Sports Medicine*, vol. 41, no. 12, pp. 1043–1069, 2011.

[39] M. H. El-Maghrabey, N. Kishikawa, K. Ohyama, and N. Kuroda, "Analytical method for lipoperoxidation relevant reactive aldehydes in human sera by high-performance liquid chromatography-fluorescence detection," *Analytical Biochemistry*, vol. 464, pp. 36–42, 2014.

[40] L. Sun, W. Shen, Z. Liu, S. Guan, J. Liu, and S. Ding, "Endurance exercise causes mitochondrial and oxidative stress in rat liver: effects of a combination of mitochondrial targeting nutrients," *Life Sciences*, vol. 86, no. 1-2, pp. 39–44, 2010.

[41] R. B. Ceddia, "The role of AMP-activated protein kinase in regulating white adipose tissue metabolism," *Molecular and Cellular Endocrinology*, vol. 366, no. 2, pp. 194–203, 2013.

[42] M. Ríos, M. Foretz, B. Viollet et al., "Lipoprotein internalisation induced by oncogenic AMPK activation is essential to maintain glioblastoma cell growth," *European Journal of Cancer*, vol. 50, no. 18, pp. 3187–3197, 2014.

[43] V. A. Narkar, M. Downes, R. T. Yu et al., "AMPK and PPARδ agonists are exercise mimetics," *Cell*, vol. 134, no. 3, pp. 405–415, 2008.

[44] M. G. Bonini and B. N. Gantner, "The multifaceted activities of AMPK in tumor progression—why the 'one size fits all' definition does not fit at all?" *IUBMB Life*, vol. 65, no. 11, pp. 889–896, 2013.

[45] Y.-G. Wang and T.-L. Yang, "Liraglutide reduces oxidized LDL-induced oxidative stress and fatty degeneration in Raw 264.7 cells involving the AMPK/SREBP1 pathway," *Journal of Geriatric Cardiology*, vol. 12, no. 4, pp. 410–416, 2015.

[46] H.-I. Lee, K. W. Yun, K.-I. Seo, M.-J. Kim, and M.-K. Lee, "Scopoletin prevents alcohol-induced hepatic lipid accumulation by modulating the AMPK-SREBP pathway in diet-induced obese mice," *Metabolism: Clinical and Experimental*, vol. 63, no. 4, pp. 593–601, 2014.

[47] Y. Zhao, Y. Sun, Y. Ding et al., "GL-V9, a new synthetic flavonoid derivative, ameliorates DSS-induced colitis against oxidative stress by up-regulating Trx-1 expression via activation of AMPK/FOXO3a pathway," *Oncotarget*, vol. 6, no. 28, pp. 26291–26307, 2015.